DOT/FAA/AR-xx/xx

Federal Aviation Administration
William J. Hughes Technical Center
Aviation Research Division
Atlantic City International Airport
New Jersey 08405

Annex A to Task A14: UAS Ground Collision Severity Evaluation 2017-2018

Date 24 May 2019

Final Report

This document is available to the U.S. public through the National Technical Information Services (NTIS), Springfield, Virginia 22161.

This document is also available from the Federal Aviation Administration William J. Hughes Technical Center at actlibrary.tc.faa.gov.

U.S. Department of Transportation
Federal Aviation Administration

NOTICE

TABLE OF CONTENTS

Page

LIST OF FIGURES

Figure **Page**

LIST OF TABLES

LIST OF ACRONYMS

3aω – Three linear accelerometers and three angular rate sensors placed in an orthogonal array, measuring both linear acceleration and angular velocity
6aω – Six linear accelerometers and three angular rate sensors attached to a tetrahedron fixture, used to measure linear acceleration, angular velocity, and used to algebraically calculate angular acceleration
AIS[1] – Abbreviated Injury Scale (1=Minor, 2=Moderate, 3=Serious, 4=Severe, 5=Critical, 6=Maximal)
6DOF - Six-Degree of Freedom
AGL – Above Ground Level
ARC – Advisory and Rulemaking Committee
ATD - Anthropomorphic Test Device
BC – Blunt Criterion
BrIC – Brain Injury Criterion
CG – Center of Gravity
COESA - 1976 Committee on Extension to the Standard Atmosphere
EKF - Extended Kalman Filter
ESC – Electronic Speed Controller, Electronic Supervisory Control
FAA – Federal Aviation Administration
FE – Finite Element
FEA – Finite Element Analysis
FEM – Finite Element Model
GPS - Global Positioning System
GSO – Ground Station Operator
HIC – Head Injury Criterion
IMU – Inertial Measurement Unit
JAA – Joint Aviation Authority
KE – Kinetic Energy
MRI – Magnetic Resonance Imaging
MSU – Mississippi State University
NAS - National Air Space
NI – National Instruments
NIAR - National Institute for Aviation Research
Nij – Neck Injury Criterion
OSU – The Ohio State University
PID - Proportional–Integral–Derivative Controller
PMHS – Post Mortem Human Surrogate, commonly referred to as a cadaver
PWM – Pulse Width Modulation, the type of digital signal used to control sUAS components
RPM – Revolutions Per Minute
RSESC – Rotorcraft Systems Engineering and Simulation Center
SC_D - Flat plate drag area
SFC – Skull Fracture Correlate

[1] Association for the Advancement of Automotive Medicine Website, [Website], URL: https://www.aaam.org/abbreviated-injury-scale-ais/ [cited 20 January, 2017]

SI – Gadd Severity Index
sUAS – Small Unmanned Aircraft System
THUMS - Total Human Model for Safety
TIM – Technical Interchange Meeting
UAH – University of Alabama in Huntsville
UAS – Unmanned Aircraft System
WGS84 - 1984 World Geodetic System
WSU – Wichita State University
VT – Virginia Tech

1. SCOPE

1.1. Research Tasks

The University of Alabama in Huntsville's (UAH) role in the Task A14 project was divided into the following primary tasks occurring over an 18-month period of performance:

1.1.1. Task A: Simplified Test Development and Analysis (UAH, NIAR)

Task A was to develop a clear and easily repeatable test method to determine the injury potential to a person impacted by a UAS under various conditions and scenarios. This task incorporated analysis of skull fracture, concussion, and neck injury probability and severity. UAH conducted failure flight testing and aerodynamic analysis of each vehicle used in both UAH and the National Institute for Aviation Research (NIAR) at Wichita State University's (WSU) impact testing as a means of developing high-speed test points that were representative of each aircraft impacting near terminal velocity. This task also included tests for the DJI S800 and DJI Inspire 2 that replicated impact of an aircraft descending under a parachute recovery system, both vertically and under high winds. The parachute impact test points were determined based on flight tests and modeling of the DJI Inspire 2 and S800 using the Vendor 2 parachute. Aerodynamic properties of the parachute system were analyzed and modeled based on known test conditions and then extended to estimate impact velocity and trajectory under winds up to 30 kt. For most aircraft common to both UAH and NIAR testing, UAH conducted vertical drop impact testing of the aircraft in multiple orientations as a means of determining the stiffest impact orientation. NIAR continued testing the aircraft at higher velocities and a range of impact trajectories and head impact locations using the stiffest or worst case impact orientation. In total, flight and impact testing included seven multirotor aircraft, five fixed wing aircraft, and four solid objects to represent falling aircraft and components, or to serve as benchmarks for different levels of rigidity. Based on the project timeline, FAA guidance and resources, not all aircraft were common to both UAH and NIAR. For example, UAH conducted impact testing with five fixed wing aircraft and NIAR only tested on one fixed wing aircraft as a lower cost means of assessing the effects of fixed wing mass and configuration for aircraft made of similar materials.

1.1.1 Task F: Program Management (UAH)

Task F was required for coordination and oversight of the entirety of the research by all participants and was the responsibility of the UAH Principal Investigator. UAH managed the test matrix for all participants in Task A14, coordinated scheduling of meetings, developed the reporting formats and timeline, coordinated technical and administrative review of documents, coordinated administrative actions, and supplied test aircraft to NIAR and OSU during Task A14.

1.2 Research Questions.

The proposed research was intended to answer the following research questions and any related questions that may be developed through the research process:

1.2.1 Task A (UAH, NIAR):

a. What is a clear and easily repeatable test method to determine the injury potential to a person upon impact by a UAS under various conditions and scenarios?
b. What should an acceptable level of safety for the non-participating public be for such a test described above? This task will address the acceptable levels of safety for the non-participating public including neck injury, skull fracture and concussion.
c. Does the test method work when a parachute is engaged? And how do the results differ?
d. What research data (both rotorcraft and fixed wing UAS examples), detailed test methods, and other information is necessary to develop and validate this type of test?

Task A: Assumptions and Limitations. The research will assume the following operating limitations:

a. Development of the simplified test method will utilize test data from 50th percentile Anthropomorphic Test Device (ATD) to quantify the initial test method and conduct an initial validation of results.
b. Data from Task B will be used to further validate the test method using a broader range of scenarios that could be accomplished via testing.
c. Energy absorption will not be used as part of this test. The test approach will leverage injury potential as developed in Figure 21 and Figure 22 of the Task A4 Final Report, Revision 2.
d. Testing will be limited to twelve aircraft (seven multirotor and five fixed wing platforms). These vehicle types will be coordinated with the FAA prior to conducting the test.
e. ATD testing is limited by the number of available vehicles as well as overall cost. Exhaustive testing would require over 640 test points per vehicle which is neither practical nor feasible within the scope of time and funding available. Testing will be limited to a maximum of 40 test points per vehicle; however, logistics and availability of vehicles may further limit testing.

1.3 Objectives

The overall goal of UAH's research was to conduct testing and analysis to estimate the injury potential of falling multirotor and fixed wing aircraft, and aircraft components based on credible impact conditions and aircraft contstruction. Impact Kinetic Energy (KE) forms the potential to cause injury due to the vehicle's mass and speed just prior to the collision while the material and structural response of the vehicle influence its ability to transfer KE to an impacted person and cause injury. UAH's technical approach had three main efforts that included failure flight testing, post-failure aircraft dynamic modeling, and simplified impact testing (Table 1). All uses of the term impact KE in this document specifically refer to the kinetic energy of the impacting vehicle or object immediately prior to impact. Flight testing and failure modeling was completed as a means of developing relevant impact test points and identifying trends in falling aircraft behavior. The simplified impact testing was a new experimental approach to impact testing, which employed an FAA Hybrid III 50th percentile male ATD head and neck versus a full FAA Hybrid III test device for measuring head accelerations and rates and upper neck forces and moments. The UAH test method was intended to determine if a simplified apparatus could be used to estimate head and neck injury severity and probability, and to address how testing should be designed for characterization of aircraft with regard to worst case impact orientations and their likely injury severity.

Table 1. Test, Test Conditions, and Test Outputs

Test/Simulation	Conditions	Key Output(s)
UAH Test Flight	**Multi-Rotor UAS:** No wind or as close as possible to no wind; single, multi, and all-motor failures at hover and maximum stabilized mode speeds **Fixed-wing UAS:** No wind or as close as possible to no wind; loss of propulsion, maximum pitch up/down, and maximum roll	**Multi-Rotor UAS:** V_{term} in vertical fall, Vertical and horizontal flat plate drag area estimates, identification of aircraft post-failure dynamics **Fixed Wing UAS:** Aircraft glide ratio, aircraft glide airspeed, stall dynamics, aircraft roll/spin dynamics, peak velocity/Kinetic Energy (KE).
UAH Post-Failure Dynamic Simulation	**Multi-Rotor UAS:** Single failure simulations that match vehicle state and environmental conditions from flight testing. Modeling of vehicle descent under high winds. **Fixed-wing UAS:** Single failure simulations that match vehicle state and environmental conditions from flight testing.	**Multi-Rotor UAS:** Flight test validated dynamic model for estimation of terminal velocity, impact KE as a function of time, and impact angle/trajectory, and vehicle drag characteristics. **Fixed Wing UAS:** Linearized vehicle model from flight test data for modeling of post-failure dynamics.
UAH Simplified Drop Test	Lower velocity vertical impacts using an FAA 50th Percentile ATD Head and Neck only	**Determination of** worst case impact orientation, assessment of how lower speed impact tests correlated with high speed ATD impacts, determination of a simplified test apparatus,
ATD Impact Tests	High velocity impact tests (> 36 ft/s) in worst case impact orientation over a range of head impact locations and impact trajectories	Head Peak Resultant Acceleration, Neck Compression, Probability of AIS ≥ 2 Skull Fracture, 15 ms Head Injury Criteria, Probability of AIS ≥ 2 Head Injury, Probability of AIS ≥ 3 Head Injury, Neck Injury Criteria, Probability of AIS ≥ 3 Neck Injury, 3ms Minimum g-loading, Combined Probability of Concussion (AIS 1 with no loss of consciousness), Brain Injury Criteria

1.4 Relation of UAH's Efforts with Other Universities on the Task A14 team

Research Tasks A-D, as described in the Task A14 Final Report Cover Letter, are mutually supporting tasks to understand the human injury potential of sUAS. Figure 1 shows the role each test and simulation effort plays in defining human injury potential for a specific aircraft. The effort leverages the research efforts conducted as part of Task A4 and Task A11 including the evaluation of the linear relationship between peak resultant acceleration as a function of impact kinetic energy (KE) and determining whether this relationship is consistent with human injury potential as defined by PMHS testing. UAH also supported NIAR and OSU through the development of test points based on flight testing and modeling, through test matrix management, and by supplying the other schools with test aircraft.

The relationships between the various elements of the research shown in Figure 1. UAH's Flight Testing determined impact velocities, KE, angles and orientations for Simplified and ATD testing and modeling efforts. The flight testing activity also provided validation data for the Aircraft Failure Dynamics Modeling depicted by the linkage between Aircraft Failure Dynamics Flight Test and Aircraft Failure Dynamics Modeling. UAH was unable to extend the dynamics modeling to running complete Monte Carlo simulations during this project. Simplified Testing developed lower velocity impact data points, estimated the slope of the test data curve fits, and refined higher velocity impact test points for NIAR. While no single test or modeling effort was exhaustive for any one vehicle (with the exception of the DJI Phantom 3), the research approach further refined three specific test methods; modeling, and simplified and extensive tests for evaluating vehicles in terms of human injury potential. The tests were intended to increase the body of knowledge for the FAA in terms of rulemaking for flight over people by evaluating the various injury potential test methods and comparing them with actual PMHS injuries.

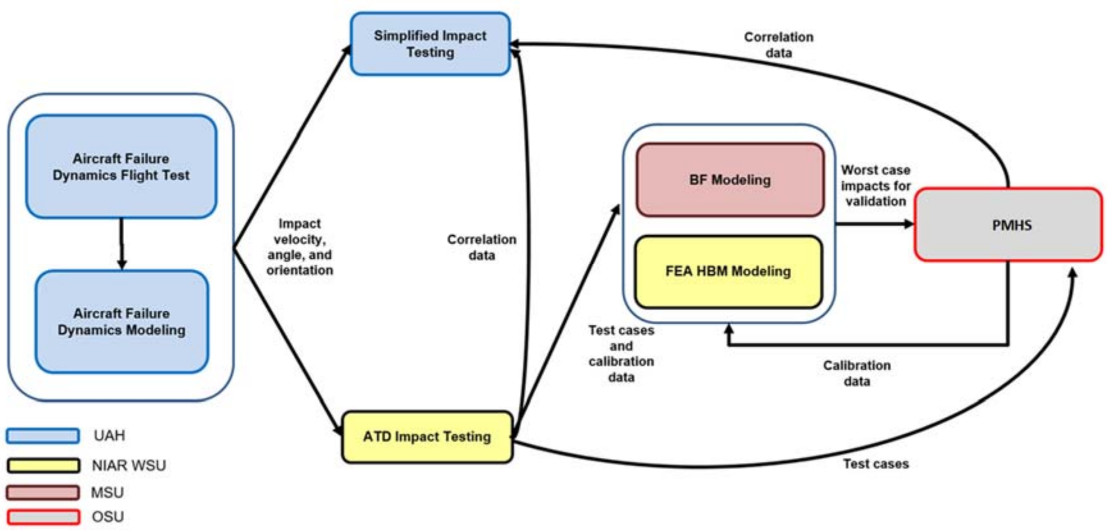

Figure 1. Task A14 Data Dependencies

2 UAH TEST AND SIMULATION TASK METHODS

2.1 Flight Test Method

A series of in-flight failure tests were performed with each aircraft to determine the aircraft's impact angle, impact kinetic energy, terminal velocity, and any other unique behaviors observed following four specific induced failure conditions for multirotor and fixed wing platforms. Flight test data was used to develop a dynamic model of each aircraft to run failure simulations across a range of failure conditions (vehicle state and environmental conditions). The most probable impact orientations, impact trajectory angles, and terminal velocities from flight test and dynamic modeling were used to determine impact test points for full ATD and PMHS impact testing.

Failure mode test points were selected to represent the corner cases of the most probable and worst-case failures to occur in a commercial UAS operation. Four test points were selected to define these corner case scenarios for multi-rotor aircraft: single-motor failure, complete aircraft motor failure, two-motor on-axis failure, and two-motor off-axis failure. The single motor failure is representative of any individual component failure such as the motor itself, the ESC, or the flight controller output. The complete aircraft motor failure is representative of a battery failure, battery disconnect, or flight controller output failure. The 2-motor failure test points are representative of a chain reaction failure due to an initial component failure. These 2-motor failures were tested in an on-axis and off-axis failure configuration to observe the dynamic behavior in response to these failures to determine if one of these failure modes could produce a higher impact energy than the other failure modes. UAH did not conduct three-motor failures because the two-motor off-axis failure was assumed to be a sufficient representation of aircraft descent initiated with unbalanced moments.

Four test points were selected to define the corner case scenarios for fixed-wing aircraft: control surfaces deflected for maximum pitch up, control surfaces deflected for maximum pitch down, control surfaces deflected for maximum roll, and motor off with control surfaces controlled by the flight controller. The first three test points are representative of a flight controller output failure. The motor-off failure test point is representative of any single component failure such as the motor itself, ESC, or the flight controller output.

For multirotor aircraft that required parachute mitigation to reduce the impact kinetic energy to acceptable levels, only the complete aircraft motor failure test point was flown. It was assumed that in the event of any in-flight failure, the parachute recovery system would turn off all motors prior to deploying the parachute.

Each failure mode test point was conducted at the hover and the aircraft's maximum stabilized horizontal flight velocity. Although most aircraft are capable of a horizontal velocity greater than the maximum stabilized horizontal flight velocity, it was assumed the FAA would only approve flights over people with the aircraft operating in an attitude-stabilized flight mode.

Each aircraft was equipped with a flight data logger and a custom RSESC failure board microcontroller to initiate the in-flight failures. A parachute recovery system was used on all multirotor test flight aircraft to preserve the airframe for additional tests. A parachute recovery system was not used on the fixed-wing aircraft since the pilot could exit the failure mode and regain control.

2.1.1 Data Logging,

Test flight data was recorded independent of the aircraft's sensors using a Pixhawk Mini flight controller. The data logger recorded Global Positioning System (GPS) data at 5 Hz, Inertial Measurement Unit (IMU) data at 25 Hz, Extended Kalman Filter (EKF) data at 25 Hz, and radio control (RC) inputs at 25 Hz for the multirotor aircraft. The data logger recorded GPS data at 5 Hz, IMU data at 50 Hz, EKF data at 50 Hz, and radio control inputs at 50 Hz for the fixed-wing aircraft. The difference in sampling rates was due to the different firmware installed on the

Pixhawk for multirotor and fixed-wing aircraft. The firmware was not configurable. In most cases, the Pixhawk Mini flight controller served the role of the aircraft flight controller in addition to the data logging functions. The data logger recorded the entire flight from takeoff to landing. The data was recorded in metric units as a single delimited data file with each parameter indexed by timestamp. A custom MATLAB and Python script was used to separate the GPS, IMU, EKF, and RC input parameters with their respective timestamps into individual data sets. The recorded parameters used from each sensor for analysis is shown in Table 2.

Table 2. Flight Test Recorded Parameters

Parameter	Units	Source
Processor Clock Time	µs	GPS, IMU
Date	YYYY-MM-DD	GPS, IMU
Local Time	HH:MM:SS.xxxxxx	GPS, IMU
Rotation, X-Axis	rad/s	IMU
Rotation, Y-Axis	rad/s	IMU
Rotation, Z-Axis	rad/s	IMU
Latitude	degrees (decimal)	GPS
Longitude	degrees (decimal)	GPS
Relative Altitude (AGL)	m	GPS
Horizontal Speed	m/s	GPS
Vertical Speed	m/s	GPS
Position North	m	EKF
Position East	m	EKF
Position Down	m	EKF
Velocity North	m/s	EKF
Velocity East	m/s	EKF
Velocity Down	m/s	EKF
Euler Roll Angle	degrees	EKF
Euler Pitch Angle	degrees	EKF
Euler Yaw Angle	degrees	EKF
RC Inputs	µs	RCIN

2.1.2 Failure Initiation

Two types of hardware solutions were used to initiate the in-flight failures. On aircraft where the Pulse Width Modulation (PWM) signals from the flight controller to the ESCs were accessible, a custom RSESC Failure Board Microcontroller was placed in line with the signals between the flight controller and Electronic Supervisory Control (ESC). Under normal operation, the failure board read the incoming PWM signals from the flight controller and passed them through to the ESC. When a failure was initiated, the flight controller outputs were ignored and a 900 µs PWM signal was sent from the failure board to the ESC to turn off the motor. The 900 µs signal pulse-width is below the minimum pulse-width that an ESC typically recognizes as a valid signal and causes the ESC to disarm and disable its output.

Relays were installed on the positive DC wire between each ESC and battery connection on aircraft that had the ESCs integrated into the internal circuit board where the individual ESC PWM signals were not accessible. When a failure was initiated, the failure board would cause the respective relays to open which disconnected the battery power from the ESC causing the ESC to turn off and the motor to stop. Relays were installed on one of the three motor wires on each motor for aircraft where the ESCs and the power distribution for each ESC was integrated into the internal circuit board. When the relay was opened, one of the phases for the brushless motor was disconnected and the motor stopped spinning.

The failure board on multirotor aircraft had an automated failure sequence program that was executed once the pilot initiated the failure. This sequence was characterized by the following events: failure initiation, remaining non-failed motors received outputs from flight controller for 3 seconds after initial failure, all motors were turned off 3 seconds after initial failure, and parachute was deployed 3.5 seconds after initial failure. This automated failure sequence was used to ensure repeatability and to reduce pilot workload. During Vendor 1 Quadrotor flights with the blade guards removed, the fall time was extended to 5.5 sec because there was sufficient altitude to recover the aircraft under parachute.

The failure board on fixed-wing aircraft was programmed to allow the pilot to activate and deactivate the failure mode via a switch on the pilot transmitter. This feature, combined with the fixed-wing aircraft's ability to recover from a dynamic state, negated the need for a parachute recovery system. Additionally, this allowed for multiple repeat test points on the same flight without having to land.

2.1.3 Flight Test Configurations

Each aircraft had to be modified for failure flight testing to accommodate the data logger, failure board and recovery parachute system. An attempt was made to preserve as much of the control and hardware functionality of the stock aircraft configuration, such as programming automatic motor shutoff in the case of excessive roll in the case of Vendor 1 Quadrotor. Externally mounted equipment integrated for failure flight testing was mounted in such a way to minimize the addition of vertical projected area. The additional equipment was distributed around the aircraft to minimize any change in CG location from the stock configuration CG location. Impact testing was conducted with stock-weight aircraft. In cases where stock batteries, flight controllers, or payloads were not available, representative masses were installed to replicate the components. The impact and flight test configuration weights for each aircraft and impacting component are shown in Table A1 - Table A3.

2.1.3.1 Vendor 1 Quadrotor

The Vendor 1 Quadrotor aircraft in its stock configuration could only be flown using proprietary hardware from Vendor 1 Quadrotor that was not supplied for this testing. As a result, the stock electronics were completely removed from the airframe, with the exception of the motors, and commercially available ESCs, battery, radio control receiver, flight controller, telemetry radio, GPS receiver, parachute release servo, and parachute were integrated to create a flyable aircraft.

The Pixhawk Mini data logger served as the aircraft flight controller in this aircraft integration. Since commercially available ESCs were used in the integration, the PWM signal for each ESC was directly accessible and the PWM based failure method was used to initiate the in-flight failures. The GPS receiver, parachute, and battery were mounted externally on the top of the aircraft. The parachute was secured with an elastic strap connected to the parachute release servo. The radio control receiver, failure board, flight controller, and telemetry radio were mounted internally within the aircraft body.

2.1.3.2 DJI Phantom 3

The DJI Phantom 3 was flown in the flight test configuration using the stock configuration DJI flight controller. Since the DJI Phantom 3 has the ESCs integrated into the internal circuit board along with the power distribution for each ESC, a relay was installed on one of the three motor wires on each motor within the internal body of the aircraft to initiate the in-flight failures. The failure board, data logger, and a Mars Mini parachute recovery system were installed on the bottom side of the aircraft. The camera payload was removed from the aircraft to make room for this equipment. The GPS receiver for the data logger was mounted externally on the top of the aircraft but not blocking the GPS receiver for the DJI flight controller.

Six of the eight flight test points were flown with the aircraft configuration described above. The aircraft was damaged on the sixth flight due to a parachute release failure which resulted in catastrophic damage to the stock DJI flight controller. No other DJI Phantom 3 aircraft with operable DJI flight controllers were available for this test flight effort, so a new aircraft was built using a new airframe shell, commercially available components, and a Pixhawk Mini for the flight controller. For this configuration, the Pixhawk Mini flight controller was integrated within the internal body of the aircraft and also served as the flight data logger. The GPS receiver, radio control receiver, and ESCs were also integrated within the internal body of the aircraft. With the addition of commercially available ESCs, the in-flight failure initiation was changed from relay based failures to PWM based failures. Since most of the previously externally mounted equipment was moved inside the aircraft body for this configuration, the stock camera payload was reinstalled to match the weight and horizontal projected area of the previous configuration.

2.1.3.3 DJI Mavic Pro

The DJI Mavic Pro was flown in the flight test configuration using the stock configuration DJI flight controller. Since the DJI Mavic Pro has the ESCs integrated into the internal circuit board along with the power distribution for each ESC, a relay was installed on one of the three motor wires on each motor to initiate the in-flight failures. The failure board, failure relays, data logger, and parachute recovery system was installed in a plastic box on the top side of the aircraft. The parachute was mounted externally on this plastic box and secured by an elastic strap that was connected to the parachute release servo.

2.1.3.4 Sensefly eBee+

The Sensefly eBee+ in its stock configuration can only be flown using proprietary hardware from Sensefly that was not supplied for this testing. As a result, the stock electronics were completely removed from the airframe, with the exception of the motor and servos, and a commercially available ESC, battery, radio control receiver, flight controller, telemetry radio, and GPS receiver were integrated to create a flyable aircraft. The Pixhawk Mini data logger served as the aircraft flight controller in this aircraft integration. Since a commercially available ESC was used in the integration, the ESC PWM signal was directly accessible and the PWM-based failure was used to initiate the in-flight failures.

2.1.3.5 Go Pro Karma

The Go Pro Karma failure integration was attempted using relays on the brushless motor wires, however, the introduction of the relay introduced a feedback anomaly within the Karma flight controller and produced an error that prevented the aircraft from arming the ESCs. As a result, the internal circuits were removed from the airframe to make room for the Pixhawk Mini flight controller, which also served the role of the flight data logger. The stock Go Pro Karma battery and motors were reused in this new integration. The failure board, GPS receiver, and parachute were mounted externally on the top of the aircraft. The commercially available ESCs and parachute release servo were mounted externally on the bottom of the aircraft. The parachute was secured with an elastic strap that was connected to the parachute release servo. Since commercially available ESCs were used in the integration, the PWM signal for each ESC was directly accessible and the PWM based failure method was used to initiate the in-flight failures.

2.1.3.6 DJI Inspire 1

The DJI Inspire 1 was flown in the flight test configuration using the stock configuration DJI flight controller. Since the DJI Inspire 1 uses a different communication protocol between the flight controller and ESCs than PWM, a relay was installed on the positive DC wire between the battery and each ESC to initiate the failures. The failure board and relays were mounted externally on each motor arm. The data logger was mounted externally on the bottom of the aircraft behind the camera gimbal. The GPS receiver for the data logger was mounted externally on the top of the aircraft, forward of the aircraft's GPS receiver. The parachute was mounted externally on the top of the aircraft with an elastic strap securing it to the parachute release servo. The parachute release servo was mounted externally on the aft, left side of the aircraft next to the battery.

2.1.3.7 Vendor 3 Quadrotor

The Vendor 3 Quadrotor was flown in the flight test configuration using the stock configuration flight controller. The failure board was integrated between the flight controller PWM outputs and the ESC PWM inputs to initiate PWM based failures. The camera payload was removed and the data logger and failure board was mounted in the space previously occupied by the camera payload. An Opale ST60-X parachute recovery system was modified with a proprietary release mechanism to provide more reliable deployments. The parachute system was installed on a custom interface mount on the front of the aircraft with the parachute launcher aligned vertically.

2.1.3.8 Parachute Flight Testing

Based on low-order aerodynamic and kinetic analysis of the DJI Inspire 2 and S800 aircraft, both were determined to be too large to conduct safe operations over humans without a parachute mitigation system installed to reduce the injury potential of the platform. The parachute flight test effort provided experimental and modeling data showing the impact energy of a UAS using a parachute as a mitigation following an in-flight failure. These results enable development of impact test points that replicate an impact while descending under a parachute recovery system. The test points were selected to bracket the aircraft's least severe and worst-case impact energy threat after experiencing and in-flight failure (Table 3). The least severe scenario is a complete aircraft motor failure at hover flight conditions. The worst-case scenario is a complete aircraft motor failure when the aircraft is flying at the maximum stabilized, controlled, horizontal flight velocity. These corner case scenarios represent the minimum and maximum resultant velocity values the aircraft can achieve in stabilized, controlled flight. These test points were flown with the parachute deployment immediately after failure. An additional set of these corner case test points were flown in which the aircraft was allowed to free-fall for 3 seconds before the parachute was deployed. The primary reason for this was to support aerodynamic modeling of the aircraft for use in the ground collision severity study modeling effort. However, this additional free-fall time allows for the parachute system to be tested to maximum structural stresses to ensure no part of it fails during, or after deployment.

Table 3. Flight Test Matrix for the DJI S800 with Vendor 2 72-inch Parachute System and DJI Inspire 2 aircraft with the DJI Inspire 2 with Vendor 2 72-inch Parachute System

Aircraft	Motor Failure	Target Horizontal Velocity at Failure (m/s)	Deployment Delay (s)
S800	M1, M2, M3, M4, M5, M6	0	0
S800	M1, M2, M3, M4, M5, M6	0	3
S800	M1, M2, M3, M4, M5, M6	15	0
S800	M1, M2, M3, M4, M5, M6	15	3
Inspire 2	M1, M2, M3, M4	0	3
Inspire 2	M1, M2, M3, M4	20	3
Inspire 2	M1	20	3

2.1.3.8.1 DJI S800

The DJI S800 was flown in the flight test configuration using the stock configuration DJI flight controller. The failure board was integrated between the flight controller PWM outputs and the ESC PWM inputs to initiate PWM based failures. The camera gimbal was removed and the Vendor 2 parachute system was mounted horizontally on the camera gimbal support rails.

2.1.3.8.2 DJI Inspire 2

The DJI Inspire 2 was flown in the flight test configuration using the stock configuration DJI flight controller. Since the DJI Inspire 2 uses a different communication protocol between the flight controller and ESCs than PWM, a relay was installed on the positive DC wire between the battery and each ESC to initiate the failures. The failure board and relays were mounted externally on each motor arm. The data logger was mounted externally on the bottom of the aircraft behind the camera gimbal. The Vendor 2 parachute system was mounted horizontally on the right arm. The GPS receiver for the data logger was mounted externally on the top of the aircraft, forward of the aircraft's GPS receiver.

2.1.3.8.3 Parachute Deployment Key Events

There were five key events observed during parachute flight test and subsequent analysis. These events and their respective nomenclature are listed below:

- Failure Onset: T0
- Parachute Deployment: T1
- Parachute Inflation: T2
- Initial Steady-State Velocity Reached: T3
- Start of Steady-State Descent: T4
- Ground Impact: T5

2.2 Aerodynamic Analysis and Dynamic Modeling

The studies of blunt trauma injury potential of small UAS are rooted in an understanding of vehicle impact characteristics. The essential characteristics of the vehicle impact are its impact KE, trajectory, impact orientation and structural response. The structural response of the vehicle depends on material properties, construction and collision behavior of the vehicle and target (human, building, cars, etc.). Other characteristics like trajectory, vehicle impact KE and impact orientation depend on the vehicle's state, defined by its position, velocity, attitude and attitude rates ($x, y, z, u, v, w, \varphi, \theta, \psi, p, q, r$) at impact. The vehicle state prior to impact is dependent upon the type of failure, the vehicle state at the time of failure, and the ambient conditions (wind speed and direction, gravity and air density) at the time of failure and during the aircraft's fall. It is expensive and time-consuming to conduct a large number of failure flight tests to quantify the effects of failure types, vehicle state before failure and environmental conditions. However, a calibrated sUAS model developed from a limited number of flight tests can be used to simulate various failures while varying vehicle states at failure and environment conditions to develop an exhaustive understanding of the aerodynamic and dynamic characteristics of the vehicle that can lead to blunt trauma injury.

Ballistic modeling of a multirotor sUAS following a four-motor failure was previously performed at UAH during the first phase of FAA ground collision severity research task. This work was documented in final report published in April 2017[2],[3]. CFD modeling was performed on a DJI Phantom 2 aircraft to estimate flat plate drag coefficients along vehicle body axis. This modeling method assumes that for a freely-falling vehicle with four motor failure, the weight and drag are the dominant forces acting on the body, while the body-induced lift and resulting aerodynamic moments are negligible. By integrating the acceleration due to external forces on the body, its

[2] Arterburn, D., Ewing, M., Prabhu, R., Zhu, F., & Francis, D., "FAA UAS Center of Excellence Task A4: UAS Ground Collision Severity Evaluation," FAA ASSURE, 2016.

[3] Arterburn, D., Duling, C. and Goli, N., "Ground Collision Severity Standards for UAS Operating in the National Airspace System (NAS)." Paper AIAA 2017-3778, *17th AIAA Aviation Technology, Integration, and Operations Conference*, Denver, CO, 2017.

position and velocity are calculated. The XY scatter of the vehicle, defined as the displacement of the vehicle in X and Y direction based on the position at failure, and the impact KE are calculated. This modeling was validated by comparing with experimental flight tests. The flight tests involved flying the vehicle at pre-defined altitude and known horizontal ground speed and cutting power to all four motors. The vehicle log files were processed to plot vehicle trajectory and compare with simulated trajectory obtained from ballistic modeling. Figure 2 shows a comparison of ballistic modeling with flight tests. This method provides an acceptable method for estimating impact energy following complete loss of propulsive power for a multi-rotor sUAS without additional lifting surfaces. The ballistic model can account for initial conditions like failure altitude, failure velocities in x, y, and z, wind speed and direction, and air density, although it requires the drag coefficient values as input values to estimate drag. The model has some limitations. The model treats velocity and drag force components as linearly superposed quantities versus being a function of vehicle angle of attack. This was a simplifying assumption that provided accurate results for a four-motor failure on multirotor with a generally level attitude during descent. This assumption broke down for fixed wing aircraft, which are not purely ballistic entities with dominant mass, and for partial failures on a multi-rotor UAS. Also, the ballistic model only had drag and did not have a force and moment model that estimated lift and moment contributions from the body (multirotor), functioning props (multirotor and fixed-wing), lifting surfaces (fixed-wing), and effectors (fixed-wing). The dynamic behavior of the body and the vehicle controller behavior during partial failure (single or multiple rotor failure, stuck actuator, etc.) cannot be modeled with ballistics alone.

During Tasks A4 and A11, UAH used CFD-generated drag coefficients as ballistic model inputs. CFD flow field simulation is resource intensive because it requires vehicle CAD models, software licenses, and in-house CFD analysis expertise. UAH and the FAA determined that a more practical approach for development of aircraft certification methods is to conduct limited flight testing to gather data used to estimate vehicle aerodynamic properties.

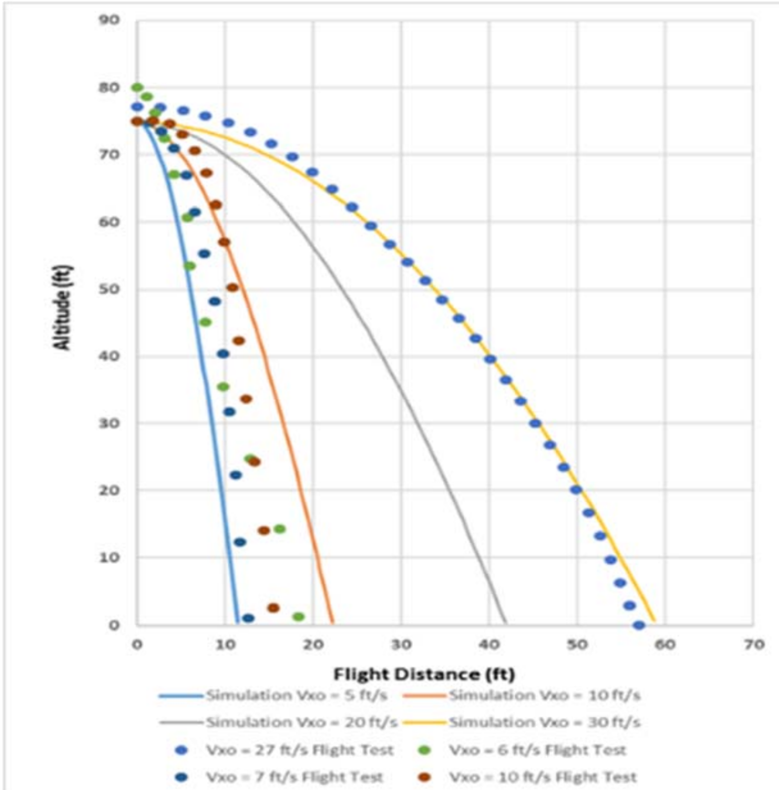

Figure 2. DJI Phantom 2 Ballistic Modeling versus Fight Test

A Simulink®-based model was developed to model the dynamics of a falling multirotor sUAS with an active controller under partial and full propulsive failure conditions. It is a time stepping model that uses Ordinary Differential Equation solvers to integrate the vehicle equations of motion (angular velocity and accelerations) to estimate positions, velocity and attitude at any time step. The model consists of blocks that simulate environmental conditions, vehicle dynamic state, vehicle flight control system and vehicle desired trajectory (or pilot commands) and provides trajectory visualization (Figure 3). The important parameters required to run this model are vehicle aerodynamic coefficients, motor and rotor parameters, vehicle mass and inertia properties, and ambient conditions. Aerodynamic coefficients, motor and rotor parameters, inertia properties, etc., are measured experimentally from flight tests, static thrust stand testing and bifilar pendulum testing for moment of inertia, respectively. The simulation outputs include the vehicle position, velocity, orientation and angular rates. If a failure occurs during flight, the simulation calculates and records the vehicle state data as it falls. The model outputs are validated against the flight test telemetry data by comparing real trajectories with simulated trajectories. When the error in position, velocity and kinetic energy is within ±10% of flight tests, the simulation is assumed to be accurate. Following validation, a Monte Carlo simulation can be performed on the model with variable factors, namely, wind gust speed and direction, failure mode (single or multiple motor failure, etc.), and vehicle states (position, velocity, orientation, and angular rates) immediately before failure. The simulation can provide impact energies, trajectories and the XY scatter of the vehicle with respect to the point of failure.

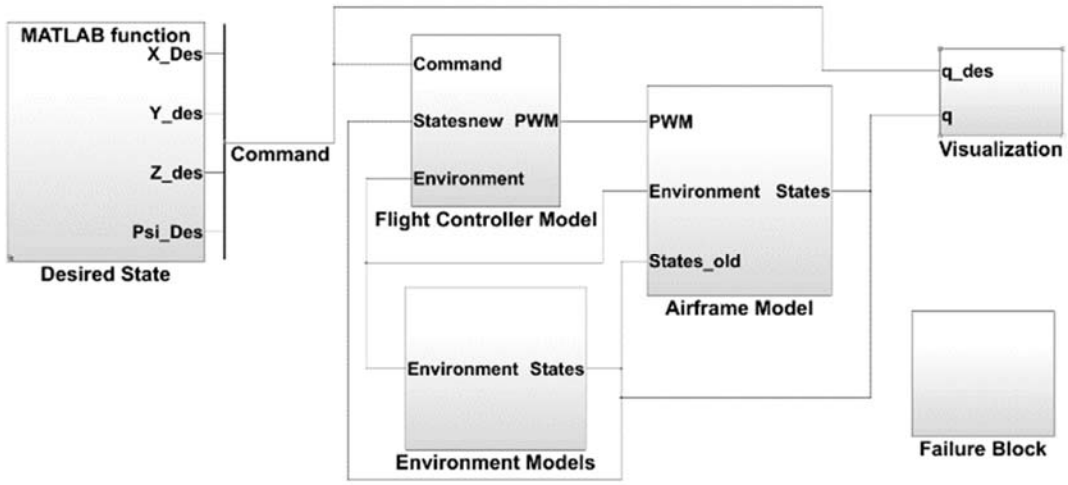

Figure 3. Simulink model of a sUAS

Figure 3 is a block diagram of the Simulink® Model. The desired state block defines the desired trajectory and vehicle velocity. The Environment Model defines ambient conditions including wind gusts, wind direction, gravity and air density. The Flight controller block models the vehicle autopilot. For a multirotor sUAS, a proportional–integral–derivative controller (PID) control is used to control the thrust and torque of each motor to create the required vehicle thrust, roll, pitch and yaw moment in order to achieve a desired state[4]. For a Fixed wing sUAS, an outer loop-inner loop PID control is used to perform trajectory tracking and control of the aircraft about the roll, pitch, and yaw axes. Based on the desired and current state, this block calculates the required PWM inputs to the motors needed to increase thrust and torque to drive the aircraft to the desired state. The control block is modeled based off a generic PID control for a multirotor and fixed wing sUAS vehicle. Exact manufacturer control design cannot be modeled due to inability to access proprietary information. However, certain aspects of specific vehicle control can be modeled to replicate vehicle controller behavior which will be discussed later. The vehicle airframe block defines the dynamic model of the vehicle. Under this block, the vehicle aerodynamic coefficients, motor/rotor parameters and mass and inertia properties are defined. Based on the current vehicle state, input PWM signals and ambient conditions, the block calculates the forces and moments acting on the vehicle that cause it to move to a new state. The visualization block displays the vehicle trajectory and stores the state variables. The Failure block defines the time at which the failure occurs and the type of failure. Fifteen modes of failures are defined for a Multirotor sUAS as shown in Table 4. These include single and multiple motor failures. For fixed wing sUAS, power loss and stuck effector positions were defined. Sensitivity Analysis (Monte Carlo) can be performed on these models by varying wind gusts and direction, vehicle states at failure, and vehicle failure types. The Monte Carlo simulations can provide data about the worst-case impact

[4] Fahimi, F., *Autonomous robots: Modeling, path planning, and control,* Springer, New York, Nov 2008, Chapter 10

energies and the maximum XY scatter following a failure. The following sub-sections discuss in detail how the inputs to the model have been estimated, the modeling method and the outputs.

Table 4. Failure types for Multirotor sUAS used in the UAH Simulation

Multirotor Failure Type	Combinations of Motor Failure	Failure types possible
One motor Failure	Any motor fails	4 types for Quadrotor
Two motor Failure	Any two motors fail	6 types for Quadrotor
Three motor Failure	Any three motors fail	4 types for Quadrotor
Four motor Failure	All four motors fail	1 type for Quadrotor

2.2.1 Aerodynamic Analysis Method

The important parameters required to run the dynamic model are vehicle aerodynamic coefficients, motor and rotor parameters, vehicle mass and inertia properties, and ambient conditions. Moment of Inertia for each vehicle was obtained experimentally using the bifilar pendulum method[5]. Table 5 outlines the MOI calculated for each vehicle in its flight test configuration. The environmental parameter that requires estimation is wind. For model validation purposes, the wind data from a weather station nearest to the test flight location, during the flight test, is used. This data consists of the wind speed and direction measured at a height of 20 feet above the ground. The next section describes how this data is used to estimate wind for the flight profile.

Table 5. Measured Moment of Inertia values of Flight Test vehicles

Vehicle	Weight (lbf)	Moment of Inertia		
		Mxx (kg/m^2)	Myy (kg/m^2)	Mzz (kg/m^2)
DJI Phantom 3	3.13	7.16E-02	7.16E-02	1.34E-01
Vendor 1 Quadrotor	0.95	9.44E-04	9.44E-04	2.13E-03
DJI Mavic Pro	2.47	4.22E-03	6.60E-03	7.30E-03
DJI Inspire 2	9.82	11.39E-02	9.26E-02	8.78E-02
GoPro Karma	5.07	1.84E-02	2.14E-02	3.62E-02
Sensefly eBee+	2.87	2.89E-02	2.93E-02	4.07E-02

The motor and rotor parameters that are required are the thrust and torque coefficient. The thrust and torque coefficient are calculated from static thrust stand testing at UAH. The static thrust stand tests run the motor-propeller combination at various speeds (RPM) and measure the thrust and torque coefficient for each motor speed (RPM). The motor speed (RPM) is attained by sending a PWM signal to the motor. From these test results, a curve fit is developed between RPM and thrust and torque coefficients, respectively.

These static thrust and torque curve fits are used in the simulations. Ideally, researchers would be using thrust and torque curves that represent a range of advance ratios since the model represents

---

[5] Habeck, Joseph; Seiler, Peter. (2016). *"Moment of Inertia Estimation Using a Bifilar Pendulum."* Retrieved from the University of Minnesota Digital Conservancy, http://hdl.handle.net/11299/182514.

edgewise, falling, and tumbling flight which all have unique inflow characteristics and thrusting states. UAH did not have access to wind tunnels for this study based on timeline and resources allotted. Additionally, UAH altered the thrust modeling for the DJI Phantom 3, based on flight test data, to examine the effect of improving the thrust model fidelity. There were few changes to the accuracy of the model, in terms of resultant velocity, impact KE, and trajectory, so this change was not made to the other aircraft models.

The aerodynamic parameter that is required for multirotor sUAS is the flat plate drag area (SC_D) as a function of vehicle angle of attack. This can be estimated from the unpowered, free-fall flight tests. In free-fall, the only forces acting on the vehicle are weight and drag. The data logger payload integrated by UAH and attached to every flight test vehicle records position, velocity, attitude and attitude rates at 10 Hz frequency. Equations 1-4 are used to measure the flat plate drag area and angle of attack.

$$Acceleration_{Res,t} = \frac{{v_t}^2 - {v_{t-1}}^2}{2(s_t - s_{t-1})} \quad \text{Eqn. 1}$$

$$Acceleration_{Drag,t} = Acceleration_{Res,t} - g \quad \text{Eqn. 2}$$

$$SCd_t = \frac{2 \times mass \times Acceleration_{Drag,t}}{\rho {V_t}^2} \quad \text{Eqn. 3}$$

$$AoA = \tan^{-1} \frac{w_{body}}{u_{body}} \quad \text{Eqn. 4}$$

The resultant acceleration of the vehicle at time t sec is calculated from the measured displacement and velocity values at time t sec and t – 0.1 sec as shown in Eqn. 1. The acceleration due to drag forces is calculated from Eqn. 2 by subtracting the gravity acceleration from the resultant acceleration. This acceleration multiplied by mass gives the Drag force at each time step. This force is acting opposite to the flight velocity direction (negative wind axes). Flat plate drag area at each time step is then calculated by dividing the drag force by the dynamic pressure as shown in Eqn. 3. The angle of attack of the vehicle is calculated at each time step from the vehicle velocity components in the body frame as shown in Eqn.4. Initially, a curve fit is established between angle of attack and flat plate drag area using the measured values. The shape of these curves is sinusoidal with minimum flat plate drag area values in the vehicle XY plane and maximum flat plate drag area values in a plane perpendicular to the vehicle XY plane. Figure 4 shows the Flat Plate Drag Area – Angle of Attack curve fit derived from Vendor 1 Quadrotor four motor failure flight test. During the simulation, the angle of attack at each time step gives the flat plate drag area at that time step. The flat plate drag area along with the dynamic pressure at that time step gives the drag force at that time step. This drag force, acting along a direction opposite to the wind direction, is then transformed to the vehicle body frame.

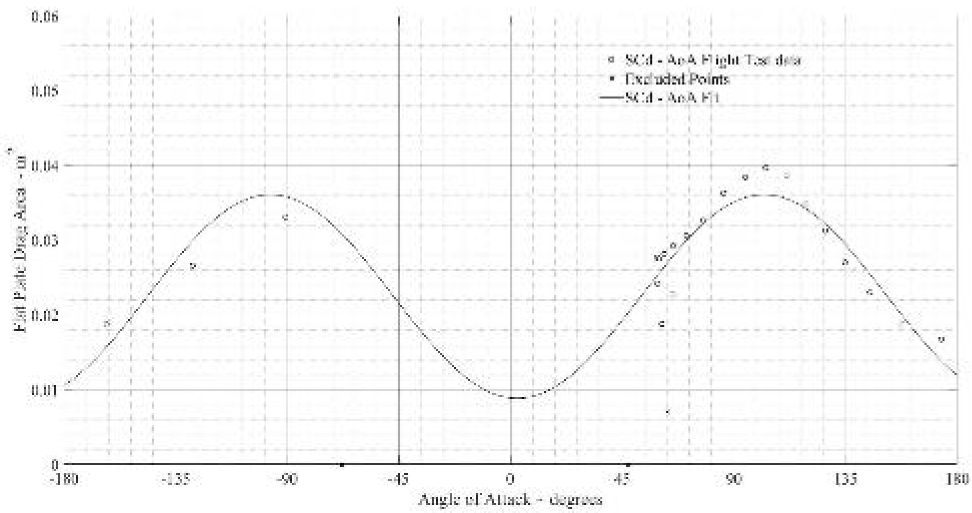

Figure 4. Flat Plate Drag Area and Angle of Attack curve fit

The above method of deriving flat plate drag area from the curve fit provided an accurate set of aerodynamic inputs to the simulation; however, this method had a drawback. When the vehicle flips, the angle of attack changes from -180 to + 180 or vice versa. The fitted curve is not continuous when the angle of attack changes from 180º to -180º. This created a sudden rise or reduction of the drag when the vehicle flipped. Instead of using a curve fit, a sinusoidal equation, as defined in Eqn. 5 and shown in Figure 5, was defined to calculate the flat plate drag area from the angle of attack.

$$SC_D = \left(SC_{D_{max}} - SC_{D_{min}}\right)\sin^2(\alpha - \varphi) + SC_{D_{min}} \qquad \text{Eqn. 5}$$

Where SC_{Dmax} and SC_{Dmin} are the maximum and minimum flat plate drag area as observed from the flight test values, φ is the angle of attack at which SC_{Dmin} occurs as obtained from the curve fit. This equation keeps the curve continuous when the vehicle flips. From Figure 4, the values of SC_{Dmax}, SC_{Dmin} and φ chosen are 0.038 m^2, 0.016 m^2 and 10º, respectively. These values are then substituted in Eqn. 5, and the resulting flat plate drag area-Angle of attack curve is plotted in Figure 5.

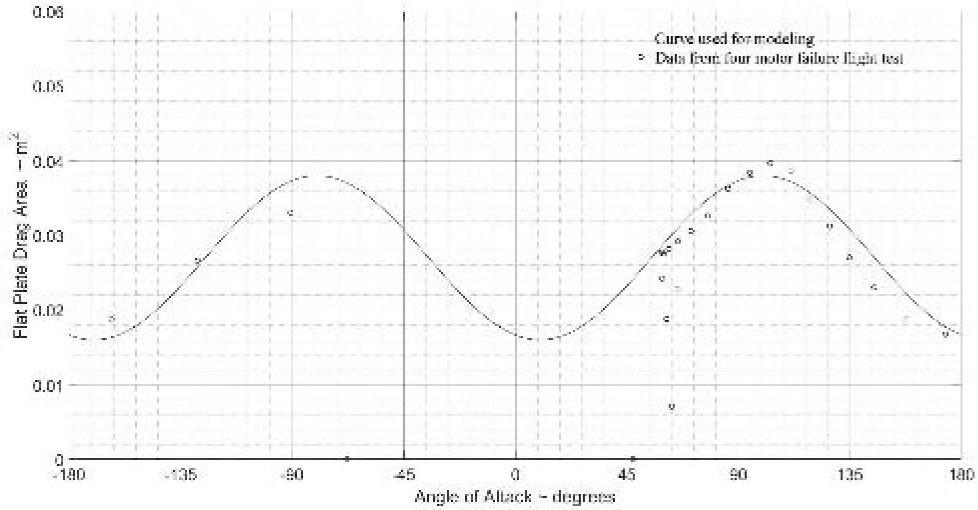

Figure 5. Flat Plate Drag Area and Angle of Attack curve

Table 6 shows the average flat plate drag area values estimated for each vehicle. For the sinusoidal drag area curves, the average flat plate drag area values are estimated as the mean of SC_{Dmax}, and SC_{Dmin}.

Table 6. Average Flat Plate Drag Area values for the Multirotor UAS flown

Vehicle	Weight (Flight Test Configuration)	Average Flat Plate Drag Area - sq. ft (m^2)
DJI Phantom 3	3.13 lbf	0.484 (0.045)
Vendor 1 Quadrotor (with Cage)	0.95 lbf	0.29 (0.027)
Vendor 1 Quadrotor(without Cage)	0.84 lbf	0.161 (0.015)
DJI Mavic Pro	2.47 lbf	0.215 (0.02)
GoPro Karma	5 lbf	0.807 (0.075)
DJI Inspire 2	9.82 lbf	0.409 (0.038)

For the fixed wing sUAS, many aerodynamic coefficients are required to define its dynamic model. The force (both lift and drag) and moment coefficients depend on the vehicle angle of attack, sideslip, angular velocities, vehicle velocity and actuator deflections. These coefficients are typically estimated from wind tunnel testing, computational models or flight testing. Initially, a parametric aircraft geometry tool called OpenVSP was used to estimate the force and moment coefficient derivatives. A 3D model of the fixed wing sUAS is created in OpenVSP to estimate force and moment coefficients for the aircraft. These coefficient derivatives are defined in the vehicle dynamic model to determine the force and moments acting on the vehicle. However, this method was not successful in estimating the eBee+ aerodynamic coefficients since the complex flying wing design and the unknown airfoil sizing lead to erroneous coefficients that created a poor force and moment model that could not be controlled in simulation.

The next method used the data from flight tests performed on the eBee+ and developed a parameter estimation simulation to estimate the coefficients and define the dynamic model. Only failure flight tests were performed on the eBee+. UAH is in the process of flying frequency sweep test flights in order to generate a linearized model for simulation.

2.2.2 Multirotor sUAS Dynamic Modeling Method

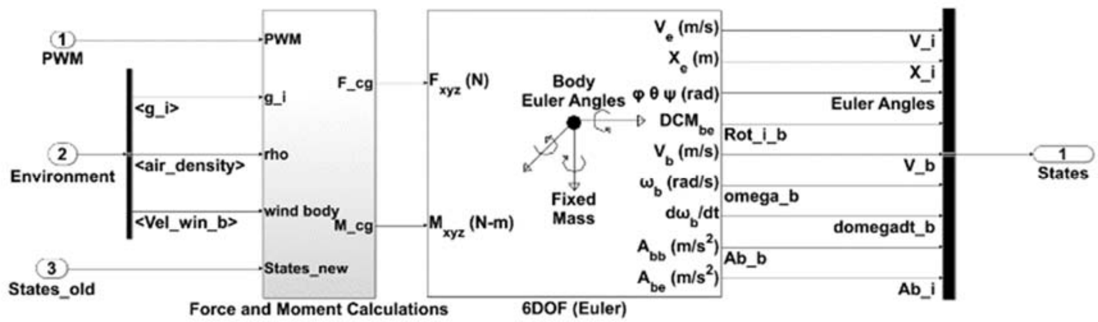

Figure 6. Airframe Model

An outline of the dynamic model is shown in Figure 3 as part of an introduction to the entire modeling and analytical effort. This section describes the dynamic model in detail. The airframe dynamic block shown in Figure 6 calculates the new states of the vehicle based on the previous states and environment conditions and applies motor PWM signal. The six-degree of freedom (6DOF) (Euler) block integrates Eqns. 6 and 7 twice to calculate the twelve states of position, velocity, attitude (Euler Angles) and attitude rates (Angular Rates). The inputs to the 6DOF block, forces and moments are in body frame coordinates.

$$m\begin{bmatrix}\ddot{x}_1\\ \ddot{x}_2\\ \ddot{x}_3\end{bmatrix} = F_B \qquad \text{Eqn. 6}$$

$$I\begin{bmatrix}\ddot{\omega}_1{}^B\\ \ddot{\omega}_2{}^B\\ \ddot{\omega}_3{}^B\end{bmatrix} = M_B \qquad \text{Eqn. 7}$$

The Force and Moment Calculations block calculates the forces and moments on the vehicle due to gravity, rotor thrust and torque, and vehicle drag. The body-induced lift and aerodynamic moments of the vehicle body are assumed to be very small and neglected. Equations 8 and 9 define the components of the forces and moments fed to the 6DOF Euler block.

$$F_B = T^B + D^B + R_{BI}W \qquad \text{Eqn. 8}$$

$$M_B = Q^B - \omega^B \times I\omega^B \qquad \text{Eqn. 9}$$

W (=mg) is the weight of the vehicle. I is the Moment of Inertia of the vehicle, and ω is the angular velocity (different from angular rate). D^B is the vehicle drag in the body frame defined by Eqn. 10,

$$D^B = \frac{1}{2}\rho S C_D {V_B}^2 \quad \text{Eqn. 10}$$

where ρ is density, and V_B is vehicle resultant velocity in body coordinates, and SC_D is the flat plate drag area. TB is the sum of the thrust from the four rotors. Eqn. 11 describes how total vehicle thrust due to rotors is calculated,

$$T_B = T_1 + T_2 + T_3 + T_4 \quad \text{Eqn. 11}$$

where T_i (i=1-4) is the thrust produced by each rotor/motor. The motors are numbered 1-4 starting from forward right and in anti-clockwise direction as shown in Figure 7.

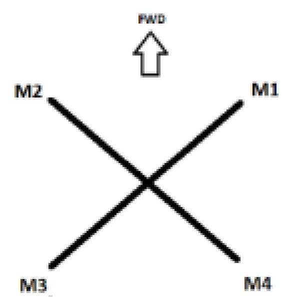

Figure 7. Naming convention for Quadrotor motors

Thrust produced from each motor is given by Eqn. 12 below,

$$T_i = \frac{1}{2}\rho A C_T (\Omega_i R)^2 \quad \text{Eqn. 12}$$

where A is the rotor disk area, R is the rotor radius, Ω is the rotor angular velocity, i represents motors 1-4 and C^T is the rotor thrust coefficient. Q^B is the moment acting on the vehicle due to difference in motor spin direction and the torque of the motors. Eqn. 13 describes the equations for roll, pitch and yaw moment acting on the vehicle,

$$Q^B = \begin{bmatrix} M_\varphi \\ M_\omega \\ M_\psi \end{bmatrix} = \begin{bmatrix} d(T_2 + T_3 - T_1 - T_4) \\ d(T_1 + T_2 - T_3 - T_4) \\ Q_1 + Q_2 + Q_3 + Q_4 \end{bmatrix} \quad \text{Eqn. 13}$$

where d is the distance between motor center and vehicle center of gravity, and Q_i is the torque of each motor defined in Eqn. 14 below,

$$Q_i = \frac{1}{2}\rho A R C_Q (\Omega_i R)^2 \quad \text{Eqn. 14}$$

where C_Q is the rotor torque coefficient.

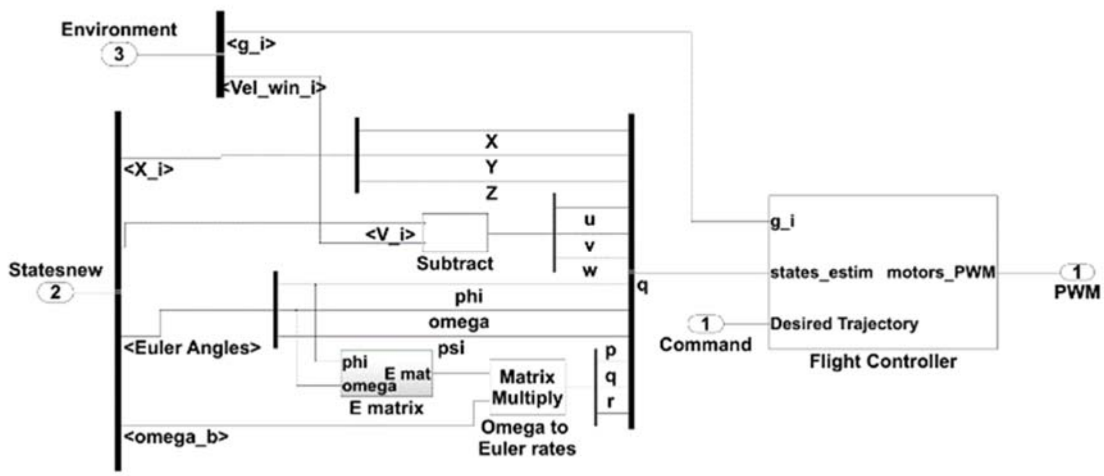

Figure 8. Flight Controller Block

The Flight Controller model block shown in Figure 8 takes the desired trajectory or pilot commands, current vehicle states and environmental conditions and outputs the PWM signal to be sent to the vehicle dynamic model. In the vehicle dynamic model, these PWM signals are applied to the motors to run at an RPM that would further create forces and moments on the vehicle. Most sUAS flight controls use a PID based control.[6] First, longitudinal and lateral control law (Eqn. 15) is applied to control the vehicle position along its x and y axis,

$$\begin{bmatrix}\phi_c \\ \theta_c\end{bmatrix} = \begin{bmatrix}-\sin\psi & \cos\psi \\ -\cos\psi & -\sin\psi\end{bmatrix}\begin{bmatrix}(k_{x1P})e_1 + (k_{x1D})\dot{e}_1 + (k_{x1I})\int_0^t e_1 t \\ (k_{x2P})e_2 + (k_{x2D})\dot{e}_2 + (k_{x2I})\int_0^t e_2 t\end{bmatrix} \qquad \text{Eqn. 15}$$

where $e_1 = x - x^{desired}$; $e_2 = y - y^{desired}$; $\dot{e}_1 = u - u^{desired}$; $\dot{e}_2 = v - v^{desired}$; k_{x1P}, k_{x2P}, k_{x1D}, k_{x2D}, k_{x1I}, k_{x2I} are the proportional, differential and integral constants. Next, the altitude and attitude control law (Eqn. 16-19) is applied to control the vehicle altitude and attitude,

$$T = mg + \left[(k_{x3P})e_3 + (k_{x3D})\dot{e}_3 + (k_{x3I})\int_0^t e_3 t\right] \qquad \text{Eqn. 16}$$

$$M_\phi = -\left[(k_{\phi P})e_4 + (k_{\phi D})\dot{e}_4 + (k_{\phi I})\int_0^t e_4 t\right] \qquad \text{Eqn. 17}$$

[6] Fahimi, F., Autonomous robots: Modeling, path planning, and control, Springer, New York, Nov 2008, Chapter 10.

$$M_\theta = -\left[(k_{\theta P})e_5 + (k_{\theta D})\dot{e}_5 + (k_{\theta I})\int_0^t e_5 t\right] \quad \text{Eqn. 18}$$

$$M_\psi = -\left[(k_{\psi P})e_6 + (k_{\psi D})\dot{e}_6 + (k_{\psi I})\int_0^t e_6 t\right] \quad \text{Eqn. 19}$$

where $e_3 = z - z^{desired}$; $e_4 = \varphi - \varphi_c$; $e_5 = \theta - \theta_c$; $e_6 = \psi - \psi^{desired}$; $\dot{e}_3 = w - w^{desired}$; $\dot{e}_4 = p$; $\dot{e}_5 = q$; $e_6 = r$; k_{x3P}, $k_{\varphi P}$, $k_{\theta P}$, $k_{\psi P}$, k_{x3D}, $k_{\varphi D}$, $k_{\theta D}$, $k_{\psi D}$, k_{x3I}, $k_{\varphi I}$, $k_{\theta I}$, $k_{\psi PI}$, are the proportional, differential and integral constants, respectively. The thrust and the moment values above are the desired values that the vehicle must attain to follow the trajectory. The desired individual motor thrust and torque values are obtained from the total thrust and moment values by using Eqn. 11 and 13. Next, the desired angular velocity values for each motor are calculated. Angular velocities are further converted to PWM based on a factor that is calculated during thrust stand testing. The control model then sends these PWM signals to the Airframe model to simulate thrust and moment generation by each motor/rotor pair.

The Environmental block shown in Figure 9 uses the current vehicle altitude to estimate the gravity, pressure, density and wind velocity values. The wind speed and direction measured at the nearest weather station is fed into a Simulink wind shear model based on military specification MIL-F-8785C to estimate wind velocities at different heights[7]. Figure 10 depicts how wind varies with altitude for seven different wind conditions at 20 feet altitude. The legend of this plot provides the wind velocity values at 400 feet altitude for the seven different wind conditions at 20 feet above ground level (AGL). Gravity is estimated using 1984 World Geodetic System (WGS84) representation of Earth's gravity[8]. Atmospheric values are estimated using the mathematical representation of the U.S. standard atmosphere as defined in the 1976 Committee on Extension to the Standard Atmosphere (COESA) model.

[7] U.S. Military Specification MIL-F-8785C, 5 November 1980.
[8] NIMA TR8350.2: "Department of Defense World Geodetic System 1984, Its Definition and Relationship with Local Geodetic Systems."

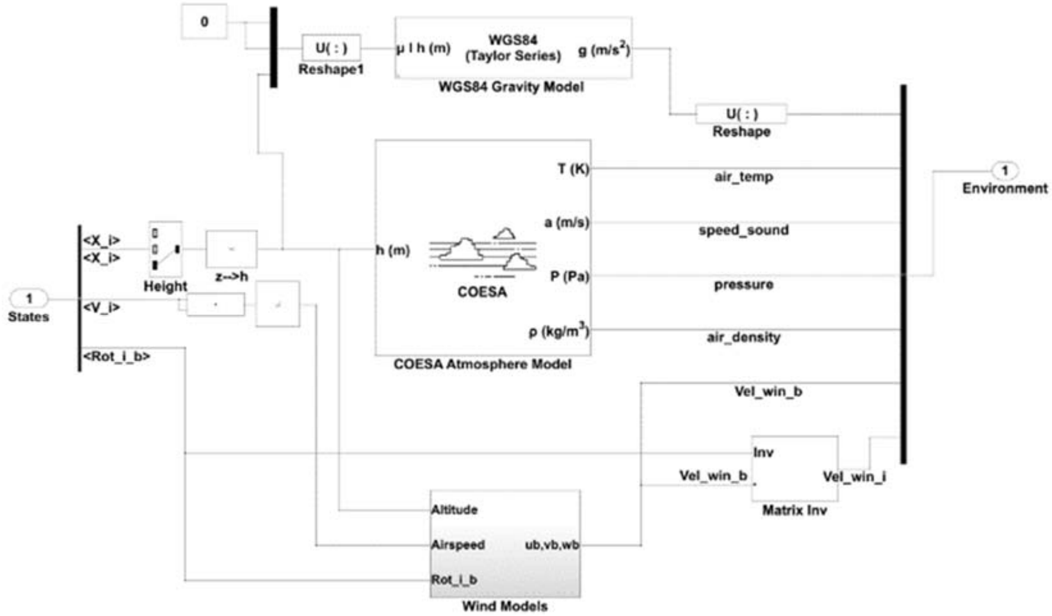

Figure 9. Environmental Block Estimating Gravity, Density, and Wind

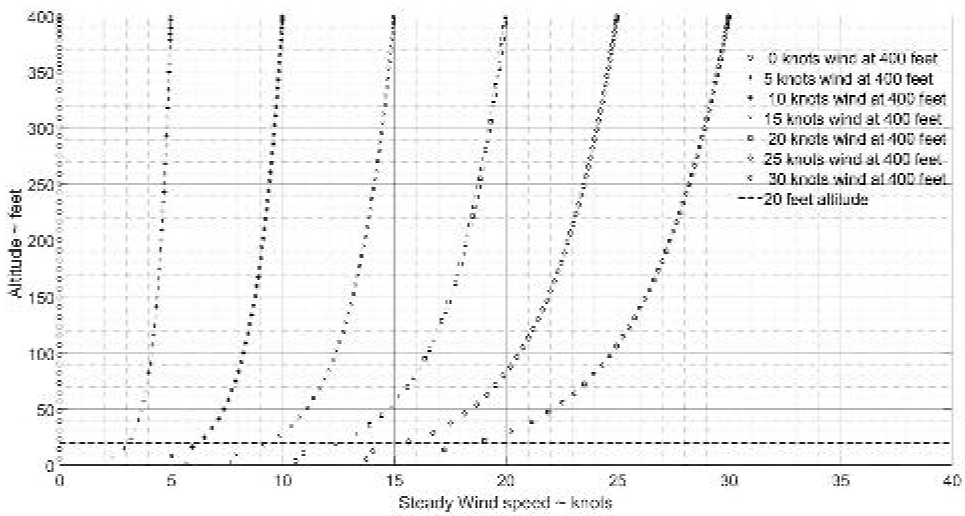

Figure 10. Wind Shear versus Altitude Model (MIL-F-8785C)

In the Failure block, fifteen types of failures are defined for a quadrotor sUAS. When the Simulink® model is replicating flight tests, a failure type is chosen to match the flight test failure. When Monte Carlo simulations are performed, the model picks any of the fifteen failure cases based on either a random, normal, or even distribution.

The desired state block outputs the desired value of position and yaw that is needed by the control model block. This block can also take the desired velocities and convert them to the desired position at every time step to feed to the control block. When failure is forced in the Simulink® model, the desired state block is defined to output the last known desired position of the vehicle to the control block in an attempt to hold position and altitude. If trajectory-tracking is enabled, the desired state block outputs the pre-defined trajectory to the control block even after a failure. When Monte Carlo simulations are performed, the desired block can output different values of desired position (or velocity) and heading for each simulation.

2.2.3 Fixed Wing sUAS Dynamic Modeling Method

The schematic outline of the fixed wing Simulink® model is same as for the multirotor aircraft. The desired state and environmental blocks are defined in the same way. The failure block is now defined to simulate power-off failures and actuator stuck failures. The major difference between the fixed wing and multirotor models are the control and dynamic models.

As shown in Figure 6, the Force and Moment calculations block calculates the forces and moments on the vehicle due to gravity, rotor thrust and torque, and vehicle aerodynamic forces and moments. Equations 20 and 21 define the components of the forces and moments fed to the 6DOF Euler block,

$$F_B = T^B + {F_{XYZ}}^B + R_{BI}W \qquad \text{Eqn. 20}$$

$$M_B = {M_{XYZ}}^B + \ Q^B \qquad \text{Eqn. 21}$$

where W (=mg) is the weight of the vehicle. T^B and Q^B are the motor/rotor thrust and torque, respectively, as defined in Eqn.11, 22 and 23. ${F_{XYZ}}^B$ and ${M_{XYZ}}^B$ are the aerodynamic forces and moments that are calculated from ${F_{XYZ}}^B = \frac{1}{2}\rho V^2 S \begin{bmatrix} CF_x \\ CF_y \\ CF_z \end{bmatrix}$ Eqn. 22 and ${M_{XYZ}}^B = \frac{1}{2}\rho V^2 Sc \begin{bmatrix} CM_x \\ CM_y \\ CM_z \end{bmatrix}$ Eqn. 23.

$${F_{XYZ}}^B = \frac{1}{2}\rho V^2 S \begin{bmatrix} CF_x \\ CF_y \\ CF_z \end{bmatrix} \qquad \text{Eqn. 22}$$

$${M_{XYZ}}^B = \frac{1}{2}\rho V^2 Sc \begin{bmatrix} CM_x \\ CM_y \\ CM_z \end{bmatrix} \qquad \text{Eqn. 23}$$

where ρ, V, S, and c are density, vehicle speed, surface area and chord length, respectively. The six force and moment coefficients are to be estimated as shown in Figure 11. The Datum Coefficients sub-system block estimates the force and moment coefficients of the vehicle at a given angle of attack and sideslip only. This sub-system contains the derivatives of coefficients with respect to angle of attack and sideslip that are estimated from either OpenVSP or flight testing.

The Actuator Increments Coefficients sub-system block estimates the force and moment coefficients of the vehicle due to control surface deflections only. This sub-system contains the derivatives of coefficients with respect to aileron, elevator and rudder deflections that are estimated from either OpenVSP or flight testing. The Body Rate Damping Coefficients sub-system block estimates the force and moment coefficients of the vehicle due to body roll, pitch and yaw rate, respectively. This sub-system contains the derivatives of coefficients with respect to body roll, pitch and yaw rate, respectively, that are estimated from either OpenVSP or flight testing.

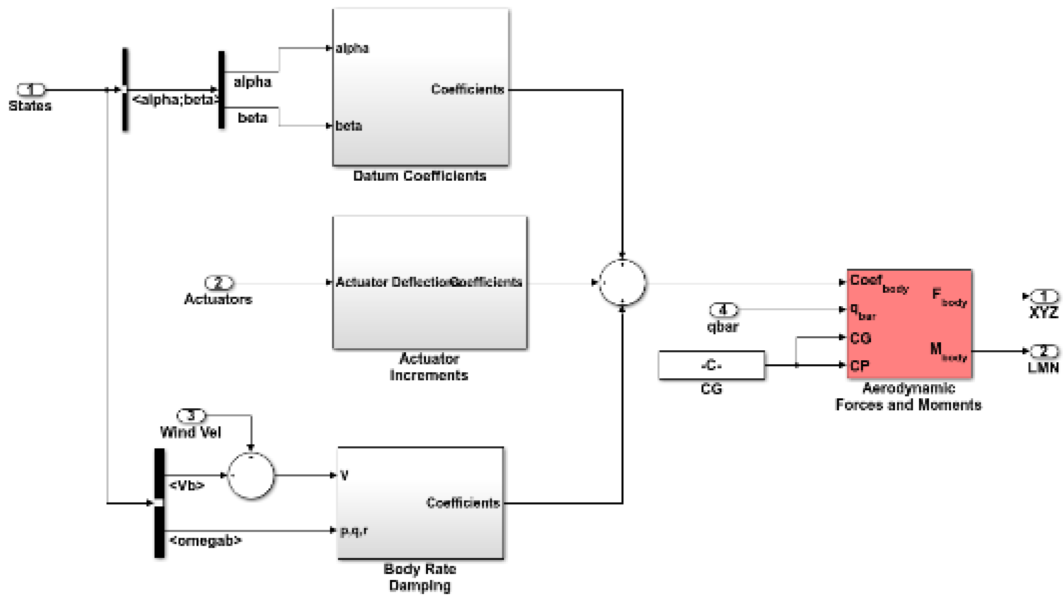

Figure 11. Fixed Wing Force and Moment Model Blocks

The outer loop-inner loop PID is used for longitudinal and lateral control as shown in Figure 12. The longitudinal control involves an outer loop to control altitude and an inner loop to control pitch angle. The output of the longitudinal control is the required elevator deflection. The lateral control involves a single loop to control heading. The output of the lateral control is the required aileron and/or rudder deflection. Thrust control is achieved by a single PID controller to achieve desired speed by outputting the desired PWM signal to the motor. The individual control blocks modeled for eBee+ model are shown in Figure 13.

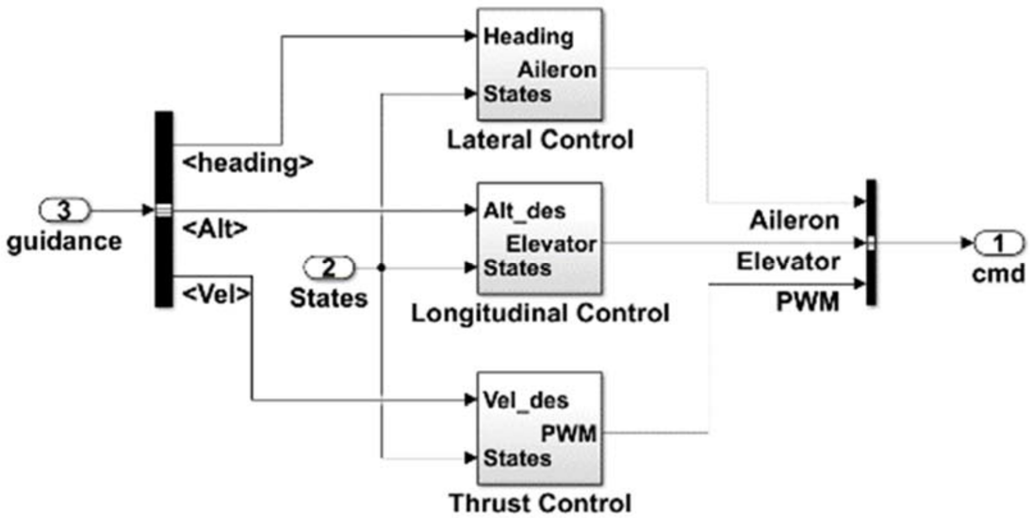

Figure 12. PID Control Block of a Fixed Wing sUAS

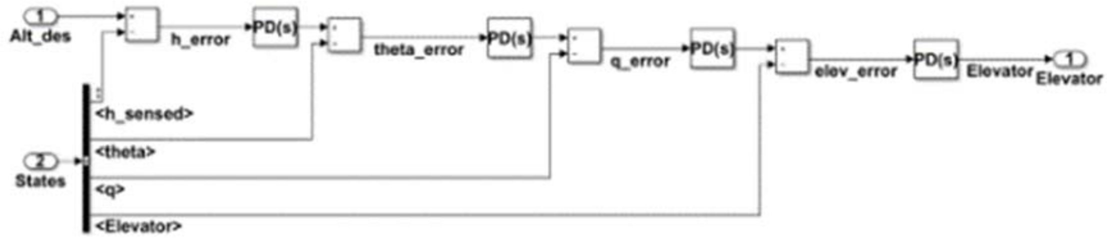

1. Longitudinal Outer Loop-Inner Loop PID Control

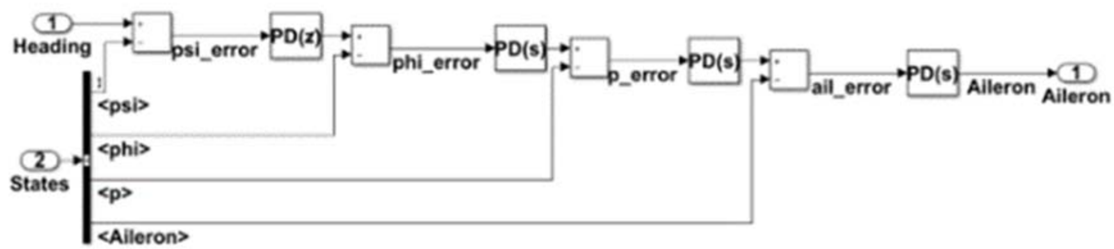

2. Lateral PID Control

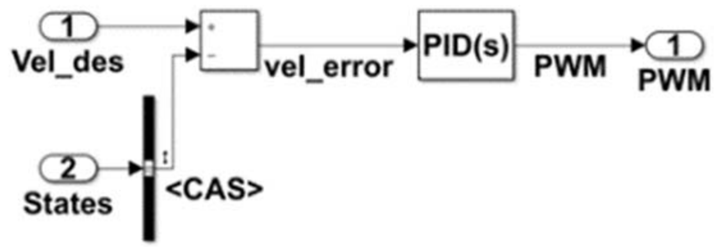

3. Thrust PID Control

Figure 13. Longitudinal, Lateral and Thrust PID control on the eBee sUAS

2.3 Simplified Test Method

The objective of the UAH simplified testing was to evaluate worst-case impact orientations by completing a set of 25 ft/s and 36 ft/s impacts (conducted from 10 ft and 20 ft vertical drops), for aircraft weighing less than 3 lbf, to determine the stiffest impact orientation. For aircraft weighing 3 lbf and over, the impacts are completed at 20 ft-lbf and 40 ft-lbf. The heavier group of aircraft was limited to 20 ft-lbf and 40 ft-lbf, because these aircraft are capable of generating significantly more KE at 25 ft/s and 36 ft/s than the lighter aircraft. The intent of the simplified test is to determine aircraft injury potential based on low velocity/energy impacts. All of the simplified tests involve vertical impacts to the top of the ATD head, with the resultant head acceleration being used to determine the stiffest impact orientation of the aircraft. Higher peak resultant acceleration indicates greater energy transfer to the head and less deformation of the aircraft during impact. This is used to identify the relative stiffness of the vehicle in any given impact orientation.

2.3.1 Test Apparatus

The UAH test apparatus consists of a 50th percentile male Humanetics Hybrid III ATD head and neck rigidly mounted to a based plate (Figure 14), a vertical drop mechanism, data collection system and high-speed cameras. UAH's data acquisition system consisted of a National Instruments (NI) PXIe-8821 computer, PXIe-107 4-slot chassis, and three PXIe-4300 8-channel, 250 ks/s, 300V analogue input modules and associated terminal blocks. Based on the rigidity of the simplified test apparatus, the team used 250 kHz per channel sampling to avoid signal aliasing due to high frequency content in accelerometer data. The UAH high-speed cameras are Sony DSC-RX100M5 Cyber-shot digital cameras capable of taking videos at 920 frames per second. The load cells and accelerometers in the dummy were used to measure Head Acceleration (g), Head Injury Criteria (HIC_{15}) , Upper Neck Tension (lbf), Upper Neck Compression (lbf), Upper Neck Flexion (lbf-ft), Upper Neck Extension (lbf-ft), Upper Neck Shear (lbf), and Upper Neck N_{ij}[9]. Upper Neck Injury Criteria (N_{ij}) is a derived term that normalizes measured loads and moments by the maximum acceptable values, such that values for Neck Injury Criteria fall between 0 and 1. Table 7 shows the instrumentation used in the UAH simplified testing apparatus.

Figure 14. UAH Simplified Testing Apparatus

[9] Eppinger, R., Sun, E., Kuppa, S., *Supplement: Development of Improved Injury Criteria for Assessment of Advanced Automotive Restraint Systems – II*, National Highway Traffic Safety Administration, Washington DC, March 2000

Table 7. FAA Hyrbid III ATD Instrumentation Used in the UAH Impact Testing

Type	Location	Signal/Direction
Accelerometer	ATD Head CG	A_x
		A_y
		A_z
Angular Rate Sensor	ATD Head	R_x
		R_y
		R_z
Force/Moment Load Cell	Upper Neck	F_x
		F_y
		F_z
		M_x
		M_y
		M_z
Laser Velocity Gate	Adjacent to Head	Impact Velocity

The simplified impact test drop apparatus is a vertical drop stand designed to impact aircraft on the top of a Humanetics Hybrid III head/neck assembly. The test apparatus is designed to be a low cost structure that can be fabricated from common materials and tools that can accommodate impact heights up to 22 feet of travel between the aircraft and the top of the head. The test apparatus consists of 4 major components: upper support structure, lower support structure, sled, and the head assembly mount. A detailed description of the test stand, drawings, pictures, and cost estimate for equipment, materials, and supplies to assemble the test stand is contained in Appendix C. The appendix includes a discussion of lessons learned and improvements that can be made to the drop stand. The total cost of the test stand was approximately $54,500.00. These costs include in excess of $35,000 for an ATD Hybrid III head and neck, $16,800 for a National Instruments data acquisition system, $1,400.00 for MiniTech extrusions and hardware, and roughly $950.00 in additional materials and supplies.

2.3.2 UAH Test Matrix Overview

UAH conducted over 80 aircraft failure flight tests with 78 tests for record. The flight test aircraft used in this study were the following: the DJI Inspire 2 with logging of rate of descent under a Vendor 2 parachute recovery system, the DJI Mavic Pro, DJI Phantom 3, DJI S800 with a logging of rate of descent under a Vendor 2 parachute recovery system, the Go Pro Karma, The DJI Inspire 1, Vendor 1 Quadrotor, Vendor 3 Quadrotor, and the eBee+ fixed wing aircraft. The multirotor flight tests were used to determine terminal velocity in vertical fall, flat plate drag area based on angle of attach, and post-failure vehicle dynamics. The eBee+ fixed wing flight tests were used to determine aircraft peak velocities after failure, and stall, roll and spin dynamics.

The simplified testing conducted by UAH included 162 record tests and 50+ calibration tests. Based on schedule limitations and, most importantly, limited test article availability, 27 test points were deleted. UAH deleted test points due to lack of available test articles so more test articles could be provided for the NIAR full ATD impact tests and OSU PMHS tests. The articles used in the record tests were the DJI Mavic Pro, DJI Phantom 3, DJI S800, Go Pro Karma, Vendor 1 Quadrotor, Vendor 3 Quadrotor, eBee Standard, eBee+, Nano Talon fixed wing, Radian fixed wing, Skyhunter fixed wing, Steel Core Foam Block, Aluminum Core Foam Block, Wood Block , DJI Phantom 3 Battery, and a Panasonic SLR Camera. The key outputs for this testing were the aircraft/object impact speed, impact orientation, impact KE, vehicle configuration, vehicle weight, ATD head linear acceleration, ATD head rotational rates, and ATD upper neck forces and moments. UAH recorded high frame rate video (920 frames per second) of all impact tests. UAH used calibration tests to verify the drop heights needed to attain required impact velocities and verify drop sled release mechanism function to ensure correct impact orientation during record tests.

2.4 ATD Test Method

2.4.1 Test Apparatus

The National Institute of Aviation Research (NIAR) at Wichita State University conducted the initial worst-case impact orientation analysis and higher speed impacts in the worst-case orientation. The NIAR test apparatus consists of a seated full FAA 50th percentile male Humanetics Hybrid III ATD (Figure 15), an aircraft launch mechanism, and high-speed cameras. Load cells and accelerometers in the dummy were used to measure Head Acceleration (g), Head Injury Criteria (HIC_{15}), Upper Neck Tension (lbf), Upper Neck Compression (lbf), Upper Neck Flexion (ft-lbf), Upper Neck Extension (ft-lbf), Upper Neck Shear (lbf), and Upper Neck N_{ij}. NIAR's head and neck instrumentation is the same as the UAH Head and Neck instrumentation (Table 7). Refer to the Annex B Report from NIAR for a complete description of the ATD test setup.

Figure 15. Hyrid III 50th Percentile Male ATD

2.4.2 NIAR Test Matrix Overview

NIAR conducted 136 tests, 112 of which were for record. NIAR conducted impact testing using the DJI Inspire 2 at parachute impact velocities and angles, DJI Mavic Pro, DJI Phantom 3, Go

Pro Karma, the Vendor 1 Quadrotor, the Vendor 3 Quadrotor, and the eBee+ fixed wing aircraft. NIAR also conducted impact testing using a Wood Block, Steel Core Foam Block, and the DJI Phantom 3 Battery. The key outputs for this testing were the aircraft/object impact speed, impact orientation, impact KE, vehicle configuration, vehicle weight, ATD head linear acceleration, ATD head rotational rates, and ATD upper neck forces and moments. NIAR also conducted calibration impact tests with the DJI Phantom 3 and eBee+ against aluminum sheets to generate FEA model calibration data.

The NIAR testing was done in order to collect injury estimate data for the various aircraft at or near terminal velocity, at realistic impact trajectories based on UAH's failure flight test data, and in the worst case impact orientations. NIAR collected peak resultant acceleration data for the ATD head in a variety of impact angles with respect to the ATD head to assess head and neck injury potential based on impact location (top, front, and sides of head). The NIAR data enabled assessment of injury potential related to peak resultant acceleration, neck compression, AIS ≥ 2 skull fracture, AIS ≥ 2 head injury based on 15 ms Head Injury Criteria, AIS ≥ 3 head injury based on Head Injury Criteria, AIS ≥ 3 Neck Injury, 3ms minimum g-loading, Brain Injury Criteria (BrIC), and Combined Probability of Concussion[10]. NIAR's data served as a reference point for evaluating the UAH data outputs to evaluate the simplified test approach and to serve as a common point for modeling when comparing the OSU PMHS test outputs against automotive and sports medicine injury risk curves.

Three parachute descent impacts were conducted at NIAR with the Inspire 2 with only one test conducted on the PMHS. The two vertical impacts represent the no wind descent conditions of 9 ft/s and 15 ft/s and bracket the average descent condition of 12 ft/s seen during flight test. The angled condition was conducted to replicate an impact during descents with 20 kt winds which is based on modeling conducted after flight test data was post-processed. The NIAR angled impact test was conducted at 30 ft/s with a 20 deg impact angle and the DJI Inspire 2 orientation representing the same impact orientation as if hanging from the Vendor 2 72-inch Parachute System when descending in a 20 kt wind. The PMHS test orientation was conducted at 30 ft/s in a horizontal impact due to limitations of the OSU launcher. Both angled impacts were conducted in a side impact condition to assess both neck injury potential and skull fracture injury potential due to the minimal number of tests conducted in parallel with other tests.

Comparison of UAH simplified testing results and NIAR full ATD impact test results was done in two different ways. When data sets had enough repeated test points to estimate the UAH experimental error, all of the NIAR test data regardless of impact angle with respect to the head was compared with the UAH 95% confidence intervals. All of the UAH upper 95% confidence intervals have slopes of up to 1.48x the slope of UAH's vertical impact test data curve fits. For data sets without enough repeated test points, the NIAR impact test data was compared with a the UAH data set curve fit and a factor of safety line with a slope 1.5x that of the UAH curve fit. That was used as a surrogate for the upper 95% confidence interval.

[10] Rowson, Steven, and Stefan M. Duma. "Brain injury prediction: assessing the combined probability of concussion using linear and rotational head acceleration." *Annals of biomedical engineering* 41.5 (2013): 873-882.

The full test matrix for UAH and NIAR test points is found in Appendix A of the FAA Task A14 Cover Letter.

3 RESULTS

3.1 Small UAS Flight Testing

3.1.1 Results Overview

The flight test effort was executed in order to collect aircraft post-failure state data that was used to estimate aircraft aerodynamic coefficients for use as model inputs. The flight testing also determined if each vehicle had a predictable dynamic response to failure, for example the Vendor 1 Quadrotor aircraft tended to roll over and fall inverted. Following partial failures, all vehicles tumble because the remaining motors still function. For illustration purposes, moderate tumbling is defined as 2-4 rotations before the parachute is deployed, and severe tumbling is defined as greater than 4 rotations before the parachute is deployed.

In some of the flight tests, it was observed on several aircraft from various vendors that the motors began to spin during freefall after a simultaneous total aircraft motor failure, regardless if the failure was initiated by PWM based failures or via relay on the ESC power. This observation was made audibly approximately 1-2 seconds into the freefall. The motors would stop spinning once the parachute was deployed. This was not observed on any of the other failure modes due to the sound of the other motors remaining powered during the free-fall. The hypothesis is that during the simultaneous total aircraft motor failures, the aircraft remains level during the freefall with the propellers oriented perpendicular to the wind vector, creating inflow that causes the propellers to spin in reverse. UAH conducted laboratory bench tests using an electric leaf blower to generate the flow through the propeller and a thrust stand to measure RPM, voltage, and current. When the wind vector was aligned perpendicular to the propeller, the propeller did spin in reverse and was capable of spinning up to several thousand RPM depending on the magnitude of the wind velocity. The propeller rotation would stop immediately when the wind was removed. The propeller was very noisy spinning in reverse, similar to the sound a propeller would make spinning in the correct direction at high RPM when powered by a motor. There was no measured voltage or current generated during the lab tests, however that could be a result of inadequate measurement equipment for this type of testing. Until further testing can be made to characterize this behavior, the assumption is made that this is an aerodynamic phenomenon independent of aircraft electrical components or software. It is not possible to attribute any sudden changes in vertical velocity slope during the freefall to the motors spinning because there are also changes in aircraft angle of attack during the same time history. Further experimental testing would need to be performed to determine the cause and effect relationship to sudden changes in vertical velocity slope during freefall after a simultaneous total aircraft motor failure.

3.1.1.1 DJI Phantom 3 Standard

In six of the eight DJI Phantom 3 standard flight tests, the DJI proprietary controller was used. For the remaining two flight tests, a Pixhawk autopilot was used. During the four motor failure at hover flight test, the vehicle falls in an upright position with slight roll and pitch moments. Following the four motor failure at stabilized forward speed flight test, the vehicle gradually flips once or twice. During one motor failure tests, the remaining motors are still ON and produce thrust as commanded by the controller. The vehicle tumbles severely following the single motor failures. During two-motor on-axis failure tests, the functioning motors maintain partial roll and pitch control, however, the vehicle yaws severely. During two motors off-axis failure tests, the remaining motors continue to function causing severe tumbling. Appendix C contains a summary of flight test and modeling plots.

3.1.1.2 Vendor 1 Quadrotor

Information about the Vendor 1 flight controller behavior was available from the manufacturer. The stock configuration Vendor 1 vehicle shuts off all four motors if its sensors measure a high pitch or roll angle (> 50 deg). For the test flight vehicles, the Vendor 1 proprietary controllers were replaced with Pixhawk controllers. The failure board integrated on the vehicle commands failures based on overriding the flight controller PWM signals sent to the ESCs. To replicate the high pitch or roll angle-based motor shutoff of the stock controller, the failure board commands full motor shutoff 0.5 seconds after the first failure command is given. The Vendor 1 vehicle was the only flight test aircraft configured to shut off all motors following the initial failure.

During a fall, the Vendor 1 quadrotor consistently flips once or twice and then stabilizes in an inverted position. This happened during all eight failure tests, for both cage-off and cage-on configurations. During four motor and two motor on-axis failures, the vehicle mostly flips only once and stabilizes in an inverted position. During the one motor and two motor off-axis failures, the vehicle flips several times before stabilizing in an inverted position. The aircraft is rotating to its most stable position as it falls. The rotors are located under the XY plane of the Vendor 1 vehicle, which means that the Center of Pressure (CP) is below the Center of Gravity (CG). The Vendor 1 aircraft inverts and achieves equilibrium with the CG below the CP.

The lower portion of Figure 16 provides a time history of the Vendor 1 cage-off, off-axis two-motor failure which was initiated from a hover. During the first 0.5 seconds, the remaining functioning motors create high moment that leads to tumbling. After the four motors are turned off, the vehicle gradually stabilizes into an inverted position in 2 seconds. The flat plate drag area of the Vendor 1 vehicle in the horizontal plane is half of what it is in the vertical plane. As the vehicle tumbles, its flat plate area is lower and the vehicle falls faster with an increasing acceleration. When the vehicle begins to stabilize in a level position, the flat plate drag area begins to increase, and a deceleration is observed. This behavior is clearly observed by plotting the Vendor 1 cage-off vehicle angle of attack and the vehicle resultant velocity as seen in Figure 16. The results from Vendor 1 cage-off four motor failure at hover and two motor off-axis failure at maximum stabilized forward velocity are shown here to show how the aircraft consistently rolls inverted under different failure scenarios. If the angle of attack is positive, the vehicle is in upright position. If the angle of attack is negative, the vehicle is in an inverted position. In the top plot of Figure 16, the vehicle maintains upright position until 4.5 seconds and then flips. The velocity of the vehicle remains stable between 2 and 4 seconds but increases as the vehicle flips. In the bottom plot of Figure 16, the vehicle tumbles severely because of the two functioning motors that are off-axis. Though all motors are turned off at 0.5 seconds, the vehicle flips eight times and then stabilizes in an inverted position. The vehicle speed steadily increases as the vehicle tumbles but reduces once the vehicle reaches a stable position where the drag is now maximum. The jagged nature of the plot is because of the fact that when the vehicle flips, its angle of attack changes from 180º to -180º or vice-versa. Appendix B contains plots of the flight test and modeling.

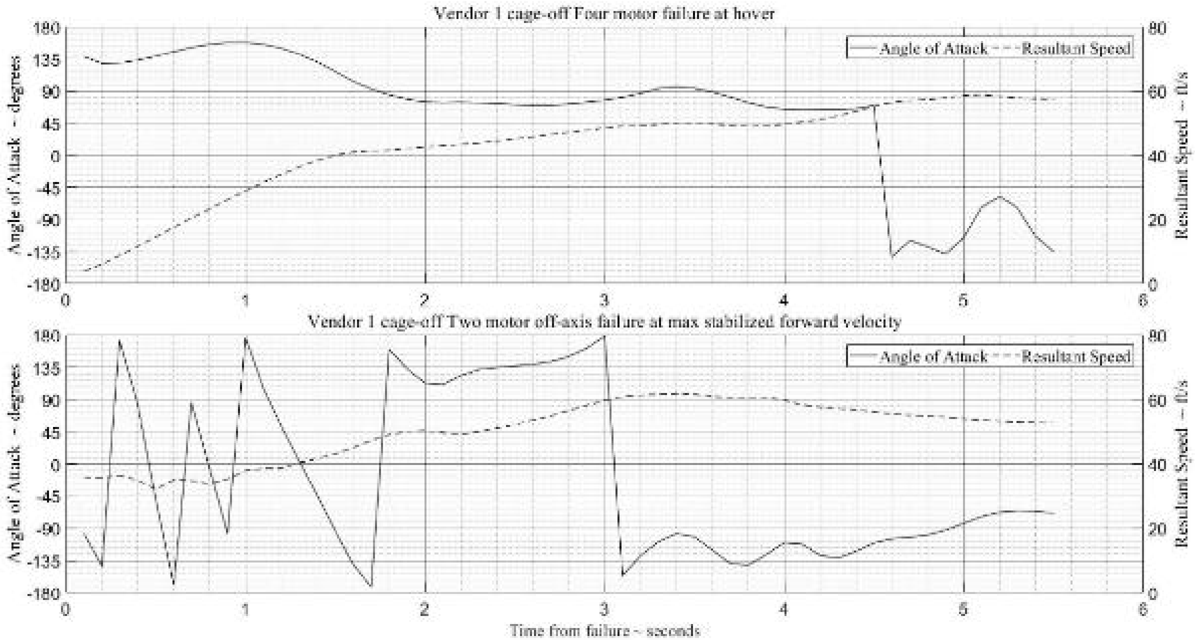

Figure 16. Angle of Attack and Resultant Velocity Time History for Vendor 1 Vehicle with Cage-Off

3.1.1.3 Sensefly eBee+

During the power-off failure mode with no lateral inputs, the vehicle descends to a lower altitude and slowly loses airspeed. Three tests of the same failure case were conducted and during these three trials, the vehicle behaved the same. Two of these trial tests recorded data for about 15 seconds. Just before the pilot restarts the motors and gains control of the vehicle, the aircraft appears to stall. The aircraft dives down, losing horizontal velocity but gaining vertical velocity quickly. The angle of attack remains approximately same during the fall except for the last three seconds where the vehicle appears to reach stall.

During the power-on, max-roll failure flight test, the vehicle rolls along its x-axis for the first seconds before it also begins to spin about its z-axis. Several seconds into the failure, the roll affects the yaw motion. Two trial tests of this failure case were performed and they both behaved similarly. These trial tests recorded data for about 6 seconds prior to pilot recovery of the aircraft. The vehicle initially loses it velocity and accelerates as it descends. The vehicle angle of attack and sideslip angle continuously oscillate between ±20º with a time period of 1 second.

During the power-on, pitch down failure flight test, the vehicle pitches down into a loop. Each loop takes approximately 4 seconds. Two trial tests of this failure case were performed and they both behave similarly for eight seconds before the pilot regains full control. The vehicle angle of attack and side-slip oscillate between ±20º with a time period of 4 seconds.

Finally, during the power-on, pitch-up failure flight test, the vehicle initially pitches up and gains vertical velocity and altitude. However, after a second, the vehicle pitches down and begins to lose altitude. During this descent, the vehicle rolls and spins. The vehicle velocity, on average, increases and the aircraft exhibits a descending phugoid motion with associated periodic accelerations and decelerations. Only one trial test was performed for this failure and data was recorded for 9 seconds. The vehicle angle of attack gradually increases and oscillates between ±180º and the side-slip oscillates between ±80º.

3.1.1.4 DJI Mavic Pro

The DJI Mavic Pro controllers are more advanced than the DJI Phantom 3 standard because they exhibit some post-failure control behavior that is different from the DJI Phantom 3 standard. Following a one-motor failure, the vehicle did not lose altitude rapidly nor did it tumble. The vehicle maintained its level position with small roll and pitch disturbances. After 3 seconds, all four motors were shut off before deploying the parachute. The stock DJI controller may have a control response designed to prevent sudden loss of altitude. This behavior was observed only for the one-motor failures. For two-motor failures, the thrust from the two remaining motors may be insufficient to maintain level position. During the four-motor failure and the two motor on-axis failure at hover, the vehicle flips once or twice only, but during the four-motor failure and two motor off-axis failure at maximum stabilized forward speed, the vehicle exhibits moderate tumbling. During the two-motor off-axis failures, the vehicle is seen to tumble severely.

Next, due to the physical construction of the DJI Mavic Pro, which is more compact than the DJI Phantom 3, the vehicle resultant speed after 3 seconds is higher than that of DJI Phantom 3. The average resultant speed of the DJI Phantom 3 and DJI Mavic Pro vehicle, based on the eight flight tests, is 60 ft/s and 66 ft/s. Also, the external data logger and failure board attached near the CG of the DJI Mavic Pro increases its mass by 50%. The DJI Mavic Pro at nominal configuration would fall slower than the test vehicle and reach lower speeds. It was assumed that the vertical planform flat plate drag area of the test flight vehicle does not vary substantially from its nominal configuration since the payload was tightly packed closer to the CG. Appendix 156 contains plots of the flight test and modeling.

3.1.1.5 DJI S800

The DJI S800 was flown in the flight test configuration using the stock configuration DJI flight controller. The failure board was integrated between the flight controller PWM outputs and the ESC PWM inputs to initiate PWM based failures. The camera gimbal was removed and the Vendor 2 parachute system was mounted horizontally on the camera gimbal support rails. The data logger was mounted externally on the top of the aircraft forward of the aircraft's GPS receiver.

3.1.1.6 DJI Inspire 2

The DJI Inspire 2 was flown in the flight test configuration using the stock configuration DJI flight controller. Since the DJI Inspire 2 uses a different communication protocol between the flight controller and ESCs than PWM, a relay was installed on the positive DC wire between the battery and each ESC to initiate the failures. The failure board and relays were mounted externally on each motor arm. The data logger was mounted externally on the bottom of the aircraft behind the camera gimbal. The Vendor 2 parachute system was mounted horizontally on the right arm. The GPS receiver for the data logger was mounted externally on the top of the aircraft, forward of the aircraft's GPS receiver.

3.1.1.7 DJI Inspire 1

The DJI Inspire 1 was flown in the flight test configuration using the stock configuration DJI flight controller. Since the DJI Inspire 1 uses a different communication protocol between the flight controller and ESCs than PWM, a relay was installed on the positive DC wire between the battery and each ESC to initiate the failures. The failure board and relays were mounted externally on each motor arm. The data logger was mounted externally on the bottom of the aircraft behind the camera gimbal. The GPS receiver for the data logger was mounted externally on the top of the aircraft, forward of the aircraft's GPS receiver. The parachute was mounted externally on the top of the aircraft with an elastic strap securing it to the parachute release servo. The parachute release servo was mounted externally on the aft, left side of the aircraft next to the battery.

3.1.1.8 GoPro Karma

The GoPro Karma proprietary controller was replaced by a Pixhawk controller to log data as well as fly the vehicle. Following a one or two-motor failure, the remaining motors were allowed to run as commanded by the controller.

Its behavior was expected to be similar to that of the DJI Phantom 3, however, during initial four motor failure tests, the GoPro Karma motors would turn back on during the descent even though all four motors were turned off when the failure was forced. This phenomena was described in Paragraph 3.1.1.

During four motor failure at a hover, after initial oscillations, the vehicle begins to stabilize in its maximum drag area attitude, which is an upright level attitude. This increased drag decelerates the vehicle to a lower resultant velocity than is observed during tumbling. The re-start of the motors do not significantly accelerate or decelerate the vehicle. It is assumed that the motors operate at a minimum thrust condition.

Similar to the Vendor 1 vehicle, following a four-motor and two-motor on-axis failure, the vehicle gradually flips and maintains this position until the parachute is deployed 3 seconds after failure. Following the one-motor failure at maximum stabilized forward velocity and the two motor off-axis failures, the vehicle tumbles severely but then stabilizes before parachute is deployed. The effect of this is clearly seen in the flight test plots, in APPENDIX B – FLIGHT TEST AND MODELING PLOTS, where the vehicle decelerates after 2 seconds. Following the one motor failure at hover, the vehicle continues to tumble severely until the parachute is deployed.

3.1.1.9 Vendor 3 Quadrotor

The Vendor 3 Quadrotor was flown in the flight test configuration using the stock configuration flight controller. The failure board was integrated between the flight controller PWM outputs and the ESC PWM inputs to initiate PWM based failures. The camera payload was removed and the data logger and failure board was mounted in the space previously occupied by the camera payload.

A modified Opale ST60-X parachute recovery system was installed on a custom interface mount on the front of the aircraft with the parachute launcher aligned vertically. The stock Opale parachute release mechanism was replaced with a custom RSESC release mechanism to provide more reliable deployments.

The Vendor 3 Quadrotor is integrated with the Pixhawk Controller and its post-failure behavior was similar to other vehicles that also used the Pixhawk Controller. The data logger was still integrated to this vehicle to fail the motors and it also recorded the vehicle states post-failure. Due to vehicle impacting the ground following the one motor failure at hover, data from only two tests were available. The Vendor 3 Quadrotor did not tumble during the free-fall following the four motor failure at hover test flight. However, slight yawing (a 45 deg yaw over 2.5 sec) was observed from the data. Similar to many other vehicles, the motors seem to have turned back on around 2.3 sec. This was initially observed during flight testing and was later confirmed from the flight data recorder on the data logger. Following the one motor failure at hover, the remaining motors continue to spin as the controller tries to stabilize the vehicle. The three motors could not provide sufficient thrust to keep the vehicle from falling to ground. However, they reduce the descent speed of the vehicle falling down. This can be observed from the plots provided for Vendor 3 Quadrotor in APPENDIX B – FLIGHT TEST AND MODELING PLOTS.

3.1.2 Failure Flight Testing

Failure flight testing is an integral part of methods for evaluating the injury potential of aircraft and developing strategies to mitigate injury risk during operations over people. Researchers and certifying organizations need failure flight test telemetry data to design impact test points around probably impact conditions in terms of impact velocity and trajectory. Failure flight testing is essential for evaluating a vehicle's post-failure dynamic behavior to determine if the aircraft tumbles or stabilizes in a predictable orientation while falling. This, too, enables development of relevant impact test points. UAH recommends that regulators incorporate failure flight testing as a gated event prior to any impact testing in support of evaluating an aircraft for flight over people.

UAH conducted aircraft failures from a maximum altitude of 400 feet AGL in accordance with Part 107 operating limitations. Based on this altitude, most multirotor flights had 3-3.5 sec of falling aircraft state data. Longer periods of data logging would further improve the fidelity of aerodynamic analysis and follow-on failure modeling and simulation. It is recommended that failure flight testing be conducted under a Part 107 altitude waiver in order to initiate failures from at least 800 feet AGL to allow the aircraft to accelerate up to and stabilize at terminal velocity prior to recovery under a parachute.

All aircraft flight test data is impacted by winds and this is especially true with lightweight sUAS flight testing. A number of UAH's flight tests were repeated because of high winds during initial flight testing.

Conclusion: Failure flight testing is essential for evaluating a vehicle's post-failure dynamic behavior to determine if the aircraft tumbles or stabilizes in a predictable orientation while falling. Longer periods of data logging would further improve the fidelity of aerodynamic analysis and follow-on failure modeling and simulation. Flight testing must be conducted under as low of winds as possible in order to provide solid data for aerodynamic analysis. Winds and gusty conditions during flight test lead to inaccurate estimates of aircraft aerodynamic properties.

Recommendation: Testing standards should stipulate that flight testing only be conducted under light winds (less than 5 kt) as part of any multi-rotor or fixed wing failure testing used to support impact energy evaluations. Failure flight testing be conducted from at least 800 feet AGL to allow the aircraft to accelerate up to and stabilize at terminal velocity prior to recovery under a parachute.

3.2 Parachute Mitigations

3.2.1 Flight Test Results

3.2.1.1 Unplanned In-Flight Failures

S800 test flights 02, 04, 07, and 08 all experienced some form of directional loss of control while conducting the flight test experiments. The initial test site used for these flights had several large radio towers in the vicinity which likely contributed to the loss of directional control. As a result, these flights did not achieve the desired initial conditions at the time of failure for the desired test point but did provide additional data for the parachute system analysis. These in-flight failures highlight the value of using a manual parachute deployment for experimental flight testing. While the aircraft was not able to be precisely controlled back to the ground, the pilot did have marginal control in which the aircraft could be maneuvered to a safe location to shut down the motors and deploy the parachute.

S800 test flight 03 experienced entanglement of the parachute lines with the parachute canopy on the 72-inch Parachute System after deployment of the parachute. The parachute recovery system deployed successfully and the parachute did not become entangled with the aircraft, but one of the canopy shroud lines became wrapped around the parachute canopy, preventing a complete inflation of the parachute canopy. This failure was attributed to the packing method that was used in the 72-inch Parachute System. As a result, Vendor 2 identified the need for a line rigging tool to be used in the parachute packing process to mitigate the potential for line entanglement and this type of failure in the future.

S800 test flight 10 experienced an in-flight failure of 2 motors while climbing to the desired failure altitude. At approximately 60 ft altitude, motor M5 failed but the aircraft remained in stable, controlled flight. Since the aircraft was at such low altitude, the pilot made the decision to attempt a landing at the current position. Immediately after beginning the landing descent, motor M2 failed. This did not result in a loss of control either, but the pilot made the immediate decision to go to 100% throttle to gain any additional altitude before initiating the full aircraft motor shut-down so the parachute could be deployed. This was the lowest parachute deployment altitude ever tested by Vendor 2 on a S800 aircraft with a deployment altitude of 72 ft. The parachute was successfully deployed and reached the initial steady-state descent resultant velocity 1.16 seconds after deployment with an altitude loss of 34 ft.

3.2.1.2 Deployment to Initial Steady-State Descent Velocity Trends

After reducing the data, neither the horizontal velocity at the time of failure, nor the free-fall time from failure to deployment had an impact in the time between parachute deployment (T1) and inflation (T2), time between deployment (T1) and reaching steady state descent (T3), or the altitude loss between deployment (T1) and reaching steady state descent (T3) for either aircraft. Additionally, there was little difference in the averaged results between each aircraft tested. UAH grouped individual flights together based on the horizontal velocity at the time failure and then averaged. The results of the grouped flights for each aircraft, as well as the total average for each aircraft is shown below in Table 8. S800 test flight 03 was omitted from the averaged results since the parachute became entangled with the shroud lines after deployment. S800 test flight 10 was omitted from the averaged results since the steady-state duration before ground impact was small due to the low altitude deployment.

Table 8. Deployment to Initial Steady-State Descent Velocity Average Flight Test Results

Aircraft	Tests Included in Average	T1 - T2	T1 - T3		Horizontal Flight Velocity at Failure (m/s)
		Time (s)	Time (s)	Altitude Loss (m)	
S800	01, 11	0.73	1.59	18.62	0.18
S800	02, 07	0.71	2.50	16.89	2.88
S800	10	0.72	1.16	10.60	7.72
S800	05, 08, 09, 12	0.69	1.73	15.40	15.83
S800	All except 03, 04, 06, 10	0.71	1.94	16.97	
Inspire 2	01	0.61	1.47	22.55	0.05
Inspire 2	02, 03	0.58	2.41	19.36	20.43
Inspire 2	All	0.60	1.94	20.96	

3.2.1.3 Steady-State Vertical and Horizontal Velocity Trends

The average steady-state descent velocities, corresponding impact angles, and impact KE are shown below in Table 9. The S800 configured at 14.5 lbf with 4.85 kt (8.18 ft/s) wind speed had an average vertical descent rate of 11.48 ft/s and an average descent resultant velocity of 19.6 ft/s. The resulting impact angle and KE was 37.4° and 87.7 ft-lbf, respectively. The DJI Inspire 2 configured at 9.83 lbf was flown with an average wind speed of 4.6 kt (8.2 ft/s) had an average vertical descent rate of 8.9 ft/s and an average descent resultant velocity of 13.2 ft/s. Based upon these results, the zero wind impact speed used for the ATD impact tests was rounded to 9 ft/s. The test series included 4-motor failure at hover (Test 1), 4-motor failure at maximum speed (Test 2), and 1-motor failure at maximum speed (Test 3). The resulting impact angle and KE was 44.7° and 26.5 ft-lbf, respectively. Except for Inspire test flight 01, all flights had an average horizontal steady-state descent velocity greater than the wind speed reported at the time of the flight. Wind speed data was collected from Weather Underground by averaging the wind speed reported by multiple nearby weather stations at the time of flight. The Oceanview and Botanical weather stations were used for S800 test flights 01-08 weather data. The Hillside and Rabbit Creek weather stations were used for S800 test flights 09-12 and DJI Inspire 2 test flights 01-03 weather data. Each weather station used was less than 1.2 miles from the test site. The variation in reported wind speed and average horizontal velocity can be attributed to the parachute pendulum mode and well as inaccurate wind speed data collected by the weather stations due to terrain, turbulence, or other unknown measurement errors.

Table 9. Steady-State Descent Flight Test Results

Aircraft	Average Results						
	Tests Included in Average	Wind Speed (kts)	Horizontal Velocity (ft/s)	Vertical Velocity (ft/s)	Resultant Velocity (ft/s)	Impact Angled (deg)	Impact Energy (ft-lbf)
S800	1,11	4.44	15.1	12.1	19.4	39.5	89.1
	2,7	5.9792	16.4	11.5	20.3	35.2	92.7
	10	2.5456	21.6	18.7	28.9	40.5	188
	5,8,9,12	3.848	14.8	11.2	19	37.6	81.4
	All Except 3,4,6,10	4.8544	15.4	11.5	19.7	37.4	87.8
DJI Inspire 2	1	5.2	8.2	10.2	13.1	50.5	25.8
	2	4.3	11.8	8.2	14.4	34.7	32.5
	3	4.3	8.9	8.2	12.1	42.9	22.2
	All	4.6	9.6	8.9	13.2	42.7	26.8

3.2.1.4 Impact Orientation

The S800 descends under parachute in an aft-side down orientation as shown below in Figure 17. The DJI Inspire 2 descends under parachute in a nose-down orientation as shown below in Figure 18. These orientations present a larger contact area of the aircraft at impact than it would if the aircraft was suspended in a bottom-down orientation, considering the impact angles due to wind. When the wind speed is equal to or greater than vertical descent rate, the impact angle is equal to or less than 45°, assuming steady-state descent. These shallow impact angles would make it difficult to achieve a center of mass impact to the head due to the large aircraft size without first striking another part of the body. However, this impact orientation can lead to increased damage to the aircraft when it impacts the ground during normal recovery. 10 out of 12 S800 flights resulted in 1 or more broken motor arms due to impacting the ground aft-side first.

Figure 17. S800 Aft-Side Down Orientation during Parachute Descent

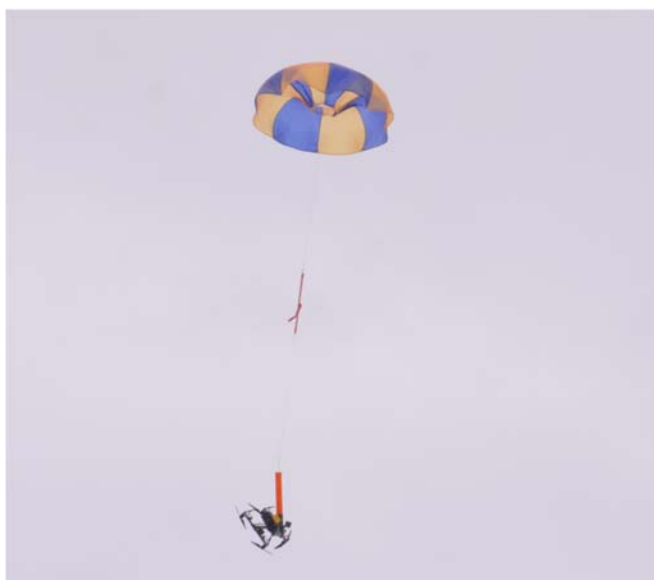

Figure 18. DJI Inspire 2 Nose Down Orientation during Parachute Descent

3.2.1.5 Motors Turning On During Free-Fall After Failure

It was observed on several of the flights in which the aircraft was allowed to free-fall for some time before the parachute was deployed that some or all of the motors would turn back on during the fall. When initially observed on the S800, it was thought that something in the RSESC failure board code or hardware was allowing the motor's ESCs to receive a non-zero throttle signal. However, this phenomenon was observed on the DJI Inspire 2 flights in which the motor failures were initiated by relays which completely disconnected the battery power to each motor's ESC. The motors would stop spinning as soon as the parachute was deployed. The current hypothesis is the inflow through the propeller during the free-fall causes the motor to spin at a high enough RPM that generates enough current to cause the ESC circuit to function in some capacity. When the parachute is deployed, the flow conditions change and cause the motors to stop spinning. Further testing will be performed to identify the mechanisms that lead to this phenomenon. However, this is not a concern for the commercial Nexus I2 parachute system as it is designed to deploy immediately after a failure where the aircraft does not free-fall for any significant amount of time.

3.2.2 Comparison of Parachute Deployment Methods

Parachute recovery systems were installed on each aircraft used in an attempt to preserve the aircraft and data logger when conducting failure test flights. Three types of parachute deployment systems were used during the flight test program based on the physical space available on each aircraft. The parachute deployment system selected for each aircraft was one that would minimize the increase in projected cross-sectional area of the aircraft with the parachute system integrated. This is important because the projected cross-sectional area of the aircraft affects the aircraft's freefall dynamics, which is used to estimate the aircraft's flat plate drag area for the dynamic modeling effort.

3.2.2.1 Elastic Retention Strap Deployment System

An elastic retention strap with a servo release was used as the deployment mechanism for the DJI Mavic, GoPro Karma, and Vendor 1 aircraft. In all cases, the parachute was mounted on the top of the aircraft. This parachute deployment system was used successfully in all failure modes tested for the DJI Mavic and GoPro Karma and never experienced entanglement with the aircraft. This parachute deployment system worked well on all the failure modes tested for the Vendor 1 aircraft, with the exception of the 4-motor failure modes. The Vendor 1 aircraft would consistently fall and aerodynamically stabilize in an inverted attitude after experiencing a 4-motor failure at hover or at maximum stabilized horizontal flight velocity. This causes the parachute to be below the aircraft at the time of parachute release. As a result, the aerodynamic drag force would keep the parachute pressed against the aircraft and prevent it from opening. This was not an issue on the other failure modes in which the aircraft had a high rotational rate at the time of deployment. This parachute system was the lowest cost, lightest weight, and easiest to integrate of the parachute deployment systems tested.

3.2.2.2 Spring-Based Kinetic Deployment System

A spring-based kinetic deployment system was used on the DJI Phantom 3, DJI Inspire 2, DJI Inspire 1, and Vendor 3 Quadrotor. The Mars Mini parachute system installed on the DJI Phantom 3 aircraft has a spring that is compressed in a tube when the parachute is installed in the deployment tube. A hinged lid is closed at the top of the tube and the servo control arm on a servo is rotated across the lid to retain the parachute until deployment. When deployment is commanded, the servo arm rotates out of the way of the lid allowing the spring to push the parachute out of the tube. The Mars Mini parachute system was used successfully in all failure modes tested for the DJI Phantom 3 aircraft.

The Opale ST60-X parachute recovery system installed on the DJI Inspire 2 aircraft has a spring that is compressed in a tube with a cylindrical retention pin that protrudes through the base of the tube that is held in place by a release pin. This release pin is connected to the servo control arm on a servo. When deployment is commanded, the servo arm rotates to pull the release pin, allowing the spring to push the parachute out of the tube. The stock configuration Opale ST60-X failed to deploy the parachute during several bench tests. The cause was attributed to the kinematic relationship of the release pin, servo arc path, and height difference between the servo control arm and the retention pin. The servo mount was modified to improve the release pin kinematics. The DJI Inspire 2 flight test had a successful deployment with this modifications, however the aircraft was damaged upon landing as the parachute size was inadequate for the 8.5 lb flight test configuration weight despite being marketed for aircraft systems up to 10.8 lbf. The data logger failed to collect data for this flight, but Opale predicts a 15 ft/s descent rate at this configuration weight.

The same modified Opale ST60-X used on the DJI Inspire 2 flight tests was also used for the DJI Inspire 1 flight tests. Although improvements were made to the kinematics of the release pin mechanism, on the first DJI Inspire 1 flight, the release pin failed to fully disengage from the retention pin and the parachute was not deployed. As a result, the aircraft was destroyed upon impact. Parachute systems that use this type of parachute release mechanisms should be designed to optimize the kinematic relationship of the deployment mechanisms as well as minimizing the torque required from the servo needed to pull the release pin.

The Opale ST60-X parachute system was modified again and installed on the Vendor 3 Quadrotor. The modifications included removing the servo-based release pin mechanism, installing a proprietary UAH parachute release mechanism, and fabrication of a custom interface plate for installation on the Vendor 3 Quadrotor. The modified parachute system successfully deployed the parachute for all failure modes tested for the Vendor 3 Quadrotor, however the parachute failed to open on one flight due to parachute entanglement with the shroud lines.

3.2.2.3 Pneumatic-Based Kinetic Deployment System

The Vendor 2 parachute system was installed on the DJI S800 and DJI Inspire 2 aircraft. The Vendor 2 parachute system features a pressurized, high velocity deployment device to rapidly eject the parachute away from the tumbling aircraft. Additionally, the system was designed so the parachute attachment point was at a point outside of the aircraft's rotation radius to prevent the parachute from becoming entangled in the aircraft during tumbling or dynamic failures. The Vendor 2 parachute system was used successfully on all failure modes tested for the S800 and DJI Inspire 2 aircraft, with the exception of one S800 flight in which the parachute shroud lines became entangled with the parachute after deployment as a result of parachute packing error.

3.3 Aerodynamic Analysis and Dynamic Modeling

3.3.1 Results Overview

Simulations were performed to estimate the worst-case impact KE for each vehicle. First, the model was validated against flight test data and flight test conditions in order to determine model accuracy and extensibility to Monte Carlo simulation. The models have many parameters that are estimated from flight test, bifilar pendulum swing, and static thrust testing. Drag coefficients values are estimated from the flight test data. Rotor parameters are obtained from static thrust stand data. Steady state winds were estimated using weather reports from nearby weather station. Wind conditions at the field were also recorded by the pilot using a hand-held anemometer. It is important that the model outputs, i.e., trajectory and velocities are similar to the actual flight vehicle trajectory and velocities during the fall. Researchers assumed that 10% error between flight test and simulation was an acceptable threshold for establishing the accuracy of simulations. This is necessary for performing any further analysis to estimate the worst-case impact KE, impact orientation and vehicle displacement at impact.

The model initial states are identical to the flight vehicle states at the instant failure is commanded. Failure occurs at time, t=0, in the simulation. The failure type in the simulation is the same as the failure in the flight test. A thrust bleed off is modeled by reducing thrust to zero in 0.1 seconds rather than instant cut-off to zero to replicate the actual rotor slow-down from its thrusting RPM to a zero RPM condition. The simulation is run and the velocity and impact angles of the model during the fall is compared with flight data. Eqn. 24 defines the method used to calculate Resultant Speed, Horizontal Displacement and Kinetic Energy error, respectively, between modeling and flight test.

$$\text{Modeling Error in Res. Speed \%} = \frac{\int_{t=0s}^{t'} V_{Res_{Model}}\, dt - \int_{t=0s}^{t=t} V_{Res_{Flight\,Test}}\, dt}{\int_{t=0s}^{t=t} V_{Res_{Flight\,Test}}\, dt} \qquad \text{Eqn. 24}$$

where the parameter being evaluated is either resultant velocity, horizontal displacement or KE. Flight test resultant velocity is integrated from time of failure (t=0) to t seconds after failure, where t represents the time for which the data logger recorded the descent data. Modeling resultant velocity output is integrated from time of failure (t=0) to t' seconds after failure, where t' is defined as the time taken by the model to lose the same altitude as the flight test vehicle loses in t sec. The difference in t and t' values is due to the fact that a model behavior is unlikely to be a 100% match with the flight test behavior. A positive error shows that the model overestimates the parameter when compared to the flight test. Negative error shows underestimation of the parameter by model compared to flight test.

$$Impact\ Angle = \tan^{-1} \frac{w}{\sqrt{u^2 + v^2}} \qquad \text{Eqn. 25}$$

The impact angle of the vehicle calculated using Eqn. 25 defines the angle at which the vehicle collides with a person. Here, u, v, w represents the vehicle velocity components in inertial frame. An impact angle of 90^o implies a pure vertical collision with a person or object. An impact angle of 0^o describes a pure horizontal collision with a person or object. The model replicates position, velocity, KE and impact angle very closely to actual flight tests but is inconsistent in comparing flight test vehicle tumbling and vehicle model tumbling in simulation. For one and two motor off-axis failures, the flight test vehicle exhibits moderate-to-severe tumbling. The model also exhibited moderate-to-severe tumbling although not the exact same number of flips as the flight test vehicle. For the four-motor and two-motor on-axis failures, the flight test vehicles do not completely flip prior to parachute deployment. For the four-motor and two-motor on-axis failures, the model either does not flip or flips more than once. This is a limitation in generating aerodynamic data from the failure flight tests. The model makes accurate predictions for the aircraft behavior as a point mass but needs refinement in order to accurately predict rotational dynamics. During the modeling of Vendor 1 Quadrotor cage and no-cage flight tests, the model was modified to approximately replicate tumbling and the auto-stabilization behavior of Vendor 1 Quadrotor. This modification did not change the modeling outputs that directly relate to injury potential (impact velocity, impact angle and trajectory) which were already close to flight test values. Given that the most important outputs for this study are resultant velocity and impact angle and that these parameters where insensitive to changes made to improve the modeling of rotational behavior, the other models were not modified to account for rotational dynamics. This method is briefly discussed in the Vendor 1 Quadrotor modeling results section. Accurate drag modeling proved to be the dominant factor in terms of accurate prediction of impact conditions. The wind speed and direction from nearby weather stations was used in the wind model.

APPENDIX B – FLIGHT TEST AND MODELING PLOTS provides a summary of plots comparing all the flight tests and modeling effort. In these plots, the flight test vehicle and model resultant speed, vertical speed, horizontal speed, altitude loss and impact angle, respectively, are plotted with time. Once the model is validated with the flight test, further analysis is performed on the vehicle to develop trends and assess the effects of environment conditions, failure types and vehicle state at the instant of failure on the vehicle trajectory, impact velocity and orientation.

3.3.1.1 DJI Phantom 3 Standard

Two different controllers were integrated on the flight test vehicle. Six flight tests had the DJI Phantom 3 standard proprietary controller but two flight tests had the open-source Pixhawk controller. The exact functioning of the DJI Phantom 3 standard proprietary controller is unknown. The open-source Pixhawk controller uses a PID based algorithm for flight vehicle control. In the model, the flight control block was designed based off a generic PID control for all eight test cases. During the flight tests, it was observed that following the one and two motor failures, the remaining motors were still ON and producing thrust. The maximum and minimum flat plate drag areas and phase angle are estimated from the four motor failure at hover flight test. The flat plate drag area and Angle of Attack curve is defined using these terms, as shown in Figure 19. The flight test flat plate drag area values are between 90º and 130º only. This implies that the vehicle did not flip during this particular test. When flight test data does not span the entire range of angles, the maximum and minimum values are chosen from the available data and the phase angle is chosen to best match the fit with the flight data. This fit still provides a good approximation of impact conditions with ± 10% accuracy. A thrust bleed off for about 0.1 seconds was also implemented to approximate rotor performance following a failure.

Table 10 shows a summary of the flight tests and modeling. The estimated average terminal velocity for the DJI Phantom 3 in the flight test configuration is 74 ft/s. The flight test configuration weighs more than the stock vehicle, which accounts for the higher terminal velocity. Additionally, these aircraft did not have blade guards installed as in Task A4/A11, which increased aircraft drag and yielded at 64 ft/s terminal velocity. The eight flight tests are modeled successfully and the modeling error in KE, velocity and displacement error is within ± 10%. The time of fall was based on being limited to 400 feet AGL under Part 107 operating rules and being able to successfully recover the aircraft under parachute for reuse. Under the flight test column, the table summarizes the vehicle distance fallen, velocity and KE attained after 3 seconds (3.5 seconds for two cases marked with *). The time taken by the model to fall the same altitude as the flight test is listed under the Dynamic Model column. The modeling error in estimating horizontal displacement, Impact Velocity and Impact KE for each of the eight cases is also shown.

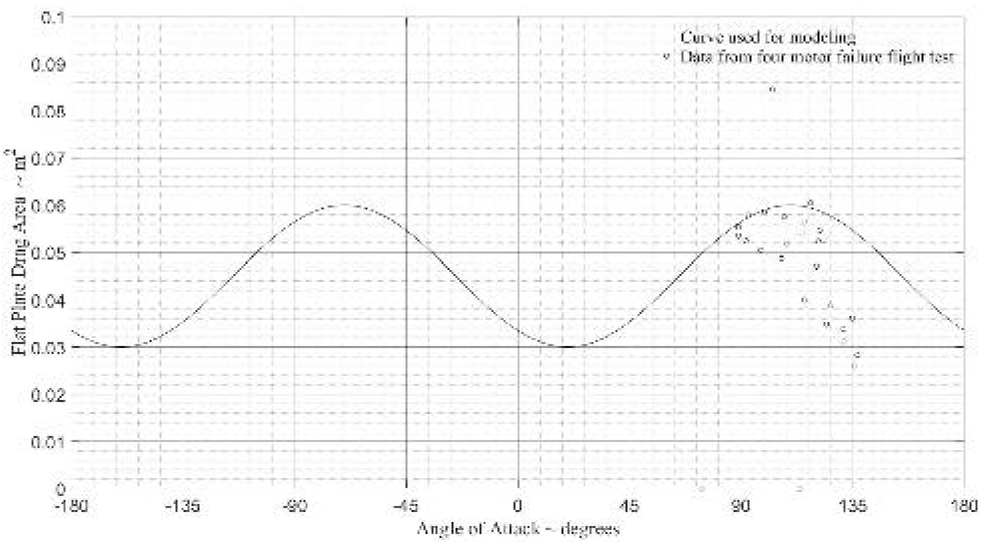

Figure 19. Flat Plate Drag Area – Angle of Attack Curve for DJI Phantom 3 Standard

Table 10. DJI Phantom 3 Standard – Flight Tests and Modeling Summary

Failure Type	Vehicle Forward Ground Speed at Failure (ft/s)	Flight Test			Dynamic Model			
		Distance Fallen (ft)	Speed reached (ft/s)	KE (ft-lbf)	Time of Sim. (sec)	Avg. Disp. Error	Avg. Res. Speed Error	Avg. KE Error
4 motor fail at hover	0	105	59	169	2.9	-4 %	1 %	3 %
4 motor fail at max stabilized forward flight speed	42	105	57	158	3	0 %	2 %	4 %
1 motor fail at hover	0	105	63.5	196	3	-10 %	-2 %	-1 %
1 motor fail at max stabilized forward flight speed	40	98.5	62	187	3	-2 %	-4 %	-4 %
2 motor on-axis (M1M3) fail at hover	0	92	49	117	3.1	4 %	-2 %	1 %
2 motor on-axis (M1M3) fail stabilized forward flight speed*	40	123	55	141	3.6	-1 %	-4 %	-5 %
2 motor off-axis (M1M2) fail at hover	0	102	62	187	3	-1 %	-3 %	-4 %
2 motor off-axis (M1M2) fail at stabilized forward flight speed*	40	122	68	215	3.6	0 %	-4 %	-7 %

3.3.1.2 Vendor 1 Quadrotor

A Pixhawk flight controller was used on the Vendor 1 Quadrotor test vehicles. The failure board forced the various failures and after a 0.5 seconds delay it forces all motors to turn off. The same PID controller used in DJI Phantom 3 modeling was integrated with the Vendor 1 Quadrotor model but with a modification where the model would also shut off all four motors after 0.5 seconds. A thrust bleed off for about 0.05 seconds was also designed for each rotor following a failure.

Researchers worked to replicate the vehicle's inherent stability observed during flight test in the model. The goal was to create a restoring moment which could negate the angular velocity of the vehicle. Initial effort involved turning on all four motors two seconds after all four motors were turned off. The motor RPM was varied from very low to high but this did not provide any auto-stabilization so this method was rejected. The next method involved adding a constant body moment coefficient to the vehicle to reduce the body pitching and rolling moment once motors were off. This unidirectional moment was never able to stabilize the vehicle. Finally, it was speculated that the up wash on the rotors due to angular velocity could provide a restoring moment to stabilize the vehicle. Figure 20 describes this phenomenon. When a positive roll or pitch moment causes a high angular velocity along the vehicle x-axis or y-axis, the rotors see an up wash (Eqn. 26) in addition to the wind velocity due to losing altitude.

$$w_B(new) = w_B(old) + (-1)^{i+1}pr + \frac{-i+2.5}{|-i+2.5|}qr \qquad \text{Eqn. 26}$$

$$Drag_{rotor,i} = \frac{1}{2}\rho S C_{D,rotor} w_B(new)^2 \quad \text{Eqn. 27}$$

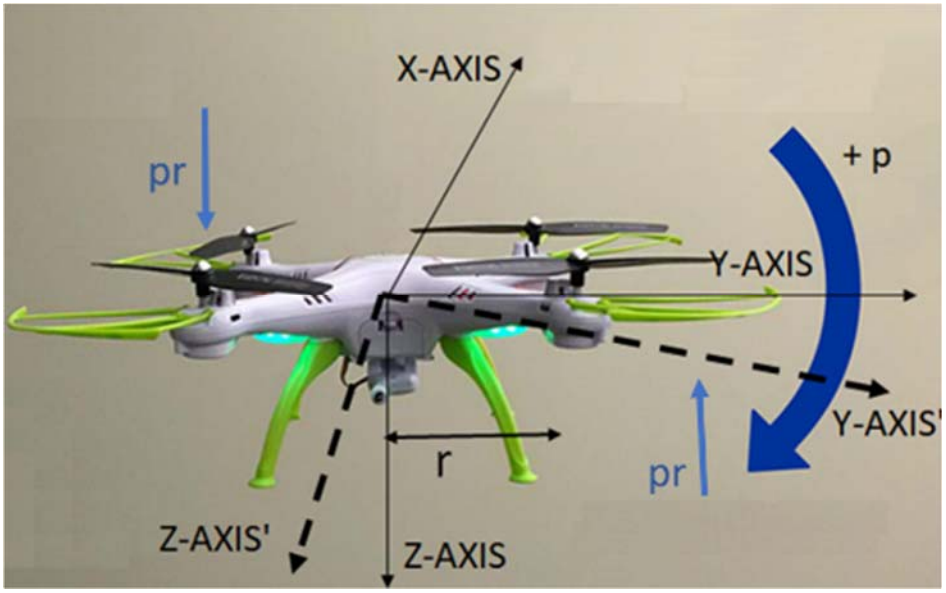

Figure 20. Roll rate creates an additional velocity on the motors

From CFD analysis performed during FAA A4 project on a DJI Phantom 3 standard, it was observed that the rotors contribute between 30-40% of the total flat plate drag area. For the Vendor 1 Quadrotor vehicle, a 30% of total flat plate drag area was used to estimate the flat plate drag area contribution of the rotors. Individual rotors would contribute one-fourth of the total rotor drag area. The flat plate drag area of each rotor and the wind velocity at each rotor including the velocity due to angular velocity is used to find the drag at each rotor. The drag force of each rotor is slightly different because of the different velocity values at each rotor as the vehicle pitches and rolls. The difference in drag at each of the rotors creates a restoring moment that stabilizes the vehicle gradually. However, unlike the flight test vehicle, the model stabilizes in either upright or inverted position versus consistently stabilizing in an inverted position like the actual aircraft. The total drag area of the vehicle is still calculated from the sinusoidal formula mentioned in Eqn. 5. The effect of the angular velocity on total vehicle drag is negligible because if two rotors see more drag, the two remaining rotors see less drag. The plots of flat plate drag area and angle of attack for the cage-on and cage-off configuration are shown in Figure 21 and Figure 22, respectively. The vehicle drag is reduced when the cage is removed. Also, note the amplitude of the flat plate drag area and angle of attack curve for the cage-on and cage-off configurations. In the cage-on configuration, a flip can cause the drag area to reduce by half. But in the cage-off configuration, a flip can reduce the drag area by five times. Therefore, tumbling in the later configuration causes a sudden increase of the vehicle speed during descent as seen in the plots in Appendix B.

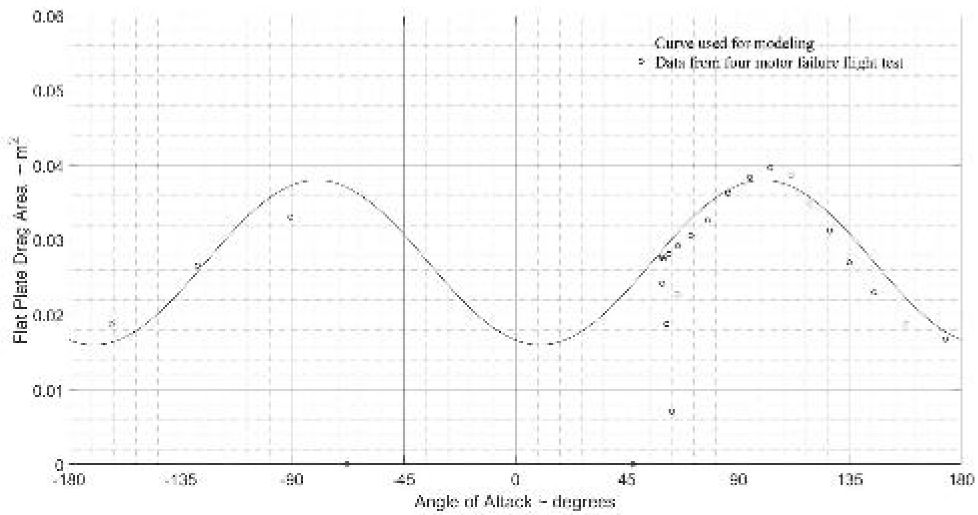

Figure 21. Flat Plate Drag Area – Angle of Attack Curve for Vendor 1 Quadrotor cage-ON vehicle

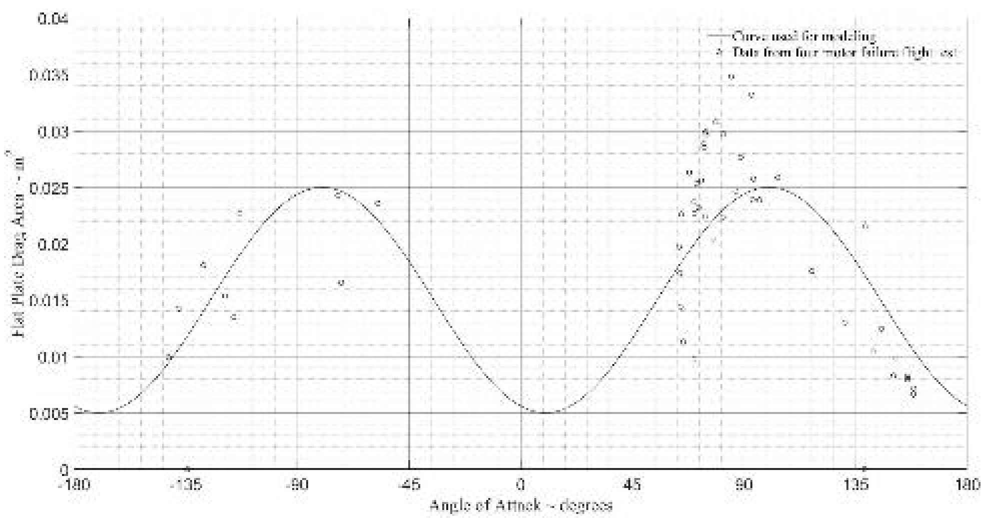

Figure 22. Flat Plate Drag Area – Angle of Attack Curve for Vendor 1 Quadrotor cage-OFF vehicle

The eight cage-off and cage-on flight tests are modeled successfully and the modeling error in KE, velocity and displacement error are within ± 10%. Table 11 and Table 12 show the summary of the flight tests and modeling for the cage-on and cage-off vehicles. The estimated average terminal velocity for the Vendor 1 Quadrotor cage-on vehicle in the flight test configuration is 49 ft/s. The estimated average terminal velocity for the Vendor 1 Quadrotor cage-off vehicle in the flight test configuration is 54 ft/s. The time of fall for the cage-on condition was 3 seconds and for the cage-off configuration is 5.5 seconds, because the pilot had determined there was still sufficient time for recovery of the aircraft.

Table 11. Vendor 1 Quadrotor Cage-on – Flight Tests and Modeling Summary

Failure Type	Vehicle Forward Ground Speed at Failure (ft/s)	Flight Test			Dynamic Model			
		Distance Fallen (ft)	Speed reached (ft/s)	KE (ft-lbf)	Time of Sim. (sec)	Avg. Disp. Error	Avg. Res. Speed Error	Avg. KE Error
4 motor fail at hover	0	92	46	31	2.7	-1 %	3 %	5 %
4 motor fail at max stabilized forward flight speed	20	90	40	24	3	4 %	6 %	13 %
1 motor fail at hover	0	102	49	36	2.7	0 %	-6 %	-10 %
1 motor fail at max stabilized forward flight speed	46	111.5	52	40	2.7	8 %	-2 %	-4 %
2 motor on-axis (M1M2) fail at hover	0	82	49	36	2.7	-8 %	6 %	9 %
2 motor on-axis (M1M2) fail at stabilized forward flight speed	29	95	42	26	2.7	7 %	1 %	4 %
2 motor off-axis (M1M3) fail at hover	0	102	46	31	2.8	0 %	2 %	4 %
2 motor off-axis (M1M3) fail at stabilized forward flight speed	28	113	51	38	2.7	3 %	-5 %	-9 %

Table 12. Vendor 1 Quadrotor Cage-off– Flight Tests and Modeling Summary

Failure Type	Vehicle Forward Ground Speed at Failure (ft/s)	Flight Test			Dynamic Model			
		Distance Fallen (ft)	Speed reached (ft/s)	KE (ft-lbf)	Time of Sim. (sec)	Avg. Disp. Error	Avg. Res. Speed Error	Avg. KE Error
4 motor fail at hover	0	225	58	44	5.4	-1 %	4 %	8 %
4 motor fail at max stabilized forward flight speed	43	205	52	35	5.1	-7 %	-4 %	-6 %
1 motor fail at hover	0	200	45	26	5.2	-5 %	2 %	6%
1 motor fail at max stabilized forward flight speed	38	250	58	44	5.9	8 %	-2 %	-4 %
2 motor on-axis (M1M2) fail at hover	0	210	48	30	5.4	-1 %	-1 %	-3 %
2 motor on-axis (M1M2) fail at stabilized forward flight speed	36	190	45	26	4.9	-10 %	1 %	3 %
2 motor off-axis (M1M3) fail at hover	0	250	52	35	5.4	-1 %	-3 %	-6 %
2 motor off-axis (M1M3) fail at stabilized forward flight speed	36	250	54	38	5.7	4 %	-5 %	-9 %

3.3.1.3 Sensefly eBee+

The dynamic modeling on the Sensefly eBee+ model has been unsuccessful. The aerodynamic coefficients estimated from OpenVSP were unable to trim the aircraft in steady conditions. Initially, a symmetric airfoil was defined for the wing inside OpenVSP. Later, a reflex airfoil was defined for the wing inside OpenVSP. Both methods did not improve the dynamic model stability. During some simulations, the model was able to achieve trim condition for a short time after which it became unstable. During this short period when trim was achieved, power off failure was forced on the model to compare its behavior to the flight tests. The dynamic model became unstable immediately after the failure and once it achieves infinite velocity.

Researchers were not able to predict aerodynamic coefficients, using OpenVSP, that worked well within the simulation. Researchers were unable to develop accurate aerodynamic parameter estimates based on failure flight test data. Based on these setbacks, UAH is conducting frequency sweep flight tests to develop a linearized eBee+ model.

Despite the failure in developing the eBee+ model, the failure flight tests were performed over a larger time duration when compared to the multirotor sUAS and provide sufficient data to determine the worst case impact KE and orientation of the eBee+ vehicle.

3.3.1.4 DJI Mavic Pro

The DJI Mavic Pro flight test vehicle used the DJI proprietary controller for flight control. The external failure board and data logger were used only to force failures directly to the ESC's and record state data. Since no information on the proprietary controller was available, a generic PID controller was defined in the model. The DJI Mavic Pro controller is likely to be more advanced than the DJI Phantom 3. The unique stabilizing controller behavior that reduced the post-failure rate of descent was observed during the single motor failure but not for the two motor failures. Therefore, the simulation was performed only on the four and two motor failures using the generic PID controller.

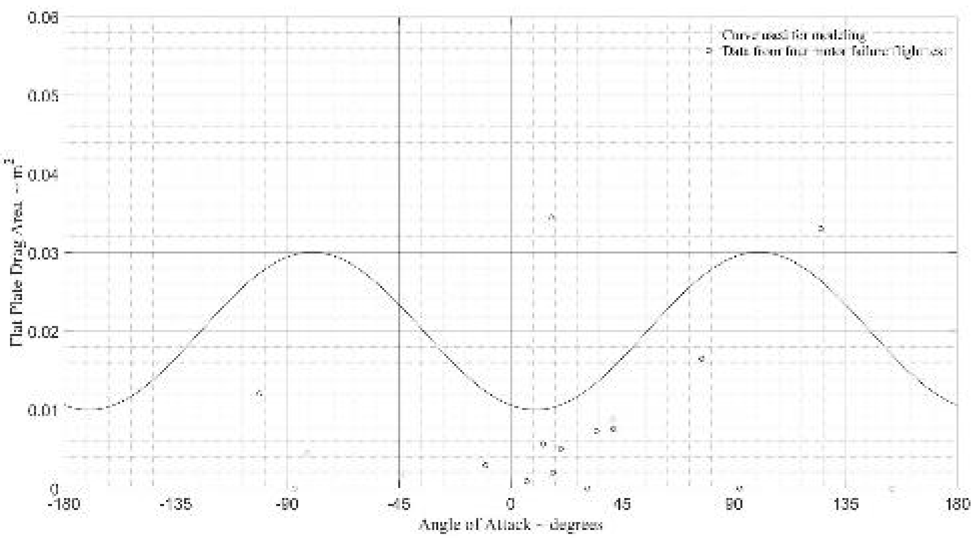

Figure 23. Flat Plate Drag Area – Angle of Attack Curve for DJI Mavic Pro

The flat plate drag area versus angle of attack curve used for the DJI Mavic Pro model is shown in Figure 23. For the DJI Mavic Pro, flight test data was insufficient by itself to arrive at the best flat plate drag area versus angle of attack curve. An adjustment was made to the fitted curve to best match flight tests with models until model accuracy was within ± 10%. The six flight tests match well with the models. The one motor failure simulation was not performed since the controller behavior is unknown. The summary of DJI Mavic Pro flight tests is shown in Table 13. The estimated average terminal velocity for the DJI Mavic Pro vehicle in the flight test configuration is 82 ft/s. The flight test vehicle data was recorded for 3 seconds. The DJI Mavic Pro reached higher velocity than the DJI Phantom 3 in the first 3 seconds of fall because of its much lower drag. The impact KE after 3 seconds is much smaller than that of DJI Phantom 3 due to the lower weight of the test vehicle. The weight of the DJI Mavic Pro flight test configuration is 50% greater than the DJI Mavic Pro nominal configuration. The nominal configuration DJI Mavic Pro saw much lower velocities and KE as discussed later in the trends section.

Table 13. DJI Mavic Pro – Flight Tests and Modeling Summary

Failure Type	Vehicle Forward Ground Speed at Failure (ft/s)	Flight Test			Dynamic Model			
		Distance Fallen (ft)	Speed reached (ft/s)	KE (ft-lbf)	Time of Sim. (sec)	Avg. Disp. Error	Avg. Res. Speed Error	Avg. KE Error
4 motor fail at hover	0	118	66	167	3.2	-4 %	4 %	4 %
4 motor fail at max stabilized forward flight speed	34	125	67	172	3.4	0 %	-2 %	-3 %
1 motor fail at hover	0	52	30	34.5	NA	NA	NA	NA
1 motor fail at max stabilized forward flight speed	23	8	48	88	NA	NA	NA	NA
2 motor on-axis (M1M3) fail at hover	0	106	61.5	145	3.4	4 %	-1 %	7 %
2 motor on-axis (M1M3) fail stabilized forward flight speed	59	110	76	222	2.9	-1 %	1 %	0 %
2 motor off-axis (M1M2) fail at hover	0	100	61.5	145	3.4	-1 %	-3 %	3 %
2 motor off-axis (M1M2) fail at stabilized forward flight speed	60	81	66	167	3.3	0 %	-5 %	-8 %

3.3.1.5 DJI Inspire 2 without Parachute

The DJI Inspire 2 test vehicle used its own proprietary controller for control of the vehicle. Only three flight tests were performed. The DJI Inspire 2 is also advanced similar to the DJI Mavic Pro and performs recovery action following a partial failure. The four motor failures required cutting power to all four motors via an electrical relay on the ESC. Following the one motor failure, the vehicle was able to maintain altitude and level flight similar to the DJI Mavic Pro. It was assumed that the controller sent certain pre-programmed commands following partial failure and the vehicle had a given power margin that afforded a specific level of performance despite the one-motor failure. Simulation was only performed on the four motor failures because the simulation did not accurately estimate performance and dynamics under this partial power condition. Figure 24 shows the relation between the flat plate drag area and the angle of attack used for the DJI Inspire 2 model. Again, the calculated flight points are very spread out and the curve was fitted to best match flights tests with models until model accuracy was within ± 10%. Table 14 shows the summary of the DJI Inspire 2 flight tests and simulation results. Flight test data was recorded for approximately 4.2 seconds as it was manually triggered. The estimated average terminal velocity for the DJI Inspire 2 vehicle in the flight test configuration is 83 ft/s.

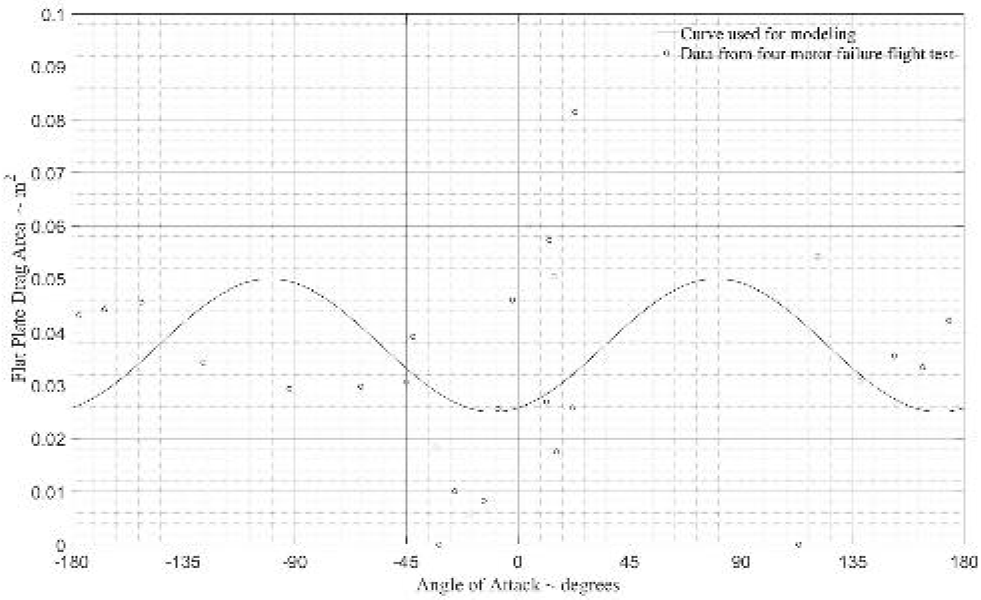

Figure 24. Flat Plate Drag Area – Angle of Attack Curve for DJI Inspire 2

Table 14. DJI Inspire 2 – Flight Tests and Modeling Summary

Failure Type	Vehicle Forward Ground Speed at Failure (ft/s)	Flight Test			Dynamic Model			
		Distance Fallen (ft)	Speed reached (ft/s)	KE (ft-lbf)	Time of Sim. (sec)	Avg. Disp. Error	Avg. Res. Speed Error	Avg. KE Error
4 motor fail at hover	0	187	80	984	4.1	-3%	0 %	-3 %
4 motor fail at max stabilized forward flight speed	66	154	69	722	3.8	4 %	1 %	3 %
1 motor fail at max stabilized forward flight speed	68	108	49	367	NA	NA	NA	NA

3.3.1.6 GoPro Karma

The Go Pro Karma proprietary controller was replaced by the Pixhawk controller and uses the generic PID controller only. The GoPro Karma is large in size and heavier than the DJI Phantom 3 Standard. Its flat plate drag area and angle of attack curve is plotted in Figure 25. The highest flat plate drag areas are around the -90º angle of attack which represents a flat, level position. The vehicle did not tumble following the four motor failure. For the Go Pro Karma, flight test data was insufficient by itself to arrive at the best flat plate drag area versus angle of attack curve. An adjustment was made to the fitted curve to best match flights tests with models until model accuracy was within ± 10%, except for the two-motor off-axis failures at a hover and in maximum stabilized speed. There two simulation cases had Average KE Error values greater than 10%. The most likely cause of this was uncommanded motor restart after the failure was initiated. The restart because could not be effectively replicated in the simulation as the data logger did not record a pwm signal or other parameter that allowed researchers to develop a representative motor command signal that minimized the error between the simulation and flight test.

As can be seen in the plots in Appendix A, when the vehicle stabilizes, drag increases and the velocity decreases. Table 15 summarizes the results of the flight test and simulation results. The flight test data is recorded for 3.5 seconds on the Karma. The estimated average terminal velocity for the GoPro Karma vehicle in the flight test configuration is 73 ft/s.

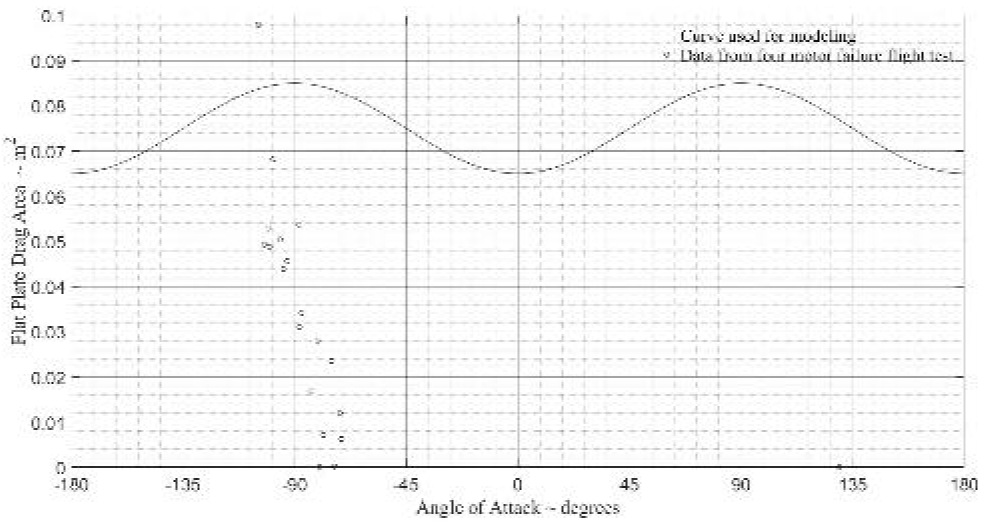

Figure 25. Flat Plate Drag Area – Angle of Attack Curve for GoPro Karma

Table 15. GoPro Karma – Flight Tests and Modeling Summary

Failure Type	Vehicle Forward Ground Speed at Failure (ft/s)	Flight Test			Dynamic Model			
		Distance Fallen (ft)	Speed reached (ft/s)	KE (ft-lbf)	Time of Sim. (sec)	Avg. Disp. Error	Avg. Res. Speed Error	Avg. KE Error
4 motor fail at hover	0	131.5	66	345	3.4	-1 %	1 %	-3 %
4 motor fail at max stabilized forward flight speed	55	103	61	295	3.2	-3%	1 %	3 %
1 motor fail at hover	0	144	77	472	3.6	-1 %	-4 %	-5 %
1 motor fail at max stabilized forward flight speed	66	109	59	271	3.5	0 %	2 %	4 %
2 motor off-axis (M1M2) fail at hover	0	109	50	194	3.4	-2%	3 %	18 %
2 motor off-axis (M1M2) fail at stabilized forward flight speed	58	128	54	232	3.6	-1 %	4 %	10%
2 motor on-axis (M1M3) fail at hover	0	80	45	160	3.4	-1 %	6 %	11 %
2 motor on-axis (M1M3) fail stabilized forward flight speed	60	90	68	362	3.3	-2%	-5 %	-9 %

3.3.1.7 Vendor 3 Quadrotor

The Vendor 3 Quadrotor uses the generic PID controller only. The Vendor 3 Quadrotor is similar in size to the GoPro Karma. Its flat plate drag area and angle of attack curve is plotted in Figure 26. The highest flat plate drag areas of the curve are around the -90º angle of attack which represents a flat, level position. The vehicle did not tumble following the four motor failure. For the Vendor 3 Quadrotor, flight test data was insufficient by itself to arrive at the best flat plate drag area versus angle of attack curve. An adjustment was made to the fitted curve to best match flights tests with models until model accuracy was within ± 10%.

Table 16 summarizes the results of the flight test and simulation results. The flight test data is recorded for 3 seconds on the Vendor 3 Quadrotor. However, for the four motor failure at hover only, 2.2 sec of data was used since the motors spin back ON. The estimated average terminal velocity for the Vendor 3 Quadrotor in the flight test configuration is 74 ft/s. The estimated terminal velocity of the Vendor 3 Quadrotor at stock weight is 70 ft/s. Based on delays in flight testing because of aircraft damage, this estimate is based on limited data; however, on an intuitive level, the higher terminal velocity makes sense based on the aircraft's weight, low profile arms, and more aerodynamic fascia.

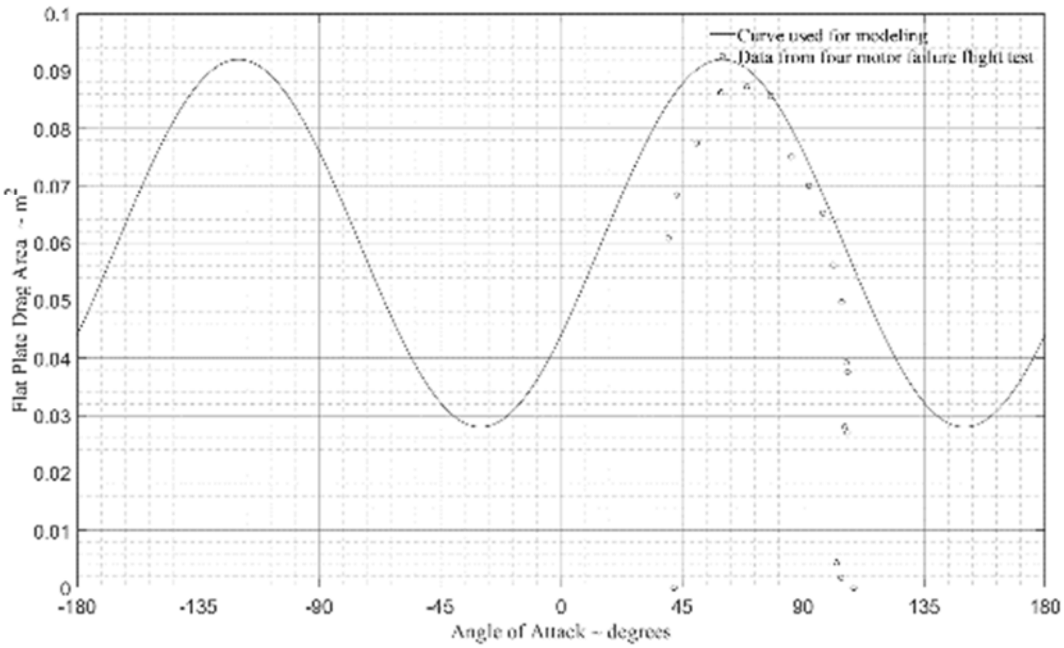

Figure 26. Flat Plate Drag Area – Angle of Attack Curve for Vendor 3 Quadrotor

Table 16. Vendor 3 Quadrotor Flight Tests and Modeling Summary

Failure Type	Vehicle Forward Ground Speed at Failure (ft/s)	Flight Test			Dynamic Model			
		Distance Fallen (ft)	Speed reached (ft/s)	KE (ft-lbf)	Time of Sim. (sec)	Avg. Disp. Error	Avg. Res. Speed Error	Avg. KE Error
4 motor fail at hover	0	71	52.2	224	2.3	0 %	6.5 %	14 %
1 motor fail at hover	0	110	58	274	3.2	-2 %	6 %	20 %

Conclusion: A UAS dynamic model, validated with flight test data, enables simulation of a larger number of failure scenarios (failure type and environmental conditions) than can be feasibly evaluated through flight test alone. The ability to run mass simulation of a range of vehicle failure types, states at failure, and environmental conditions is extensible to sensitivity studies and Monte Carlo Simulation.

Conclusion: The modeling conducted by UAH was successfully validated for aircraft linear velocity and impact KE estimates, but was not accurate at predicting aircraft rotational dynamics. It appeared that the prediction of impact KE and comparison with flight test data was relatively insensitive to this model shortcoming.

3.3.2 Analysis and Modeling of S800 and DJI Inspire 2 Descent under Parachute

3.3.2.1 Use of Resultant Values

Throughout this analysis, resultant acceleration and velocity values are used to identify different events during the flight. The resultant acceleration value at each time step is the root-mean-square (RMS) of the x-, y-, z-axis components. The resultant velocity value at each time step is the RMS of each vertical and horizontal velocity component. While it is of interest to obtain some results in a particular axis, it's difficult to identify the exact timestamp in which a particular event occurred only through analyzing a single axis because the aircraft dynamics are often coupled. For example, parachutes tend to have a pendulum mode while descending that results in an oscillatory response in the vertical and horizontal velocity. As the pendulum swings upward, the vertical velocity decreases and the horizontal velocity increases. Motion in one axis causes a change in the other axis. By analyzing the resultant magnitude of the individual components, a better trend over the time history can be observed.

The following sections illustrate how the events T0 – T5 are identified within flight test data for analysis.

3.3.2.2 Failure Onset – T0

Since the data logger is operated independently of the aircraft system, there was no trigger available to indicate the time the failure was initiated by the pilot. To determine the time of failure, first the maximum altitude for that flight was located. Next, the vertical velocity was analyzed to find the first major slope change from the stable maximum altitude condition. The data point right before the vertical velocity slope change is marked as the time of failure. A subset of the data from the 4-motor hover failure flight with the time of failure highlighted in green is shown in

Table 17 and graphically in Figure 27. Once the point of failure was identified, all data prior to the failure was removed from the analysis data set and the time index was modified so the first data point was at t = 0.0 seconds.

Table 17. Data subset showing change in vertical velocity to indicate time of failure

Time (μs)	Altitude (m)	Vz (m/s)
751913627	97.95	0.129
752114561	97.89	0.086
752295742	97.84	0.186
752516965	97.78	0.134
752698194	97.63	1.2
752898993	97.21	2.641
753099906	96.49	4.223

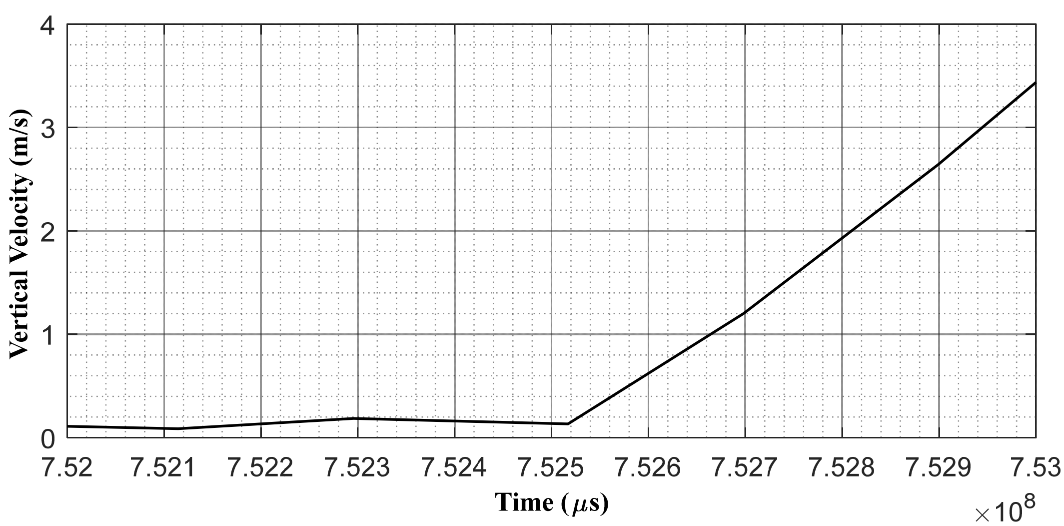

Figure 27. Slope Change in Vertical Velocity Used to Determine Time of Failure

3.3.2.3 Parachute Deployment – T1

Vendor 2 parachute system featured a pressurized, high velocity deployment device to rapidly eject the parachute away from the tumbling aircraft. This kinetic deployment applied a force to the aircraft, resulting in a rapid acceleration change. This resultant acceleration was used to identify the parachute deployment as the first acceleration spike since the time of failure, shown in Figure 28. In some cases, there was another spike immediately after the first which could be attributed to pressurization dynamics of the deployment mechanisms.

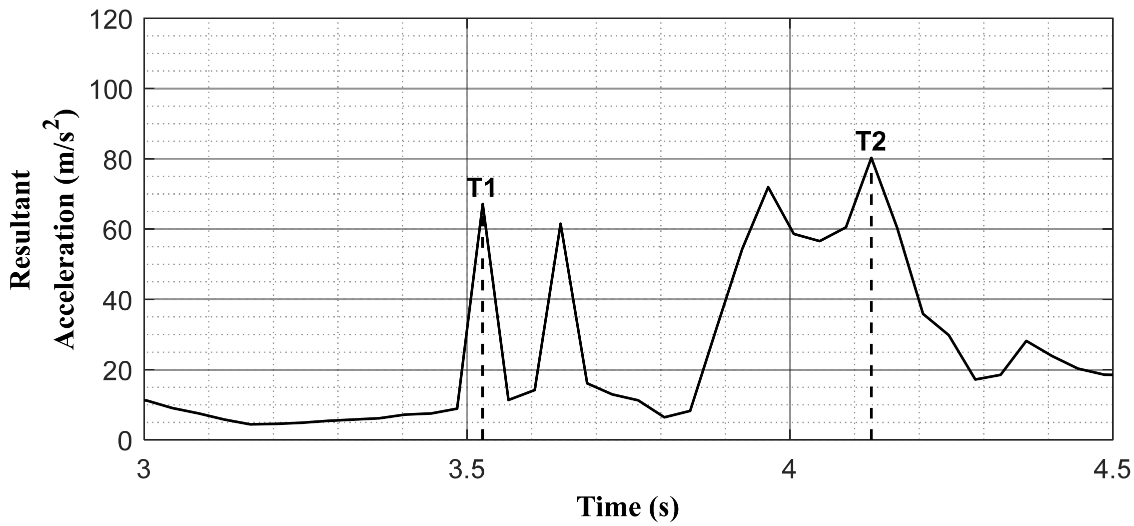

Figure 28. Resultant Acceleration Spikes Used to Identify Parachute Deployment and Inflation

3.3.2.4 Initial Steady-State Velocity Reached – T3

This event represents the point in which the resultant velocity of the aircraft first becomes equal to or less than the average steady-state descent resultant velocity as shown in Figure 5. Although the aircraft has not yet reached a stabilized descent rate, this point can be used to evaluate the performance of a parachute deployment system by identifying the time from deployment to safe descent rate and the altitude lost during this period.

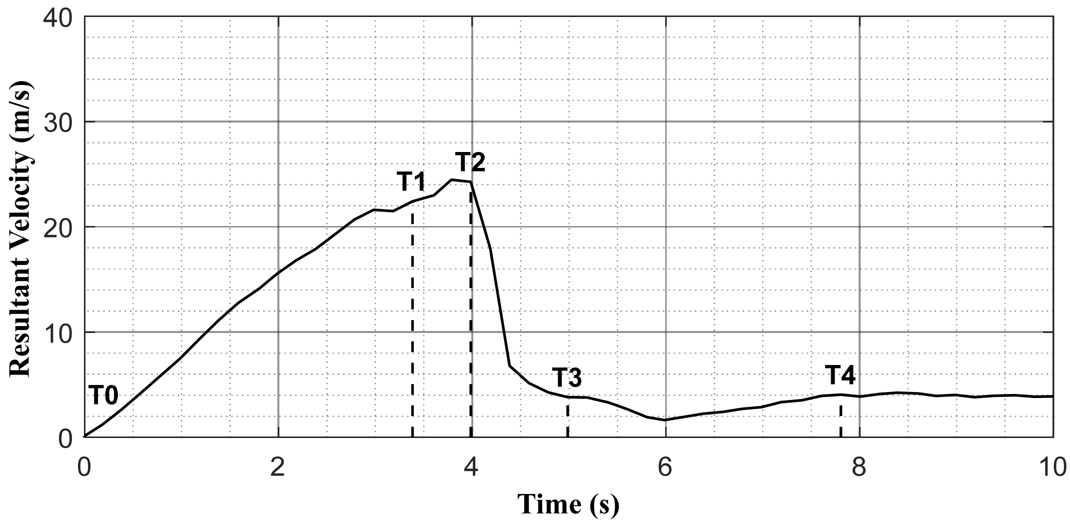

Figure 29. Resultant velocity from failure to steady-state descent

3.3.2.5 Start of Steady-State Descent – T4

The start of steady-state descent was identified as the first peak resultant velocity value since the initial minimum resultant velocity after parachute inflation, as shown in Figure 30.

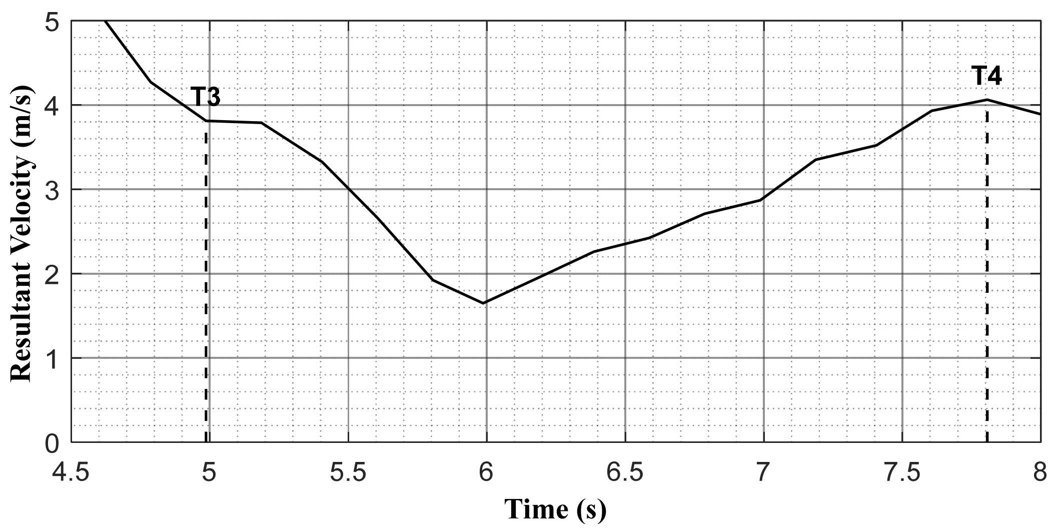

Figure 30. Start of steady-state descent identified as the first resultant velocity peak after inflation

3.3.2.6 Ground Impact – T5

Similar to the failure onset identification, the change in slope of the resultant velocity was used to identify the time of ground impact. The last value prior to the large slope change was used as the ground impact time, shown by the green line in Table 18 and graphically in Figure 31.

Table 18. Resultant velocity data subset used to identify time of ground impact

Time (s)	Vz (m/s)	Vr (m/s)	Δ Vr (m/s)
15.988	2.742	3.720	0.017
16.188	2.632	3.721	0.001
16.408	3.298	4.110	0.389
16.588	3.176	3.891	-0.219
16.788	0.859	2.437	-1.454
16.988	0.301	2.167	-0.270
17.188	0.251	2.120	-0.047

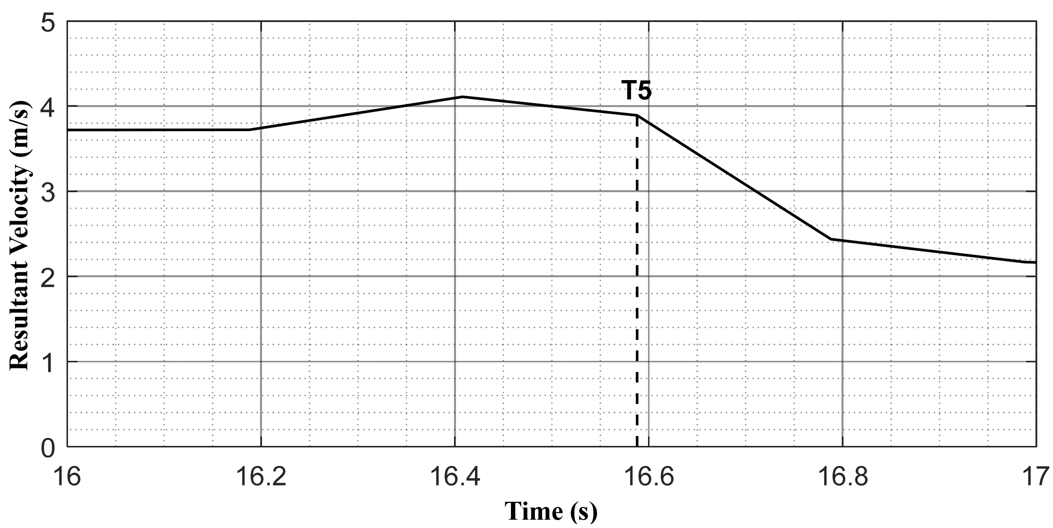

Figure 31 - Ground impact identified by resultant velocity slope change

3.3.2.7 Average Steady-State Descent Velocities

The average steady-state vertical, horizontal, and resultant velocities were each calculated by averaging the data of each respective velocity vector between the timestamps T4 and T5.

3.3.2.8 Horizontal Position Displacement

The inertial reference frame x-axis and y-axis positions are converted to a resultant position at each time step with an initial position of (X,Y) = (0,0) at the time of failure. This resultant value is referred to as the horizontal displacement. This is useful for determining impact radius from initial failure point based on altitude, wind speed, and horizontal velocity at the time of failure. However, the actual horizontal position displacement values obtained are less useful since the displacement radius can increase and decrease with wind direction changes during the descent. The magnitude of the resultant horizontal position displacement was calculated at each time step to remove the effects of changing wind direction. Presenting the horizontal position in this form makes it easier to identify trends and make comparisons with parachute descent models. Figure 32 shows the difference between actual and magnitude of the horizontal position displacement.

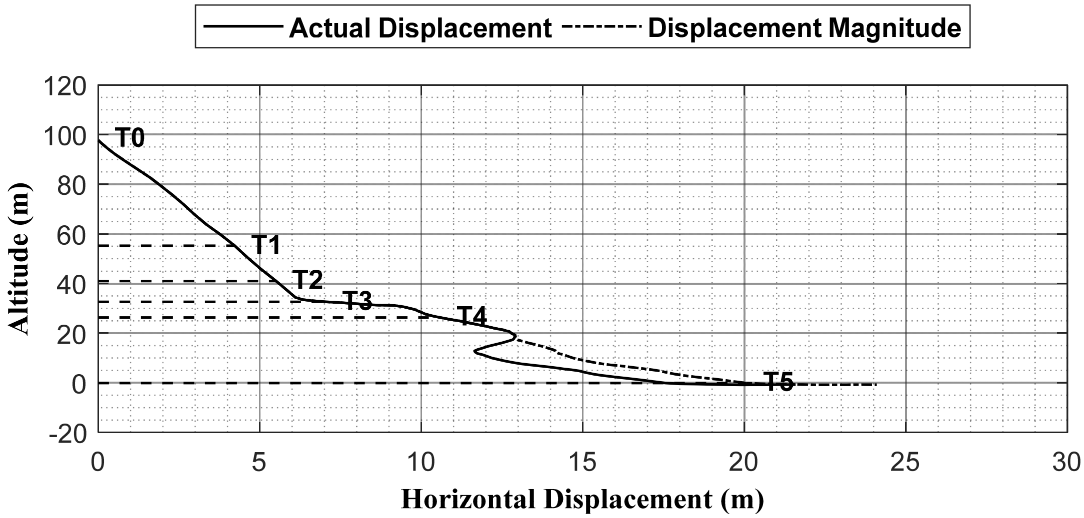

Figure 32. Altitude vs Displacement from time of failure to ground impact

3.3.2.9 Pendulum Frequency

A Fast-Fourier-Transform (FFT) frequency domain analysis was performed on the steady-state descent resultant velocity time domain data to calculate the pendulum frequency. The peaks on an Amplitude vs. Frequency plot of the transformed data represent the fundamental frequencies of the individual signals in a combined signal waveform. In this case, the signal is the periodic motion of the pendulum mode. Typically, two fundamental frequencies appear in the FFT results. One frequency, typically around 0.05 Hz, can be attributed to minor changes in the air mass over time as well as the drag force balance of the system when the steady-state horizontal velocity is in equilibrium with the wind velocity. The higher frequency peak, typically around 0.2 Hz, can be attributed to the pendulum motion of the 2-body parachute-aircraft system. The higher frequency identified by the second peak in the FFT is used as the reported pendulum frequency. The FFT results are shown below in Figure 33 on the left, with the steady-state resultant velocity time domain data shown on the right. The red sinusoid illustrates the 0.05 Hz frequency, and the green sinusoid illustrates the 0.2 Hz frequency.

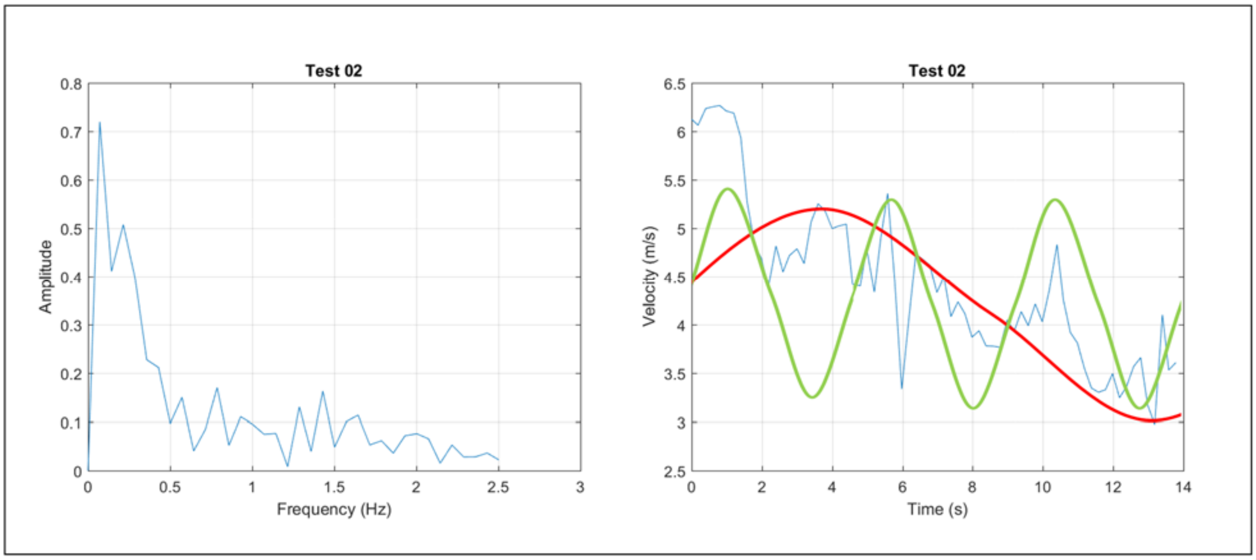

Figure 33. FFT results from DJI Inspire 2 test flight 02

3.3.2.10 Impact Angle

Two impact angles are presented in the results tables: actual impact angle and resultant impact angle. Actual impact angle is calculated using with the respective vertical and horizontal velocities at ground impact. Average impact angle is calculated using Eqn. 28 with the respective average steady-state descent vertical and horizontal velocities.

$$\theta = \tan^{-1}\left(\frac{v_z}{v_h}\right) \qquad \text{Eqn. 28}$$

3.3.2.11 Impact Kinetic Energy

Similar to the impact angle calculations, actual impact kinetic energy is calculated using Eqn. 29, where m is the mass and v is the resultant velocity at the time of ground impact. Average impact angle is calculated using the average steady-state descent resultant velocity.

$$KE = \frac{mv^2}{2} \qquad \text{Eqn. 29}$$

3.3.2.12 Drag Coefficient Estimation

3.3.2.12.1 Assumptions

A low order parachute velocity dynamic model was developed to correlate flight test data trends and estimate drag coefficients. Parachute inflation and descent characteristics are a very complicated study of fluid dynamics[11] in which many of the relationships are highly non-linear. In order to make estimations from flight data collected on a single body, several assumptions were made to simplify the model.

[11] 1. Li Y., Han C., Ya'nan Z., Shaoteng L., "Study of Parachute Inflation Process Using Fluid-Structure Interaction Method", Chinese Journal of Aeronautics, (2014), 27(2):272-279, February 28, 2014.

1. The 2-body parachute-aircraft system is reduced to a single, lumped mass, rigid body where all the forces are acting at the center of mass.
2. The oscillatory pendulum motion was neglected.
3. Inflation dynamics are neglected.
4. The parachute angle of attack at inflation was 0° and remained constant for the remainder of the descent.
5. Wind speed during flight test was constant with no direction change.
6. The wind velocity vector is always parallel to the horizontal axis.
7. Lift from the parachute and the resulting drag due to lift was neglected.
8. Drag from the aircraft body and the parachute shroud lines was neglected.
9. The vertical projected area is based only on the inflated parachute outer diameter, neglecting the area loss due to the center spill hole.
10. The maximum horizontal velocity during steady-state descent cannot be greater than the wind speed.
11. At t = 0 seconds, the model vertical velocity is already at the steady-state vertical descent velocity.
12. At t = 0 seconds, the model horizontal velocity is set to the body horizontal velocity at the time of parachute inflation from the flight test data.
13. The subsequent horizontal velocity calculations at each time step are based on the acceleration due to difference in wind and body velocities.
14. Drag coefficient estimations neglect the drag due to the aircraft body.

3.3.2.13 Parachute Velocity Model Inputs

The parachute dynamic model takes the inputs shown in Table 19 to calculate the wind velocity, body acceleration, and body velocity of the parachute-aircraft system.

Table 19. Parachute Dynamic Model Inputs

Parameter	Units
Wind Velocity at 6 meters	m
Horizontal Velocity at Inflation	m/s
Altitude at Inflation	m
Density	kg/m^3
Aircraft Takeoff Mass	kg
Parachute Vertical Area	m^2
Parachute Horizontal Area	m^2
Parachute Vertical Drag Coefficient	N/A
Parachute Horizontal Drag Coefficient	N/A

3.3.2.14 Vertical Drag Coefficient Estimation

The standard drag equation is given below in Eqn. 30:

$$F_D = ma_D = \frac{1}{2}\rho v^2 S C_D \qquad \text{Eqn. 30}$$

where m is the mass, a_D is the acceleration due to drag, ρ is the air density, v is the velocity, S is the reference area, and C_D is the drag coefficient. Rearranging Eqn. 30 to solve for C_D and substituting the correct values for the vertical axis yields Eqn. 31:

$$C_{D,Z} = \frac{2mg}{\rho {v_{Z,AVG}}^2 S_Z} \qquad \text{Eqn. 31}$$

where $v_{z,AVG}$ is the average steady-state vertical descent rate, a_D becomes g, the gravitational constant, as the acceleration due to drag in the vertical axis is only a result of the acceleration due to gravity at steady-state conditions, and S_Z is the vertical projected area of the inflated parachute. The calculated drag coefficient represents the drag coefficient of the 2-body parachute-aircraft system. Further aerodynamic analysis of the aircraft is required to isolate the parachute's drag coefficient.

3.3.2.15 Wind Velocity, Body Velocity, and Acceleration Relationship

In the horizontal axis, the only force acting on the body is the drag force due to the resulting acceleration from the difference in wind and body velocity. If the body horizontal velocity is less than the wind velocity at the initial condition, then the resulting force due to drag accelerates the body in the positive horizontal axis. This acceleration causes an increase in the body velocity. As the body is accelerated along the positive horizontal axis, the velocity difference between the body and the wind becomes smaller, resulting in a decrease in acceleration. When the two velocities become equal, there is no longer an acceleration due to drag and the body is now traveling along the horizontal axis at the wind velocity. However, acceleration changes occur before changes in velocity, and as a result, the body velocity may become larger than the wind velocity. When this occurs, the force due to drag is now in the negative horizontal axis direction since the force vector always points in the direction of the velocity. This is the restoring action that causes the body velocity to always be approximately equal to the wind velocity at steady-state conditions as shown in Figure 34.

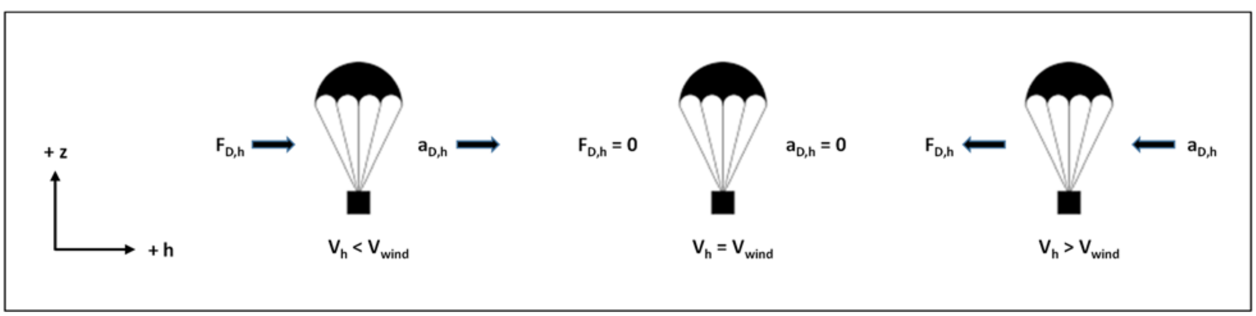

Figure 34. Force and acceleration relationship based on velocity vector

The equation for the force due to drag in the horizontal axis is shown below in Eqn. 32.

$$F_{D,h} = ma_{D,h} = \frac{1}{2}\rho(v_{wind} - v_h)^2 S_h C_{D,h} \qquad \text{Eqn. 32}$$

3.3.2.16 Wind Shear Model

The wind speed at low altitude is significantly impacted by the surface boundary layer. The logarithmic wind shear velocity as a function of height above surface, valid for heights $1 \leq h \leq 300$ meters, is given by Eqn. 33:

$$v_{wind,h} = v_{wind,6} \frac{ln\left(\frac{h}{z_0}\right)}{ln\left(\frac{6}{z_0}\right)} \qquad \text{Eqn. 33}$$

where $v_{wind,6}$ is the wind velocity measured at 6 meters above the surface, h is the height above the surface, and z_0 is the coefficient used to define the air stability based on the surface roughness.[12] A value of $z_0 = 0.04573$ is typically used for smooth, level, grass-covered terrain. A plot of the wind shear profile from surface to 120 meters altitude, with $v_{wind,6} = 3$ m/s, is shown below in Figure 35.

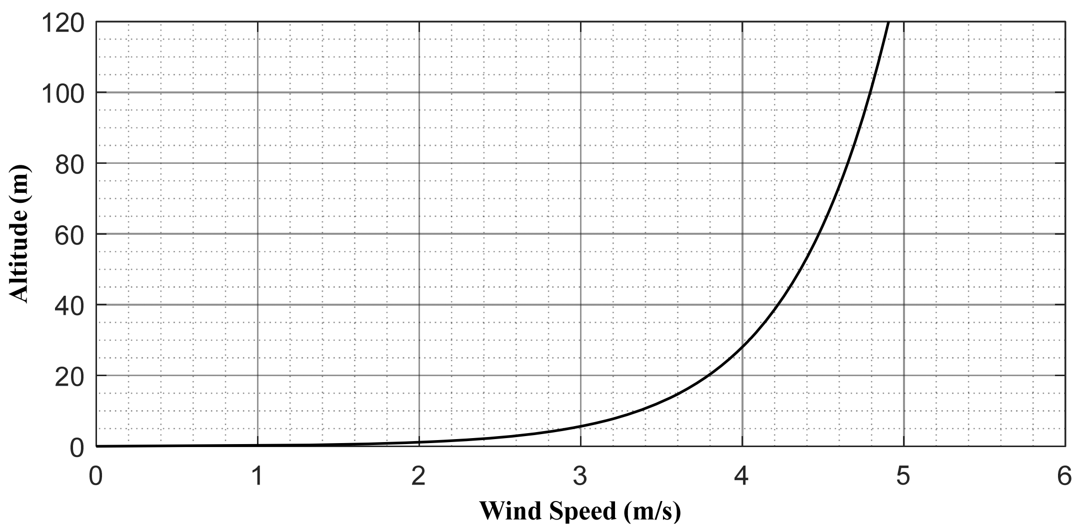

Figure 35. Wind shear profile with wind velocity at 6 meters = 3 m/s

3.3.2.17 Horizontal Drag Coefficient Estimation

A trend of the flight test horizontal velocity from the time of inflation to the start of steady-state descent was developed using the saturation-growth-rate (SGR) equation, shown in Figure 36, as a method of comparison between flight test data and the model results. The SGR equation is well suited for characterizing non-linear growth with limiting conditions.[13]

---

[12] https://www.mathworks.com/help/aeroblks/windshearmodel.html, Accessed: July 09, 2018
[13] Chapra, Steven C., "Applied Numerical Methods with MATLAB for Engineers and Scientists 3rd Edition", McGraw-Hill Education, January 27, 2011.

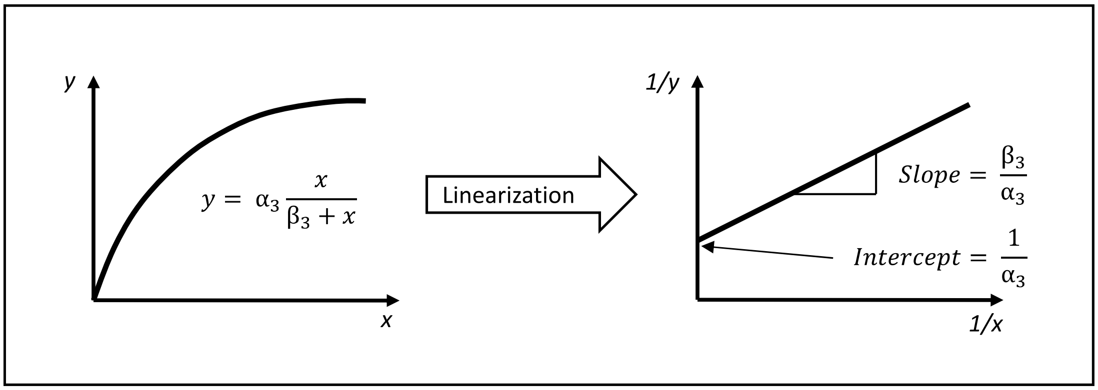

Figure 36. Saturation-growth-rate equation and linearization step to solve for equation coefficients

This works well for describing the horizontal velocity profile from parachute inflation to steady-state descent since the horizontal velocity grows from a low, or zero, velocity initial condition to the wind-velocity, which is the limiting condition. The time scale index from the flight test data is modified to start at t = 0 since the parachute dynamic model starts at t = 0, however, this data set represents the time history between T2 and T3. The horizontal velocity data from flight test was modified so that once the transient velocity reached the average steady-state horizontal velocity, the horizontal velocity remained constant at the average steady-state velocity. This removed oscillations in the velocity due to wind and pendulum motion to allow for a better fit for the SGR equation. The modified set of transient horizontal velocity from parachute inflation to initial stead-state horizontal velocity is shown in Figure 37.

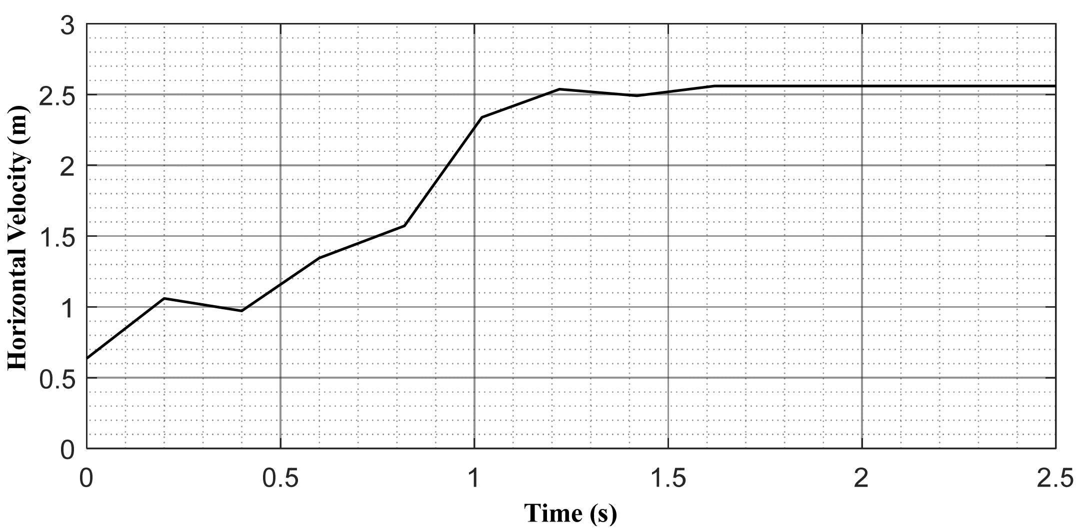

Figure 37. Modified horizontal velocity data set from T2 to T3 used for SGR equation fit

To solve for the coefficients of the SGR equation, a linear fit is applied to the reciprocal of the modified horizontal velocity flight test data. The y-axis intercept of the linear fit solves for the α_3 coefficient. After solving for α_3, the β_3 coefficient can be obtained from the slope of the linear fit. The linearization of the modified data set is shown in Figure 38.

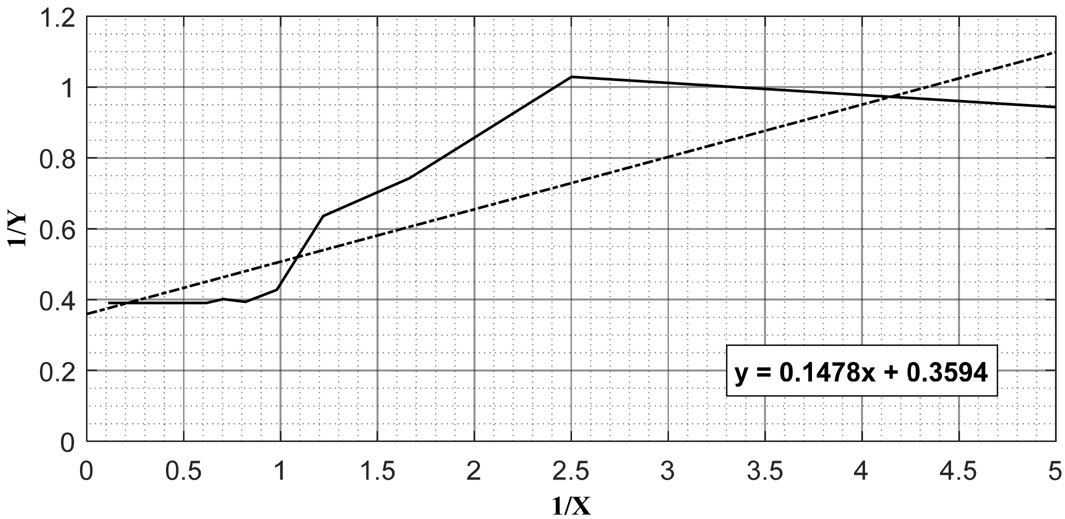

Figure 38. Linearization of modified data set to solve for SGR equation coefficients

With the SGR coefficients obtained, the horizontal velocity for the SGR fit can be calculated. The results of the SGR fit and modified horizontal velocity flight data set on an extended time scale is shown in Figure 39.

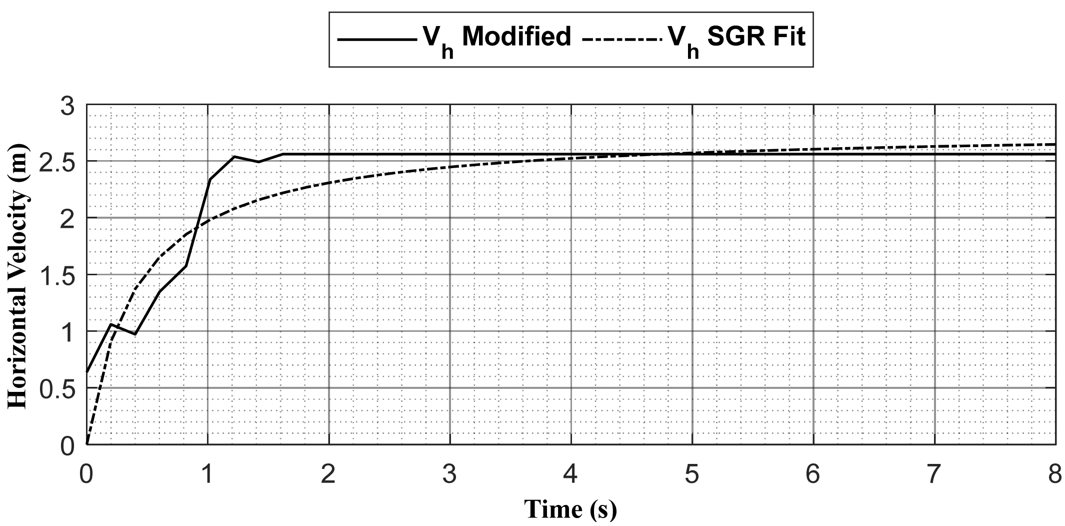

Figure 39 SGR fit with modified data set and extended time scale

To solve for the horizontal acceleration at each time step, *i*, Eqn. 32 is rearranged to yield Eqn. 34, shown below.

$$a_{D,h,i} = \frac{\rho\left(v_{wind,i} - v_{h,i-1}\right)^2 S_h C_{D,h}}{2m} \qquad \text{Eqn. 34}$$

The horizontal velocity at each time step, i, is calculated using Eqn. 35 below.

$$v_{h,i} = v_{h,i-1}(a_{D,i})(t_i - t_{i-1}) \quad \text{Eqn. 35}$$

The parachute horizontal drag coefficient was iterated upon until the maximum horizontal velocity achieved in the dynamic model converged with the horizontal velocity from the SGR fit, as shown in Figure 40. The dynamic model horizontal velocity goes to zero right before t = 10s because the aircraft has landed after the elapsed time given the initial altitude and vertical descent rate. The SGR fit continues because the horizontal velocity is only a function of time based on the SGR equation.

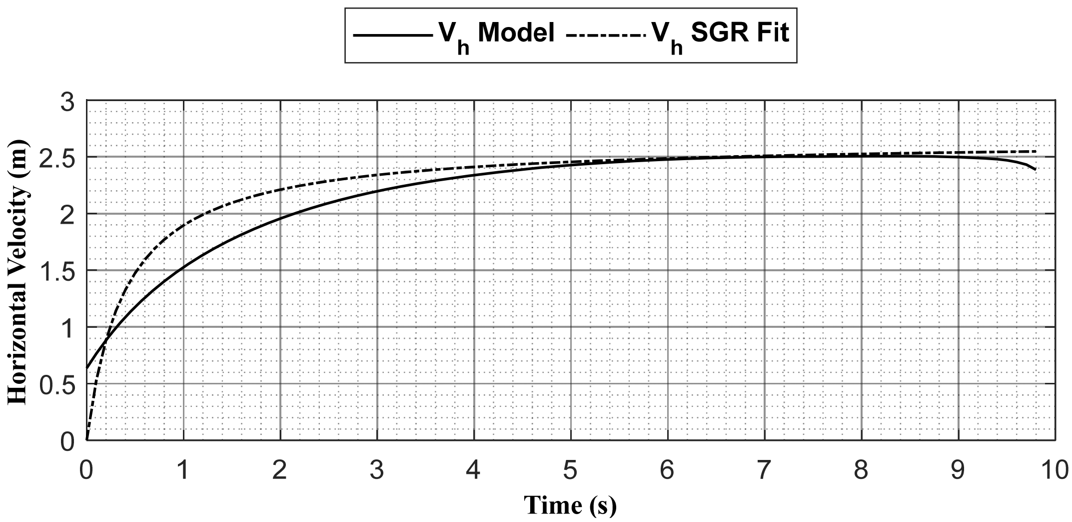

Figure 40. Dynamic model horizontal velocity results compared to SGR fit from test flight data

The dynamic model input parameters used to solve for the horizontal drag coefficient for the DJI Inspire 2, 4-motor failure at hover conditions, are shown in Table 20.

Table 20. Parachute dynamic model inputs used to calculate $C_{D,h}$ from DJI Inspire 2 test flight 01

Parameter	Value	Units
Wind Velocity at 6 meters	2.50	m
Horizontal Velocity at Inflation	0.64	m/s
Altitude at Inflation	30.06	m
Density	1.2788	kg/m^3
Aircraft Takeoff Mass	4.46	kg
Parachute Vertical Area	2.63	m^2
Parachute Horizontal Area	0.77	m^2
Parachute Vertical Drag Coefficient	2.79	N/A
Parachute Horizontal Drag Coefficient	1.5	N/A

The drag coefficient obtained from iteration of the parachute dynamic model represents the drag coefficient of the 2-body parachute-aircraft system. Further aerodynamic analysis of the aircraft is required to isolate the parachute's drag coefficient.

3.3.2.18 Ideal Flight Test Profile for Horizontal Drag Coefficient Estimation

While this low order parachute dynamic model is useful for estimating the horizontal drag coefficient, it is heavily dependent on the flight test profile and accuracy of the wind measured at 6 meters. The ideal flight test conditions would be:

1. Test flight location over flat terrain, far away from tree lines to reduce wind turbulence that would affect wind velocity measurements at 6 meters.
2. Test flight conducted as early as possible after sunrise when the air mass is most stable.
3. Steady-wind conditions from a constant direction.
4. A complete aircraft motor failure immediately followed by parachute deployment.
5. A non-kinetic parachute deployment system or parachute deployment system aligned with the aircraft z-axis to minimize accelerations in the horizontal axis due to the kinetic deployment. This helps insure the initial parachute inflation occurs with an angle of attack of 0° so the reference area used for the drag estimation is purely that of the parachute horizontal projected area and not a component of the horizontal and vertical project area when the angle of attack ≠ 0.°

As a result, the flight tests that were conducted at maximum horizontal flight velocity at the time of failure were not used for a horizontal drag coefficient estimation since the parachute angle of attack after inflation ≠ 0° due to the large horizontal velocity component at the time of inflation.

3.3.3 Modeling and Simulation Trends

In the previous sections, the simulation results were summarized for each vehicle separately. These simulations were performed for each vehicle at their respective flight test configurations and for the various failures. It was also important to perform the simulations for each vehicle at their nominal configurations without additional payloads (data logger) nor parachutes. Table 21 below summarizes the estimated average terminal velocity and KE at these velocities for each vehicle in their nominal and flight test configuration.

Table 21. Summary of Estimated Average Terminal Velocities and impact KE at Terminal Velocities for Multirotor Aircraft

Vehicle	Configuration/Weight	Estimated Average Terminal Velocity (ft/s)	KE at Estimated Average Terminal Velocity (ft-lbf)	Altitude to Reach 90% Estimated Average V_{term} (ft)	Impact Trajectory after 3 sec Fall from Max Stabilized Velocity (deg)
DJI Phantom 3	Flight Test Config. / 3.13 lbf	74	266	175	84
	Nominal Config. / 2.67 lbf	68	225	155	82
Vendor 1 Quadrotor (with cage)	Flight Test Config. / 0.95 lbf	49	117	60	87
	Nominal Config. / 0.727 lbf	42	86	45	85
Vendor 1 Quadrotor (without cage)	Flight Test Config. / 0.85 lbf	54	142	75	60
	Nominal Config. / 0.6 lbf	48	112	60	66
DJI Mavic Pro	Flight Test Config. / 2.47 lbf	82	327	175	82
	Nominal Config. / 1.64 lbf	68	225	145	86
GoPro Karma	Flight Test Config. / 5.07 lbf	73	259	140	58
	Nominal Config. / 4.07 lbf	65	206	120	58
DJI Inspire 2	Flight Test Config. /9.82 lbf	83	335	180	66
	Nominal Config. / 8.14 lbf	74.5	270	160	67
Vendor 3 Quadrotor	Flight Test Config. /5.2 lbf	74	266	140	*
	Nominal Config. / 4.2 lbf	70	238	130	*

Table 22 and Table 23 provide estimates of impact resultant velocity, impact angle, and impact KE for the S800 and DJI Inspire 2 aircraft based on inflation altitude and wind at 20 ft. The highlighted cells in these tables show where impact KE exceeds 180 ft-lbf, which can serve as a threshold for determining wind limitations of a parachute recovery system. Vendor 2 Parachute is able to maintain a 9.82 lbf DJI Inspire 2 aircraft at less than 180 ft-lbf of impact KE with winds up to 25 kt depending on failure altitude, which is a considerable mitigation of impact KE for this heavy of a multirotor. The Vendor 2 parachute is shown to be able to maintain a 14.6 lb DJI S800 at less than 180 ft-lbf of impact KE with winds up to 15 kt depending on failure altitude.

Table 22. S800 Parachute Dynamic Model Results

Altitude Loss (ft)	Horizontal Velocity at Failure (ft/s)	Resultant Velocity (ft/s) / Impact Angle (deg) / Impact KE (ft-lb)						
		Wind at 20 ft (kt)						
		0	5	10	15	20	25	30
100	0	12/90/33	14/61/44	20/38/87	26/28/155	33/22/242	39/18/338	44/16/443
200	0	12/90/33	15/54/51	22/34/106	28/25/183	35/20/278	41/17/384	47/15/503
300	0	12/90/33	16/51/55	22/33/113	25/29/193	36/20/292	42/17/405	48/23/534
400	0	12/90/33	16/51/56	22/34/109	28/26/179	34/21/263	40/18/357	50/14/558

Table 23. DJI Inspire 2 Parachute Dynamic Model Results

Altitude Loss (ft)	Horizontal Velocity at Failure (ft/s)	Resultant Velocity (ft/s) / Impact Angle (deg) / Impact KE (ft-lb)						
		Wind at 20 ft (kt)						
		0	5	10	15	20	25	30
100	0	10/90/15	13/53/24	18/34/49	23/26/82	28/21/118	32/18/156	36/16/193
200	0	10/90/15	13/49/27	19/32/56	25/24/91	30/20/133	34/17/179	39/15/227
300	0	10/90/15	14/47/28	19/31/58	25/24/96	30/19/141	36/16/192	40/14/247
400	0	10/90/15	14/47/29	20/31/59	25/23/99	31/19/147	36/16/202	42/14/262

3.4 ATD AND SIMPLIFIED IMPACT TESTING

The following section will provide a review of aggregate test results based on families of aircraft, e.g. multirotor and fixed wing, or aircraft components. Individual aircraft test result plots are presented in appendices.

3.4.1 Background on UAH Test Execution and NTS Stop Work

The UAH research team originally contracted with National Technical Systems (NTS) in Huntsville, AL for completion of the simplified testing; however, NTS was unable to execute the testing and data reduction per their contract with UAH. UAH issued a stop-work order to NTS in May of 2018 and took over the simplified testing effort. Following the stop-work order, UAH procured a data acquisition system, designed and fabricated a new impact test stand, installed the test stand at the UAH Aerophysics Research Center, conducted calibration drops, and then began conducting simplified testing for Task A14.

3.4.2 Family of Aircraft Results Overview

The figures in this section show the aggregate peak resultant acceleration, probability of AIS ≥ 2 skull fracture, probability of AIS ≥ 2 head injury, probability of AIS ≥ 3 head injury, and probability of AIS ≥ 3 neck injury results for multirotor aircraft, fixed wing aircraft, and aircraft components and solid objects. Based on its experimental nature and a need for more statistically significant testing related to basic parameters like peak resultant acceleration, the simplified test apparatus data was not used to calculate concussion severity metrics that are currently being refined like Combined Probability of Concussion or Brain Injury Criteria. It's hard to quantify the meaning of experimental test device results relating to severity criteria where injury thresholds may be changing in the near future, and doing so may lead to publishing erroneous or misleading results. An exhaustive set of plots for each aircraft's ATD and/or simplified test results is included in Appendix D through Appendix T.

3.4.2.1 Family of Multirotor Aircraft Test Results

The plots in this section provide a review of test data relating to the head and neck injury potential of the multirotor aircraft used in Task A14. Where both NIAR and UAH data for a vehicle were available, NIAR data is shown since the full ATD should be considered the standard test apparatus for use in evaluating injury potential based on FMVSS 208 and NCAP. Later in the results section, there are comparisons between the UAH and NIAR test outputs.

The first comparison between multirotor aircraft is based on relating the peak resultant head acceleration in the full ATD and simplified tests to impact KE for each vehicle (Figure 41). The wood block serves as a common reference point for all impact testing because it is essentially a rigid object and has the steepest slope relating impact KE to peak resultant acceleration of the head. The Vendor 1 Quadrotor impacts show that it has the most rigid structural response out of the group of multirotor vehicles tested at UAH and NIAR; however, its low mass resulted in a maximum impact KE of less than 25 ft-lbf, so it has very low likelihood of exceeding any injury thresholds (Figure F 4). This is backed up by the OSU PMHS tests where the Vendor 1 Quadrotor impacts did not cause any injuries even with impact KE far beyond what it can generate during a fall. The DJI Mavic Pro is more compliant than the Vendor 1 Quadrotor when impacting in its stiffest orientation, which is top-down (Figure E 1). Based on review of test videos from UAH's worst case orientation testing, the DJI Mavic Pro inverted or top-down orientation appears to have the least compliance because none of the arms can naturally fold toward the body when impacting in an inverted orientation. The DJI Mavic Pro's arm folding is used for making the aircraft compact for storage, but it also seems to mitigate impact severity in some orientations. The bottom-down and side-into-head impact orientations allow the arms to fold. When impacting nose first into the head, the vehicle has compliance in its nose (Figure E 1). During the nose into head impact tests conducted at UAH, there was less than a 10g resultant acceleration increase between 25ft/s and 36 ft/s impacts because the nose crumpled at the higher impact speed and extended out the period of deceleration. The NIAR DJI Phantom 3 test data shown in Figure 41 is based on the aircraft impacting the ATD head between the arms on the front of the aircraft. The slope of the Phantom 3 line is roughly ½ of the slope of the Vendor 1 Quadrotor line, although its higher mass enables development of up to 192 ft-lb of impact KE at terminal velocity, so mass is the dominant factor in the Phantom 3's injury potential. The next most compliant aircraft is the 4.2 lbf Vendor 3 Quadrotor, which has a carbon fiber, printed circuit board (PCB) and 3D printed plastic frame (Figure 41). Based on the NIAR testing, the DJI Inspire 2, when impacting at velocities and angles representative of descent under parachute, has the lowest injury potential of the multirotor aircraft that were tested in this study.

The terminal velocity impact KE levels of the Vendor 1 Quadrotor, DJI Mavic Pro, Karma, and Phantom 3 are represented in Figure 41. The lines of constant terminal velocity impact KE for the DJI Mavic Pro, Karma, and Phantom 3 intersect the impact test curve fits of KE vs Peak Resultant Acceleration data for each of these aircraft above the 198g skull fracture threshold limit, which indicates that these aircraft have some potential for causing AIS ≥ 2 skull fractures if they impact at or near the respective terminal velocity for each aircraft. The 198g limit was chosen as an injury threshold during Task A4[2]. Subsequent evaluation of the 198g peak resultant acceleration threshold shows that is a conservative threshold with a 9% chance of an AIS ≥ 2 skull fracture based on automotive medicine research.[14] Based on flight test and modeling experience with the multi-rotor aircraft, it takes 150-200 ft of unpowered descent to reach near terminal velocity. However, when equipped with stock camera payloads, many of these aircraft are flown at lower altitudes for collecting aerial imagery, which can lower injury potential. Whether by virtue of payload limitations or operational procedures, altitude restrictions are an effective way to mitigate the risk of injury.

[14] Mertz, H., Irwin, A., Prasad, P., Biomechanical and Scaling Basis for Frontal and Side Impact Injury Assessment Reference Values, Stapp Car Crash Journal, Vol. 60 (November 2016), pp. 625-657.

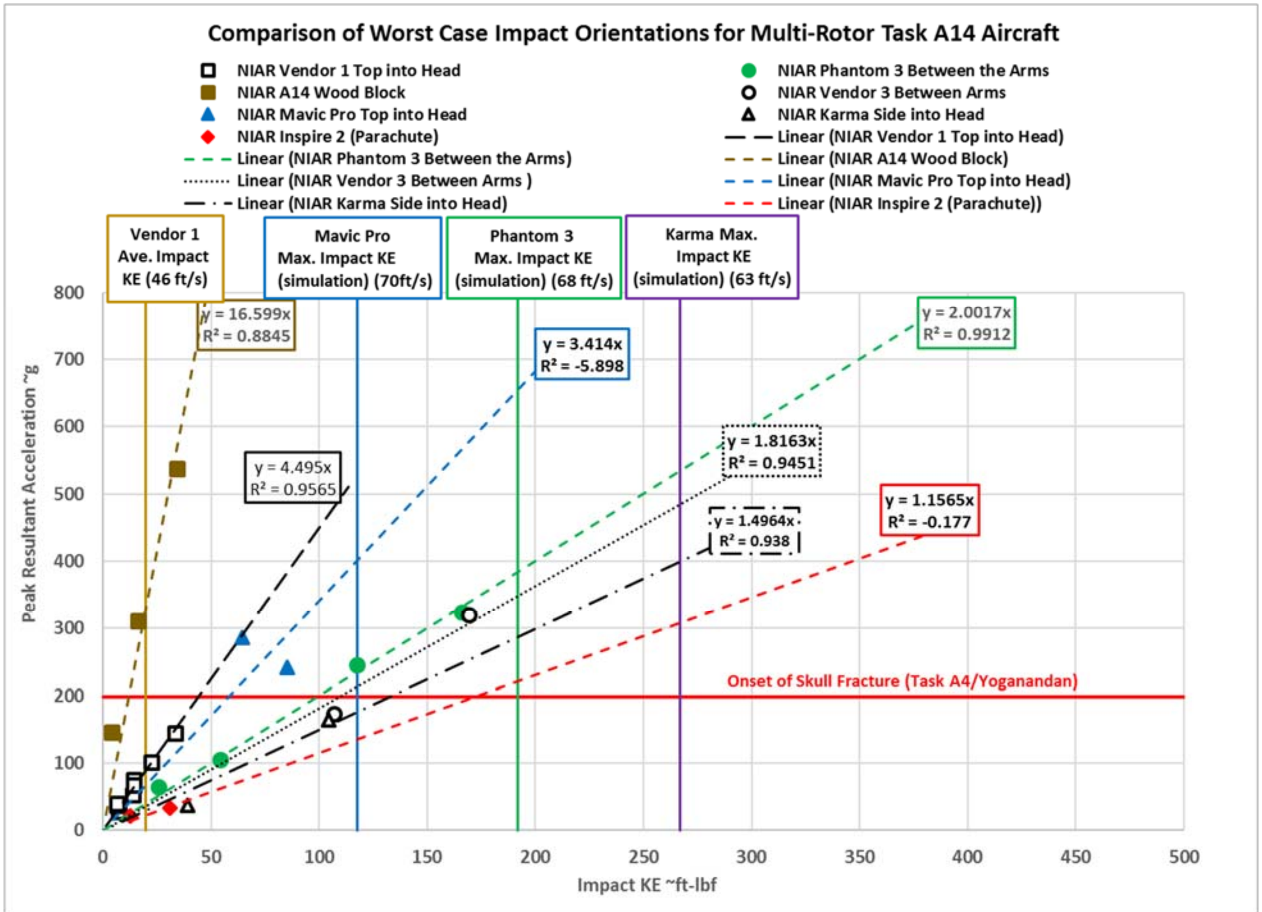

Figure 41. Comparison of Worst Case Vehicle Orientations for Multi-Rotor Task A14 Aircraft

The assessment of skull fracture potential that is indicated by Figure 41 is further validated by relating the peak resultant acceleration observed in each the NIAR and UAH testing via a log normal cumulative distribution with a mean of 262 and standard deviation of 48 as defined by Mertz.[14] This relation is shown in Figure 42. While Figure 41 only shows vertical impacts, since that impact trajectory is common to both the full ATD and Simplified testing, Figure 42 includes test points from all impact angles in the test matrix. The 198g peak resultant acceleration threshold correlates to just over 9% probability of an AIS ≥ 2 skull fracture by way of the Mertz relationship. Figure 42 shows that there is greater than a 9% probability of AIS ≥ 2 skull fracture for the DJI Mavic Pro, Go Pro Karma, Vendor 3 Quadrotor, and Phantom 3 when impacting at higher velocities. 9% is being used as a reference point in this analysis because it serves as a common point between the 198g threshold in Figure 41 and the peak resultant acceleration to probability of skull fracture relation shown in Figure 42. For the DJI Mavic Pro, this elevated risk was observed in tests with impact velocities greater than 50 ft/s, which is 73% of its estimated terminal velocity (Table 21). For the Go Pro Karma, there is elevated risk of AIS ≥ 2 skull fracture at impact velocities of 40 ft/s or more, which is roughly 60% of its estimated terminal velocity. Based on the Task A14 test data, the DJI Phantom 3 has 9% or more probability for AIS ≥ 2 skull fractures at impact velocities greater than 50 ft/s, which is 73% of its estimated terminal velocity based on the UAH aerodynamic modeling results presented in Table 21. The DJI Inspire 2, when descending under a parachute recovery system either vertically or in winds up to 30 kt, has very low potential to cause AIS ≥ 2 skull fractures because the peak resultant acceleration of the NIAR ATD head was well under 198g at these impact velocities (Figure 41 and Figure 42). Parachute recovery systems and limiting operating altitude over people are effective ways to manage impact KE and skull fracture potential for small UAS.

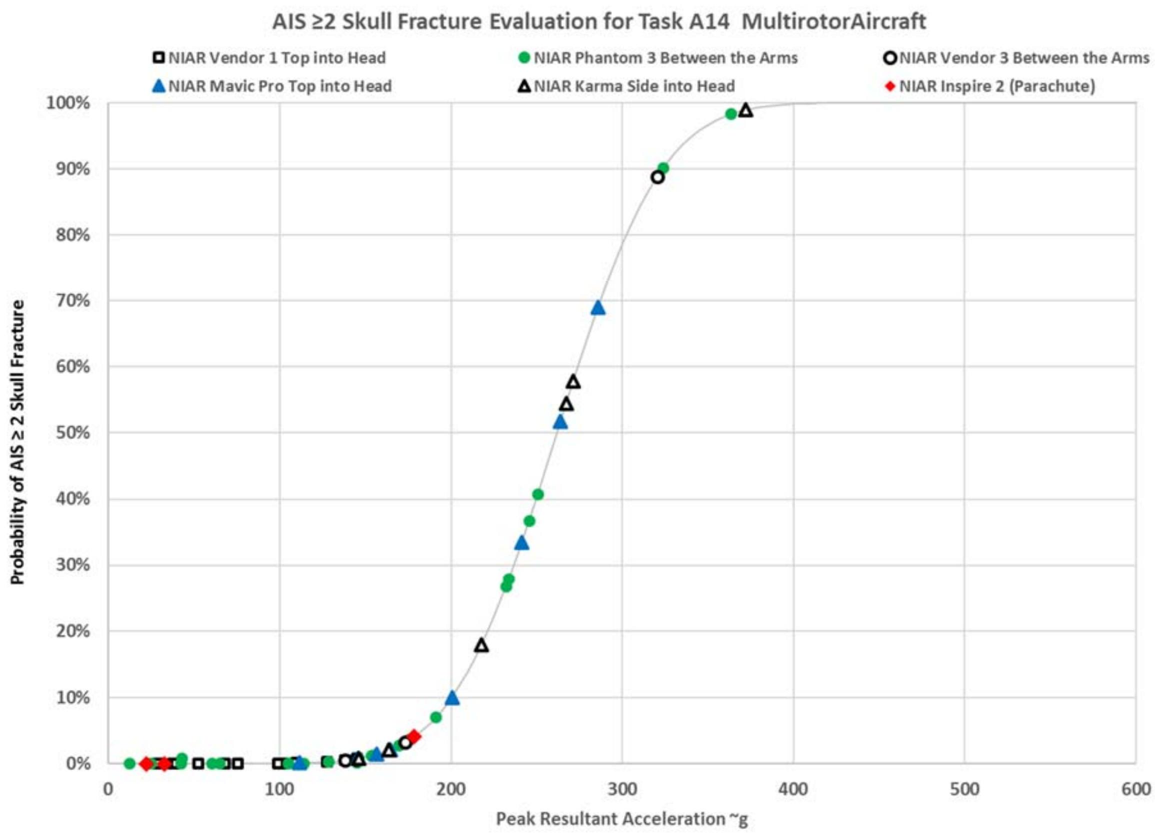

Figure 42. Probability of an AIS ≥ 2 Skull Fracture Evaluation for Task A14 Multirotor Aircraft

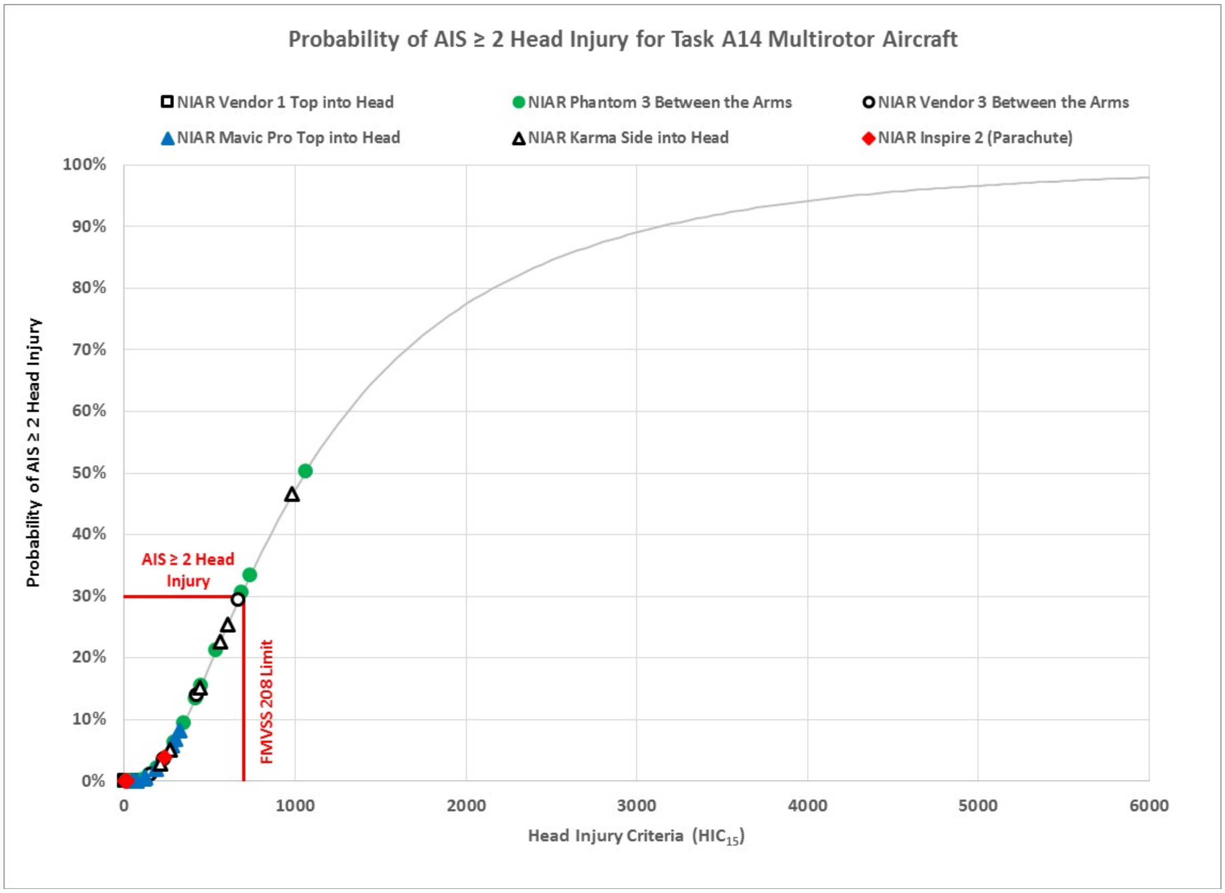

Figure 43. Probability of AIS ≥ 2 Head Injury for Task A14 Multirotor Aircraft

The estimated probabilities of AIS ≥ 2 and AIS ≥ 3 head injuries based on HIC_{15}, for the Task A14 multirotor aircraft are shown in Figure 43 and Figure 44. In Figure 43, $HIC_{15} = 700$ is used as an injury severity threshold because it correlates to 30% probability of an AIS ≥ 2 head injury based on FMVSS 208[9]. Only the DJI Phantom 3, Go Pro Karma, and Vendor 3 Quadrotor show potential for 30% or more probability of AIS ≥ 2 head injury (Figure 43). In Figure 44, $HIC_{15} = 1170$ is used as an injury severity threshold because it correlates to 30% probability of an AIS ≥ 3 head injury based on NCAP[15]. None of the multirotor aircraft exceeded 30% probability of an AIS ≥ 3 head injury during the NIAR impact testing.

UAH developed a simple parachute recovery system that was used during failure flight testing of every Task A14 aircraft, including the Vendor 1 Quadrotor, to prevent damage to the aircraft after failures were induced. While it is feasible to install parachute recovery systems on many small UAS; UAH has not yet done specific analysis to determine how much these recovery systems reduced the injury potential of any aircraft other than the DJI S800 and DJI Inspire 2.

[15] Consumer Information; New Car Assessment Program. Federal Register, Vol 73, No. 134. National Highway Traffic Safety Administration (Docket No. NHTSA-2006-26555), Department of Transportation, Final Decision Notice, July 2008.

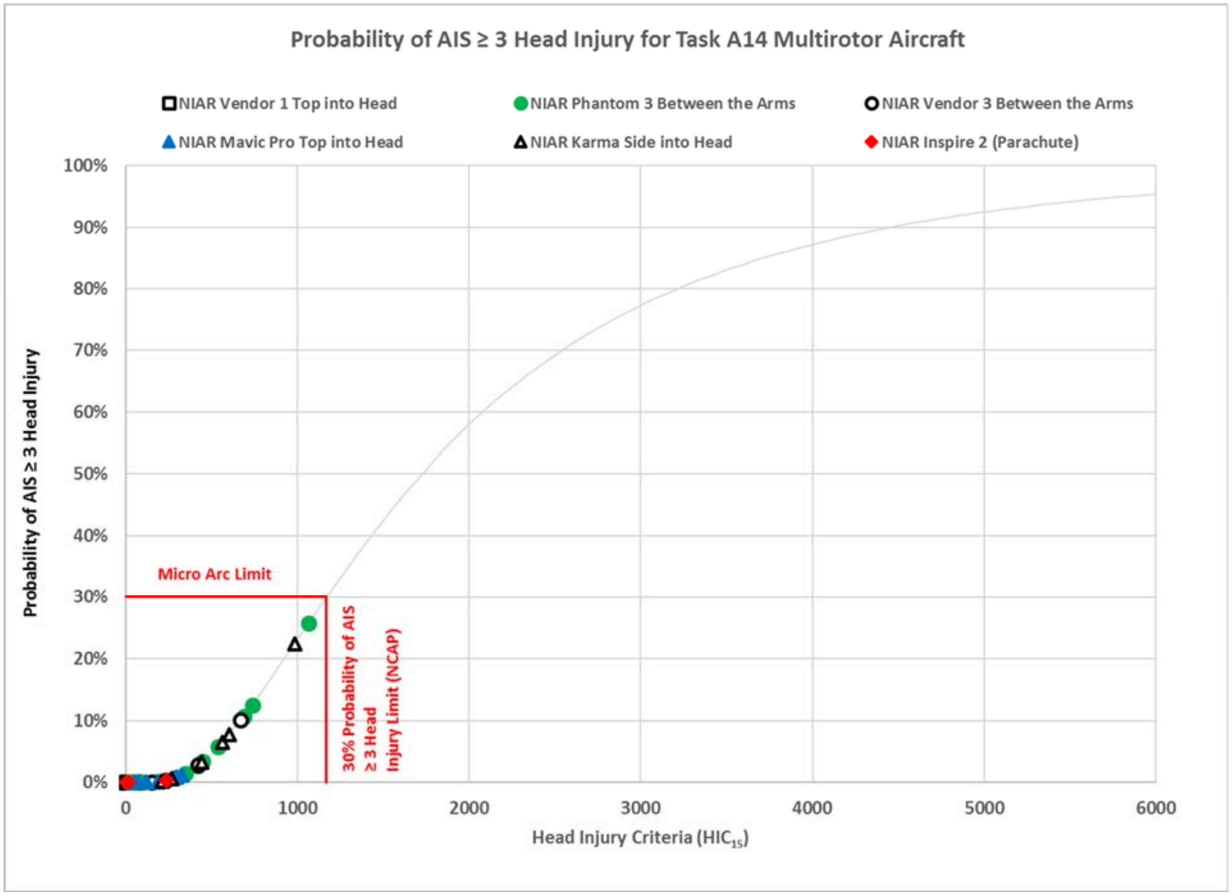

Figure 44. Probability of AIS ≥ 3 Head Injury for Task A14 Multirotor Aircraft

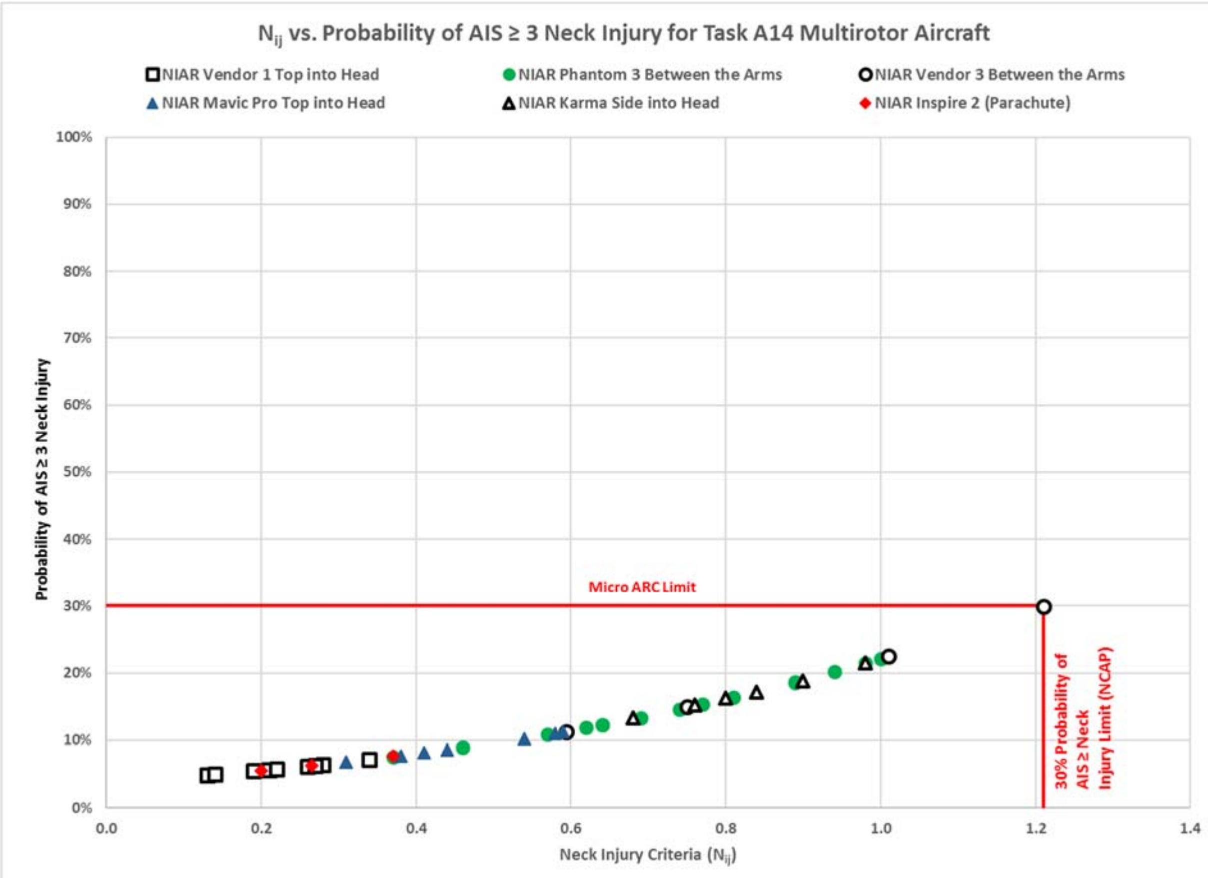

Figure 45. N_{ij} vs. Probability of AIS ≥ 3 Neck Injury for Task A14 Multirotor Aircraft

The majority of Task A14 multirotor aircraft impacts resulted in less than 30% probability of AIS ≥ 3 neck injury (Figure 45). The lone impact test with approximately 30% probability of AIS ≥ 3 was a vertical impact test of the Vendor 3 Quadrotor at 51 ft/s. The dominant factor in this impact that led to the threshold exceedance was compressive loading, which had a value of 1663 lbf. Flexion and extension moments in this impact were 6.5 and 5.5 ft-lbf, respectively, which are well within the flexion and extension load limits for this testing. All other impact tests results had less than 23% probability of an AIS ≥ 3 neck injury. In comparison with the fixed wing tests, many of these multi-rotors were tested close to their terminal velocities or near their maximum horizontal speeds as shown in their respective test results in Appendix C of this report.

3.4.3 Individual ATD and Simplified Multirotor Test Results

3.4.3.1 Overview.

Individual test results for all multirotor aircraft shown in APPENDIX D – DJI PHANTOM 3 SIMPLIFIED AND FULL ATD TEST DATA through APPENDIX J – DJI S800 SIMPLIFIED TEST DATA. These results are used on conjunction with the family of multirotor results to assess each individual vehicles test results and assessments on safe envelope using the ATD and simplified testing methods.

3.4.3.2 DJI Phantom 3

Complete DJI Phantom 3 ATD and Simplified Test Results are shown in Appendix D

Based on the ATD impact points conducted by NIAR, the DJI Phantom 3, impacting in its worst case impact orientation, has low potential to exceed 30% probability of an AIS ≥ 3 head or neck injury for impacts at velocities up to its terminal velocity (Table 24). The DJI Phantom 3's terminal velocity and terminal velocity impact KE are 68 ft/s and 194 ft-lbf, respectively. UAH testing determined that the worst case impact orientation of the DJI Phantom 3 occurred when impacted between the arms of the aircraft and all NIAR ATD impacts were conducted in this orientation (Figure D 1). The NIAR test points used in this analysis were cg-to-cg impacts with minimal angular or lateral offset from the intended point of impact and impact orientation. Impact offsets result in aircraft rotation after impact and reduce injury severity even for deviations as small as ½ inch and pitch angles of the vehicle of 4-9 deg.

Table 24. DJI Phantom 3 Injury Potential Summary

Injury Metric	DJI Phantom 3 Values
Nominal Configuration Weight (lbf)	2.67
Terminal Velocity (ft/s)	68
Impact KE at Terminal Velocity (ft-lbf)	194
PMHS Injury	Yes, at 104% of V_{term}
Worst Case Orientation 198g Crossing Impact KE (ft-lbf)	100 (Note 1)
Safe Altitude for impact KE associated with the 198g Crossing Point (ft)	< 60
Cross 198g Threshold below Terminal Velocity	Yes
9% Probability of Skull Fracture	Yes, within flight profile
Neck Compression Risk	Exceed NCAP limit at 61% of V_{term}
AIS ≥ 2 Skull Fracture	48% Probability at 96% of V_{term}
AIS ≥ 2 Head Injury	31% Probability at 96% of V_{term}
AIS ≥ 3 Head Injury	13% Probability at 96% of V_{term}
AIS ≥ 3 Neck (N_{ij})	21% Probability at 96% of V_{term}
Exceed 80g for 3ms	No
VT CP	99% Probability of AIS 1 Concussion at 96% of V_{term}
BrIC	Exceed 0.69 at 84% of V_{term}

Notes:
1. Crossing point of 198g is conservative with no AIS ≥ 2 or AIS ≥ 3 head or neck injuries occurring at these values during any of the PMHS tests.
2. The 198g crossing point is a method for how injury metrics can be used to define operating envelopes based upon ATD type testing and is deemed very conservative.
3. All parameters in this table are deemed as conservative since these worst case impacts can occur in only one orientation of the DJI Phantom 3 and only during center of mass collisions. Any offset from these collisions dramatically reduces the severity of the collision. Data in this table is also conservative based upon the PMHS results.

The DJI Phantom 3's curve fit on the Impact KE vs Peak Resultant Acceleration plot crosses the 198g threshold at 49 ft/s and 100 ft-lbf (Figure D 2). This impact KE is achieved in a vertical fall from approximately 60 ft. NIAR's testing shows a 90% probability of AIS ≥ 2 skull fracture for a vertical impact at 65 ft/s and 166 ft-lbf (Figure D 8). During OSU's PMHS testing, there was one AIS ≥ 2 skull fracture associated with the DJI Phantom 3 in a angled impact to the front of the head at 71 ft/s which is 104% of the DJI Phantom 3's average estimated terminal velocity. The highest probability of AIS ≥ 2 skull fracture from ATD testing is 98% for a 58 deg angled impact to the front of the head at 71 ft/s and 202 ft-lbf. The next highest probability of AIS ≥ 2 skull fracture is a 41% probability based on an angled impact to the rear of the head at 65 ft/s and 169 ft-lbf followed by a vertical impact with 37% probability of AIS ≥ 2 skull fracture at 55 ft/s and 117 ft-lbf. There is correlation between NIAR's ATD impact test results which show higher probabilities of an AIS ≥ 2 skull fracture at impact speeds of 55-71 ft/s and PMHS testing that resulted in an AIS ≥ 2 skull fracture during an angled impact to the front of the head at 71 ft/s.

The DJI Phantom 3's maximum probability of an AIS ≥ 3 head injury was 26% and this occurred during a 71 ft/s angled impact, which is beyond the average estimated terminal velocity of the aircraft. The DJI Phantom 3's maximum probability of an AIS ≥ 3 head injury within its flight envelope was 13% during a vertical impact to the head at 64 ft/s, 166 ft-lbf, which is 96% of terminal velocity (Figure 46). During OSU's PMHS testing, there was one AIS ≥ 2 skull fracture associated with the DJI Phantom 3 in a angled impact to the front of the head; however, this impact was at 71 ft/s that is 104% of the DJI Phantom 3's average estimated terminal velocity.

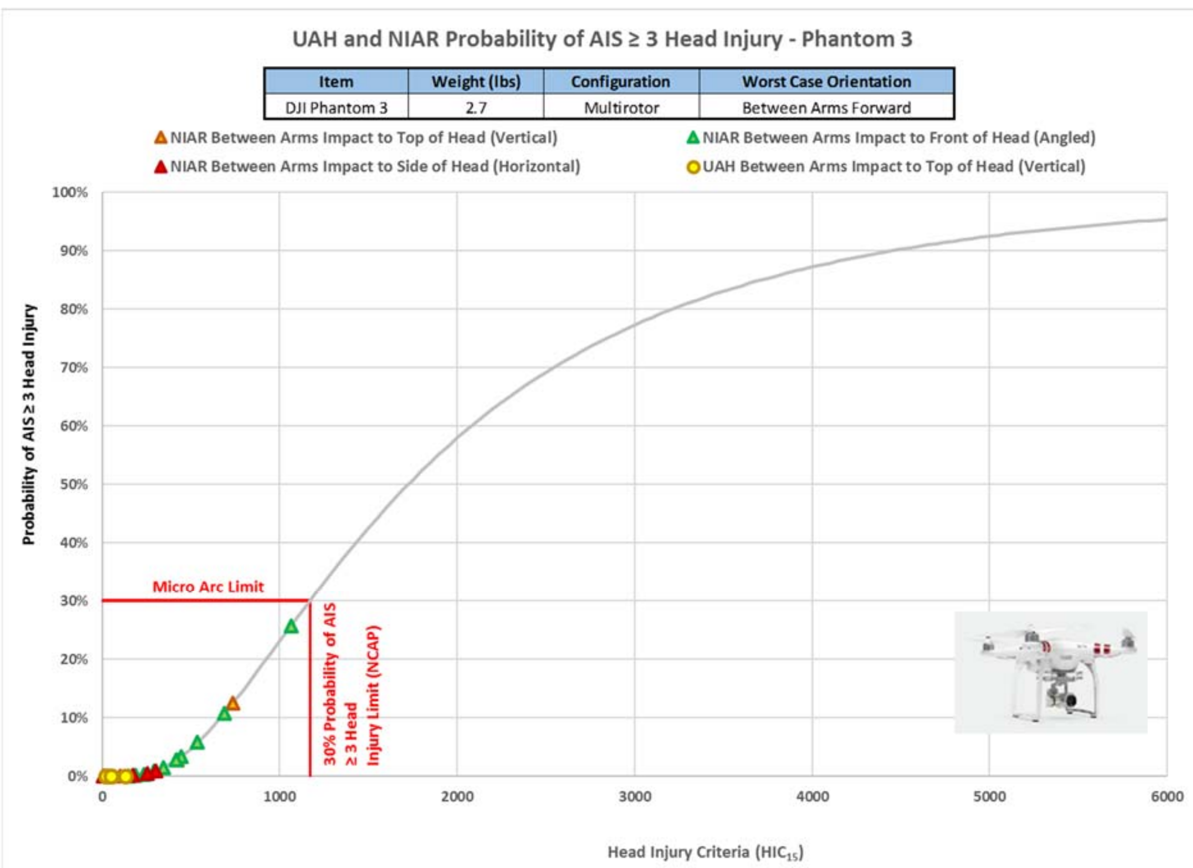

Figure 46. UAH and NIAR Probability of AIS ≥ 3 Head Injury - Phantom 3

The maximum likelihood of an AIS ≥ 3 neck injury was 21% based an impact at 65 ft/s and 177 ft-lbf, which is 96% of the DJI Phantom 3's terminal velocity (Figure 47). A curve fit of impact KE vs. N_{ij} trends indicates that the DJI Phantom 3 may exceed 30% probability of an AIS ≥ 3 neck injury in a cg-to-cg vertical impact between the arms at velocities in excessive of 66 ft/s and 180 ft-lbf (Figure 48). This requires additional test data to verify the curve fit trend and threshold exceedance at velocities up to terminal velocity; however, PMHS testing did not agree with this estimated level of neck injury probability and severityfor impacts occurring at greater impact KE across multiple PMHS.

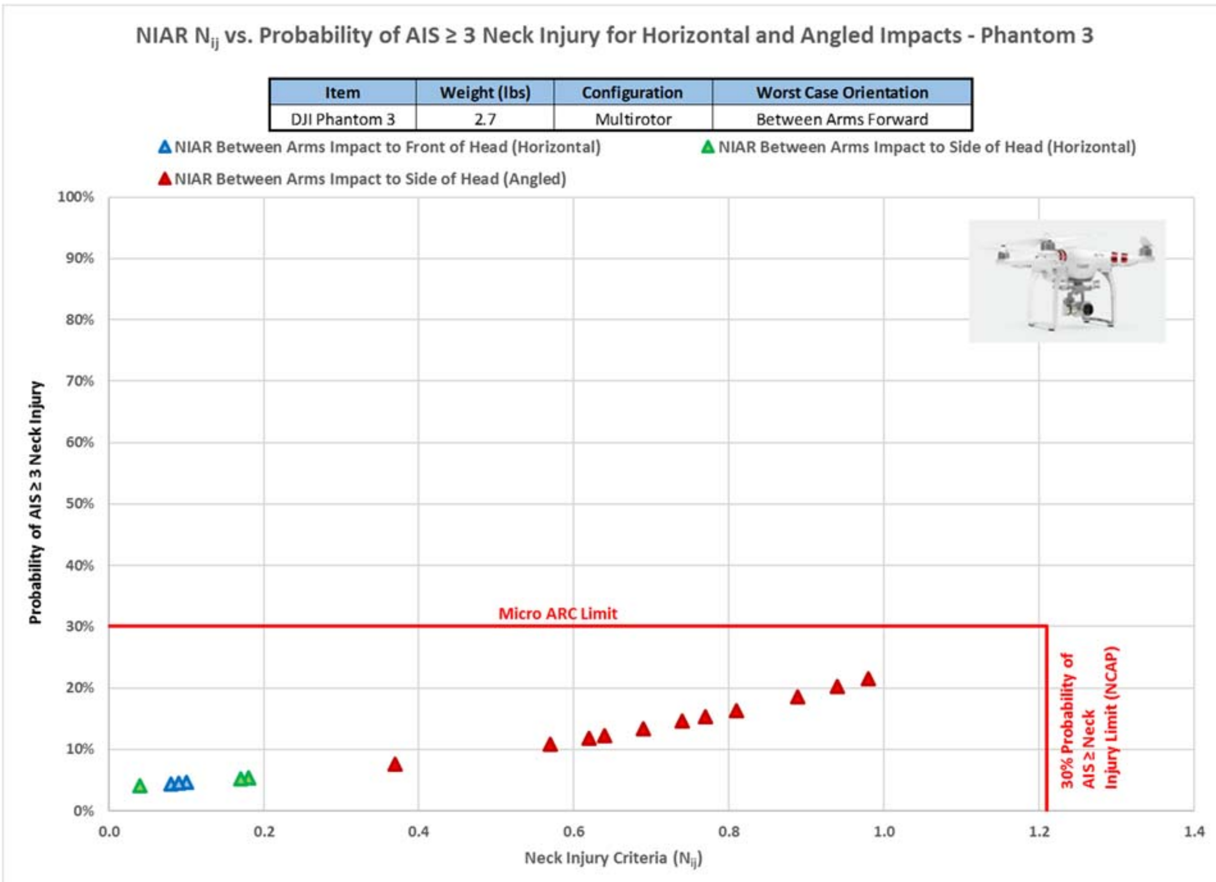

Figure 47. NIAR N_{ij} vs. Probability of AIS ≥ 3 Neck Injury for Horizontal and Angled Impacts - Phantom 3

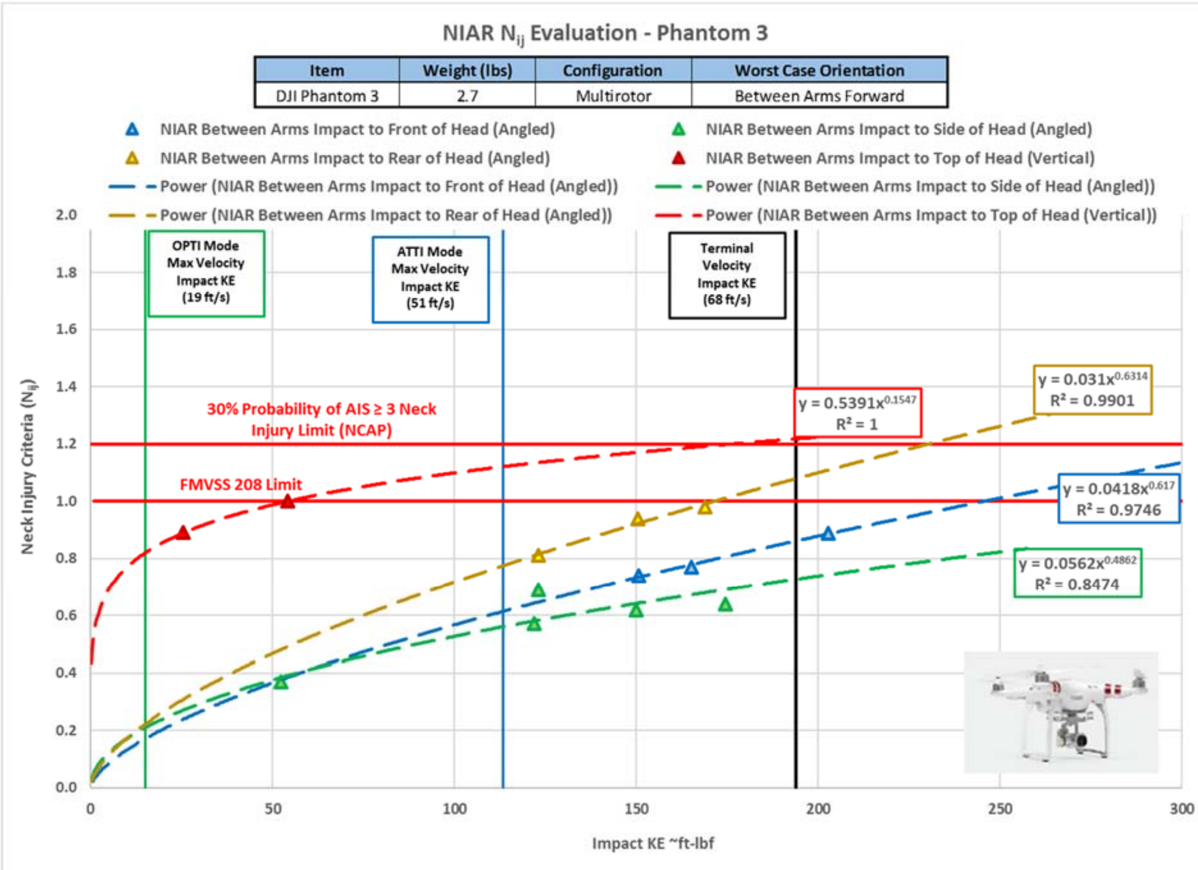

Figure 48. NIAR N_{ij} Evaluation - Phantom 3

Several NIAR impact tests conducted at or near terminal velocity resulted in BrIC values greater than 0.69. All of these impacts occurred at over 60 ft/s and 151 ft-lbf, which shows that there is at least 30% probability of AIS ≥ 3 concussion for the DJI Phantom 3 when it impacts at terminal velocity (Figure 49). However altitude and velocity restrictions can mitigate this concussion risk. The probability of concussion is further reduced if the aircraft cg is offset from the cg of the head during impact, which will result in greater aircraft rotation after impact and lower resultant linear and angular accelerations of the head.

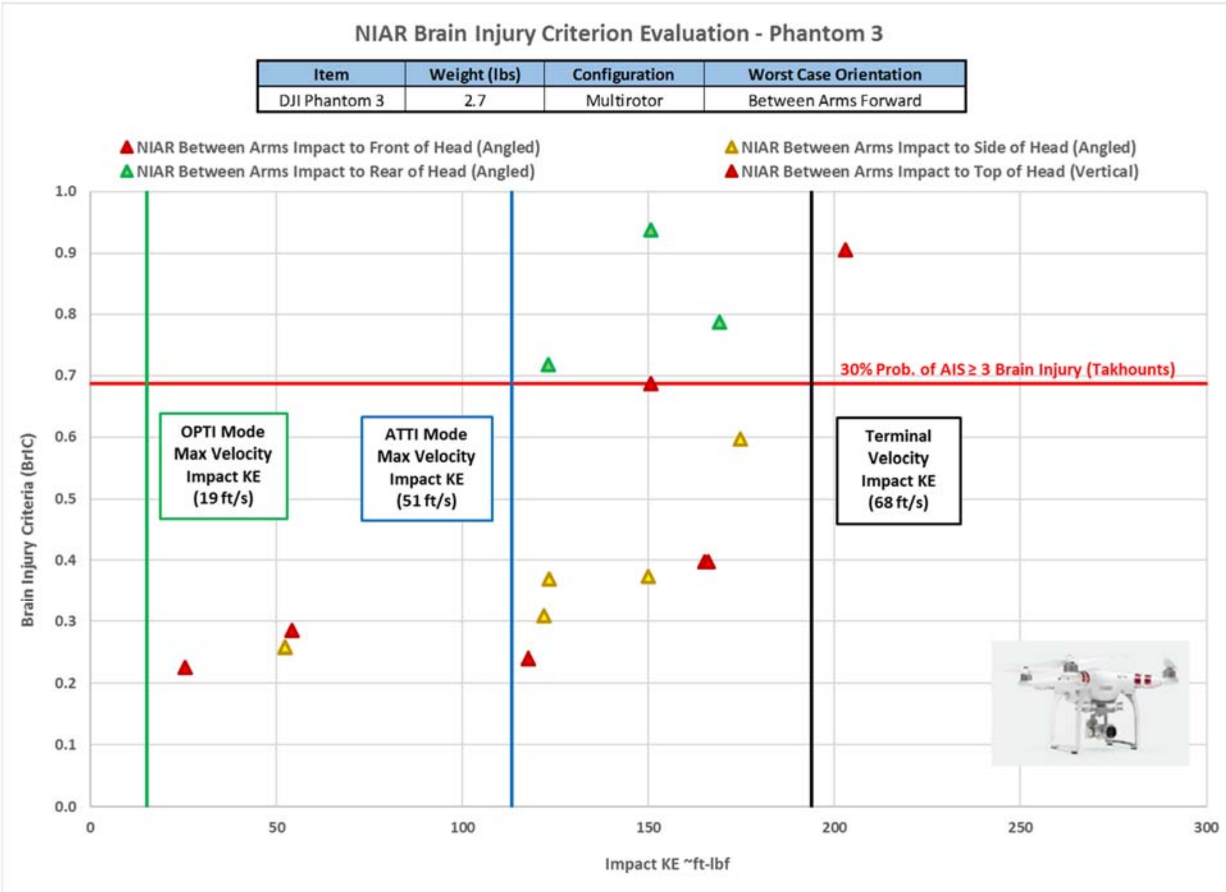

Figure 49. NIAR Brain Injury Criterion Evaluation - Phantom 3

While the ATD impact data using automotive injury metrics would suggest the DJI Phantom 3 should be flow at altitudes below 60 ft to avoid the potential of a skull fracture, the 60 ft altitude cap is associated with the 198g peak resultant acceleration threshold presented in the A4 Final Report. The 198g threshold represents a 9% probability of AIS ≥ 2 skull fracture. The PMHS data and ATD data, using of the automotive injury metrics, indicates the 198g threshold is overly conservative. The development of the injury metrics for evaluation is defined by the FAA and the A4 team strongly encourages more testing to better refine these metrics.

3.4.3.3 DJI Mavic Pro

Complete DJI Mavic Pro ATD and Simplified Test Results are shown in Appendix E

Based on the ATD impact points conducted by NIAR, the DJI Mavic Pro, impacting in its worst case impact orientation, does not exceed 30% probability of an AIS ≥ 3 head or neck injury for impacts at velocities up to its terminal velocity (Table 25). The DJI Mavic Pro's terminal velocity and terminal velocity impact KE are 68 ft/s and 118 ft-lbf, respectively. UAH testing determined that the worst case impact orientation of the DJI Mavic Pro occurred when impacted in an inverted position, also referred to as top into head, and all NIAR ATD impacts were conducted in this orientation (Figure E 1). The NIAR test points used in this analysis were cg-to-cg impacts with minimal angular or lateral offset from the intended point of impact and impact orientation. Impact offsets result in aircraft rotation after impact and reduce injury severity even for deviations as small as ½ inch and pitch angles of the vehicle of 4-9 deg.

Table 25. DJI Mavic Pro Injury Potential Summary

Injury Metric	DJI Mavic Pro Values
Nominal Configuration Weight (lbf)	1.64
Terminal Velocity (ft/s)	68
Impact KE at Terminal Velocity (ft-lbf)	117
PMHS Injury	None
Worst Case Orientation 198g Crossing Impact KE (ft-lbf)	58 (Note 1)
Safe Altitude for impact KE associated with the 198g Crossing Point (ft)	< 51
Cross 198g Threshold below Terminal Velocity	Yes
9% Probability of Skull Fracture	Yes, within flight profile
Neck Compression Risk	None based on testing; however, trend needs verification
AIS ≥ 2 Skull Fracture	69% Probability at 75% of V_{term}
AIS ≥ 2 Head Injury	8.19% Probability at 75% of V_{term}
AIS ≥ 3 Head Injury	1.21% Probability at 75% of V_{term}
AIS ≥ 3 Neck (N_{ij})	10.31% Probability at 75% of V_{term}
Exceed 80g for 3ms	Not within ATD test points
VT CP	99% Probability of AIS 1 Concussion at 96% of V_{term}
BrIC	None within ATD test points

Notes:
1. Crossing point of 198g is conservative with no AIS ≥ 2 or AIS ≥ 3 head or neck injuries occurring at these values during any of the PMHS tests.
2. The 198g crossing point is a method for how injury metrics can be used to define operating envelopes based upon ATD type testing and is deemed very conservative.
3. All parameters in this table are deemed as conservative since these worst case impacts can occur in only one orientation of the DJI Mavic Pro and only during center of mass collisions. Any offset from these collisions dramatically reduces the severity of the collision. Data in this table is also conservative based upon the PMHS results.

The DJI Mavic Pro's curve fit on the Impact KE vs Peak Resultant Acceleration plot crosses the 198g threshold at 58 ft-lbf (Figure E 3). This impact KE is achieved in a vertical fall from approximately 51 ft. The DJI Mavic Pro's terminal velocity is 68 ft/s with an associated impact KE of 117 ft-lbf. NIAR's testing shows a 69% probability of AIS ≥ 2 skull fracture for a vertical impact at 108 ft-lbf (Figure E 5). During OSU's PMHS testing, there were no skull fractures caused by DJI Mavic Pro impacts even at 103% of terminal velocity; however, i the OSU testing was done with the aircraft impacting sideways between the arms with the PMHS because the OSU launcher was not able of accommodating the aircraft for top into head impacts. Based on this difference in vehicle impact orientation (top vs. side) it isn't possible to correlate the PMHS test results for the AIS ≥ 2 skull fracture injury assessment with the ATD impact tests.

The DJI Mavic Pro's maximum probability of an AIS ≥ 3 head injury was 1.21% during a vertical impact to the head at 65 ft-lbf and 75% of terminal velocity (Figure E 7). Given this low probability and that Figure 51 indicates the DJI Mavic Pro will not exceed a HIC_{15} value of 1170 below its terminal velocity, it is likely that the DJI Mavic Pro cannot produce an AIS ≥ 3 head injury.

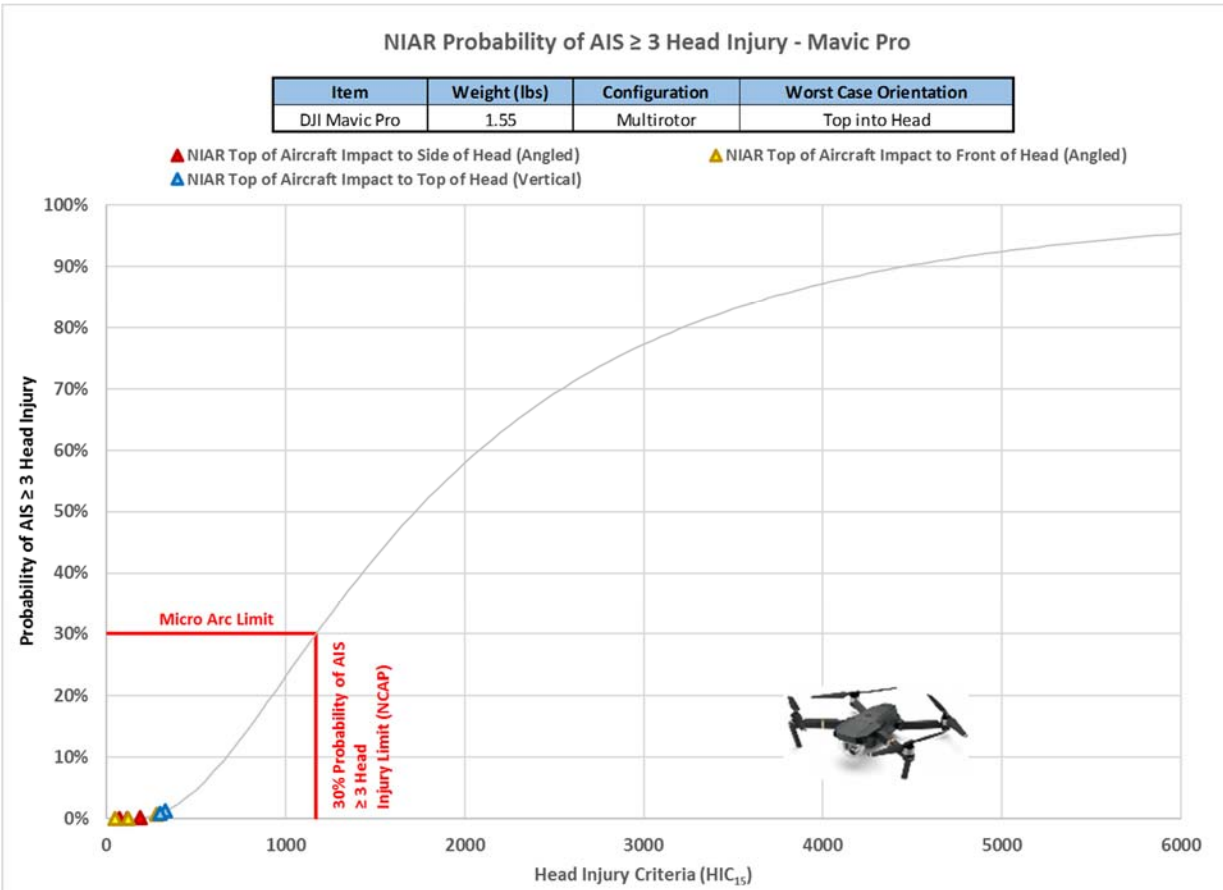

Figure 50. UAH and NIAR Probability of AIS ≥ 3 Head Injury - Mavic Pro

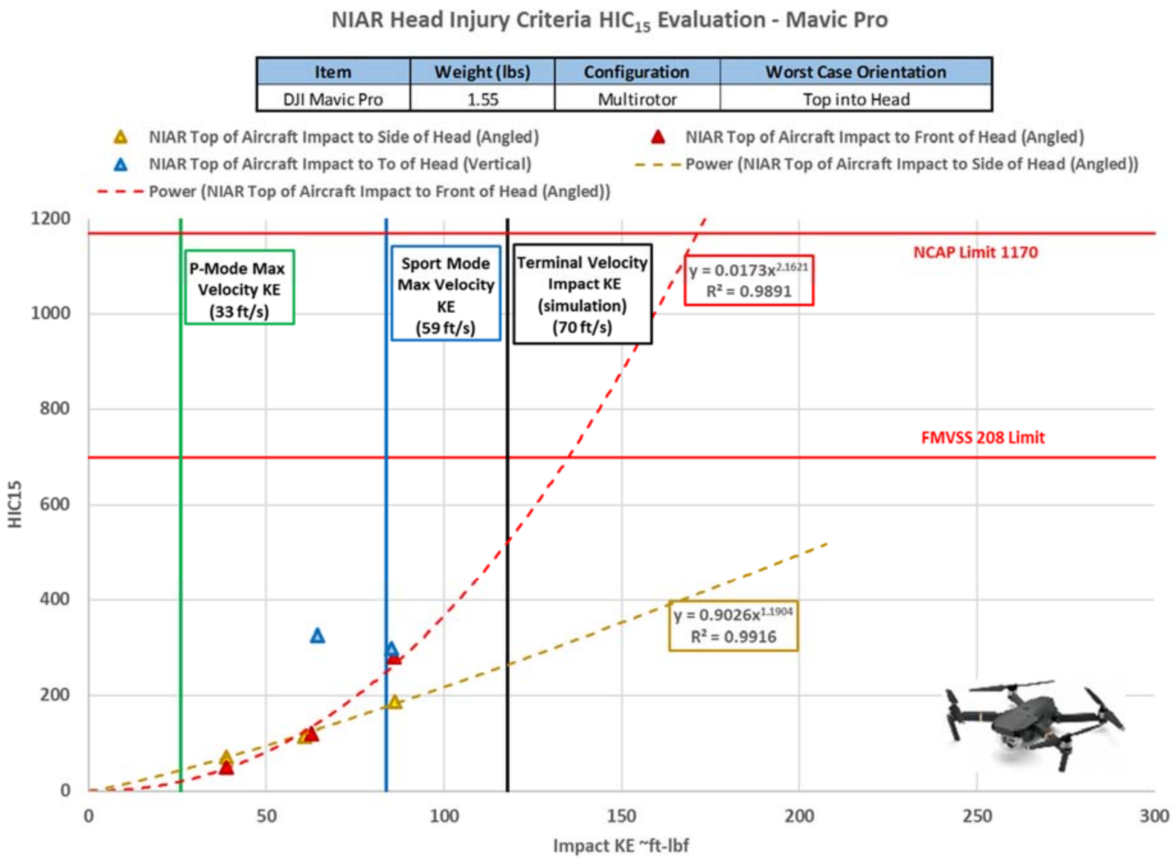

Figure 51. NIAR Head Injury Criteria HIC_{15} Evaluation - Mavic Pro

The maximum likelihood of an AIS ≥ 3 neck injury was 10.31% based an impact at 65 ft/s and 68 ft-lbf, which is 75% of the DJI Mavic Pro's terminal velocity (Figure 52). A curve fit of impact KE vs. N_{ij} trends indicates that the DJI Mavic Pro is unlikely to exceed the 30% probability of AIS ≥ 3 neck injury threshold at any flight condition at or below its terminal velocity (Figure 53). While the PMHS impacts where conducted in a different impact orientation, there were no PMHS neck injuries during the four DJI Mavic Pro PMHS impact tests.

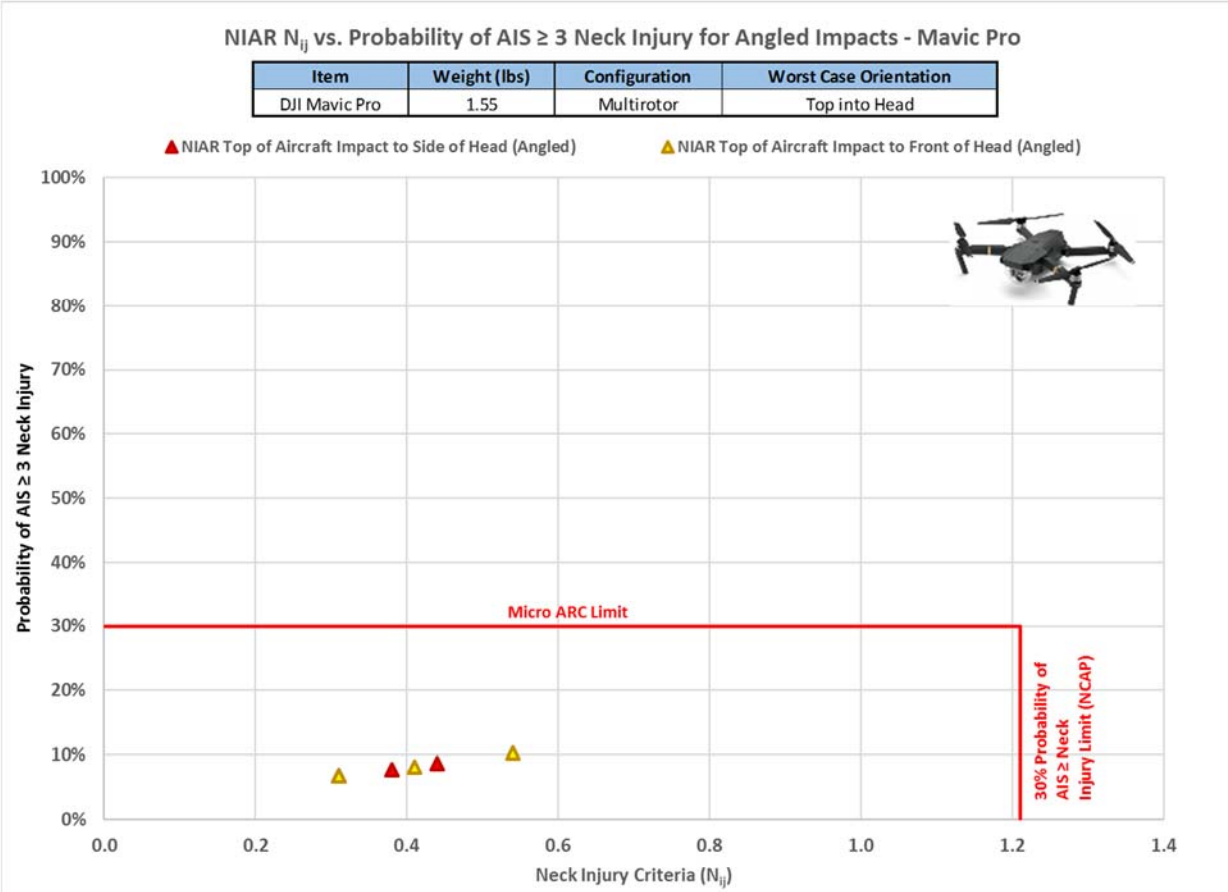

Figure 52. NIAR N_{ij} vs. Probability of AIS ≥ 3 Neck Injury for Horizontal and Angled Impacts - Mavic Pro

NIAR Worst Case N_{ij} Evaluation - Mavic Pro

Item	Weight (lbs)	Configuration	Worst Case Orientation
DJI Mavic Pro	1.55	Multirotor	Top into Head

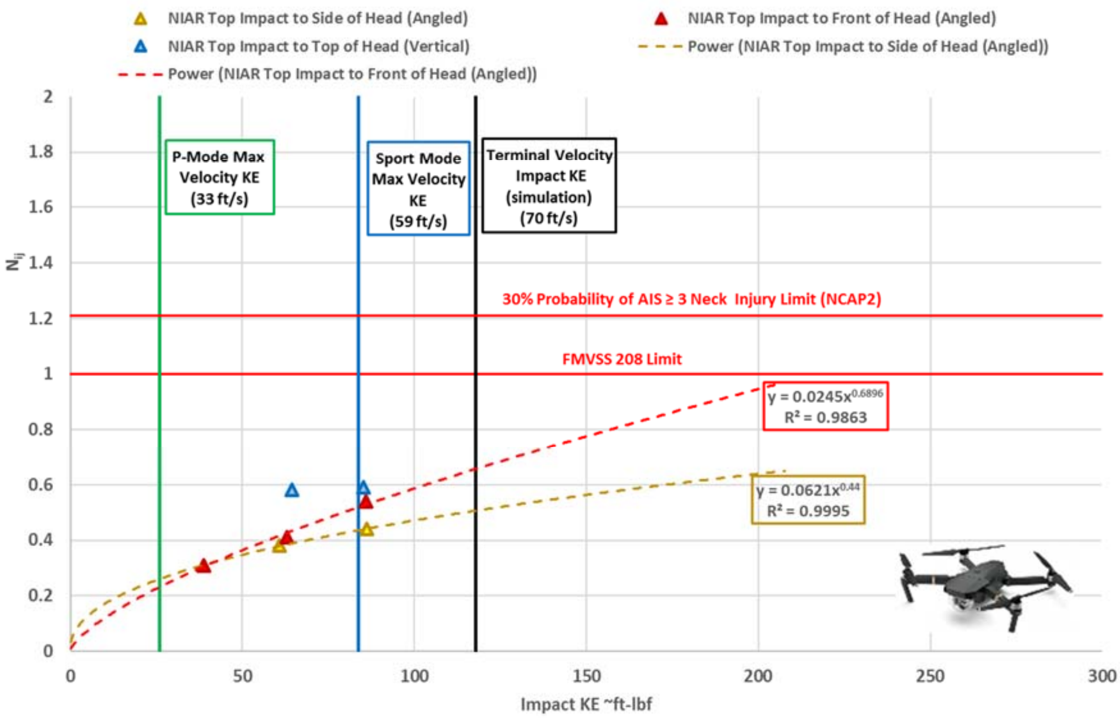

Figure 53. NIAR N_{ij} Evaluation - Mavic Pro

The maximum BrIC value achieved during the NIAR testing was 0.4 for an impact at 75% of the DJI Mavic Pro's terminal velocity. Based on the ATD test points, the DJI Mavic Pro appears to have a low risk of AIS ≥ 3 concussion at impact velocities up to terminal velocity (Figure 54). The probability of concussion is further reduced if the aircraft cg is offset from the cg of the head during impact, which will result in greater aircraft rotation after impact and lower resultant linear and angular accelerations of the head.

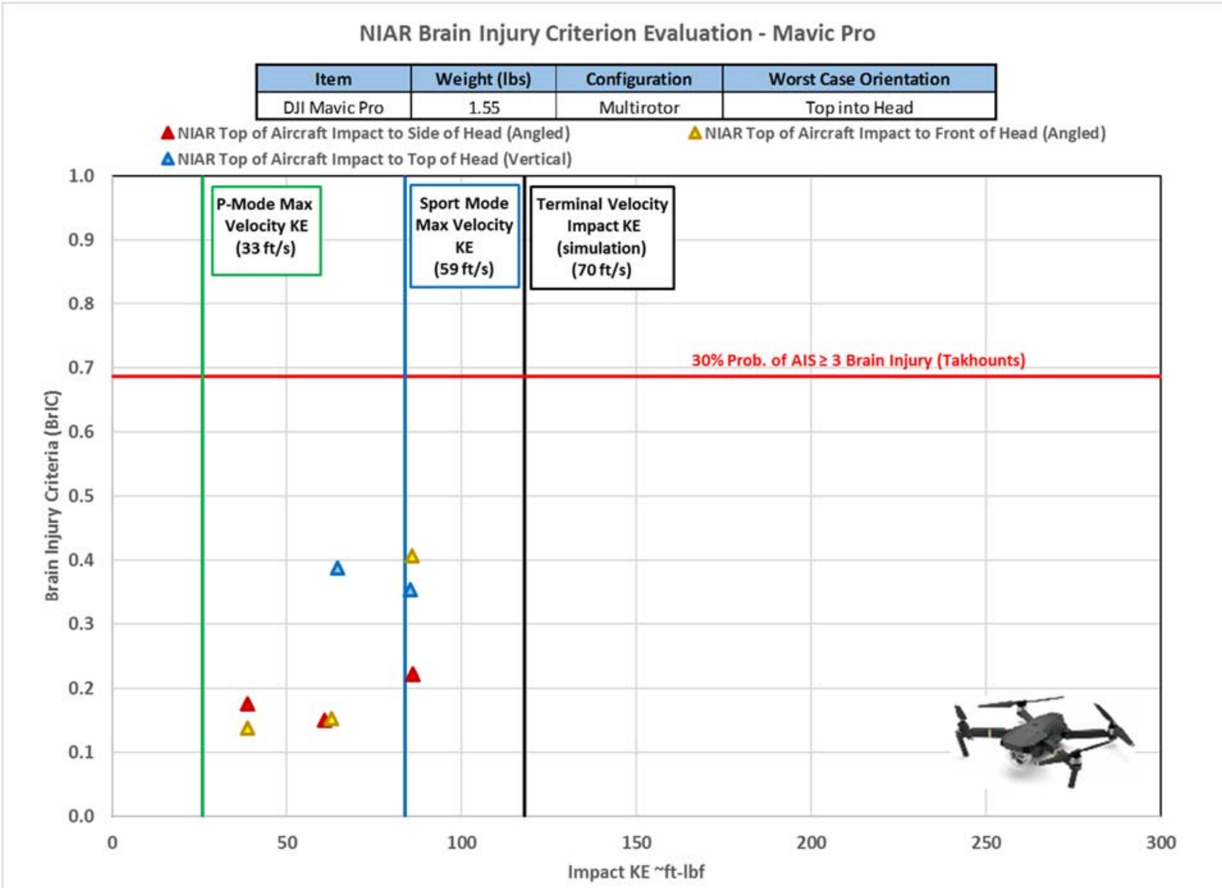

Figure 54. NIAR Brain Injury Criterion Evaluation - Mavic Pro

While the ATD impact data using automotive injury metrics would suggest the DJI Mavic Pro should be flown at altitudes below 51 ft to avoid the potential of a skull fracture, the 51 ft altitude cap is associated with the 198g peak resultant acceleration threshold presented in the A4 Final Report. While these altitudes are derived from the 198g threshold developed on the A4 Final Report, the 198g threshold represents a 9% probability of AIS ≥ 2 skull fracture. Based upon the Mavic Pro tests conducted on the PMHS that did not result in any AIS ≥ 2 skull fractures and the ATD data shown in Figure 50 and Figure 51, the 198g threshold and the altitudes derived from this injury threshold are overly conservative. The development of the injury metrics for evaluation is defined by the FAA and the A4 team strongly encourages more testing to better refine these metrics.

3.4.3.4 <u>Vendor 1 Quadrotor</u>

Vendor 1 Quadrotor ATD and Simplified Test Results are shown in Appendix F

Based on the ATD impact points conducted by NIAR, the Vendor 1 Quadrotor, impacting in its worst case impact orientation, does not exceed 30% probability of an AIS ≥ 3 head or neck injury for impacts at velocities up to 130% of its terminal velocity (Table 26). The Vendor 1 Quadrotor's terminal velocity and terminal velocity impact KE are 42 ft/s and 20 ft-lbf in the cage on nominal configuration, respectively. UAH and NIAR testing determined that the worst case impact orientation of the Vendor 1 Quadrotor occurred when impacted in an inverted position, also referred to as top into head, and all NIAR ATD impacts were conducted in this orientation (Figure F 1 and Figure F 3). The NIAR test points used in this analysis were cg-to-cg impacts with minimal angular or lateral offset from the intended point of impact and impact orientation. Impact offsets result in aircraft rotation after impact and reduce injury severity even for deviations as small as ½ inch and pitch angles of the vehicle of 4-9 deg.

Table 26. Vendor 1 Quadrotor Injury Potential Summary

Injury Metric	Vendor 1 Quadrotor Values
Nominal Configuration Weight (lbf)	0.727
Terminal Velocity (ft/s)	42
Impact KE at Terminal Velocity (ft-lbf)	20
PMHS Injury	None
Worst Case Vehicle Orientation 198g Crossing Impact KE (ft-lbf)	42 (Note 1)
Safe Altitude for impact KE associated with the 198g Crossing Point (ft)	Any
Cross 198g Threshold below Terminal Velocity	No
9% Probability of Skull Fracture	Not at or below terminal velocity
Neck Compression Risk	None based on testing
AIS ≥ 2 Skull Fracture	Less than 0.1% Probability at 130% of V_{term}
AIS ≥ 2 Head Injury	Less than 0.1% Probability at 130% of V_{term}
AIS ≥ 3 Head Injury	Less than 0.1% Probability at 130% of V_{term}
AIS ≥ 3 Neck (N_{ij})	7% Probability at 130% of V_{term}
Exceed 80g for 3ms	Not within ATD test points
VT CP	81% Probability of AIS 1 Concussion at 96% of V_{term}
BrIC	None within ATD test points

Notes:
1. Crossing point of 198g is conservative with no AIS ≥ 2 or AIS ≥ 3 head or neck injuries occurring at these values during any of the PMHS tests.
2. The 198g crossing point is a method for how injury metrics can be used to define operating envelopes based upon ATD type testing and is deemed very conservative.
3. All parameters in this table are deemed as conservative since these worst case impacts can occur in only one orientation of the DJI Mavic Pro and only during center of mass collisions. Any offset from these collisions dramatically reduces the deverity of the collision. Data in this table is also conservative based upon the PMHS results.

The Vendor 1 Quadrotor's curve fit on the Impact KE vs Peak Resultant Acceleration plot crosses the 198g threshold at 43 ft-lbf (Figure E 3). This impact KE is 215% of the aircraft's terminal velocity impact KE and cannot be achieved during freefall or powered flight. NIAR's testing shows a less than 0.1% probability of AIS ≥ 2 skull fracture for a vertical impact at 34 ft-lbf, which is 170% of its terminal velocity impact KE (Figure E 5). During OSU's PMHS testing, there were no skull fractures during the Vendor 1 Quadrotor impact testing at impacts up to 316% of terminal velocity impact KE. The PMHS test result provides some correlation with the low estimated probability of AIS ≥ 2 skull fracture from the ATD testing, although an actual injury, associated impacted conditions for the injury, and a greater number of tests are required for a complete comparison of the results.

The Vendor 1 Quadrotor's maximum probability of an AIS ≥ 3 head injury was less than 0.1% during a vertical impact to the head at 34 ft-lbf and 170% of terminal velocity impact KE (Figure 55). It is unlikely that the Vendor 1 Quadrotor can achieve any probability of AIS ≥ 3 head injury over 1% during an impact at terminal velocity.

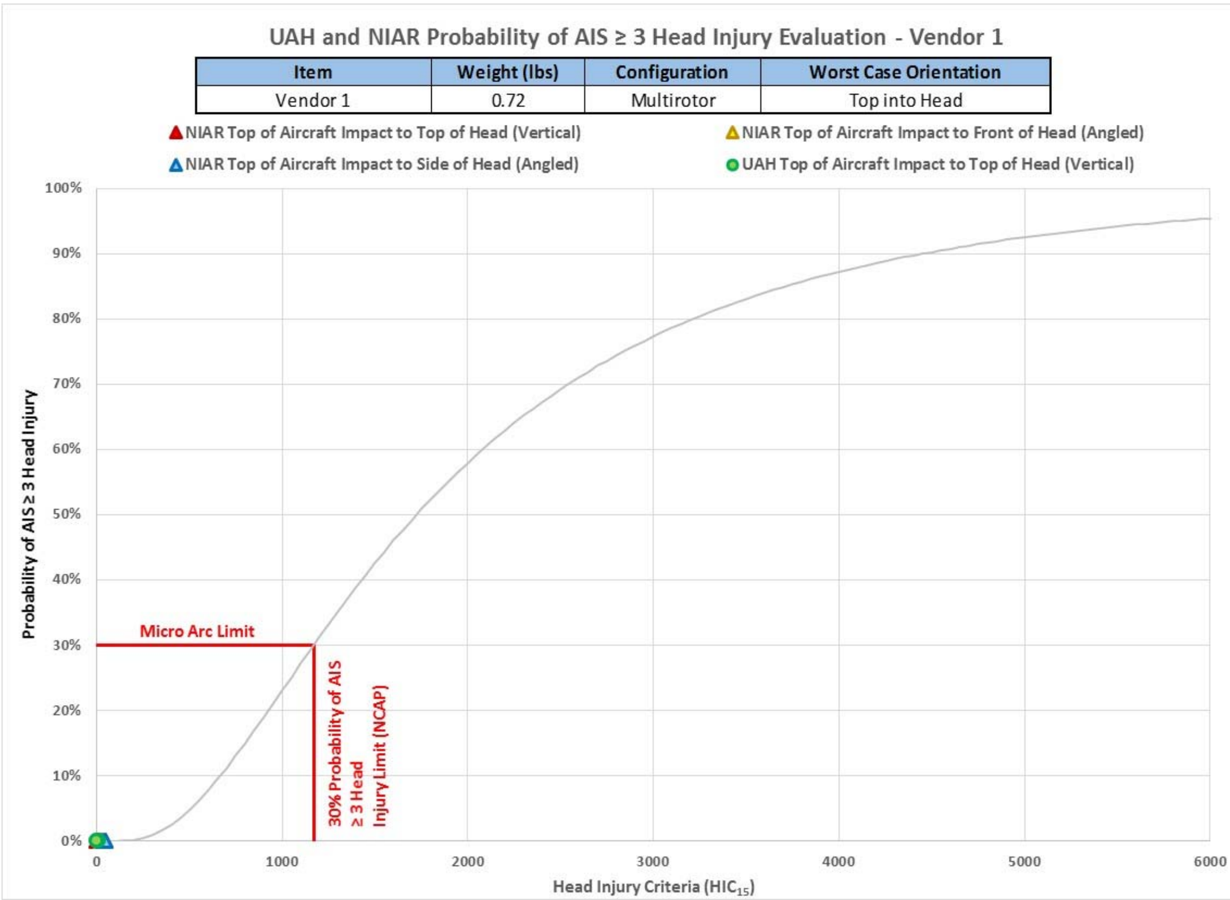

Figure 55. UAH and NIAR Probability of AIS ≥ 3 Head Injury – Vendor 1 Quadrotor

The maximum likelihood of an AIS ≥ 3 neck injury was 7% based an impact at 56 ft/s and 34 ft lbf, which is 170% of the Vendor 1 Quadrotor's terminal velocity impact KE (Figure 56). A curve fit of Impact KE vs. N_{ij} trends indicates that the DJI Mavic Pro is unlikely to exceed the 30% probability of AIS ≥ 3 neck injury threshold at any flight condition at or below its terminal velocity (Figure 57). There were no PMHS neck injuries during the two Vendor 1 Quadrotor PMHS impact tests which were conducted at 315% of the aircraft's terminal velocity impact KE.

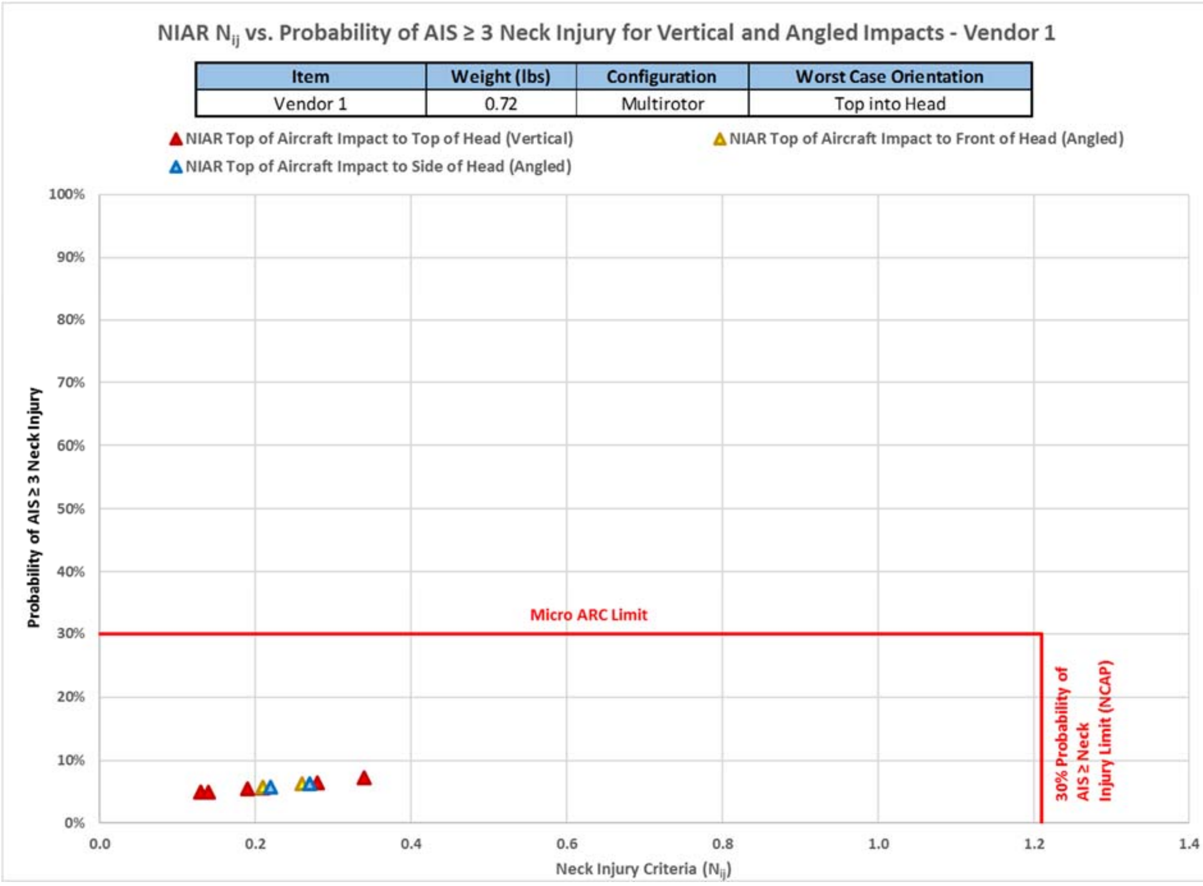

Figure 56. NIAR N_{ij} vs. Probability of AIS ≥ 3 Neck Injury for Horizontal and Angled Impacts – Vendor 1 Quadrotor

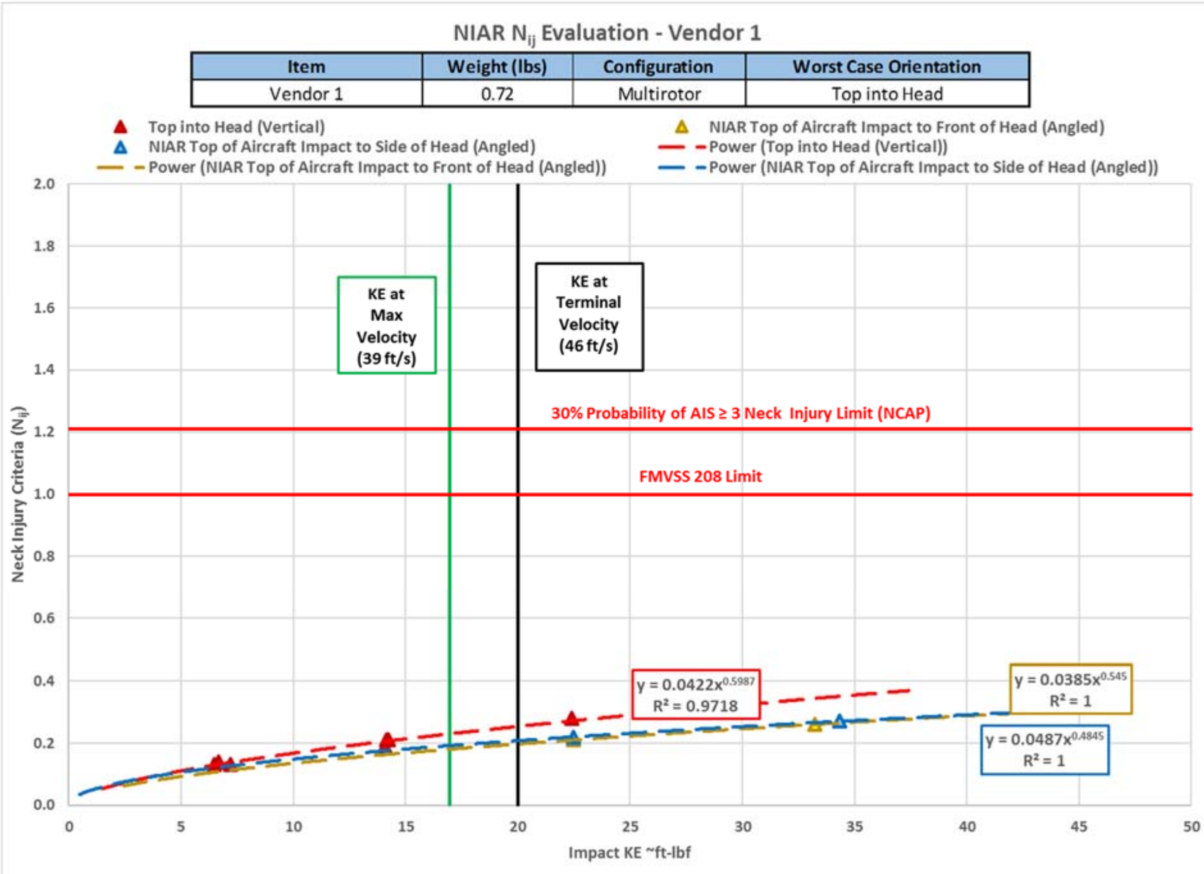

Figure 57. NIAR N_{ij} Evaluation – Vendor 1 Quadrotor

Several NIAR impact tests conducted at or near terminal velocity resulted in a peak BrIC values of 0.43 for an impact at 170% of terminal velocity impact KE. Based on the ATD test points, the DJI Mavic Pro appears to have a low risk of AIS ≥ 3 concussion at impact velocities up to terminal velocity (Figure 58). The probability of concussion is further reduced if the aircraft cg is offset from the cg of the head during impact, which will result in greater aircraft rotation after impact and lower resultant linear and angular accelerations of the head.

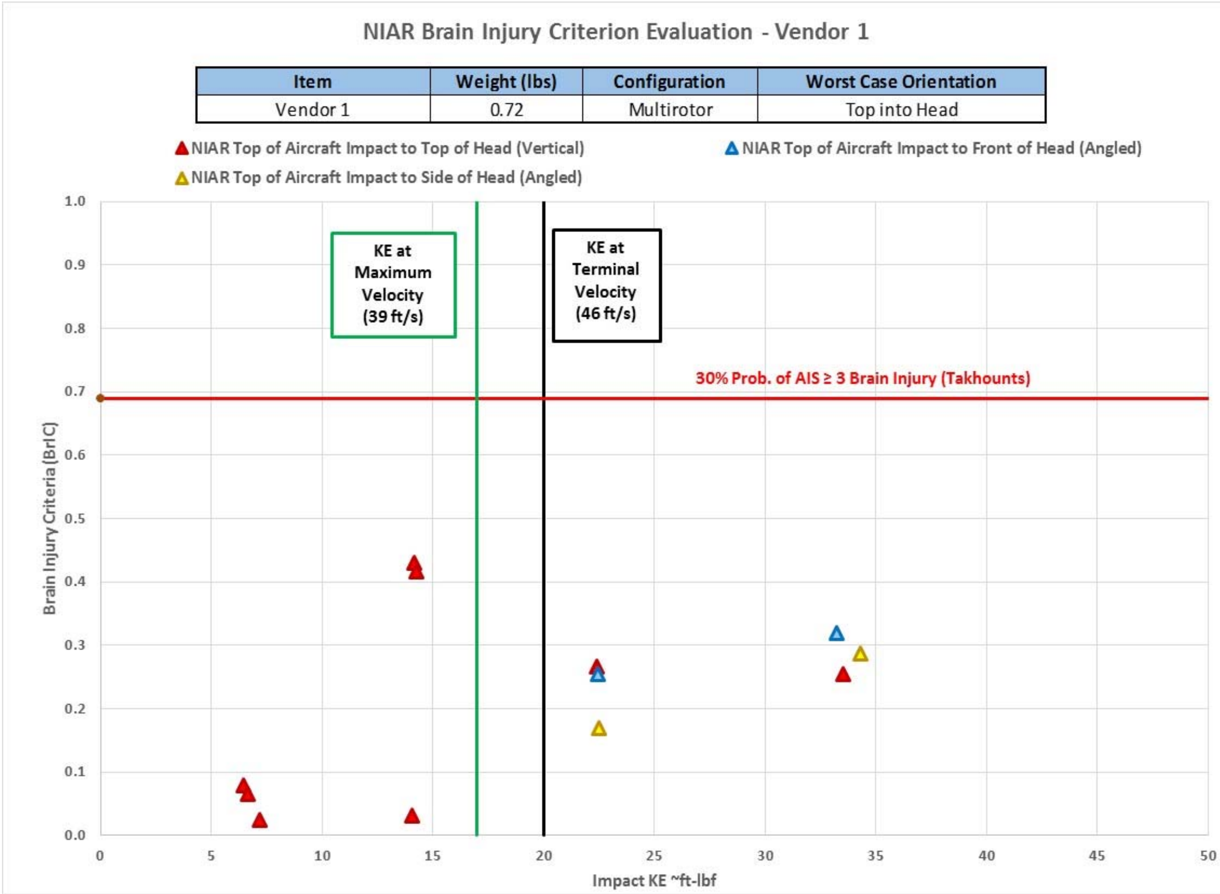

Figure 58. NIAR Brain Injury Criterion Evaluation – Vendor 1 Quadrotor

The ATD impact data using automotive injury metrics would suggest that the Vendor 1 Quadrotor can be flown at any altitude without exceeding the 1% probability of an AIS ≥ 3 injury of any type.

3.4.3.4.1 Go Pro Karma

Go Pro Karma ATD and Simplified Test Results are shown in Appendix G

Based on the ATD impact points conducted by NIAR, the Go Pro Karma, impacting in its worst case impact orientation, has strong potential to exceed 30% probability of an AIS ≥ 3 head or neck injury for impacts at velocities up to its terminal velocity (Table 27). The Go Pro Karma's terminal velocity and terminal velocity impact KE are 65 ft/s and 267 ft-lbf in the vehicle's nominal configuration, respectively. UAH testing determined that the worst case impact orientation of the Go Pro Karma occurred when impacted between the arms on the side of aircraft and all NIAR ATD impacts were conducted in this orientation (Figure G 1). The NIAR test points used in this analysis were cg-to-cg impacts with minimal angular or lateral offset from the intended point of vehicle impact and impact orientation.

Table 27. Go Pro Karma Injury Potential Summary

Injury Metric	Go Pro Karma Values
Nominal Configuration Weight (lbf)	4.07
Terminal Velocity (ft/s)	65
Impact KE at Terminal Velocity (ft-lbf)	267
PMHS Injury	No Go Pro Karma PMHS Test Points
Worst Case Impact Orientation 198g Crossing Impact KE (ft-lbf)	88 (Note 1)
Safe Altitude for impact KE associated with the 198g Crossing Point (ft)	26
Cross 198g Threshold below Terminal Velocity	Yes at 57% of V_{term}
9% Probability of Skull Fracture	Yes, within flight profile
Neck Compression Risk	80 ft-lbf at 55% of V_{term}
AIS ≥ 2 Skull Fracture	99% Probability at 76% of V_{term}
AIS ≥ 2 Head Injury	47% Probability at 76% of V_{term}
AIS ≥ 3 Head Injury	22% Probability at 76% of V_{term}
AIS ≥ 3 Neck (N_{ij})	21% Probability at 76% of V_{term}
Exceed 80g for 3ms	Not within ATD test points
VT CP	99% Probability of AIS 1 Concussion at 76% of V_{term}
BrIC	No Exceedances of 30% Probability of AIS ≥ 3 Brain Injury

Notes:
1. Crossing point of 198g is conservative with no AIS ≥ 2 or AIS ≥ 3 head or neck injuries occurring at these values during any of the PMHS tests.
2. The 198g crossing point is a method for how injury metrics can be used to define operating envelopes based upon ATD type testing and is deemed very conservative.
3. All parameters in this table are deemed as conservative since these worst case impacts can occur in only one orientation of the DJI Mavic Pro and only during center of mass collisions. Any offset from these collisions dramatically reduces the severity of the collision. Data in this table is also conservative based upon the PMHS results.

The Go Pro Karma's curve fit on the Impact KE vs Peak Resultant Acceleration plot crosses the 198g threshold at 37 ft/s and 88 ft-lbf (Figure D 2). This impact KE is achieved in a vertical fall from approximately 26 ft. NIAR's testing shows a 99% probability of AIS ≥ 2 skull fracture for a vertical impact at 158 ft-lbf, which is achieved at 59% of its terminal velocity impact KE (Figure G 8). The Go Pro Karma was not included in PMHS testing, so there are no correlating test points for reference with PMHS injuries. While the ATD impact data using automotive injury metrics would suggest the Go Pro Karma should be flow at altitudes below 26 ft to avoid the potential of a skull fracture, the 26 ft altitude cap is associated with the 198g peak resultant energy threshold presented in the A4 Final Report. As was previously stated, the 198g threshold is likely an overly conservative and more testing is needed to develop and refine automotive injury risk thresholds so that they are representative of the risk associated with sUAS impact kinematics.

The Go Pro Karma's maximum probability of an AIS ≥ 3 head injury was 22% during an angled 58 deg impact to the side of the head at 158 ft-lbf which is 59% of its terminal velocity impact KE (Figure 59). Additional testing up to an impact at terminal velocity would be needed to determine if a 30% probability of AIS ≥ 3 head injury can be achieved by this aircraft. Based on the current test points, it seems plausible that there could be 30% or more probability of this injury in a cg-to-cg side into head impact. A curve fit of the Go Pro Karma's HIC_{15} vs Impact KE data indicates that the 30% probability of AIS ≥ 3 head injury could be achieved by an angled impact at 172 ft-lbf of impact KE which is achieved at 64% of the vehicles terminal velocity (Figure 60); however, this value is based on a sample of two test points so more testing would be needed to verify the trend and experimental error.

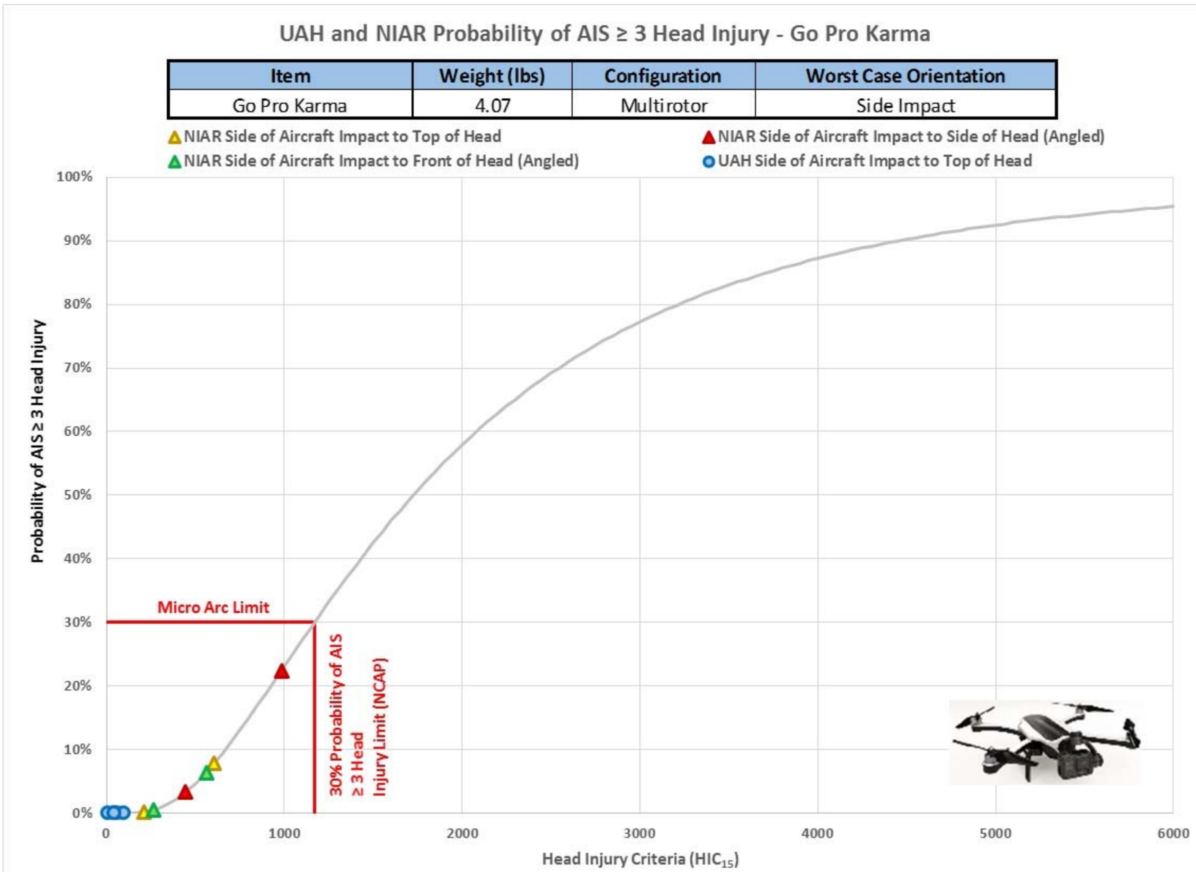

Figure 59. UAH and NIAR Probability of AIS ≥ 3 Head Injury - Go Pro Karma

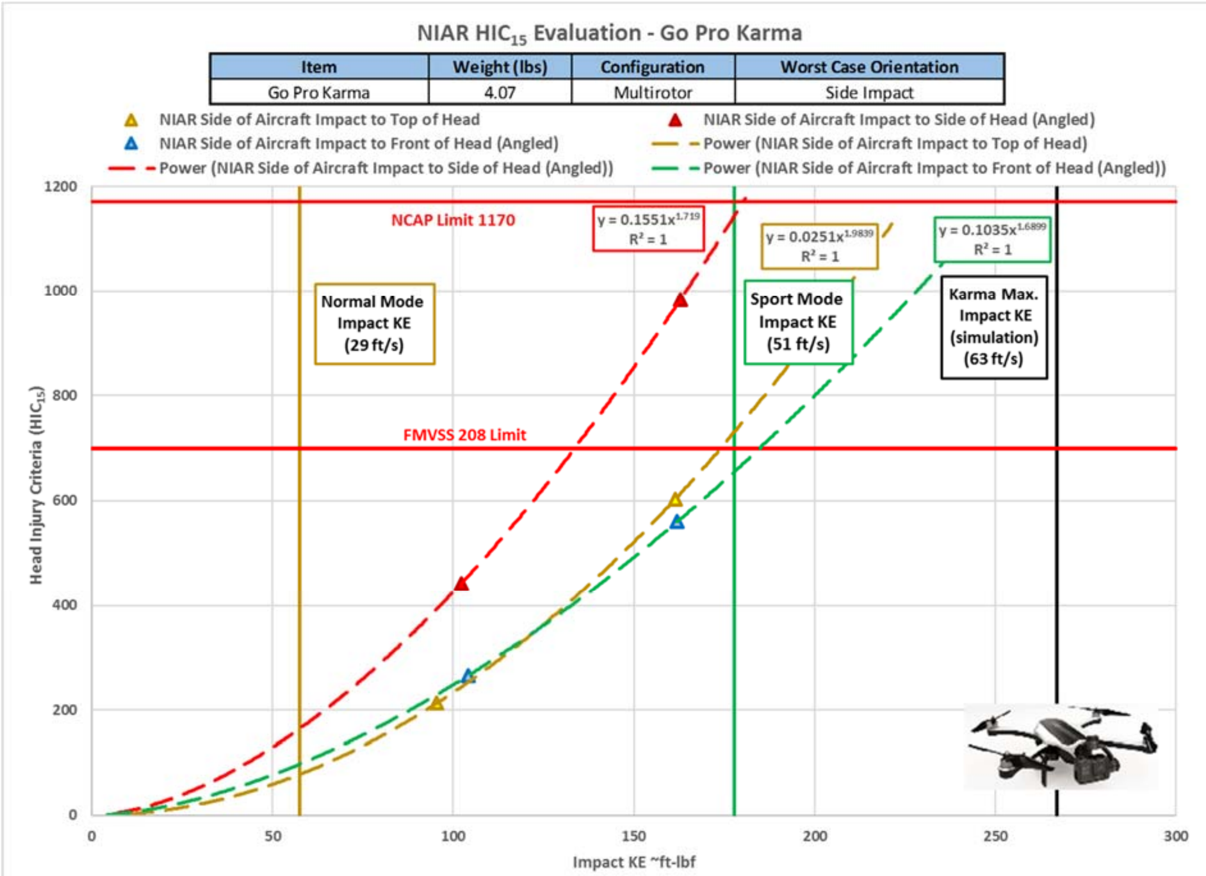

Figure 60. NIAR HIC_{15} Evaluation - Go Pro Karma

The maximum likelihood of an AIS ≥ 3 neck injury was 21% based an impact at 158 ft-lbf, which is achieved at 59% of the Go Pro Karma's terminal velocity impact KE (Figure 61). A curve fit of impact KE vs. N_{ij} indicates that the Go Pro Karma would lead to 30% probability of an AIS ≥ 3 neck injury in a cg-to-cg vertical impact on the side of the aircraft at velocities in excessive of 65 ft/s and 267 ft-lbf which is very close to the vehicle's terminal velocity impact KE (Figure 62). Additional test data is required to verify the curve fit trend and determine if there is threshold exceedance at velocities up to and including terminal velocity.

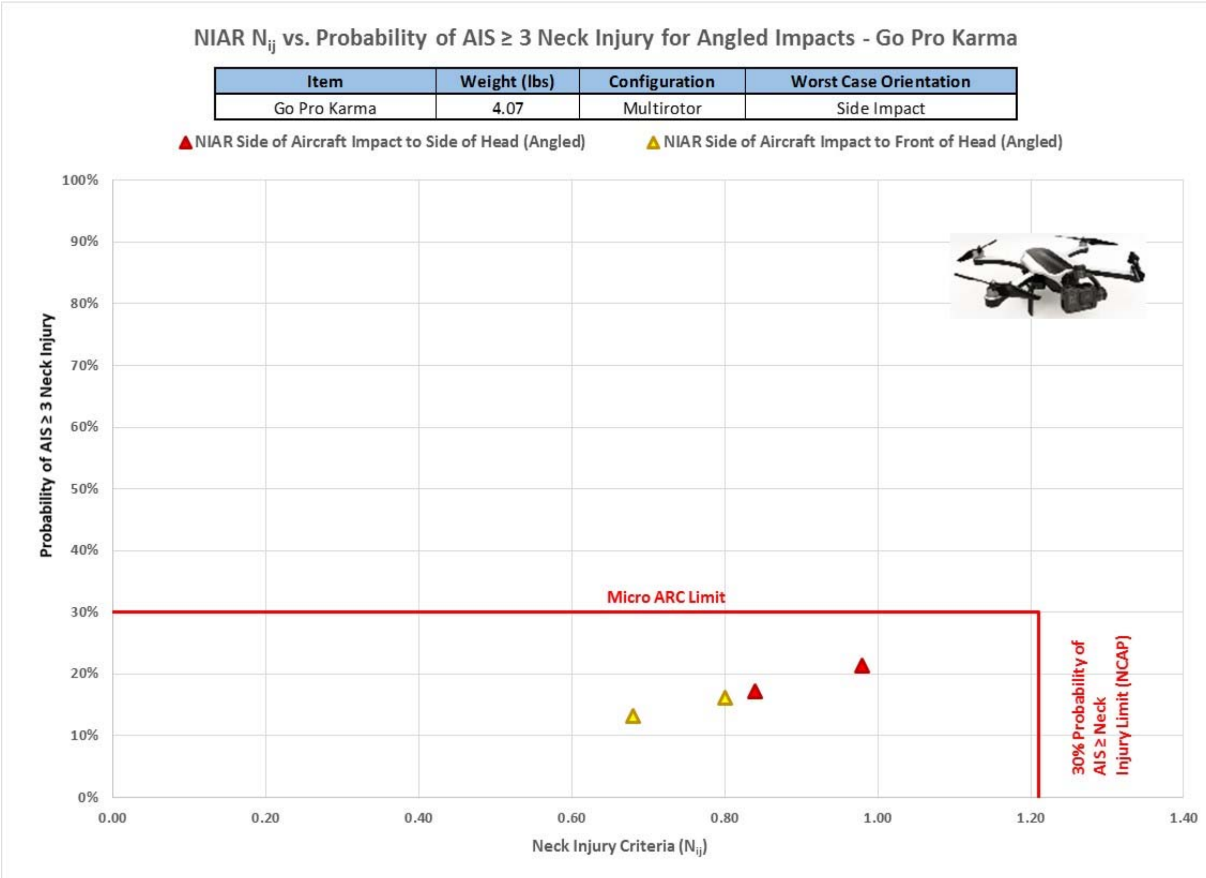

Figure 61. NIAR N_{ij} vs. Probability of AIS ≥ 3 Neck Injury for Horizontal and Angled Impacts - Phantom 3

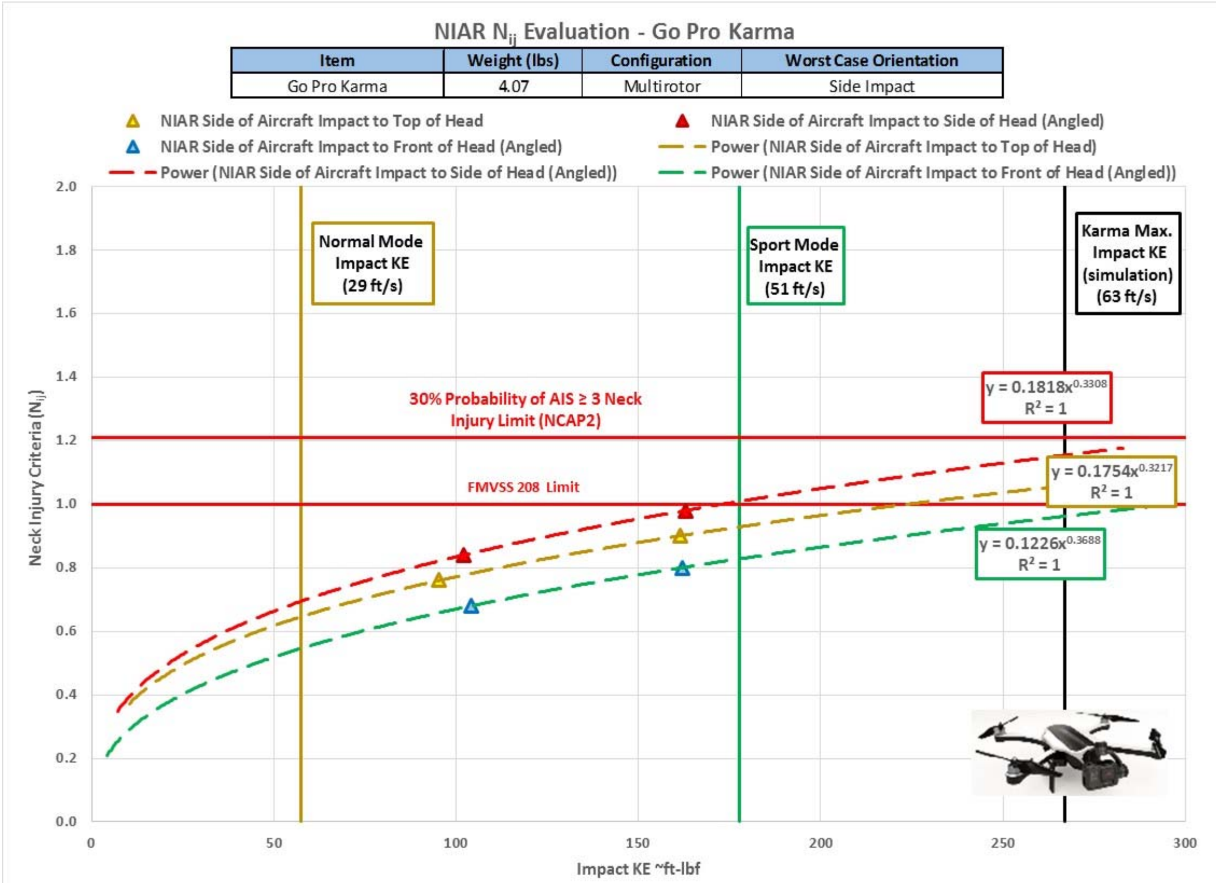

Figure 62. NIAR N_{ij} Evaluation - Go Pro Karma

None of the NIAR Go Pro Karma impact test points conducted at 59% of terminal velocity impact KE exceeded a BrIC score of 0.69; however five out six tests achieved at least a BrIC value of 0.5. This trend indicates the Go Pro Karma in its' worst case orientation impact at terminal velocity would exceed 30% probability of AIS ≥ 3 concussion (Figure 63). However, altitude and velocity restrictions could potentially mitigate this concussion risk. The probability of concussion is further reduced if the aircraft cg is offset from the cg of the head during impact, which will result in greater aircraft rotation after impact and lower resultant linear and angular accelerations of the head.

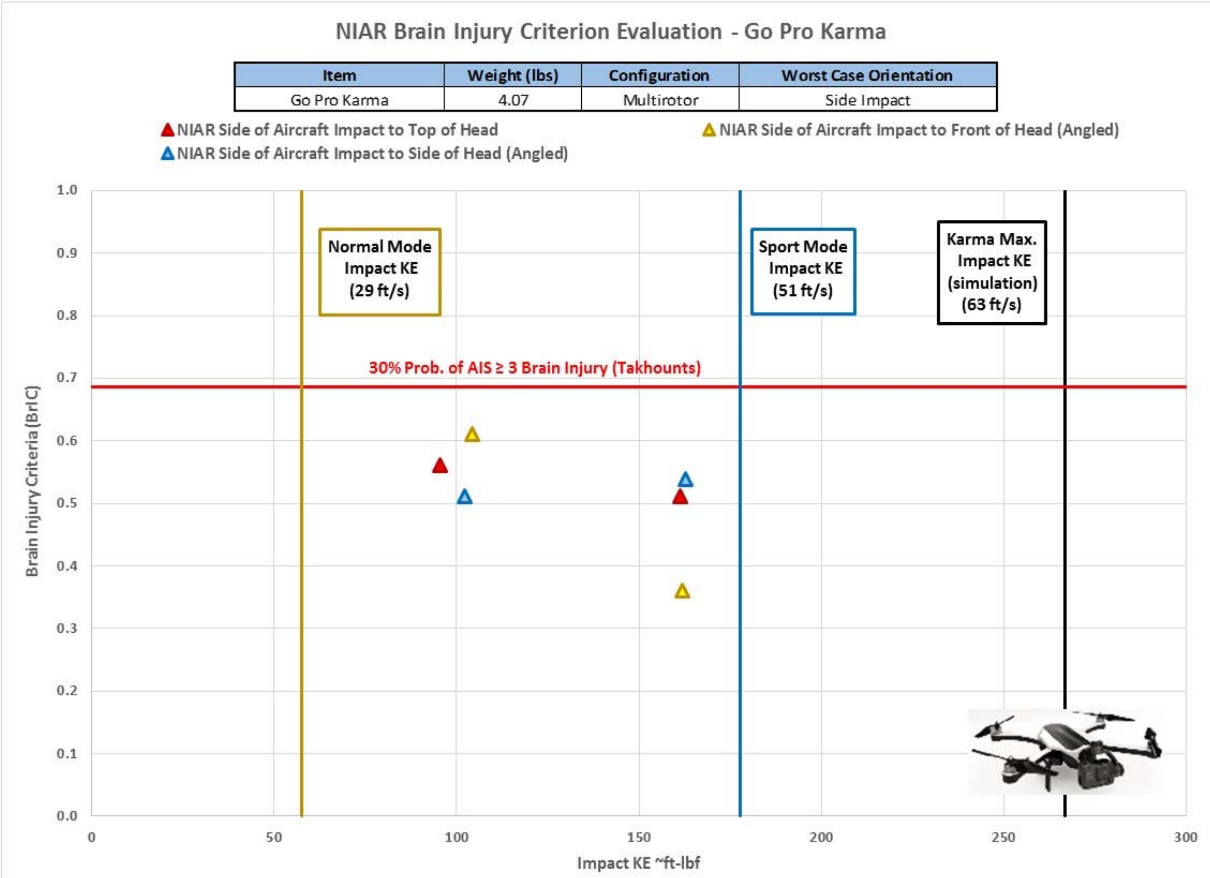

Figure 63. NIAR Brain Injury Criterion Evaluation - Go Pro Karma

3.4.3.4.2 Vendor 3 Quadrotor

Vendor 3 Quadrotor ATD and Simplified Test Results are shown in Appendix H

Based on the ATD impact points conducted by NIAR, the Vendor 3 Quadrotor, impacting in its worst case impact orientation, is likely to exceed 30% probability of an AIS ≥ 3 head or neck injury for impacts at velocities up to its terminal velocity impact KE (Table 28). The Vendor 3 Quadrotor's terminal velocity and terminal velocity impact KE are 70 ft/s and 320 ft-lbf, respectively. UAH testing determined that the worst case impact orientation of the Vendor 3 Quadrotor occurred when impacted between the arms on the front of aircraft and all NIAR ATD impacts were conducted in this orientation (Figure H 1). The NIAR test points used in this analysis were cg-to-cg impacts with minimal angular or lateral offset from the intended point of impact and impact orientation.

Table 28. Vendor 3 Quadrotor Injury Potential Summary

Injury Metric	Vendor 3 Quadrotor Values
Nominal Configuration Weight (lbf)	4.2
Terminal Velocity (ft/s)	70
Impact KE at Terminal Velocity (ft-lbf)	320
PMHS Injury	Not included in PMHS testing
Worst Case Orientation 198g Crossing Impact KE (ft-lbf)	106 (Note 1)
Safe Altitude for impact KE associated with the 198g Crossing Point (ft)	35
Cross 198g Threshold below Terminal Velocity	Yes at 53% of impact KE at V_{term}
9% Probability of Skull Fracture	Yes, within flight profile
Neck Compression Risk	Trend indicated exceedance at 37% of V_{term}
AIS ≥ 2 Skull Fracture	89% Probability at73% of V_{term}
AIS ≥ 2 Head Injury	29% Probability at 73% of V_{term}
AIS ≥ 3 Head Injury	10% Probability at 73% of V_{term}
AIS ≥ 3 Neck (N_{ij})	29% Probability at 73% of V_{term}
Exceed 80g for 3ms	Reached 80g at 73% of V_{term}
VT CP	99% Probability of AIS 1 Concussion at 73% of V_{term}
BrIC	Exceed 30% Probability of AIS ≥ at 72% of V_{term}

Notes:
1. Crossing point of 198g is conservative with no AIS ≥ 2 or AIS ≥ 3 head or neck injuries occurring at these values during any of the PMHS tests.
2. The 198g crossing point is a method for how injury metrics can be used to define operating envelopes based upon ATD type testing and is deemed very conservative.
3. All parameters in this table are deemed as conservative since these worst case impacts can occur in only one orientation of the DJI Mavic Pro and only during center of mass collisions. Any offset from these collisions dramatically reduces the severity of the collision. Data in this table is also conservative based upon the PMHS results.

The curve fit of the Vendor 3 Quadrotor's Impact KE vs Peak Resultant Acceleration plot crosses the 198g threshold at 27 ft/s and 106 ft-lbf (Figure H 3). This impact KE is achieved in a vertical fall from approximately 35 ft. NIAR's testing shows 89% probability of AIS ≥ 2 skull fracture for a vertical impact at 169 ft-lbf, which is achieved at 53% of its terminal velocity impact KE (Figure H 7). The Vendor 3 Quadrotor was not included in PMHS testing, so there are no correlating test points for reference with PMHS injuries. While the ATD impact data using automotive injury metrics would suggest the Vendor 3 Quadrotor should be flow at altitudes below 35 ft to avoid the potential of a skull fracture, the 35 ft altitude cap is associated with the 198g peak resultant energy threshold presented in the A4 Final Report. As was previously stated, the 198g threshold is likely an overly conservative threshold and more testing is needed to develop and refine automotive injury risk thresholds so that they are representative of the risk associated with sUAS impact kinematics.

The Vendor 3 Quadrotor's maximum probability of an AIS ≥ 3 head injury was 10% during a vertical impact to the top of the head at 53% of its terminal velocity or 169 ft-lbf (Figure 64). Additional testing up to an impact at terminal velocity would be needed to determine if a 30%

probability of AIS ≥ 3 head injury can be achieved by this aircraft. Based on the current test points, it seems plausible that there could be 30% or more probability of this injury in a cg-to-cg side into head impact. A curve fit of the Vendor 3 Quadrotor's HIC_{15} vs Impact KE data indicates that the 30% probability of AIS ≥ 3 head injury could be achieved during an angled impact at 295 ft-lbf which is 92% terminal velocity impact KE (Figure 65). This trend is based on a sample of two test points so more testing would be needed to verify the trend and experimental error. The likelihood of this injury may be much lower given the difficulty in achieving a cg-to-cg type impact in an operational environment when an aircraft can tumble following failure and non-participants on the ground can move relative to the vehicle. The Vendor 3 Quadrotor was not included in PMHS testing, because it was added to the testing matrix during the last half of the project after the set of OSU impactor vehicles was finalized.

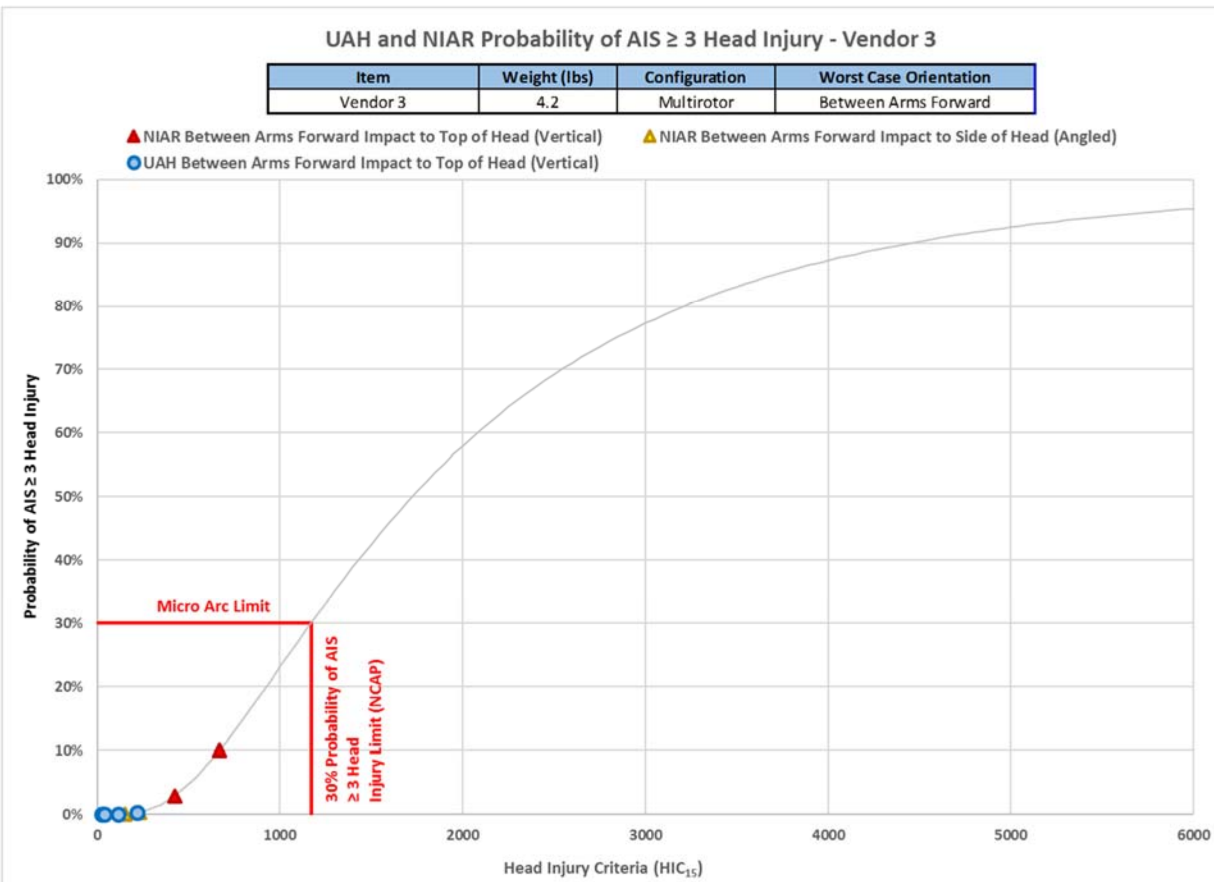

Figure 64. UAH and NIAR Probability of AIS ≥ 3 Head Injury - Vendor 3 Quadrotor

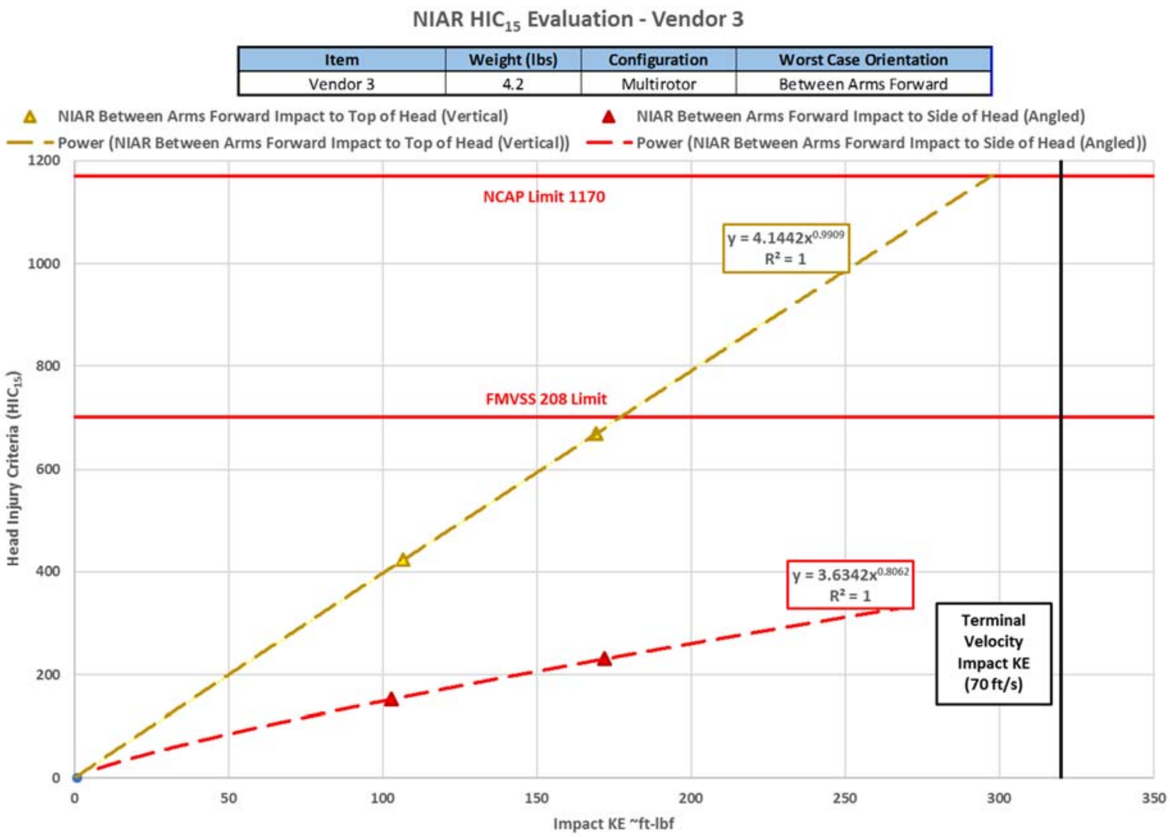

Figure 65. NIAR HIC_{15} Evaluation - Vendor 3 Quadrotor

The maximum likelihood of an AIS ≥ 3 neck injury was 29% based an impact at 169 ft-lbf, which is achieved at 59% of the Vendor 3 Quadrotor's terminal velocity impact KE (Figure 66). A curve fit of impact KE vs. N_{ij} trends indicates that the Vendor 3 Quadrotor would 30% probability of an AIS ≥ 3 neck injury in a cg-to-cg vertical impact at 170 ft-lbf which is 53% of the terminal velocity impact KE (Figure 67). This trend requires additional test data to verify the curve fit and associated threshold exceedances at velocities up to and including terminal velocity.

NIAR N_{ij} vs. Probability of AIS ≥ 3 Neck Injury for Vertical and Angled Impacts - Vendor 3

Item	Weight (lbs)	Configuration	Worst Case Orientation
Vendor 3	4.2	Multirotor	Between Arms Forward

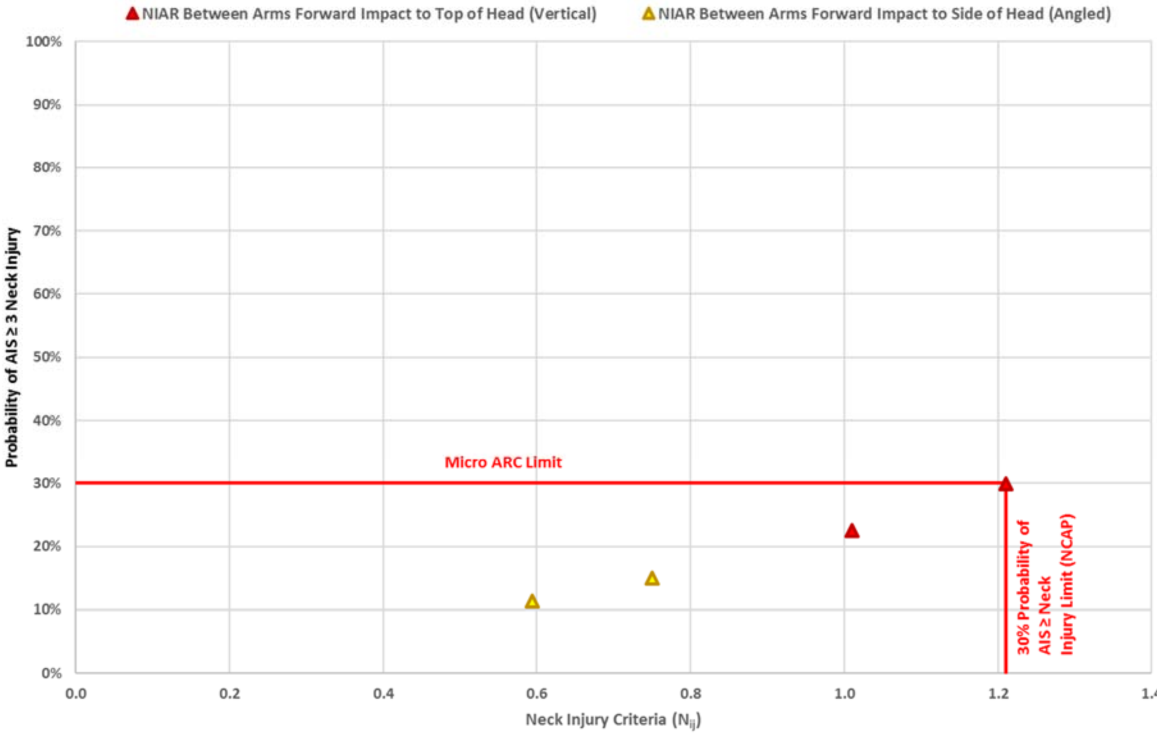

Figure 66. NIAR N_{ij} vs. Probability of AIS ≥ 3 Neck Injury for Horizontal and Angled Impacts - Vendor 3 Quadrotor

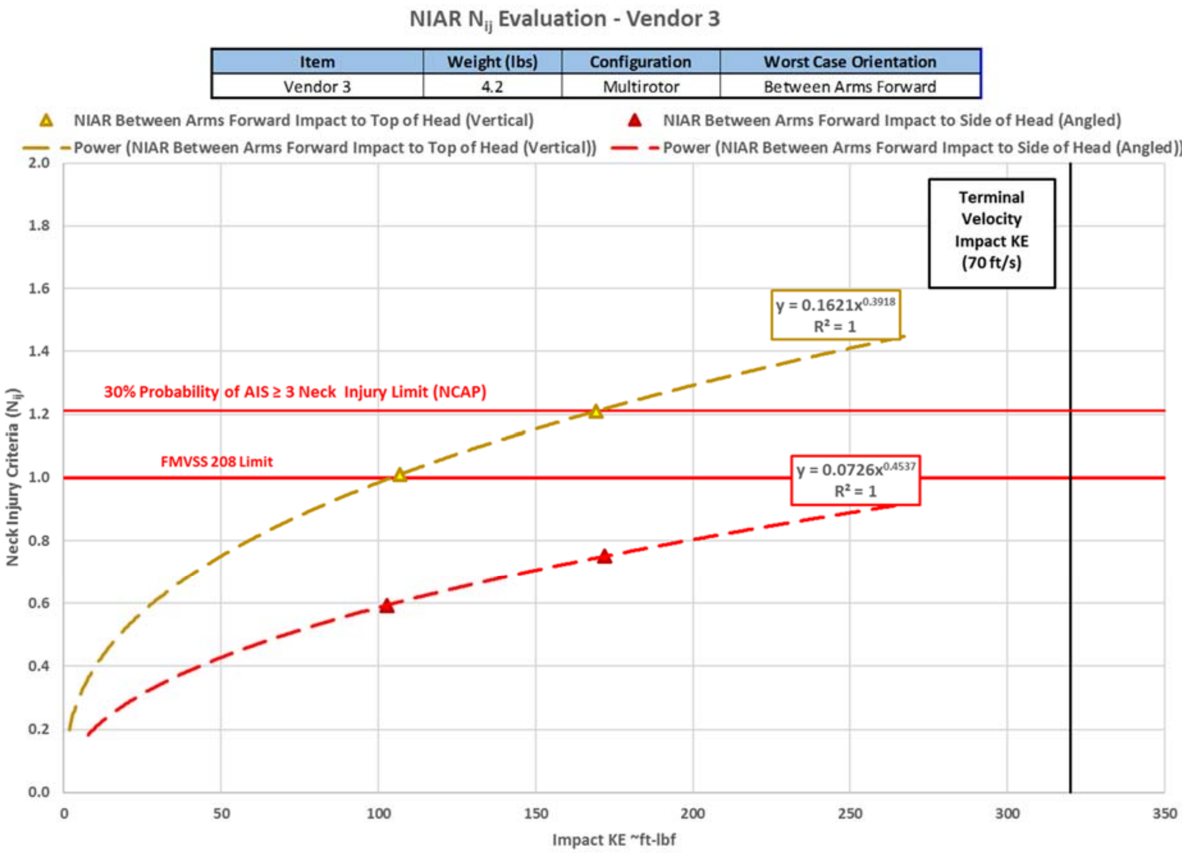

Figure 67. NIAR N_{ij} Evaluation - Vendor 3 Quadrotor

One of the NIAR Vendor 3 Quadrotor impact test points conducted at 73% of terminal velocity exceeded a BrIC score of 0.69 and several tests achieved at least a BrIC value of 0.45. This trend indicates an impact by the Vendor 3 Quadcopter in the worst case orientation at terminal velocity would exceed 30% probability of AIS ≥ 3 concussion (Figure 68). Altitude and velocity restrictions may mitigate this concussion risk. The probability of concussion is further reduced if the aircraft cg is offset from the cg of the head during impact, which will result in greater aircraft rotation after impact and lower resultant linear and angular accelerations of the head.

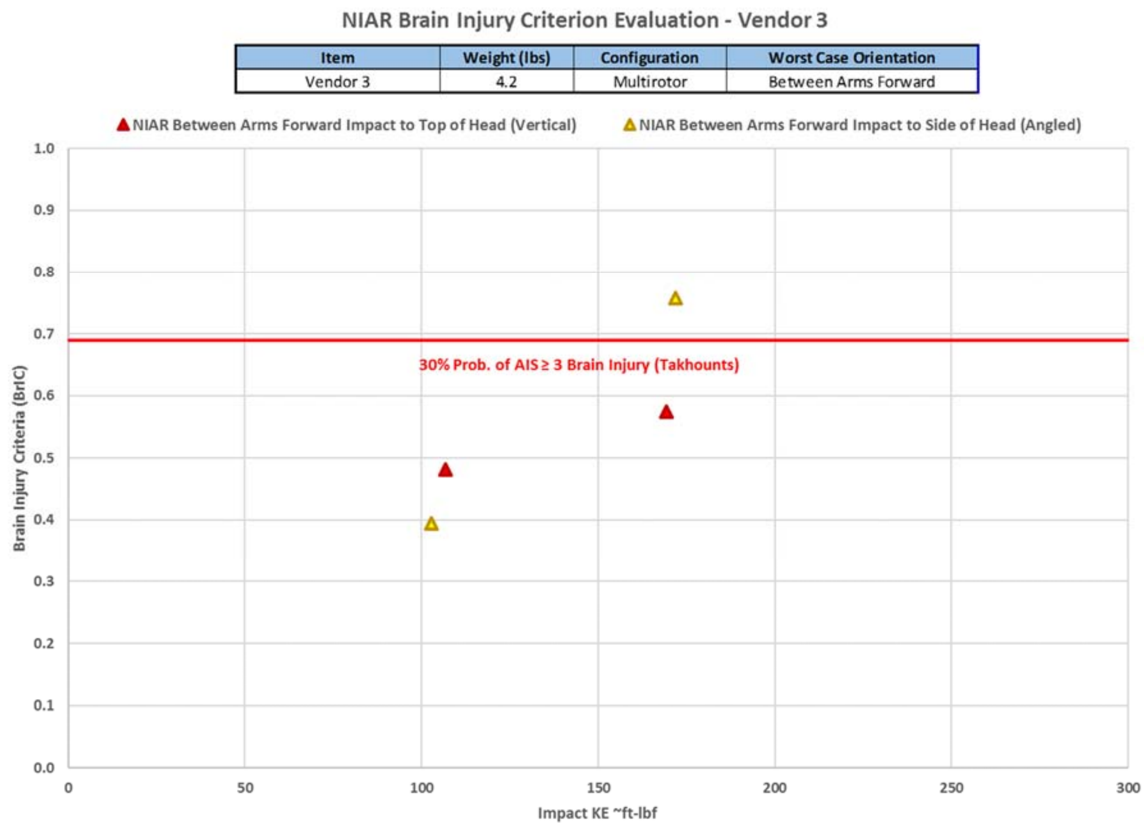

Figure 68. NIAR Brain Injury Criterion Evaluation - Vendor 3 Quadrotor

3.4.3.5 DJI Inspire 2 (Parachute)

DJI Inspire 2 (Parachute) ATD Test Results are shown in Appendix I

Based on the ATD impact points conducted by NIAR, the DJI Inspire 2, impacting under parachute descent conditions has very low potential to exceed 30% probability of AIS ≥ 3 head or neck injuries (

Table 29). There were no PMHS injuries observed during the DJI Inspire 2 parachute impact tests. Under the Vendor 2 72-inch Parachute System, the DJI Inspire 2 impacts with a maximum impact KE of 147 ft-lbf when descending with a 20 knot winds. The NIAR impact testing and PMHS tests used were cg-to-cg impacts with minimum angular or lateral offset from the intended point of impact and impact orientation.

Table 29. DJI Inspire 2 (Parachute) Injury Potential Summary

Injury Metric	Inspire 2 (Parachute) Values
Nominal Configuration Weight (lbf)	8.14
Nominal Configuration Weight with Vendor 2 Parachute System (lbf)	8.82
Impact Velocity when Descending under Parachute in a 20 kt wind (ft/s)	30
Impact KE when Descending under Parachute in a 20 kt wind (ft-lbf)	147
PMHS Injury	None
Worst Case Orientation 198g Crossing Impact KE (ft-lbf)	171 (Note 1)
Safe Altitude for impact KE associated with the 198g Crossing Point (ft)	Any altitude allowing parachute deployment for wind speeds up to 20 kt
Cross 198g Threshold below Max Parachute Descent Impact Velocity	No
9% Probability of Skull Fracture	Not at or below max parachute impact velocity
Neck Compression Risk	None based on testing
AIS ≥ 2 Skull Fracture	4% Probability at max parachute impact velocity
AIS ≥ 2 Head Injury	4% Probability at max parachute impact velocity under 20 kt winds
AIS ≥ 3 Head Injury	Less than 0.1% Probability at max parachute impact velocity
AIS ≥ 3 Neck (N_{ij})	5.5% Probability at max parachute impact velocity
Exceed 80g for 3ms	Not within ATD test points
VT CP	81% Probability of AIS 1 Concussion at max parachute impact velocity
BrIC	None within ATD test points

Notes:
1. Crossing point of 198g is conservative with no AIS ≥ 2 or AIS ≥ 3 head or neck injuries occurring at these values during any of the PMHS tests.
2. The 198g crossing point is a method for how injury metrics can be used to define operating envelopes based upon ATD type testing and is deemed very conservative.
3. All parameters in this table are deemed as conservative since these worst case impacts can occur in only one orientation of the DJI Mavic Pro and only during center of mass collisions. Any offset from these collisions dramatically reduces the severity of the collision. Data in this table is also conservative based upon the PMHS results.

While testing of the DJI Inspire 2 was not exhaustive and statistically significant, Figure I 1 and Figure 69 show some valuable trends in assessing the importance of the Vendor 2 72-inch Parachute when mitigating the injury potential of the 8.82 lbf DJI Inspire 2 following failure. The DJI Inspire 2 crosses the 198g skull fracture line at approximately 171 ft-lbf that would limit the descent rate under failure conditions for an 8.82 lbf platform to 35 ft/s. The DJI Inspire 2 would not be capable of meeting these descent speeds in the presence of failure at any altitude higher than 20 ft AGL and with little or no forward speed. As such, the DJI Inspire 2 requires some mitigation to decelerate the vehicle to descent rates below 35 ft/s. Figure I 1 shows that the DJI Inspire 2 at 30 ft/s and an Impact Angle of 20 deg remains below the skull fracture limit of 198g. The 198g peak resultant acceleration threshold correlates to just over 9% probability of an AIS ≥ 2 skull fracture. Figure 69 shows that the DJI Inspire 2, when descending under the Vendor 2 72-inch

Parachute recovery system either vertically or in winds up to 30 knots, has less than a 9% probability of causing an AIS ≥ 2 skull fracture.

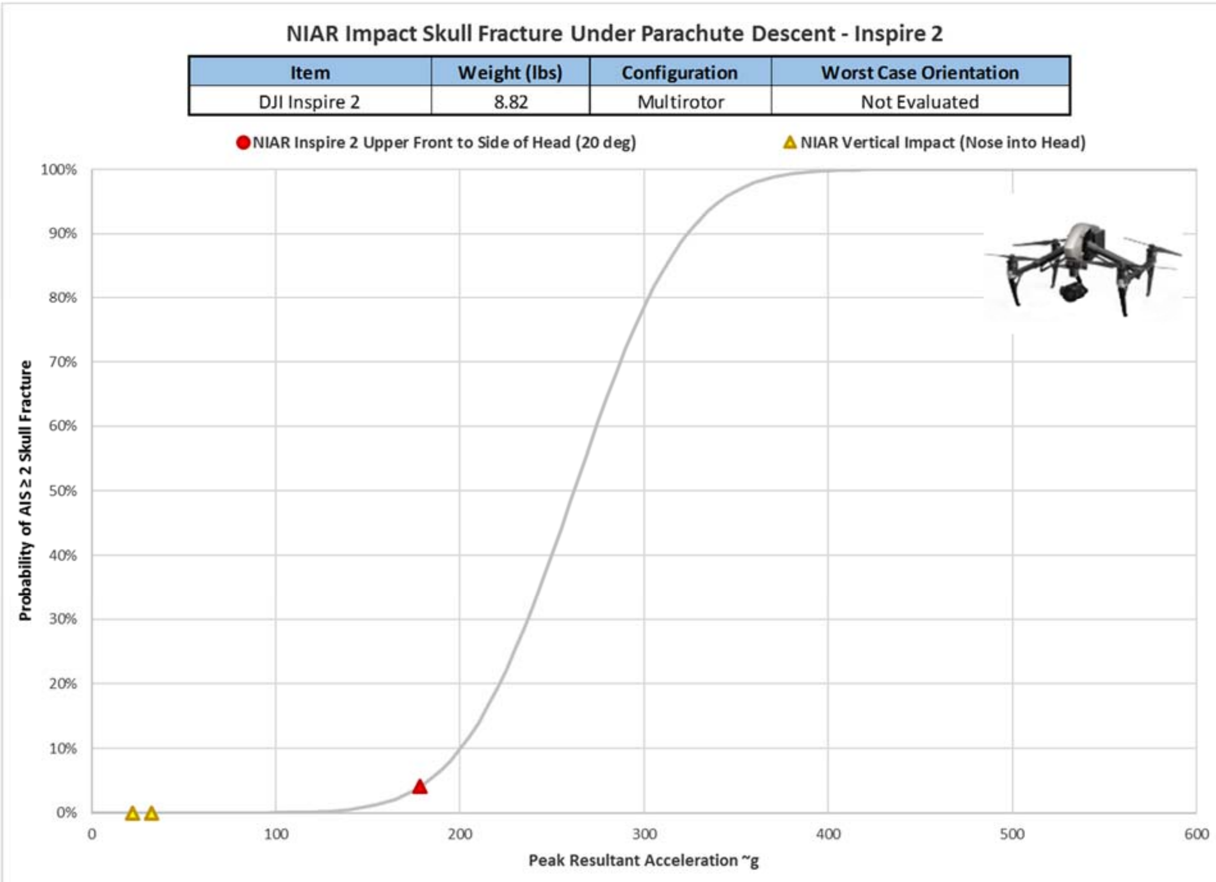

Figure 69. Worst Case Skull Fracture Evaluation for a DJI Inspire 2 under Parachute Descent

The estimated probabilities of AIS ≥ 3 head injuries based on HIC_{15}, for the DJI Inspire 2 under an Vendor 2 72-inch Parachute is shown and Figure 70. The vertical impacts at 9 and 14 ft/s represent less than a 0.1% chance of an AIS ≥ 3 Head Injury. These low values for the no wind condition are due to the descent rate and the impact characteristics of the DJI Inspire 2. More testing is required to verify these trends, but curve fits of the head injury criteria data points suggest that the DJI Inspire 2 descending under a parachute will not exceed any HIC_{15} injury thresholds related to AIS ≥ 2 or AIS ≥ 3 head injuries. The low probability of head injury for the 27 ft/s impact speed representing wind conditions are in part due to the way the DJI Inspire 2 is positioned below the Vendor 2 72-inch Parachute since the contact area exposed during the collision is below the center of gravity of the DJI Inspire 2. This causes the DJI Inspire 2 to rotate when colliding with the center of mass of the ATD or human head resulting in a less severe impact.

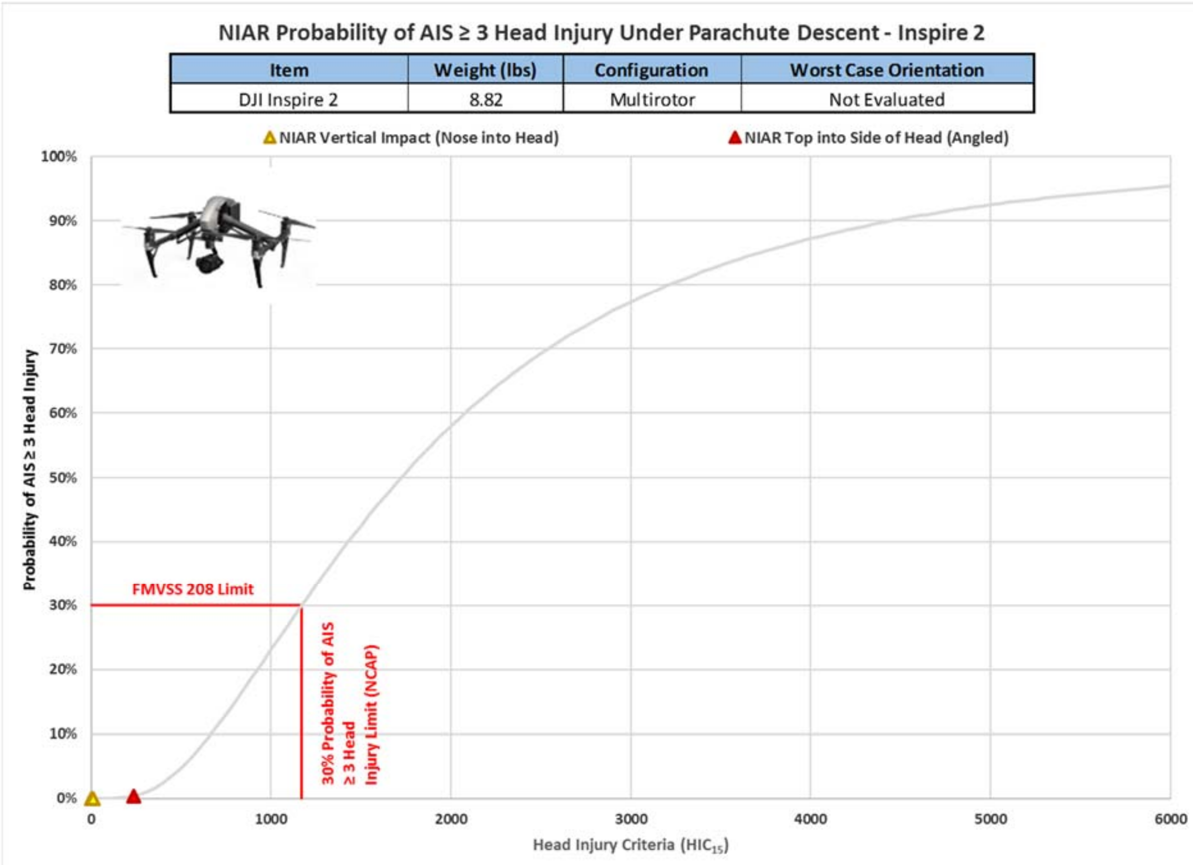

Figure 70. Probability of AIS ≥ 3 Head Injury for a DJI Inspire 2 under Parachute Descent

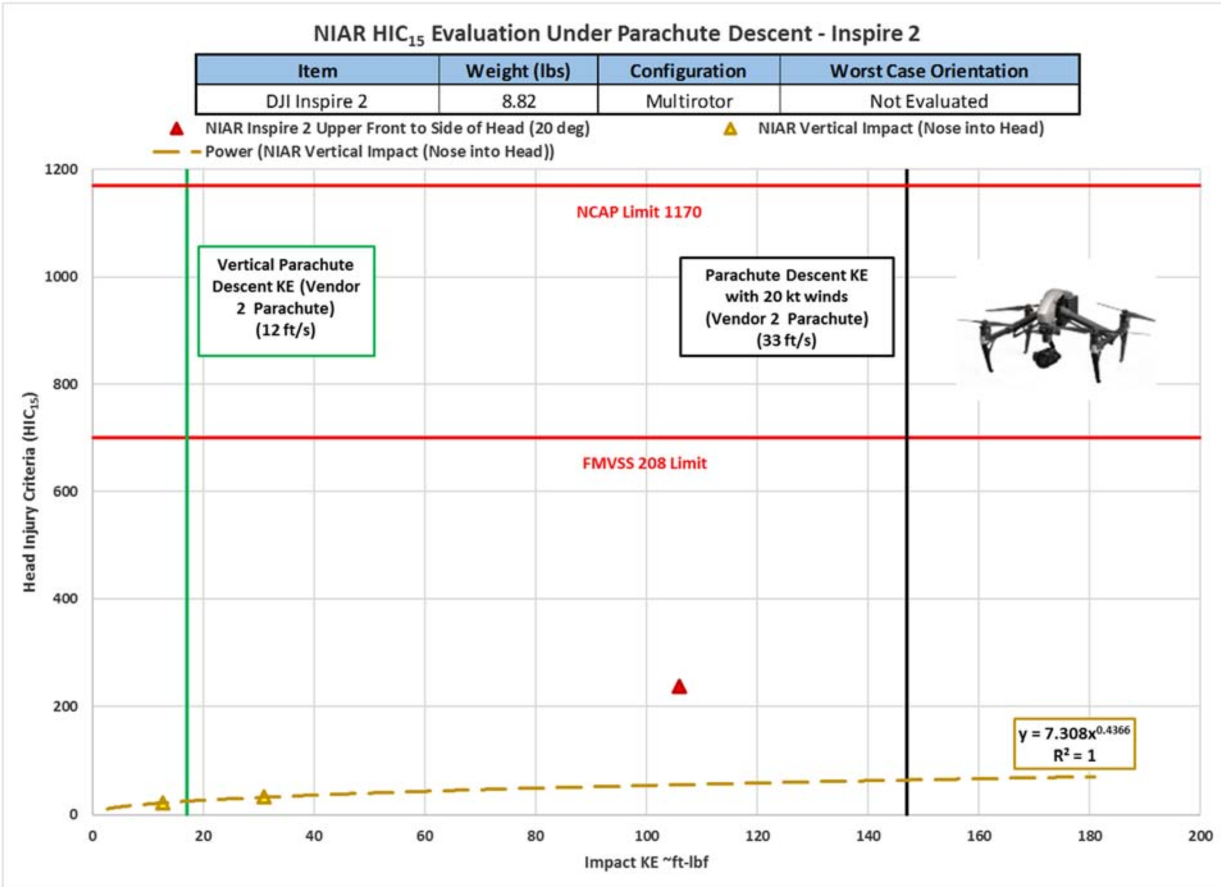

Figure 71. NIAR HIC_{15} Evaluation Under Parachute Descent - Inspire 2

NIAR evaluated neck injury potential of the DJI Inspire 2 when descending under the Vendor 2 72-inch Parachute during vertical descents by looking at the N_{ij} values for the vertical descent and impact under winds. Only the ATD impact with the side of the head could be evaluated for AIS ≥ 3 neck injury (Figure 72) using the N_{ij} criteria of FMVSS 208. For all test points, there is less than 5.5% probability of an AIS ≥ 3 neck injury.

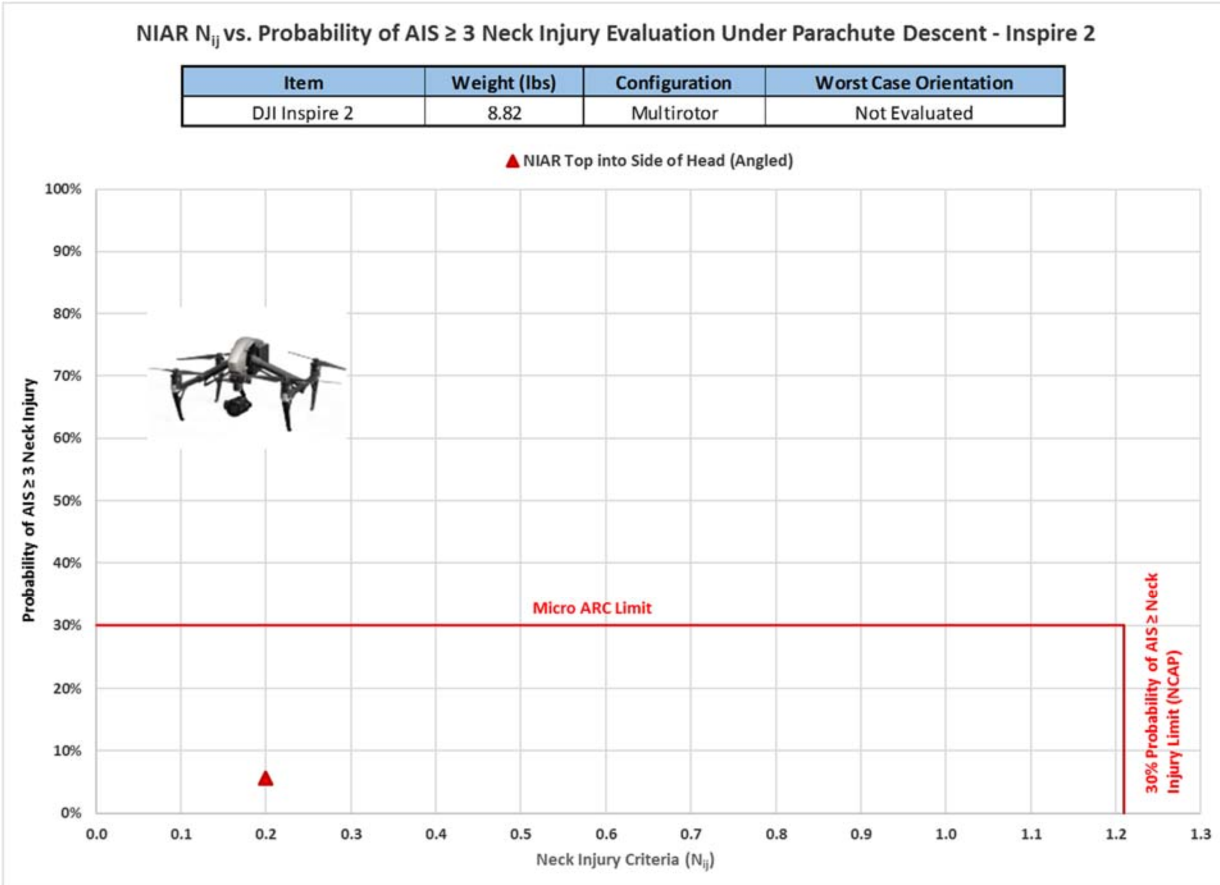

Figure 72. N_{ij} vs. Probability of AIS ≥ 3 Neck Injury for an DJI Inspire 2 under Parachute Descent

When assessing BrIC values shown in Figure 73, the DJI Inspire 2 under an Vendor 2 72-inch Parachute does not exceed the 30% probability of an AIS ≥ 3 Brain Injury. However, Figure 73 shows that the DJI Inspire 2, when descending under the Vendor 2 72-inch Parachute, may present some lower level of concussion risk than AIS ≥ 3 when descending in a 20 kt wind.

The ATD and PMHS test data suggest that the DJI Inspire 2 descending under a Vendor 2 72-inch Parachute presents a low risk of injury and is safe for flight over people at any altitude that enables complete deployment of the parachute and deceleration to steady state descent velocity.

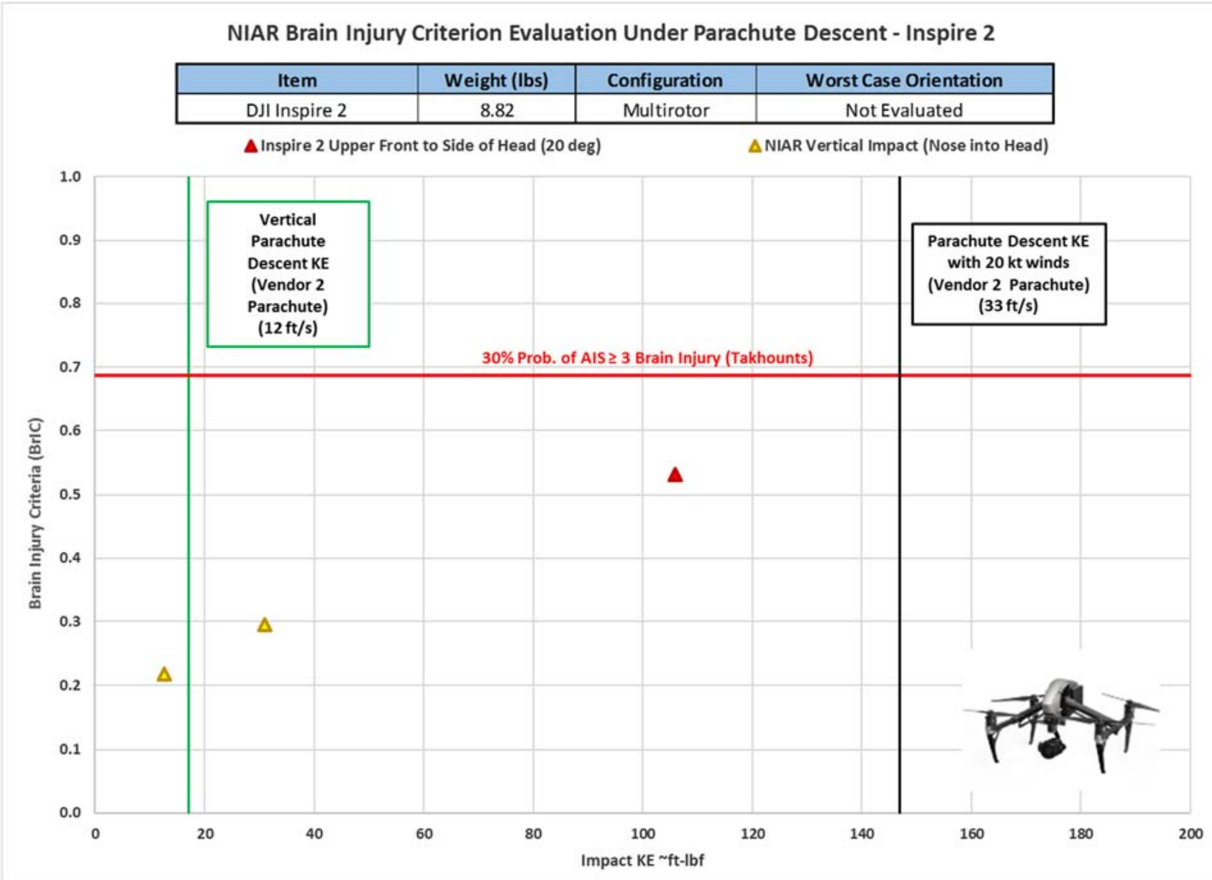

Figure 73. NIAR Brain Injury Criterion Evaluation – Inspire 2 (Parachute)

For any multirotor impact, The probability of injury is further reduced if the aircraft cg is offset from the cg of the head during impact, which will result in greater aircraft rotation after impact and lower resultant linear and angular accelerations of the head. Impact offsets result in aircraft rotation after impact and reduce injury severity even for deviations as small as ½ inch and pitch angles of the vehicle of 4-9 deg. The likelihood of injuries may actually be less than 1% given the difficulty in achieving a cg-to-cg type impact in an operational environment when an aircraft can tumble following failure and non-participants on the ground can move relative to the vehicle.

Conclusion: Impact testing using a full ATD Hybrid III or a simplified apparatus provides the capability of estimating injury potential/fatality risk based upon impact KE and resultant acceleration of the head for specific aircraft. Based on using a range of injury criterion, e.g. HIC_{15}, 3ms Minimum g-loading, Virginia Tech Combined Probability of Concussion, Brain Injury Criteria, and Peak Resultant Acceleration, impact testing provides regulators with a range of options for setting injury thresholds that address multiple injury types and mechanisms.

Conclusion: UAS impact testing using Hybrid III ATDs can provide regulators a method for evaluating injury potential and risk based assessments using the modified injury metrics established in this report for multirotor and fixed-wing platforms up to 10 lbf and larger platforms up to 55 lbf at parachute impact speeds. The use of this data also supports a risk based approach to determine when and if additional operational mitigations are required for specific Concept of Operations (CONOPS).

Conclusion: Simplified and ATD testing can be used to determine injury impact energies for sUAS as in the 8-10 lbf range such that appropriate parachute speeds can be assessed and the appropriate parachute mitigation are applied to support flight over people.

Conclusion: The estimated injury severity and probability associated with each test represent cg-to-cg type impacts in a test environment. These probabilities of head injury may actually be less than 1% based upon the PMHS tests resulting in a single AIS ≥ 2 skull fracture and the difficulty in achieving a cg-to-cg type impact in an operational environment when an aircraft can tumble following failure and non-participants on the ground can move relative to the vehicle. Impact offsets result in aircraft rotation after impact and reduce injury severity even for deviations as small as ½ inch and pitch angles of the vehicle of 4-9 deg.

3.4.3.6 Family of Fixed Wing Aircraft Test Results

Five fixed wing foam aircraft were tested as part of the Task A14 research. The aircraft and their representative weights are shown in Table 30.

Table 30. Foam Fixed Wing Platforms Configurations

Vehicle	Configuration/Weight	Maximum Test Flight Velocity (ft/s)	Impact KE (ft-lbf)
eBee+	Flight Test Config. / 2.87 lbf	103	473
	Nominal Config. / 2.58 lbf	103	425
	Configuration/Weight	**Example Cruise Velocity (ft/s)**	**Impact KE (ft-lbf)**
eBee Standard	Nominal Config. / 1.52 lbf	68	109
Nano Talon	Nominal Config. / 1.5 lbf	50	58
Radian	Nominal Config. / 2.5 lbf	100	388
Skyhunter	Nominal Config. / 6.9 lbf	90	868

The aggregate head Peak Resultant Acceleration versus Impact KE plot for the Task A14 fixed wing aircraft is shown in Figure 74. All of the fixed wing aircraft testing as part of Task A14 are made of foam. The majority of the fixed wing test data in this section comes from UAH's simplified testing and served as a means of examining the effects of mass and configuration for foam vehicles as well as pusher versus puller pro on the relation of peak resultant head acceleration to impact KE. For reference, Figure 74 also includes the NIAR wood block data and NIAR impact test data for a 2.7 lbf Steel Core Foam Block, which weighs the same amount at the Wood Block and the DJI Phantom 3. All of the test data shown in Figure 74 was developed from nose into head vertical impact tests, which serves as a common impact orientation and trajectory for benchmarking the aircraft against one another based on Peak Resultant Acceleration versus Impact KE slopes. These test results show that all of the foam fixed wing aircraft are significantly more compliant than the multirotor aircraft, with the Radian's slope being 64% of the most compliant, non-parachute descent impact test results that came from the Karma (Figure 41).

Before reviewing the test results further, there is an important point to make regarding the UAH and NIAR data. The rigidity of the UAH head and neck-only test device tended to break the nose sections of the pusher propeller aircraft, and the NIAR full ATD test device did not readily break the nose sections off of aircraft even at twice the maximum impact velocity used in UAH testing. Based on this difference in aircraft impact response, the results may not be directly comparable; however, since most of the results come from UAH's apparatus, conclusions can be made about stiffness and injury potential when only comparing between UAH-generated data sets.

There are several other key points that came from the fixed wing test data in Figure 74. First, this shows that the only puller prop aircraft used in this study, the Radian, has a slope that is roughly 3 times that the pusher prop aircraft tested by UAH. This steeper slope is due to the impact of the rigid spinner and motor on the nose of the Radian versus the pusher aircraft that impact with deformable foam noses. While only qualitative in nature, Figure 75 also illustrates the increased potential for injury posed by a puller prop fixed wing aircraft as the Radian was the only aircraft that did noticeable damage to the rubber ATD head covering. These divots do not necessarily correlate to a given injury threshold, but they do represent the potential for penetrating injuries to the skin and localized injury to the skull. The eBee+ curve fit intercept of the 198g threshold occurs at impact KE levels above the maximum descent velocity that UAH observed during failure flight testing, which leads to an initial conclusion that this aircraft has low potential to cause skull fracture (Figure K 1). Based on aircraft launcher limitations, the eBee+ was not tested at impact velocities up to 103 ft/s and the 70 ft/s impacts conducted at NIAR and OSU are just above the average cruise speed of the eBee+. While the injury potential of the eBee+ at maximum velocity observed in flight test was not tested, the data trend gives confidence that the injury potential of the eBee+ is low throughout its flight envelope. It also appears that the foam material and general construction method used to make these aircraft play the most significant role in determining the injury potential of the foam pusher propeller aircraft. The UAH curve fits for the Nano Talon, eBee Standard, and Skyhunter all have similar slopes, which range from 0.3029 g/ft-lbf to 0.3373 g/ft-lbf despite having aircraft weights that run from 1.5 to 6.9 lbf. All of these aircraft are made of foam and have hollow nose areas that house batteries and electronics. UAH and NIAR conducted tests with batteries and representative electronics masses installed in these aircraft during testing to replicate masses that are in operational aircraft. The hollow volumes with the aircraft nose sections function as crumple zones that deform during impact and reduce peak resultant acceleration of the ATD head. It is possible that the Steel Core Foam Block data, which also comes from NIAR, has a steeper slope than the NIAR eBee+ because the foam block is solid and does not have any large voids, so it has greater rigidity based on having continuous material through the structure than the pusher propeller fixed wing aircraft that were tested.

The foam fixed wing impact tests conducted in this study show low potential for skull fracture (Figure 76), AIS ≥ 2 head injury (Figure 77), or AIS ≥ 3 head injury (Figure 78). Only NIAR's eBee+ test points represent the aircraft in a cruise flight condition. The NIAR test points indicate a probability of AIS ≥ 2 skull fracture of less than 0.1%, and even lower probabilities of AIS ≥ 2 and AIS ≥ 3 head injuries for the eBee+ (Figure K 5, Figure K 6, and Figure K 7). UAH's test points are only representative of aircraft at approach airspeeds. Based on the NIAR results, it is probable that none of the pusher prop aircraft have high head injury potential unless an impact causes so much fuselage damage that an aircraft's payload, battery, or electronics are able to act as high speed head impactors. While Figure 74 shows the Radian's curve fit intercepting the 198g line (9% probability of AIS ≥ 2 skull fracture) at approximately 220 ft-lbf, it seems likely that a minor skull fracture could occur at a lower impact KE value. The Mertz relation for skull fracture is based on blunt impacts and peak resultant acceleration, versus energy density and strain rates[16]. The relatively small contact area of the Radian's spinner appears to pose a risk of skull fracture based on high impact energy density and high localized strain rates. Until more testing is done with puller prop aircraft, or a comparison of puller prop impact conditions is made with non-lethal munition impact conditions, which are not meant to be fired at human heads, the most conservative approach is to prohibit puller prop aircraft from flying over people unless they employ a parachute recovery systems.

[16] Oukara A, Nsiampa N, Robbe C, Papy A. Injury risk assessment of non-lethal projectile head impacts. Open Biomed Eng J. 2014;8:75-83. Published 2014 Oct 30. doi:10.2174/1874120701408010075

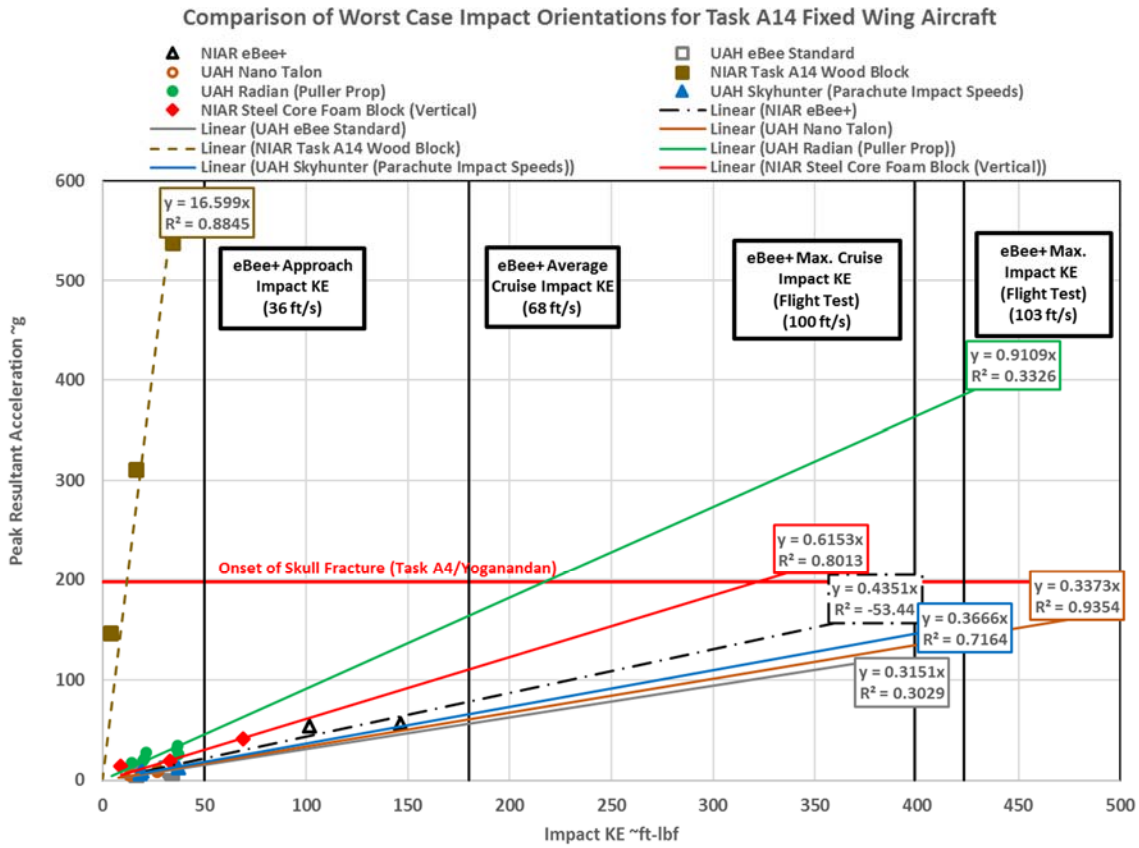

Figure 74. Comparison of Worst Case Vehicle Orientations for Task A14 Fixed Wing Aircraft

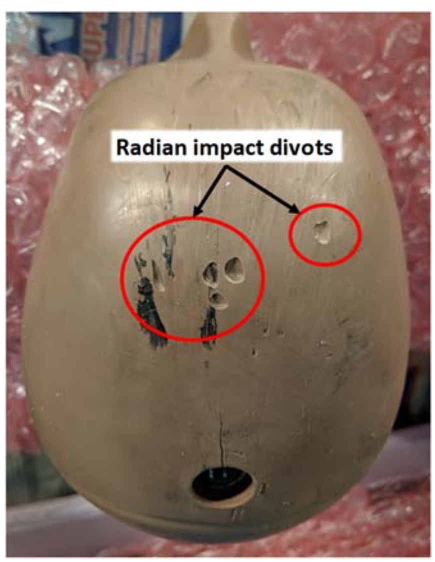

Figure 75. Top Down View of UAH ATD Head with Radian Impact Damage

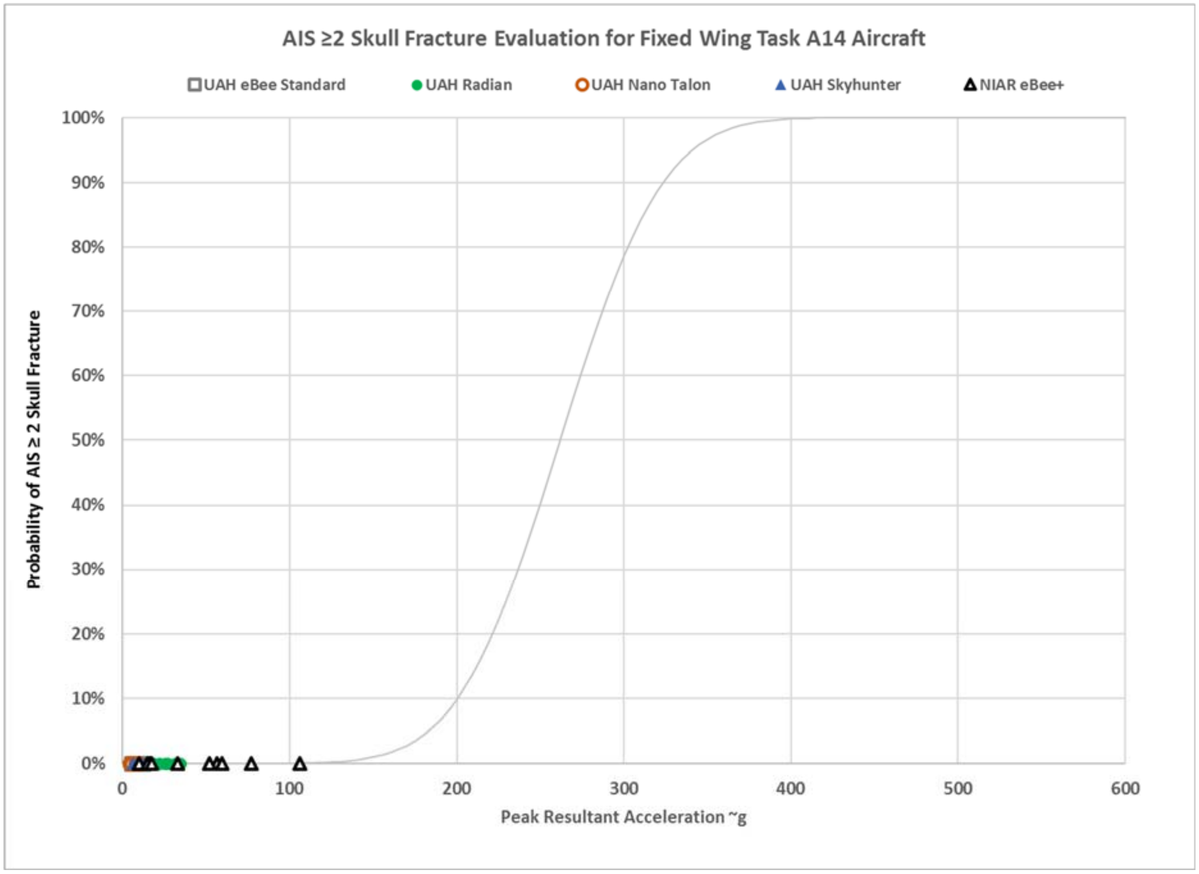

Figure 76. AIS ≥2 Skull Fracture Evaluation for Fixed Wing Task A14 Aircraft

The foam fixed wing aircraft impact results show that there is low risk of head injury due to the impact of pusher type aircraft models. In order to make a complete assessment of these aircraft for injury potential, impact testing must be conducted with test points up to maximum aircraft speed. It is necessary to conduct testing up to maximum impact velocity and KE levels in order to assess the aircraft based on its full fight envelope, as was done with several of the multi-rotor aircraft in this study. The 65 ft/s eBee+ impacts were completed at 63% of the maximum airspeed observed during failure flight testing. While the foam fuselages appear to prevent injury at high impact KE levels, it is necessary to verify that high speed impacts up to and beyond 100 ft/s do not lead to fuselage failures that result in battery and payload impacts that could increase the vehicle's injury potential. Based on the lower impact speeds used in the current simplified test method, there is insufficient test data to make detailed injury assessments of the Nano Talon, eBee Standard, Radian, and Skyhunter.

Conclusion: Simplified test methods are capable of assessing multi-rotor worst case impact orientations and have strong potential for estimating injury probability and severity for sUAS other than foam manufactured aircraft.

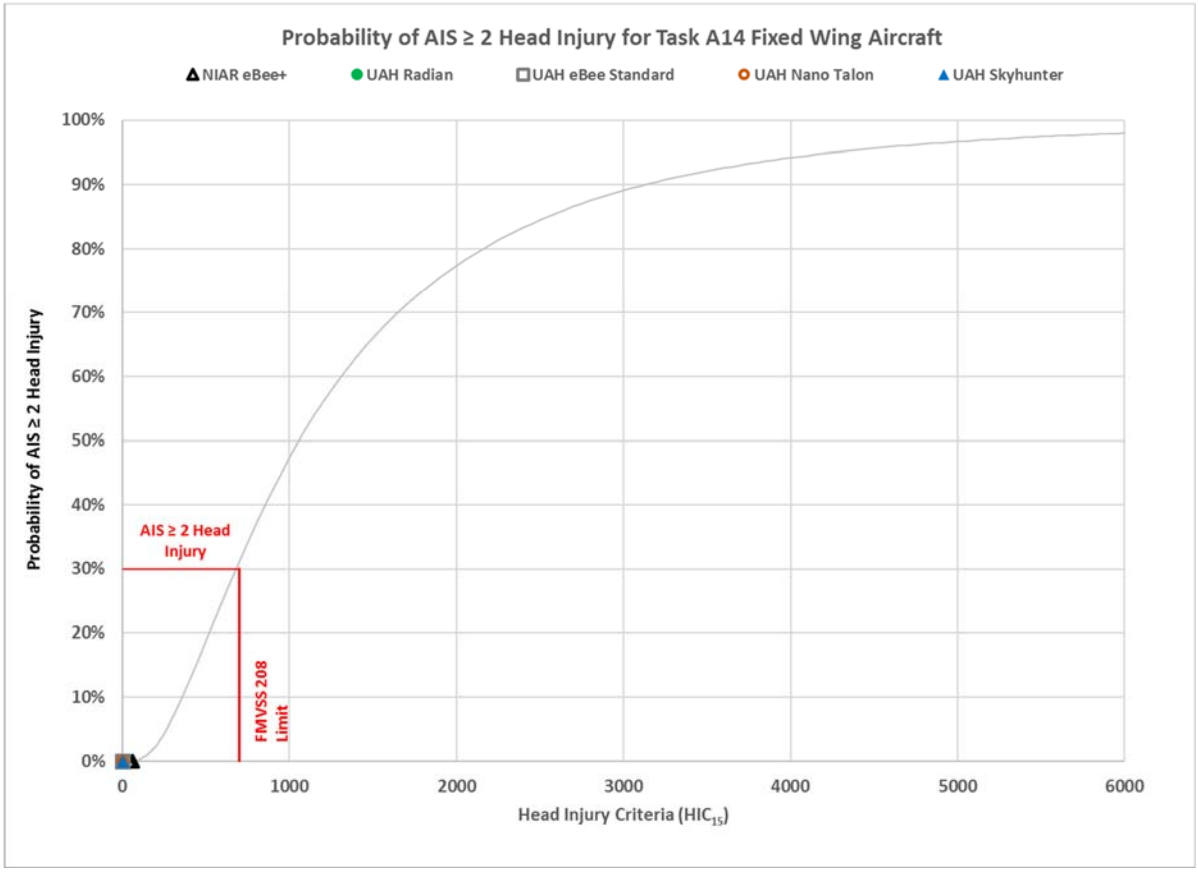

Figure 77. Probability of AIS ≥ 2 Head Injury for Task A14 Fixed Wing Aircraft

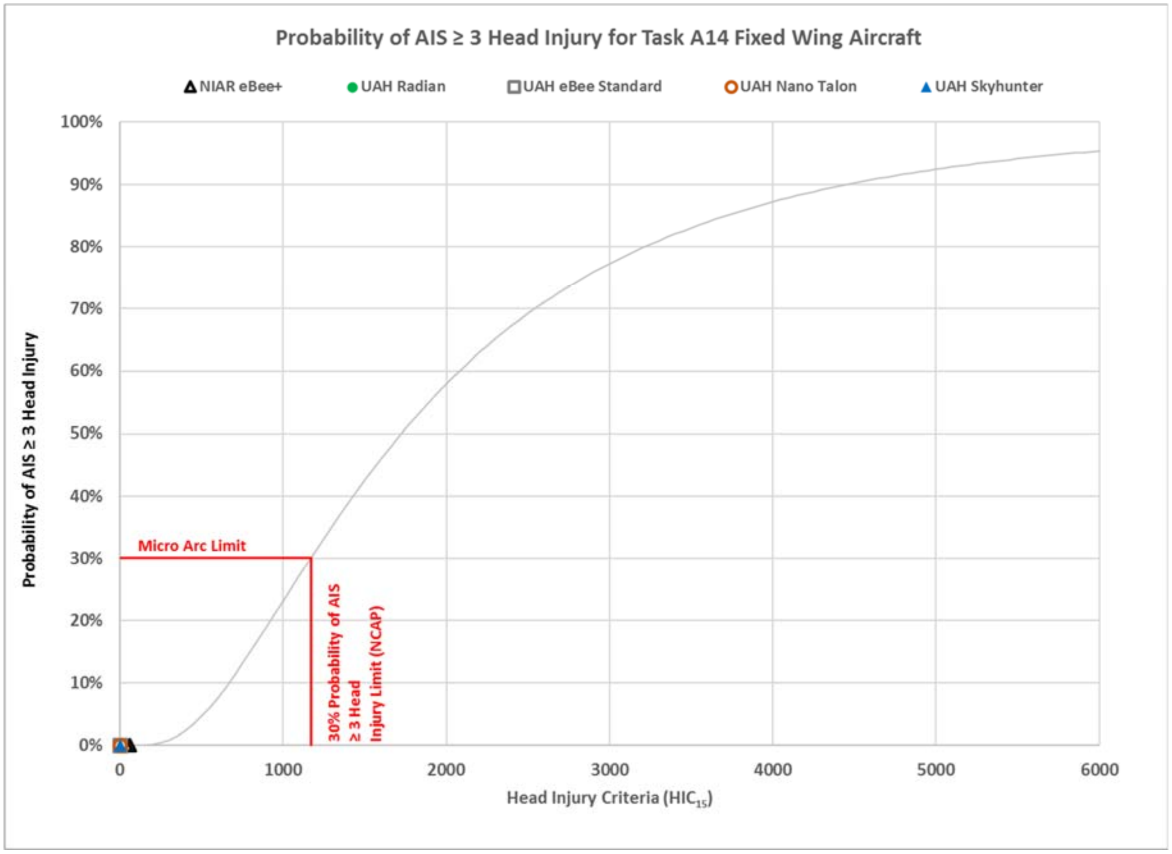

Figure 78. Probability of AIS ≥ 3 Head Injury for Task A14 Fixed Wing Aircraft

The SenseFly eBee+ was the only fixed wing platform evaluated by NIAR for angled and side impact tests. Therefore, the eBee+ was the only platform that could be evaluated in terms of neck injury criteria. The SenseFly eBee+ configurations are shown in Table 30. The NIAR eBee+ test results related to neck injury potential show a maximum of 9% probability of an AIS ≥ 3 neck injury (Figure 79 and Figure K 8). The two tests with the highest probability of neck injury were a vertical impact to the top of the head and a 58 deg angled impact to the side of the head at 60 and 64 ft/s, respectively. The dominant loading in both of these tests was compressive loading with minimal flexion or extension moment generation. It is likely that the eBee+ poses little neck injury risk even at impact velocities up to its maximum cruise speed of 100 ft/s.

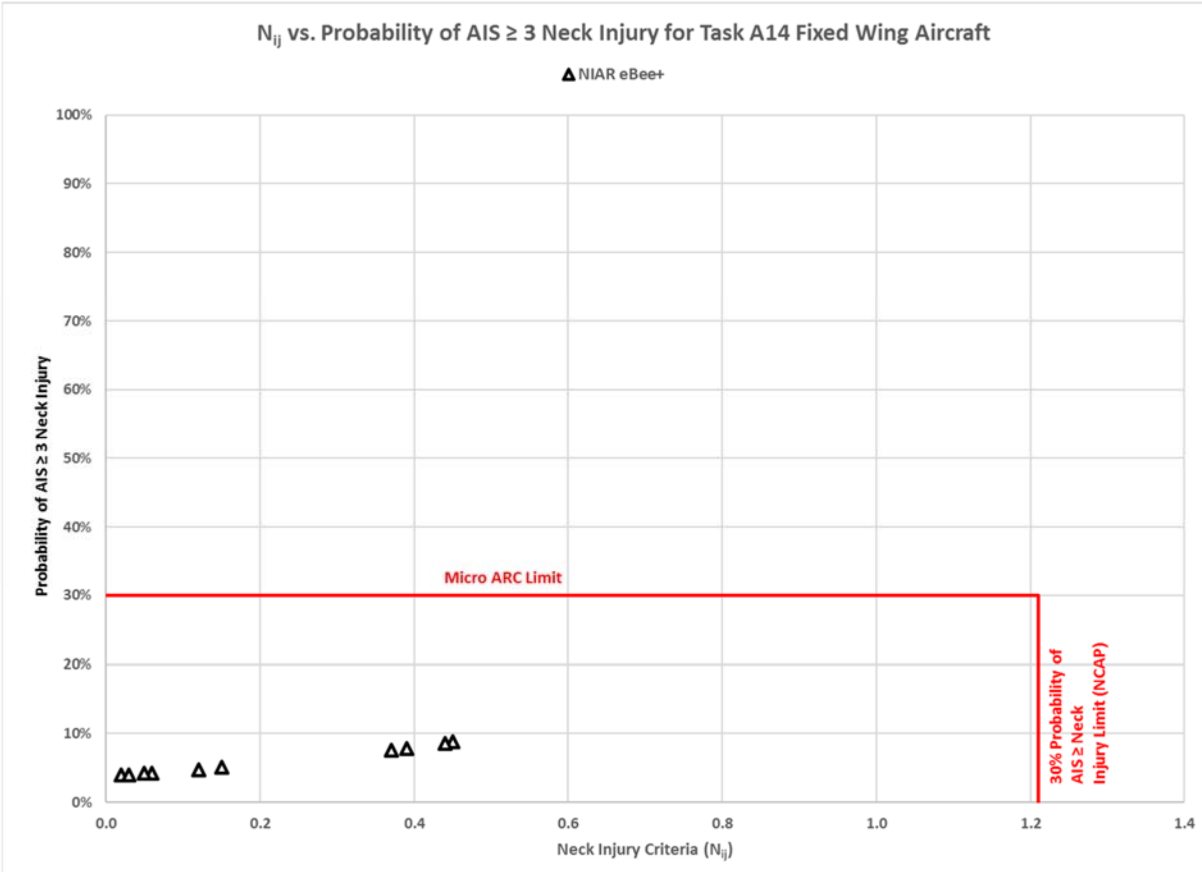

Figure 79. N_{ij} vs. Probability of AIS ≥ 3 Neck Injury for SenseFly eBee+

Conclusion: FW aircraft impact test results show that puller prop aircraft have upwards of three times the injury potential to that of a pusher prop aircraft due to the pointed spinner and the concentrated mass of the prop, spinner, and motor located at the initial contact point. Without substantial mitigations to reduce the sharpness and impact severity during ground collision, puller prop platforms are not suitable for flight over people without use of a parachute system or other decelerating mitigation system due to their increased injury potential and high impact velocities following failures.

3.4.3.7 Aircraft Component Test Results

Components/payloads tested during the Task A14 research are shown in Table 31. During Task A14, UAH and NIAR conducted impact testing of DJI Phantom 3 batteries and SLR cameras to assess the injury potential of these objects. This testing is relevant because aircraft components can separate for the aircraft if there is a midair collision with a structure or another aircraft during operations over people. Based on available test articles, this was a limited assessment that provided preliminary data to support characterization of the objects relative to aircraft and support the overall survey of UAS injury potential under Task A14.

Table 31. Task A14 Vehicle Components/Payload Configurations

Object	Configuration/Weight	Estimated Cross-Section Area (ft^2)	Estimated Drag Coefficient	Estimated Terminal Velocity (ft/s)	KE at Estimated Average Terminal Velocity (ft-lbf)
Wood Block	Impact Test Config. / 2.7 lbf	0.225	1.05	98	401
Foam Block (Steel or AL Core)	Impact Test Config. / 2.7 lbf	0.225	1.05	98	401
Phantom 3 Battery	Impact Test Config. / 0.85 lbf	0.0245	1.05	167	368
SLR Camera	Impact Test Config. / 1.7 lbf	0.201	1.05	70	129

Aircraft components, such as batteries and cameras, appear to have impact characteristics that are more similar to rigid impactors such as the wood block than multirotor and fixed wing aircraft (Figure 80 - Figure 84). These components are relatively rigid objects with lower compliance than the aircraft that were tested under Task A14. Low order aerodynamic modeling indicates that these objects can also reach higher terminal velocities than the aircraft in a fall as shown in Table 31. The SLR camera, wood block, and DJI Phantom 3 Battery have estimated terminal velocities of 70, 98, and 167 ft/s, respectively, with terminal velocity impact KE levels ranging from 129 – 401 ft-lbf. With the exception of the SLR camera, the curve fits of test data shown in Figure 80 indicate that all of these objects will readily exceed the 198g peak resultant head acceleration threshold in any impact above 10% of their terminal velocities. Such a condition is possible if the components are separated from an aircraft because of an impact with a structure during flight. Power curve fits were used in this analysis because they have higher R^2 values than linear fits do, which differs from the aircraft that were testing in Task A14. The SLR camera estimates are suspect due to the challenge of estimating an appropriate drag factor for the SLR camera due to its shape and external features. Based on per unit cost and a primary focus on conducting aircraft impact test versus component tests, there were only four SLR impact tests conducted by UAH. All of these tests used the same camera. Researchers stopped testing after they found external damage on the SLR camera during post-test inspection. Based on repeated tests using the same SLR camera and an inability to assess internal damage, it is not possible to determine if the results in Figure 80 are accurate and representative of the SLR camera's injury potential. The appearance of greater compliance in the SLR camera impact trends is questionable and requires additional testing and analysis for verification.

Only NIAR's tests clearly showed a pronounced potential for increased probability of AIS ≥ 2 skull fracture for the DJI Phantom 3 Battery (Figure 81), with a maximum value of 28%. The NIAR tests were completed with impact velocities of approximately 60 ft/s (48 ft-lbf). Aerodynamic analysis shows that this is 36% of the battery's terminal velocity. Figure 80 shows the DJI Phantom 3 Battery crosses the 198g threshold at 36 ft-lbf indicating that the 198g threshold may be conservative relative to the automotive skull fracture injury metrics. To make a complete assessment of the DJI Phantom 3 Battery's injury potential, impact testing must be conducted at or near terminal velocity that can occur within the Part 107 altitude limit of 400 ft AGL.
.
The current NIAR test results indicate that there is low probability of AIS ≥ 2 head injury, AIS ≥ 3 head injury, and AIS ≥ 3 neck injury associated with a DJI Phantom 3 Battery impact (Figure 82, Figure 83, and Figure 84). Testing at higher impact velocities is needed to determine the upper limits of the DJI Phantom 3 Battery's injury potential based on its terminal velocity. Additionally, if further battery testing is conducted, larger mass batteries that are needed to conduct flights with

aircraft of 10 lbf gross takeoff weight or more should be tested as the relatively light DJI Phantom 3 Battery does not represent the highest mass batteries on the market that are likely to be used in commercial sUAS operations.

Conclusion: Externally mounted equipment and batteries that become dislodged can present a more substantial injury risk than that of the sUAS itself at equivalent impact KE. Components like batteries and cameras are typically denser and have less flat plate drag area than a multirotor aircraft, which makes them rigid and likely to impact at higher velocities and with greater injury potential than the aircraft themselves.

Recommendation: The FAA should develop performance-based standards for component mounting latches and other mechanisms for securing components to aircraft, e.g. minimum g-loading limits for latches to retain components if an operator is seeking approval for operations over people.

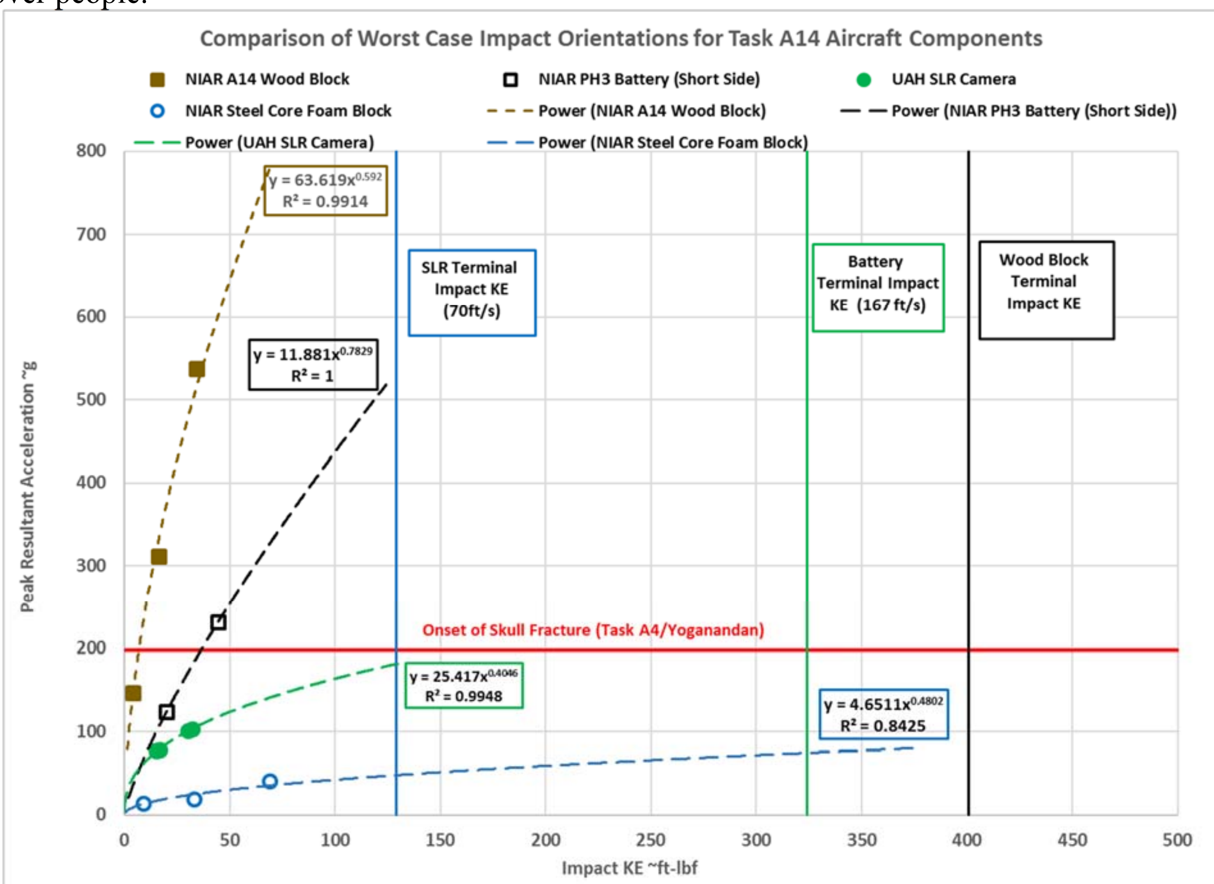

Figure 80. Comparison of Worst Case Impact Orientations for Task A14 Aircraft Components

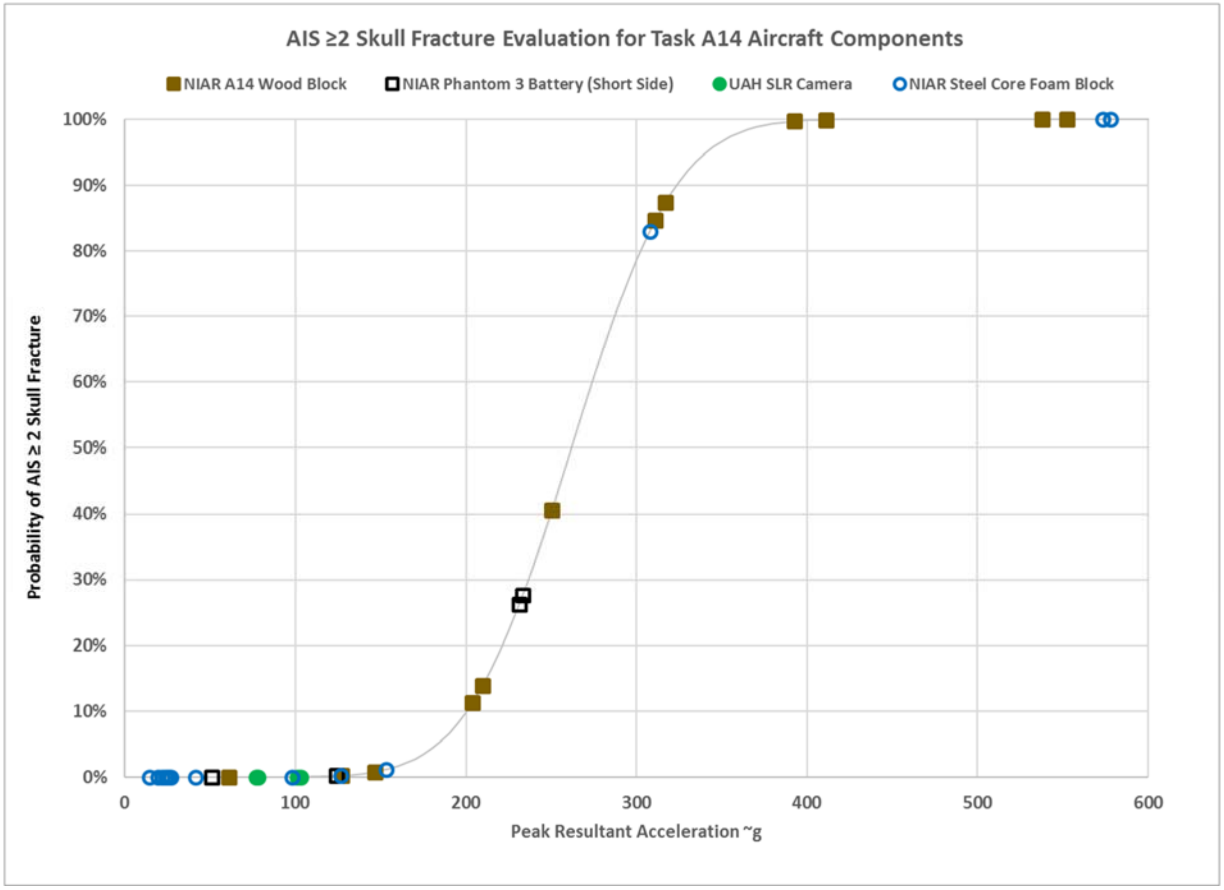

Figure 81. AIS ≥2 Skull Fracture Evaluation for Task A14 Aircraft Components

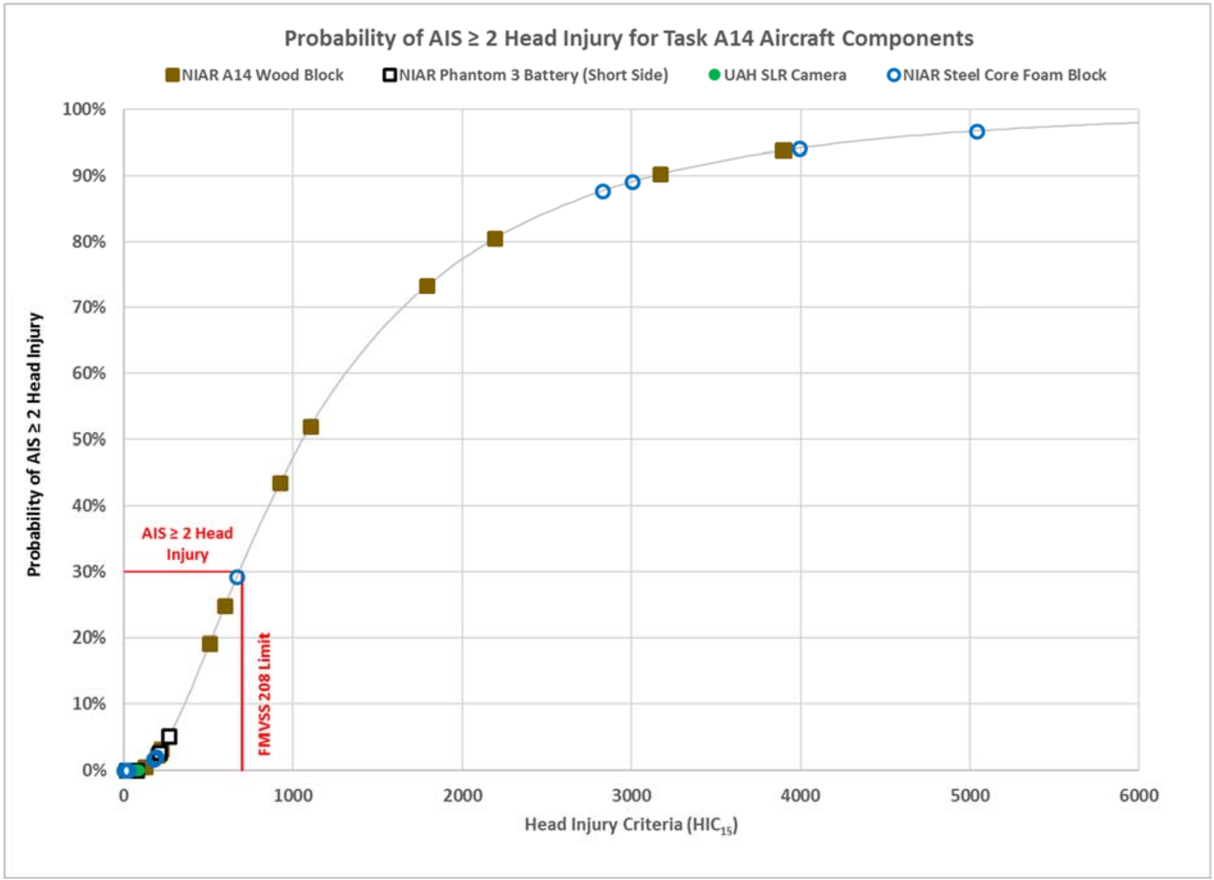

Figure 82. Probability of AIS ≥ 2 Head Injury for Task A14 Aircraft Components

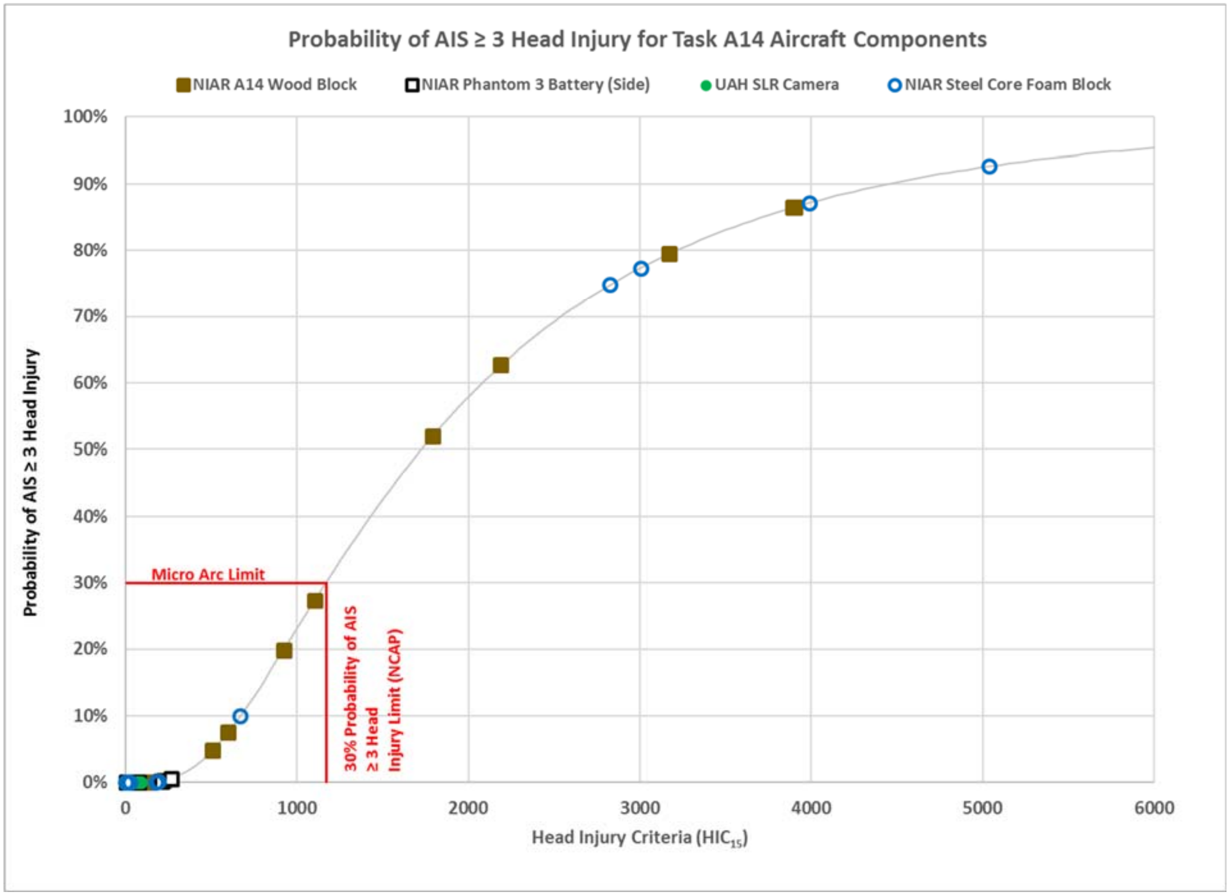

Figure 83. Probability of AIS ≥ 3 Head Injury for Task A14 Aircraft Components

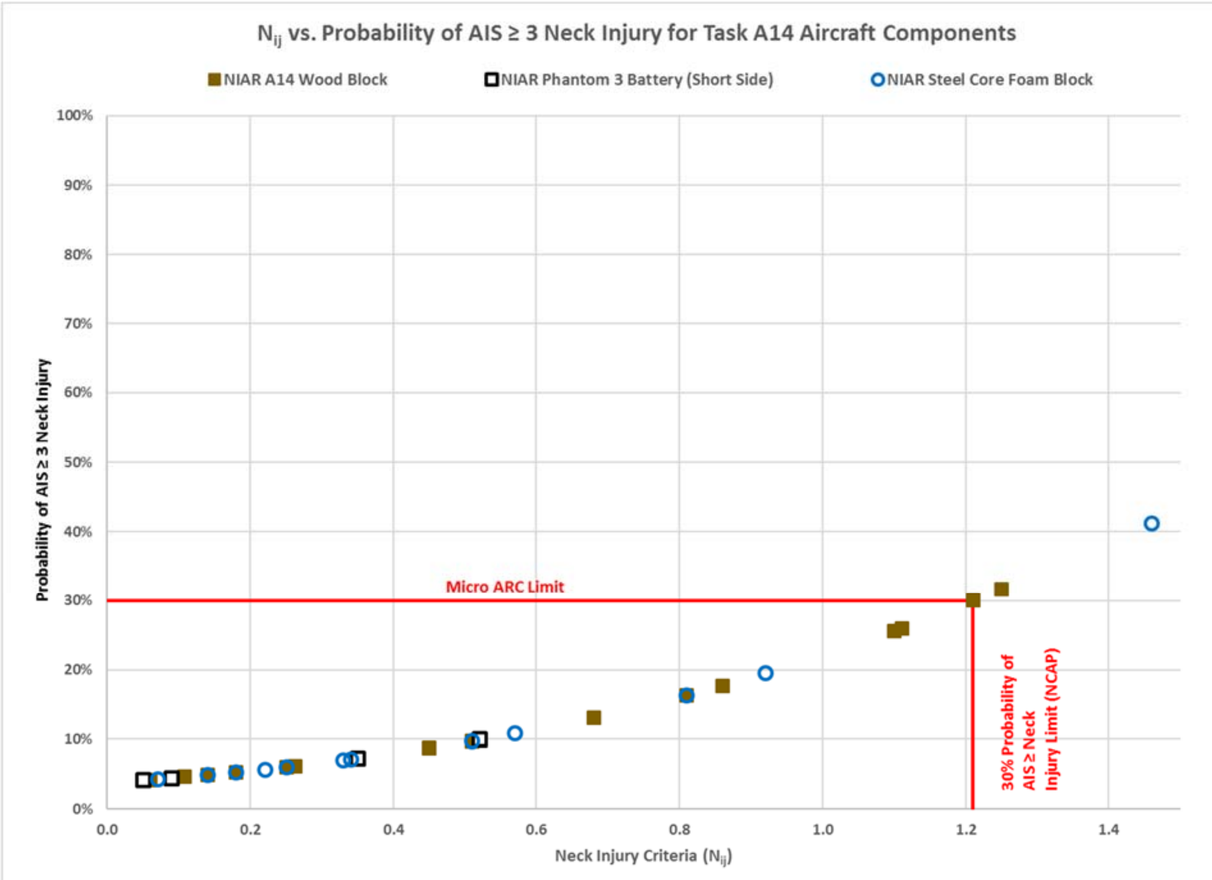

Figure 84. N_{ij} vs. Probability of AIS ≥ 3 Neck Injury for Task A14 Aircraft Components

3.4.4 Injury Data Trends

The Task A14 ATD and Simplified test results suggest that head injury potential is the dominant injury risk for sUAS impacts on people versus neck injury. With the exception of the Vendor 1 Quadcopter, flight test suggests that multirotor aircraft achieve a very steep impact angle and terminal velocity within the first 150 ft of fall following failure (Table 21). This further suggests that the head is the most vulnerable area for multirotor impacts or impacts from payloads. Overall, most aircraft do not exceed 30% probability of AIS ≥ 3 head or neck injuries when impacted at velocities up to and including terminal velocity. However, based on launcher limitations, the Go Pro Karma, Vendor 3 Quadrotor and eBee+ aircraft were not tested at impact velocities up to their terminal or maximum operating velocities. Aircraft components like the DJI Phantom 3 Battery and SLR camera had limited testing, but the results indicate that they have higher injury potential than the aircraft. Further testing at higher impact velocities is needed to make full conclusions about these components. Pusher prop foam fixed wing aircraft have significantly lower injury potential than multirotor aircraft. Puller prop aircraft that initiate impacts with a hard (and often pointed) spinner and motor have high injury potential and are less suitable for operations over people, particularly considering the higher impact velocities that these aircraft can achieve following failure, e.g. 100+ ft/s. Despite having low risk of causing neck injuries or skull fracture, both the Vendor 1 Quadrotor and eBee+ do exhibit some potential to cause concussions, as do all of the heavier multirotor aircraft. Due to inconsistency between concussion metrics measured during PMHS testing, as well as disagreement within the scientific community concerning which metric is more accurate, a concussion threshold for use in regulatory standards should be delayed until such a time when a more definitive and consensus-based criterion has been established. Task A14 impact testing with the DJI Inspire 2 and S800 aircraft show that parachute recovery systems can significantly reduce the injury potential of heavier sUAS when flight test data and wind limits are used to develop corner case impact test points for analysis against the Task A14 injury metrics. Parachute recovery systems provide the clearest means of reducing impact KE for larger aircraft. The data sets developed in Task A14 are not sufficient to provide a recommended aircraft weight over which parachutes should be required for flight over people.

It appears that vertical impacts, out of all tested impact trajectories, have the highest potential for neck injury versus the angled and horizontal impacts. The vertical impacts achieve significantly higher upper neck compression loads that more readily exceed the 50th Percentile H3 ATD limits, whereas the angled and horizontal impacts do not readily exceed these limits for compression, flexion, or extension. This is borne out by analysis of the wood block and DJI Phantom 3 N_{ij} values based on impact KE and separated by impact trajectory with respect the head seen in Figure 85 and Figure 86. In both cases, the vertical impact test data curve fits cross the NCAP N_{ij} threshold of 1.21 at lower impact KE values than the other impact orientations like angled impacts to the front, rear, and side of the head, and horizontal impacts in the case of the wood block. This indicates that flexion and extension moments due to sUAS head impacts play a smaller role in the neck injury potential of these aircraft. Further testing is needed to validate this observation, but it may play a strong role in determining which impact trajectories, with respect to the ATD head, are the most critical for testing as standards are developed.

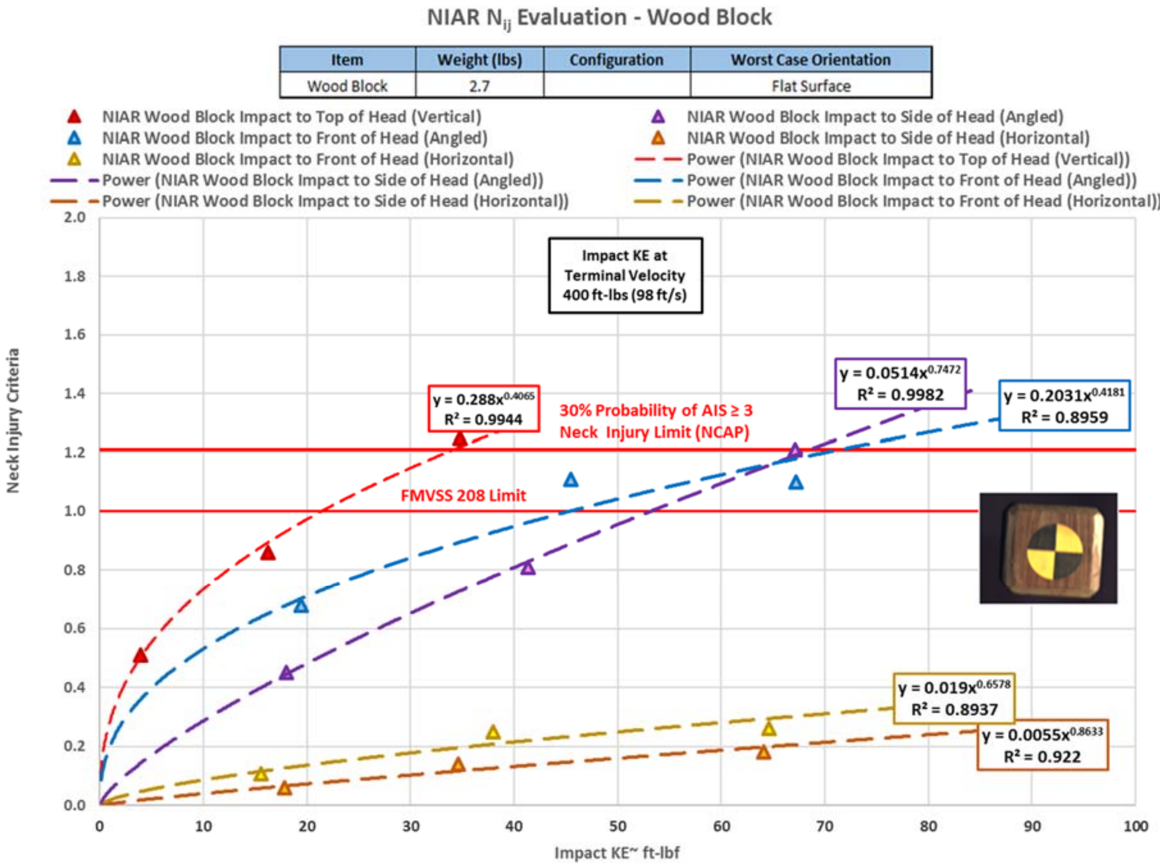

Figure 85. NIAR N_{ij} Evaluation - Wood Block

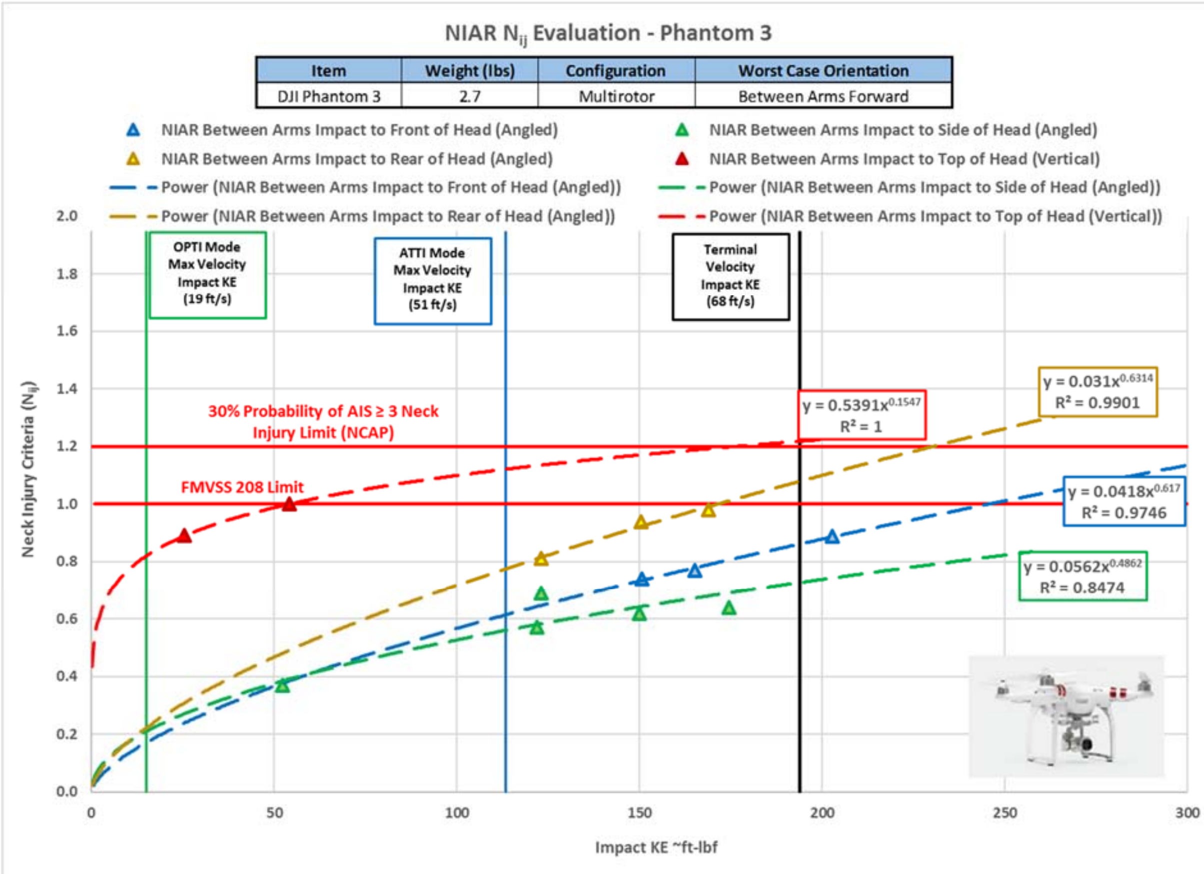

Figure 86. NIAR N_{ij} Evaluation - Phantom 3

Conclusion: The Vendor 1 Quadrotor and eBee+ fixed-wing aircraft testing showed that these aircraft have very low risk of causing skull fracture or neck injuries and are good examples of platforms appropriate for flight over people over their full flight envelope.

Conclusion: It appears that head injuries are the most probable injury type in sUAS impacts, versus neck injuries, based on the tests conducted under Task A14 to date. Aircraft and impactor object construction and materials are key factors relating to probability of and type of injury potential.

Conclusion: Vertical impacts appear to have the highest injury potential out of the testing impact trajectories with respect to the head.

Conclusion: Test results show that more rigid aircraft or impactors have a higher likelihood of causing head injuries like skull fracture because of high, short-duration linear accelerations and impulse loading on the skull. However, more compliant objects can still cause low-level concussions and neck injuries because they have longer contact times with the head and can generate greater head rotational rates and acceleration.

3.4.5 Comparison of Full ATD and Simplified Testing Results

There are two means by which the UAH (Simplified Test) and NIAR (Full ATD Test) results are compared in this study. First, when there are sufficient redundant test points for either a UAH or NIAR test series, the mean and standard deviation peak resultant head acceleration and mean impact KE value are calculated for each set of repeated tests, e.g. multiple impacts with a target velocity of 25 ft/s. The mean and standard deviation are used to establish 95% confidence intervals for the UAH impact data. The complete set of NIAR full ATD impact data, regardless of impact trajectory, is plotted to determine if it falls within the confidence interval. Based on the overall study goal to complete a broad survey of aircraft and impact orientations, and limited test assets, it was not possible to conduct statistically significant testing for every aircraft or component. For aircraft in which there were sufficient test points to generate 95% confidence intervals, the slopes of these confidence intervals where 1.35 – 1.48x the slope of the UAH curve fits. In cases where there are not repeated test points for a given aircraft, the curve fit slopes of the UAH and NIAR data are compared along with looking at whether the entire NIAR test points fall under a line with a slope 1.5 times greater than the UAH data curve fit slope. The use of the 1.5x slope of the UAH data serves as a surrogate for the upper 95% confidence interval and for evaluation as a potential Factor of Safety for analyzing simplified versus ATD impact data. This 1.5x factor of safety was chosen based on rounding up from the steepest 95% confidence interval observed during calculation of experimental error for the DJI Phantom 3, Go Pro Karma, and Vendor 1 aircraft. This is a potential conservative method for estimating the worst case injury potential of an aircraft when there are limited numbers of articles available for testing.

The current Task A14 testing of the DJI Phantom 3 was sufficient to establish confidence intervals and compare test results. The UAH DJI Phantom 3 vertical impact tests included in the evaluation were conducted with the front of the aircraft impacting the top of the ATD head between the arms. All of the NIAR test data, regardless of impact trajectory with respect to the head, was included to determine if the NIAR full ATD test data falls under the upper 95% confidence interval of the UAH tests (Figure 87). The upper 95% confidence interval of the UAH data is, effectively, a factor of safety and potentially represents the worst case injury potential of the DJI Phantom 3 aircraft. The slope of the upper confidence interval is 1.48 times the slope of the UAH data curve fit. UAH's more rigid apparatus experiences lower magnitude accelerations than the NIAR vertical impact and predicts exceeding the 198g threshold at approximately 121 ft-lbf of impact KE. The NIAR vertical impact test results, which were conducted at higher impact velocities up to 60 ft/s, are more conservative. NIAR's other impact trajectories, which are angled impacts to the front, rear, and side of head, result in generally lower peak head resultant acceleration than vertical impacts from either UAH or NIAR. The crossing point of the upper 95% confidence interval of the UAH data is at 82 ft-lbf. The upper confidence interval bound is a statistically-determined and conservative estimate of the DJI Phantom 3's worst injury potential.

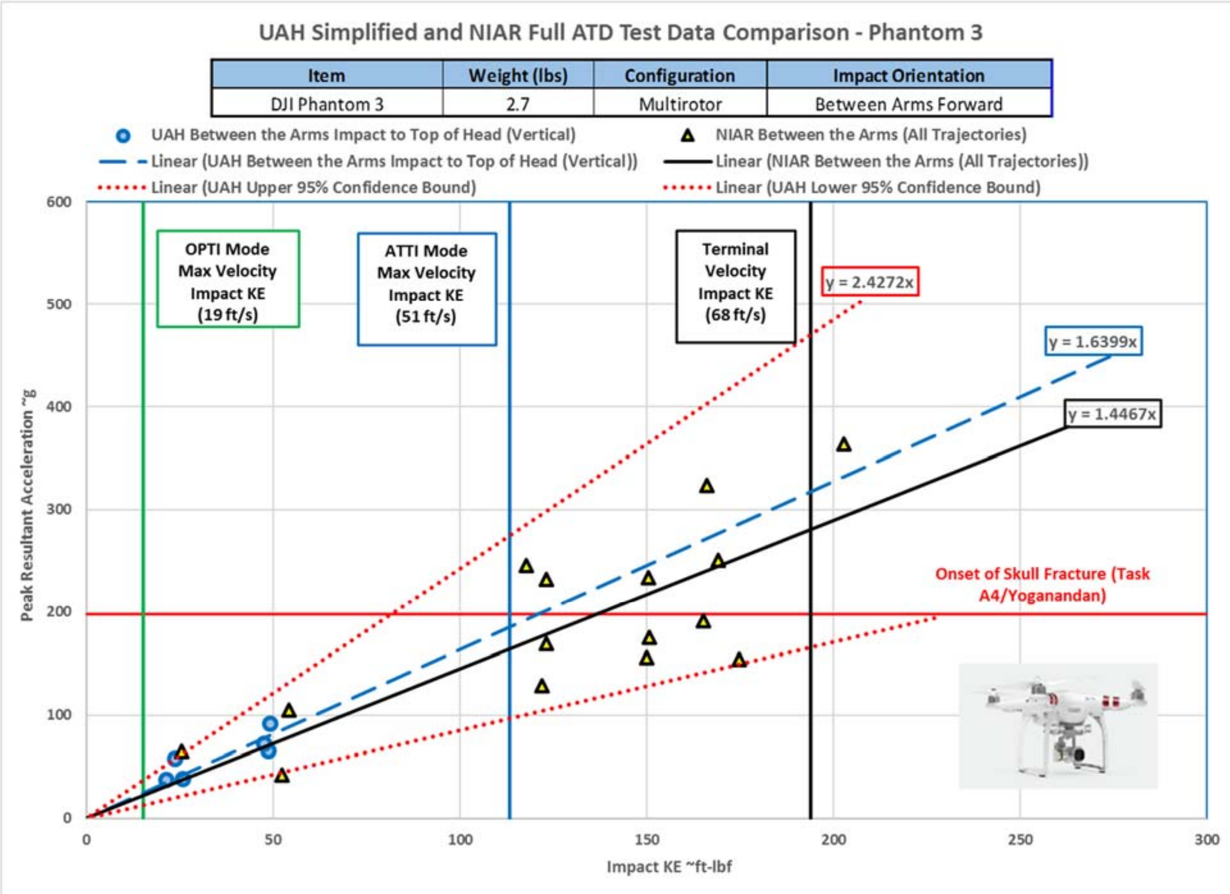

Figure 87. UAH vs. NIAR Data Comparison - DJI Phantom 3 Front into Head

There is good consistency between the Task A4 and Task A14 NIAR impact test data for the DJI Phantom 3 (Figure 88). Overall, there is a higher slope for the aggregate data compiled in Task A14 compared to the Task A4 tests. That is related to the Task A4 predominant impact test orientation of bottom into head. Bottom into head is the most compliant impact orientation for the DJI Phantom 3 which leads to a shallower slope. The Task A14 impact orientations are biased toward the stiffest orientation, which is an impact between the arms; however, there were also some low-energy top into head, arm into head, and bottom into head impacts, which work to decrease the slope of the aggregate data. This shows consistency between the two sets of test data and highlights a significant step forward in this testing. The task A14 did not aggregate vehicle impact orientations and ATD impact orientations to determine injury thresholds or to assess injury trends. The Task A14 research focused on worst case impact orientation evaluations and analysis of different impact trajectories (Figure D 2 and Figure D 4).

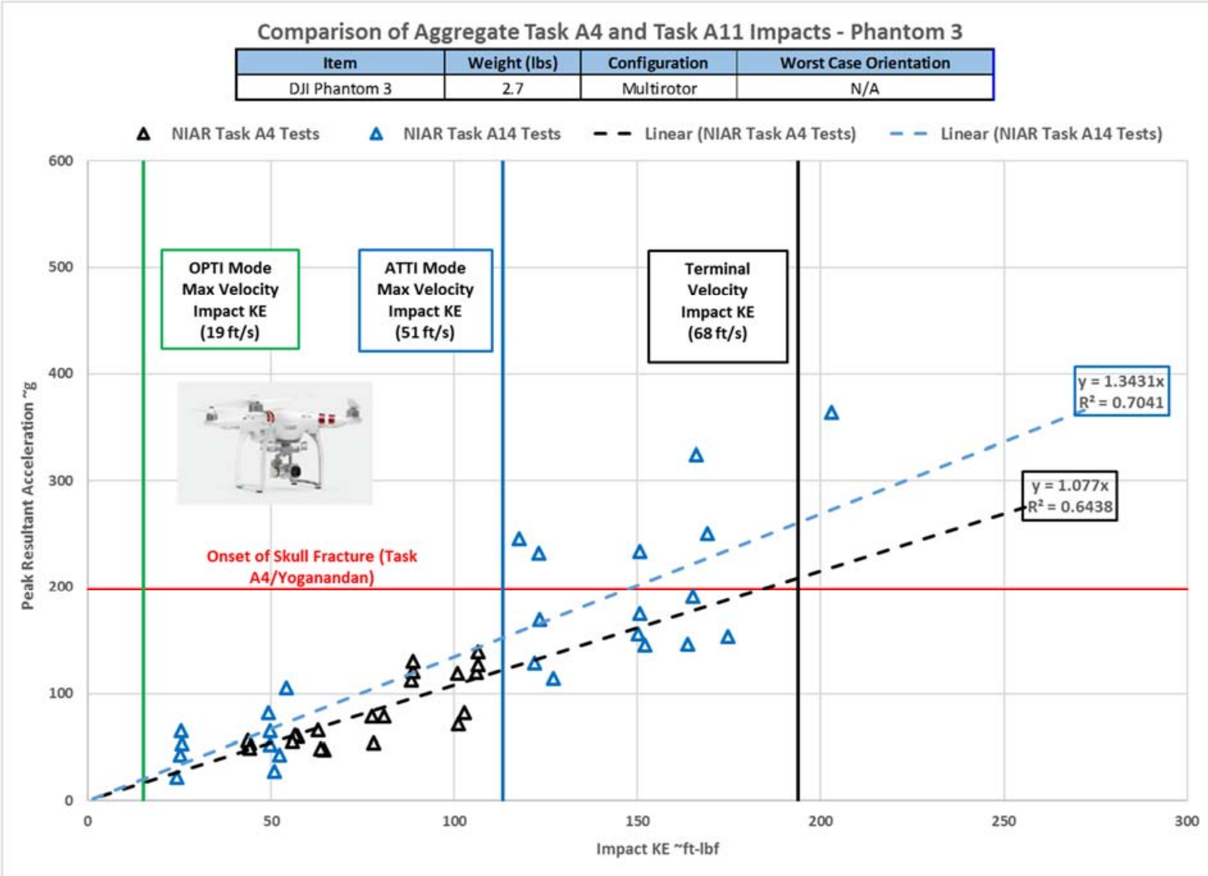

Figure 88. Comparison of Aggregate Task A4 and Task A11 Impacts - Phantom 3

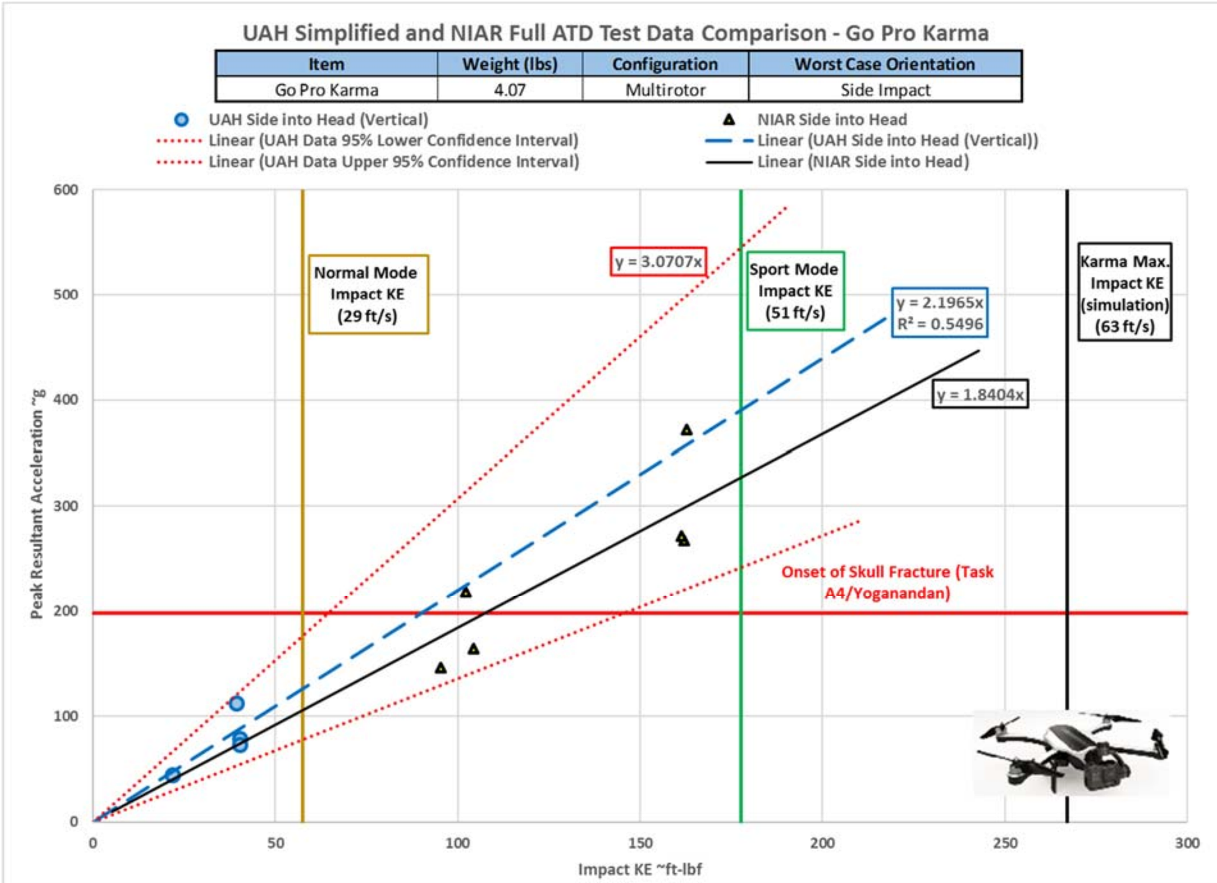

Figure 89. UAH vs. NIAR Data Comparison - Go Pro Karma

The comparison of UAH and NIAR data sets for the Go Pro Karma was based on redundant tests using a side into top of head impact orientation for vertical impacts. After some inconsistent data points based on excessive roll prior to impact were parsed from the UAH data, 95% confidence intervals were developed based on 40 ft-lbf impacts. Data from all of NIAR impact trajectories falls under the upper bound of UAH's experimental error (Figure 89). The upper 95% confidence interval of UAH's data set has a slope that is 1.39 times the slope of the UAH curve fit. Additional UAH testing at an impact energy of 20 ft-lbf would further refine these results in order to make up for the rejected data points; however, the NIAR data curve fit would most likely remain within these bounds based on the spread of the 40 ft-lbf UAH impact test points. The UAH upper 95% confidence interval crosses the 198g threshold (9% probability of AIS ≥ skull fracture) at 65 ft-lbf of impact KE and is a conservative estimate of the injury potential of the Go Pro Karma that is based on the most injurious impact test data in the aircraft's stiffest impact orientation.

Based on delays in simplified testing described in Section 3.4.1, NIAR conducted worst case orientation analysis of the Vendor 1 Quadrotor aircraft to prepare for full ATD and PMHS testing. UAH replicated the NIAR worst case orientation analysis and came to the same conclusion that the top into head or inverted impact orientation is the stiffest impact orientation for the Vendor 1 Quadrotor aircraft (Figure G 1 and Figure G 3). Figure 90 illustrates that all of the NIAR test data falls under the upper 95% confidence interval of the UAH data. The upper 95% confidence interval of UAH's data set has a slope that is 1.35 times the slope of the UAH data linear curve fit. The upper confidence interval crosses the 198g threshold for the onset of skull fracture at 29.5 ft-lbf of impact KE; however, this impact KE level is beyond what the aircraft can generate in a free fall at terminal velocity. Based on this observation, the Vendor 1 Quadrotor presents low risk of skull fracture or head injury during flight over people.

The analysis of the DJI Phantom 3, Vendor 1 Quadrotor, and Go Pro Karma data from UAH relies heavily on the extrapolation of low-velocity impact test trends to higher velocity/energy regions. This is based on an assumption that the behavior of the simplied head and neck device remains linear as the impact KE increases, and remains comparable to the NIAR impact test points conducted with velocities in excess of 36 ft/s. In order to continue advancing the use of the simplified test apparatus, future testing must validate that the head response remains approximately linear when testing the multirotor aircraft at higher impact velocities. Based on the current testing, the estimated crossing points for the 198g threshold and neck injury thresholds are good for visualization, but the head and neck device requires additional testing to be validated for estimating injury potential due to impacts with velocity in excess of 36 ft/s.

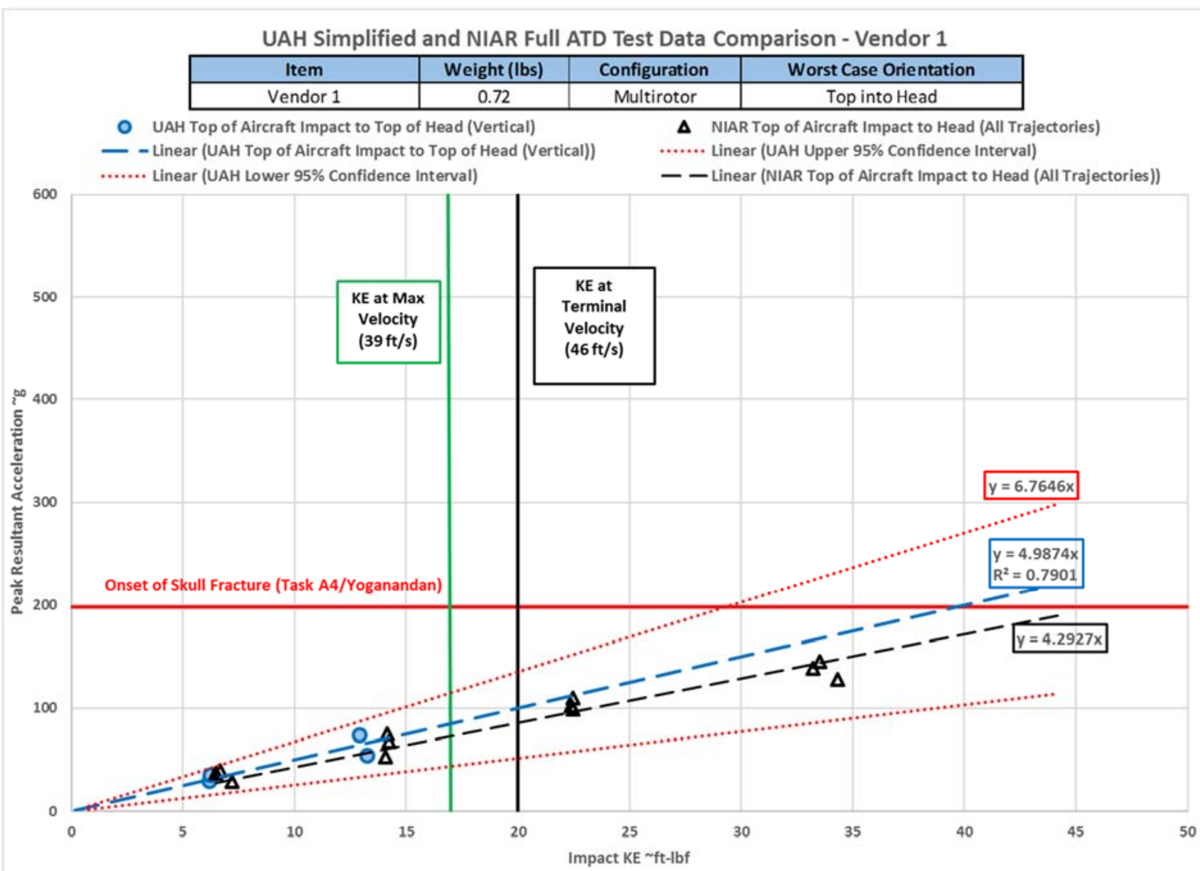

Figure 90. UAH vs. NIAR Data Comparison - Vendor 1 Quadrotor

Due to limited test articles, UAH and NIAR did not have a large enough number of repeated test points to establish confidence bounds for the DJI Mavic Pro. In lieu of establishing confidence bounds, Figure 91 provides a comparison of the UAH vertical impacts with all of the NIAR data points using the stiffest orientation of the DJI Mavic Pro, which is top into head or inverted. While the UAH and NIAR data have similar slopes, the linear curve fit is poor for the NIAR data. This may be due to differences in impact energy dissipated through battery ejection between NIAR's two impacts, which leads to a non-linear trend (decreased g-loading at higher impact velocity/KE). The video and test data do not readily indicate reasons for this trend, although test videos show differences in aircraft rebound height off of the top of the ATD. It is not possible to provide a clear comparison of the two test devices based on this data. All NIAR data points for angled impacts to the side and front of the head fall below UAH's vertical impact curve fit line. In Figure 91, a line with a slope that is 1.5 times greater than the UAH data curve fit is used as a conservative factor of safety to serve as an upper bound of the injury potential of the DJI Mavic Pro in its worst case impact orientation. This factor of safety crosses the 198g head peak resultant acceleration threshold at 31 ft-lbf of impact KE. Further testing is needed to develop an actual statistically based estimate of the aircraft's worst case injury potential; however, the factor of safety shown in Figure 91 serves as a conservative approximation of the upper confidence interval. All of the NIAR test points fall under the line representing a factor of safety of 1.5 over the UAH data curve fit.

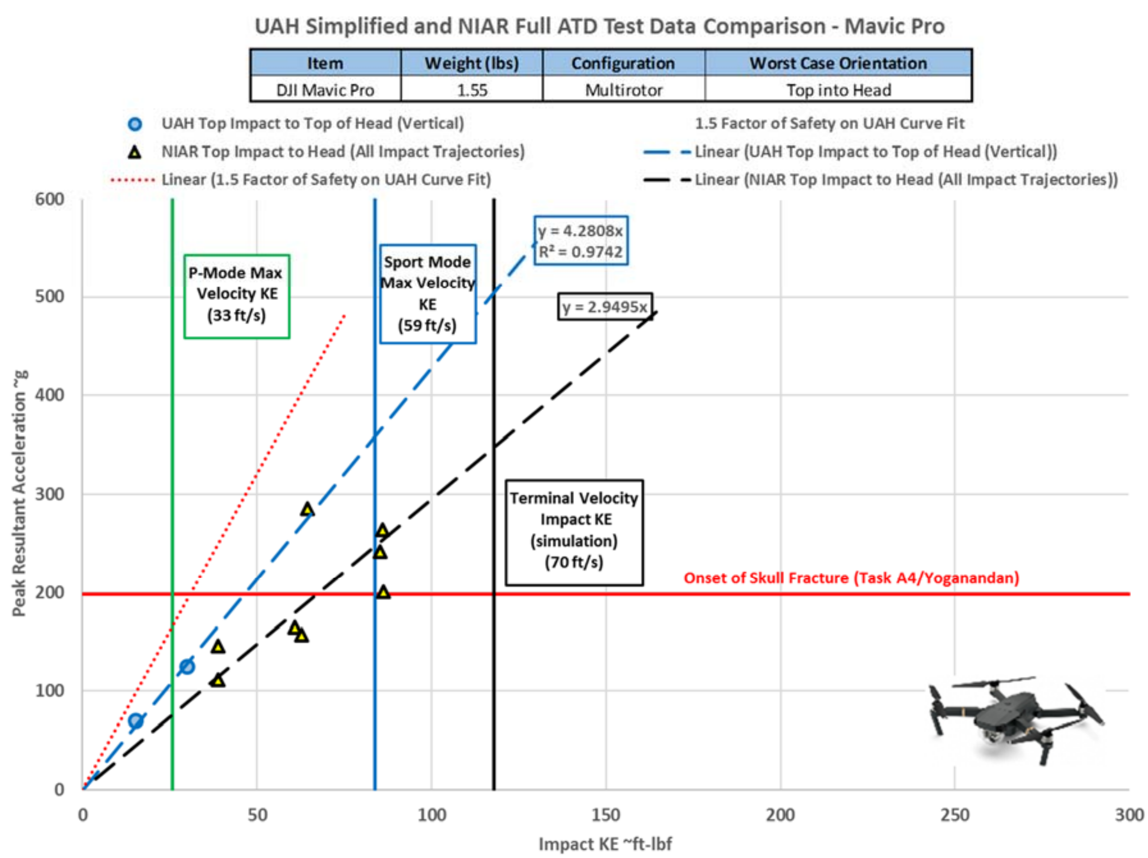

Figure 91. UAH vs. NIAR Data Comparison - DJI Mavic Pro

Figure 92 shows close agreement between the UAH and NIAR Vendor 3 Quadrotor data sets relating to vertical impacts between the arms of the aircraft. Based on limited test assets and an error in test execution, it was not possible to conduct enough tests to establish confidence interval.

UAH researchers conducted tests each at 20 ft-lbf, 40 ft-lbf, and 85 ft-lbf instead of three tests each at 20 ft-lbf, 40 ft-lbf. Referring to Figure 92, there is close agreement between the UAH and NIAR slopes for vertical impacts with the Vendor 3 Quadrotor. All NIAR test points fall below the line representing a factor of safety of 1.5 over the UAH data curve fit.

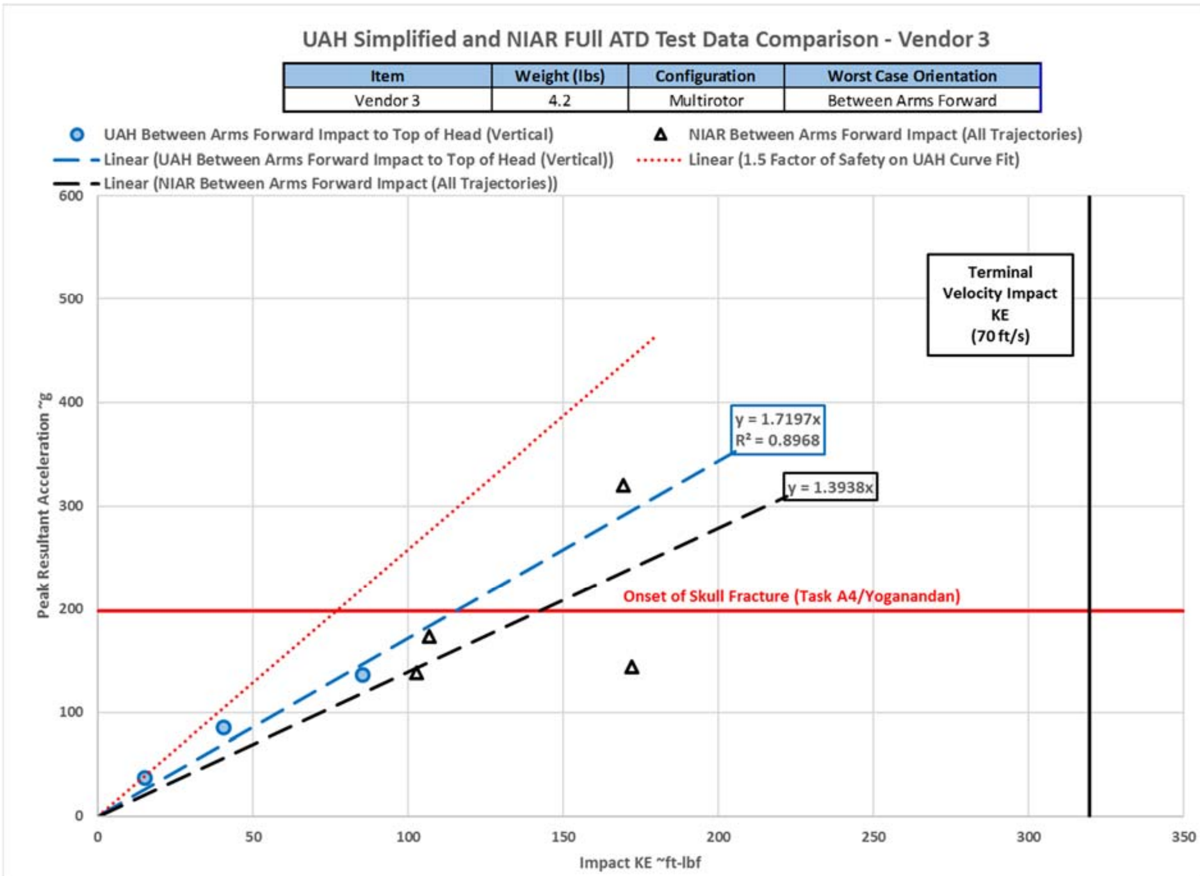

Figure 92. UAH vs. NIAR Data Comparison - Vendor 3 Quadrotor

The comparison between UAH and NIAR impact test data for the eBee+ shows that current simplified test apparatus responds in a manner differently from the full ATD device when testing aircraft with foam-based fuselages. UAH collected sufficient impact test data for the eBee+ Nose into Head impact orientation to establish 95% confidence intervals. The NIAR data fits along the upper 95% confidence bound of the UAH experimental data, which is indicative that the two test devices do not provide comparable data for this aircraft and other aircraft with foam-based fuselages (Figure 93). The clearest difference in aircraft impact response between the simplified and full ATD test setups was that the eBee+ aircraft tend to break at impact speeds of 25 ft/s and higher on the rigid simplified setup. Specifically, the forward nose section which houses the battery broke off at a hole that is designed into the fuselage at the aft end of the battery compartment. The eBee+ aircraft used in NIAR's full ATD testing remained intact with the exception of the removable wings falling off during some tests. This difference in head response may also be due to the differences in impact velocity/energy as foam has non-linear strain rate material characteristics[17]. Some of the differences in aircraft behavior, breaking versus bending may also be due to the lower velocity used in the UAH simplified test impacts and the higher velocities used in the NIAR full ATD impact tests.

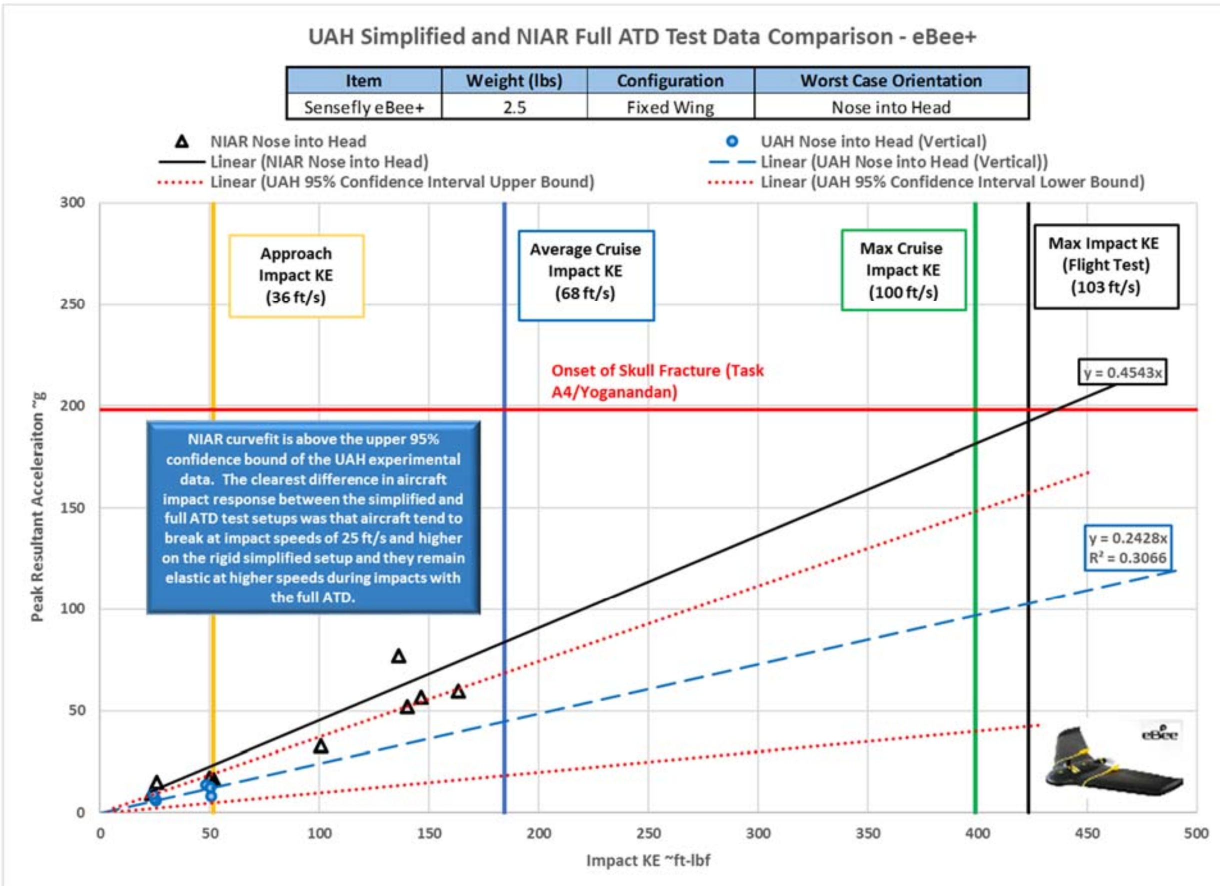

Figure 93. UAH vs. NIAR Data Comparison - eBee+

The NIAR DJI Phantom 3 Battery data curve fit is comparable to the UAH DJI Phantom 3 Battery curve fit for vertical impacts of the battery impacting the head with the smallest side of the battery (Figure 94). This impact orientation is shown in Figure 95. This comparison is based on a limited number of tests and does not employ confidence intervals, but it does use a factor of 1.5 time the slope of the UAH data curve fit. As with the multirotor aircraft, the UAH linear curve fit is above many of the NIAR non-vertical impact test points, and the 1.5 factor of safety provides a conservative estimate of the threshold for onset of injury.

It was necessary to preserve batteries for the full DJI Phantom 3 aircraft impacts at UAH, NIAR, and OSU so battery impact tests were limited. The battery cap was removed because it interfered

[17] Wei-Yang, L. Neidigk, M, Wyatt, N., "Cyclic Loading Experiement for Characterizting Foam Viscoelastic Behavior," Sandia National Laboratories, Livermore, CA, USA, 2016

with the drop stand release mechanism which resulted in incorrect impact orientations. UAH researchers assumed that the minor loss of mass was less important than correct impact orientation for recording accurate data. NIAR researchers conducted battery impact tests with the battery cap removed as well.

UAH Simplified and NIAR Full ATD Test Data Comparison - Phantom 3 Battery

Item	Weight (lbs)	Configuration	Worst Case Orientation
Phantom 3 Battery	0.75	Battery	Long Side into Head

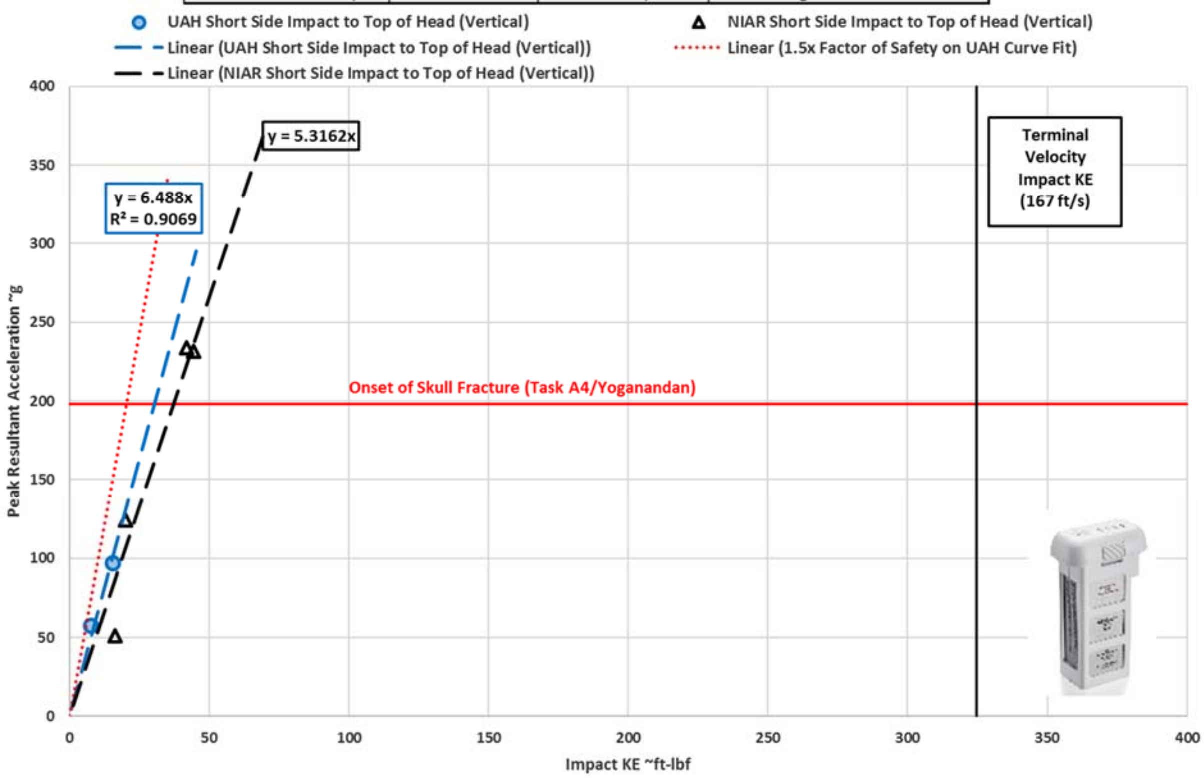

Figure 94. UAH and NIAR Vertical Test Data Comparison - DJI Phantom 3 Battery

Figure 95. DJI Phantom 3 Battery Impacting on Small Side

The rigid wood block impact test data sets from NIAR and UAH are not in good agreement. UAH conducted enough tests to establish 95% confidence intervals and the NIAR test data curve fit falls well outside of the confidence intervals (Figure 96). The UAH simplified test apparatus peak resultant acceleration is lower than the NIAR peak resultant acceleration at equivalent impact KE values. The rigidity of the simplified apparatus mount provides a markedly different response than the ATD when impacted by an object as rigid as the wooden block. The neck compression loads measured during the UAH tests were also lower than the NIAR wood block vertical impact tests with similar impact velocities. It is possible that the rigidity of the simplified device combined with the rigidity of the wood block leads to a very short contact time and less work done on both the head and neck by the block. Additionally, the head structure of the ATD and simplified devices may deform differently with the rigid impactor, e.g. greater deformation of the simplified head without as much translation of the head. The wood block serves as an essentially rigid object that can be used as a benchmark for comparison with aircraft and aircraft component impacts and it also serves as a corner case that most clearly demonstrates the differences in how these two devices respond to impacts. More impact testing, perhaps with modified instrumentation, like strain gauges on the ATD head and photogrammetry to compare head and body displacements (ATD) with head and base mount displacements (simplified device) could be used to more fully understand differences in these two test devices.

Power fits were used for this comparison because they provided higher R^2 values than linear fits with the rigid wood block. As with linear fits that fix the y-intercept at zero, the power fits have a y-intercept at zero, which is physically correct since there will be no head acceleration if there is no impact energy imparted to the head. The current scope of test data doesn't provide a clear explanation for the non-linear behavior of the head peak acceleration curves; however, it is likely that the ATD neck acts as a non-linear spring in compression. Previous government research shows that the ATD Hybrid III neck has non-linear spring properties in flexion and extension.[18] The rigid object impacts tend to highlight the dynamic properties of the head and neck since there is essentially no deformation of the impactor. Head and neck response measurements based on rigid object impacts are dominated by the neck dynamics, while the results of aircraft impacts reflect the structural response of the aircraft as well as the head and neck.

Conclusion: Simplified test methods are capable of assessing multi-rotor worst case impact orientations and have strong potential for estimating injury probability and severity for sUAS other than foam manufactured aircraft.

Recommendation: The FAA should support continued testing to develop statistically significant datasets that characterize the consistency and repeatability of the test results and help evaluate the hypothesis that the upper 95% confidence interval of the UAH test data is a true worst case transfer function for all simplified and ATD test data pertaining to a specific aircraft.

Conclusion: For an aircraft with four different impact orientations, a minimum of 12 impact tests are needed to evaluate the worst case impact orientation. If the four impact orientations are noted as orientations A-D, then characterization requires impacts at two velocities or energy levels in each orientation A-D. After the first eight tests are done, the slope for each orientation can be estimated by curve fitting the data for each orientation. After the steepest slope is determined, then a minimum of two more tests at each speed should be conducted in the stiffest orientation to verify the slope determined in the initial round of testing. Additional testing can be done in order to more accurately quantify experimental error.

Conclusion: Due to the large scope of vehicles, test orientations and impact locations selected for this testing, few statistically significant conclusions can be drawn concerning use of the simplified test apparatus in lieu of the full ATD for impact testing and injury potential estimation based on the full scope of Task A14 injury metrics that are taken from FMVSS 208 and NCAP.

Recommendation: The FAA should focus future research on statistically significant simplified and ATD impact test data sets that enable assessment of test method consistency and repeatability as well as the development of injury risk curves specific to sUAS impacts.

Recommendation: The FAA should support research to develop a simplified impact target other than a FAA Hybrid III head and neck to reduce the number of test variables for simplified testing.

Recommendation: The FAA should support the conduct of a comparative test between the simplified or ATD testing approach and tests based on energy transfer estimation to determine the appropriate injury risk curves or injury metrics associated with energy transfer based methods.

[18] Spittle, E., Shipley, B., Kaleps, I. *Hybrid II and Hybrid III Dummy Neck Properties for Computer Modeling,* Vulnerability Assessment Branch Biodynamics and Biocommunications Division, Crew Systems Directorate, Write-Patterson AFB, OH, February 1992

3.4.6 Rigid Object Impact Testing Using the Simplified Head and Neck

It appears that the UAH simplified apparatus is not well-suited for testing rigid objects because of high impulse loading and the rigidity of the head and neck-only setup. UAH data for impacts in excess of 25 ft/s were not included in this analysis (Figure 96) because the z-axis accelerometer was saturated by the high impulse loading and the shock of the rigid body impact resulted in resonant ringing of the accelerometers after the block impact was recorded (Figure 97). The measured impact signal is minimal compared to the subsequent resonant ringing. The accelerometer resonant response in this case is significant enough that it cannot be filtered out using CFC 1000 filtering per SAE J211. This creates a false peak that can be interpreted as the peak resultant acceleration. This sensor response rendered the impact data largely unusable. The current simplified test design is unsuitable for use in evaluating the injury potential of higher speed rigid body impacts over approximately 25 ft/s. The clearest option for remedying this limitation of the simplified test device is to change out the standard accelerometers installed in ATD Hybrid III heads, which have resonant frequencies of 26 kHz with gas-damped with a resonant frequency of at least 90 kHz.. The gas-damped accelerometers are likely to eliminate the resonant ringing and saturation issues experienced with the standard accelerometers.

Conclusion: Due to the stiffness of the simplified test device, wood block impacts at over 25 ft/s generated high impulse loading on the Meggit C-Series stock head cg accelerometers and high frequency response of the head.

Recommendation: Future sUAS impact test standards should require the use of gas-damped accelerometers with resonant frequencies of at least 90 kHz versus the standard accelerometers installed in ATD Hybrid III heads, which have a resonant frequency of 26 kHz..

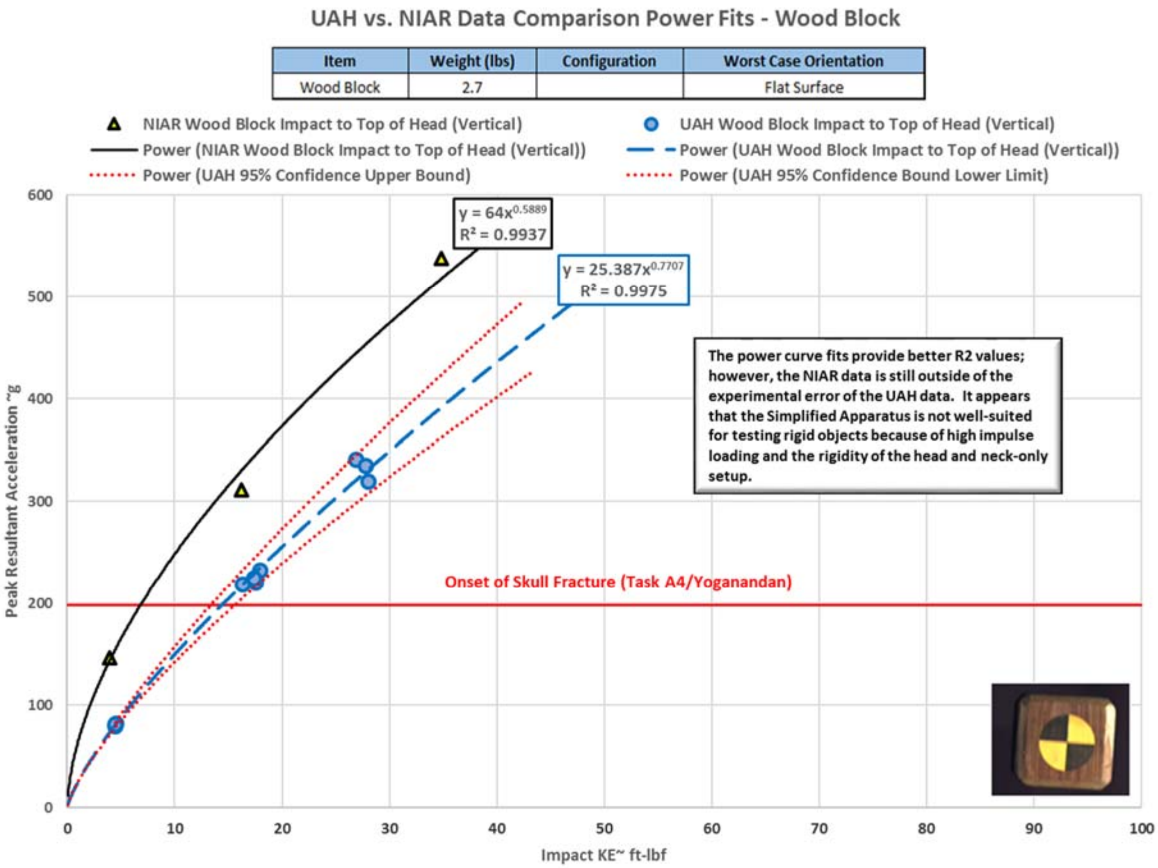

Figure 96. UAH vs. NIAR Data Comparison Power Fits - Wood Block

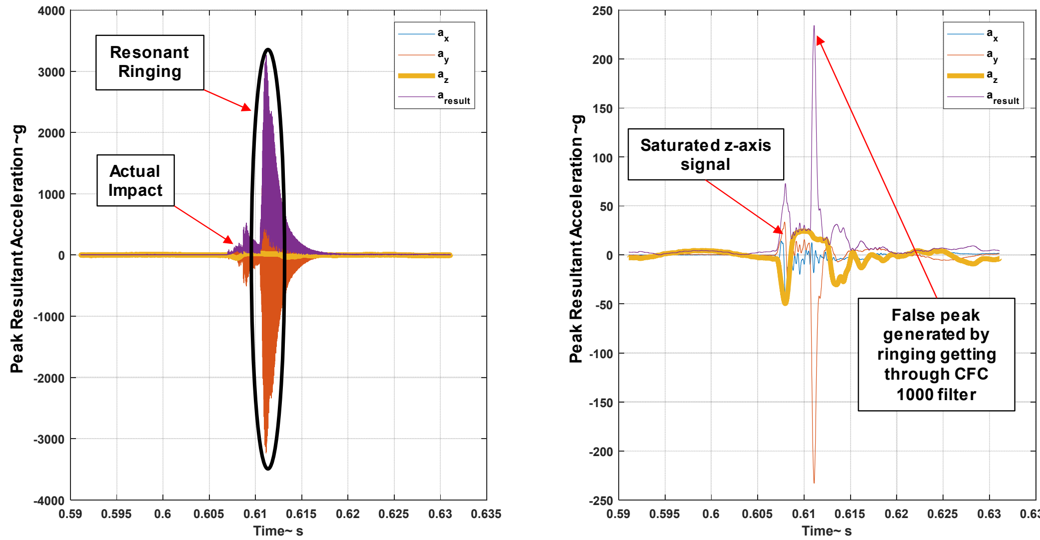

Figure 97. Unfiltered (left) and Filtered (right) Acceleromater Signals from a 36 ft/s Wood Block Impact on the Simplified Test Apparatus

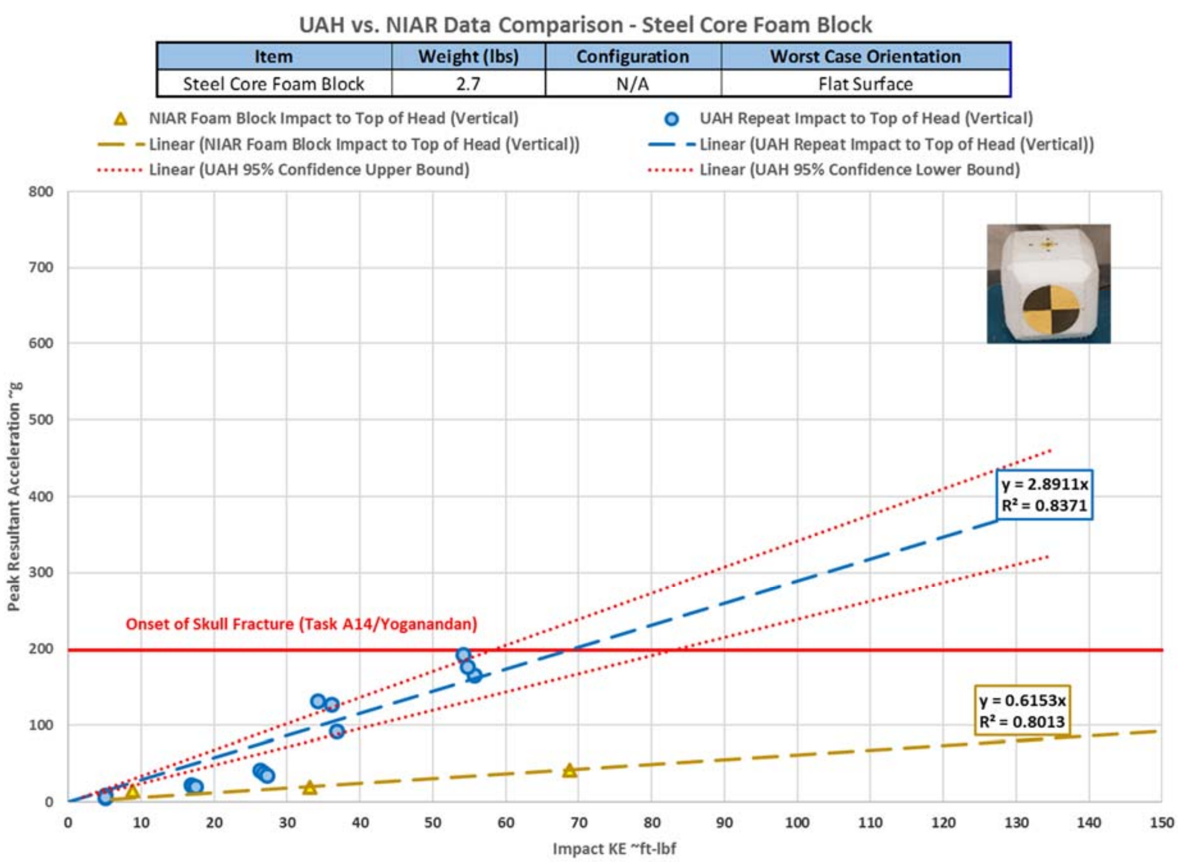

Figure 98. UAH vs. NIAR Data Comparison - Steel Core Foam Block

NIAR's steel core foam block vertical impact test data falls outside of the UAH 95% confidence interval for similar impact velocities. UAH's lower-speed impact tests of 10, 20, and 25 ft/s exhibit a generally linear increase in head peak resultant acceleration, but the head acceleration data begins to trend toward more of a g^2 relation with increasing impact KE above 25 ft/s. This trend is not seen in the NIAR vertical impact test data. The stiffness of the simplified test apparatus elicits non-linear deformation behavior in the test articles at lower impact KE-levels than the more compliant full ATD apparatus. The linear fit does not work well for the UAH data, but NIAR's vertical impact test data cannot be described well with a linear or power fit. In some cases, the NIAR data does follow a g^2 relationship, although it is not consistent for all impact orientations with respect to the head (Figure 99). In Figure 99, the UAH data is shown in purple circles, along with a second-order polynomial curve fit that has a better R^2 value than the linear fit in Figure 98. The NIAR test data curve fits for angled side of head impacts and horizontal impacts to the front and side of the head are also described well with second-order polynomial fits as well. It is possible that the linear region of these three data sets comes from foam compression and that the higher speed impacts, where g-loading increases more rapidly, represent the foam being at its maximum compression and the rigid steel core begins to dominate the head response. The rigid simplified test device is able to elicit this behavior because the foam compression is greater, relative to the NIAR impacts, during low-speed impacts. The more compliant full ATD exhibits this behavior at higher impact velocities because it takes more impact KE to fully compress the foam with the more compliant test apparatus. It is not clear, based on the available test data, why the NIAR vertical impacts and angled impacts to the front of the head are not well-described by a second-order polynomial fit.

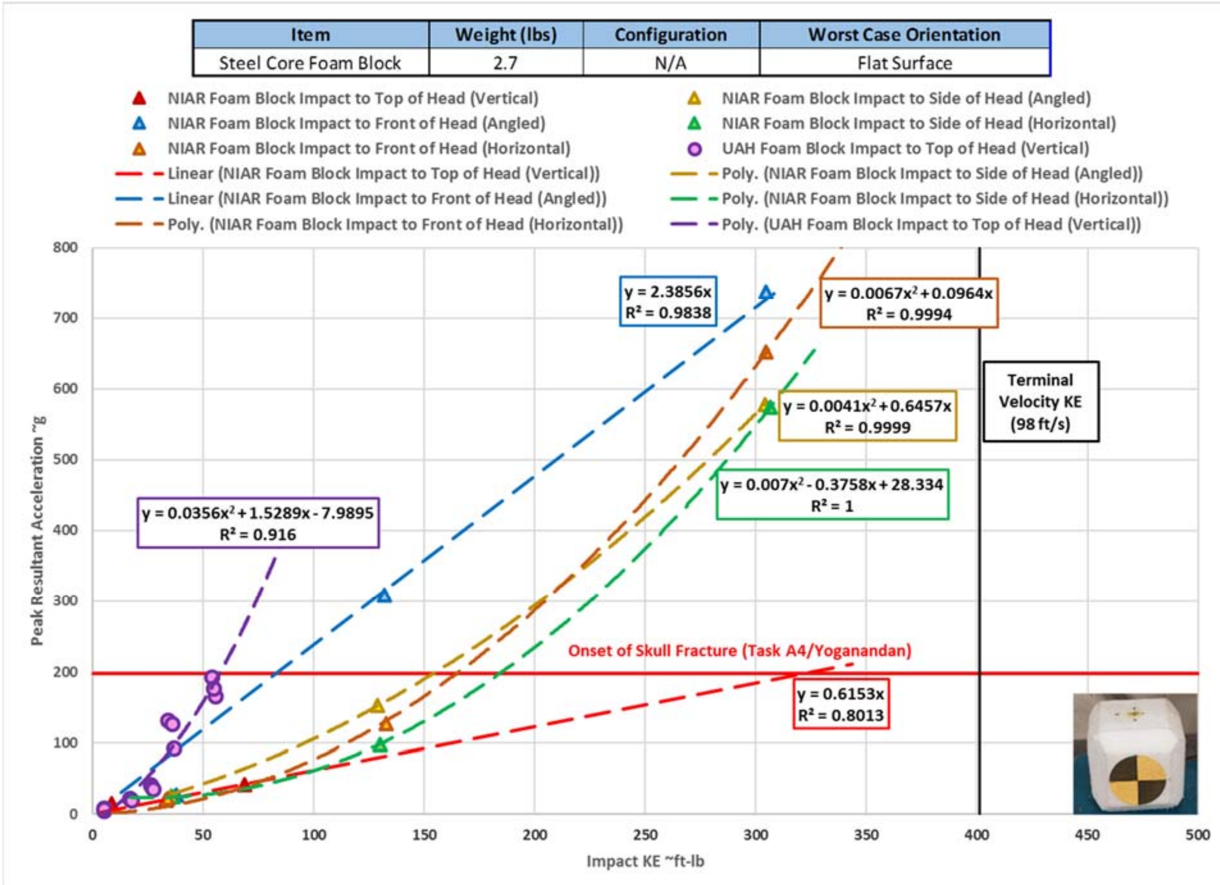

Figure 99. Comparison of Curve Fit Methods for Steel Core Foam Block Impacts

The current simplified apparatus has a limited, but unspecified, range of compliance where it is suitable for testing aircraft impacts. The simplified apparatus stiffness also made comparisons of neck forces, moments, and neck injury criteria with the NIAR test results challenging. The neck injury severity metrics from simplified testing conducted under this task are suspect and may not be useful for assessing neck injury risk.

The UAH data collected in Task A14 shows that the simplified test apparatus is capable to determining the stiffest orientation of a vehicle based on comparing the curve fit slopes of peak resultant head acceleration versus impact KE data for different impact orientations of a given vehicle. Comparison of aircraft impact test data from UAH and NIAR show that the NIAR data representing all impact trajectories for the DJI Phantom 3, Karma, and Vendor 1 Quadrotor aircraft impacts lie below the upper 95% confidence intervals of the UAH test data. In fact, the majority of the data falls below the UAH curve fit of the data from the worst case orientation. The remaining multirotor aircraft in this study did not have enough test data to conduct this analysis; however, all of the NIAR test points on these aircraft either lie below the UAH vertical impact test curve fit or below a line defined as a 1.5 factor of safety applied to the UAH curve fit. The wood and foam block data sets from UAH and NIAR were different enough that the NIAR curve fits fell outside of the UAH 95% confidence intervals.

3.4.7 Application of Wood Block PMHS Testing Results to Range Commander's Council Risk Curve

Wood block impact tests on PMHS subjects by OSU show correlation with Range Commander's Council injury risk curve probability of fatality estimates.[19] Figure 100 shows the OSU wood block impacts from the last series of PMHS test plotted on the RCC 321-00 Supplement's probability of fatality risk curve for head impacts. OSU's 30 ft/s impact appeared to cause a minor fracture during testing, and this impact is evaluated at roughly 7% probability of fatality on the RCC curve. The 40 ft/s impact resulted in a much larger set of fractures (AIS ≥ 3), and its impact conditions lead to an estimated 75% probability of fatality on the RCC risk curve. These test results appear to validate the use of the RCC risk curves for rigid objects; however, the testing results and evaluation of metrics like HIC_{15} and BrIC show significantly lower injury risk levels for multirotor aircraft impacts than the RCC curves would predict at similar impact KE levels. Given that the sUAS impacts fall into a region that is away from the injury risk curves, in terms of impact KE, this demonstrates how the RCC curves do not adequately describe the risk associated with small UAS impacts. Additionally, there is not a validated way to translate sUAS impacts and estimated energy transfer levels to the RCC risk injury curves. Another shortcoming in the RCC curves is that the estimated probability of fatality does not provide details regarding injury types like concussion, neck injury or skull fracture.

3.4.8 Use of Energy Absorption Techniques to Assess sUAS Injury Potential

Energy absorption methods were originally designed to test ballistic vests and determine how much energy passed to the human wearing these vests to assess injury following a ballistic impact to the vest. Extending these test methods to the assessment of skull fractures and neck injuries common to sUAS collisions has no clear relationship to human injury metrics. Energy absorption techniques have typically been applied solely to rigid impactors that have limited elasticity in comparison to sUAS. Contact with energy absorbing material suppresses much of the vehicles inherent flexibility of actual impacts as observed during both PMHS and ATD tests. Energy absorption approaches have also been assessed using analysis and modeling techniques with limited success due to the complexity of analyzing all of the energy absorption mechanisms analytically and validating the modeling approach via test. Without substantial comparison tests with PMHS data, energy absorption techniques should not be used as a basis for certifying sUAS for Category 2 or Category 3 operations due to the lack of scientifically validated correlation with human injury.

[19] Range Commander's Council, "Common Risk Criteria for National Test Ranges; Inert Debris," Supplement to Standard 321-00, April 2000.

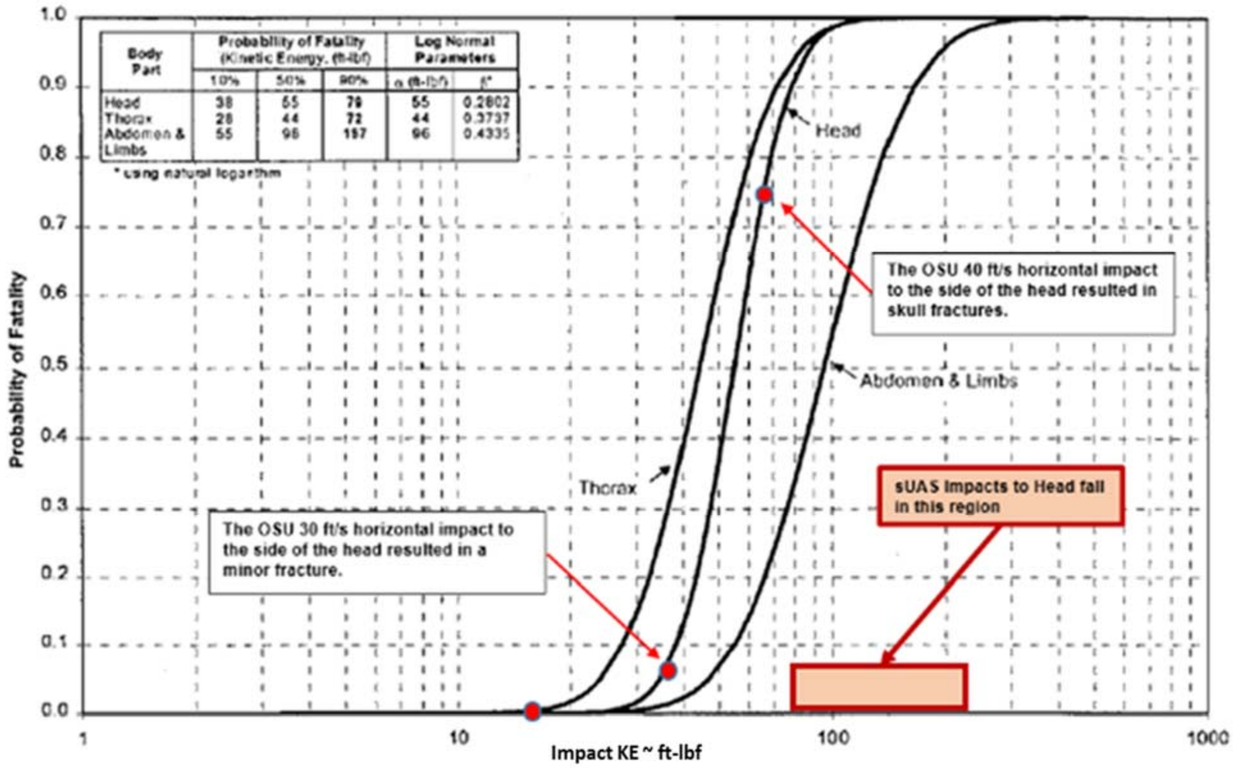

Figure 100. Wood Block Impacts Applied to RCC Injury Risk Curves

Conclusion: Energy absorption-based testing methods cannot provide data that clearly translates to existing injury severity standards while addressing multiple injury types like skull fracture and concussion.

Conclusion: The PMHS injuries and ATD testing verify that appropriateness of RCC standards for rigid objects, but automotive injury risk curves are more appropriate for compliant impactors and assessing a broad range of human injury due to sUAS collisions.

Recommendation: The FAA should support a comparison of energy based test methods and the data contained in this report to provide a clear understanding of how energy based test methods are capable of assessing injury potential for head and neck injuries typically associated with sUAS impacts following failures.

4 CONCLUSIONS AND RECOMMENDATIONS

4.1 Flight Testing of sUAS for Impact Studies

Failure flight testing is essential for evaluating a vehicle's post-failure dynamic behavior to determine if the aircraft tumbles or stabilizes in a predictable orientation while falling. Longer periods of data logging would further improve the fidelity of aerodynamic analysis and follow-on failure modeling and simulation. Flight testing must be conducted under as low of winds as possible in order to provide solid data for aerodynamic analysis. Winds and gusty conditions during flight test lead to inaccurate estimates of aircraft aerodynamic properties.

Recommendation: Failure flight testing is essential for evaluating a vehicle's post-failure dynamic behavior to determine if the aircraft tumbles or stabilizes in a predictable orientation while falling. Longer periods of data logging would further improve the fidelity of aerodynamic analysis and follow-on failure modeling and simulation. Flight testing must be conducted under as low of winds as possible in order to provide solid data for aerodynamic analysis. Winds and gusty conditions during flight test lead to inaccurate estimates of aircraft aerodynamic properties.

4.2 Impact Testing Using A Full ATD Hybrid III or a Simplified Apparatus

Impact testing using a full ATD Hybrid III or a simplified apparatus provides the capability of estimating injury potential/fatality risk based upon impact KE and resultant acceleration of the head for specific aircraft. Based on using a range of injury criterion, e.g. HIC_{15}, 3ms Minimum g-loading, Virginia Tech Combined Probability of Concussion, Brain Injury Criteria, and Peak Resultant Acceleration, impact testing provides regulators with a range of options for setting injury thresholds that address multiple injury types and mechanisms.

4.3 Energy Absorption Test Methods

Energy absorption-based testing methods cannot provide data that clearly translates to existing injury severity standards while addressing multiple injury types like skull fracture and concussion.

Recommendation: The FAA should support a comparison of energy based test methods and the data contained in this report to provide a clear understanding of how energy based test methods are capable of assessing injury potential for head and neck injuries typically associated with sUAS impacts following failures.

4.4 RCC versus Automotive Injury Standards

The PMHS injuries and ATD testing verify that appropriateness of RCC standards for rigid objects, but automotive injury risk curves are more appropriate for compliant impactors and assessing a broad range of human injury due to sUAS collisions.

4.5 Head Injures versus Neck Injuries

Overall, it appears that head injuries are the most probable injury type in sUAS impacts, versus neck injuries, based on the tests conducted under Task A14 to date. Aircraft and impactor object construction and materials are key factors relating to probability of and type of injury potential.

4.6 Injury Potential of Vertical Impacts

Vertical impacts appear to have the highest probability of head injury for the impact trajectories tested.

4.7 Weight Limitations for Use of Hybrid III ATD

UAS impact testing using Hybrid III ATDs can provide regulators a method for evaluating injury potential and risk based assessments using the modified injury metrics established in this report for multirotor and fixed-wing platforms up to 8-10 lbf and larger platforms up to 55 lbf at parachute impact speeds. The use of this data also supports a risk based approach to determine when and if additional operational mitigations are required for specific CONOPS.

4.8 Use of Simplified Test Method for sUAS

Simplified test methods are capable of assessing multi-rotor worst case impact orientations and have strong potential for estimating injury probability and severity for sUAS other than foam manufactured aircraft.

Recommendation: The FAA should support continued testing to develop statistically significant datasets that characterize the consistency and repeatability of the test results and help evaluate the hypothesis that the upper 95% confidence interval of the UAH test data is a true worst case transfer function for all simplified and ATD test data pertaining to a specific aircraft.

4.9 Number of Tests Required to Evaluate Worse Case Impact Orientations

For an aircraft with four different impact orientations, a minimum of 12 impact tests are needed to evaluate the worst case impact orientation. If the four impact orientations are noted as orientations A-D, then characterization requires impacts at two velocities or energy levels in each orientation A-D. After the first eight tests are done, the slope for each orientation can be estimated by curve fitting the data for each orientation. After the steepest slope is determined, then a minimum of two more tests at each speed should be conducted in the stiffest orientation to verify the slope determined in the initial round of testing. Additional testing can be done in order to more accurately quantify experimental error.

4.10 Statistical Significance of Task A14 Test Results

Due to the large scope of vehicles, test orientations and impact locations selected for this testing, few statistically significant conclusions can be drawn concerning use of the simplified test apparatus in lieu of the full ATD for impact testing and injury potential estimation based on FMVSS 208 and NCAP.

Recommendation: The FAA should focus future research on statistically significant simplified and ATD impact test data sets that enable assessment of test method consistency and repeatability as well as the development of injury risk curves specific to sUAS impacts.

Recommendation: The FAA should support research to develop a simplified impact target other than a FAA Hybrid III head and neck to reduce the number of test variables for simplified testing.

Recommendation: The FAA should support the conduct of a comparative test between the simplified or ATD testing approach and tests based on energy transfer estimation to determine the appropriate injury risk curves or injury metrics associated with energy transfer based methods.

4.11 Limitations

Simplified and ATD testing can be used to determine injury impact energies for sUAS in the 8-10 lbf range such that appropriate parachute speeds can be assessed and the appropriate parachute mitigation applied to support flight over people.

4.12 Injury Potential of Fixed Wing Puller Propeller Aircraft

FW aircraft impact test results show that puller prop aircraft have upwards of three times the injury potential to that of a pusher prop aircraft due to the pointed spinner and the concentrated mass of the prop, spinner, and motor located at the initial contact point. Without substantial mitigations to reduce the sharpness and impact severity during ground collision, puller prop platforms are not suitable for flight over people due to their increased injury potential and high increased impact velocities following failures with use of a parachute system or other decelerating mitigation system.

4.13 Injury Potential of Externally Mounted Equipment and Batteries

Externally mounted equipment and batteries that become dislodged can present a more substantial injury risk than that of the sUAS itself at equivalent impact KE. Components like batteries and cameras are typical denser and have less flat plate drag area than a multirotor aircraft, which makes them rigid and likely to impact at higher velocities than the aircraft themselves.

Recommendation: The FAA should develop performance-based standards for component mounting latches and other mechanisms for securing components to aircraft, e.g. minimum g-loading limits for latches to retain components if an operator is seeking approval for operations over people.

4.14 Vendor 1 and eBee+ Have Low Probability of Injury Throughout Full Envelope

The Vendor 1 Quadrotor and eBee+ fixed-wing aircraft testing showed that these aircraft have very low risk of causing skull fracture, head injuries, or neck injuries throughout their entire flight envelope and are good examples of platforms appropriate blanket flight over people over approvals.

4.15 Injury Potential of Rigid versus Compliant Impactors/Aircraft

Test results show that more rigid aircraft or impactors have a higher likelihood of causing head injuries like skull fracture because of high, short-duration linear accelerations and impulse loading on the skull. However, more compliant objects can still cause concussions and neck injuries because they have longer contact times with the head and can generate greater head rotational rates and acceleration.

4.16 Limitations of Wood Block Testing with Stock Accelerometers on FAA Hybrid III ATD Head

Due to the stiffness of the simplified test device, wood block impacts at over 25 ft/s generated high impulse loading on the Meggit C-Series stock head cg accelerometers and high frequency response of the head.

Recommendation: Future sUAS impact test standards should require the use of gas-damped Meggitt 7264H-2K-2-240 accelerometer versus the standard Meggitt 7264C-2K-2-240 11 accelerometer installed in ATD Hybrid III heads.

4.17 Extensibility of the UAS Dynamic Model

A UAS dynamic model, validated with flight test data, enables simulation of a larger number of failure scenarios (failure type and environmental conditions) than can be feasibly evaluated through flight test alone. The ability to run mass simulation of a range of vehicle failure types, states at failure, and environmental conditions is extensible to sensitivity studies and Monte Carlo Simulation.

4.18 Limitations of the UAS Dynamic Model

The modeling conducted by UAH was successfully validated for aircraft linear velocity and impact KE estimates, but was not accurate at predicting aircraft rotational dynamics. It appeared that the prediction of impact KE and comparison with flight test data was relatively insensitive to this model shortcoming.

APPENDIX A – AIRCRAFT FLIGHT AND IMPACT TEST CONFIGURATION MATRIX

Table A1. – Multirotor Test Aircraft Configurations

Multirotor Test Aircraft Configurations								
Model	**DJI Phantom 3**		**Go Pro Karma**		**Vendor 1**		**DJI Inspire 1**	
Test	Flight	Impact	Flight	Impact	Flight	Impact	Flight	
Image Payload	Stock	Stock	Stock	Stock	N/A	N/A	N/A	
Gimbal	Stock	Stock	Stock	Stock	N/A	N/A	N/A	
Datalogger Payload	Pixhawk Mini	N/A	Pixhawk Mini	N/A	Pixhawk Mini	N/A	Pixhawk Mini	
Flight Controller	Stock/Pixhawk Mini	Stock	Pixhawk Mini	Stock	Pixhawk Mini	Stock	Stock	
Parachute	Yes	N/A	Yes	N/A	Yes	N/A	2x SafeTech ST60-X	
Failure Board	Teensy 3.6	N/A	Teensy 3.6	N/A	Teensy 3.6	N/A	Indemnis	
Recovery Parachute Servo	Yes	N/A	Yes	N/A	Yes	N/A	Yes	
Battery	Stock	Stock	Stock	Stock	2S 600 mAh Li-Po	Stock	Stock	
Weight	3.13 lbs	2.44-2.67	5.07 lbs	4.07 - 4.17 lbs	0.95 lbs	0.708-0.77 lbs	7.66 lbs	
Mode	**Vendor 3**		**DJI Inspire 2**		**DJI S800**		**DJI Mavic Pro**	
Test	Flight	Impact	Flight	Impact	Flight	Impact	Flight	Impact
Image Payload	Proprietary Camera	Proprietary Camera	N/A	N/A	Panasonic GH3	Panasonic GH3	Stock	Stock
Gimbal	N/A	N/A	N/A	N/A	Zenmuse Z15-GH4	Zenmuse Z15-GH4	Stock	Stock
Datalogger Payload	Pixhawk Mini	N/A	Pixhawk Mini	N/A	Pixhawk Mini	N/A	Pixhawk Mini	N/A
Flight Controller	Pixhawk 2	Pixhawk 2	Stock	Stock	Stock Controller	Stock Controller	Stock Controller	Stock Controller
Parachute	Yes	N/A	2x SafeTech ST60-X	N/A	Indemnis	N/A	Yes	N/A
Failure Board	Yes	N/A	Indemnis	N/A	Teensy 3.6	N/A	Teensy 3.6	N/A
Recovery Parachute Servo	Parachute Launch Tube	N/A	Yes	N/A	Yes	N/A	Yes	N/A
Battery	N/A	N/A	Stock	Stock	6S Li-Po	6S Li-Po	Stock	Stock
Weight	5.2 lbs	4.2 lbs	9.82 lbs	9.11-9.59 lbs	14.56 lbs	13.2 lbs	2.47 lbs	1.58 - 1.67 lbs

Table A2. Fixed Wing Test Aircraft Configurations

Fixed Wing Test Aircraft Configurations						
Mode	**Radian**	**Nano Talon**	**Skyhunter**	**Sensefly eBee+**		**Sensefly eBee Standard**
Test	Impact	Impact	Impact	Flight	Impact	Impact
Image Payload	N/A	N/A	N/A	145g Sony Camera	145g Sony Camera	145g Sony Camera
Gimbal	N/A	N/A	N/A	N/A	N/A	N/A
Datalogger Payload	N/A	N/A	N/A	Pixhawk Mini	N/A	N/A
Flight Controller	N/A	N/A	N/A	Pixhawk Mini	120g Autopilot Ballast	N/A
Parachute	N/A	N/A	N/A	N/A	N/A	N/A
Failure Board	N/A	N/A	N/A	Teensy 3.6	N/A	N/A
Recovery Parachute Servo	N/A	N/A	N/A	N/A	N/A	N/A
Battery	N/A	N/A	N/A	3S 5000 mAh Li-Po	3S 5000 mAh Li-Po	N/A
Weight	2.5 lbs	1.5 lbs	6.91 lbs	2.87 lbs	2.43- 2.58 lbs	1.64 lbs

Table A3. Test Aircraft Component and Object Information

Aircraft Component Test Information				
Mode	**SLR Camera**	**Wood Block**	**Aluminum and Steel Core Foam Block**	**DJI Phantom 3 Battery**
Test	Impact	Impact	Impact	Impact
Image Payload	Panasonic GH3	N/A	N/A	N/A
Gimbal	N/A	N/A	N/A	N/A
Datalogger Payload	N/A	N/A	N/A	N/A
Flight Controller	N/A	N/A	N/A	N/A
Parachute	N/A	N/A	N/A	N/A
Failure Board	N/A	N/A	N/A	N/A
Recovery Parachute Servo	N/A	N/A	N/A	N/A
Battery	N/A	N/A	N/A	N/A
Weight	1.23 lbs	2.7 lbs	2.7 lbs	0.805 lbs

APPENDIX B – FLIGHT TEST AND MODELING PLOTS

Configuration	**Weight**	**Failure Altitude**	**Initial Conditions**	**Flight Test Winds***
Flight Test	3.13 lbf	400 ft AGL	Hover	1 kt SSW

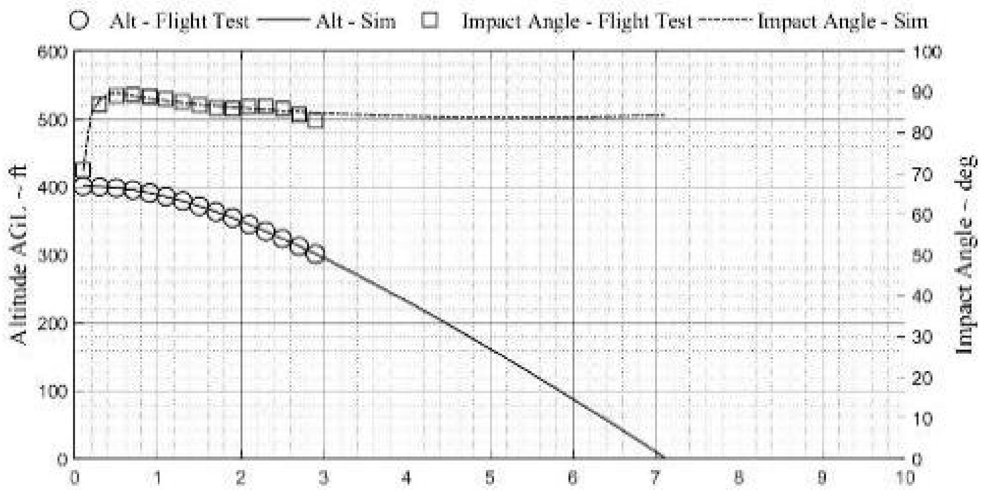

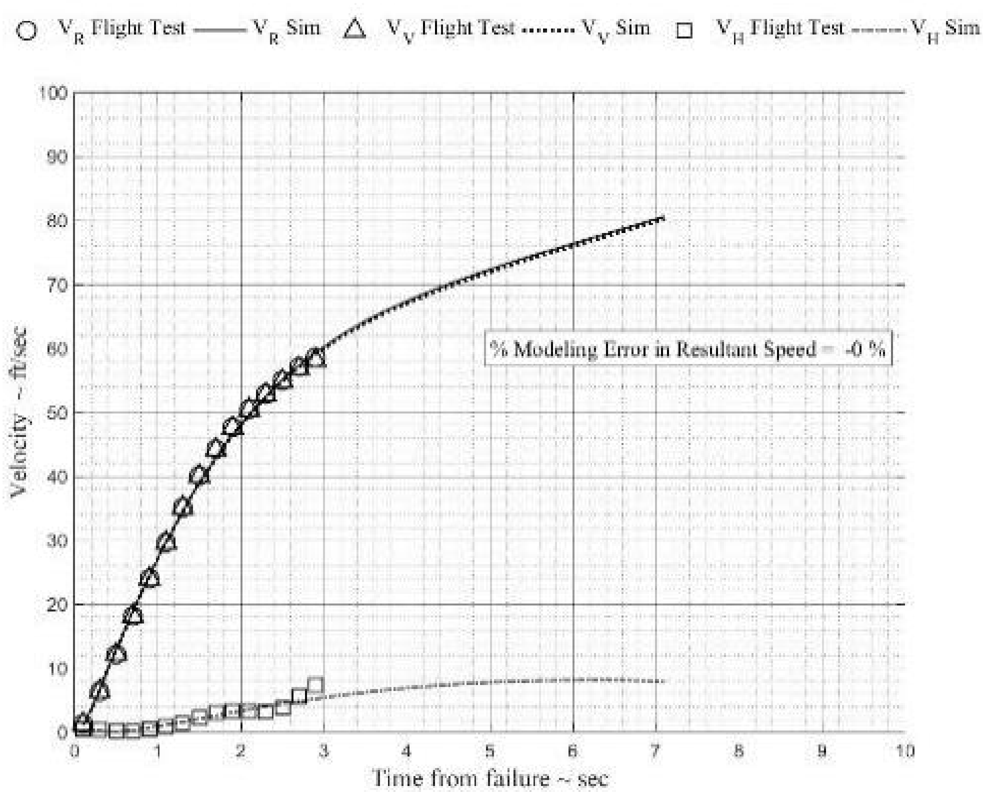

Figure B 1 .DJI Phantom 3 – Four Motor Failure at Hover

*Winds measured 20 feet AGL at a weather station less than three miles from flight test location

V_R = Resultant Speed | V_V = Vertical Speed | GS = Ground Speed
V_H = Horizontal GS | Alt = Altitude | Sim = Simulation
AGL = Above Ground Level

Configuration	Weight	Failure Altitude	Initial Conditions	Flight Test Winds*
Flight Test	3.13 lbf	400 ft AGL	42 ft/sec GS, level flight	4 kt ESE

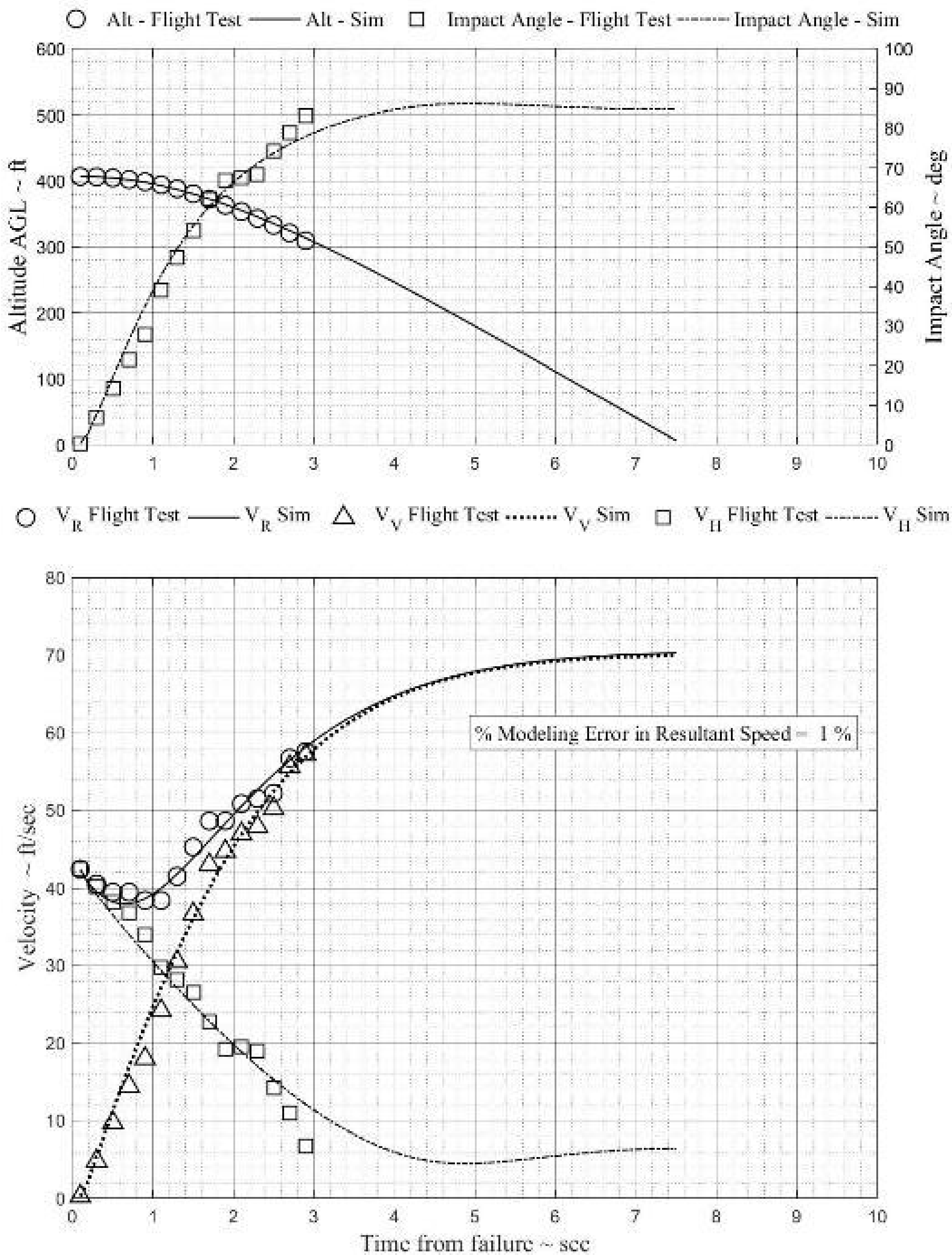

Figure B 2. DJI Phantom 3 – Four Motor Failure at Maximum Stabilized Forward Speed

*Winds measured 20 feet AGL at a weather station less than three miles from flight test location

V_R = Resultant Speed　　V_V = Vertical Speed　　GS = Ground Speed
V_H = Horizontal GS　　Alt = Altitude　　Sim = Simulation
AGL = Above Ground Level

Configuration	Weight	Failure Altitude	Initial Conditions	Flight Test Winds*
Flight Test	3.13 lbf	400 ft AGL	Hover	calm

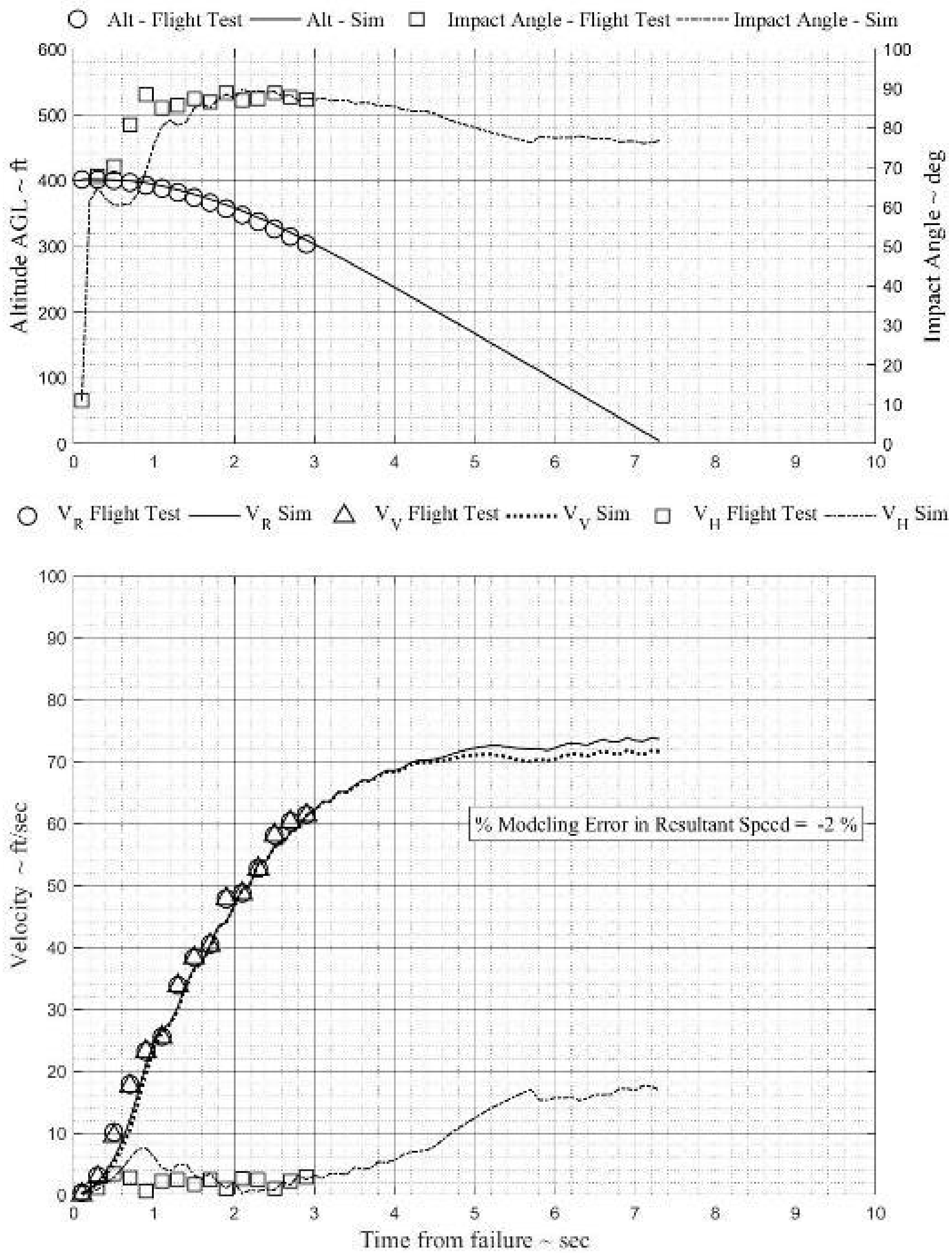

Figure B 3. DJI Phantom 3 – One Motor Failure at Hover

*Winds measured 20 feet AGL at a weather station less than three miles from flight test location

V_R = Resultant Speed V_V = Vertical Speed   GS = Ground Speed
V_H = Horizontal GS   Alt = Altitude   Sim = Simulation
AGL = Above Ground Level

Configuration	Weight	Failure Altitude	Initial Conditions	Flight Test Winds*
Flight Test	3.13 lbf	420 ft AGL	40 ft/sec GS, level flight	2 kt NNW

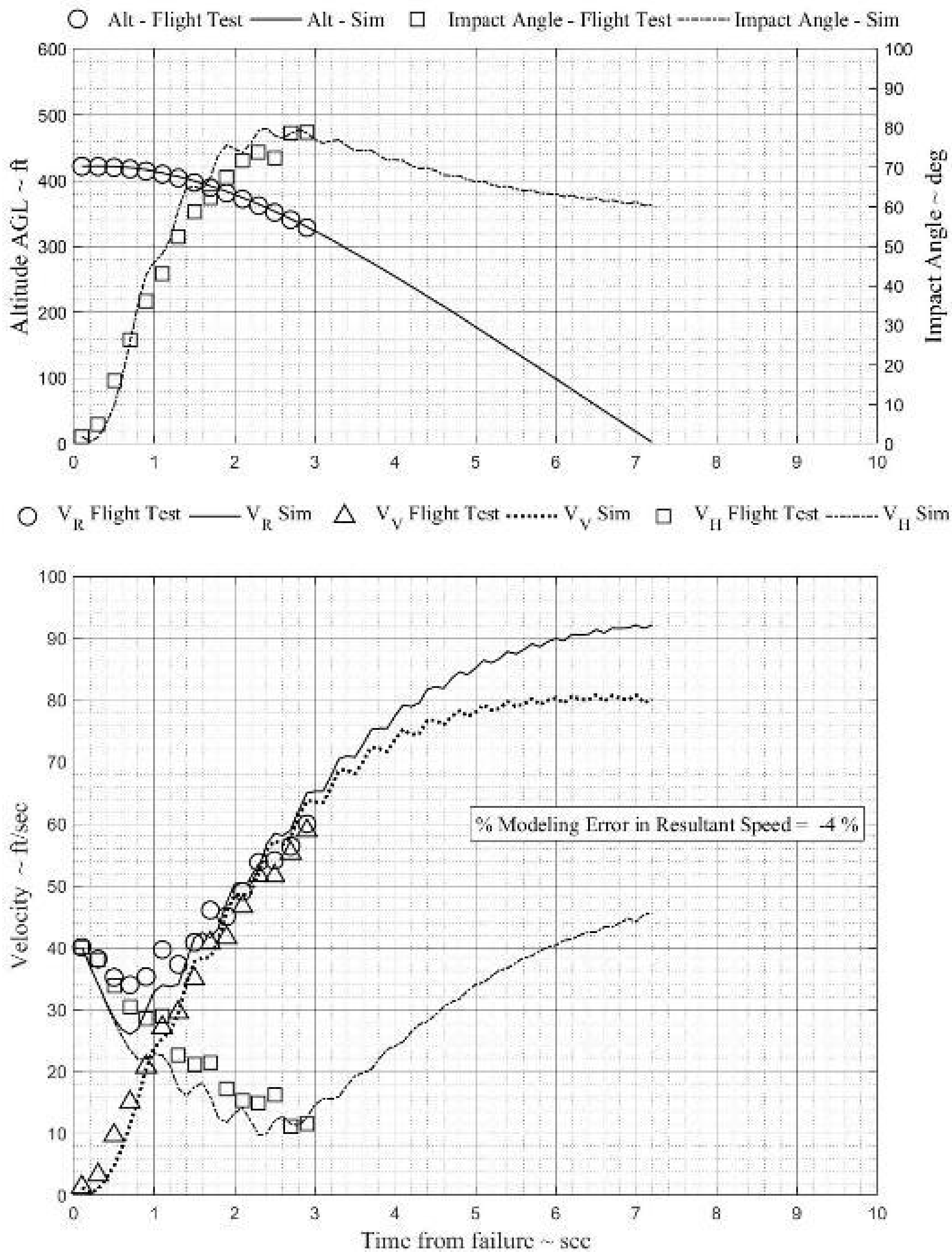

Figure B 4. DJI Phantom 3 – One Motor Failure at Maximum Stabilized Forward Speed

*Winds measured 20 feet AGL at a weather station less than three miles from flight test location

V_R = Resultant Speed V_V = Vertical Speed GS = Ground Speed
V_H = Horizontal GS Alt = Altitude Sim = Simulation
AGL = Above Ground Level

Configuration	Weight	Failure Altitude	Initial Conditions	Flight Test Winds*
Flight Test	3.13 lbf	400 ft AGL	Hover	2 kt ESE

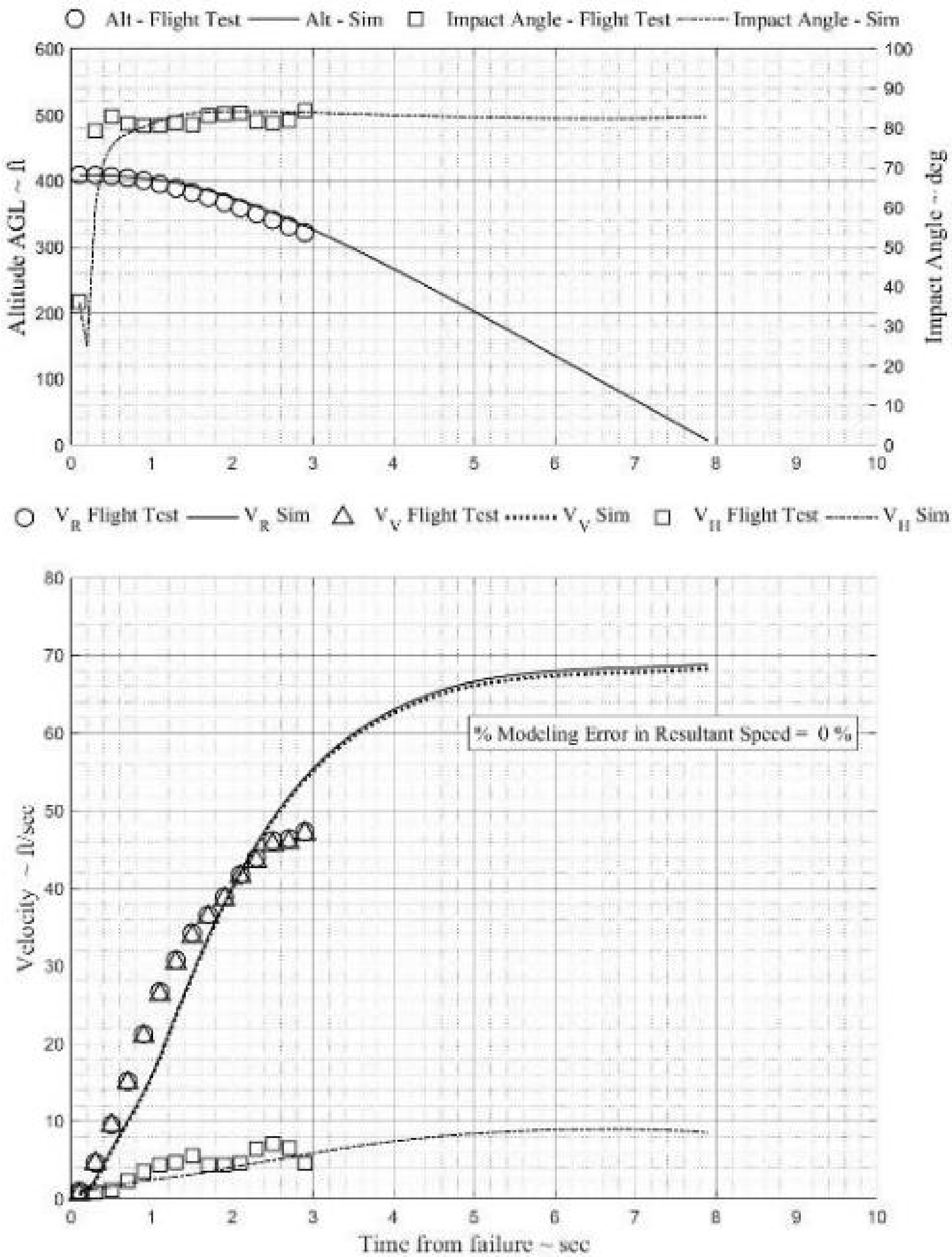

Figure B 5. DJI Phantom 3 – Two Motor (On-Axis) Failure at Hover

*Winds measured 20 feet AGL at a weather station less than three miles from flight test location

V_R = Resultant Speed | V_V = Vertical Speed | GS = Ground Speed
V_H = Horizontal GS | Alt = Altitude | Sim = Simulation
AGL = Above Ground Level

Configuration	Weight	Failure Altitude	Initial Conditions	Flight Test Winds*
Flight Test	3 lbf	480 ft AGL	40 ft/sec GS, level flight	2 kt NNE

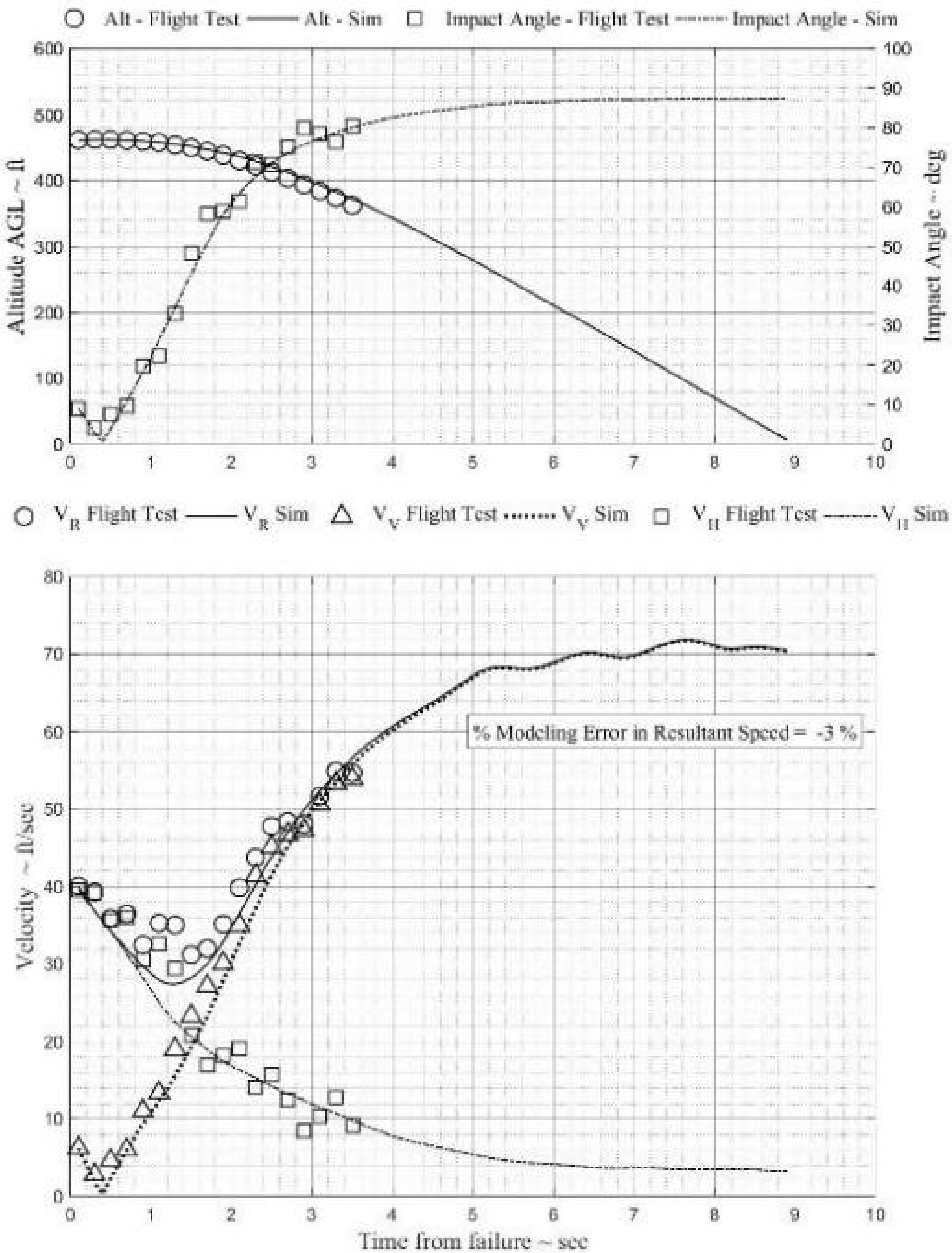

Figure B 6. DJI Phantom 3 – Two Motor (On-Axis) Failure at Maximum Stabilized Forward Speed

*Winds measured 20 feet AGL at a weather station less than three miles from flight test location

V_R = Resultant Speed V_V = Vertical Speed GS = Ground Speed

V_H = Horizontal GS Alt = Altitude Sim = Simulation

AGL = Above Ground Level

Configuration	Weight	Failure Altitude	Initial Conditions	Flight Test Winds*
Flight Test	3.13 lbf	400 ft AGL	Hover	2 kt N

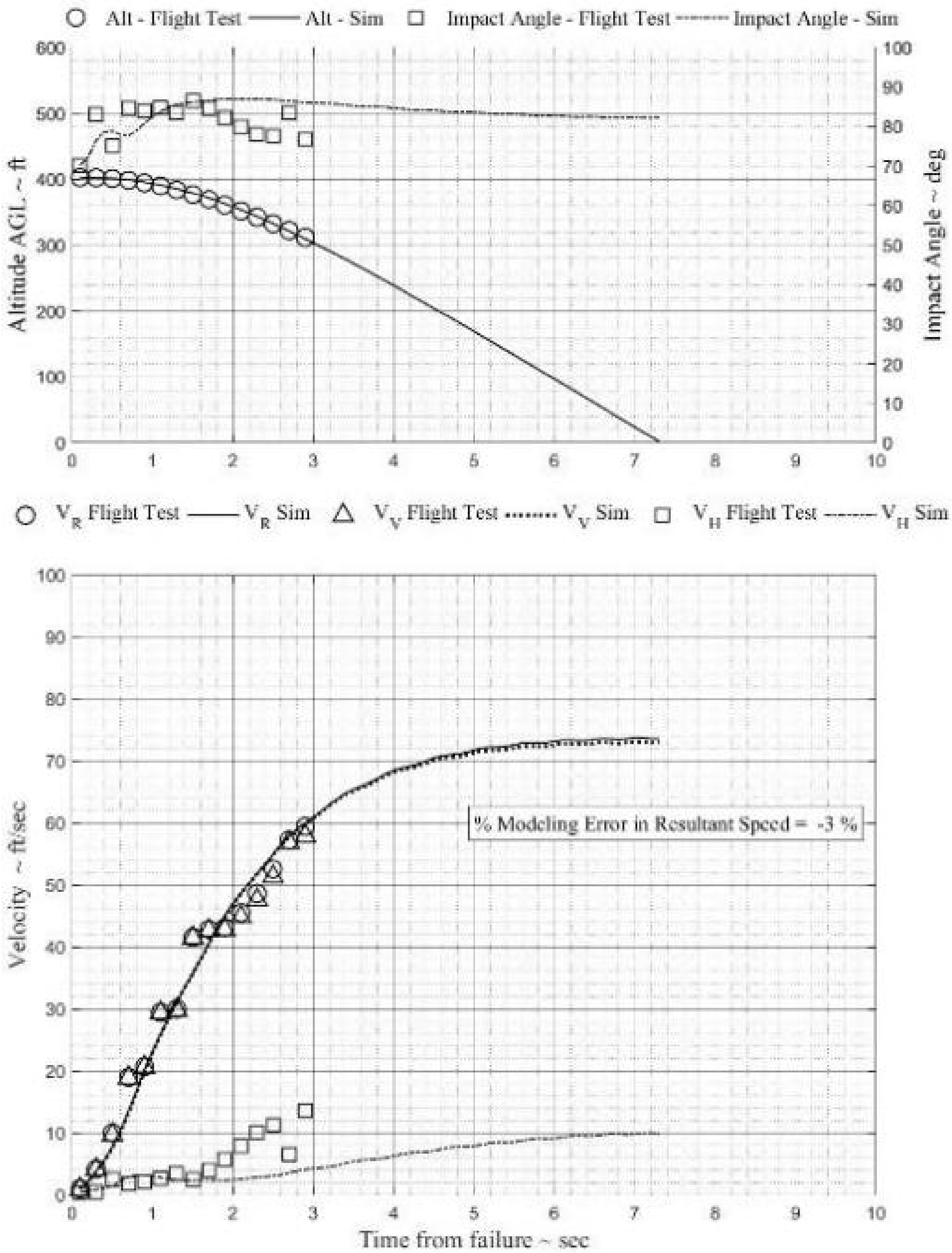

Figure B 7. DJI Phantom 3 – Two Motor (Off-Axis) Failure at Hover

*Winds measured 20 feet AGL at a weather station less than three miles from flight test location

V_R = Resultant Speed | V_V = Vertical Speed | GS = Ground Speed

V_H = Horizontal GS | Alt = Altitude | Sim = Simulation

AGL = Above Ground Level

Configuration	Weight	Failure Altitude	Initial Conditions	Flight Test Winds*
Flight Test	3 lbf	380 ft AGL	40 ft/sec GS, level flight	2 kt NNE

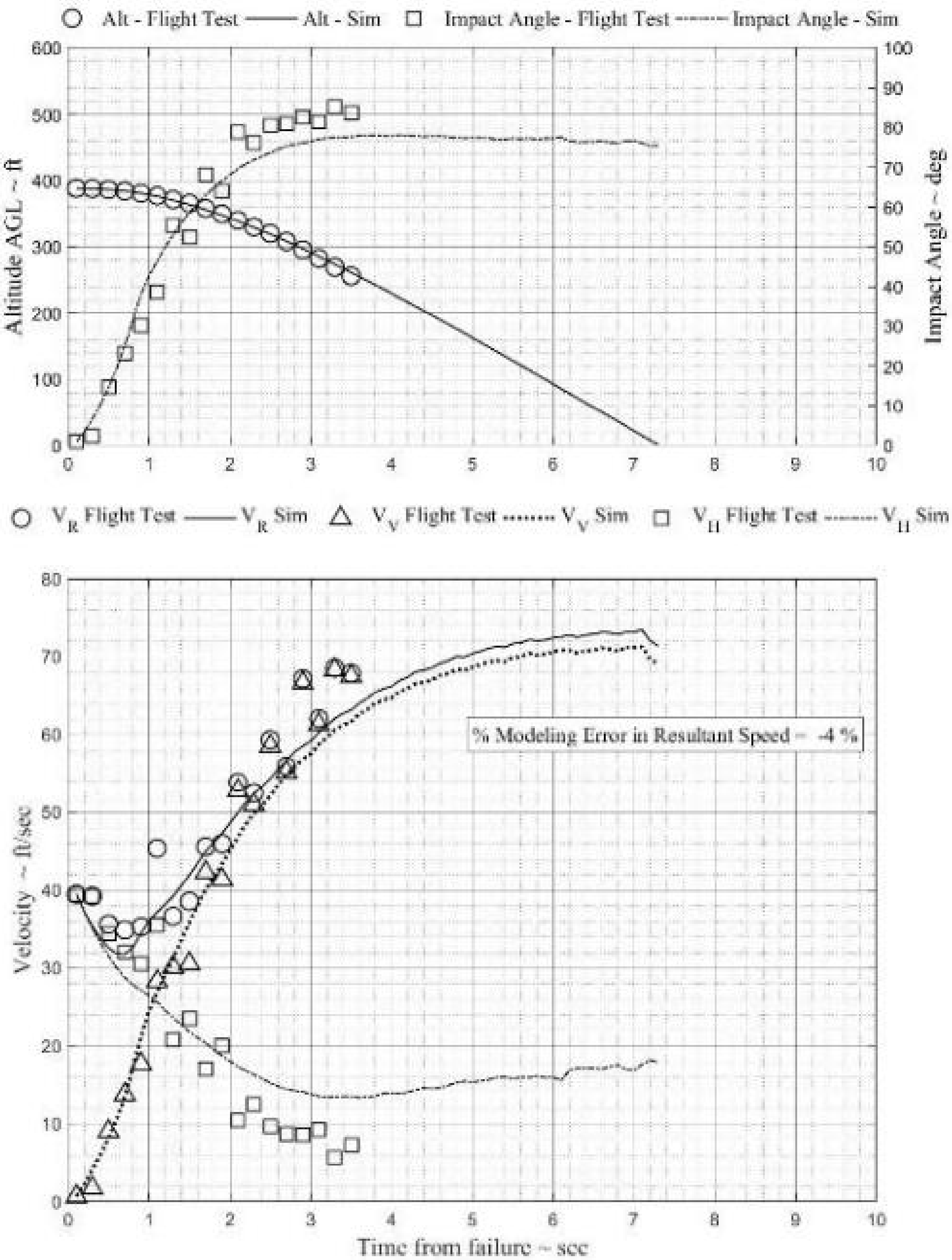

Figure B 8. DJI Phantom 3 – Two Motor (Off-Axis) Failure at Maximum Stabilized Forward Speed

*Winds measured 20 feet AGL at a weather station less than three miles from flight test location

V_R = Resultant Speed V_V = Vertical Speed GS = Ground Speed

V_H = Horizontal GS Alt = Altitude Sim = Simulation

AGL = Above Ground Level

Configuration	Weight	Failure Altitude	Initial Conditions	Flight Test Winds*
Flight Test	0.95 lbf	400 ft AGL	Hover	Calm

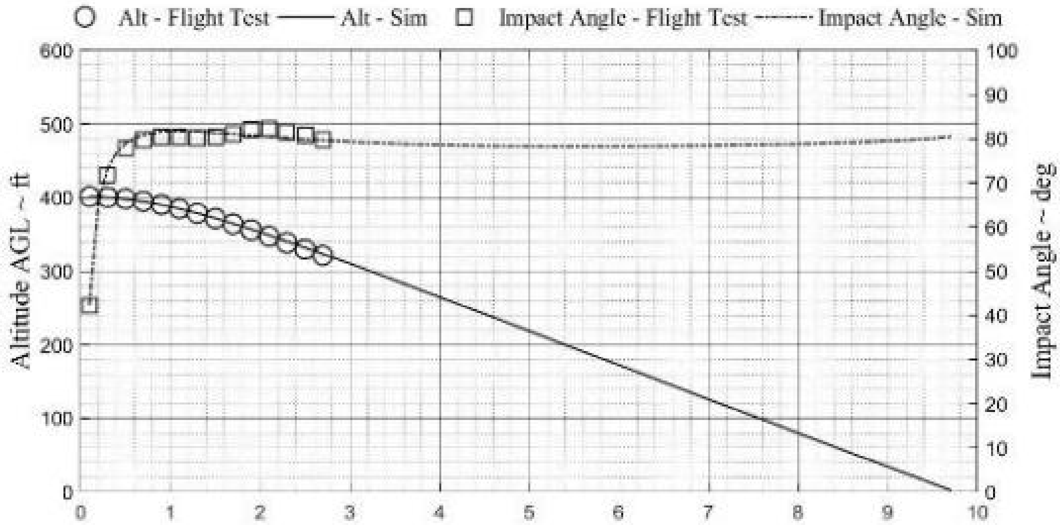

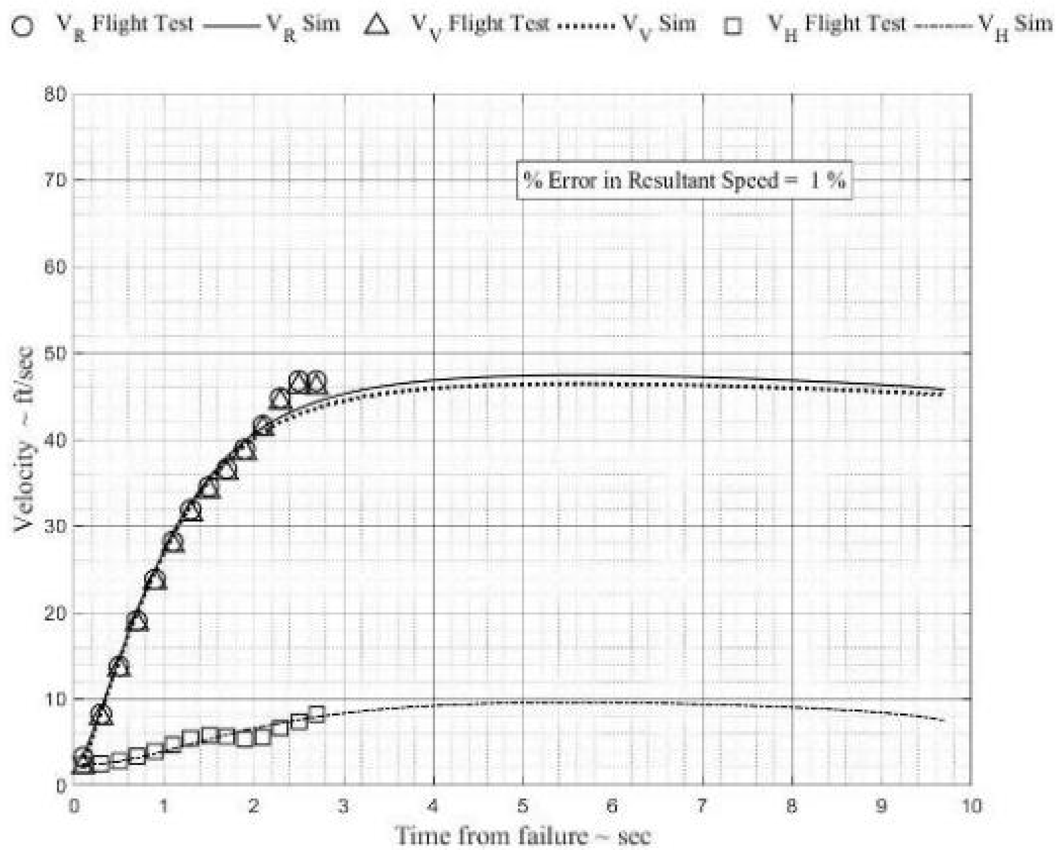

Figure B 9. Vendor 1 Quadrotor – Four Motor Failure at Hover*Winds measured 20 feet AGL at a weather station less than three miles from flight test location

V_R = Resultant Speed | V_V = Vertical Speed | GS = Ground Speed

V_H = Horizontal GS | Alt = Altitude | Sim = Simulation

AGL = Above Ground Level

Configuration	Weight	Failure Altitude	Initial Conditions	Flight Test Winds*
Flight Test	0.95 lbf	308 ft AGL	20 ft/sec GS, level flight	6 kt NE

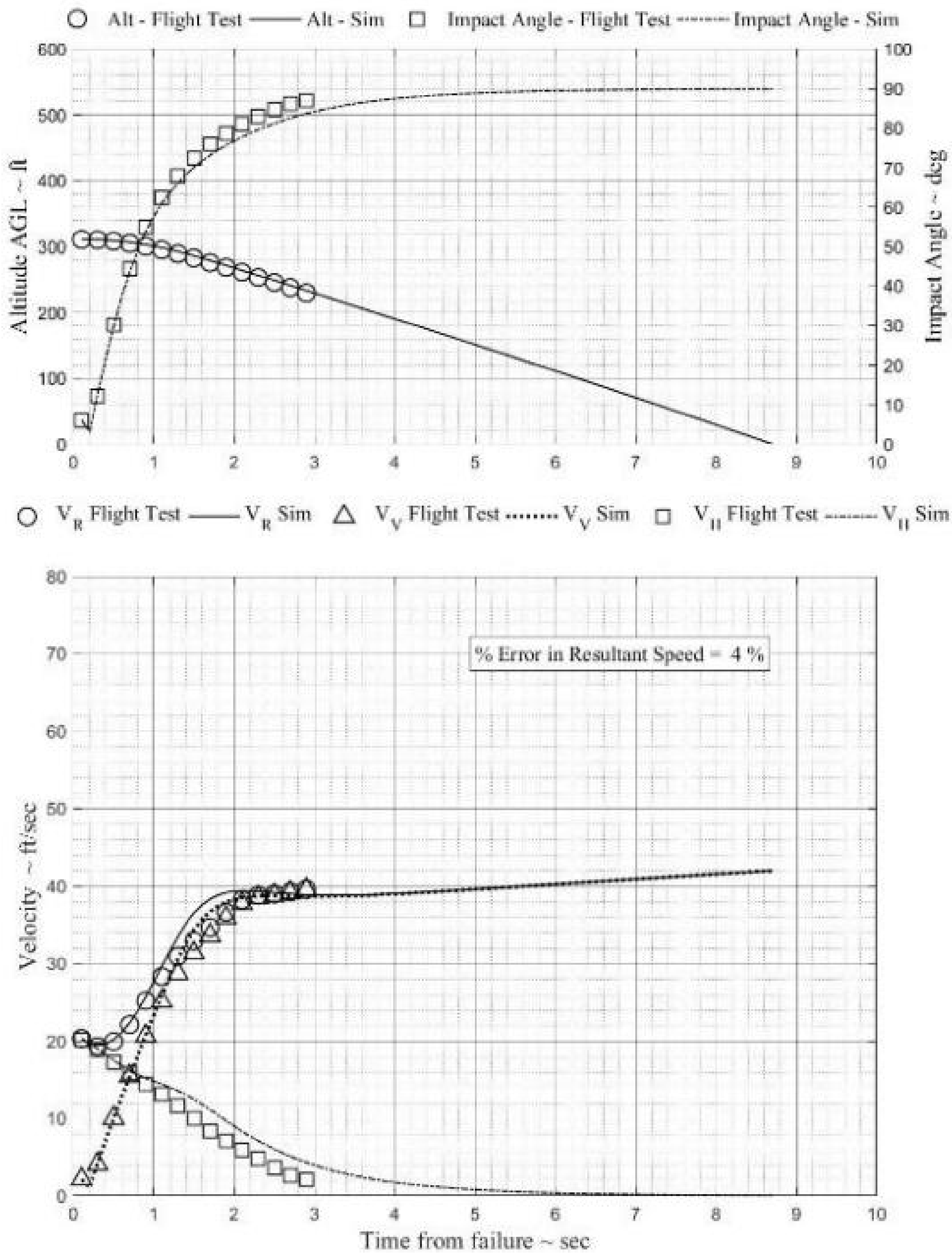

Figure B 10. Vendor 1 Quadrotor – Four Motor Failure at Maximum Stabilized Forward Speed

*Winds measured 20 feet AGL at a weather station less than three miles from flight test location

V_R = Resultant Speed
V_V = Vertical Speed
GS = Ground Speed
V_H = Horizontal GS
Alt = Altitude
Sim = Simulation
AGL = Above Ground Level

Configuration	Weight	Failure Altitude	Initial Conditions	Flight Test Winds*
Flight Test	0.95 lbf	341 ft AGL	Hover	Calm

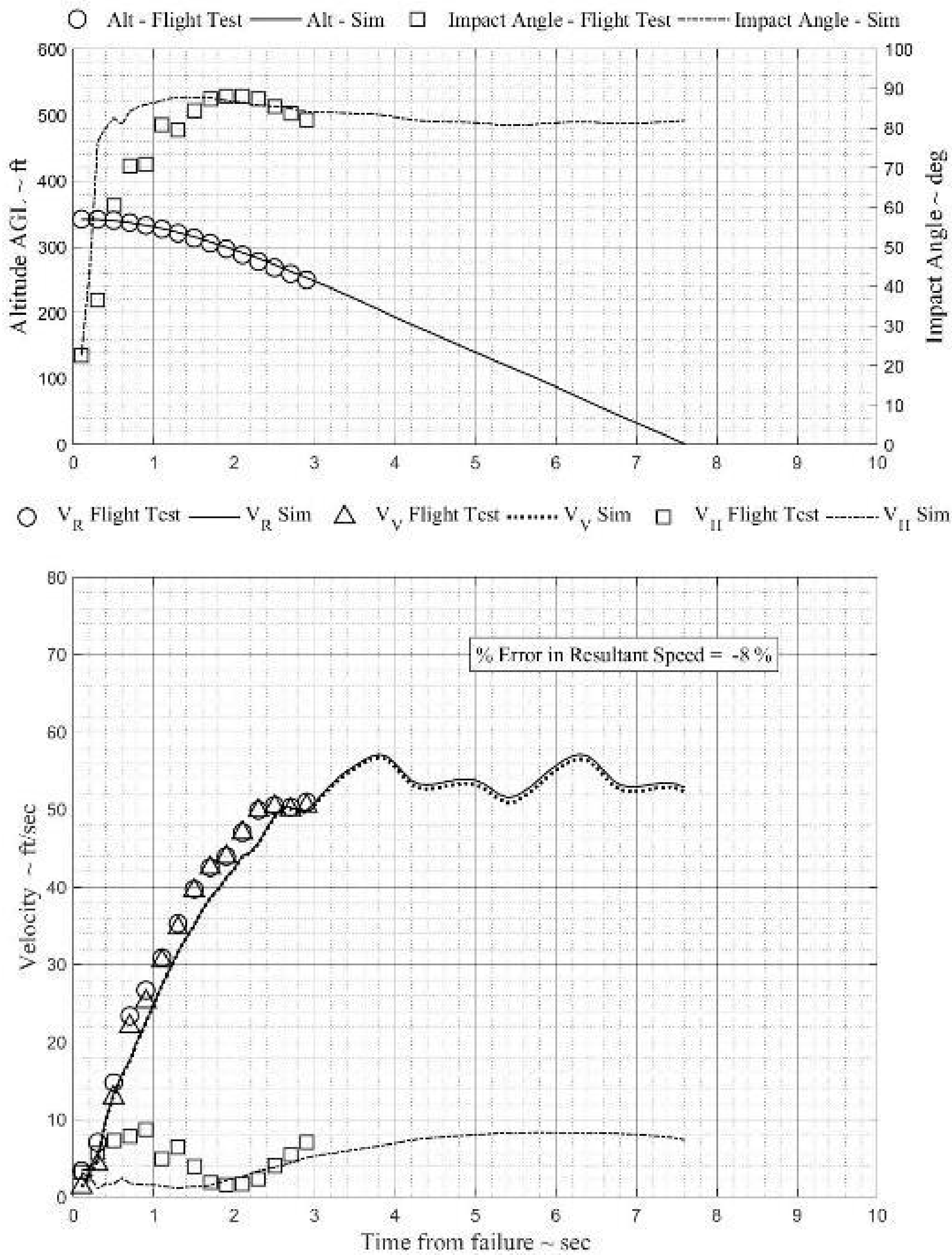

Figure B 11. Vendor 1 Quadrotor One Motor Failure at Hover

*Winds measured 20 feet AGL at a weather station less than three miles from flight test location

V_R = Resultant Speed | V_V = Vertical Speed | GS = Ground Speed

V_H = Horizontal GS | Alt = Altitude | Sim = Simulation

AGL = Above Ground Level

Configuration	Weight	Failure Altitude	Initial Conditions	Flight Test Winds*
Flight Test	0.95 lbf	344 ft AGL	46 ft/sec GS, level flight	5 kt SW

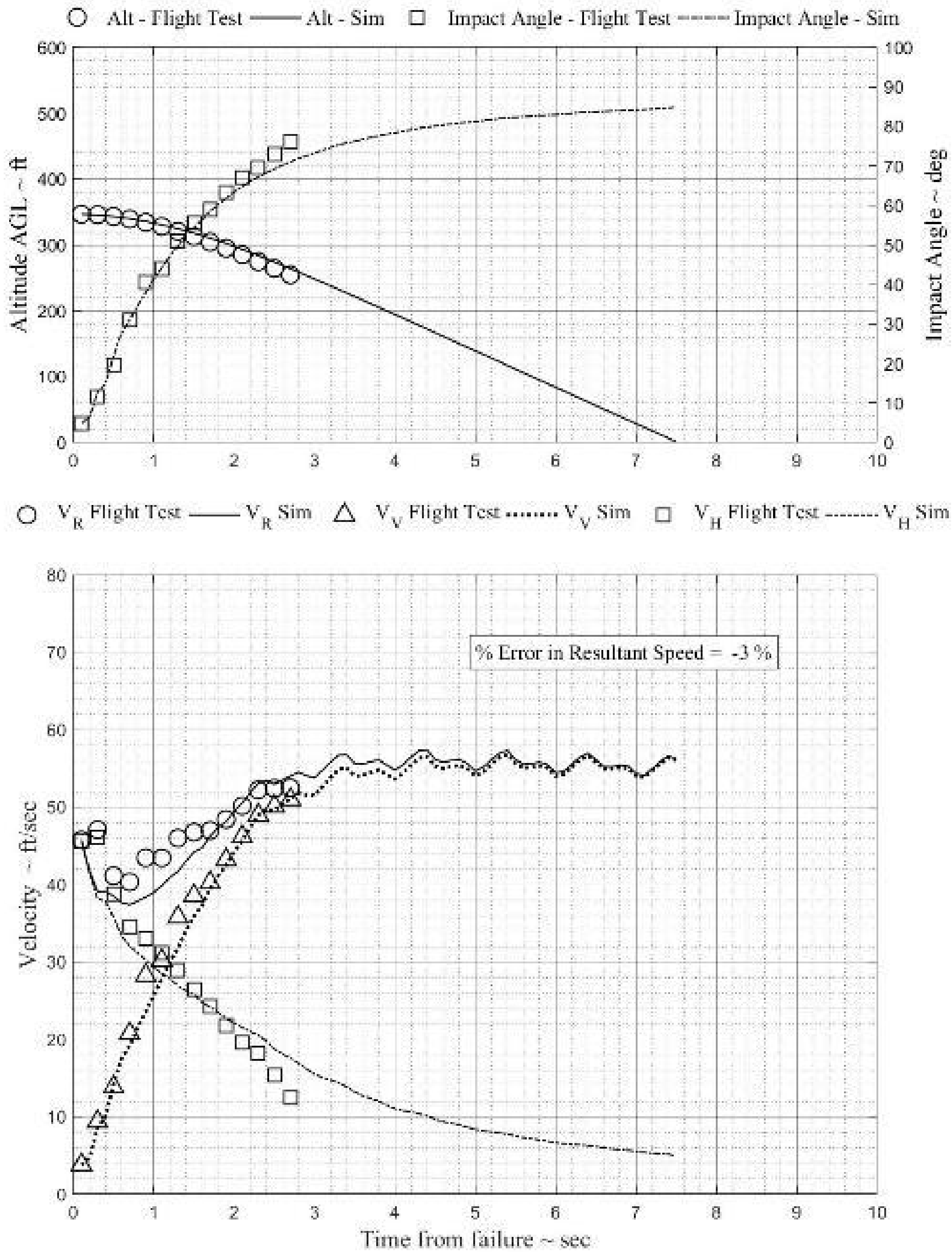

Figure B 12. Vendor 1 Quadrotor One Motor Failure at Maximum Stabilized Forward Speed

*Winds measured 20 feet AGL at a weather station less than three miles from flight test location

V_R = Resultant Speed V_V = Vertical Speed   GS = Ground Speed

V_H = Horizontal GS   Alt = Altitude   Sim = Simulation

AGL = Above Ground Level

Configuration	Weight	Failure Altitude	Initial Conditions	Flight Test Winds*
Flight Test	0.95 lbf	333 ft AGL	Hover	5 kt SW

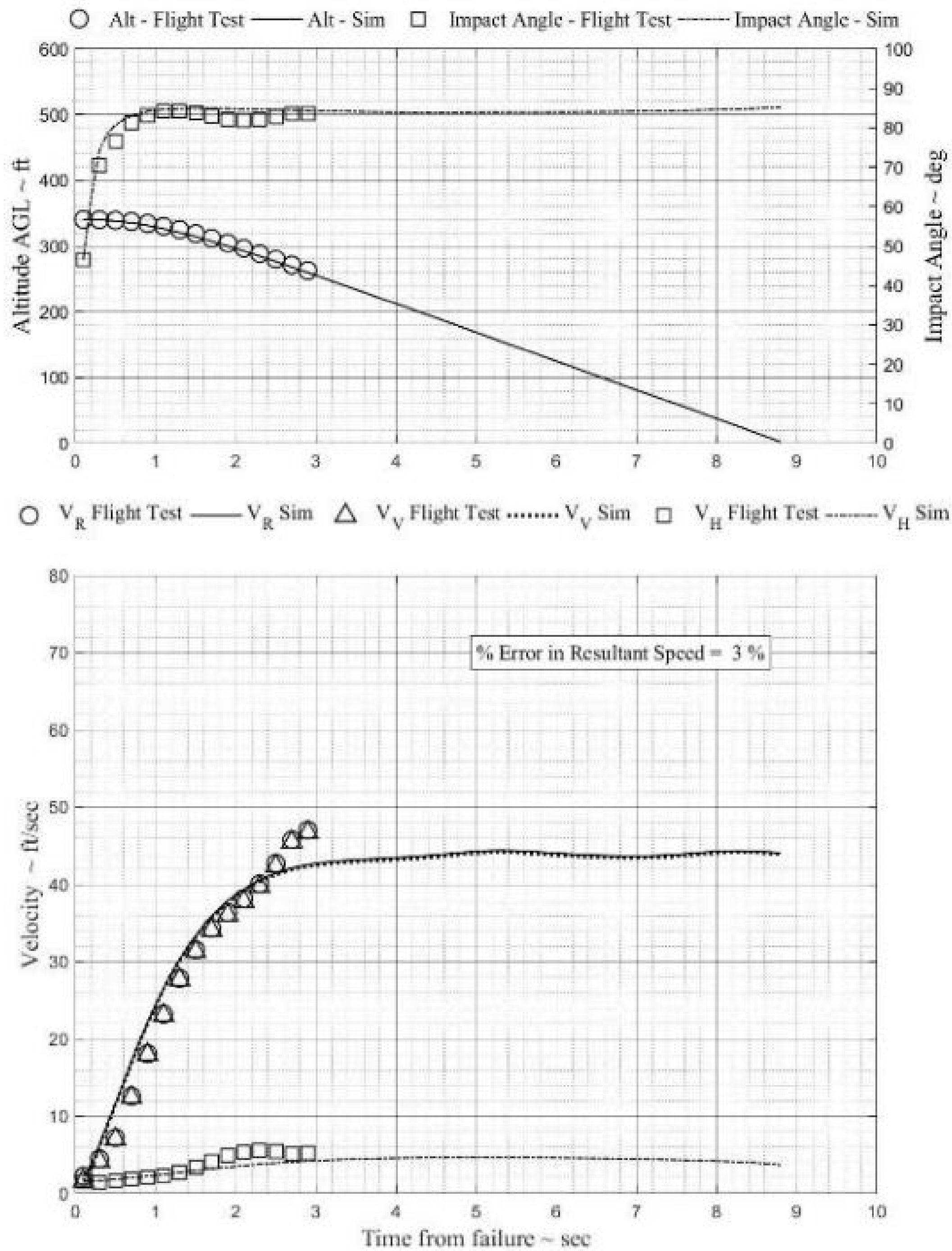

Figure B 13. Vendor 1 Quadrotor Two Motor (On-Axis) Failure at Hover

*Winds measured 20 feet AGL at a weather station less than three miles from flight test location

V_R = Resultant Speed V_V = Vertical Speed GS = Ground Speed

V_H = Horizontal GS Alt = Altitude Sim = Simulation

AGL = Above Ground Level

Configuration	Weight	Failure Altitude	Initial Conditions	Flight Test Winds*
Flight Test	0.95 lbf	379 ft AGL	29 ft/sec GS, level flight	7 kt NE

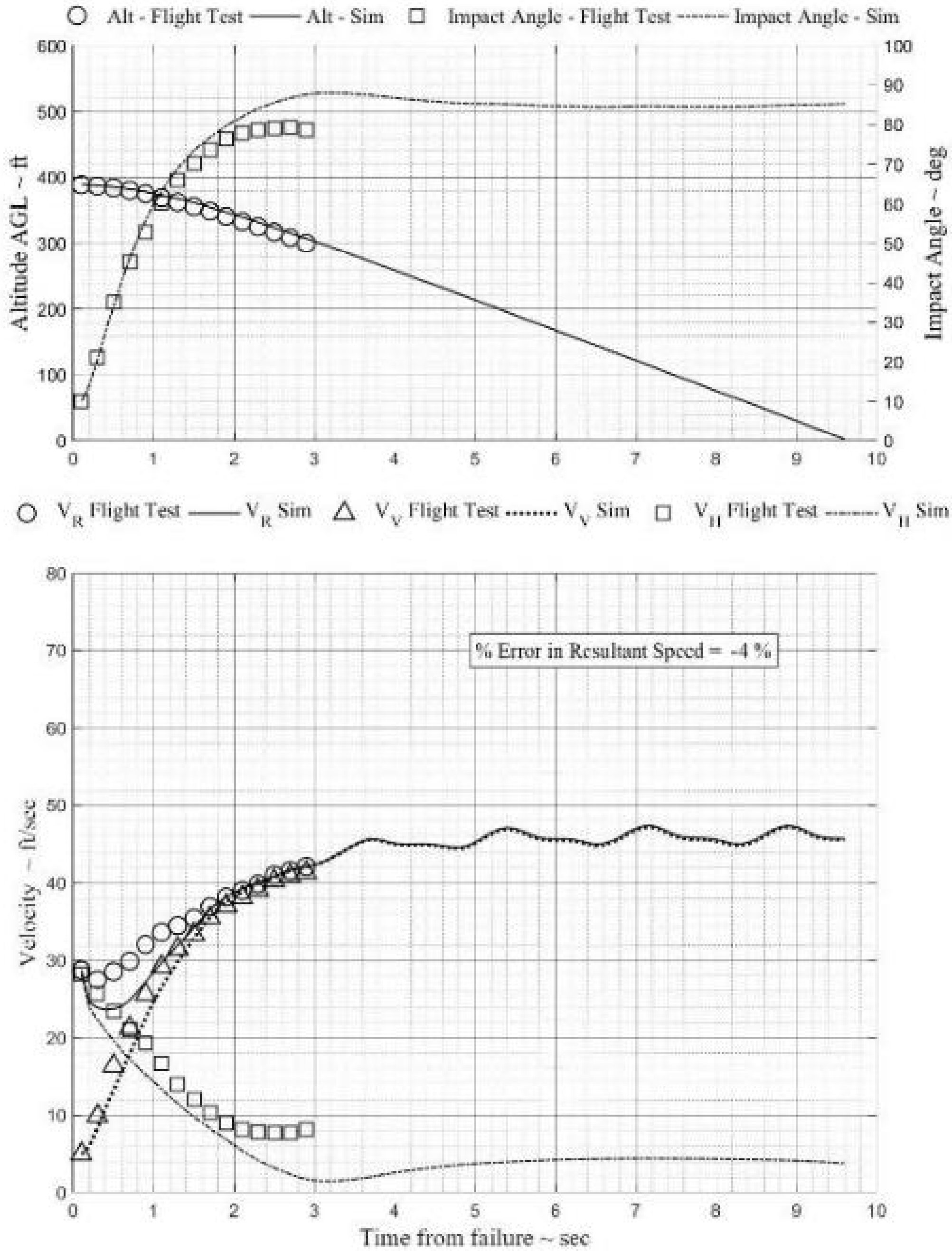

Figure B 14. Vendor 1 Quadrotor Two Motor (On-Axis) Failure at Maximum Stabilized Forward Speed

*Winds measured 20 feet AGL at a weather station less than three miles from flight test location

V_R = Resultant Speed | V_V = Vertical Speed | GS = Ground Speed
V_H = Horizontal GS | Alt = Altitude | Sim = Simulation
AGL = Above Ground Level

Configuration	Weight	Failure Altitude	Initial Conditions	Flight Test Winds*
Flight Test	0.95 lbf	333 ft AGL	Hover	5 kt SW

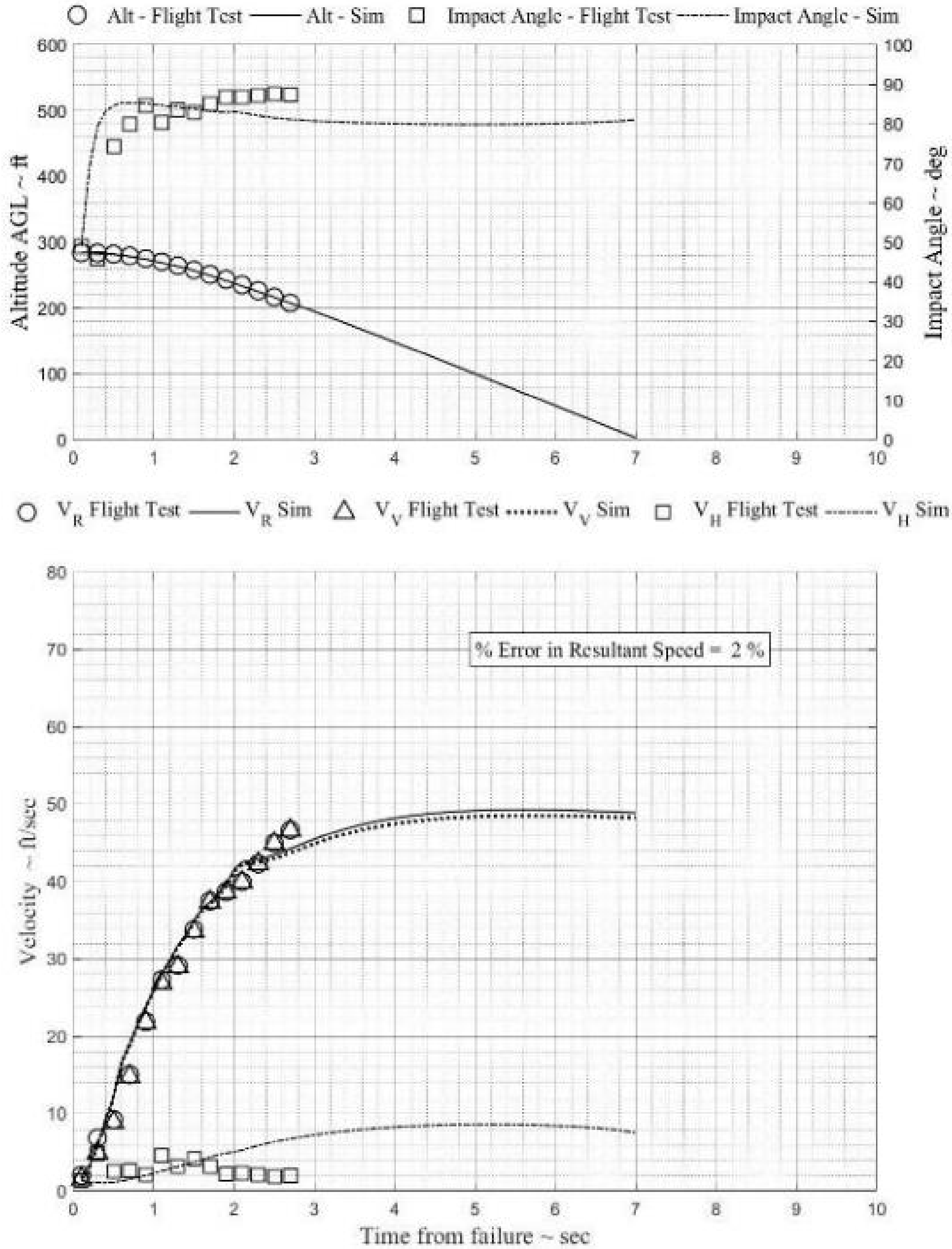

Figure B 15. Vendor 1 Quadrotor Two Motor (Off-Axis) Failure at Hover

*Winds measured 20 feet AGL at a weather station less than three miles from flight test location

V_R = Resultant Speed　V_V = Vertical Speed　GS = Ground Speed

V_H = Horizontal GS　Alt = Altitude　Sim = Simulation

AGL = Above Ground Level

Configuration	Weight	Failure Altitude	Initial Conditions	Flight Test Winds*
Flight Test	0.95 lbf	372 ft AGL	28 ft/sec GS, level flight	7 kt NE

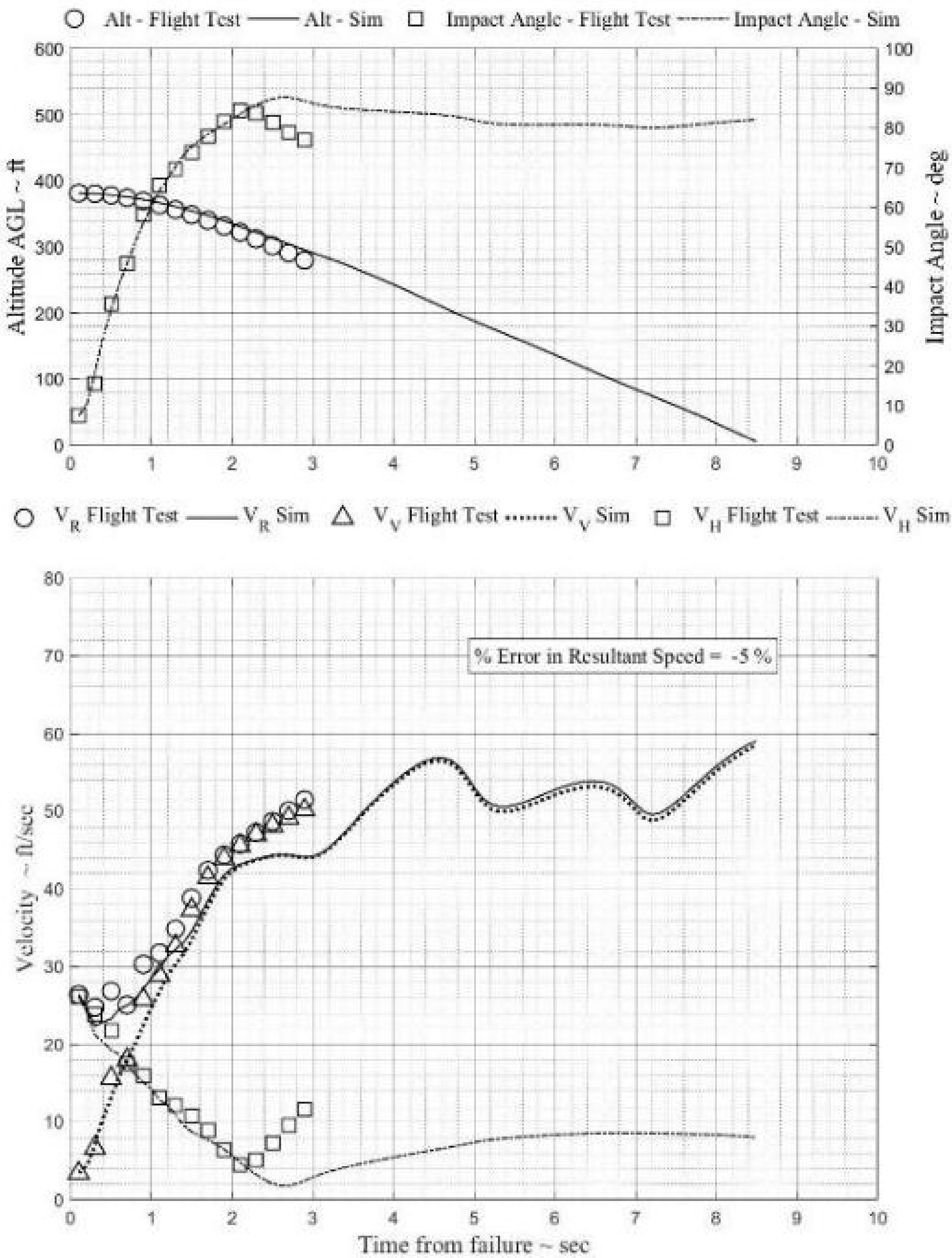

Figure B 16. Vendor 1 Quadrotor Two Motor (Off-Axis) Failure at Maximum Stabilized Forward Speed

*Winds measured 20 feet AGL at a weather station less than three miles from flight test location

V_R = Resultant Speed — V_V = Vertical Speed — GS = Ground Speed
V_H = Horizontal GS — Alt = Altitude — Sim = Simulation
AGL = Above Ground Level

Configuration	Weight	Failure Altitude	Initial Conditions	Flight Test Winds*
Flight Test	0.84 lbf	384 ft AGL	Hover	Calm

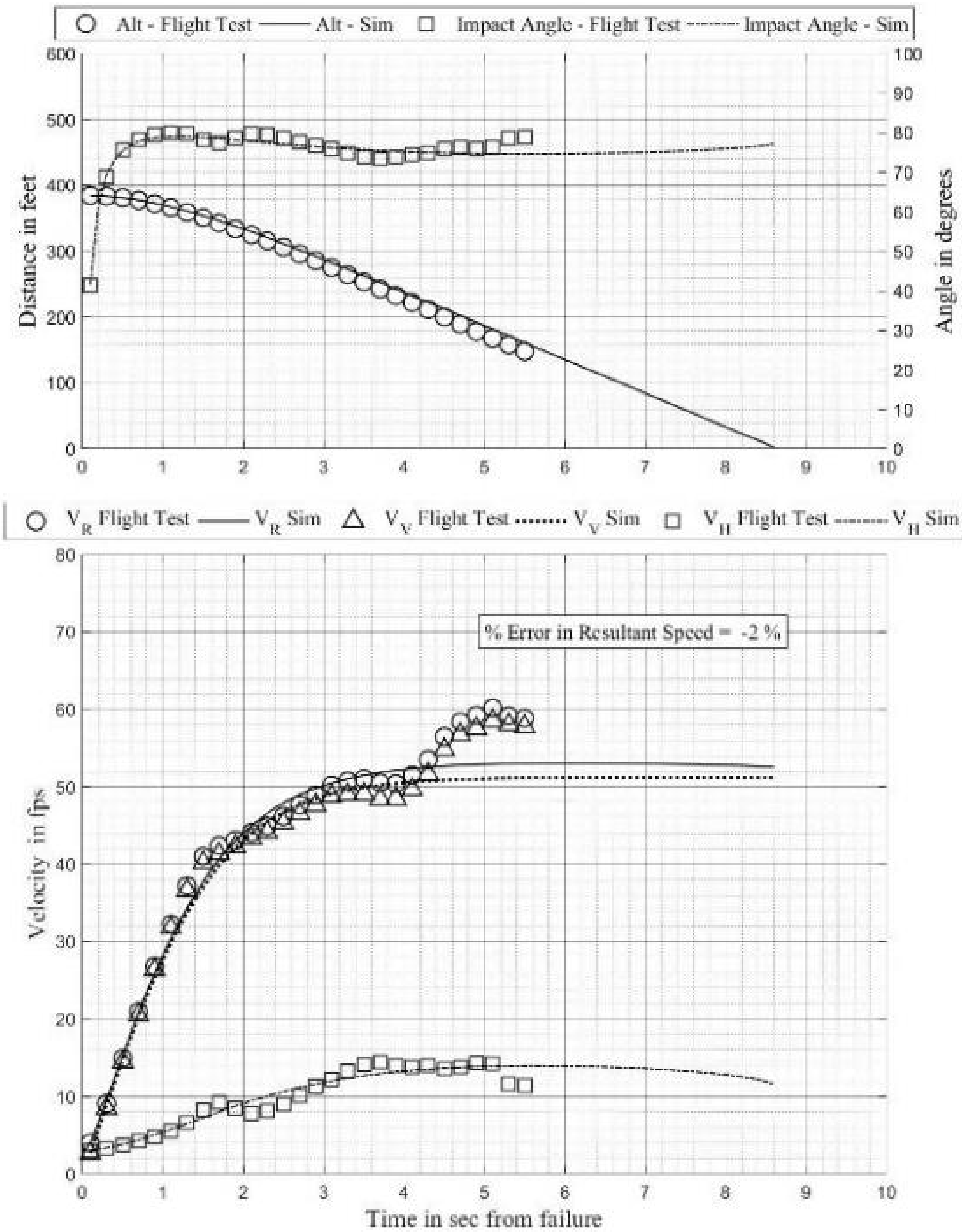

Figure B 17. Vendor 1 Quadrotor Cage-OFF Four Motor Failure at Hover

*Winds measured 20 feet AGL at a weather station less than three miles from flight test location

V_R = Resultant Speed | V_V = Vertical Speed | GS = Ground Speed
V_H = Horizontal GS | Alt = Altitude | Sim = Simulation
AGL = Above Ground Level

Configuration	Weight	Failure Altitude	Initial Conditions	Flight Test Winds*
Flight Test	0.84 lbf	469 ft AGL	43 ft/sec GS, level flight	6 kt SSE

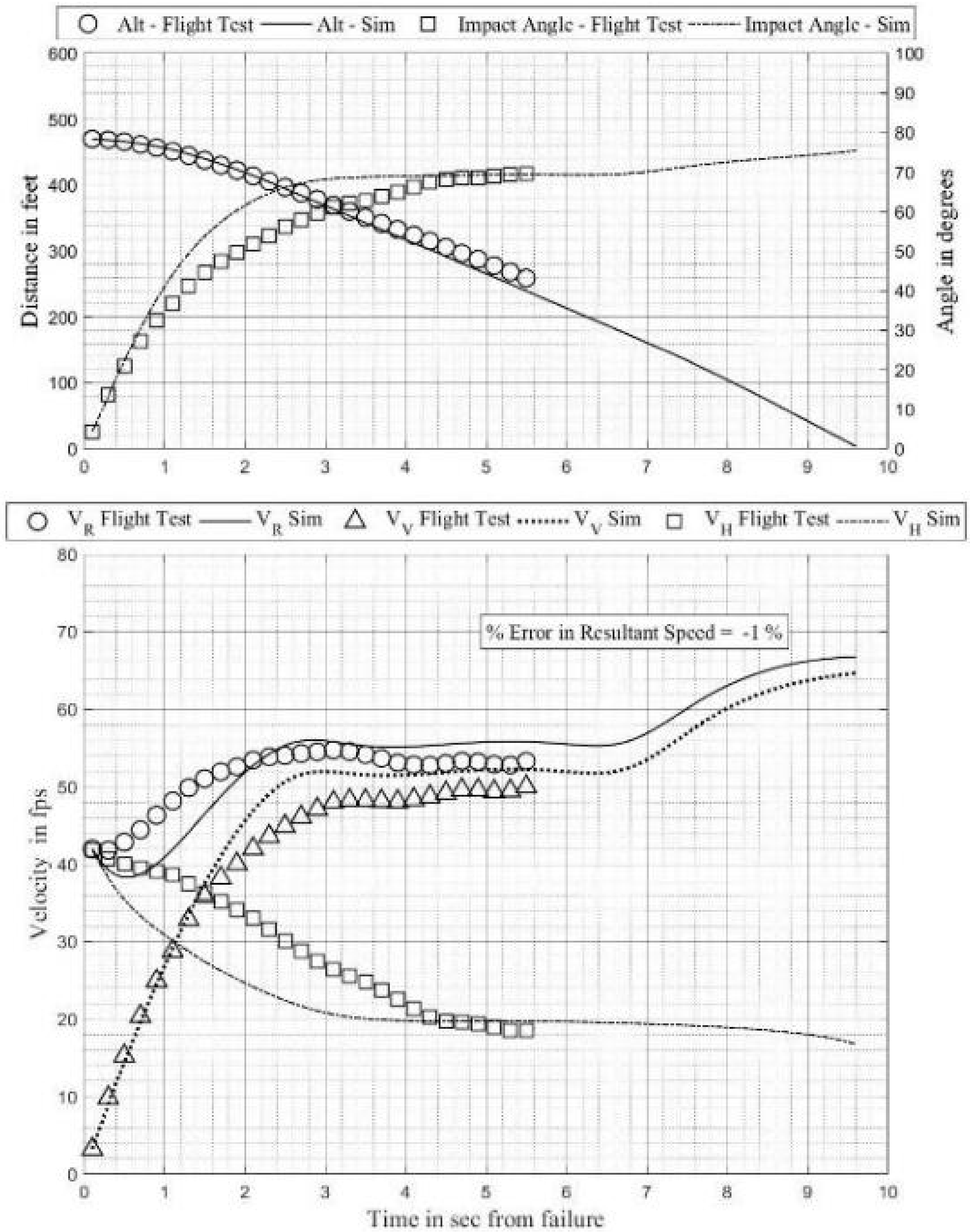

Figure B 18. Vendor 1 Quadrotor Cage-OFF Four Motor Failure at Maximum Stabilized Forward Speed

*Winds measured 20 feet AGL at a weather station less than three miles from flight test location

V_R = Resultant Speed V_V = Vertical Speed GS = Ground Speed

V_H = Horizontal GS Alt = Altitude Sim = Simulation

AGL = Above Ground Level

Configuration	Weight	Failure Altitude	Initial Conditions	Flight Test Winds*
Flight Test	0.84 lbf	390 ft AGL	Hover	Calm

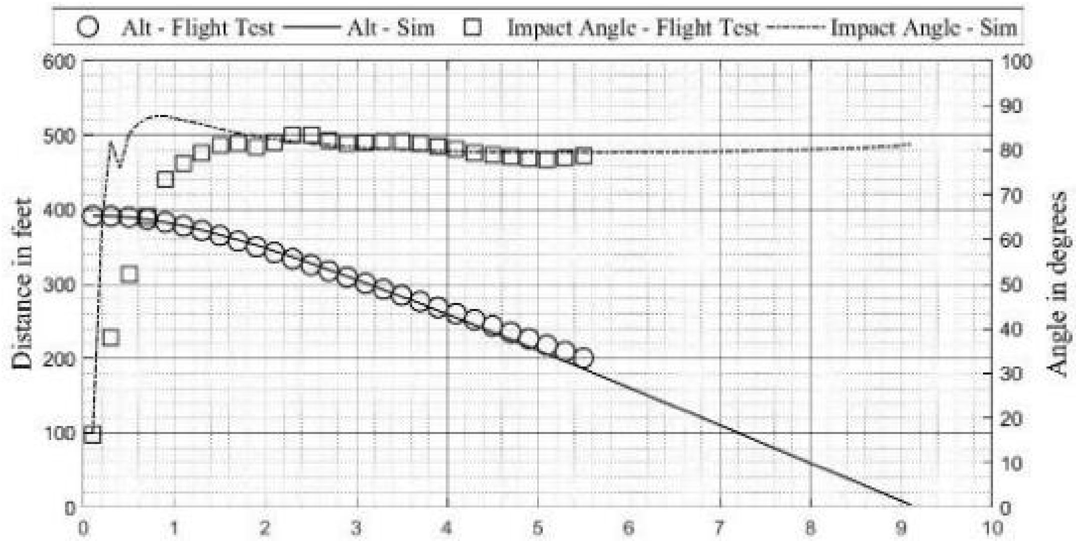

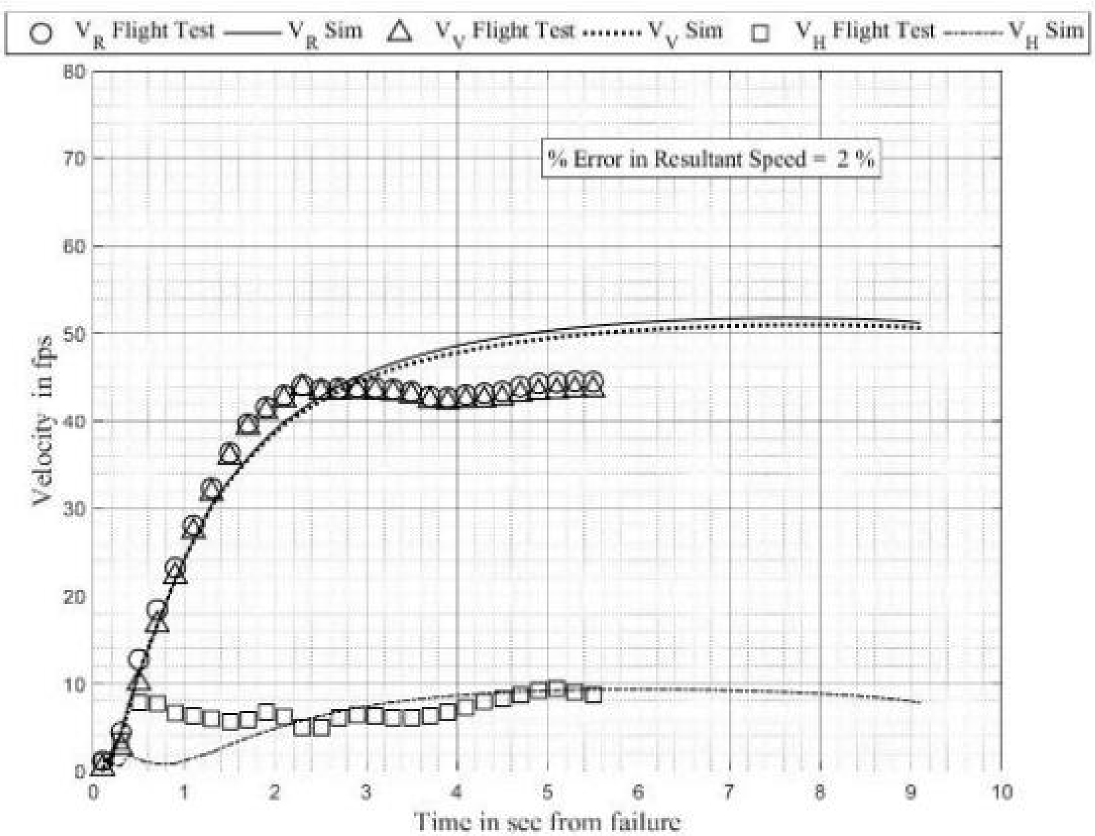

Figure B 19. Vendor 1 Quadrotor Cage-OFF One Motor Failure at Hover

*Winds measured 20 feet AGL at a weather station less than three miles from flight test location

V_R = Resultant Speed
V_V = Vertical Speed
GS = Ground Speed
V_H = Horizontal GS
Alt = Altitude
Sim = Simulation
AGL = Above Ground Level

Configuration	Weight	Failure Altitude	Initial Conditions	Flight Test Winds*
Flight Test	0.84 lbf	438 ft AGL	38 ft/sec GS, level flight	Calm

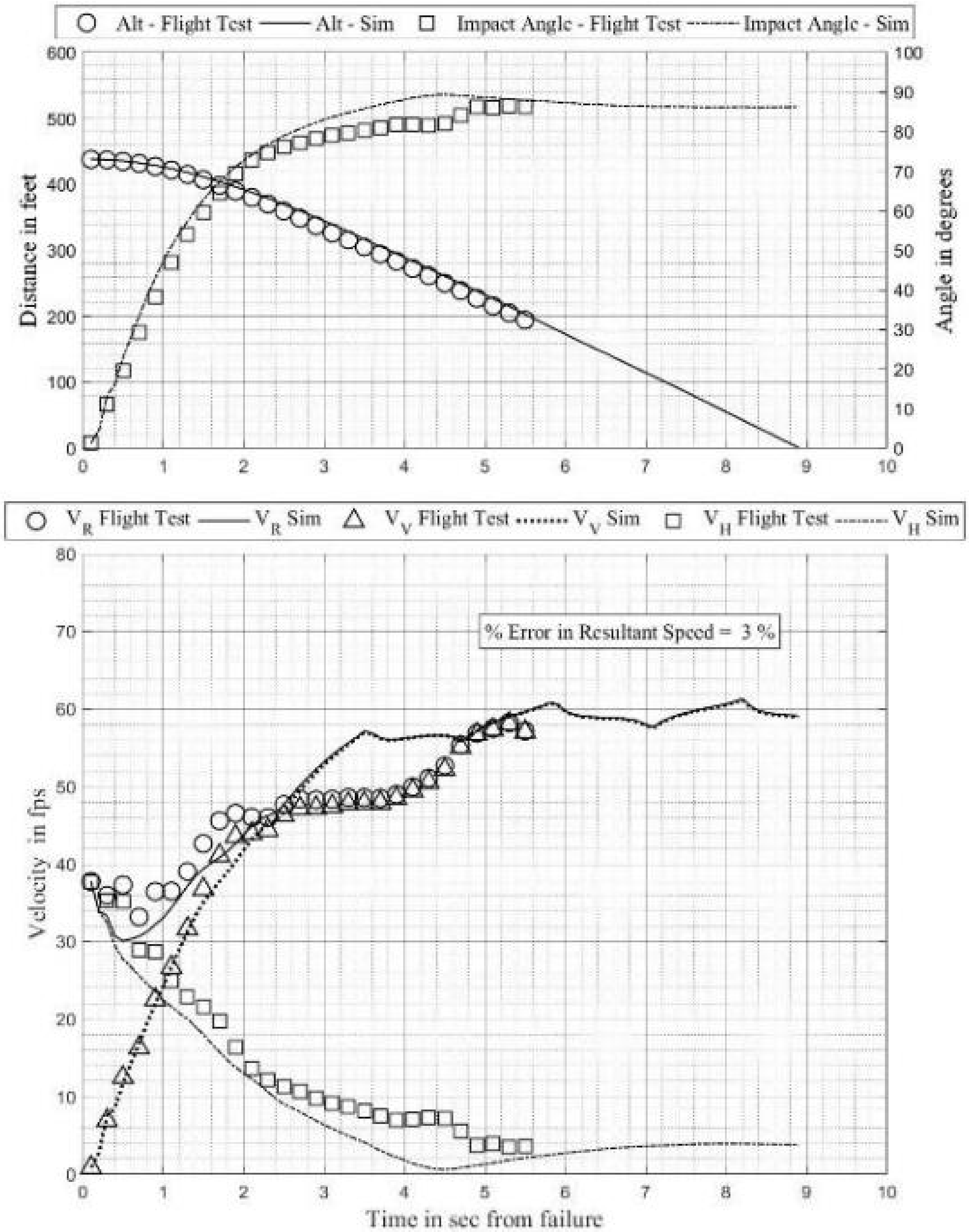

Figure B 20. Vendor 1 Quadrotor Cage-OFF One Motor Failure at Maximum Stabilized Forward Speed

*Winds measured 20 feet AGL at a weather station less than three miles from flight test location

V_R = Resultant Speed V_V = Vertical Speed GS = Ground Speed

V_H = Horizontal GS Alt = Altitude Sim = Simulation

AGL = Above Ground Level

Configuration	**Weight**	**Failure Altitude**	**Initial Conditions**	**Flight Test Winds***
Flight Test	0.84 lbf	407 ft AGL	Hover	Calm

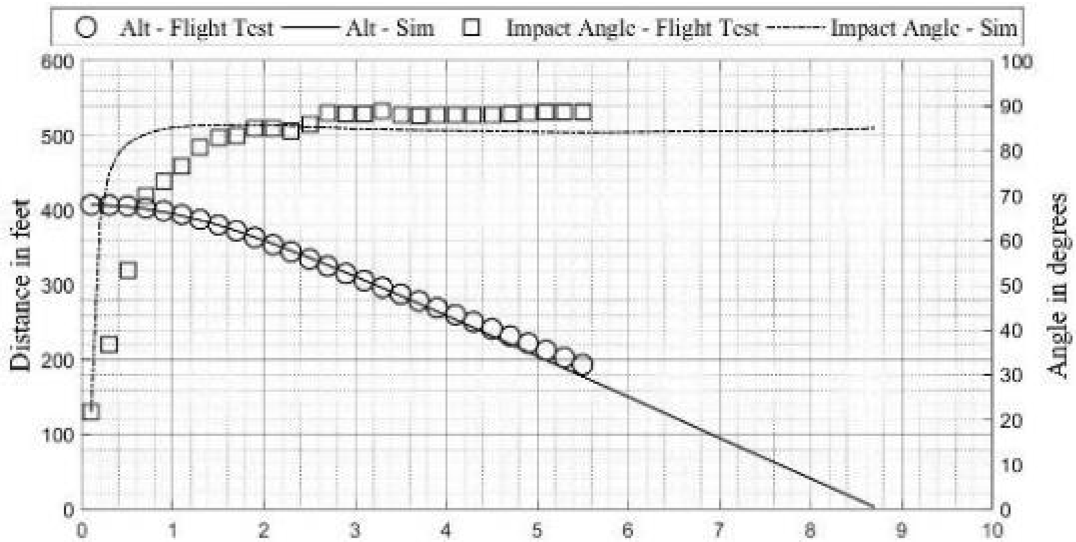

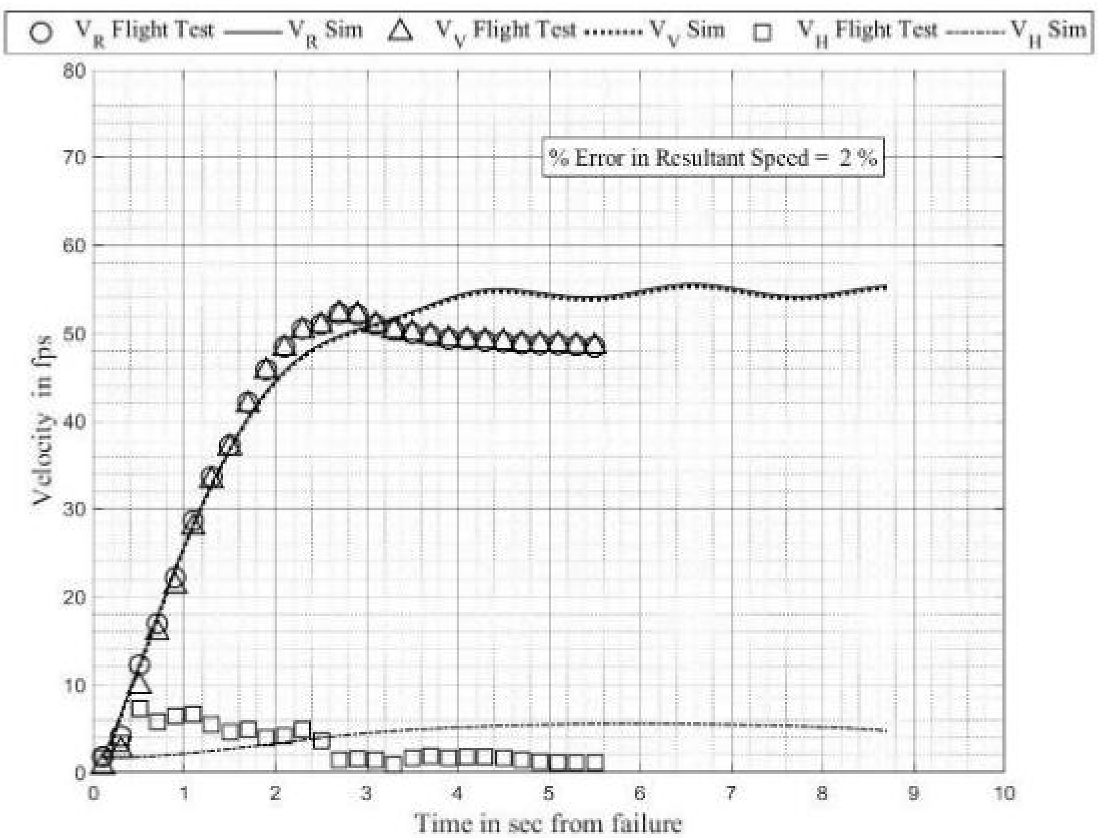

Figure B 21. Vendor 1 Quadrotor Cage-OFF Two Motor (On-Axis) Failure at Hover

*Winds measured 20 feet AGL at a weather station less than three miles from flight test location
V_R = Resultant Speed
V_V = Vertical Speed
GS = Ground Speed
V_H = Horizontal GS
Alt = Altitude
Sim = Simulation
AGL = Above Ground Level

Configuration	Weight	Failure Altitude	Initial Conditions	Flight Test Winds*
Flight Test	0.84 lbf	405 ft AGL	36 ft/sec GS, level flight	Calm

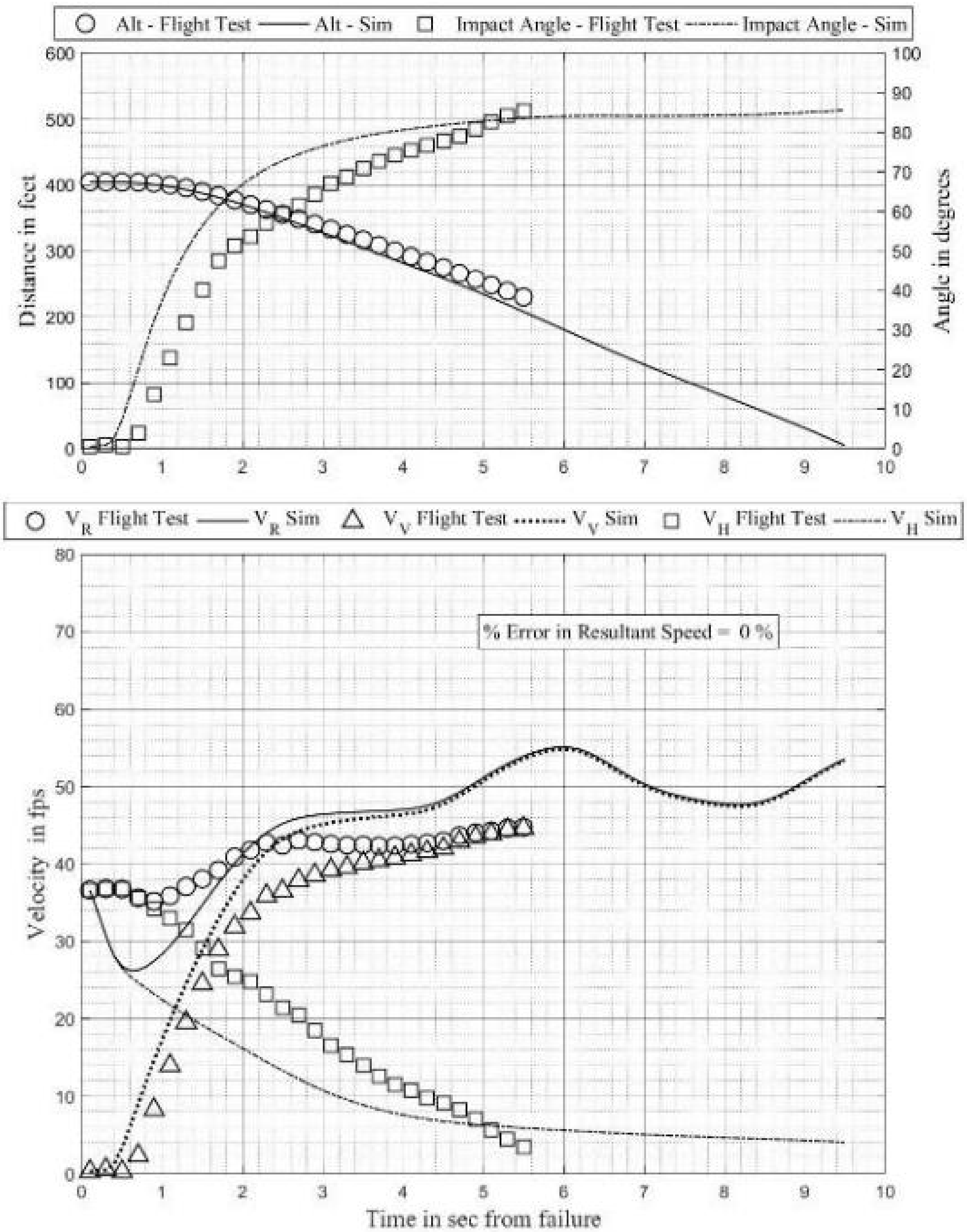

Figure B 22. Vendor 1 Quadrotor Cage-OFF Two Motor (On-Axis) Failure at Maximum Stabilized Forward Speed

*Winds measured 20 feet AGL at a weather station less than three miles from flight test location

V_R = Resultant Speed
V_V = Vertical Speed
GS = Ground Speed
V_H = Horizontal GS
Alt = Altitude
Sim = Simulation
AGL = Above Ground Level

Configuration	Weight	Failure Altitude	Initial Conditions	Flight Test Winds*
Flight Test	0.84 lbf	387 ft AGL	Hover	Calm

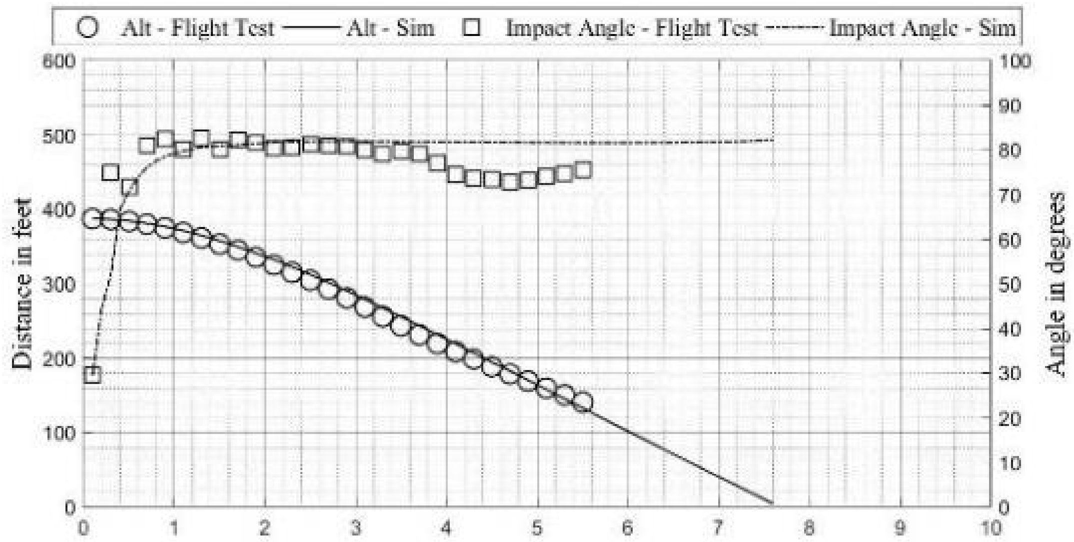

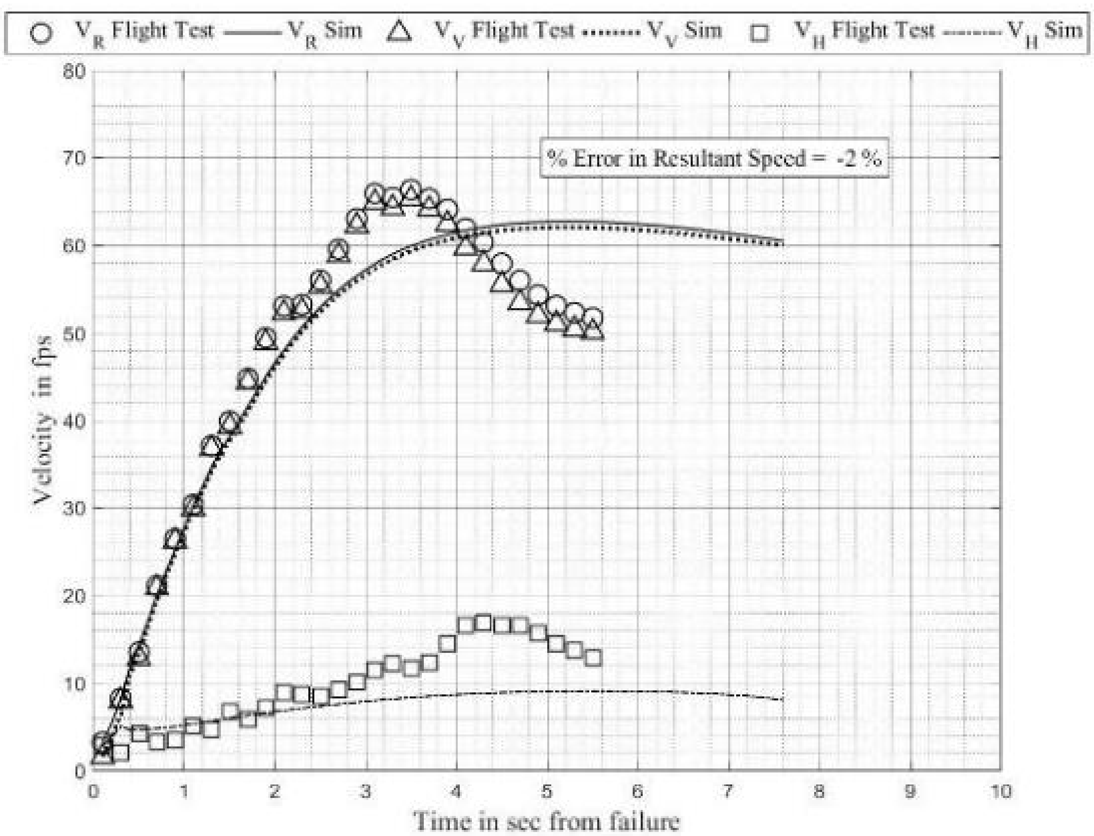

Figure B 23. Vendor 1 Quadrotor Cage-OFF Two Motor (Off-Axis) Failure at Hover

*Winds measured 20 feet AGL at a weather station less than three miles from flight test location

V_R = Resultant Speed V_V = Vertical Speed GS = Ground Speed
V_H = Horizontal GS Alt = Altitude Sim = Simulation
AGL = Above Ground Level

Configuration	Weight	Failure Altitude	Initial Conditions	Flight Test Winds*
Flight Test	0.84 lbf	400 ft AGL	36 ft/sec GS, level flight	1 kt N

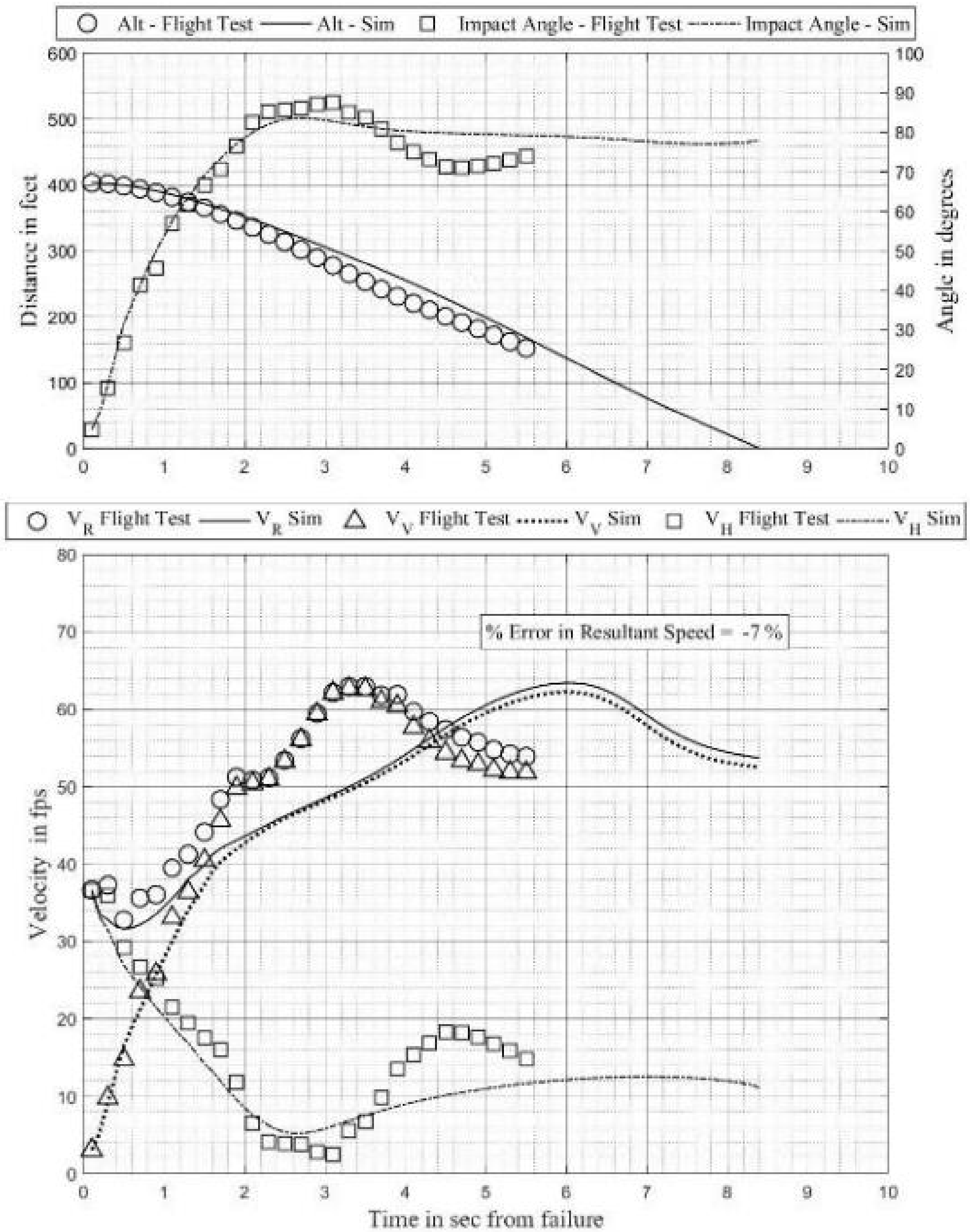

Figure B 24. Vendor 1 Quadrotor Cage-OFF Two Motor (Off-Axis) Failure at Maximum Stabilized Forward Speed

*Winds measured 20 feet AGL at a weather station less than three miles from flight test location

V_R = Resultant Speed
V_V = Vertical Speed
GS = Ground Speed
V_H = Horizontal GS
Alt = Altitude
Sim = Simulation
AGL = Above Ground Level

Configuration	Weight	Failure Altitude	Initial Conditions	Flight Test Winds*
Flight Test	2.86 lbf	318 ft AGL	98 ft/sec GS, level flight	8 kt S

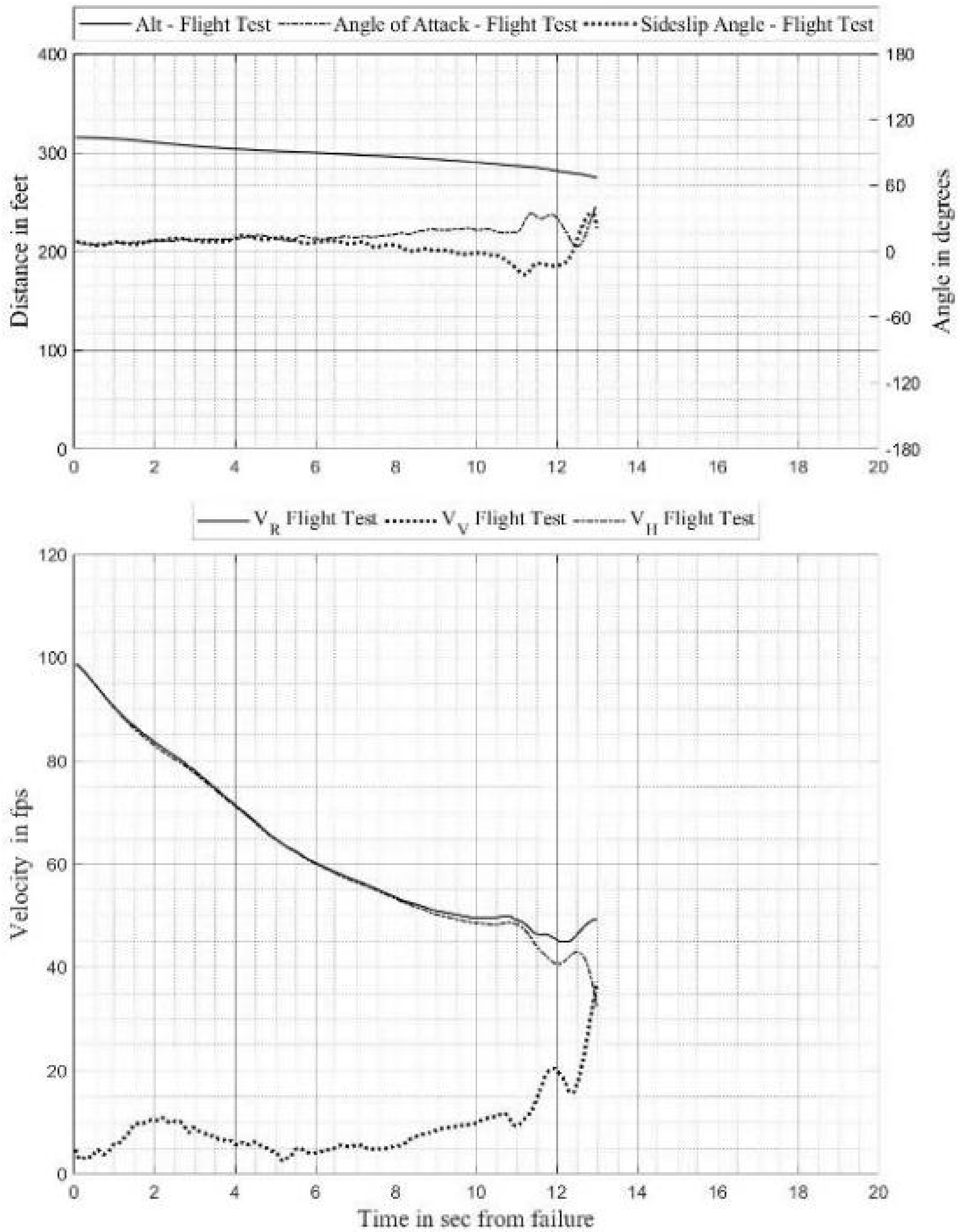

Figure B 25. Sensefly eBee + Power Off, No Lateral Inputs

*Winds measured 20 feet AGL at a weather station less than three miles from flight test location

V_R = Resultant Speed　V_V = Vertical Speed　GS = Ground Speed

V_H = Horizontal GS　Alt = Altitude　Sim = Simulation

AGL = Above Ground Level

Configuration	Weight	Failure Altitude	Initial Conditions	Flight Test Winds*
Flight Test	2.86 lbf	270 ft AGL	60 ft/sec GS, level flight	14 kt NNW

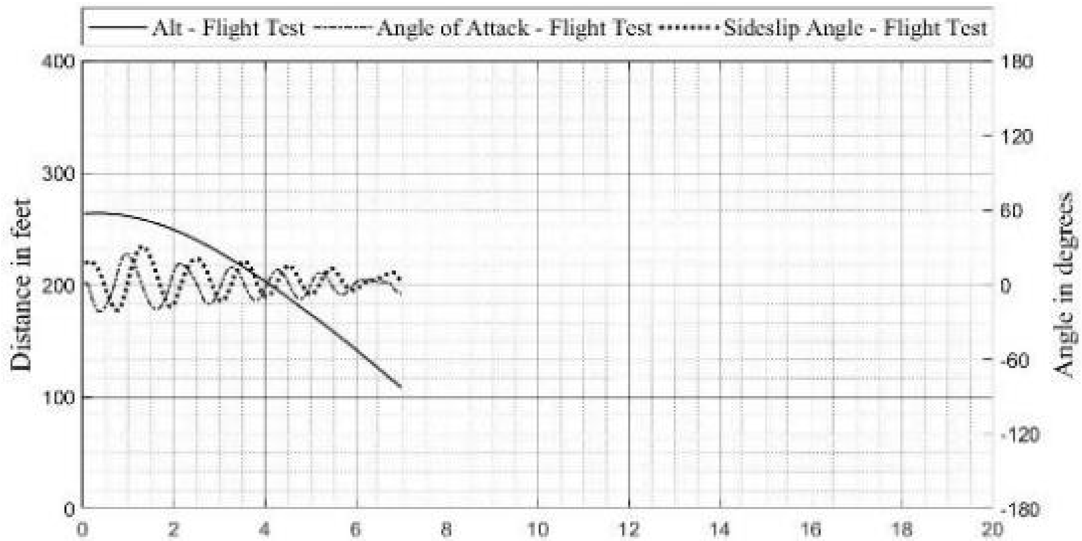

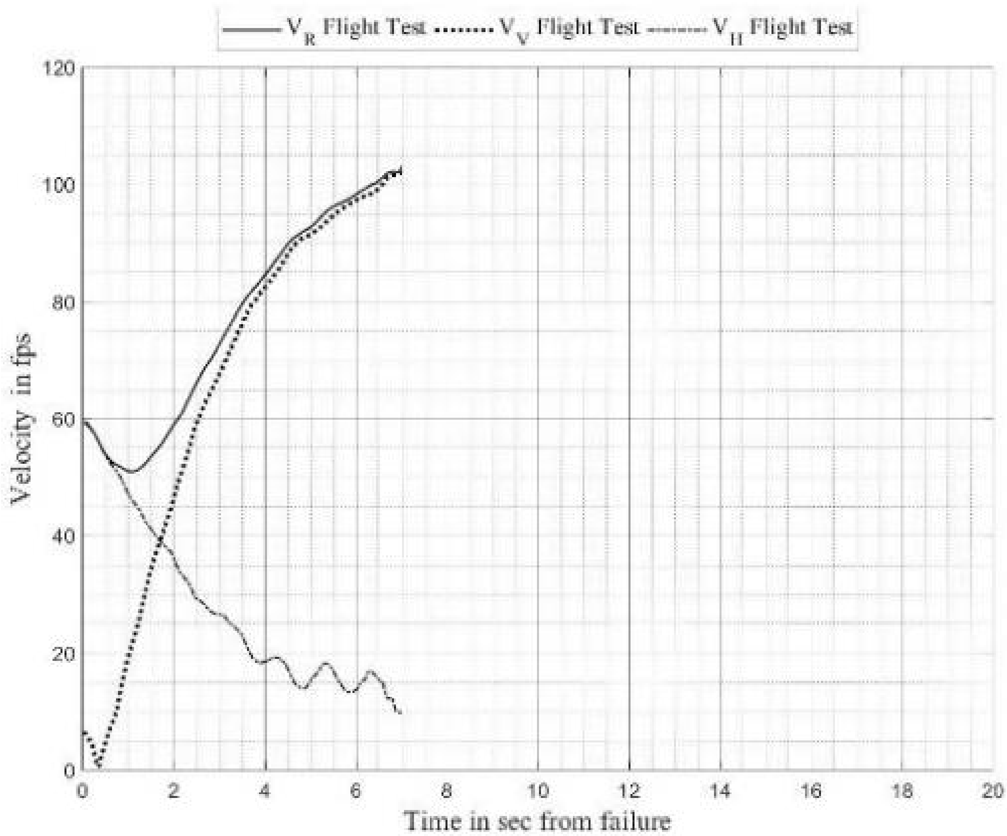

Figure B 26. Sensefly eBee + Power On, Max Roll Inputs

*Winds measured 20 feet AGL at a weather station less than three miles from flight test location

V_R = Resultant Speed | V_V = Vertical Speed | GS = Ground Speed
V_H = Horizontal GS | Alt = Altitude | Sim = Simulation
AGL = Above Ground Level

Configuration	Weight	Failure Altitude	Initial Conditions	Flight Test Winds*
Flight Test	2.86 lbf	360 ft AGL	98 ft/sec GS, level flight	8 kt S

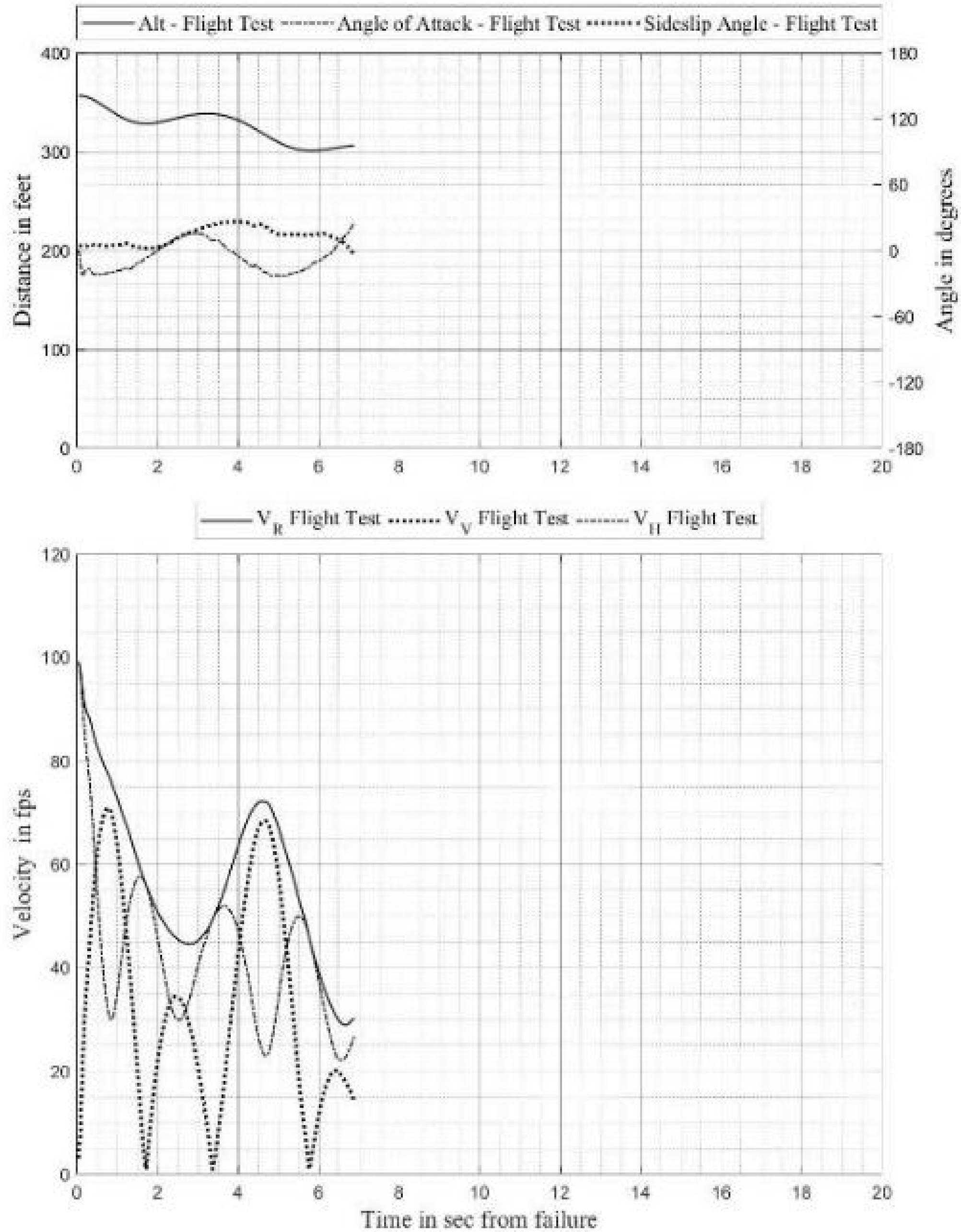

Figure B 27. Sensefly eBee + Power On, Pitch Down Inputs

*Winds measured 20 feet AGL at a weather station less than three miles from flight test location

V_R = Resultant Speed V_V = Vertical Speed   GS = Ground Speed

V_H = Horizontal GS   Alt = Altitude   Sim = Simulation

AGL = Above Ground Level

Configuration	Weight	Failure Altitude	Initial Conditions	Flight Test Winds*
Flight Test	2.86 lbf	387 ft AGL	72 ft/sec GS, level flight	14 kt NNW

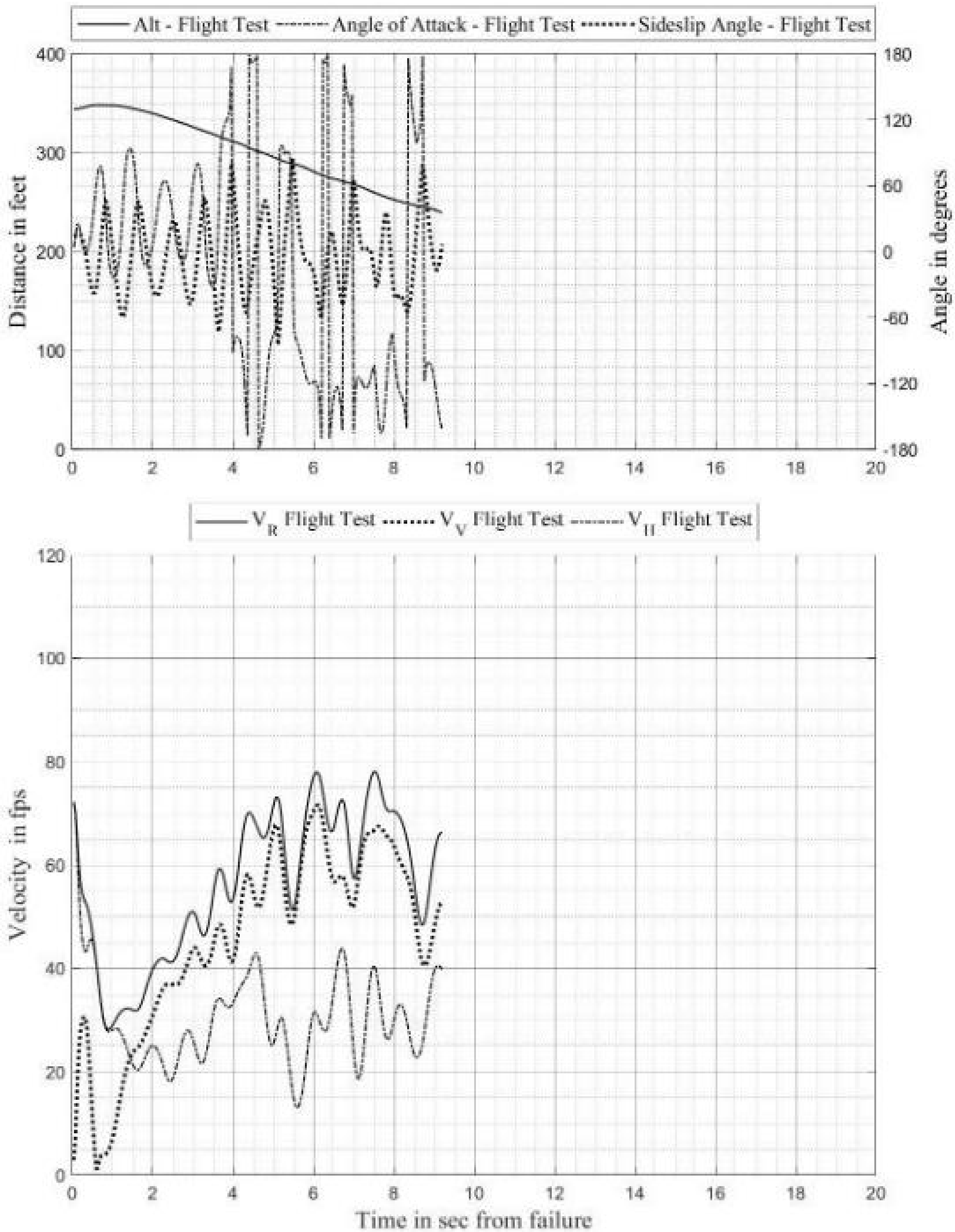

Figure B 28. Sensefly eBee + Power On, Pitch Up Inputs

*Winds measured 20 feet AGL at a weather station less than three miles from flight test location

V_R = Resultant Speed V_V = Vertical Speed GS = Ground Speed
V_H = Horizontal GS Alt = Altitude Sim = Simulation
AGL = Above Ground Level

Configuration	Weight	Failure Altitude	Initial Conditions	Flight Test Winds*
Flight Test	2.47 lbf	361 ft AGL	Hover	9 kt NE

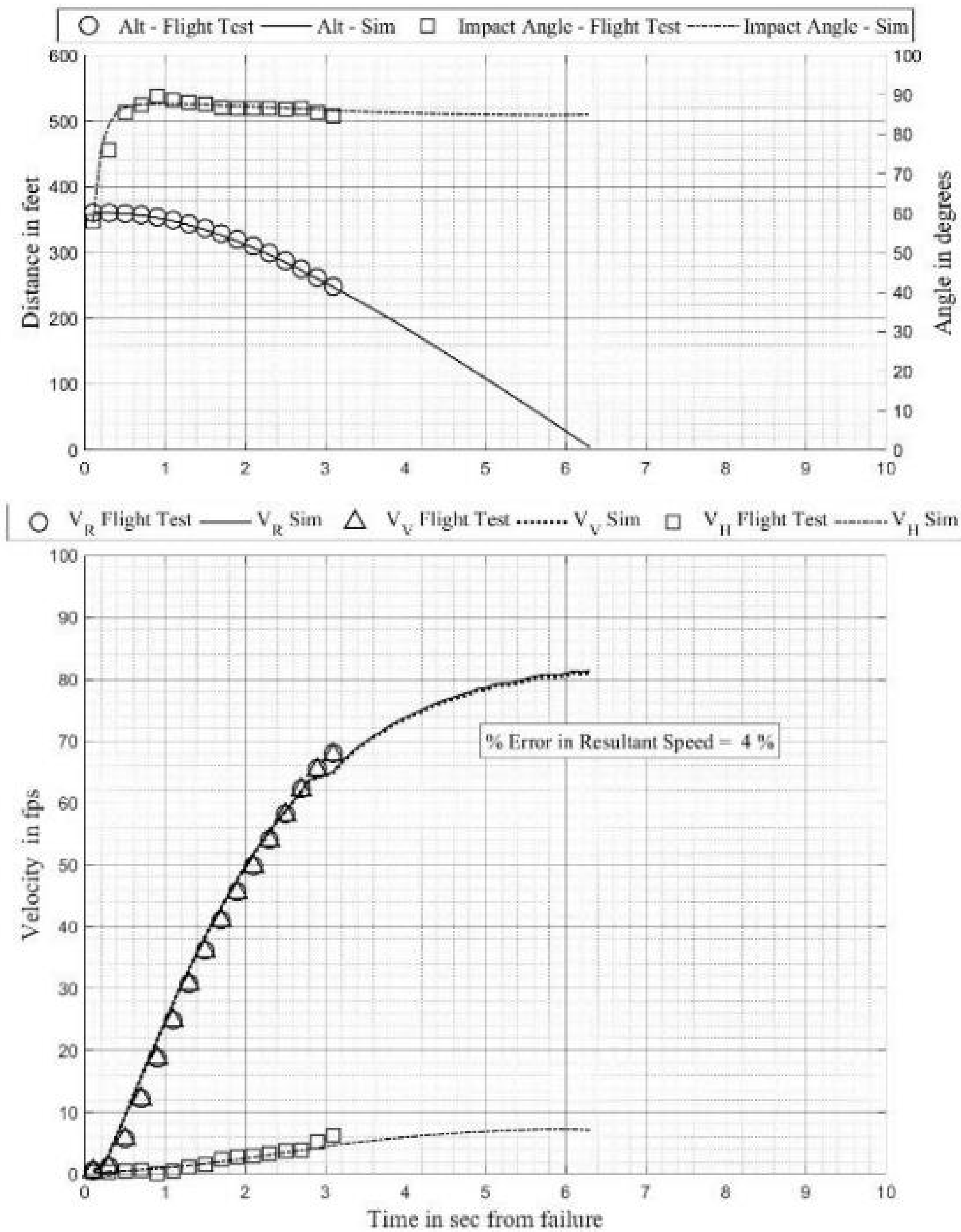

Figure B 29. DJI Mavic Pro Four Motor Failure at Hover

*Winds measured 20 feet AGL at a weather station less than three miles from flight test location

V_R = Resultant Speed
V_V = Vertical Speed
GS = Ground Speed
V_H = Horizontal GS
Alt = Altitude
Sim = Simulation
AGL = Above Ground Level

Configuration	Weight	Failure Altitude	Initial Conditions	Flight Test Winds*
Flight Test	2.47 lbf	340 ft AGL	34 ft/sec GS, level flight	9 kt NE

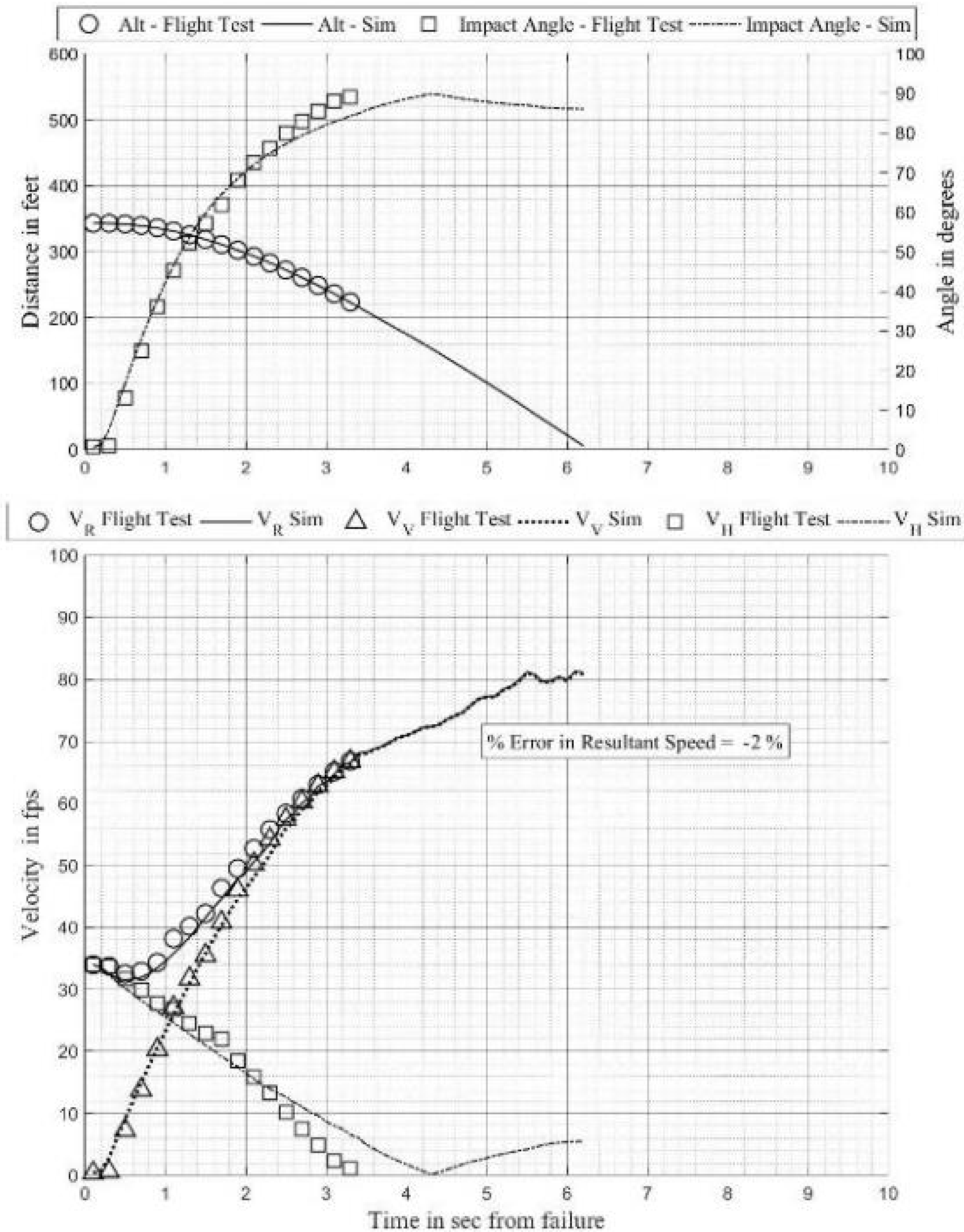

Figure B 30. DJI Mavic Pro Four Motor Failure at Maximum Stabilized Forward Speed

*Winds measured 20 feet AGL at a weather station less than three miles from flight test location

V_R = Resultant Speed
V_V = Vertical Speed
GS = Ground Speed
V_H = Horizontal GS
Alt = Altitude
Sim = Simulation
AGL = Above Ground Level

Configuration	Weight	Failure Altitude	Initial Conditions	Flight Test Winds*
Flight Test	2.47 lbf	360 ft AGL	Hover	9 kt NE

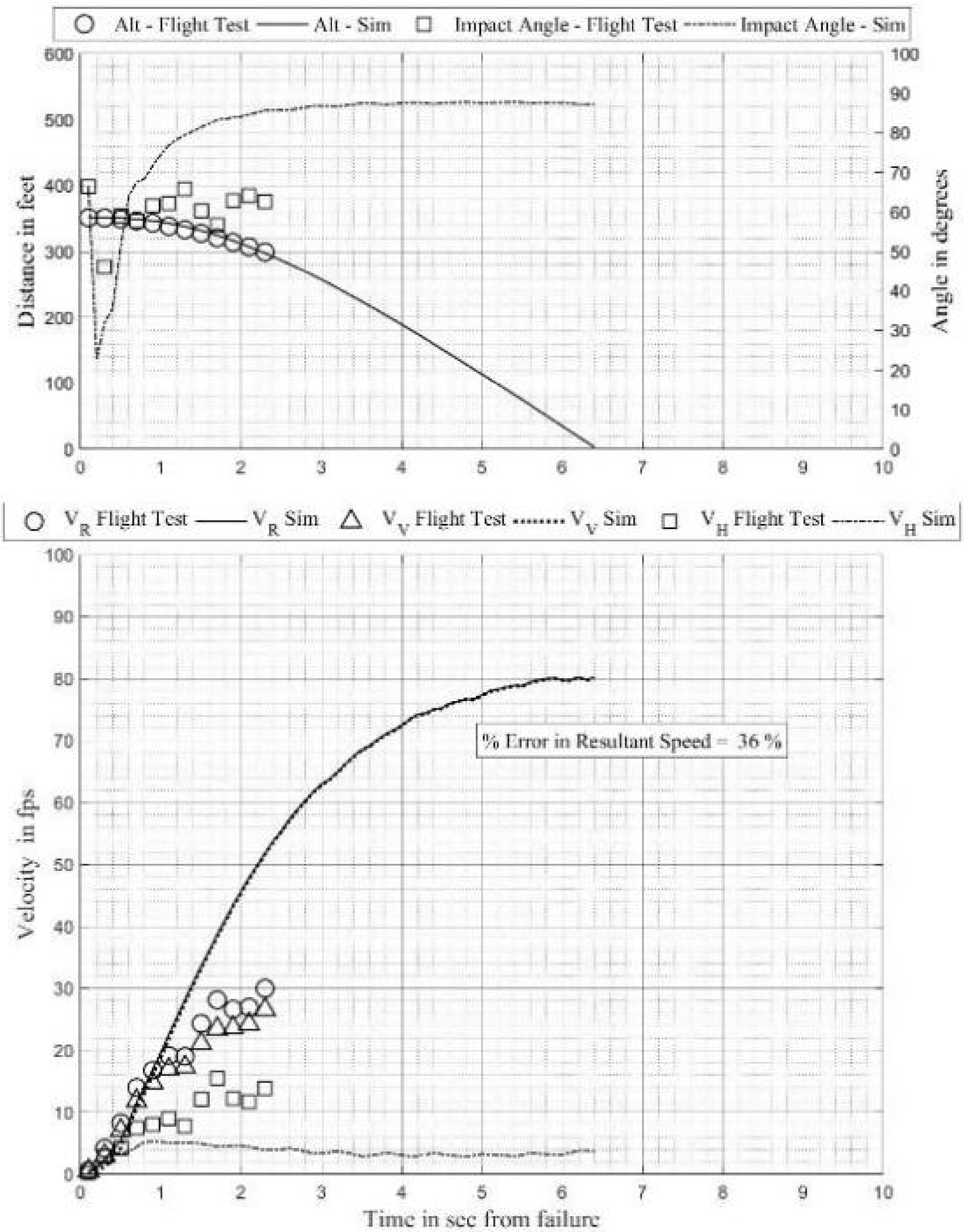

Figure B 31. DJI Mavic Pro One Motor Failure at Hover

*Winds measured 20 feet AGL at a weather station less than three miles from flight test location

V_R = Resultant Speed
V_V = Vertical Speed
GS = Ground Speed
V_H = Horizontal GS
Alt = Altitude
Sim = Simulation
AGL = Above Ground Level

Configuration	Weight	Failure Altitude	Initial Conditions	Flight Test Winds*
Flight Test	2.47 lbf	335 ft AGL	48 ft/sec GS, level flight	9 kt NE

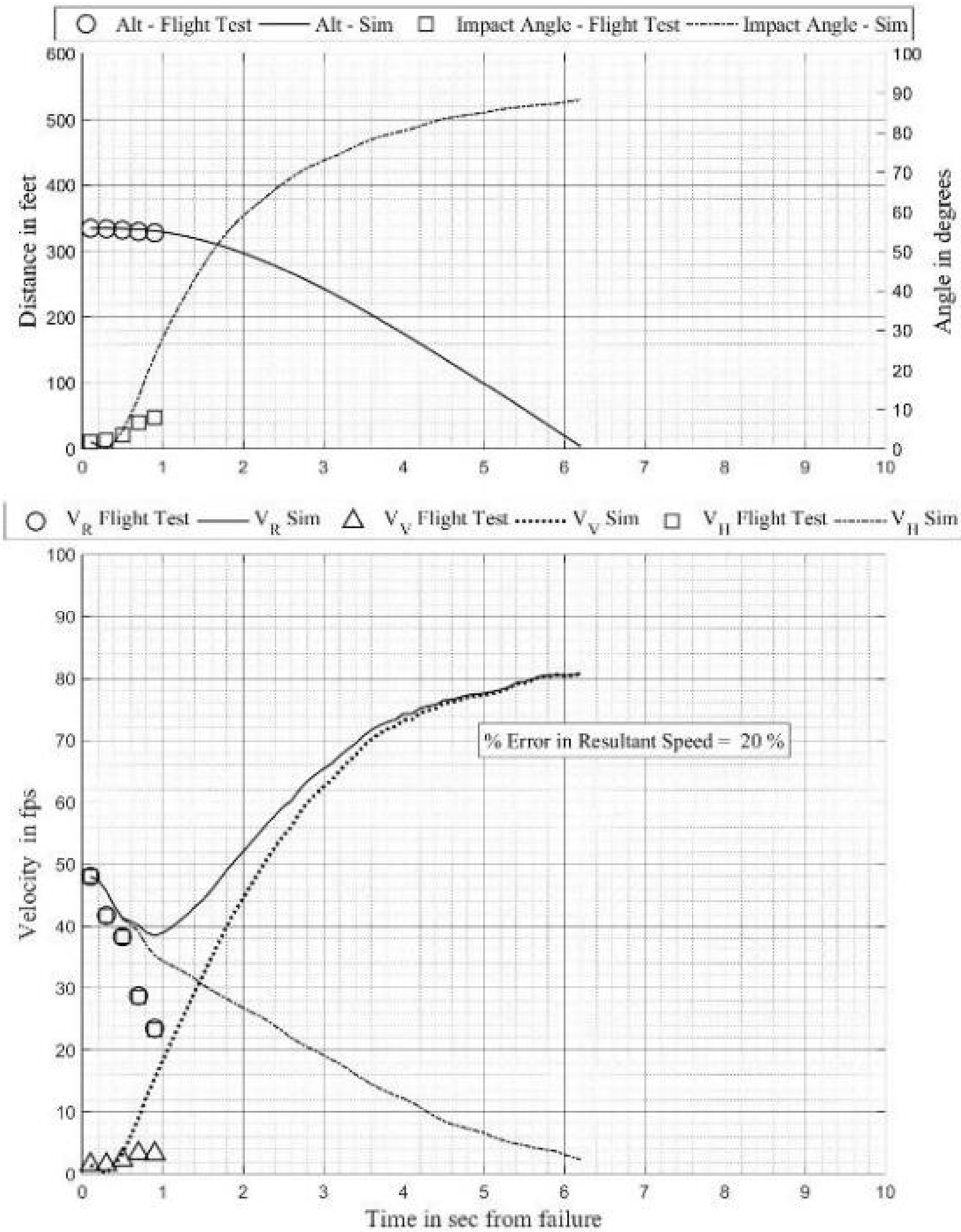

Figure B 32. DJI Mavic Pro One Motor Failure at Maximum Stabilized Forward Speed

*Winds measured 20 feet AGL at a weather station less than three miles from flight test location

V_R = Resultant Speed | V_V = Vertical Speed | GS = Ground Speed

V_H = Horizontal GS | Alt = Altitude | Sim = Simulation

AGL = Above Ground Level

Configuration	Weight	Failure Altitude	Initial Conditions	Flight Test Winds*
Flight Test	2.47 lbf	370 ft AGL	Hover	8 kt SW

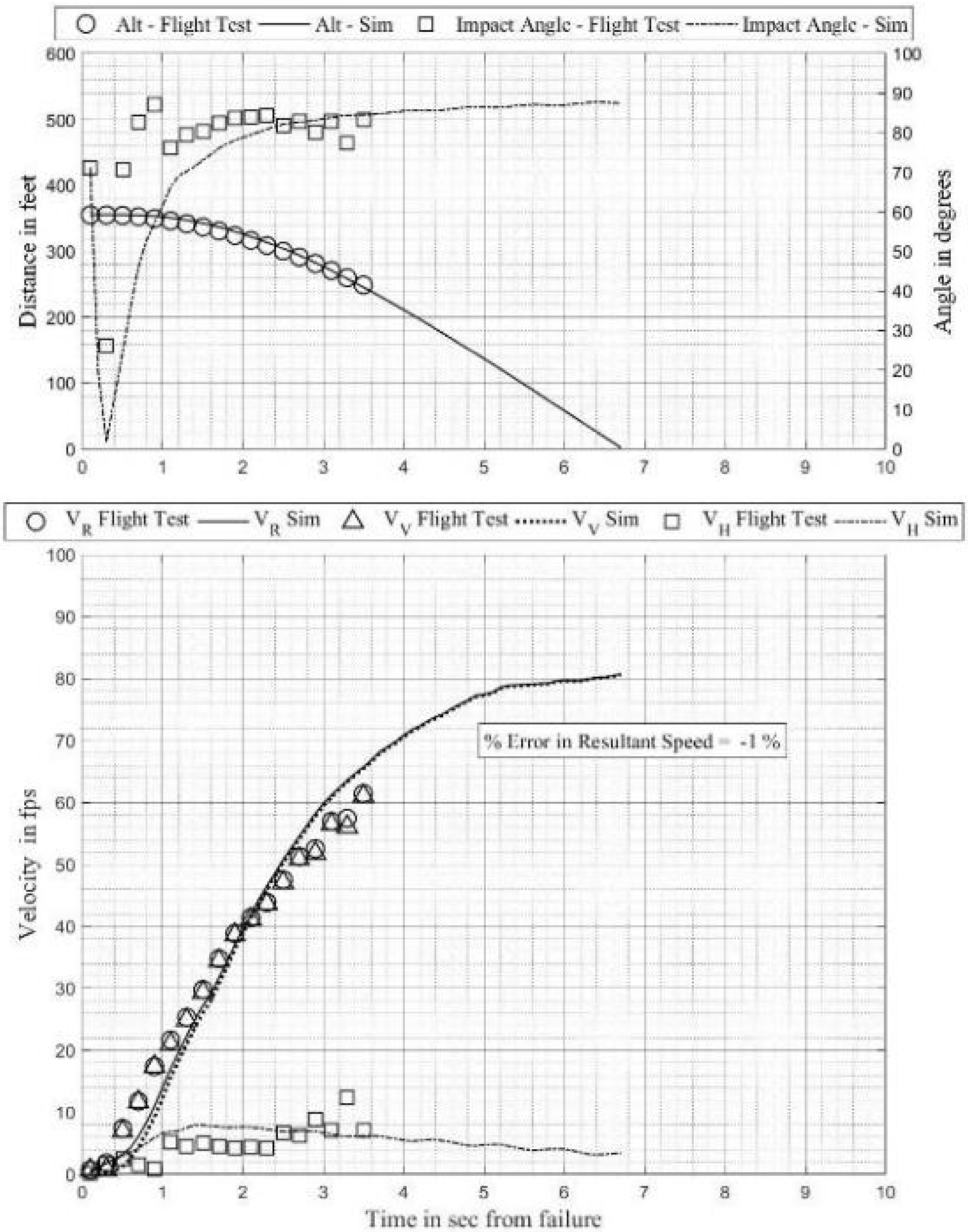

Figure B 33. DJI Mavic Pro Two Motor (On-Axis) Failure at Hover

*Winds measured 20 feet AGL at a weather station less than three miles from flight test location

V_R = Resultant Speed　V_V = Vertical Speed　GS = Ground Speed

V_H = Horizontal GS　Alt = Altitude　Sim = Simulation

AGL = Above Ground Level

Configuration	Weight	Failure Altitude	Initial Conditions	Flight Test Winds*
Flight Test	2.47 lbf	370 ft AGL	60 ft/sec GS, level flight	8 kt SW

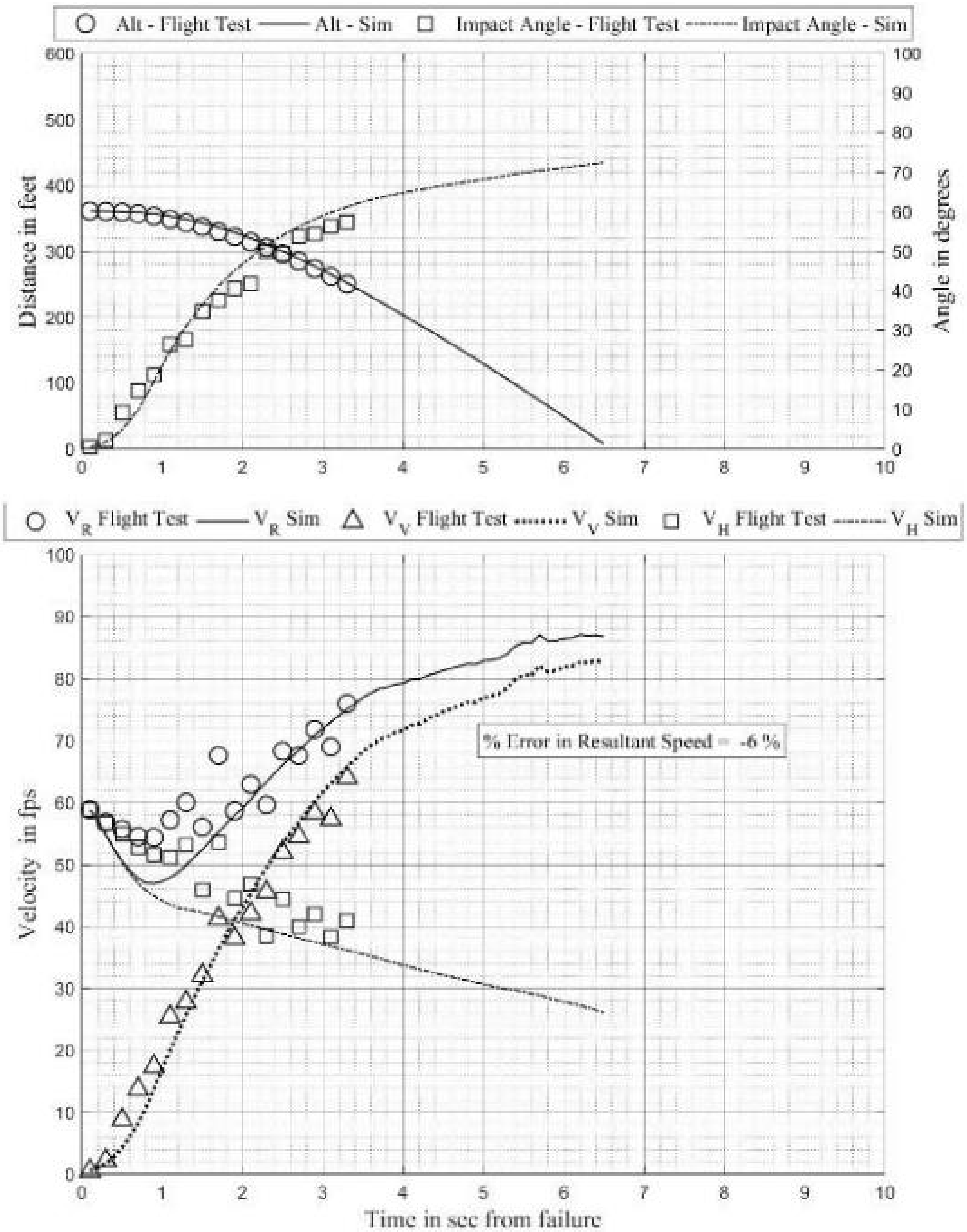

Figure B 34. DJI Mavic Pro Two Motor (On-Axis) Failure at Maximum Stabilized Forward Speed

*Winds measured 20 feet AGL at a weather station less than three miles from flight test location

V_R = Resultant Speed | V_V = Vertical Speed | GS = Ground Speed

V_H = Horizontal GS | Alt = Altitude | Sim = Simulation

AGL = Above Ground Level

Configuration	Weight	Failure Altitude	Initial Conditions	Flight Test Winds*
Flight Test	2.47 lbf	385 ft AGL	Hover	9 kt NE

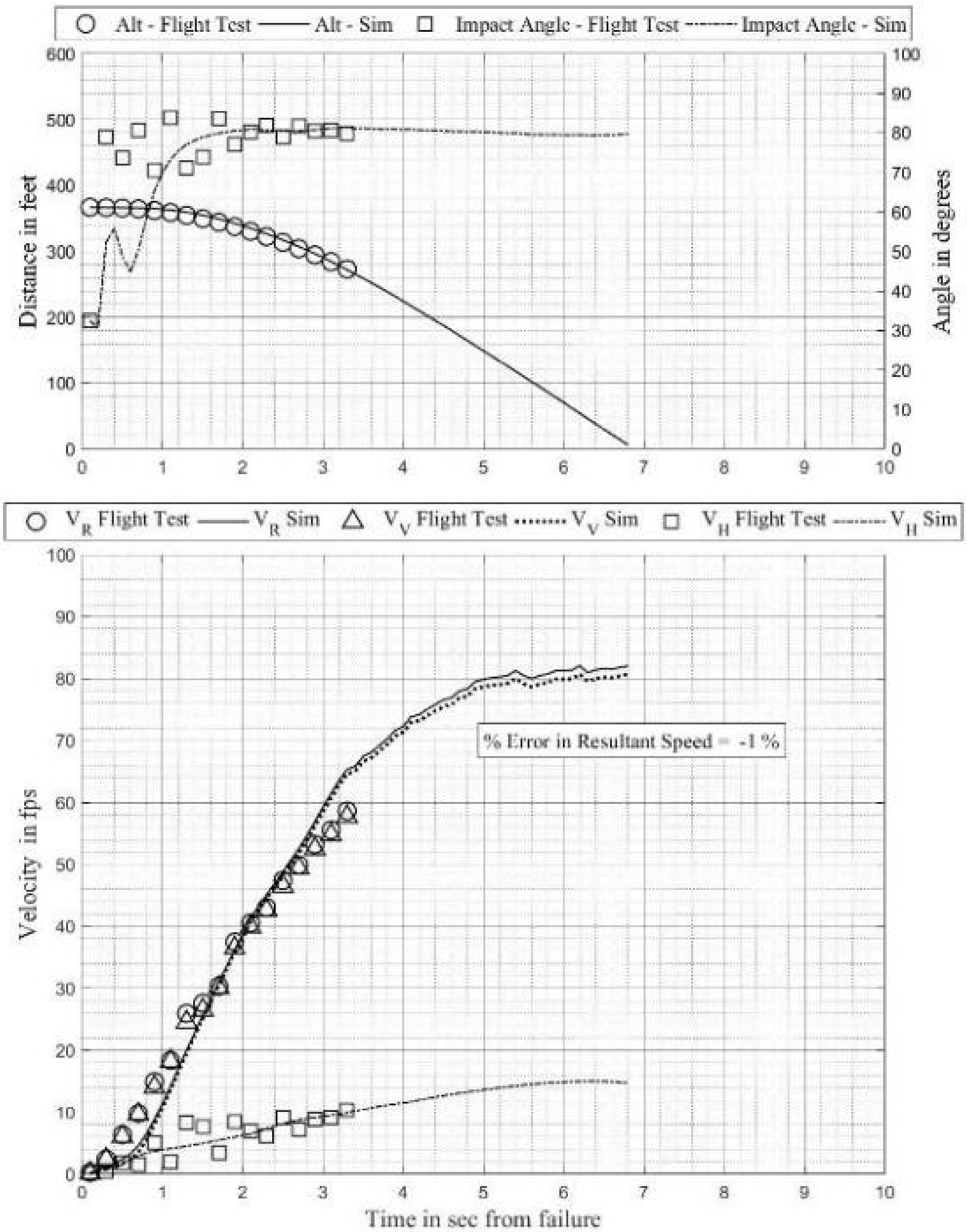

Figure B 35. DJI Mavic Pro Two Motor (Off-Axis) Failure at Hover

*Winds measured 20 feet AGL at a weather station less than three miles from flight test location

V_R = Resultant Speed
V_V = Vertical Speed
GS = Ground Speed
V_H = Horizontal GS
Alt = Altitude
Sim = Simulation
AGL = Above Ground Level

Configuration	Weight	Failure Altitude	Initial Conditions	Flight Test Winds*
Flight Test	2.47 lbf	400 ft AGL	59 ft/sec GS, level flight	8 kt SW

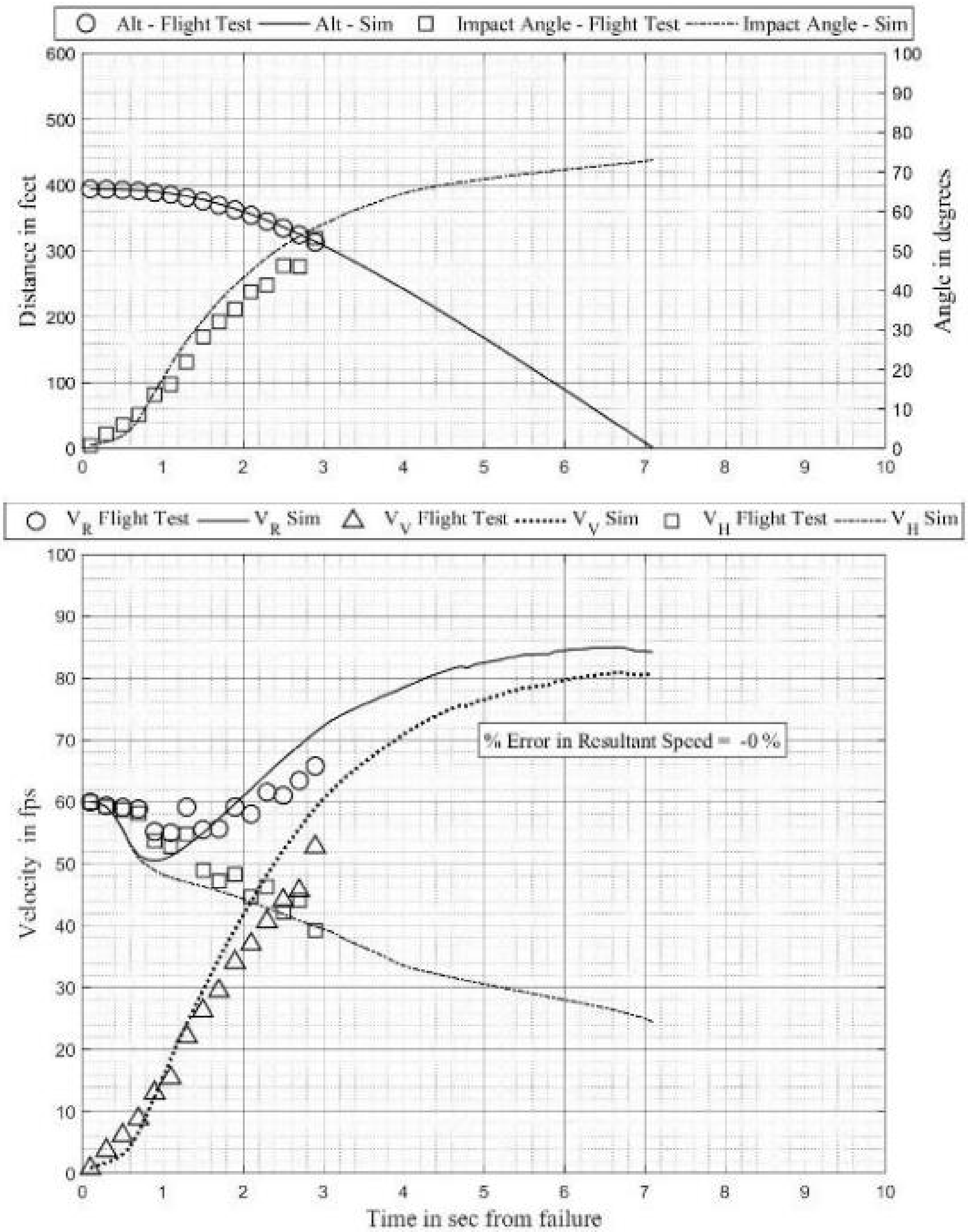

Figure B 36. DJI Mavic Pro Two Motor (Off-Axis) Failure at Maximum Stabilized Forward Speed

*Winds measured 20 feet AGL at a weather station less than three miles from flight test location
V_R = Resultant Speed V_V = Vertical Speed   GS = Ground Speed
V_H = Horizontal GS   Alt = Altitude   Sim = Simulation
AGL = Above Ground Level

Configuration	Weight	Failure Altitude	Initial Conditions	Flight Test Winds*
Flight Test	9.9 lbf	314 ft AGL	Hover	4 kt SW

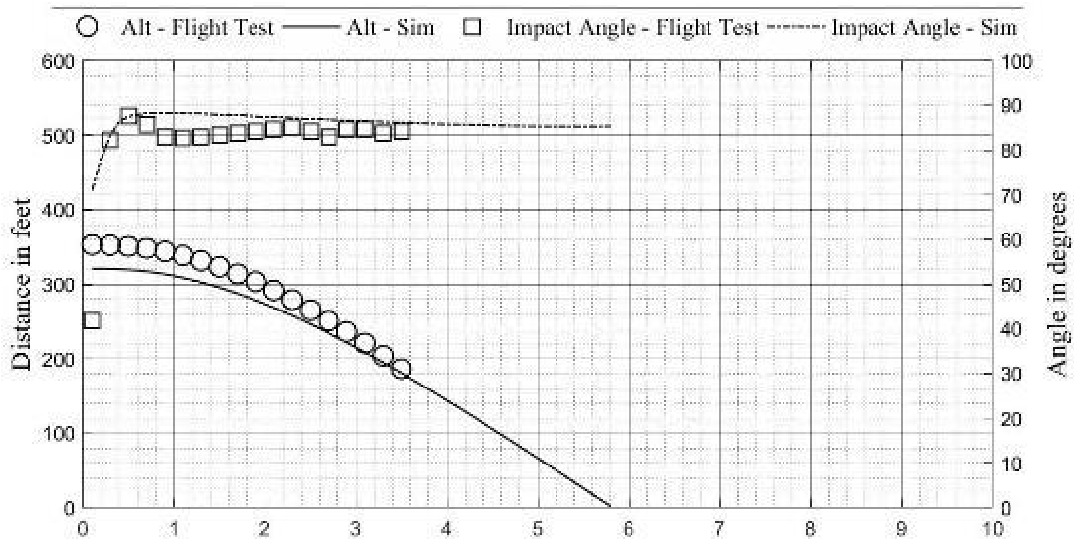

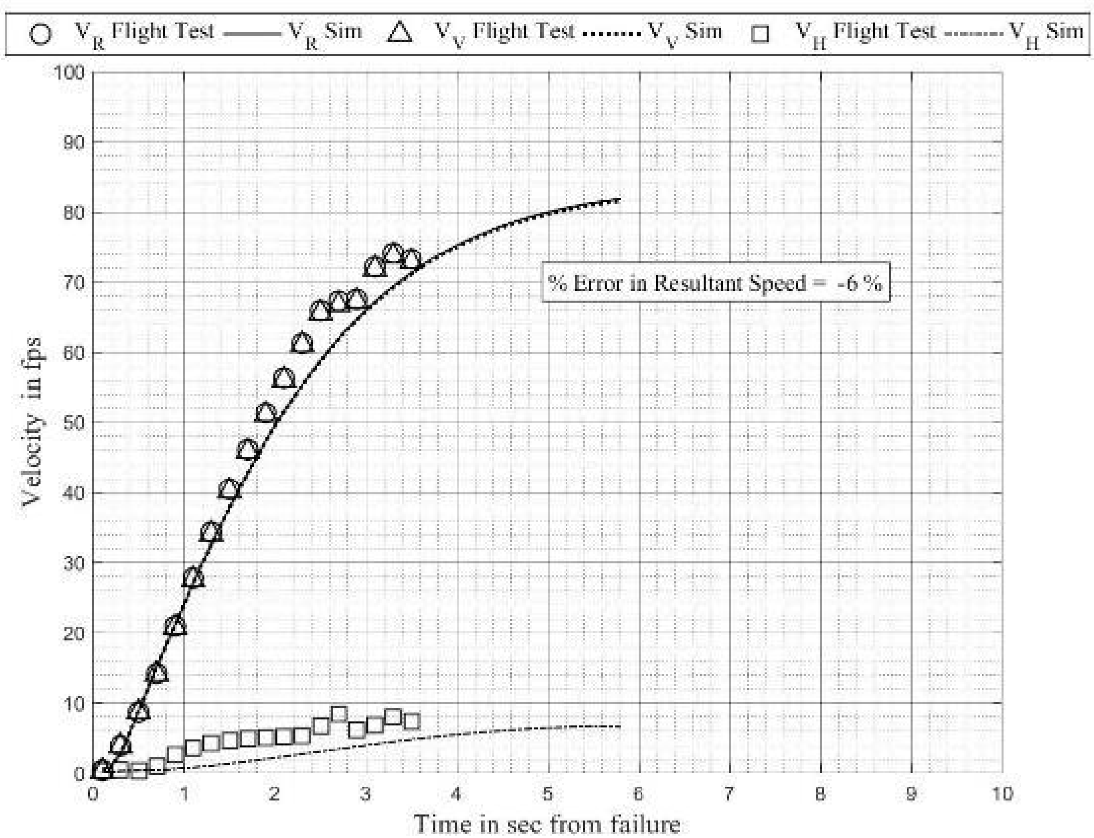

Figure B 37. DJI Inspire 2 Four Motor Failure at Hover

*Winds measured 20 feet AGL at a weather station less than three miles from flight test location

V_R = Resultant Speed
V_V = Vertical Speed
GS = Ground Speed
V_H = Horizontal GS
Alt = Altitude
Sim = Simulation
AGL = Above Ground Level

Configuration	Weight	Failure Altitude	Initial Conditions	Flight Test Winds*
Flight Test	9.9 lbf	341 ft AGL	66 ft/sec GS, level flight	4 kt SW

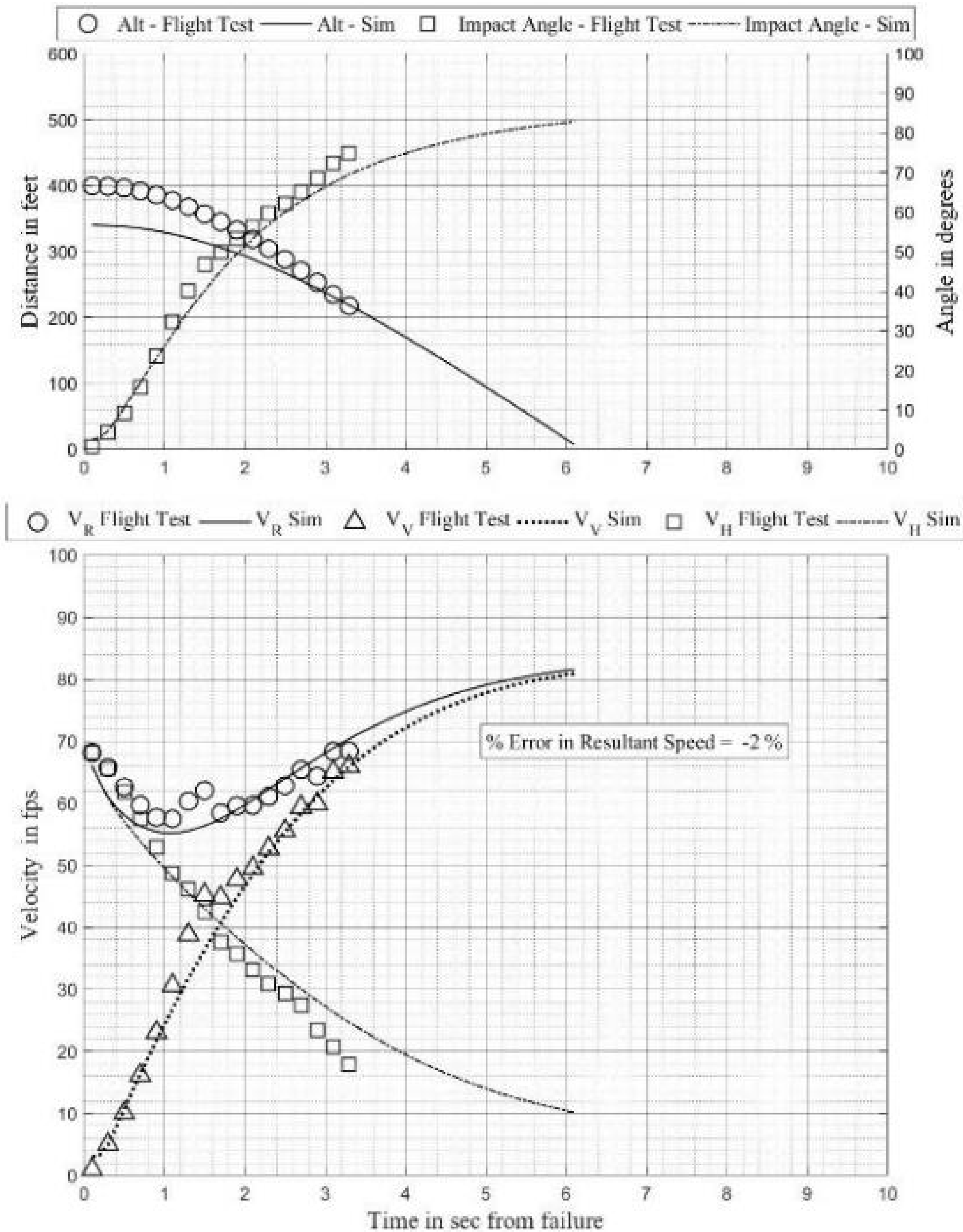

Figure B 38. DJI Inspire 2 Four Motor Failure at Maximum Stabilized Forward Speed

*Winds measured 20 feet AGL at a weather station less than three miles from flight test location

V_R = Resultant Speed | V_V = Vertical Speed | GS = Ground Speed
V_H = Horizontal GS | Alt = Altitude | Sim = Simulation
AGL = Above Ground Level

Configuration	Weight	Failure Altitude	Initial Conditions	Flight Test Winds*
Flight Test	5 lbf	400 ft AGL	Hover	8 kt N

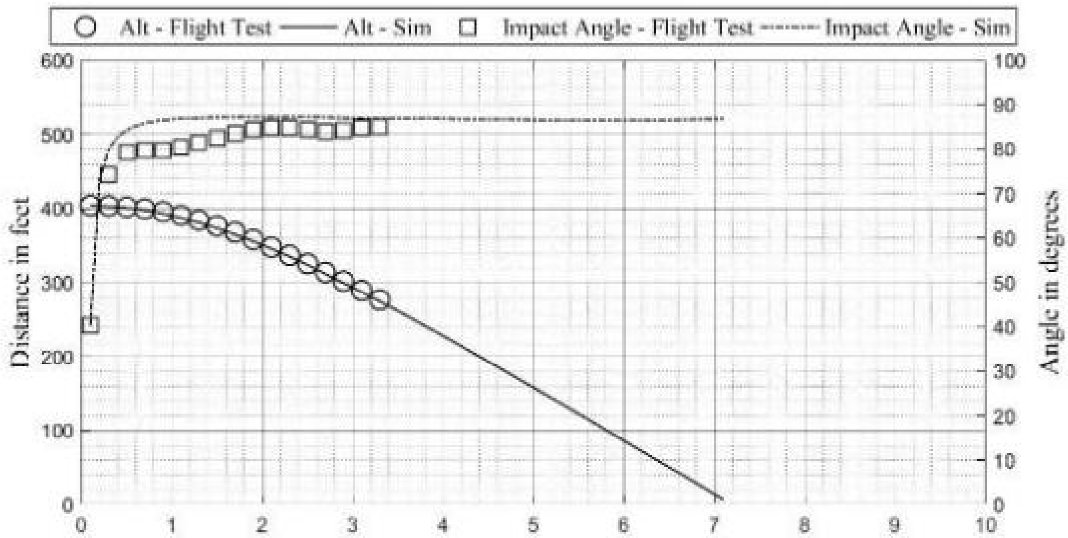

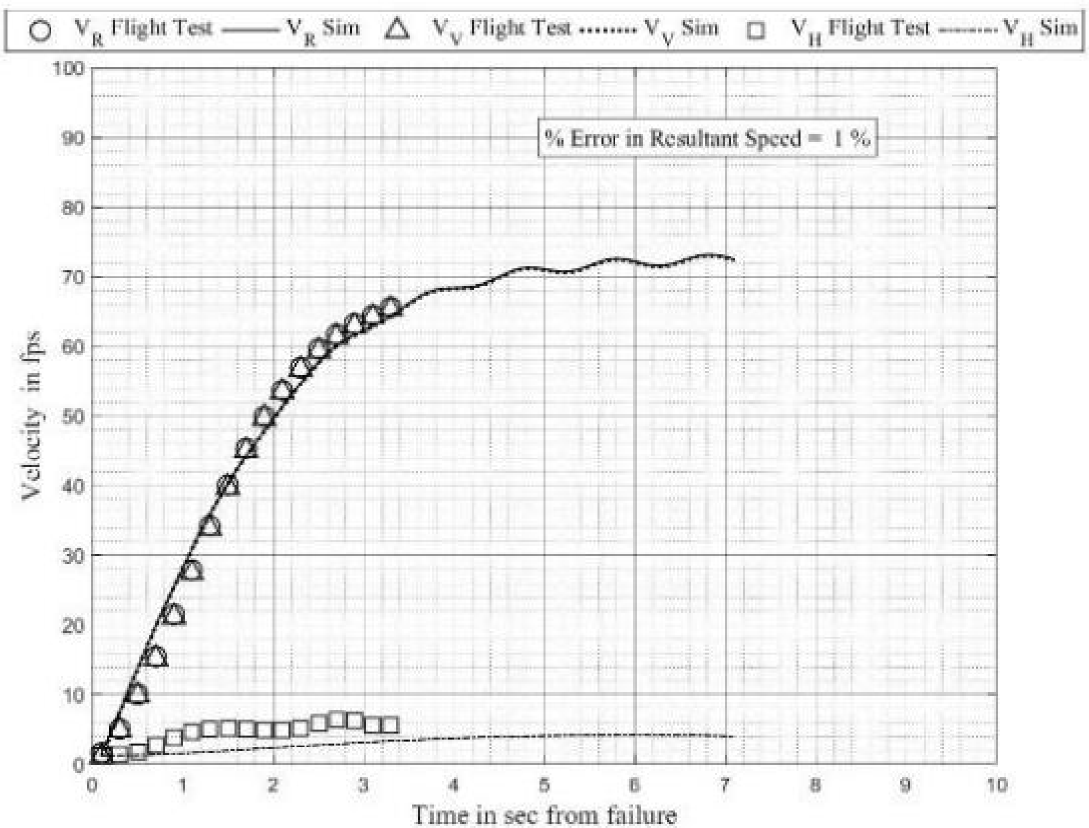

Figure B 39. GoPro Karma Four Motor Failure at Hover

*Winds measured 20 feet AGL at a weather station less than three miles from flight test location

V_R = Resultant Speed　V_V = Vertical Speed　GS = Ground Speed

V_H = Horizontal GS　Alt = Altitude　Sim = Simulation

AGL = Above Ground Level

Configuration	Weight	Failure Altitude	Initial Conditions	Flight Test Winds*
Flight Test	5 lbf	400 ft AGL	55 ft/sec GS, level flight	7 kt SW

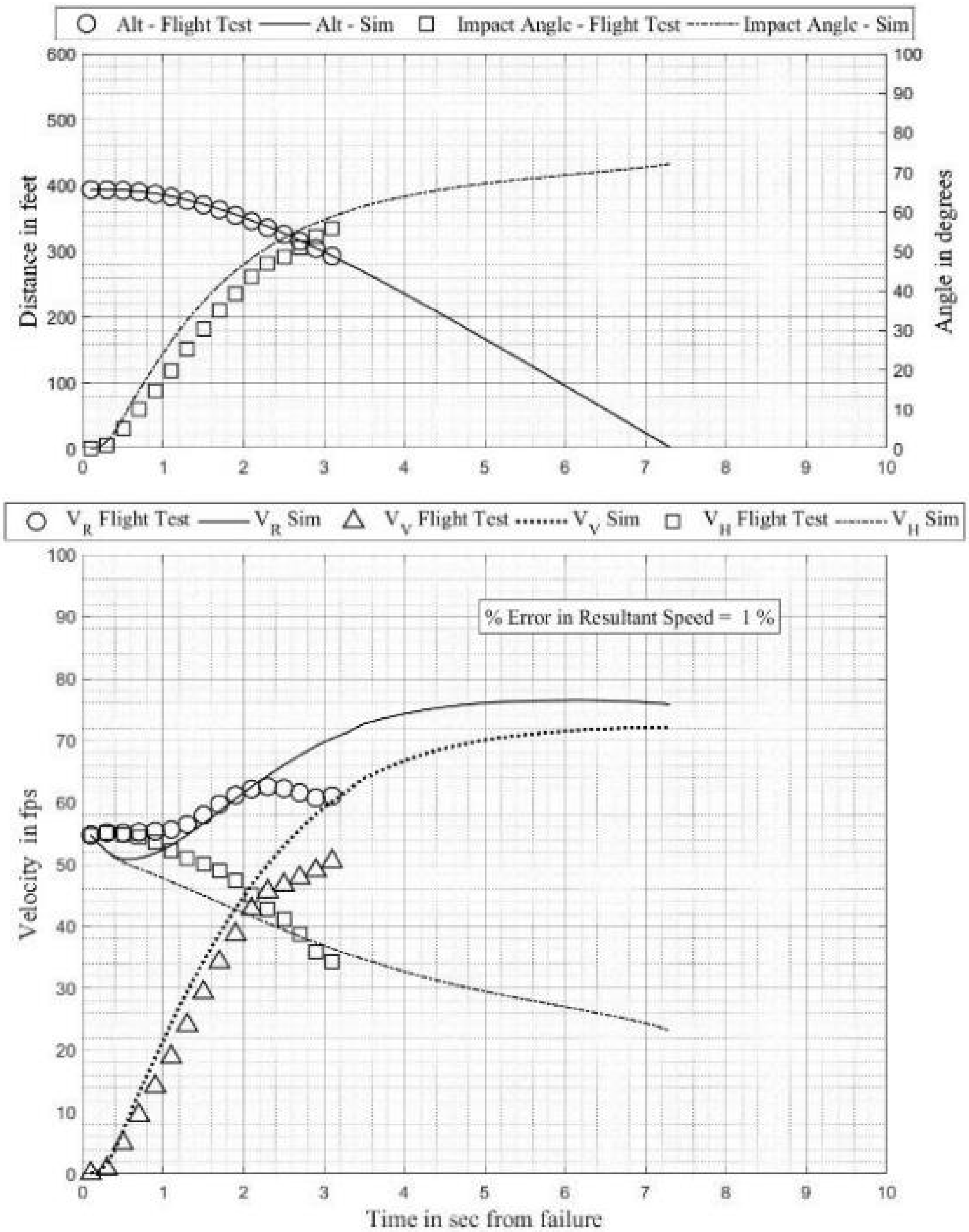

Figure B 40. GoPro Karma Four Motor Failure at Maximum Stabilized Forward Speed

*Winds measured 20 feet AGL at a weather station less than three miles from flight test location

V_R = Resultant Speed	V_V = Vertical Speed	GS = Ground Speed
V_H = Horizontal GS	Alt = Altitude	Sim = Simulation
AGL = Above Ground Level		

Configuration	Weight	Failure Altitude	Initial Conditions	Flight Test Winds*
Flight Test	5 lbf	374 ft AGL	Hover	5 kt SSE

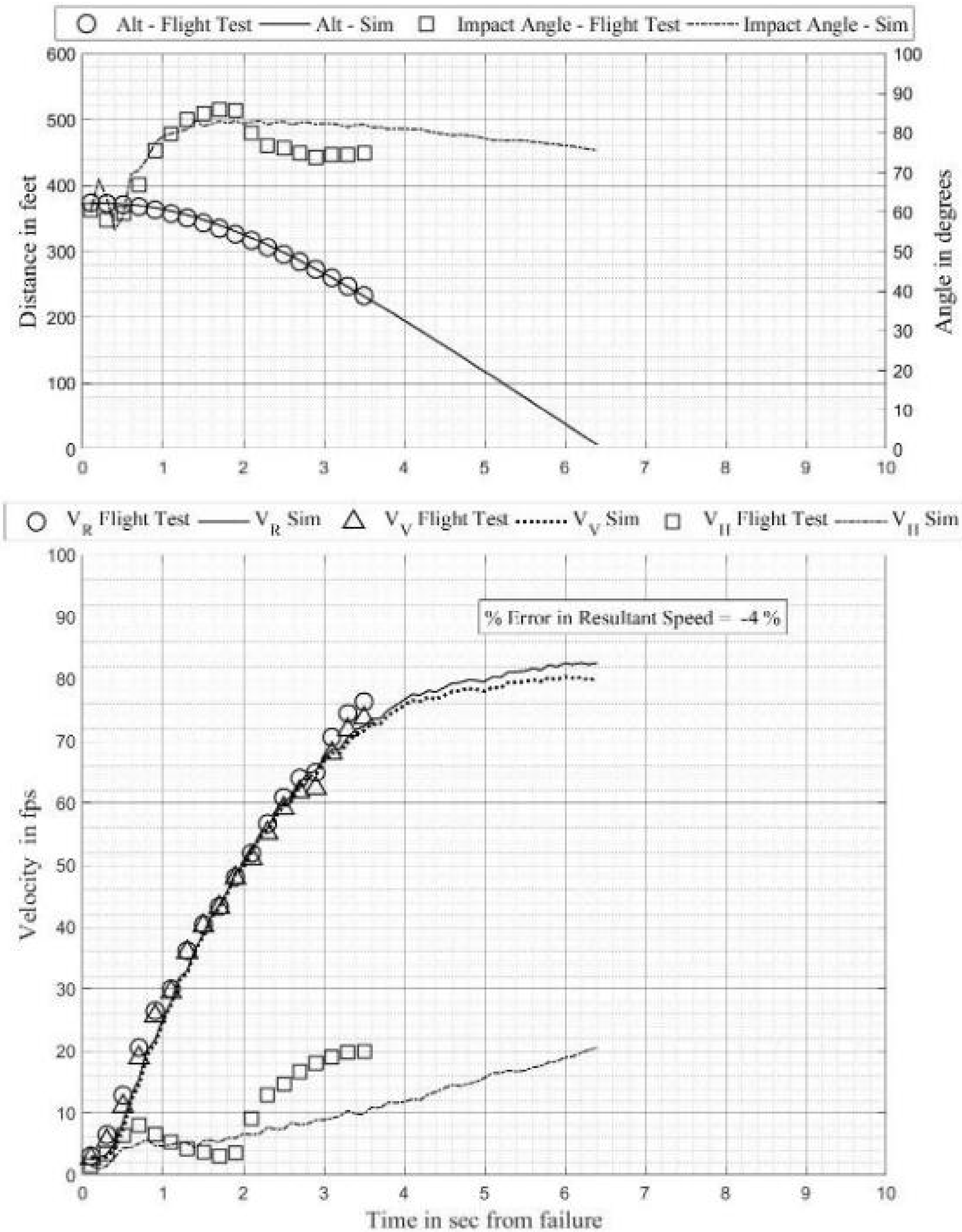

Figure B 41. GoPro Karma One Motor Failure at Hover

*Winds measured 20 feet AGL at a weather station less than three miles from flight test location

V_R = Resultant Speed
V_V = Vertical Speed
GS = Ground Speed
V_H = Horizontal GS
Alt = Altitude
Sim = Simulation
AGL = Above Ground Level

Configuration	Weight	Failure Altitude	Initial Conditions	Flight Test Winds*
Flight Test	5 lbf	388 ft AGL	66 ft/sec GS, level flight	6 kt SW

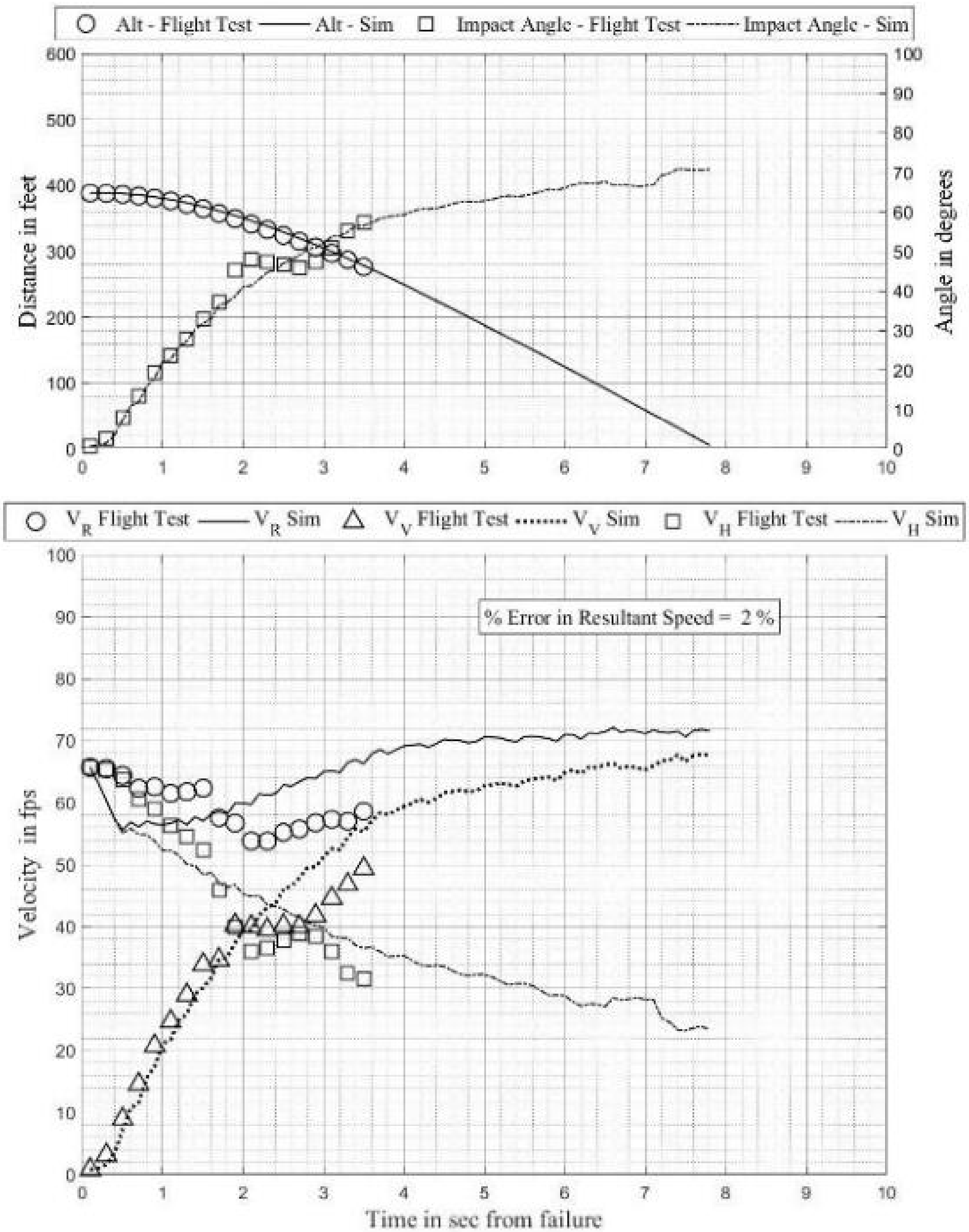

Figure B 42. GoPro Karma One Motor Failure at Maximum Stabilized Forward Speed

*Winds measured 20 feet AGL at a weather station less than three miles from flight test location

V_R = Resultant Speed
V_V = Vertical Speed
GS = Ground Speed
V_H = Horizontal GS
Alt = Altitude
Sim = Simulation
AGL = Above Ground Level

Configuration	Weight	Failure Altitude	Initial Conditions	Flight Test Winds*
Flight Test	5 lbf	290 ft AGL	Hover	5 kt NNW

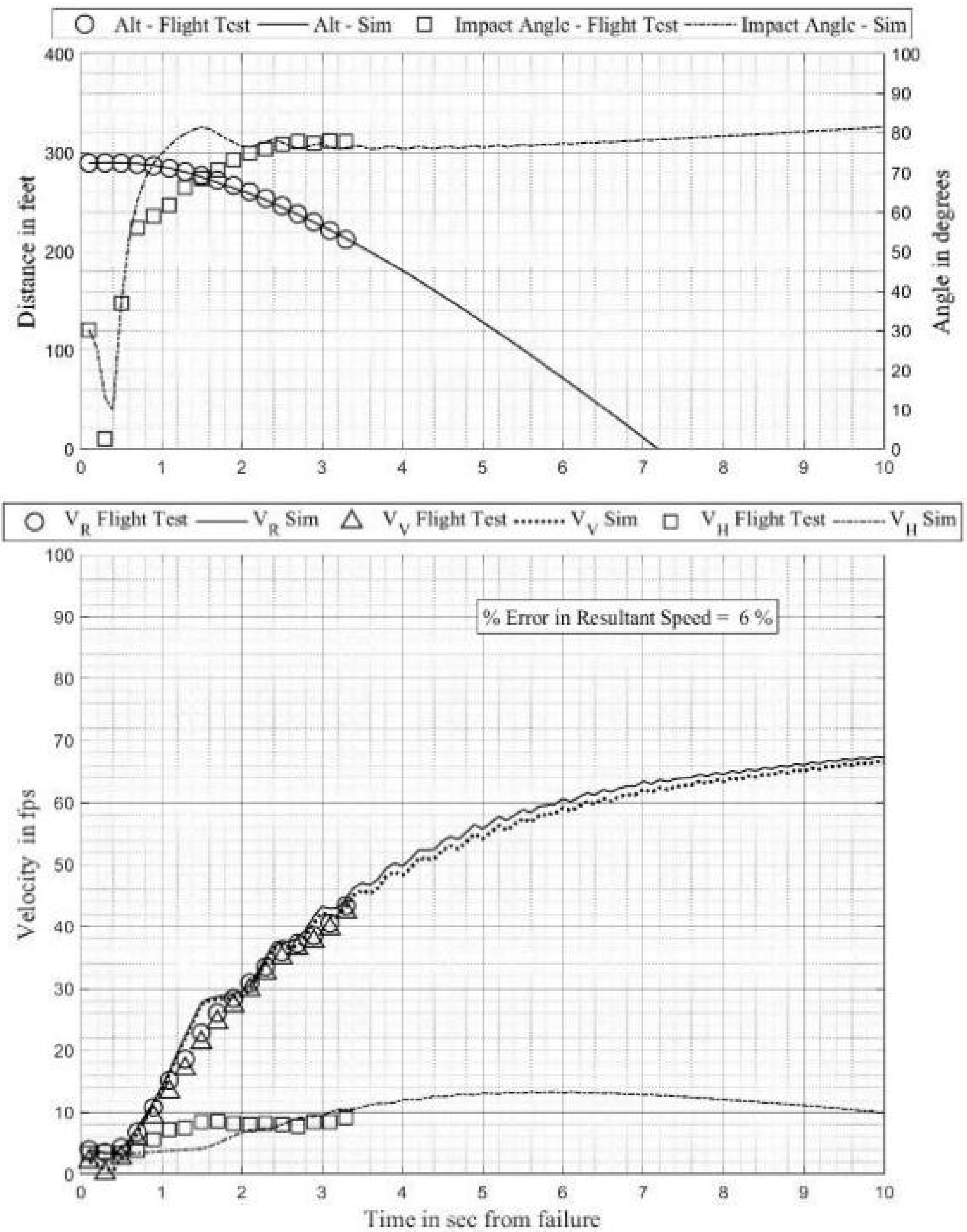

Figure B 43. GoPro Karma Two Motor (On-Axis) Failure at Hover

*Winds measured 20 feet AGL at a weather station less than three miles from flight test location

V_R = Resultant Speed
V_V = Vertical Speed
GS = Ground Speed
V_H = Horizontal GS
Alt = Altitude
Sim = Simulation
AGL = Above Ground Level

Configuration	Weight	Failure Altitude	Initial Conditions	Flight Test Winds*
Flight Test	5 lbf	420 ft AGL	60 ft/sec GS, level flight	7 kt SW

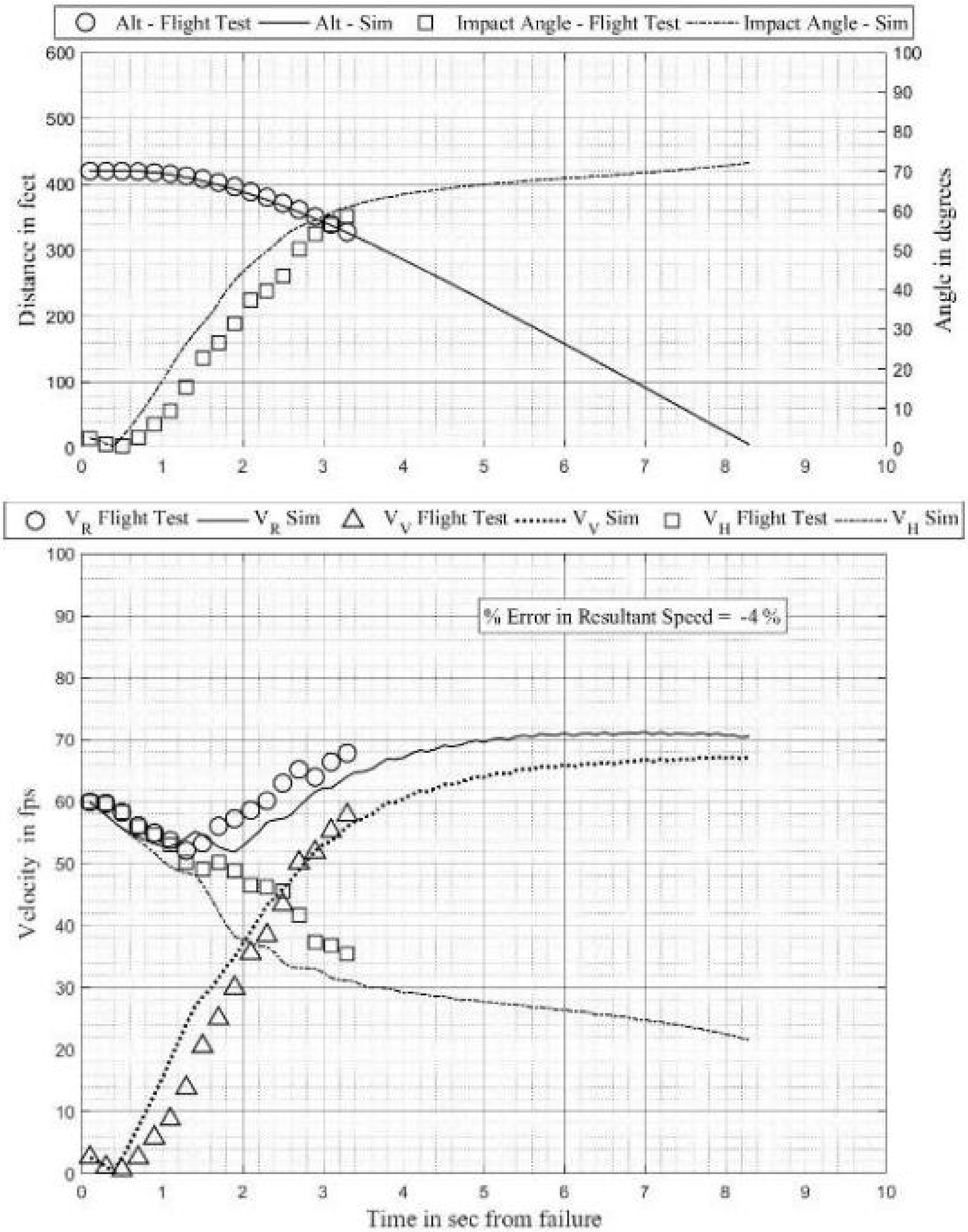

Figure B 44. GoPro Karma Two Motor (On-Axis) Failure at Maximum Stabilized Forward Speed

*Winds measured 20 feet AGL at a weather station less than three miles from flight test location

V_R = Resultant Speed | V_V = Vertical Speed | GS = Ground Speed

V_H = Horizontal GS | Alt = Altitude | Sim = Simulation

AGL = Above Ground Level

Configuration	Weight	Failure Altitude	Initial Conditions	Flight Test Winds*
Flight Test	5 lbf	326 ft AGL	Hover	Calm

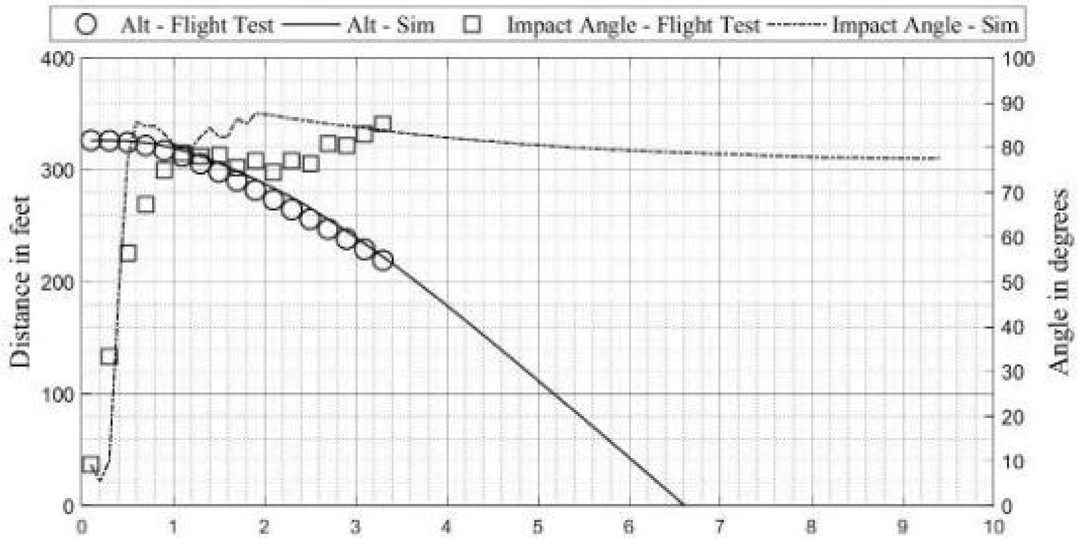

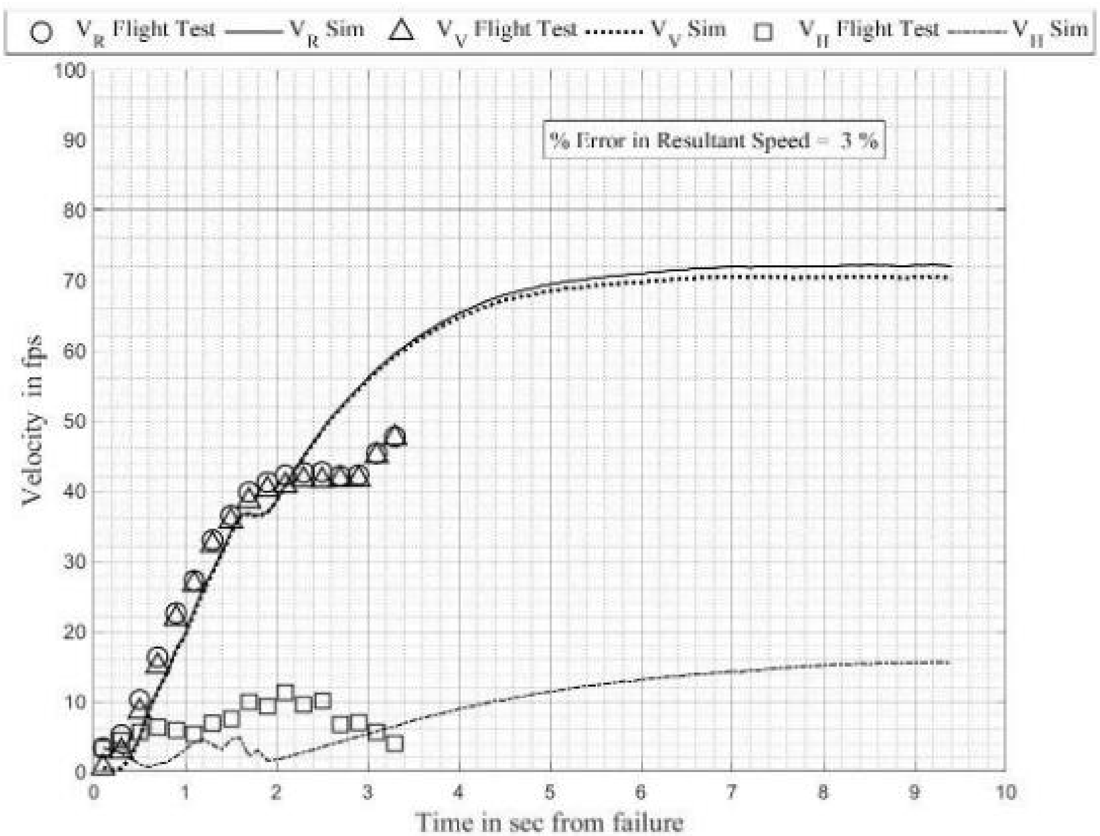

Figure B 45. GoPro Karma Two Motor (Off-Axis) Failure at Hover

*Winds measured 20 feet AGL at a weather station less than three miles from flight test location

V_R = Resultant Speed V_V = Vertical Speed   GS = Ground Speed
V_H = Horizontal GS   Alt = Altitude   Sim = Simulation
AGL = Above Ground Level

Configuration	Weight	Failure Altitude	Initial Conditions	Flight Test Winds*
Flight Test	5 lbf	430 ft AGL	58 ft/sec GS, level flight	8 kt SSW

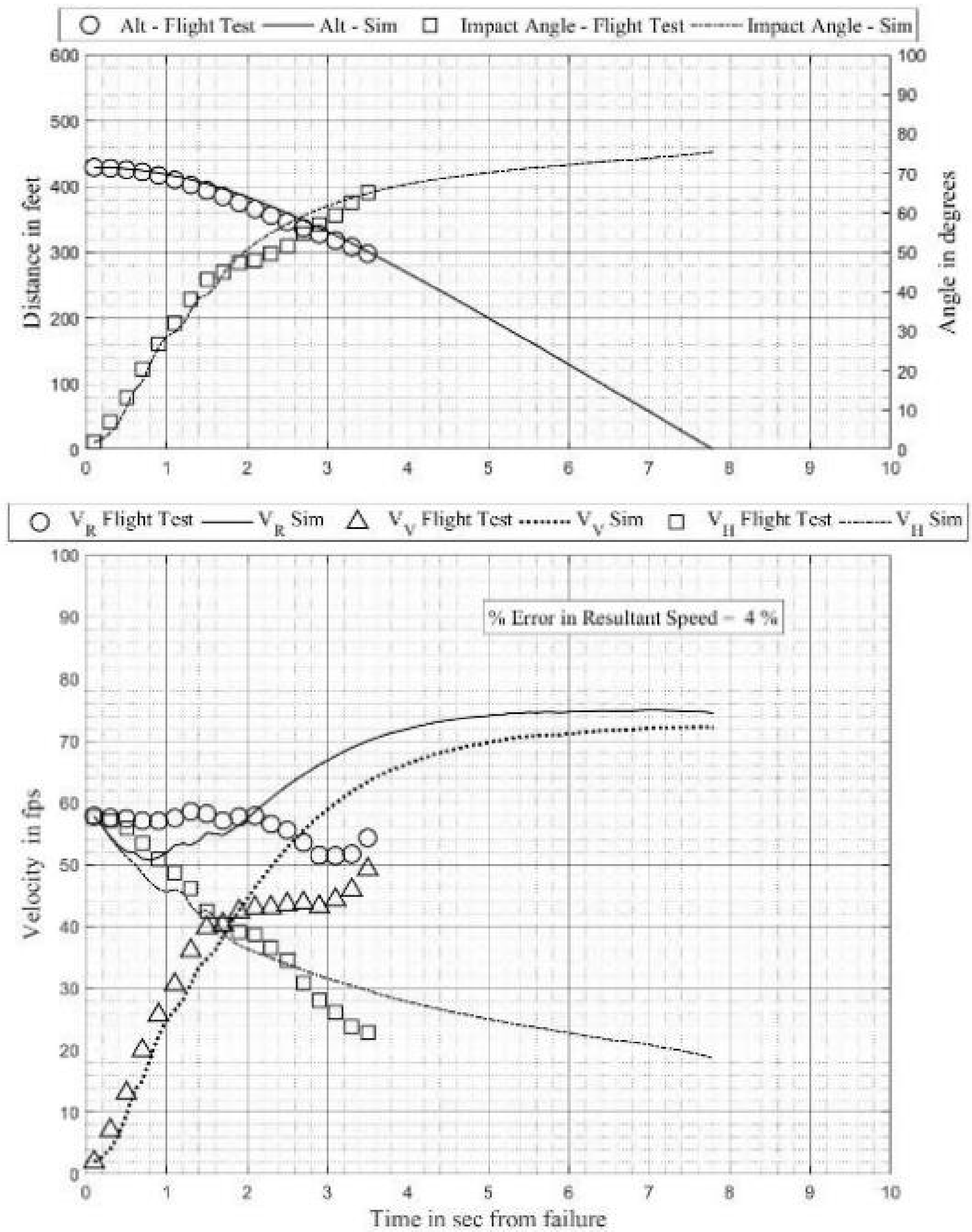

Figure B 46. GoPro Karma Two Motor (Off-Axis) Failure at Maximum Stabilized Forward Speed

*Winds measured 20 feet AGL at a weather station less than three miles from flight test location

V_R = Resultant Speed V_V = Vertical Speed GS = Ground Speed

V_H = Horizontal GS Alt = Altitude Sim = Simulation

AGL = Above Ground Level

Configuration	Weight	Failure Altitude	Initial Conditions	Flight Test Winds*
Flight Test	5.2 lbf	400 ft AGL	Hover	Calm Winds

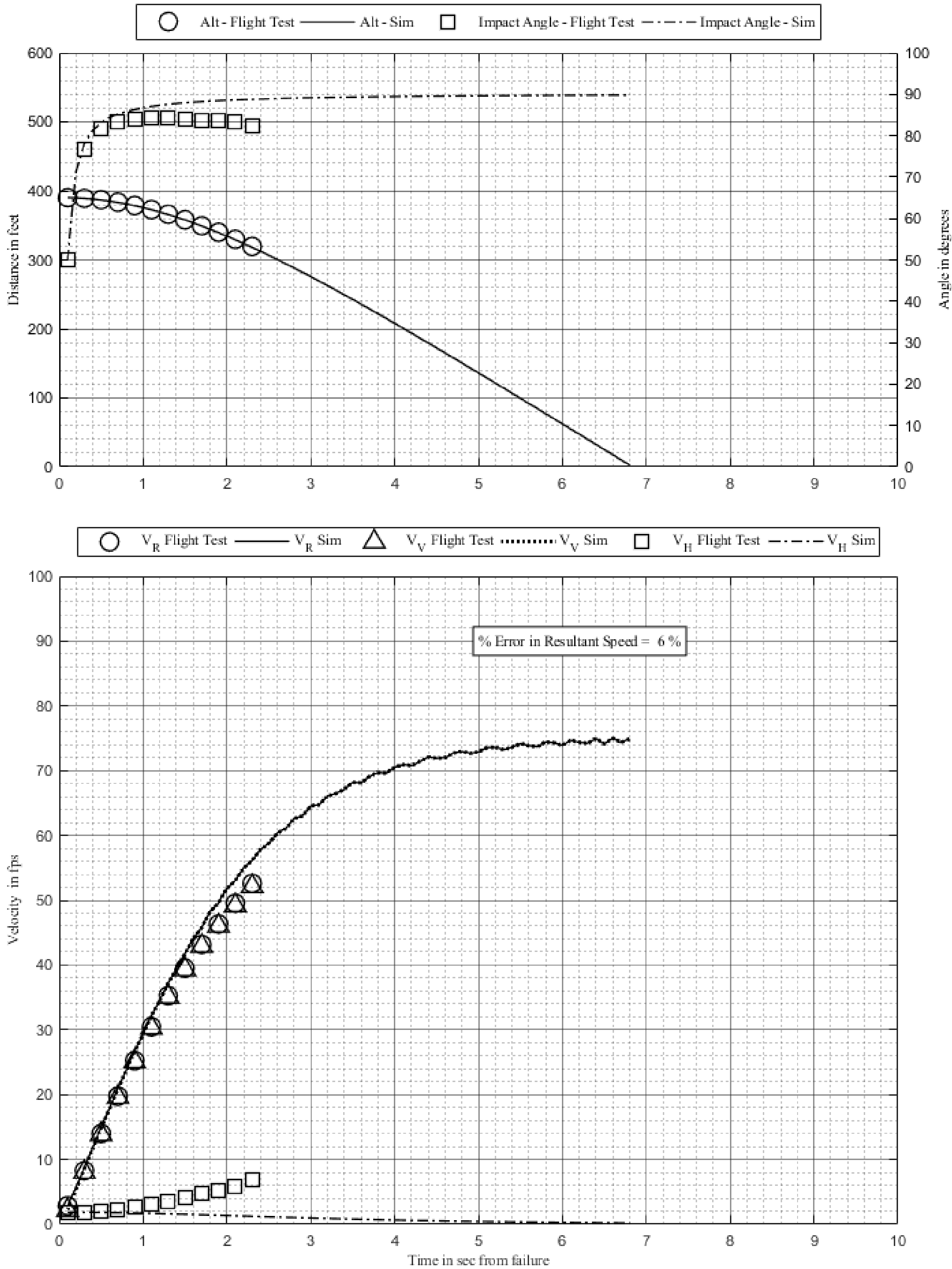

Figure B 47. Vendor 3 Quadrotor Four Motor Failure at Hover

*Winds measured 20 feet AGL at a weather station less than three miles from flight test location
V_R = Resultant Speed | V_V = Vertical Speed | GS = Ground Speed
V_H = Horizontal GS | Alt = Altitude | Sim = Simulation
AGL = Above Ground Level

Configuration	Weight	Failure Altitude	Initial Conditions	Flight Test Winds*
Flight Test	5.2 lbf	400 ft AGL	Hover	Calm Winds

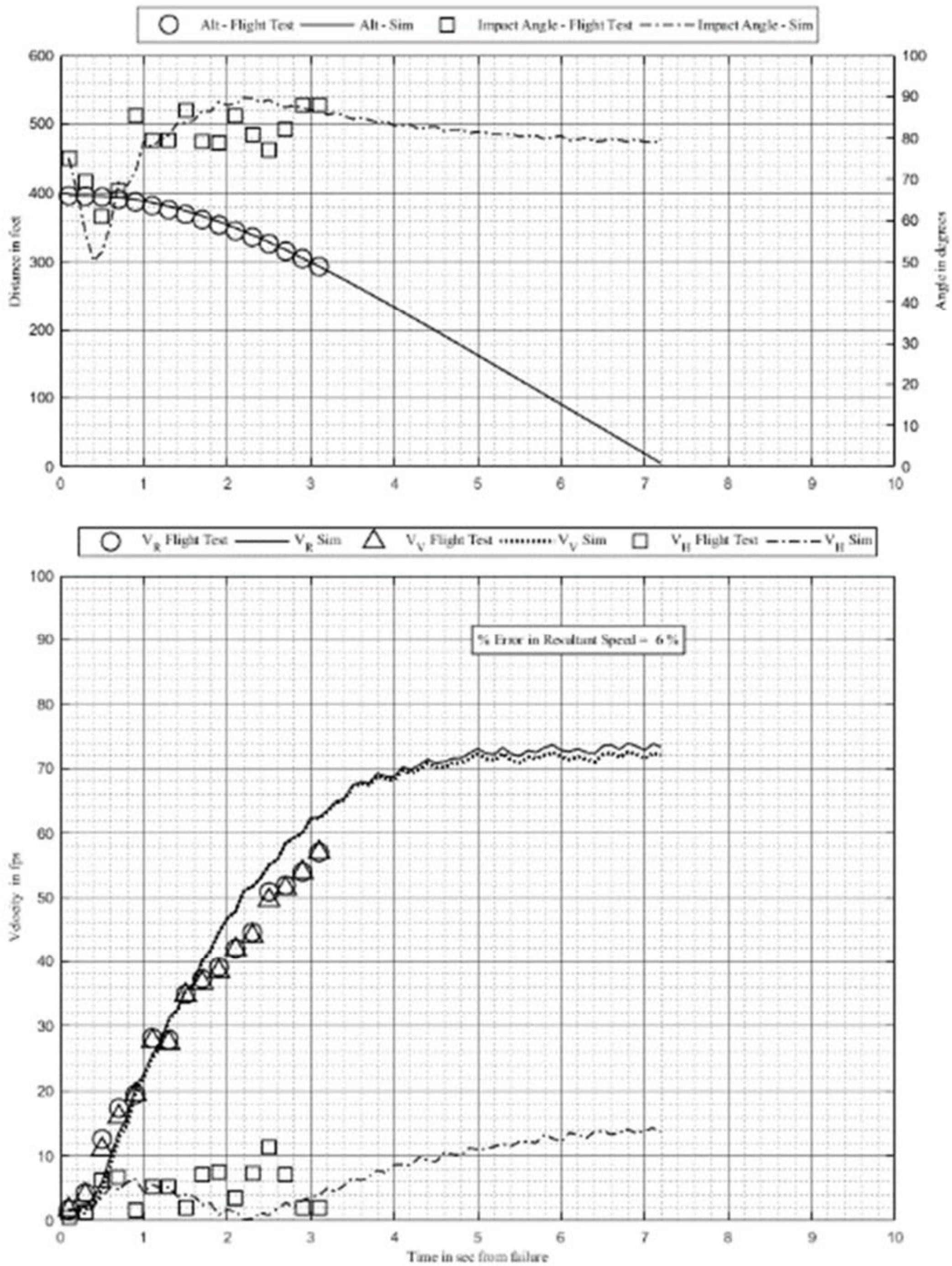

Figure B 48. Vendor 3 Quadrotor One Motor Failure at Hover

*Winds measured 20 feet AGL at a weather station less than three miles from flight test location

V_R = Resultant Speed | V_V = Vertical Speed | GS = Ground Speed
V_H = Horizontal GS | Alt = Altitude | Sim = Simulation
AGL = Above Ground Level

APPENDIX C – UAH SIMPLIFIED TEST STAND DETAILED DESCRIPTION

The upper support structure was designed to attach to an existing mezzanine mounted crane hoist structure at the UAH Aerophysics Research Center (Figure C 1). This crane hoist structure has a horizontal I-beam that could be rotated over the mezzanine railing to lift objects from the floor below. This I-beam provided a secure attachment point for the upper support structure that could withstand forces generated by the cable tension and the weight of the upper support structure. The upper support structure is a cantilever beam design to give the necessary clearance between the aircraft and structure when the aircraft is raised to its maximum height on the cables. The upper support structure was fabricated using MiniTec 45x45 UL Structural Aluminum T-Slot Framing. Eye bolts were installed on the front horizontal beam and used as the anchor points for the steel guide cables. A swivel pulley was installed at the center of this beam to guide the cable that was used to raise the sled. Crosshair laser pointers were mounted on the outside edges of the front horizontal beam pointing down at the floor to assist with aligning the lower support structure so the steel cables were mutually perpendicular to each structure. The installed upper and lower frames are shown in Figure C 2.

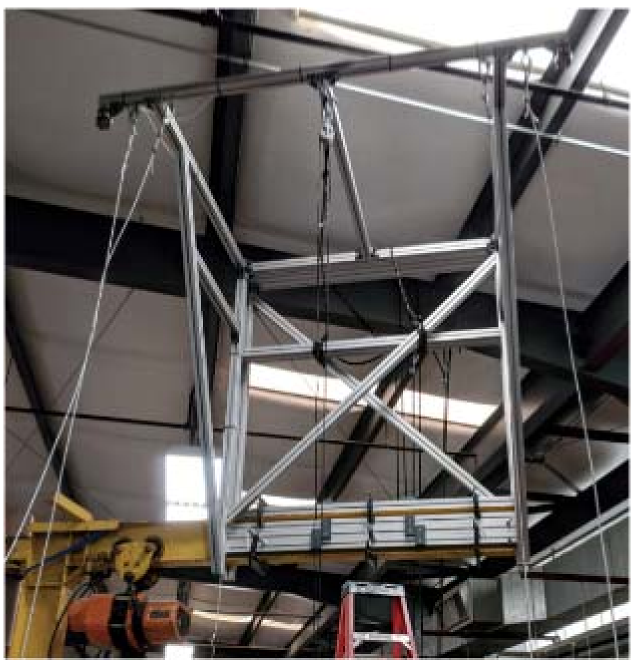

Figure C 1. Drop Stand Upper Frame Mounted on I-Beam

Figure C 2. Drop Stand without ATD Head Installed (Original Impact Columns)

The sled was fabricated using aluminum C channel, steel tubes, and MiniTec Structural Aluminum T-Slot Framing (Figure C 3). Steel tubes were used as the bearing guide surfaces for the sled to traverse along the cables. The 1/4" inside diameter of the tubes was larger than the 3/16" outside diameter of the steel cables which provided a loose enough clearance for minimizing friction, yet a tight enough clearance to prevent the sled from pitching fore and aft on the cables. The sled was installed on the steel guide cables before the guide cables were connected to the lower support structure. A single eyebolt was installed on the top of the sled to provide an attachment point for the Sea Catch TR3-RL load release mechanism. A set of spring clamps, fabricated from aluminum angle extrusion and torsion springs were used to secure the aircraft to the sled. The spring clamp design was modeled from a similar design used by NIAR. A piece of MiniTec T-slot extrusion was bolted to the bottom of the C channel to provide adjustable width spacing for the spring clamps. When the sled collides into the PVC columns installed on the lower support structure, the inertia of the aircraft pulls the aircraft out of the torsion spring clamps and allows it to freefall into the head.

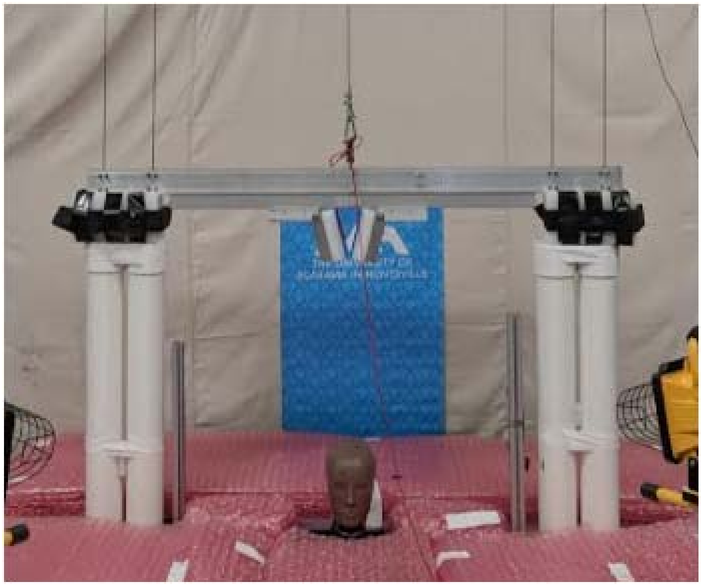

Figure C 3. Drop Sled, Spring Clamp Releases, and Column Supports

The lower support structure was also fabricated using MiniTech 45x45 UL Structural Aluminum T-Slot Framing. Eye bolts were installed on the center horizontal beam and used as the anchor points for the steel guide cables. Turnbuckles were attached to the eye bolts and used to tension the steel cables. The lower support structure was secured to the floor using 600 lbf of sand bags distributed on each side of the structure. 3/16" diameter steel cables were connected to the upper and lower support structures, tensioned, and used as guide cables for the sled to travel along. Each steel cable was routed through a 4" diameter PVC pipe, 48" in length, prior to attaching the cable to the base. These PVC pipes stood as vertical columns for the sled to collide into and initiate the release of the aircraft. Blocks of EPP foam 8" thick were installed on the top of the columns to absorb some of the energy from the sled impact.

A separate steel cable was routed through the pulley on the upper support structure and down to the sled to be used for hoisting. At this end of the cable, the Sea Catch load release mechanism was attached to the steel cable and the release jaws were closed around the eye bolt on the top of the sled. This steel cable is used to pull the sled assembly to the desired drop height and then tied off to a rigid structure. A rope attached to the release lever on the Sea Catch is pulled to release the sled from the steel hoist cable to permit freefall along the steel guide cables.

The head assembly mount was fabricated using MiniTec 45x45 UL Structural Aluminum T-Slot Framing, a 29" diameter aluminum plate with a thickness of 1.5", and an aluminum cylinder 5" in diameter and 4" in height (Figure C 4). The head and neck assembly was bolted to the cylinder and the other side of the cylinder was bolted to the 29" diameter aluminum plate. The purpose of the cylinder was to add additional height to the head/neck assembly so the sand bags used to weigh down the head assembly mount would not obscure the view of the high speed cameras. The large diameter aluminum plate was used to provide a rigid mounting surface that would not deform when impacted. The large diameter also provided a large bearing area for the attachment of the MiniTec horizontal beams. These horizontal beams provided additional surface area to lay the sand bags that were used to keep the head assembly from moving during impacts. Adjustable, self-leveling feet were installed on the bottom of the horizontal beams to raise the entire head assembly mount above the horizontal beam of the lower support structure to prevent vibrations from being transferred to the head caused by the sled colliding into the columns.

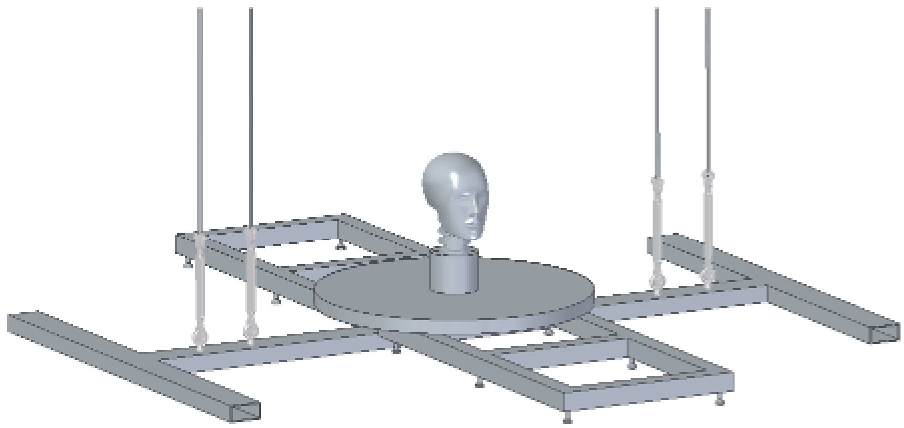

Figure C 4. Test Stand Base and ATD Head Mount

The Simplified Test Method Test Apparatus used at UAH was designed based on the facilities and structures available. While this solution worked well, a more universal vertical test stand could have been constructed using scaffold towers. A pair of towers would be positioned some distance apart, far enough to accommodate the maximum width of the aircraft to be tested, with a horizontal beam that would bridge the two towers at the top to serve as the attachment point for the steel guide cables. The lower support structure, sled, and head assembly mount designs used in the UAH Simplified Test Apparatus could be used in this configuration. Two 25' non-rolling scaffold towers retails for less than $1800[20], which is comparable to the cost of materials used in the UAH upper support structure design.

The spring clamps used to secure the aircraft to the sled worked well for most aircraft, but required significant amounts of time adjusting the proper spacing to give the desired release characteristics. Additionally, small differences in spring constants between each clamp resulted in different clamping forces on each side of the aircraft. This would allow the aircraft to start rotating as it fell from the clamps which would give a non-desirable impact orientation. To mitigate this problem, linear actuators could be used to provide the clamping force on the aircraft. The linear actuators could be triggered to open by a laser gate set at some distance above the columns to release the aircraft from the sled prior to the sled colliding into the columns.

The high speed cameras, sled release, and DAQ record start events were all triggered manually for the UAH Simplified Testing. This setup required a minimum of 3 people for each test to be

[20] 1) https://www.scaffoldexpress.com/25-Non-Rolling-Scaffold-Tower-p/psv-nrt-25.htm

conducted. This was a significant burden on coordinating schedules and personnel available considering the large test matrix that was to be completed. The personnel required for testing could be reduced to a single person if the DAQ and camera record start events were triggered via laser gates, or other sensors, positioned at different points along the steel guide cables, and the sled release was done by a remotely controlled servo or solenoid actuator.

The total cost of the test stand was approximately $54,500.00. These costs include in excess of $35,000 for an ATD Hybrid III head and neck, $16,800 for a National Instruments data acquisition system, $1,400.00 for MiniTech extrusions and hardware, and roughly $950.00 in additional materials and supplies.

APPENDIX D – DJI PHANTOM 3 SIMPLIFIED AND FULL ATD TEST DATA

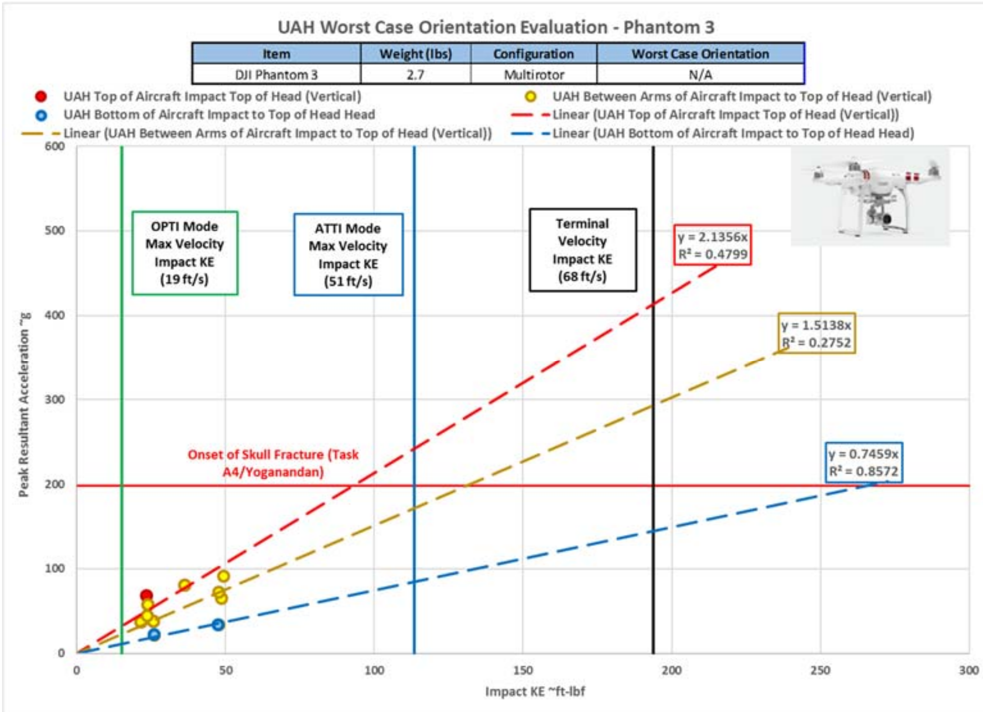

Figure D 1. UAH Worst Case Orientation Evaluation - DJI Phantom 3

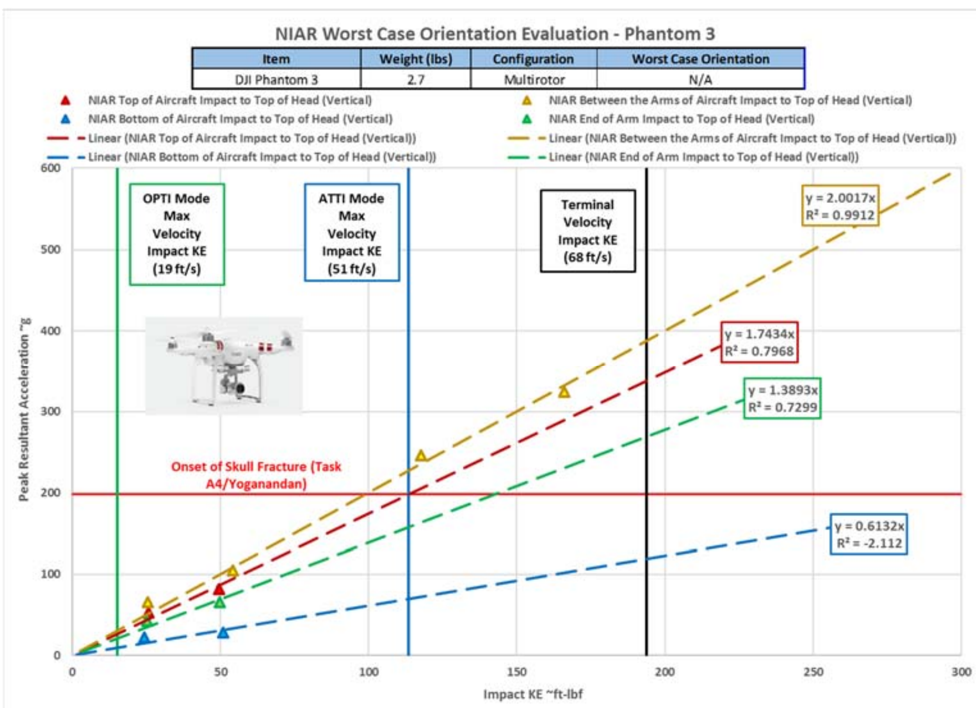

Figure D 2. NIAR Worst Case Orientation Evaluation - DJI Phantom 3

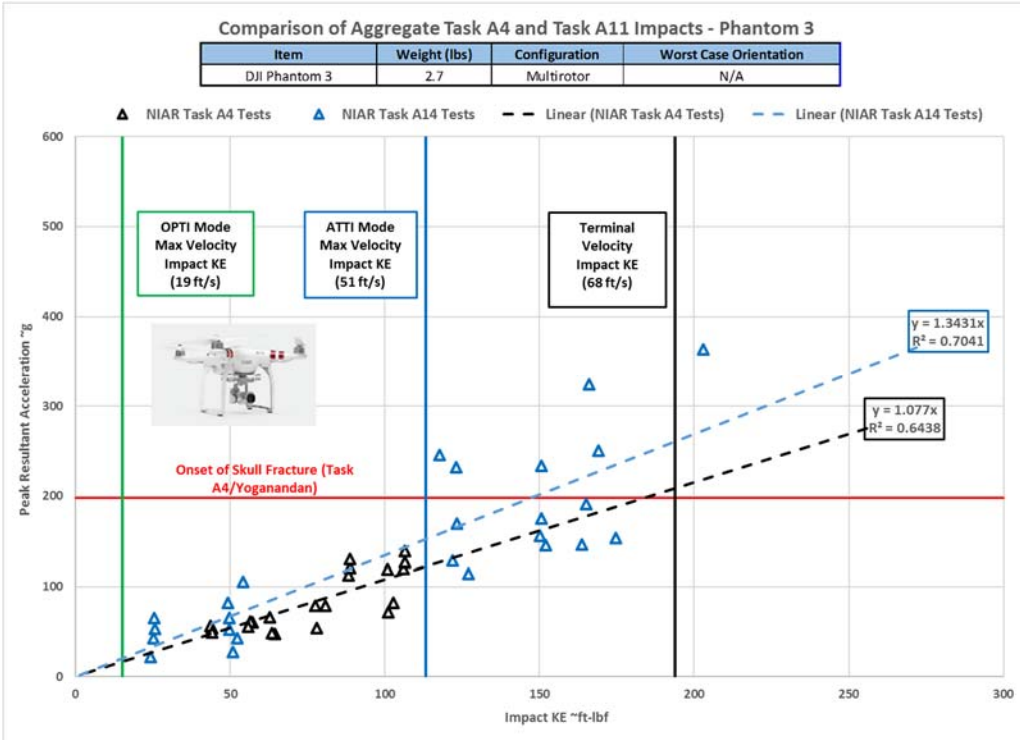

Figure D 3. UAH vs. NIAR Data Comparison - DJI Phantom 3

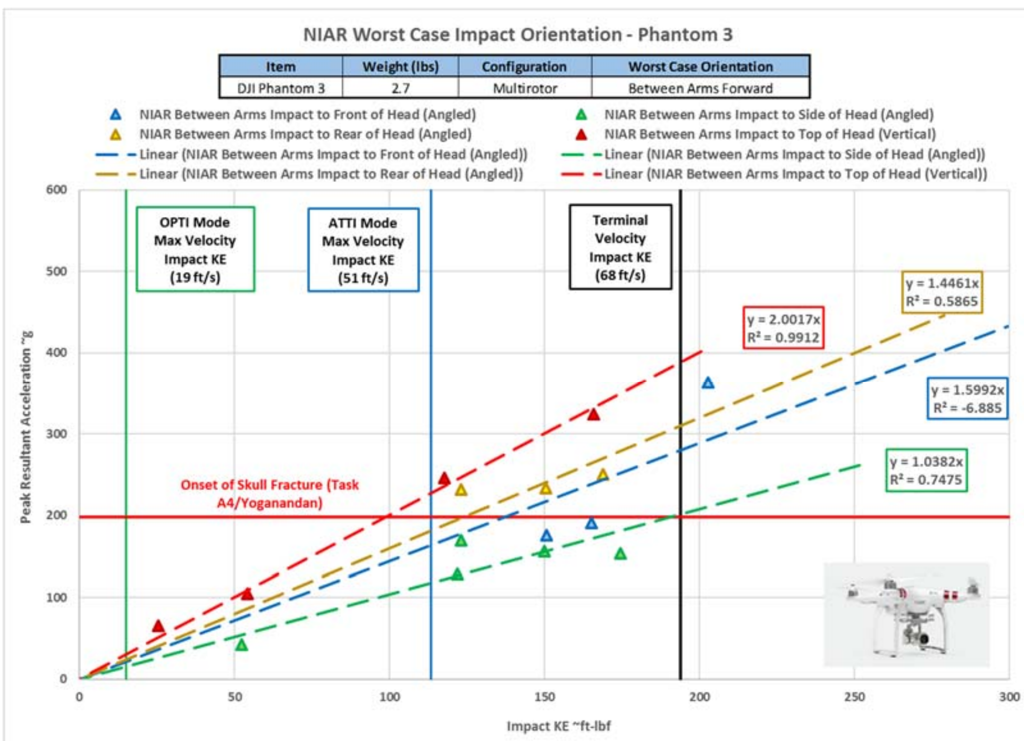

Figure D 4. NIAR Worst Case Impact Evaluation - DJI Phantom 3

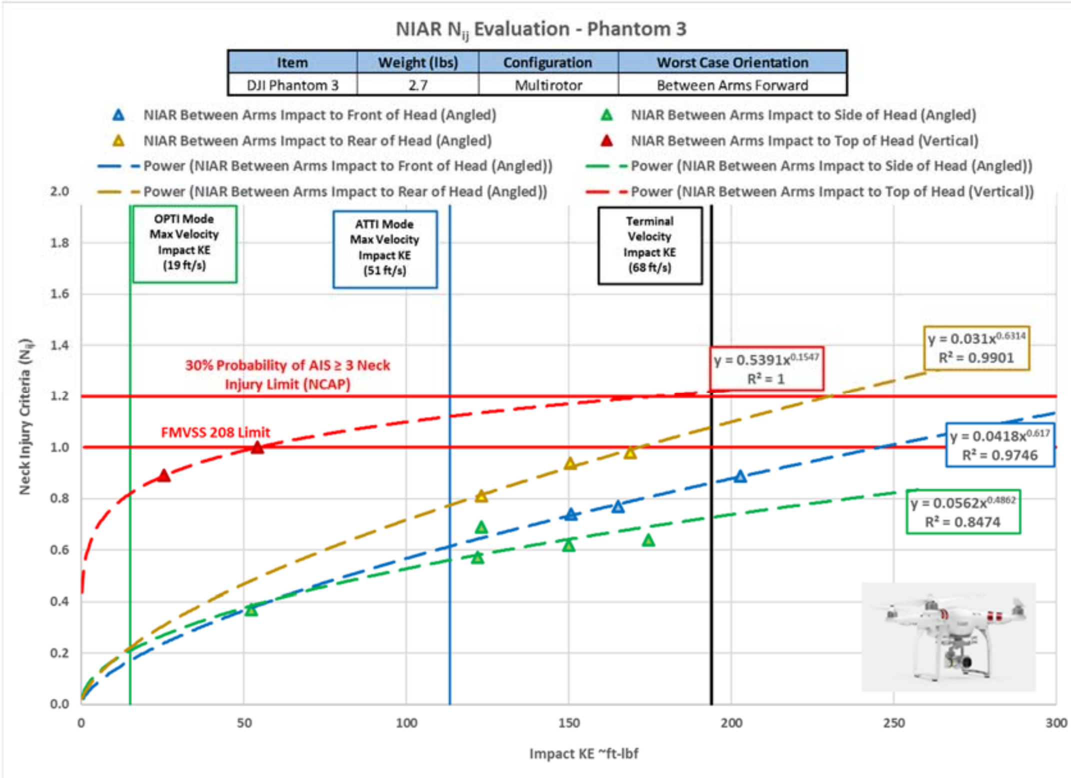

Figure D 5. NIAR N_{ij} Evaluation - Phantom 3

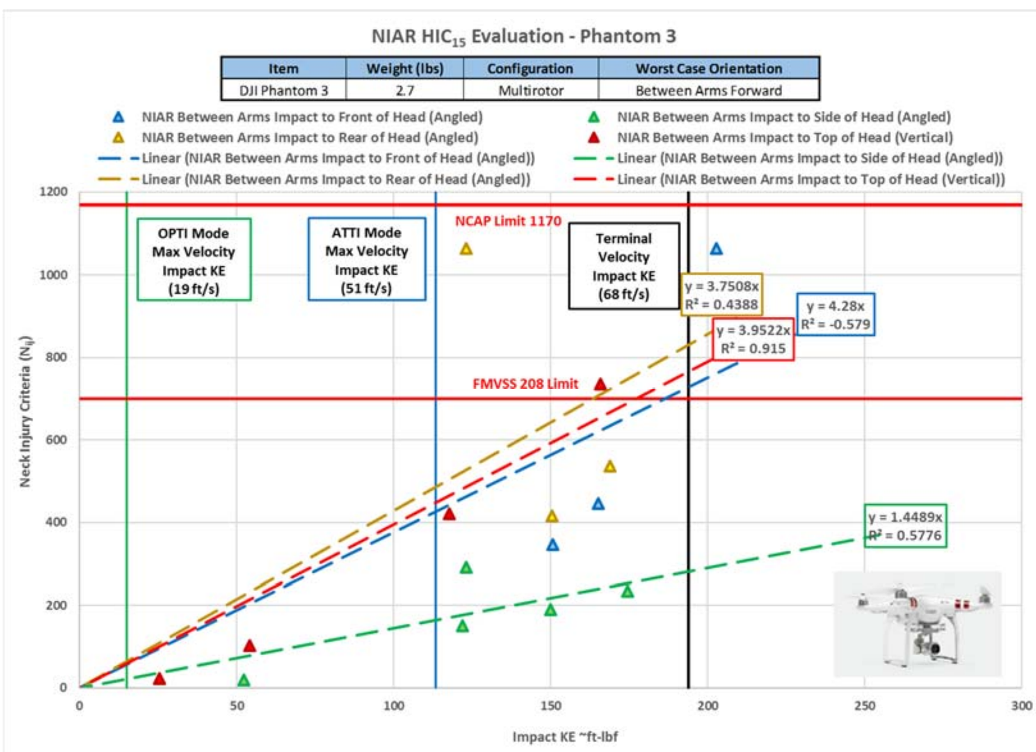

Figure D 6. NIAR HIC_{15} Evaluation - Phantom 3

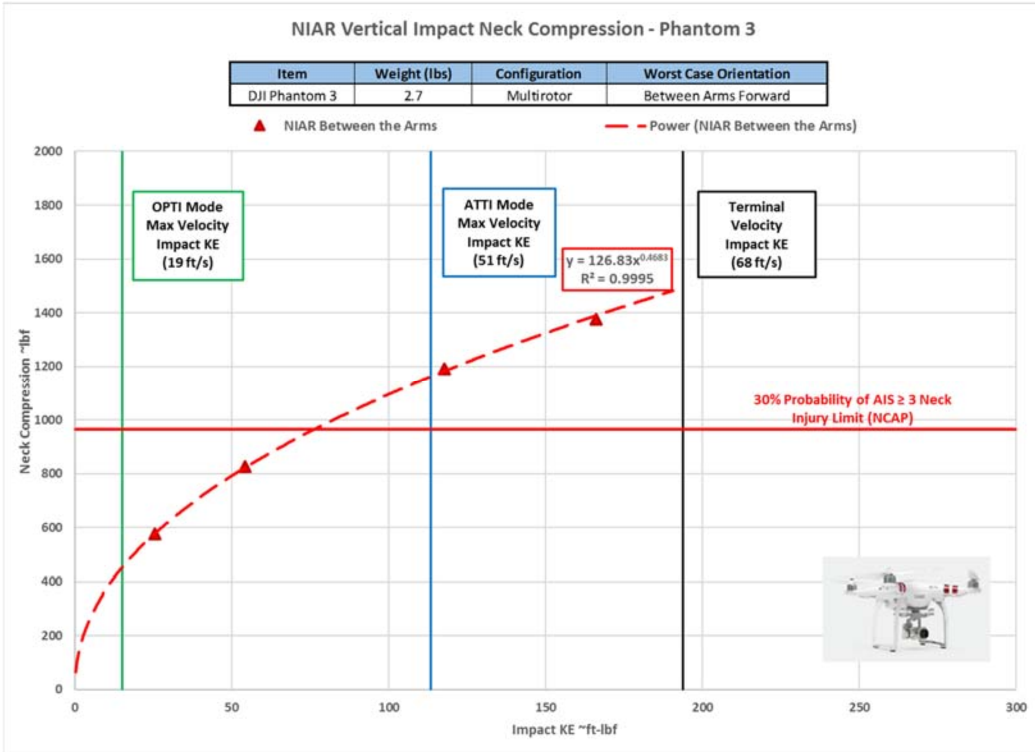

Figure D 7. NIAR Vertical Impact Neck Compression - DJI Phantom 3

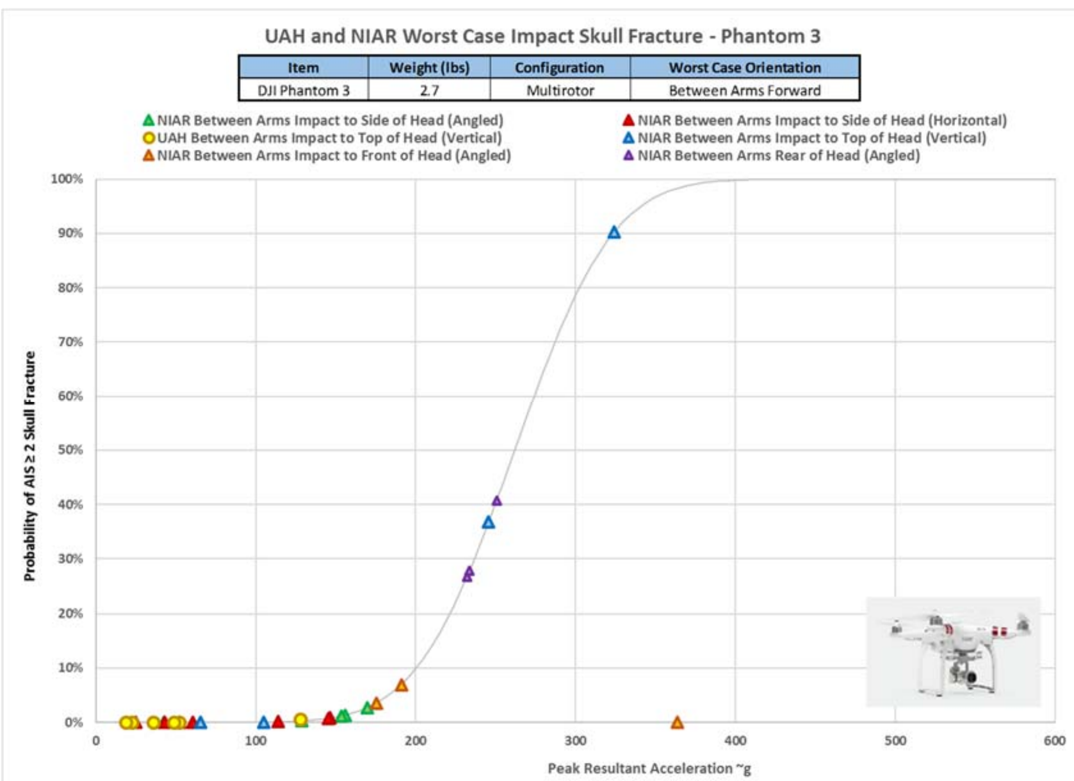

Figure D 8. UAH and NIAR Worst Case Impact Skull Fracture - DJI Phantom 3

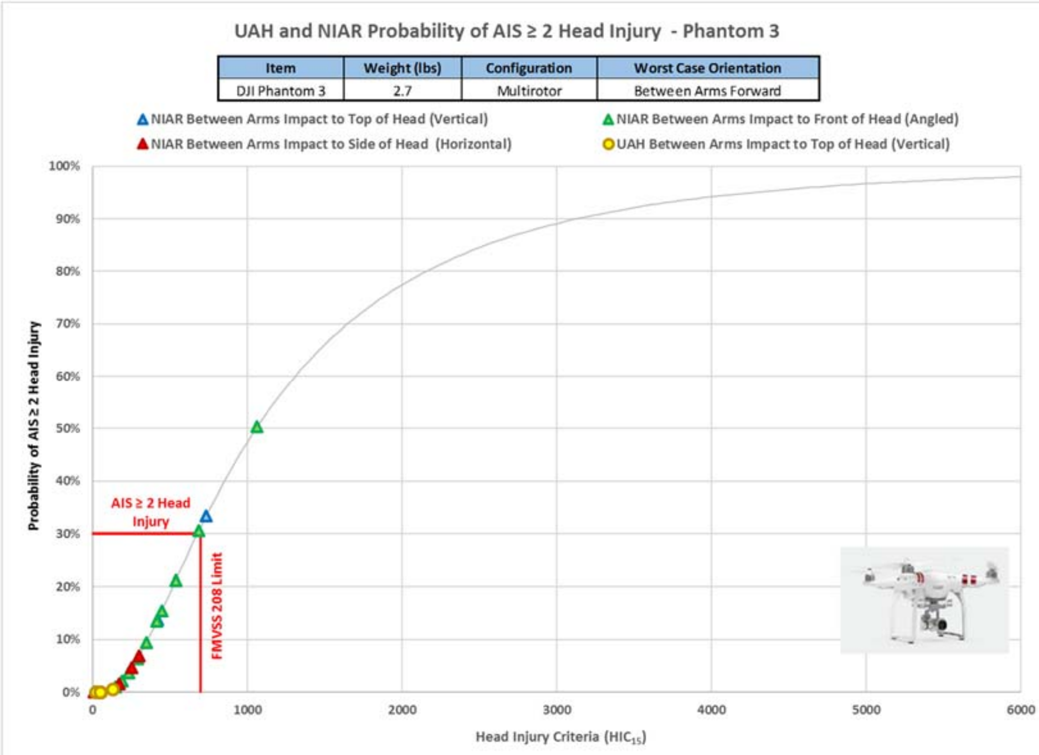

Figure D 9. UAH and NIAR Probability of AIS ≥ 2 Head Injury - DJI Phantom 3

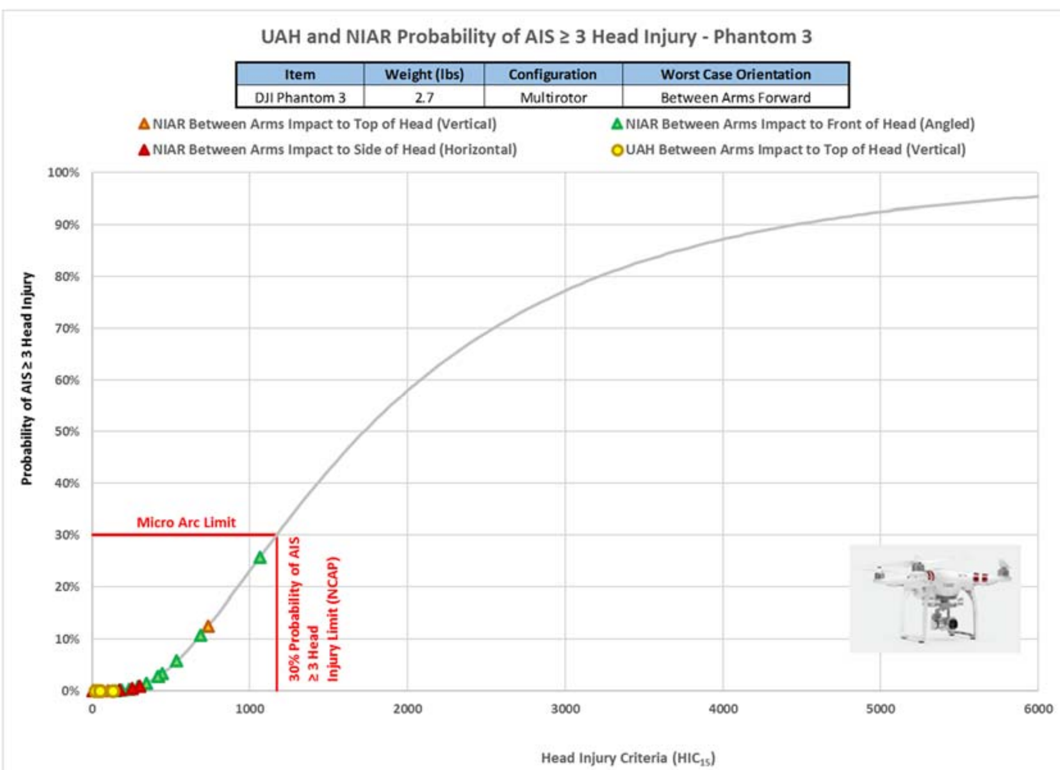

Figure D 10. UAH and NIAR Probability of AIS ≥ 3 Head Injury - DJI Phantom 3

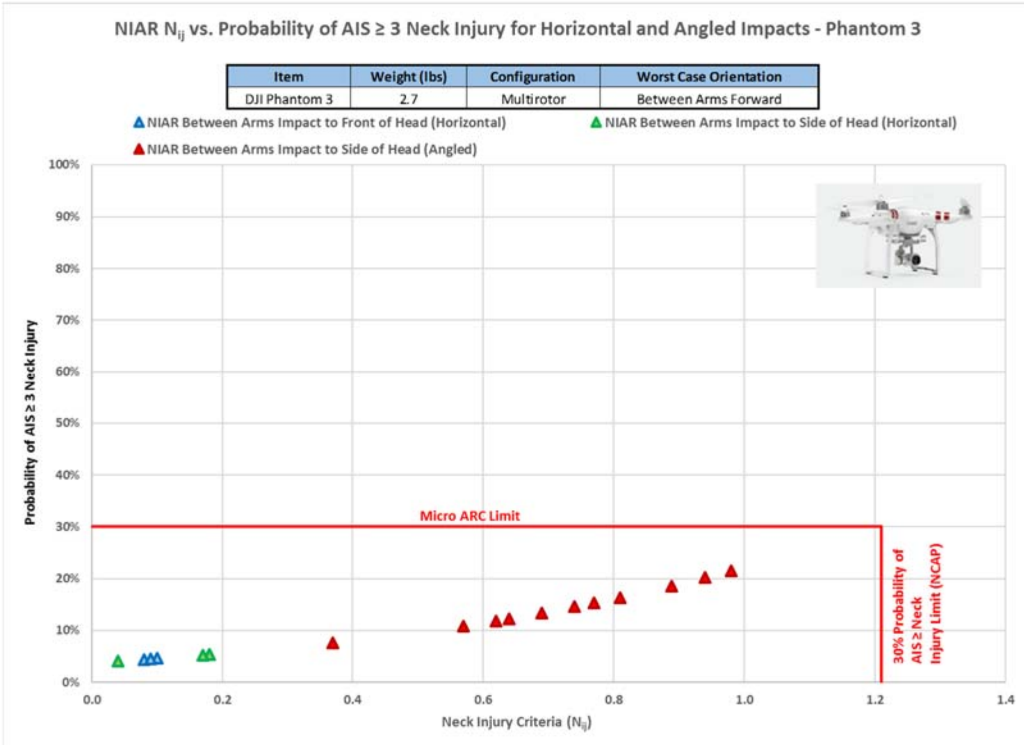

Figure D 11. NIAR N_{ij} vs. Probability of AIS ≥ 3 Neck Injury for Horizontal and Angled Impacts - DJI Phantom 3

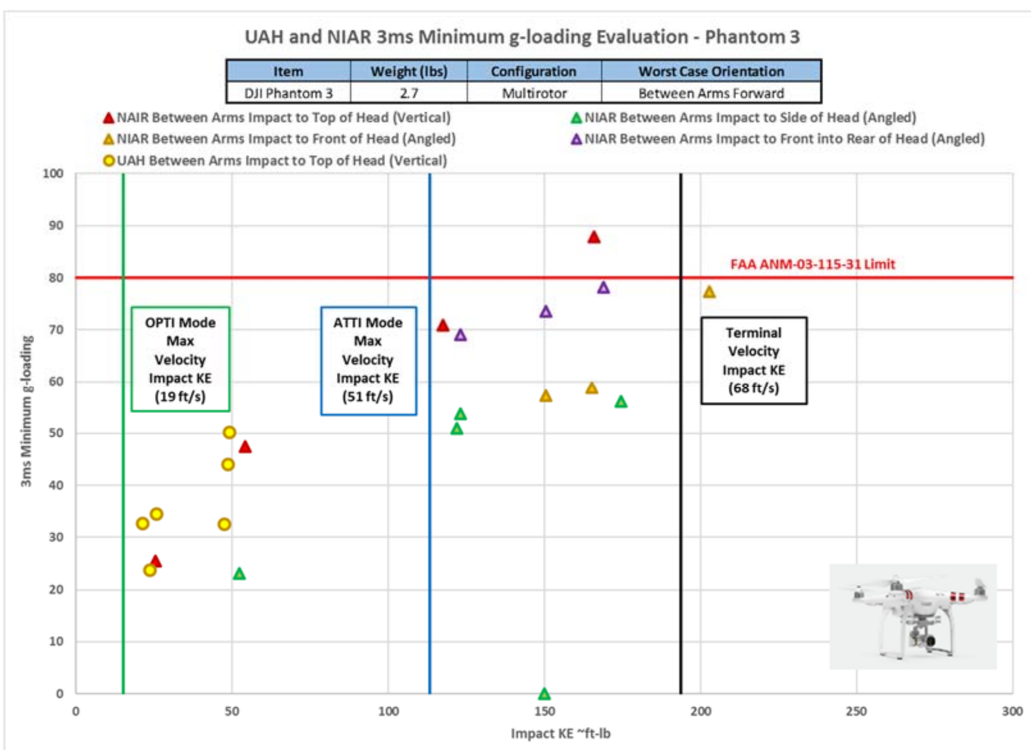

Figure D 12. UAH and NIAR 3ms Minimum g-loading Evaluation - DJI Phantom 3

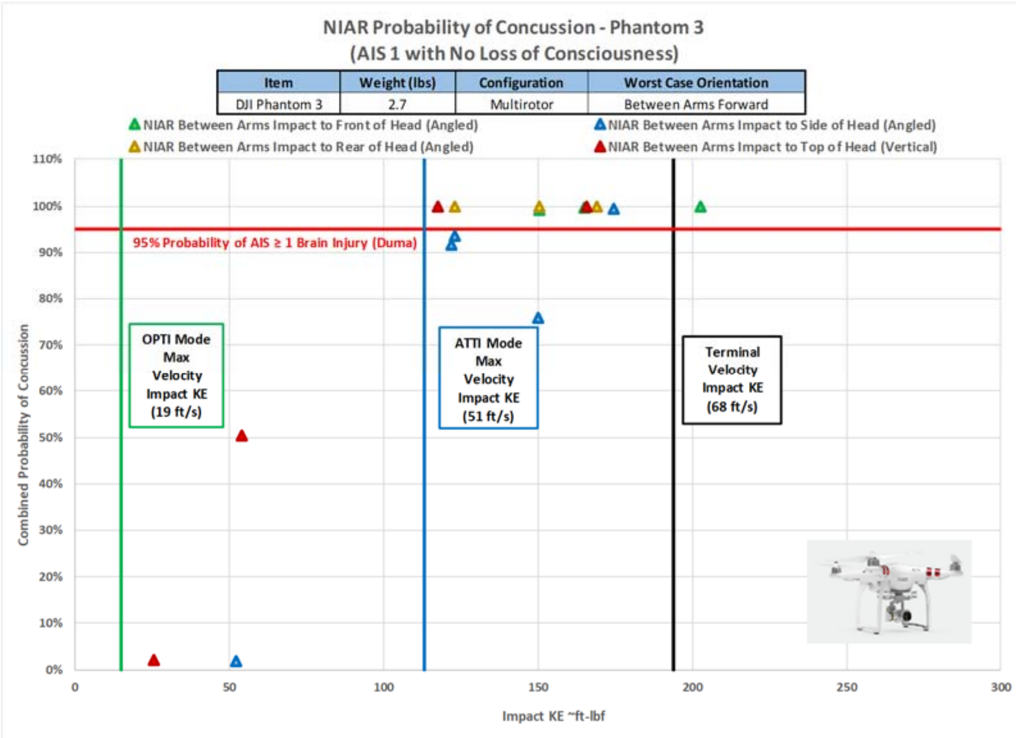

Figure D 13. NIAR Probability of Concussion - DJI Phantom 3

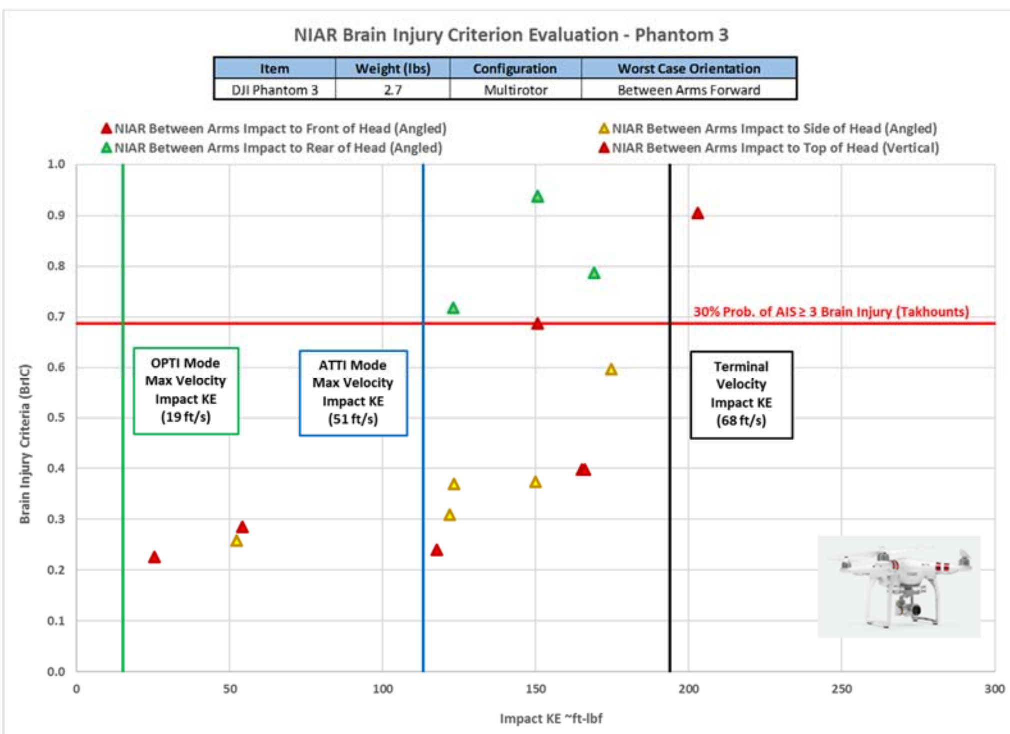

Figure D 14. NIAR Brain Injury Criterion Evaluation - DJI Phantom 3

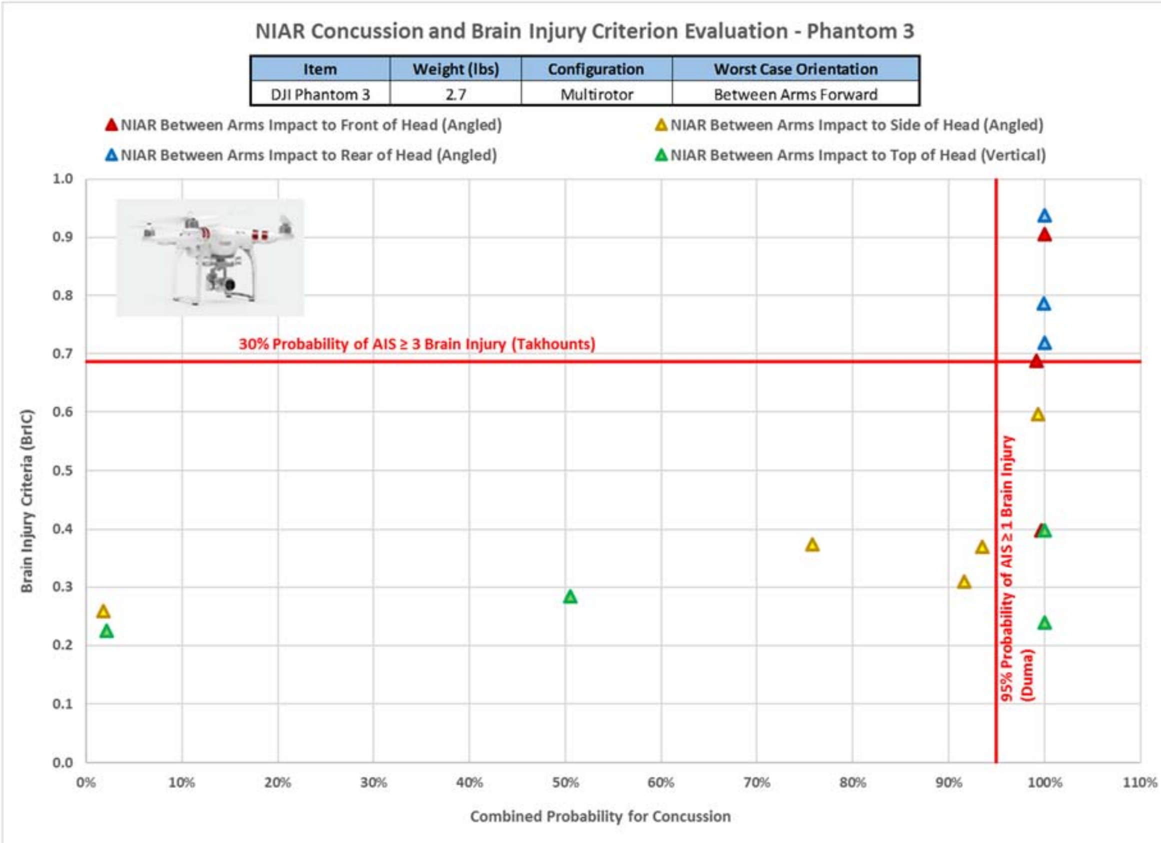

Figure D 15. NIAR Concussion and Brain Injury Criterion Evaluation - DJI Phantom 3

APPENDIX E – MAVIC PRO SIMPLIFIED AND FULL ATD TEST DATA

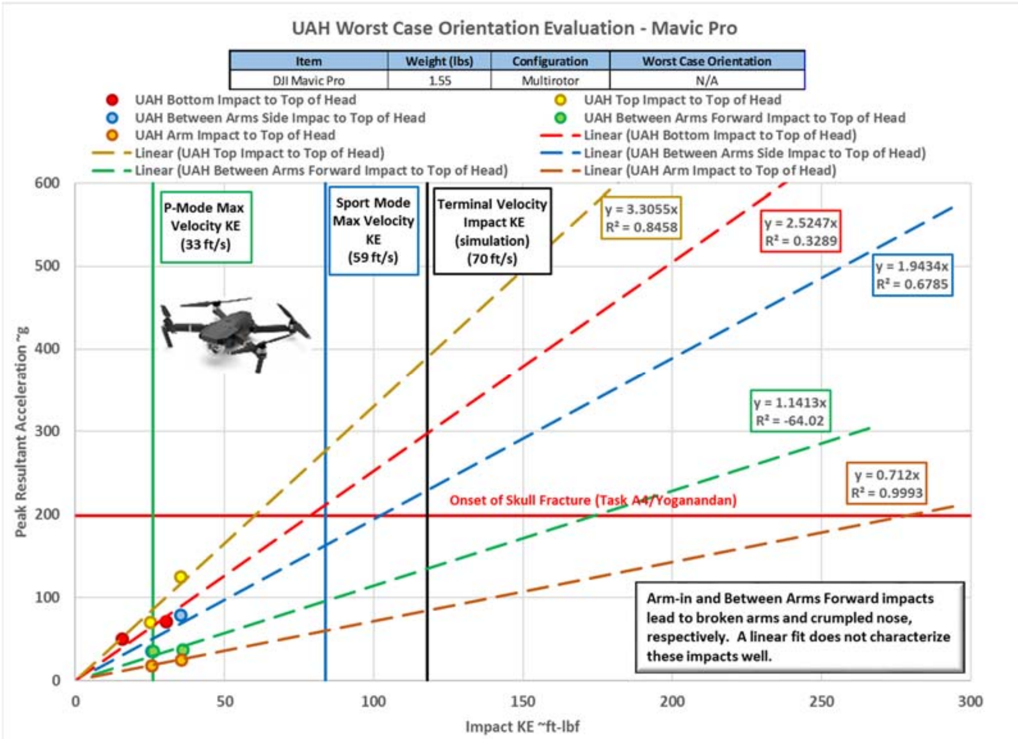

Figure E 1. UAH Worst Case Orientation Evaluation – Mavic Pro

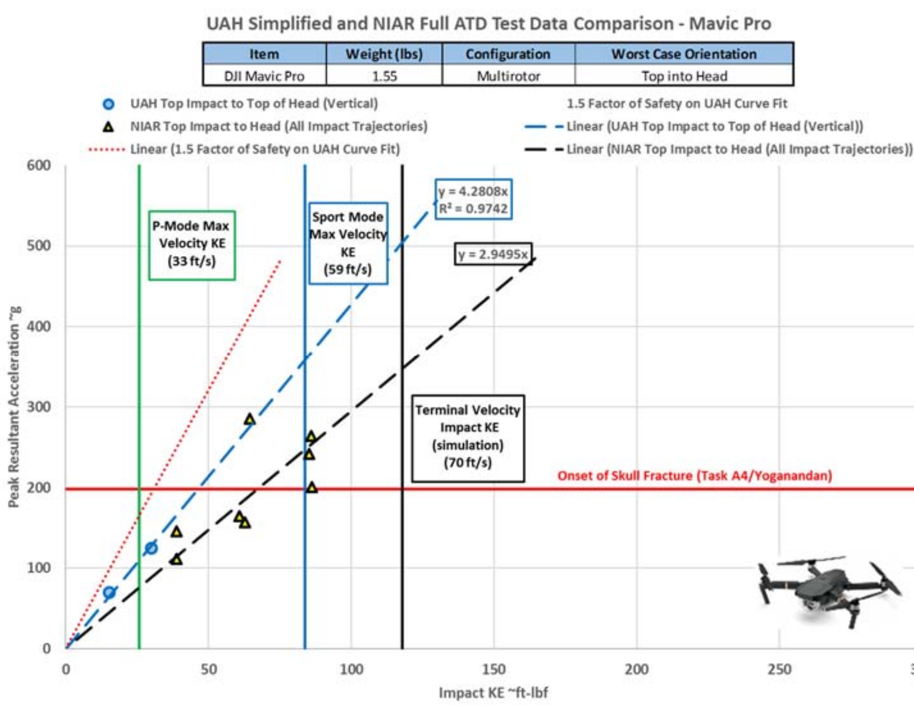

Figure E 2. UAH vs. NIAR Data Comparison - Mavic Pro

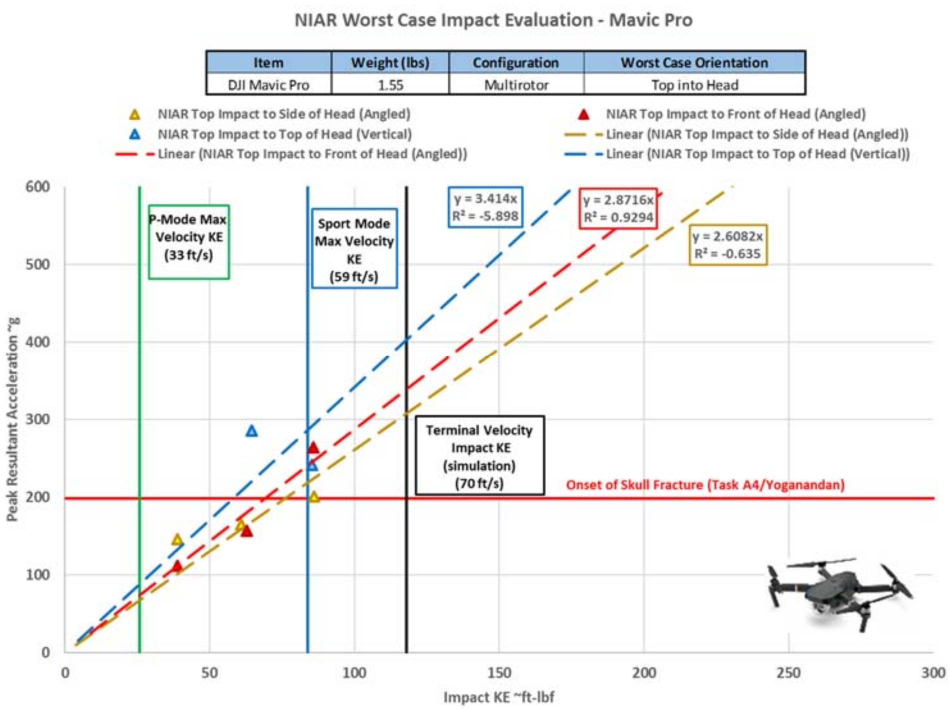

Figure E 3. NIAR Worst Case Impact Evaluation - Mavic Pro

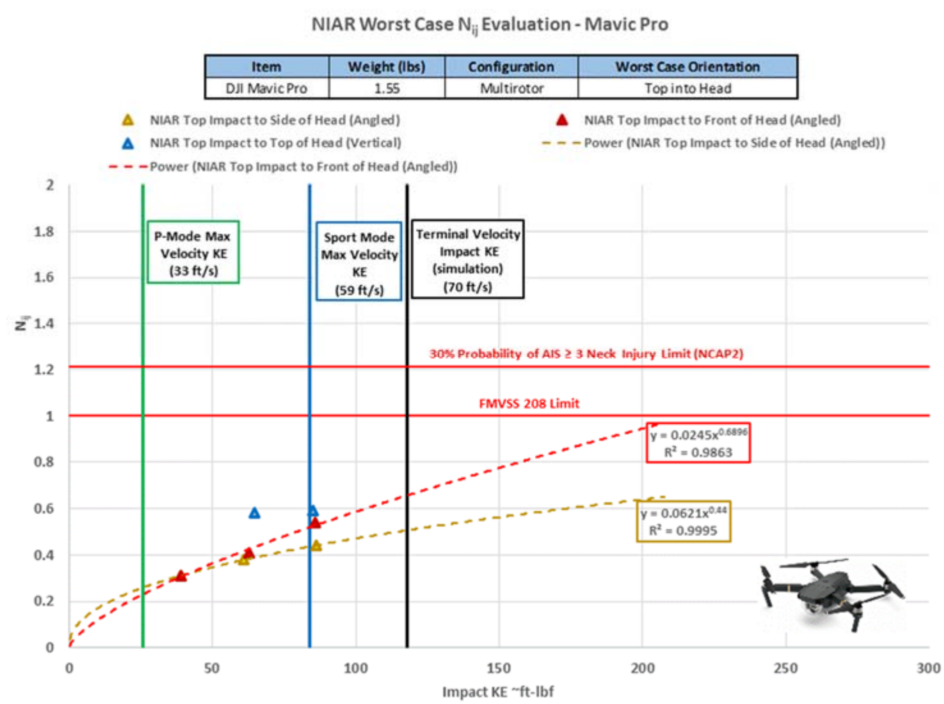

Figure E 4. NIAR Worst Case N_{ij} Evaluation - Mavic Pro

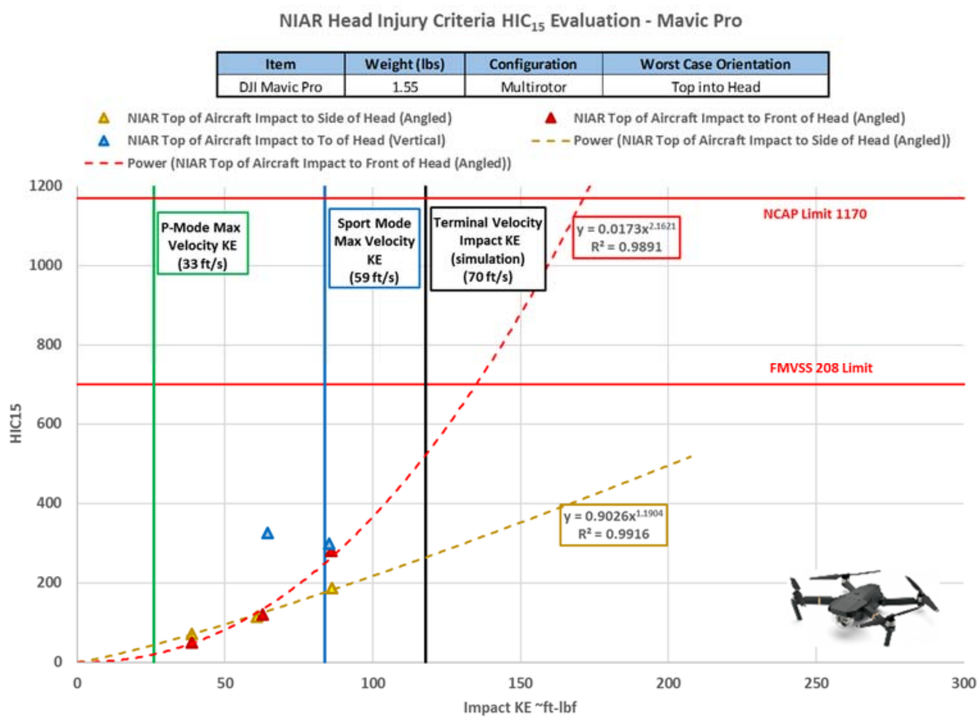

Figure E 5. Head Injury Criteria HIC_{15} Evaluation - Mavic Pro

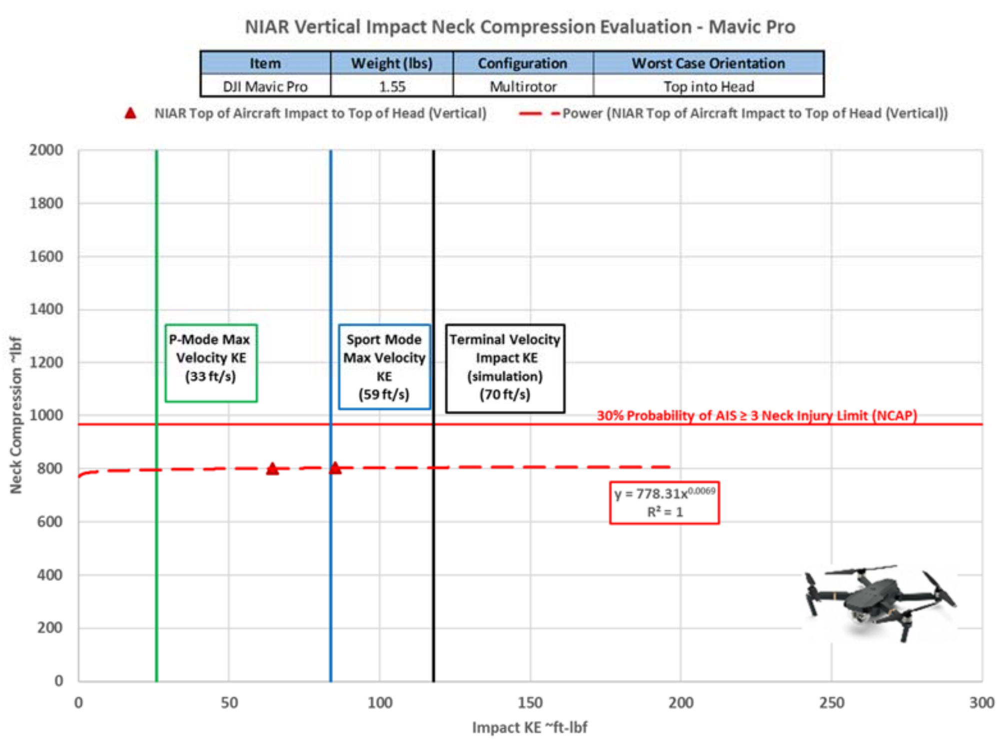

Figure E 6. NIAR Vertical Impact Neck Compression Evaluation - Mavic Pro

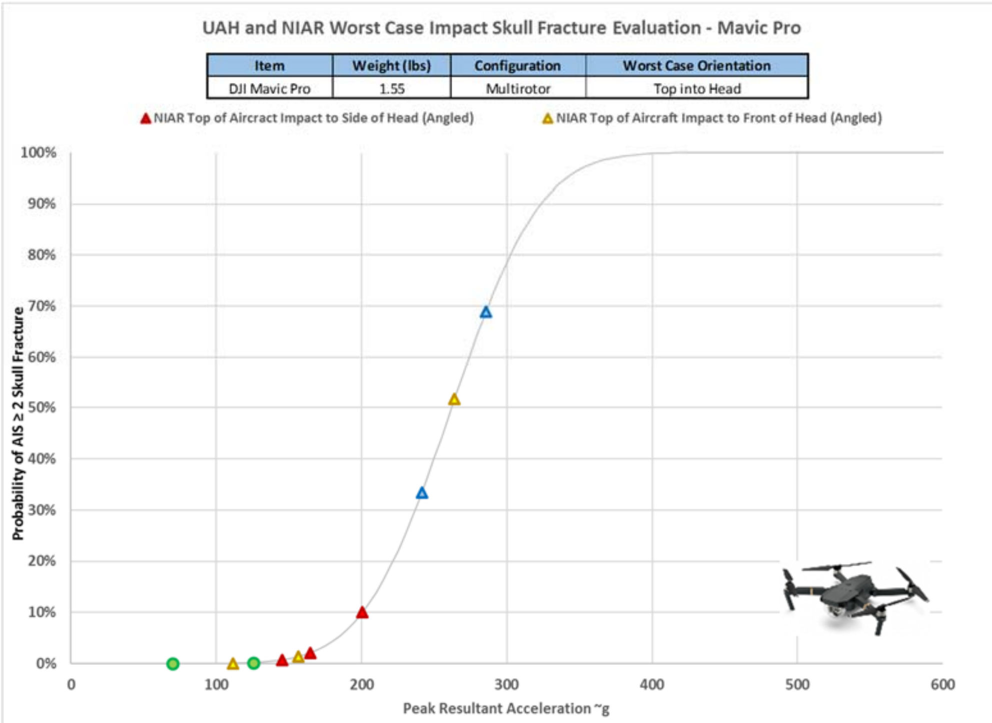

Figure E 7. UAH and NIAR Worst Case Impact Skull Fracture Evaluation - Mavic Pro

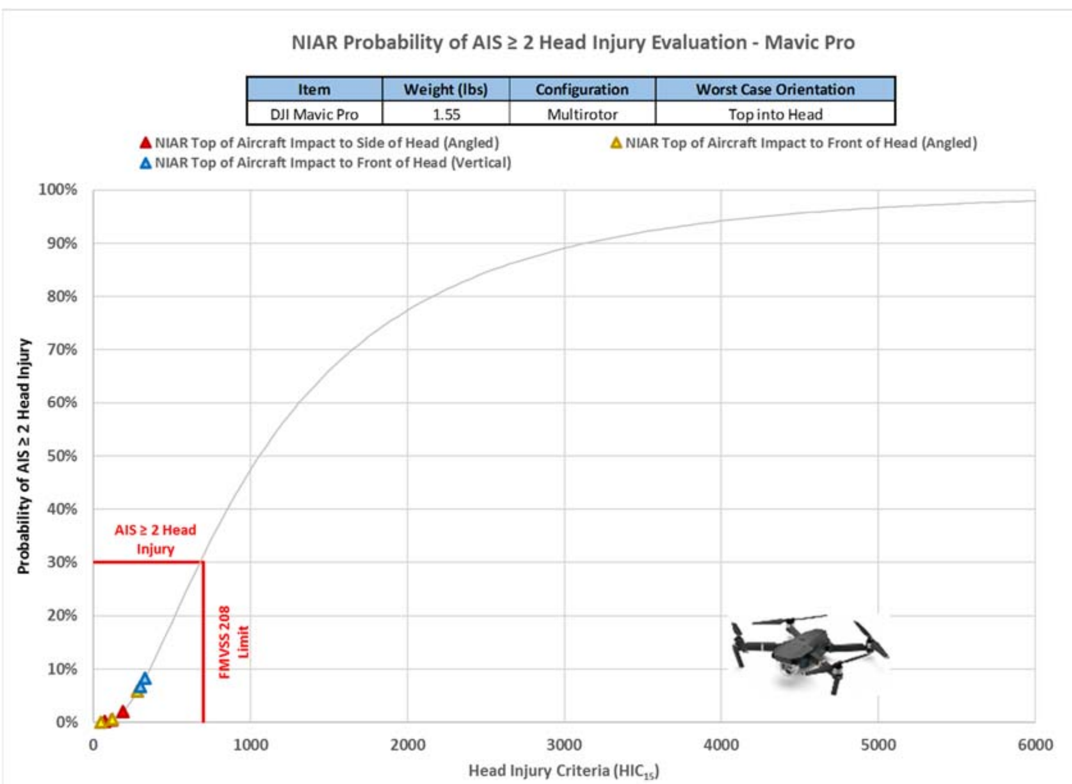

Figure E 8. NIAR Probability of AIS ≥ 2 Head Injury Evaluation - Mavic Pro

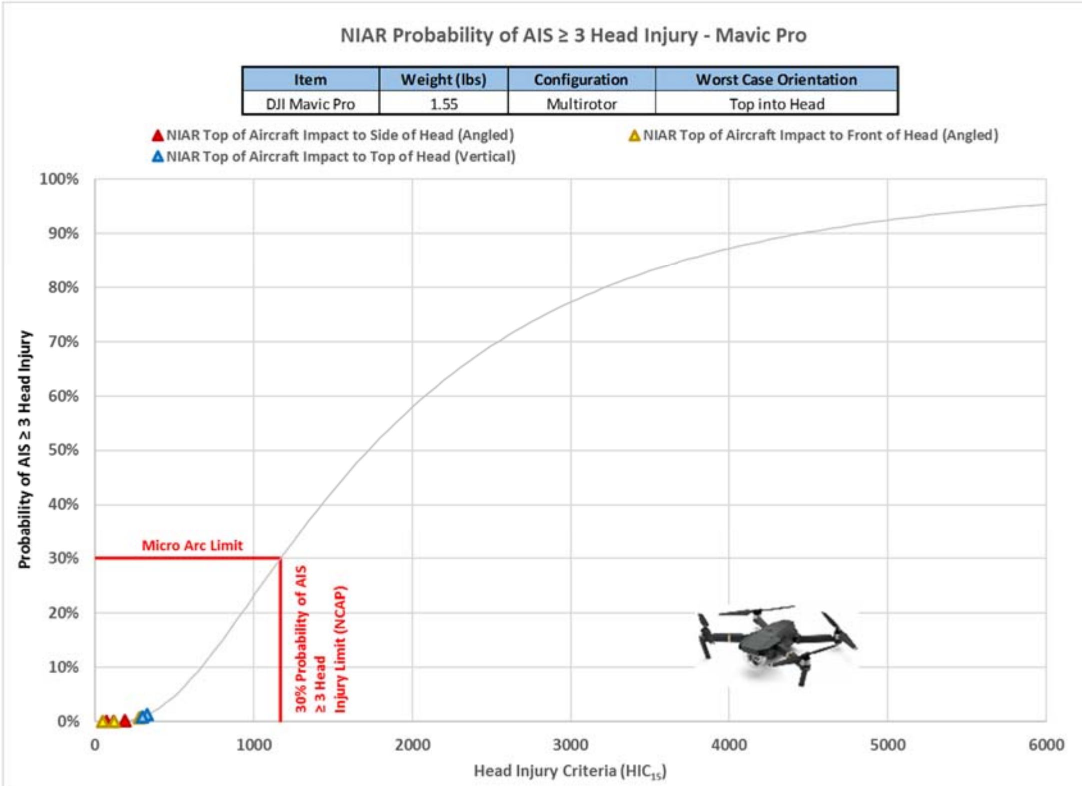

Figure E 9. NIAR Probability of AIS ≥ 3 Head Injury - Mavic Pro

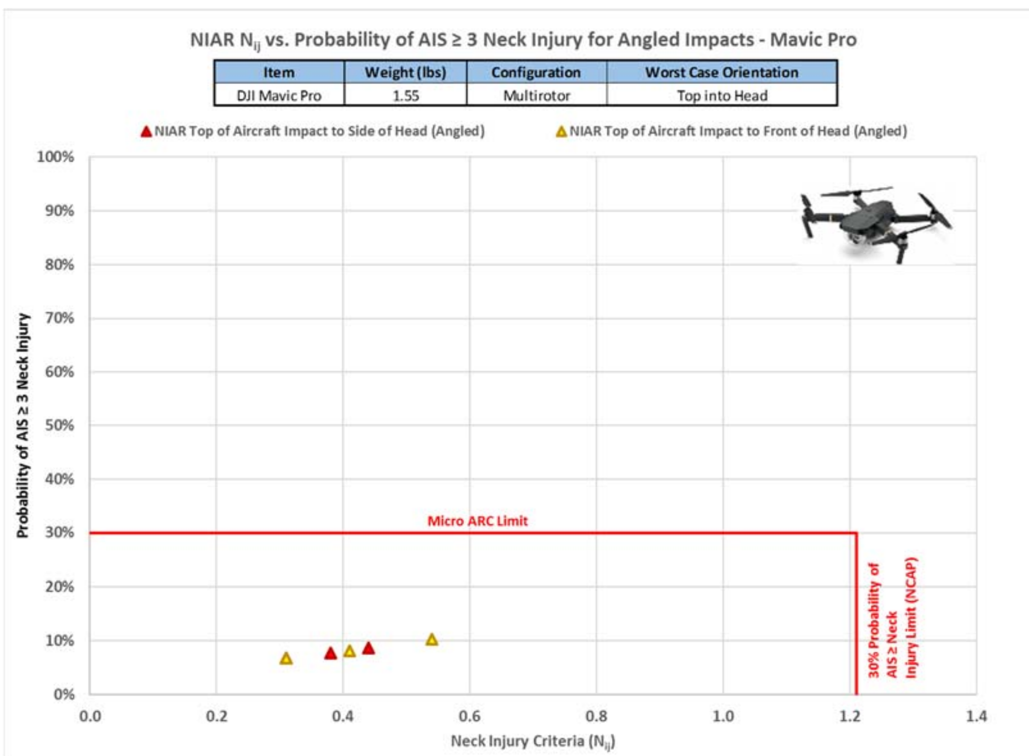

Figure E 10. NIAR N_{ij} vs. Probability of AIS ≥ 3 Neck Injury for Angled Impacts - Mavic Pro

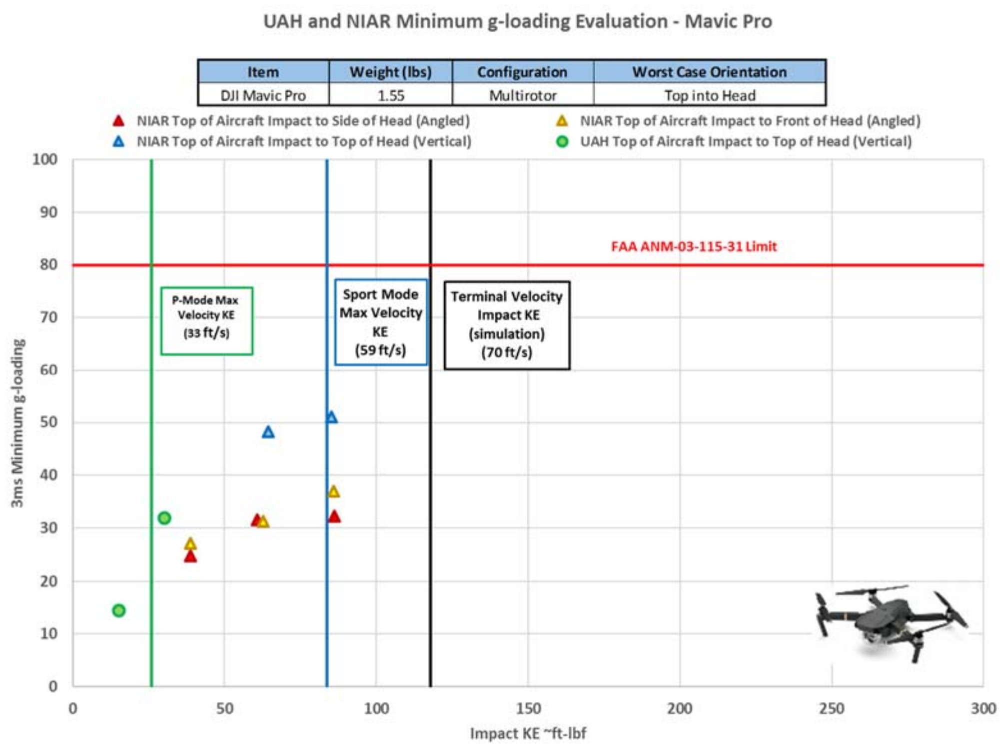

Figure E 11. UAH and NIAR Minimum g-loading Evaluation - Mavic Pro

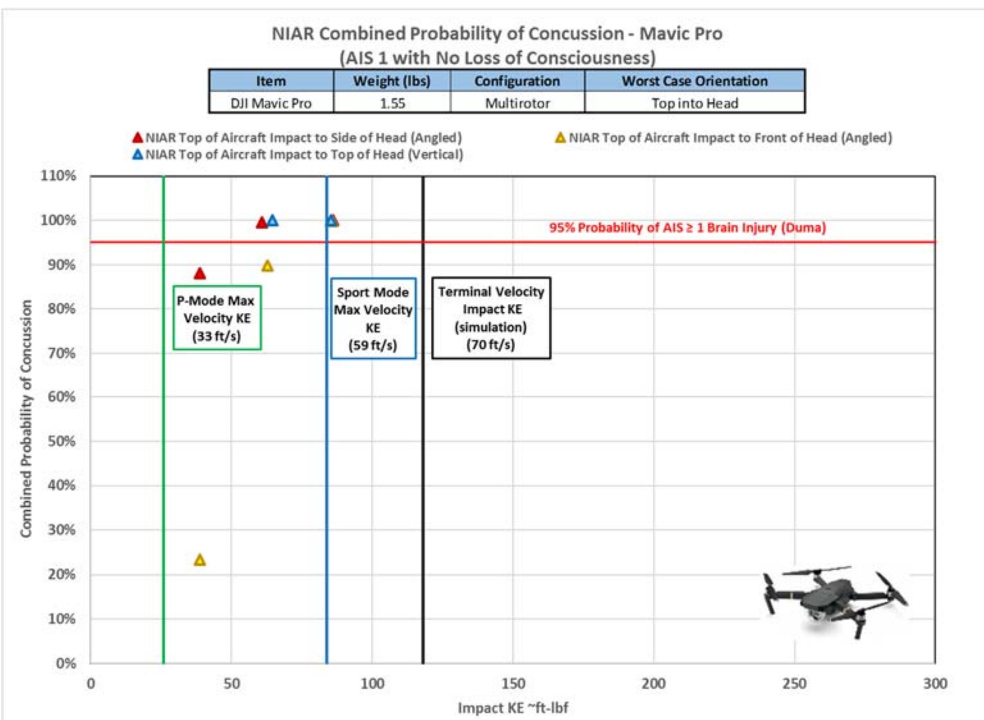

Figure E 12. NIAR Combined Probability of Concussion - Mavic Pro(AIS 1 with No Loss of Consciousness)

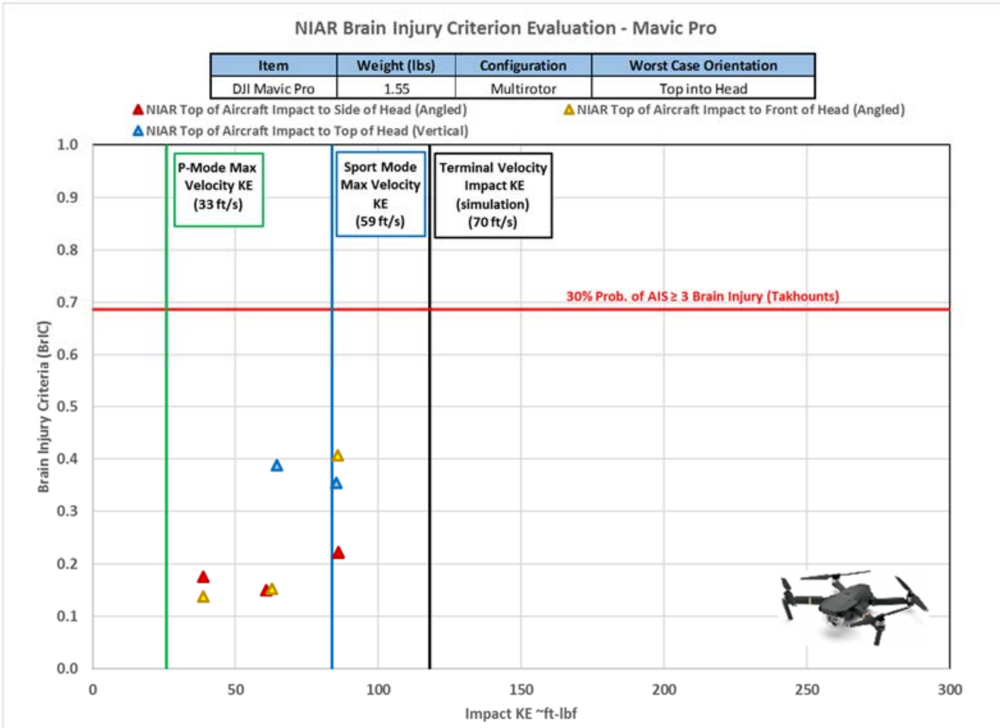

Figure E 13. NIAR Brain Injury Criterion Evaluation - Mavic Pro

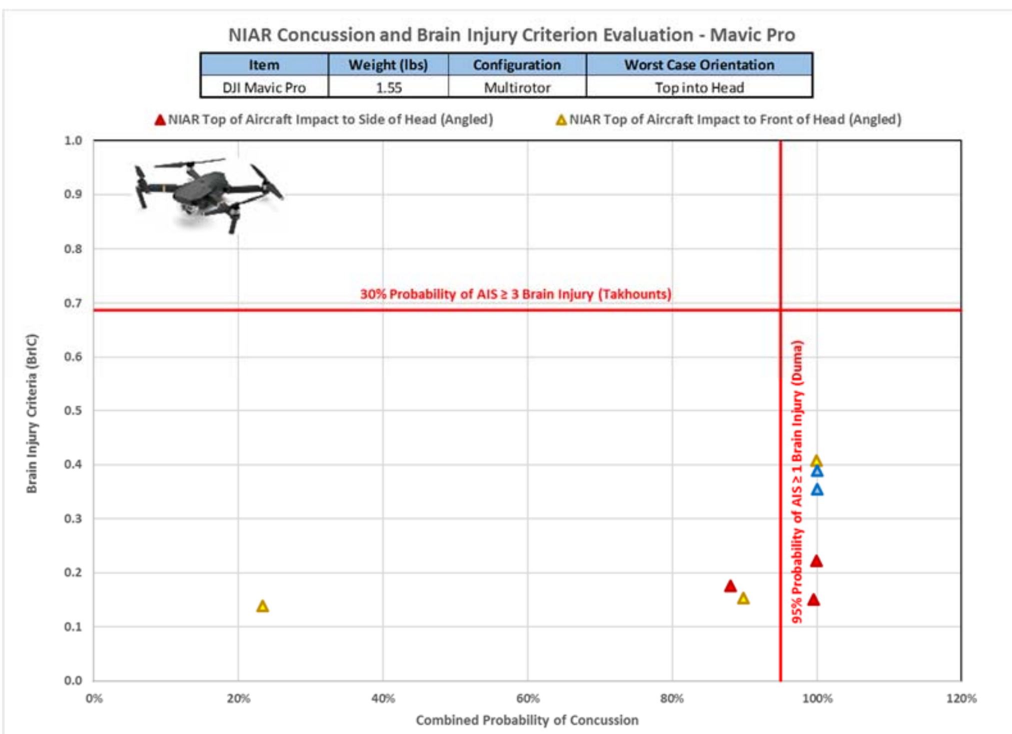

Figure E 14. NIAR Concussion and Brain Injury Criterion Evaluation - Mavic Pro

APPENDIX F – VENDOR 1 QUADROTOR SIMPLIFIED AND FULL ATD TEST DATA

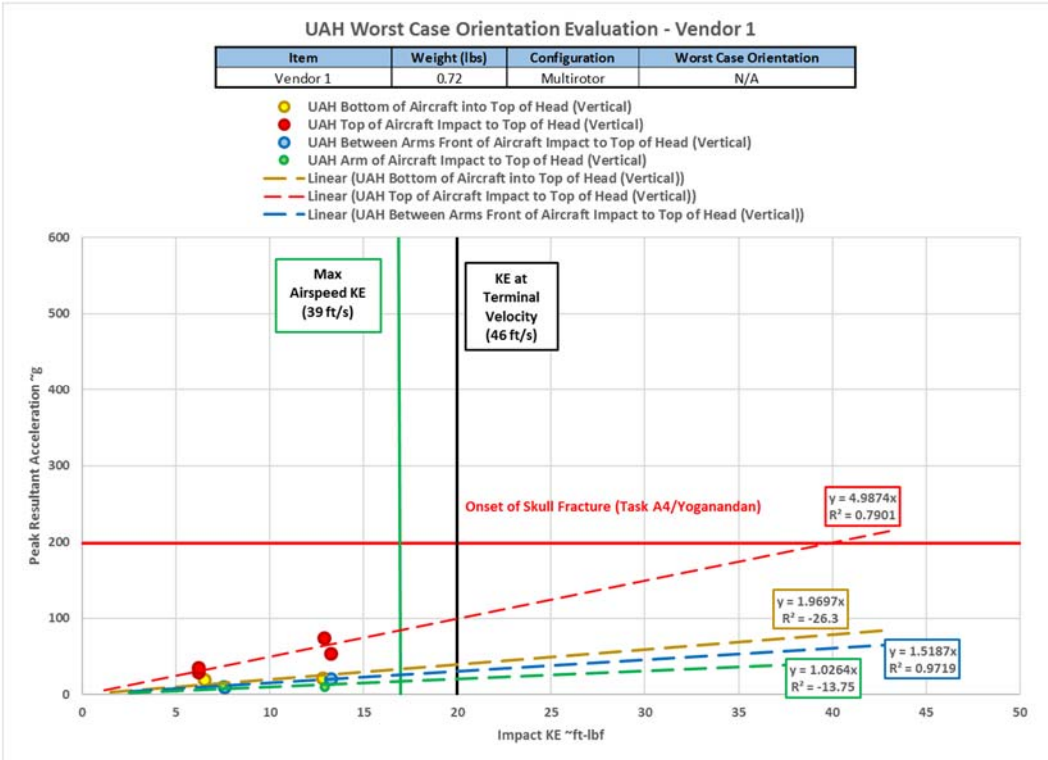

Figure F 1. UAH Worst Case Orientation Evaluation – Vendor 1 Quadrotor

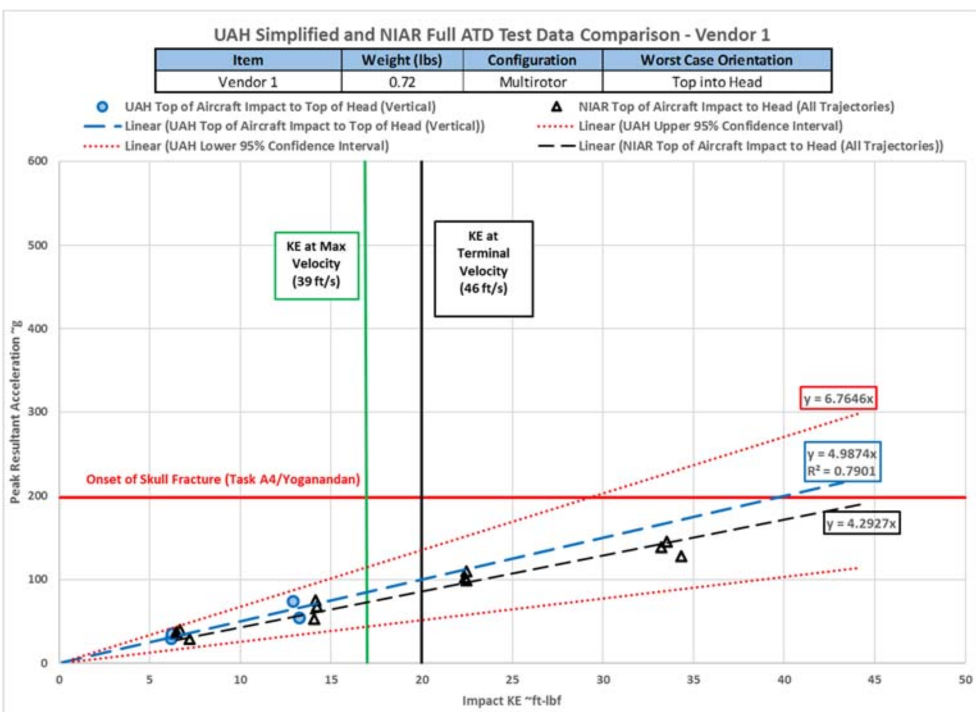

Figure F 2. UAH vs. NIAR Data Comparison - Vendor 1 Quadrotor

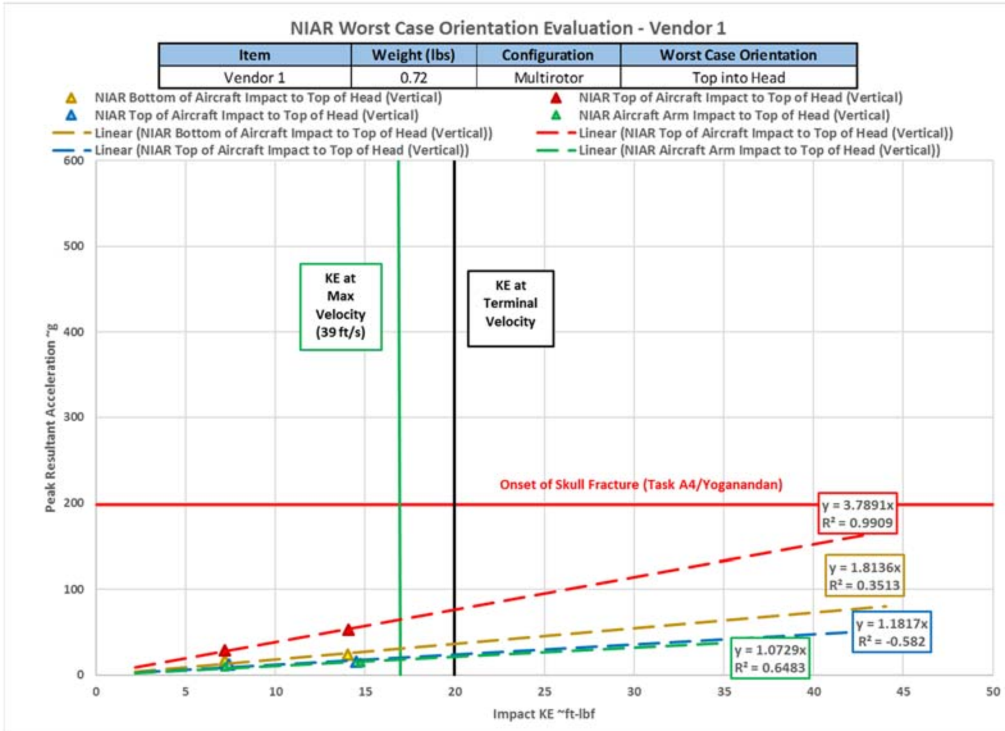

Figure F 3. NIAR Worst Case Orientation Evaluation - Vendor 1 Quadrotor

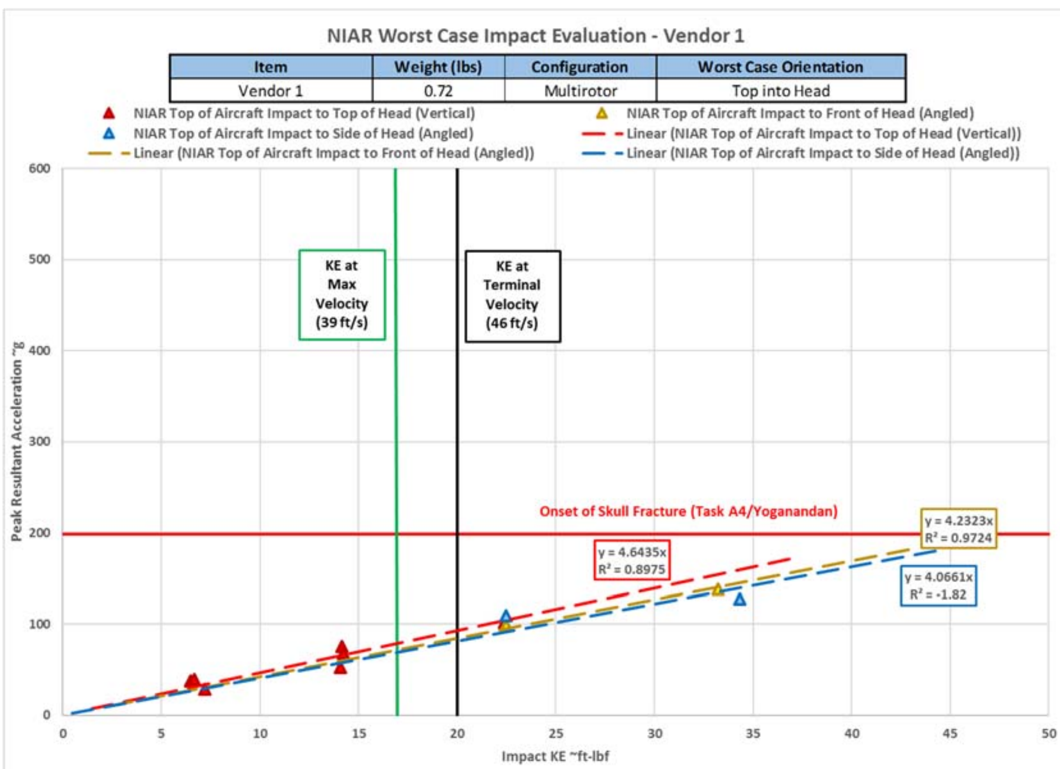

Figure F 4. NIAR Worst Case Impact Evaluation - Vendor 1 Quadrotor

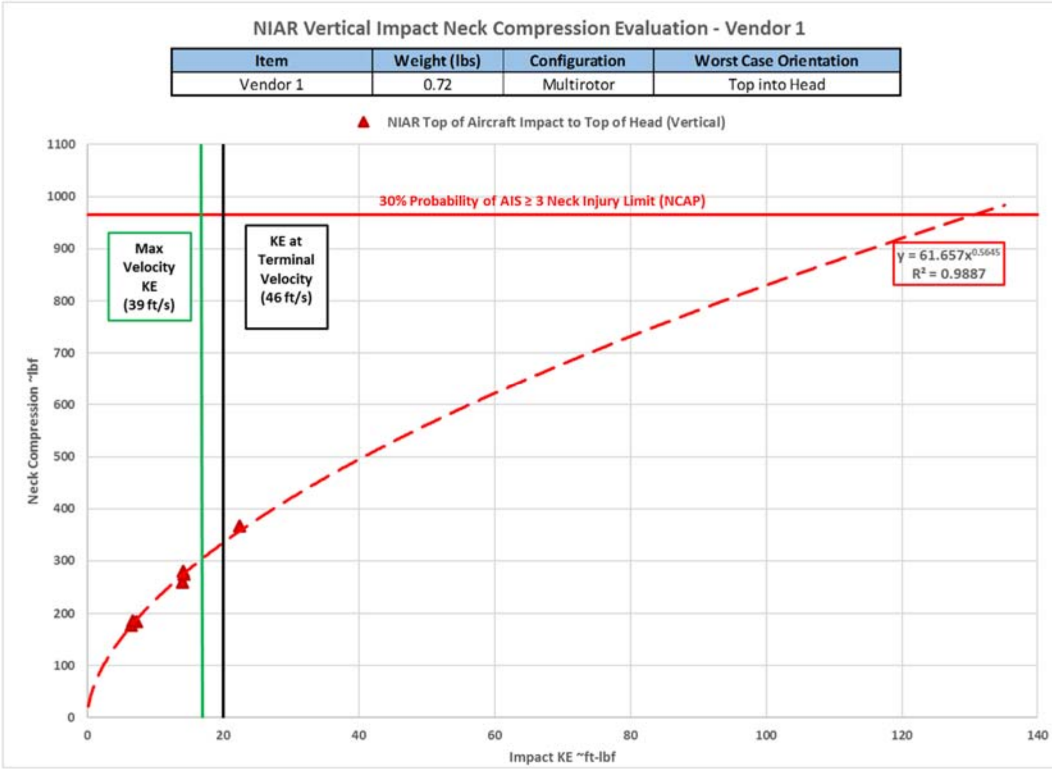

Figure F 5. NIAR Vertical Impact Neck Compression Evaluation - Vendor 1 Quadrotor

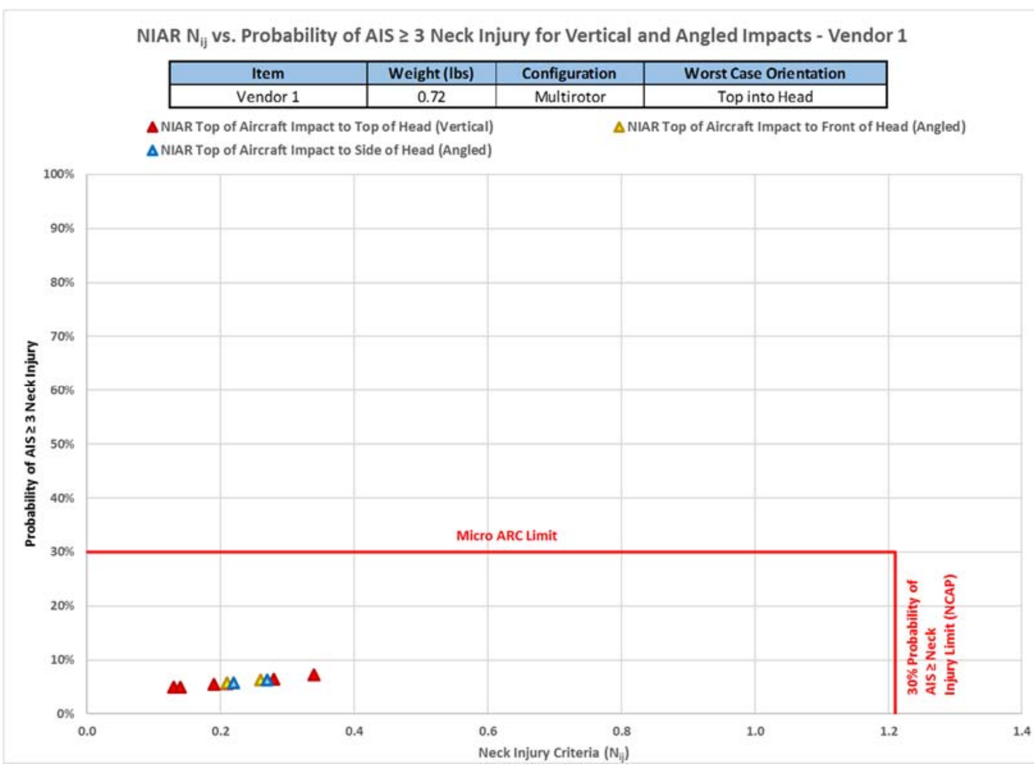

Figure F 6. NIAR N_{ij} Evaluation - Vendor 1

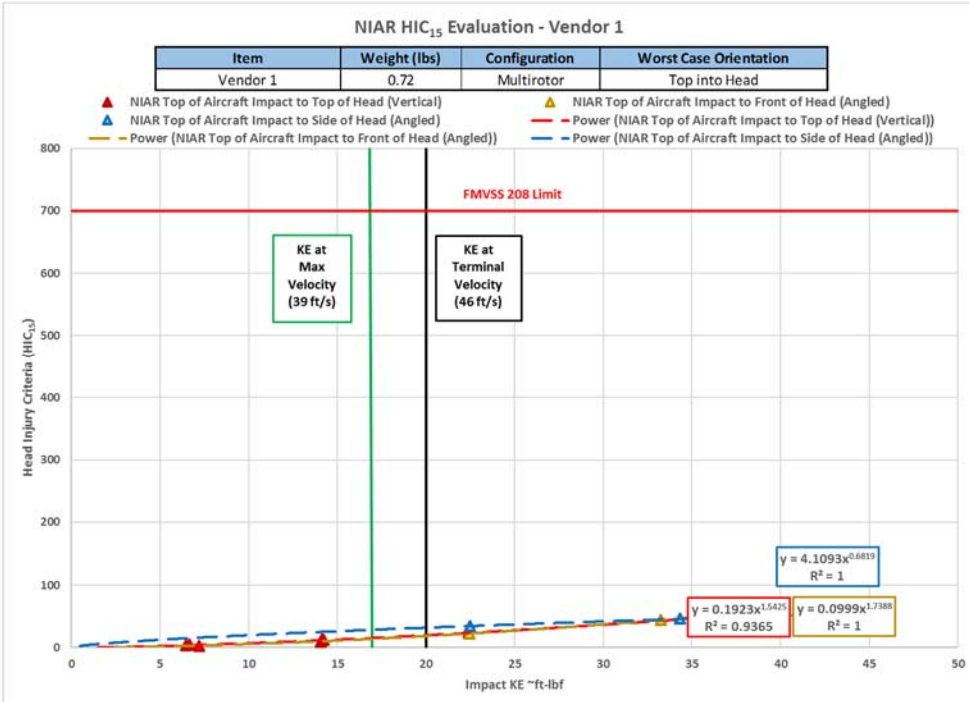

Figure F 7. NIAR HIC15 Evaluation - Vendor 1

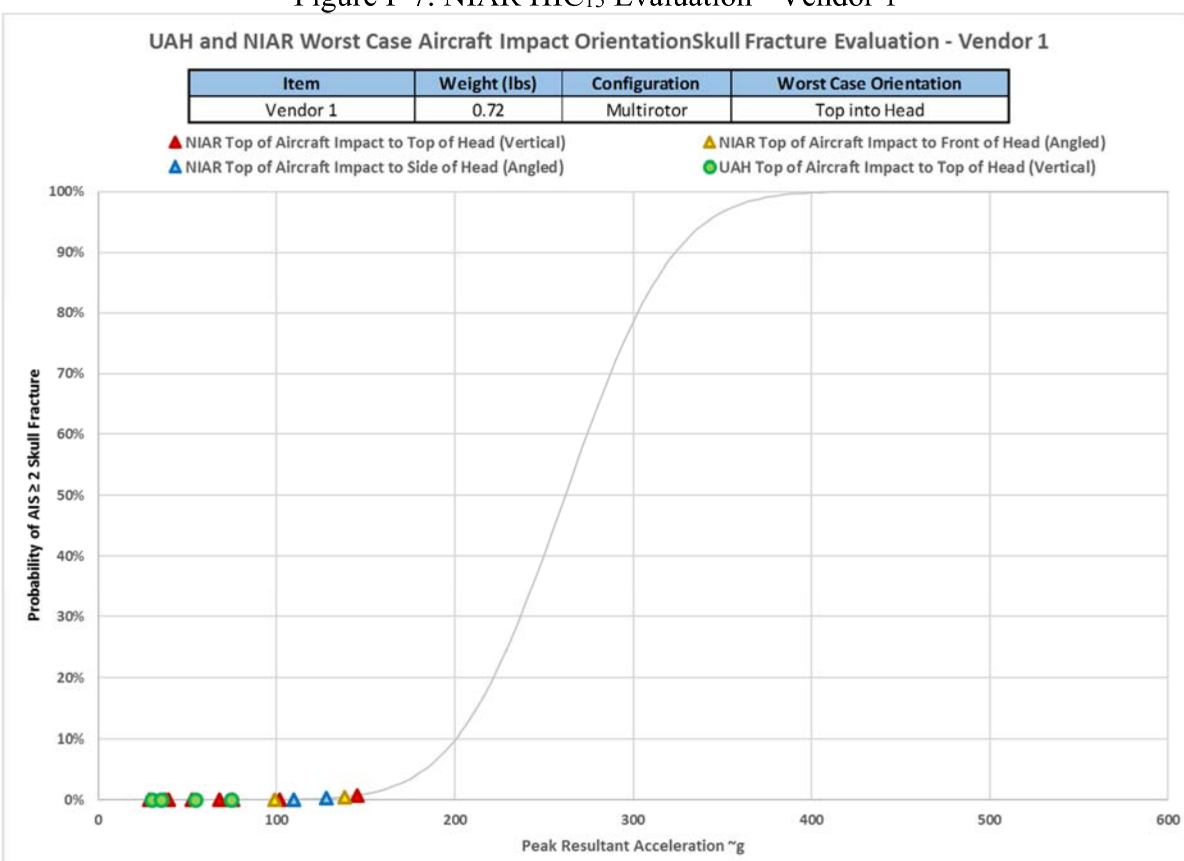

Figure F 8. UAH and NIAR Worst Case Impact Skull Fracture Evaluation - Vendor 1 Quadrotor

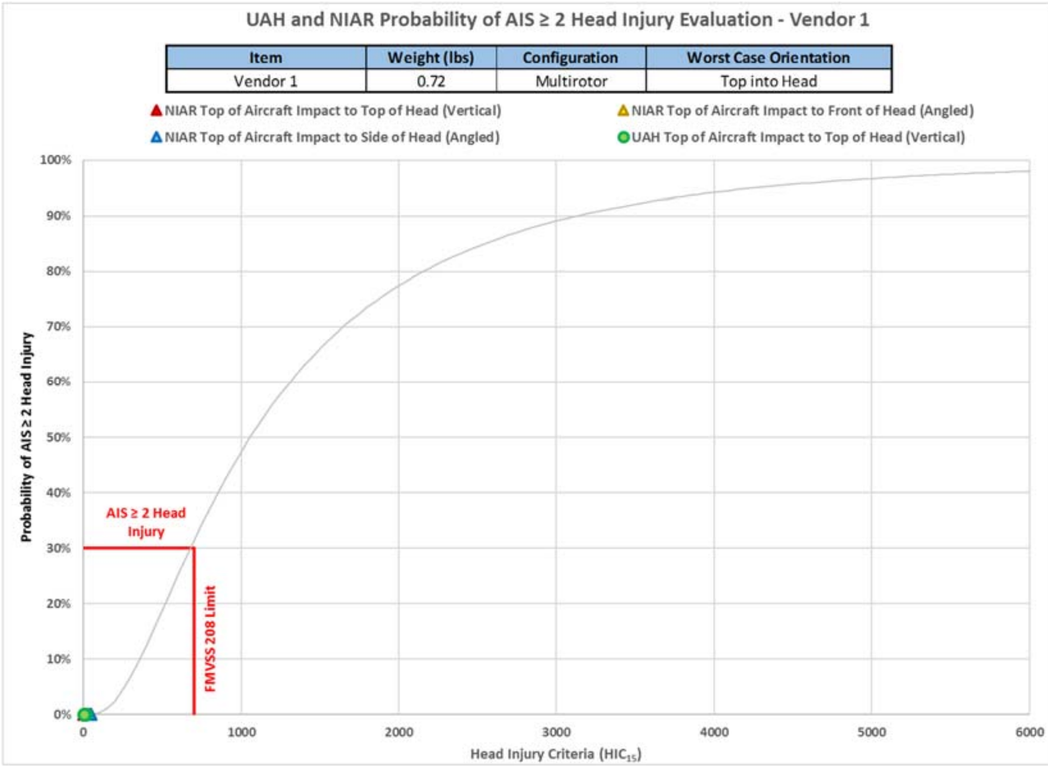

Figure F 9. NIAR Probability of AIS ≥ 2 Head Injury Evaluation - Vendor 1 Quadrotor

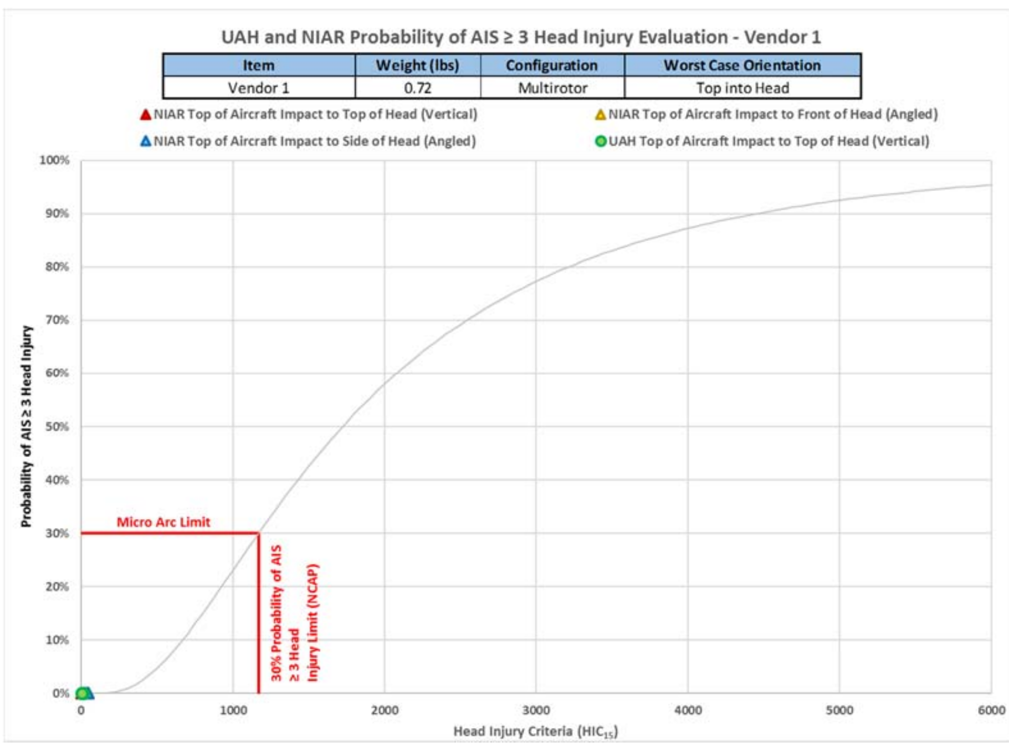

Figure F 10. NIAR Probability of AIS ≥ 3 Head Injury - Vendor 1 Quadrotor

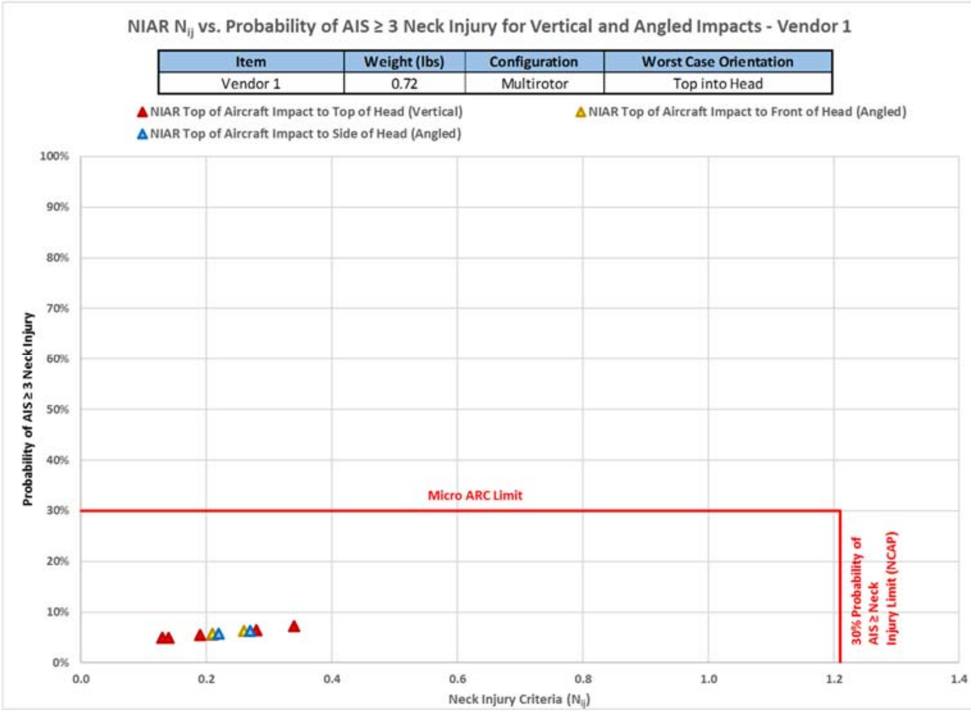

Figure F 11. NIAR N_{ij} vs. Probability of AIS ≥ 3 Neck Injury for Angled Impacts - Vendor 1 Quadrotor

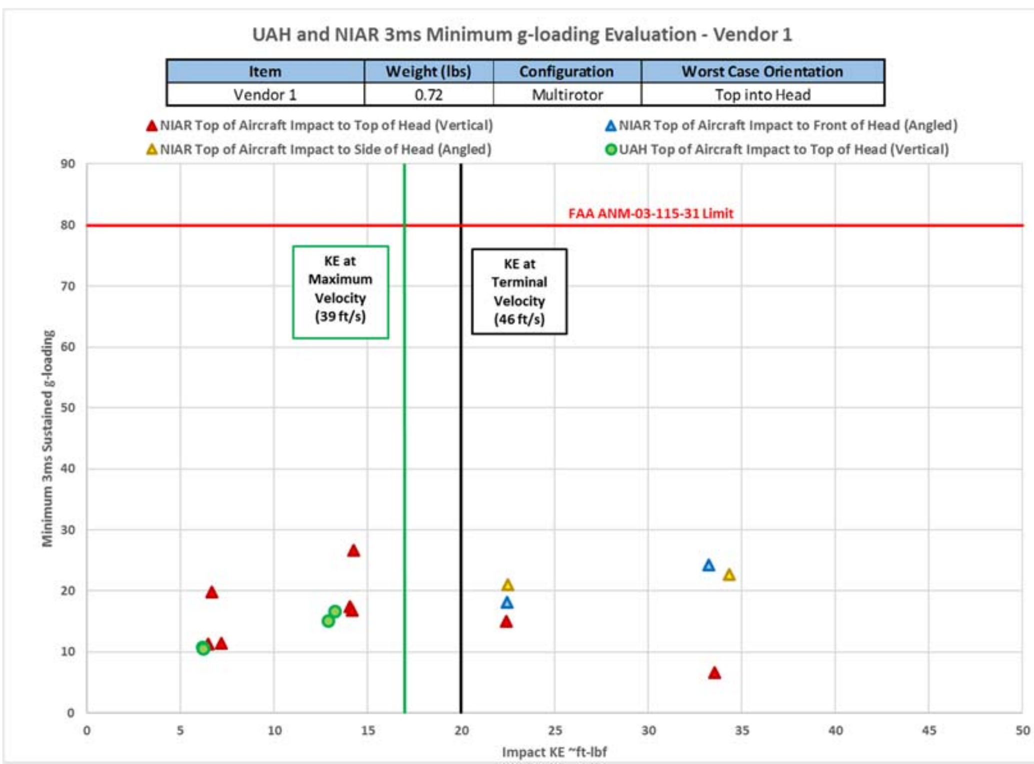

Figure F 12. UAH and NIAR Minimum g-loading Evaluation - Vendor 1 Quadrotor

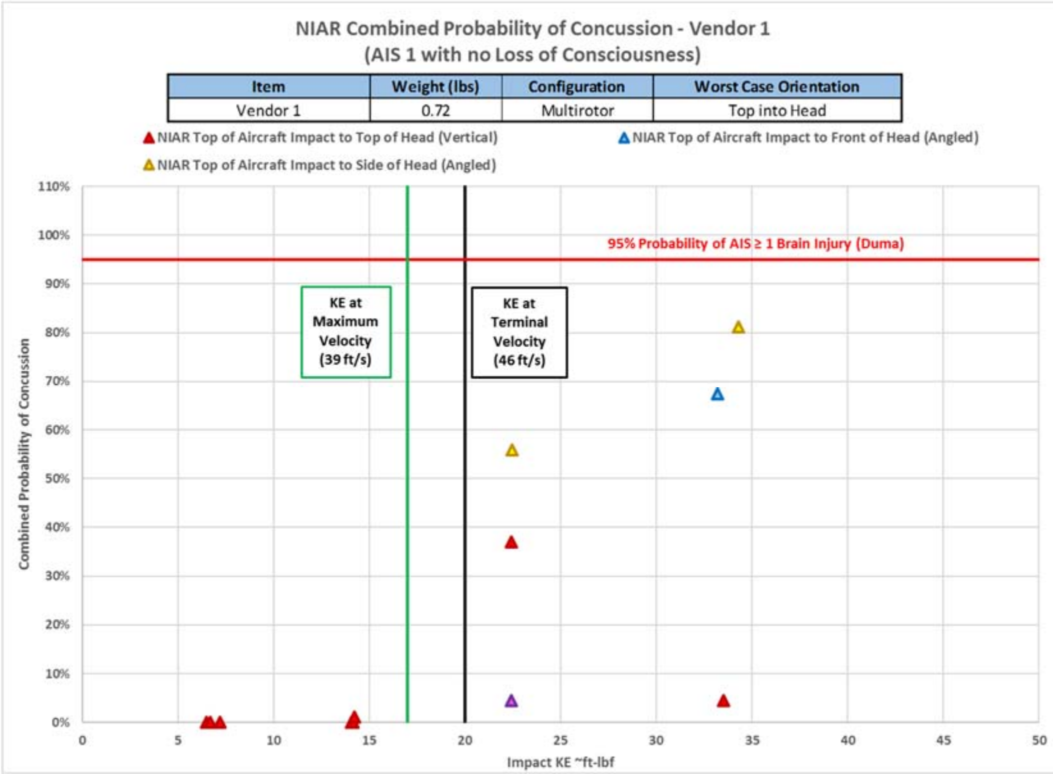

Figure F 13. NIAR Combined Probability of Concussion - Vendor 1 Quadrotor

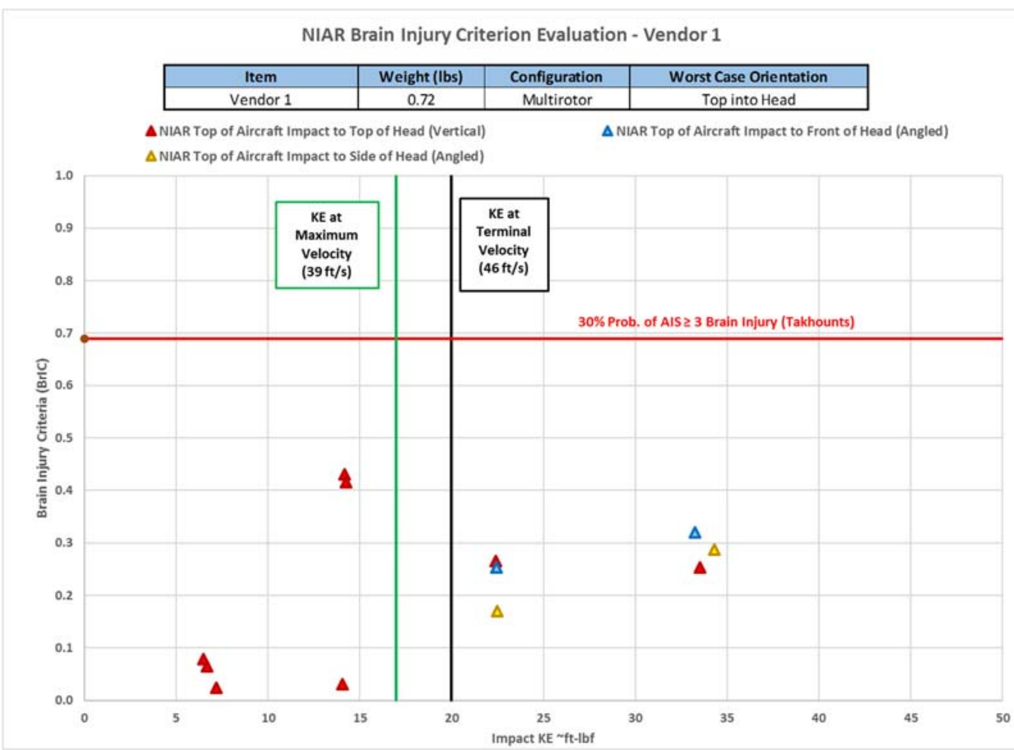

Figure F 14. NIAR Brain Injury Criterion Evaluation - Vendor 1 Quadrotor

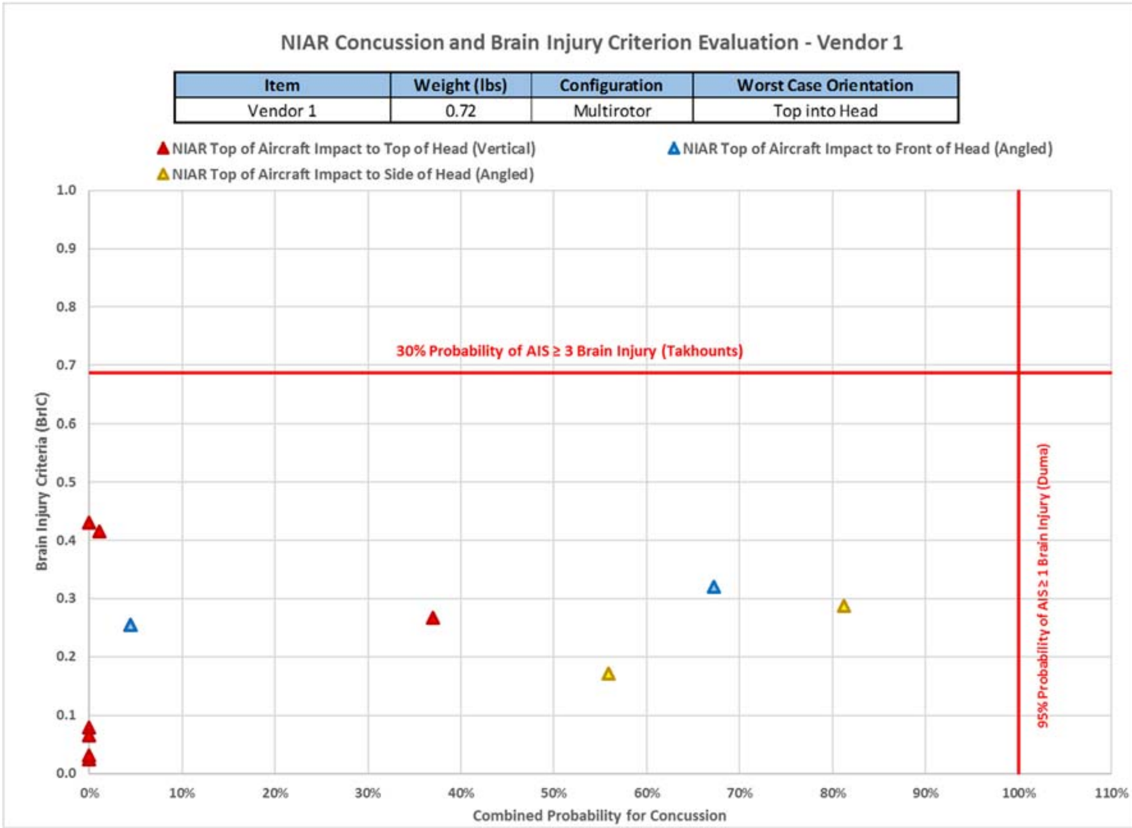

Figure F 15. NIAR Concussion and Brain Injury Criterion Evaluation - Vendor 1 Quadrotor

APPENDIX G – GO PRO KARMA SIMPLIFIED AND FULL ATD TEST DATA

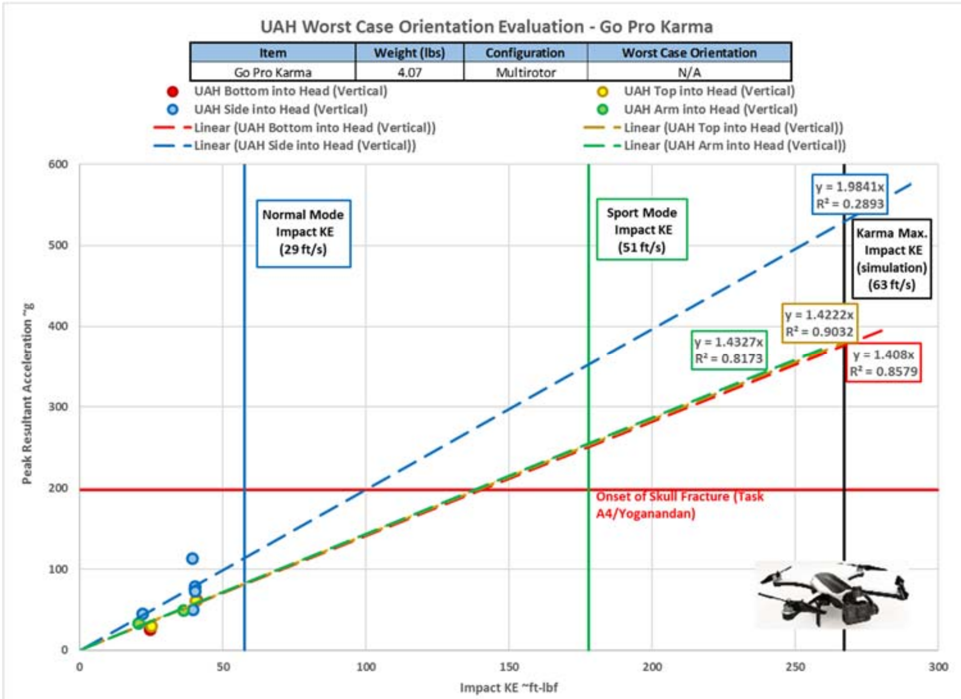

Figure G 1. UAH Worst Case Orientation Evaluation - Go Pro Karma

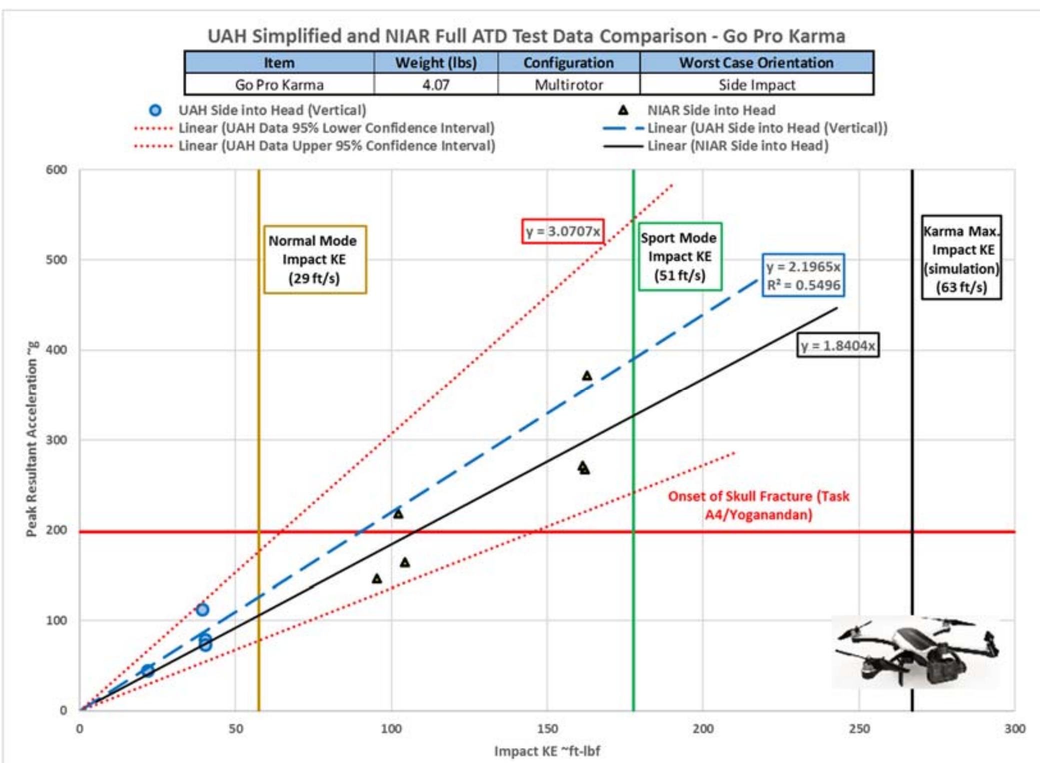

Figure G 2. UAH vs. NIAR Data Comparison - Go Pro Karma

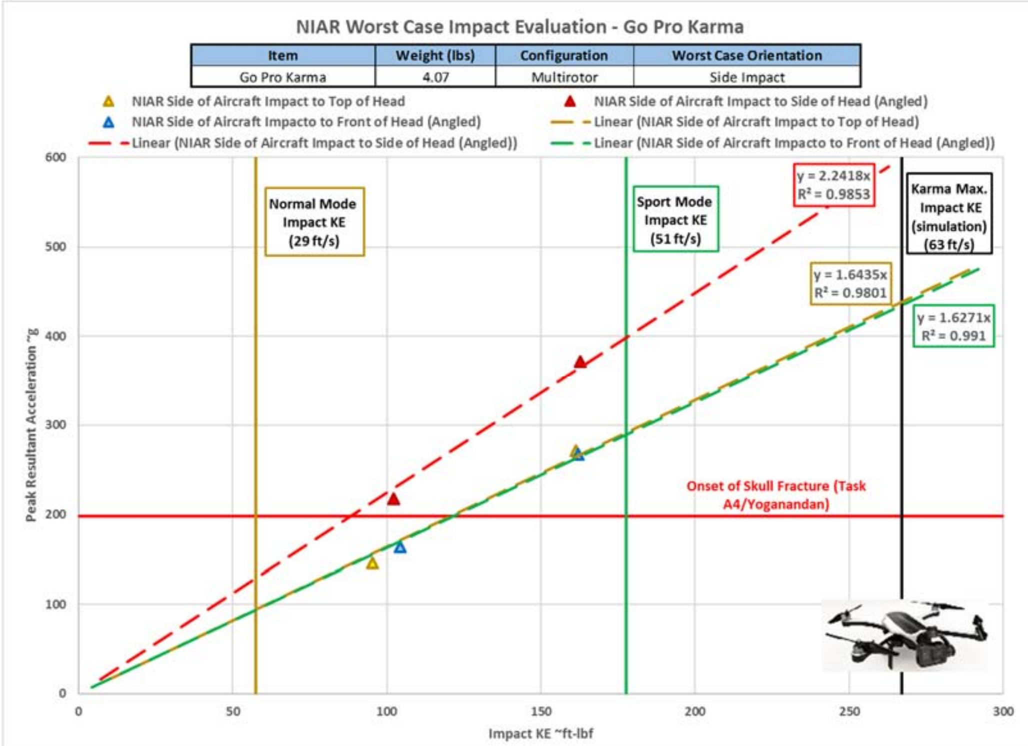

Figure G 3. NIAR Worst Case Orientation Evaluation - Go Pro Karma

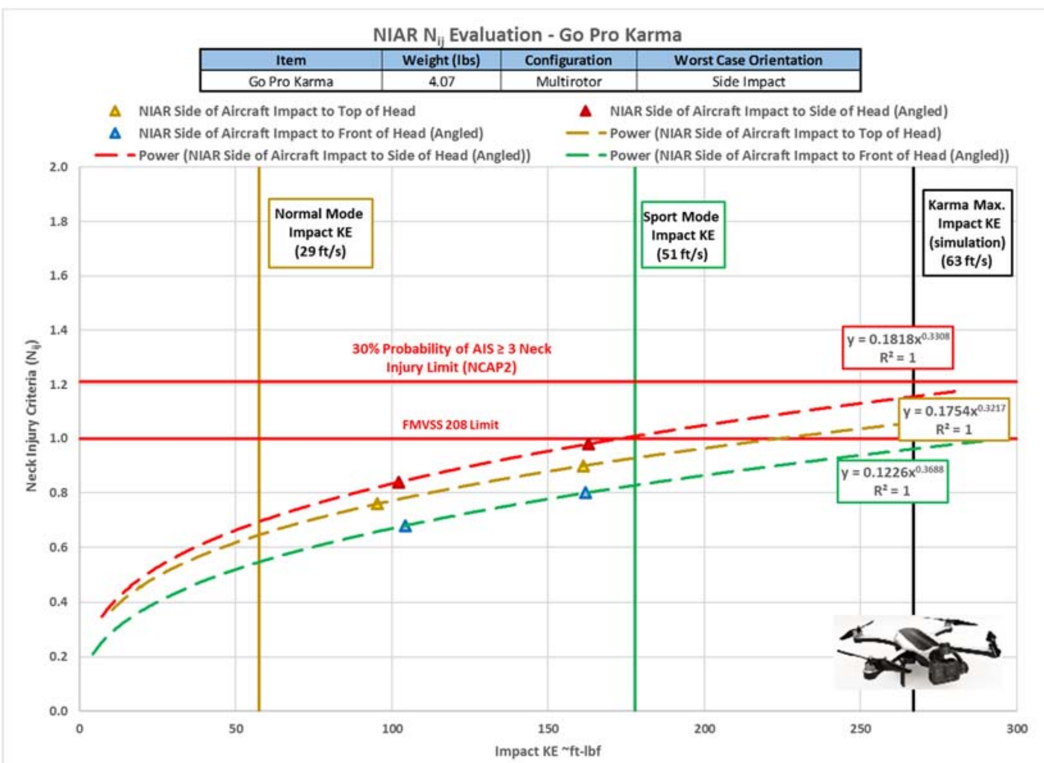

Figure G 4. NIAR N_{ij} Evaluation - Go Pro Karma

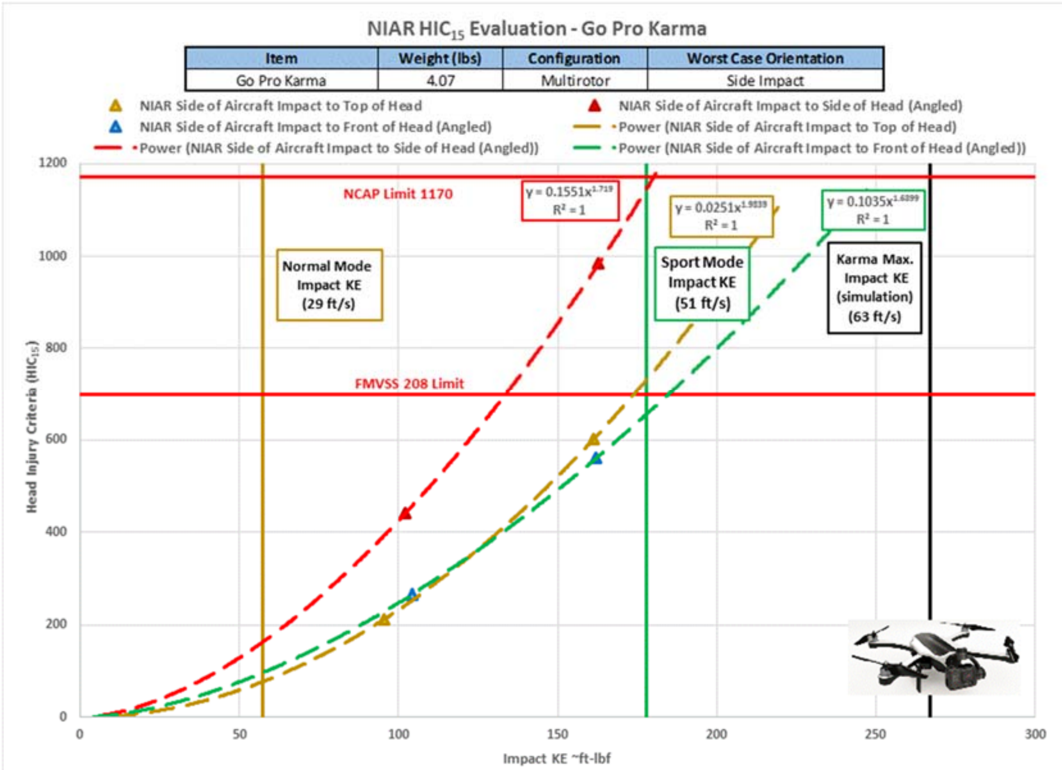

Figure G 5. NIAR HIC15 Evaluation - Go Pro Karma

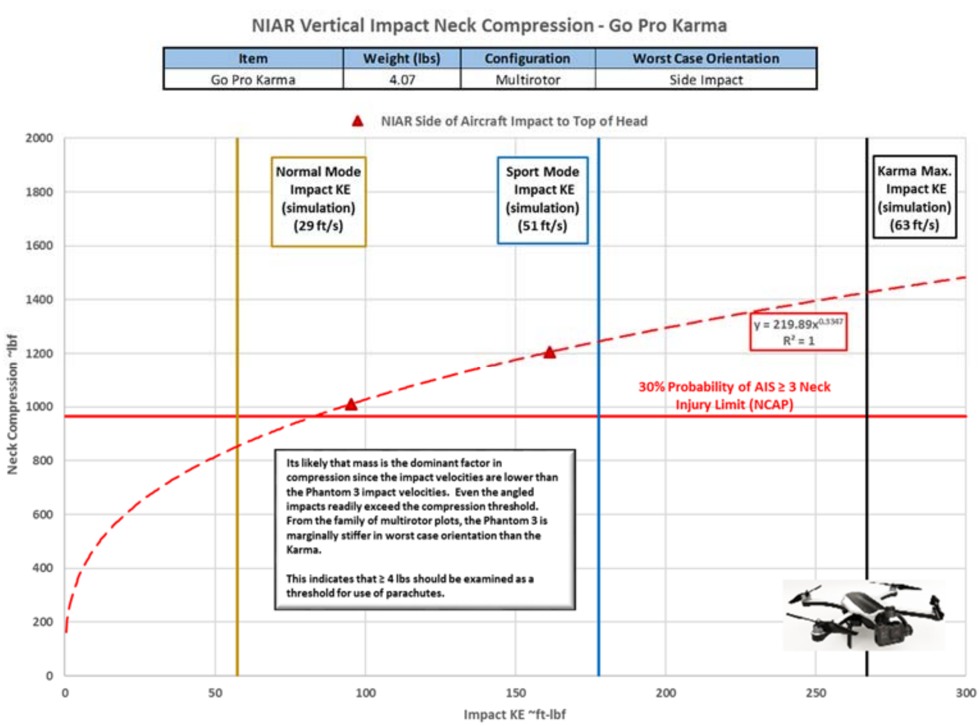

Figure G 6. NIAR Vertical Impact Neck Compression Evaluation - Go Pro Karma

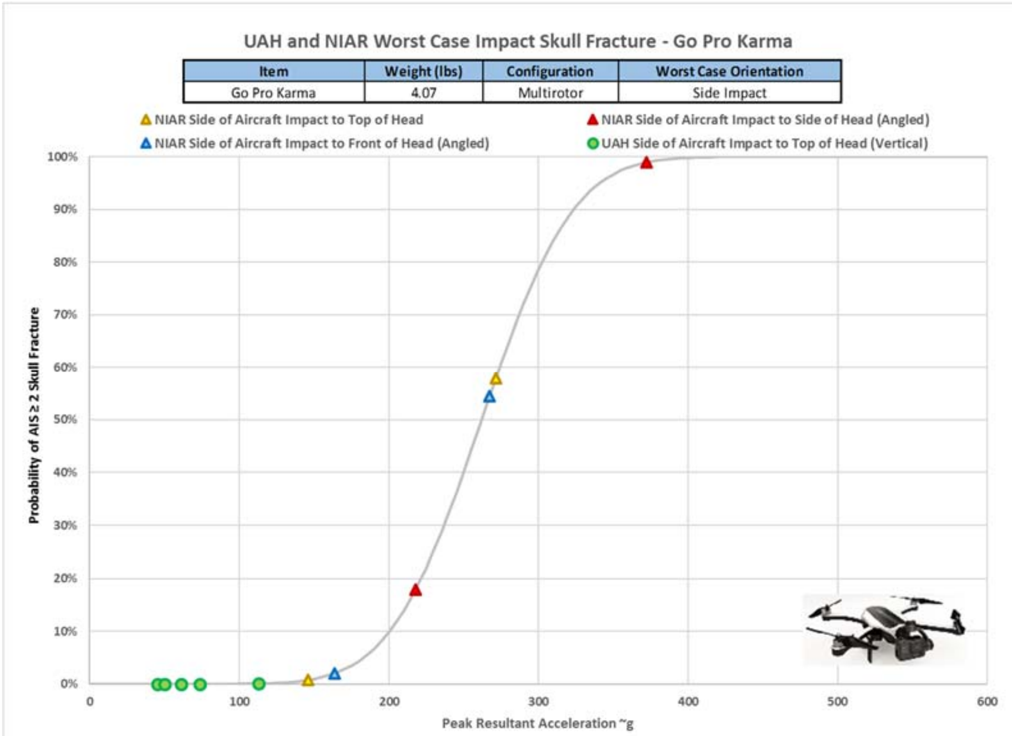

Figure G 7. UAH and NIAR Worst Case Impact Skull Fracture Evaluation - Go Pro Karma

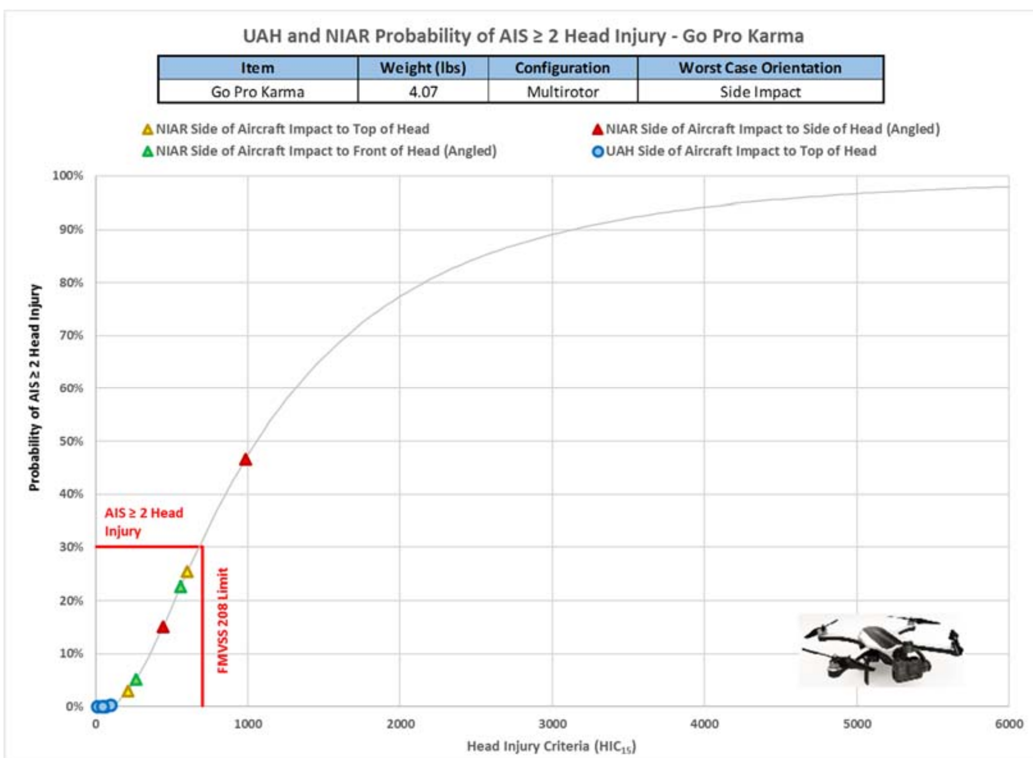

Figure G 8. UAH and NIAR Probability of AIS ≥ 2 Head Injury Evaluation - Go Pro Karma

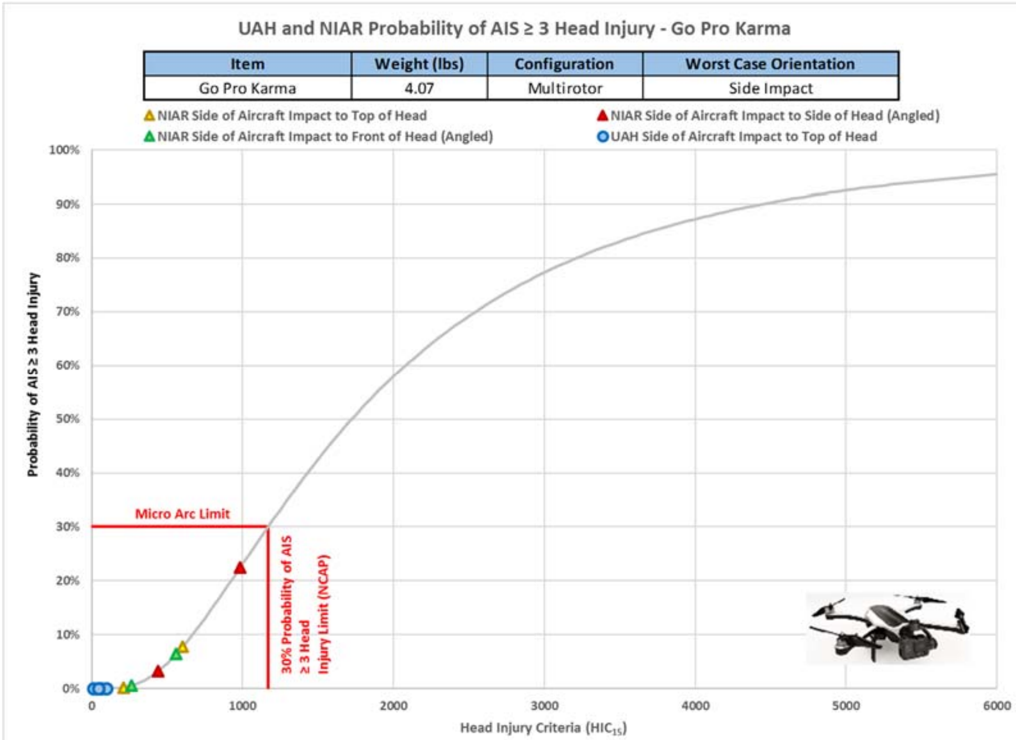

Figure G 9. UAH and NIAR Probability of AIS ≥ 3 Head Injury Evaluation - Go Pro Karma

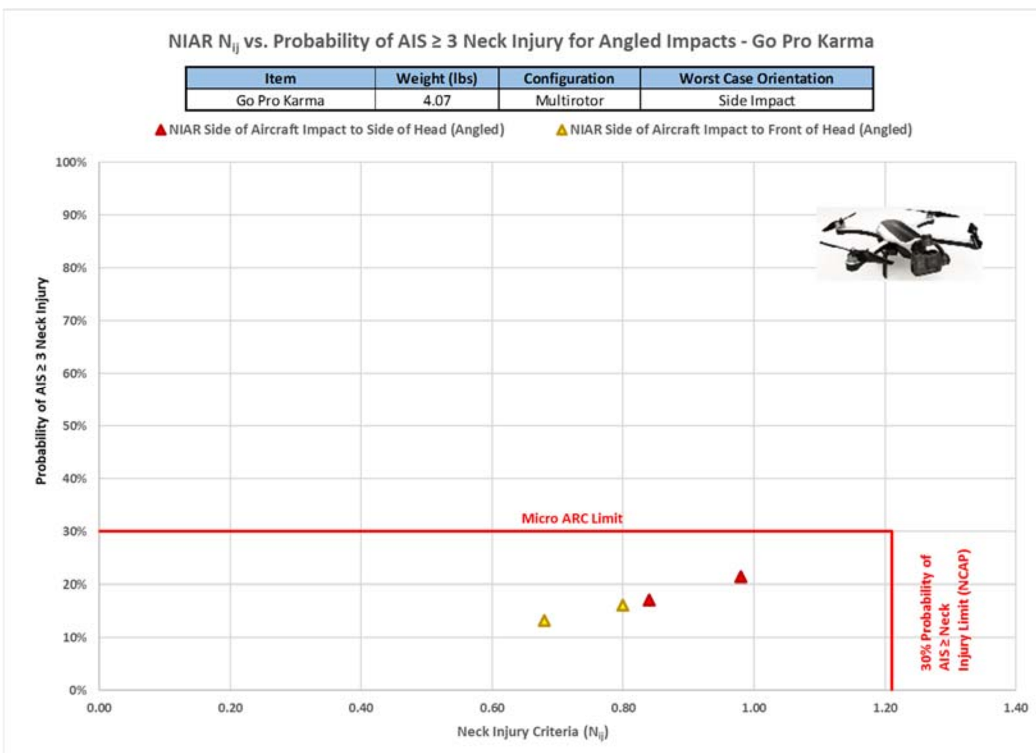

Figure G 10. NIAR N_{ij} vs. Probability of AIS ≥ 3 Neck Injury for Vertical and Angled Impacts – Go Pro Karma

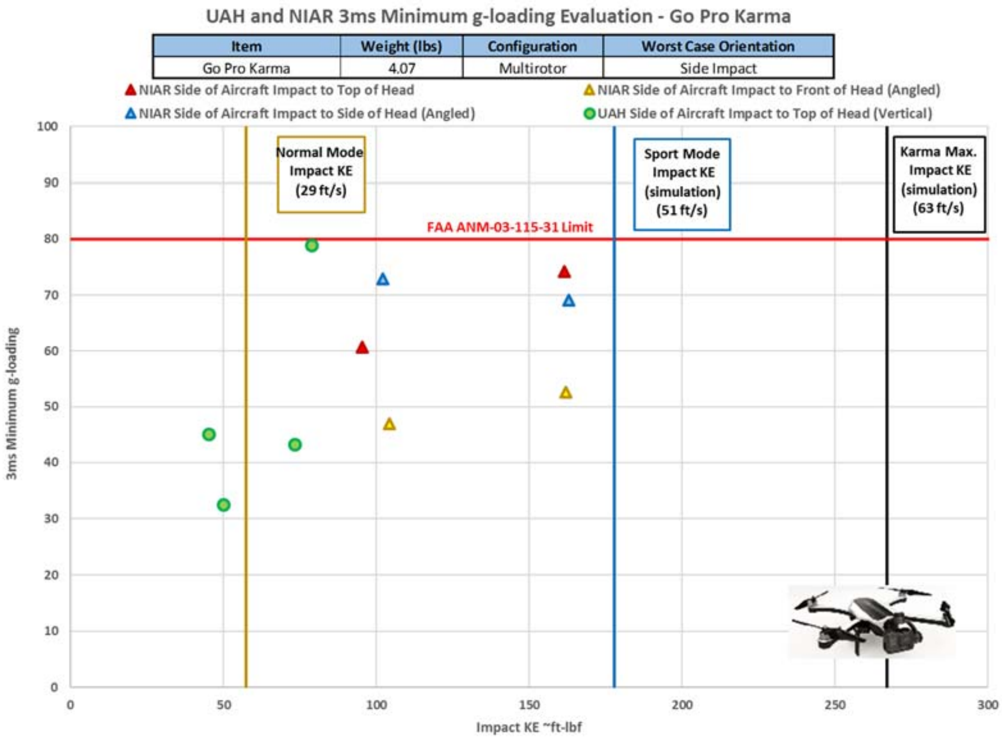

Figure G 11. UAH and NIAR 3ms Minimum g-loading Evaluation - Go Pro Karma

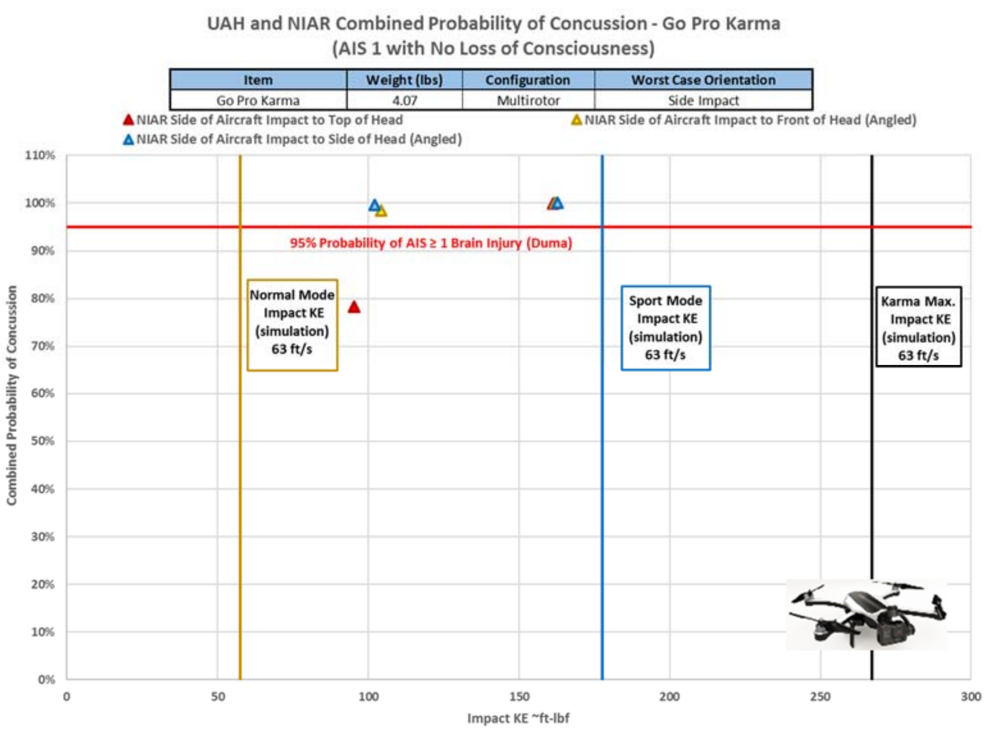

Figure G 12. NIAR Combined Probability of Concussion - Go Pro Karma

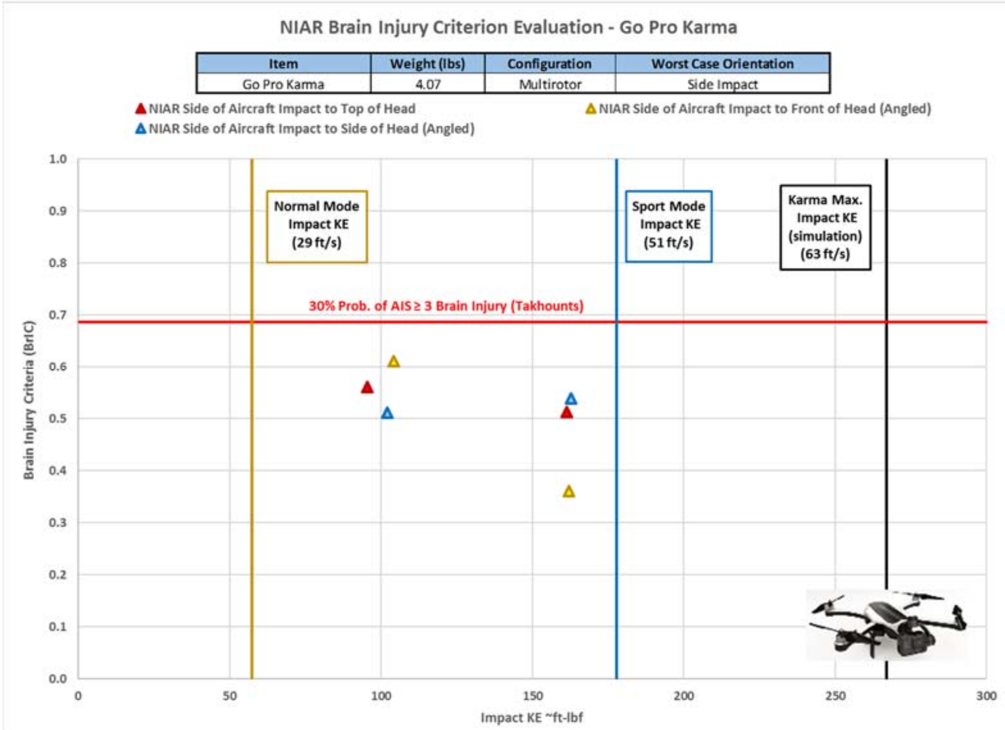

Figure G 13. NIAR Brain Injury Criterion Evaluation – Go Pro Karma

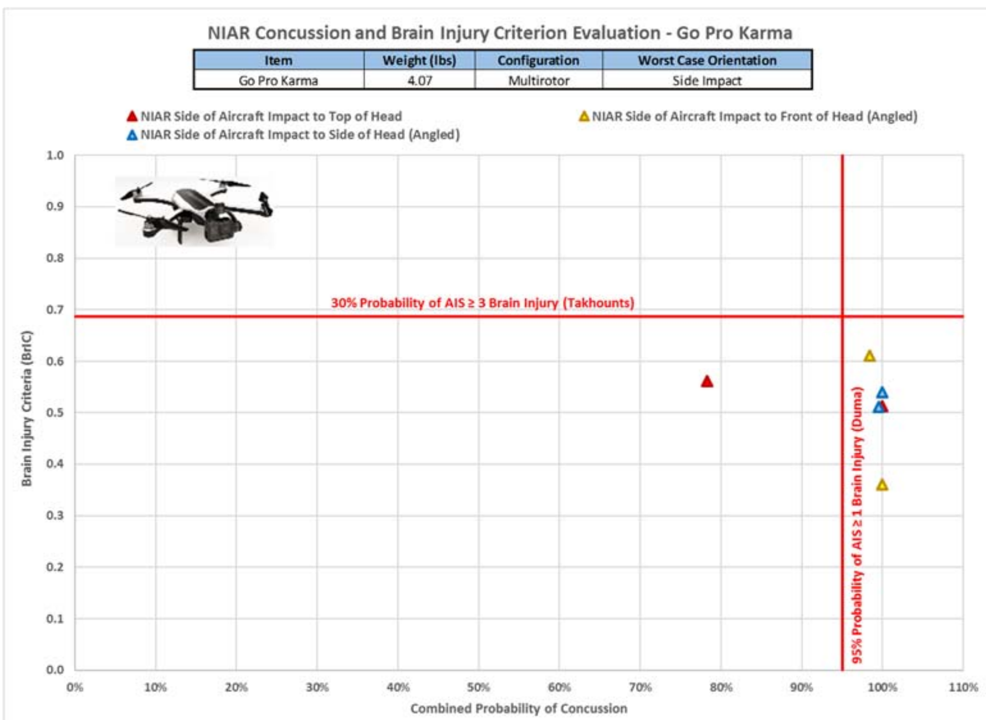

Figure G 14. NIAR Concussion and Brain Injury Criterion Evaluation - Go Pro Karma

APPENDIX H – VENDOR 3 QUADROTOR SIMPLIFIED AND FULL ATD TEST DATA

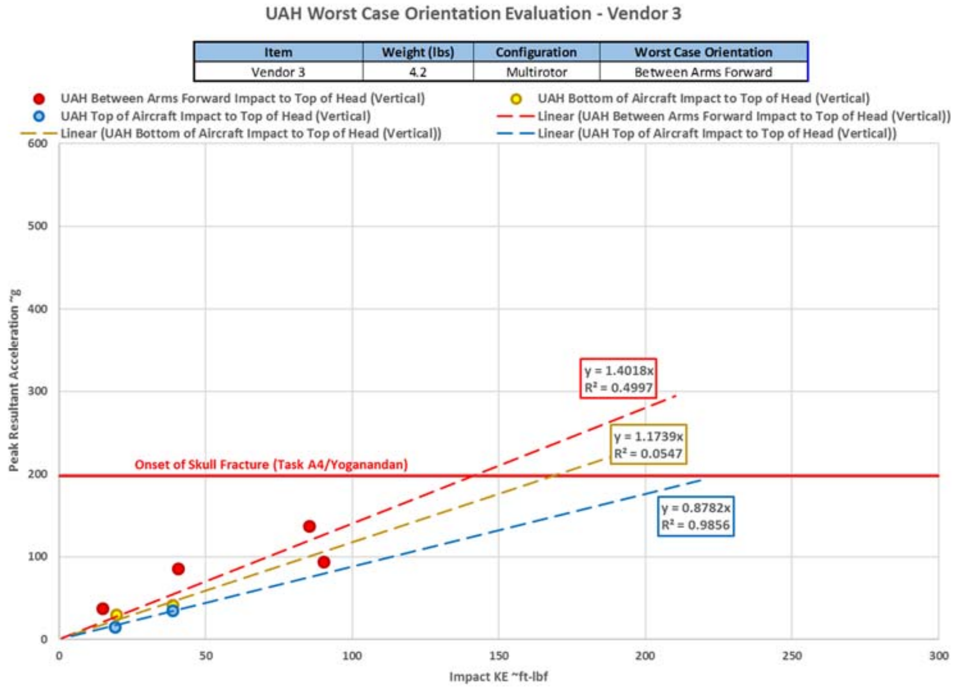

Figure H 1. UAH Worst Case Orientation Evaluation – Vendor 3 Quadrotor

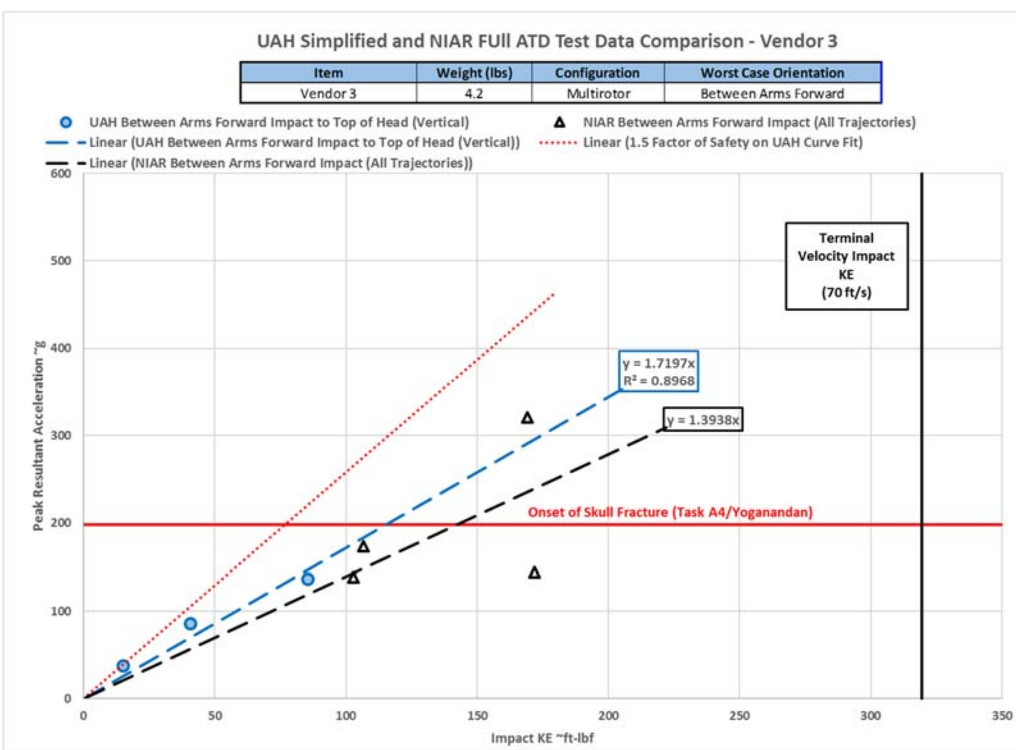

Figure H 2. UAH and NIAR Data Comparison - Vendor 3 Quadrotor

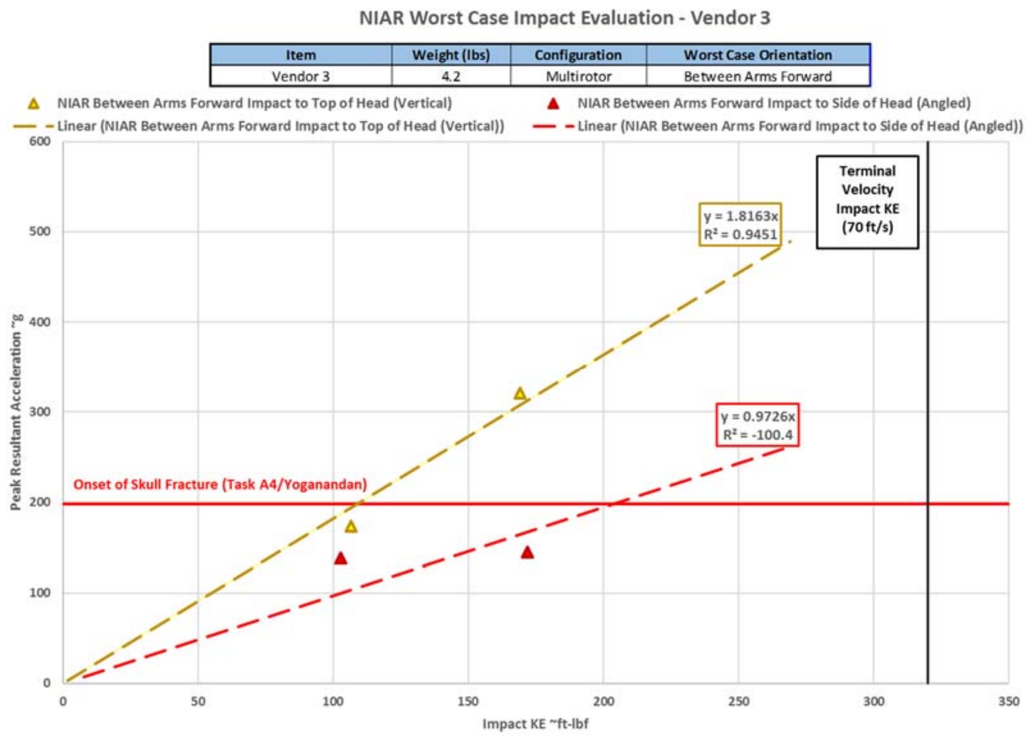

Figure H 3. NIAR Worst Case Impact Evaluation - Vendor 3 Quadrotor

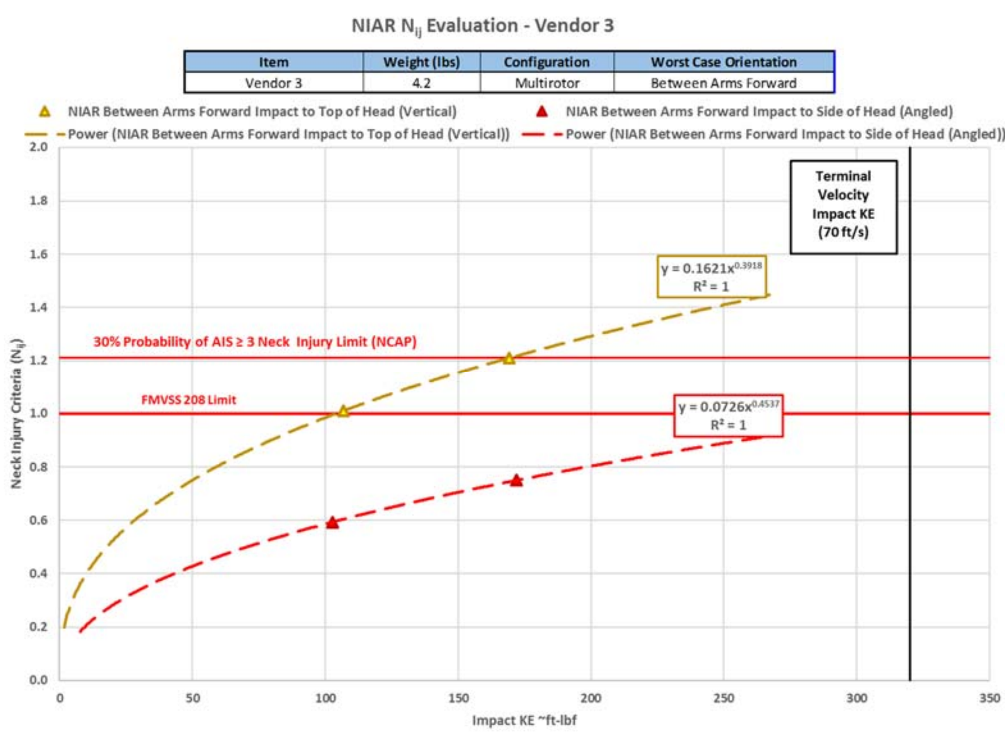

Figure H 4. NIAR N_{ij} Evaluation - Vendor 3

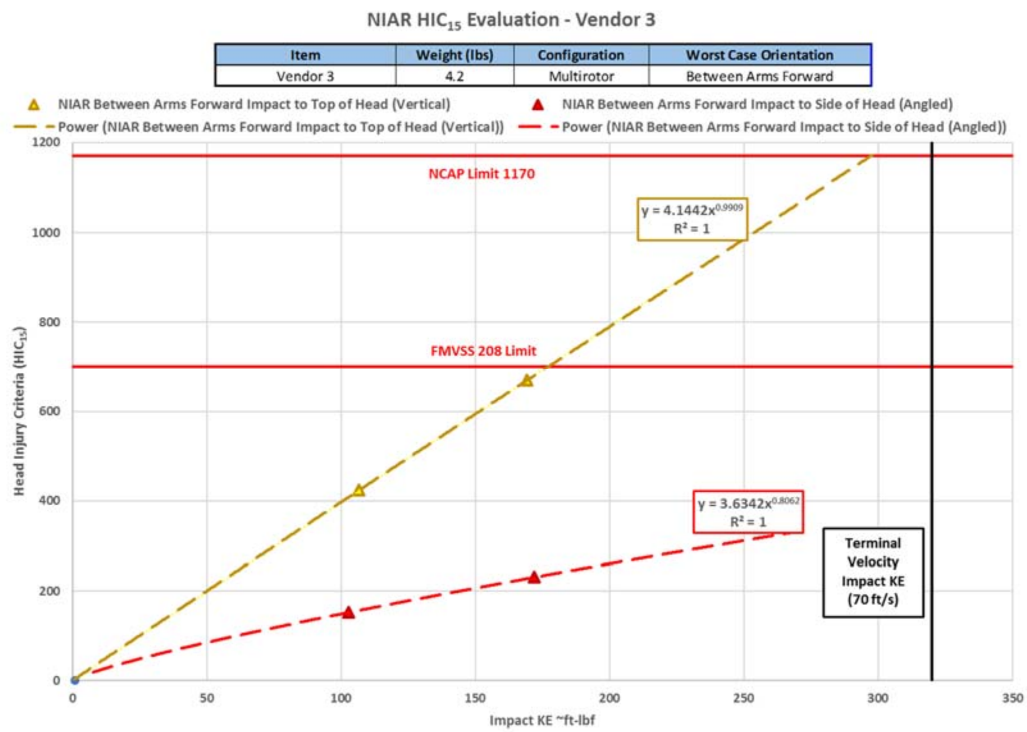

Figure H 5. NIAR HIC15 Evaluation - Vendor 3

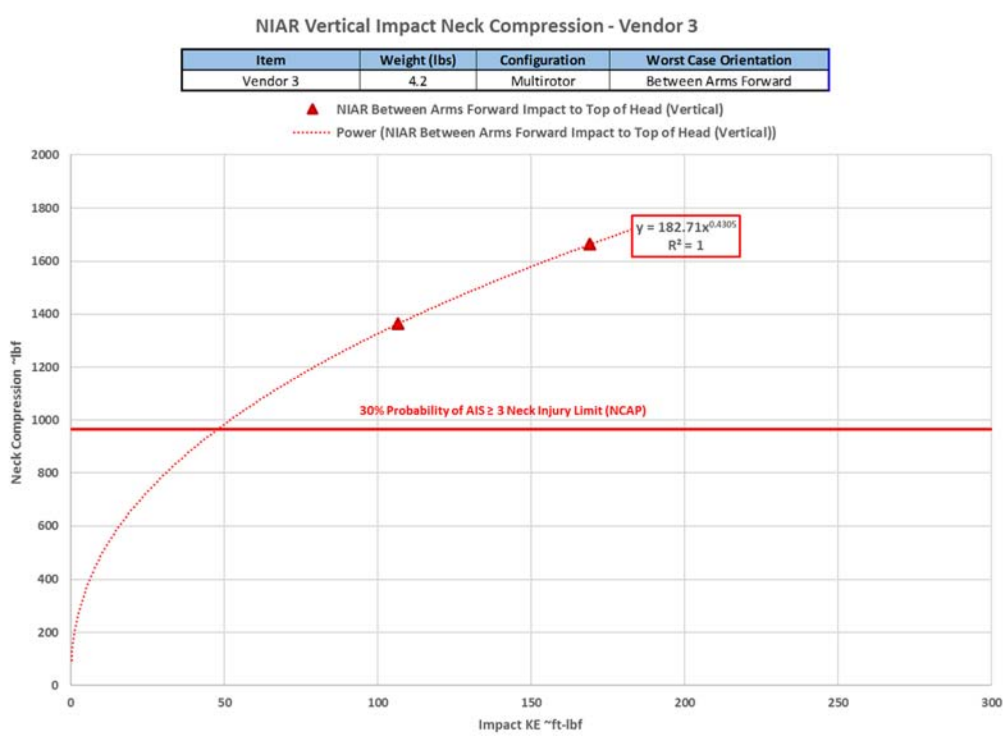

Figure H 6. NIAR Vertical Impact Neck Compression - Vendor 3 Quadrotor

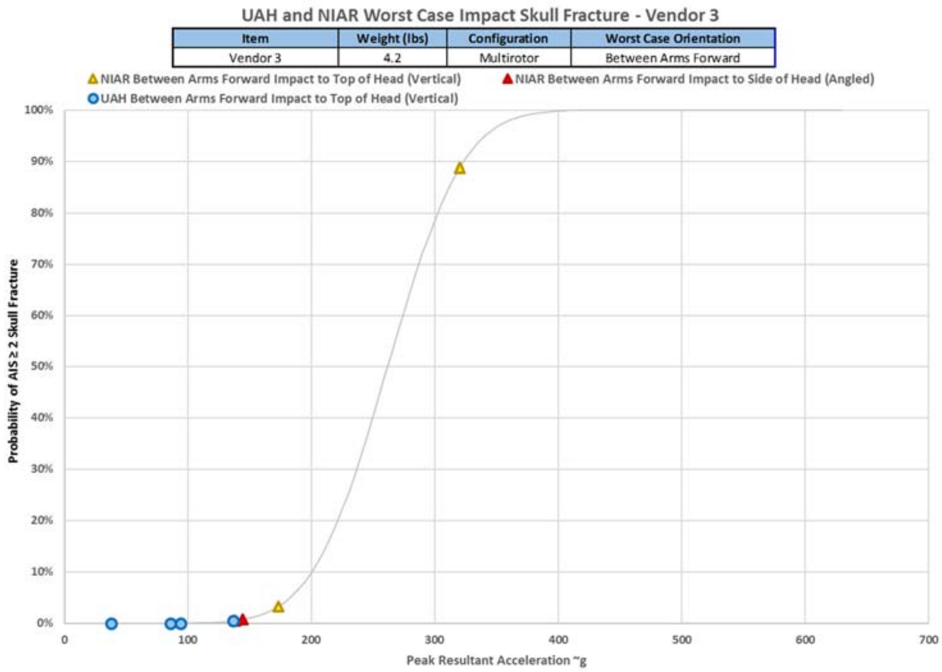

Figure H 7. UAH and NIAR Worst Case Impact Skull Fracture - Vendor 3 Quadrotor

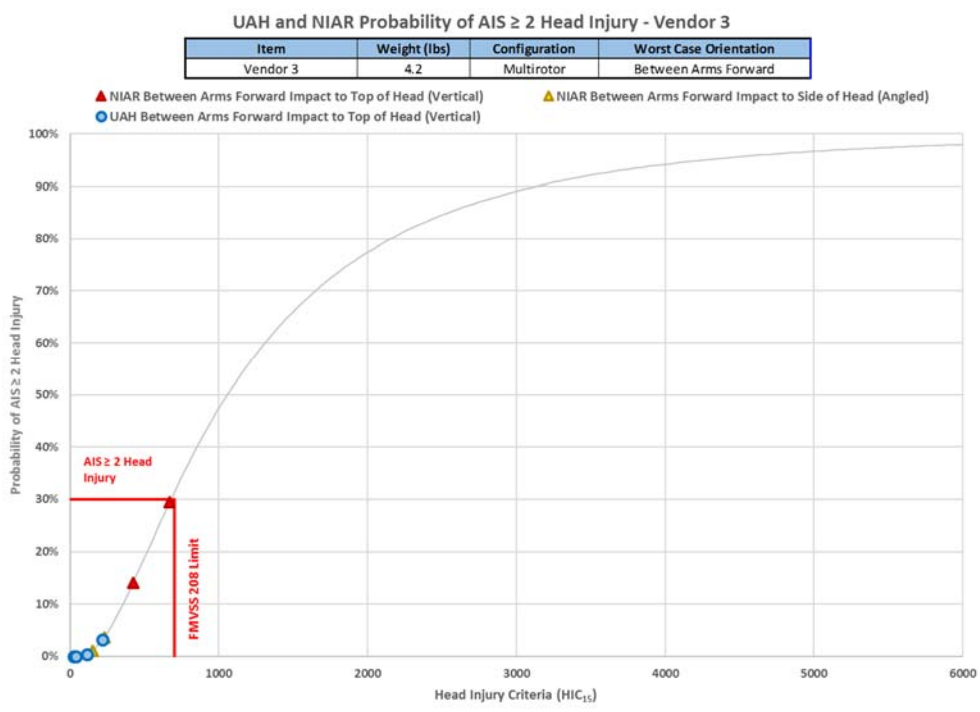

Figure H 8. UAH and NIAR Probability of AIS ≥ 2 Head Injury - Vendor 3 Quadrotor

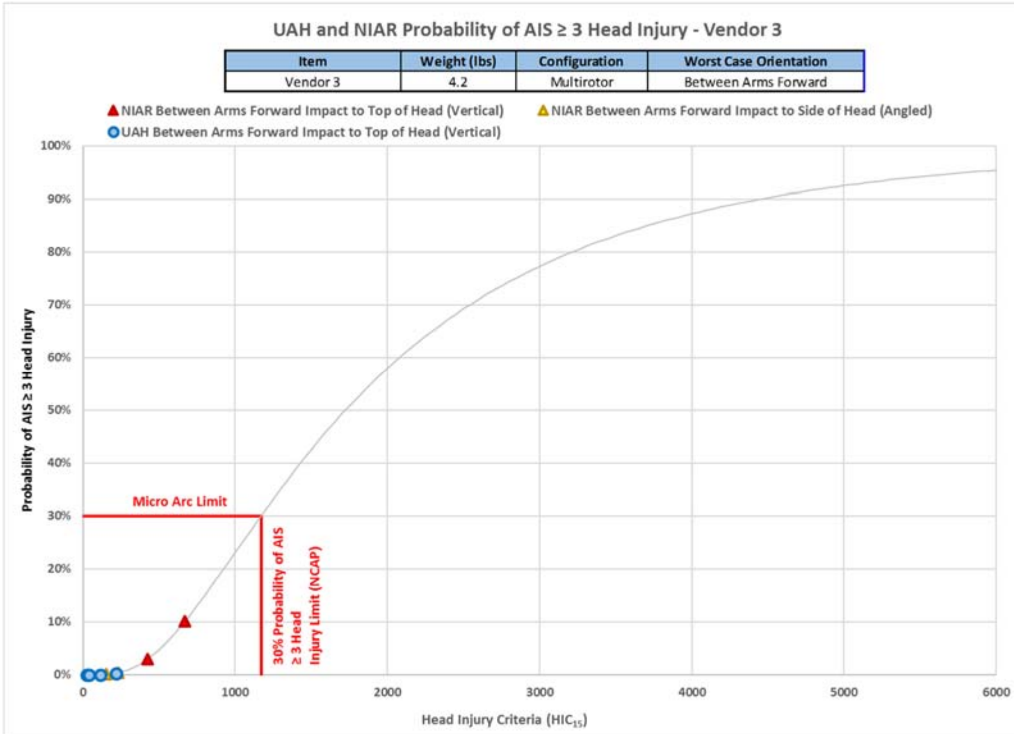

Figure H 9. UAH and NIAR Probability of AIS ≥ 3 Head Injury - Vendor 3 Quadrotor

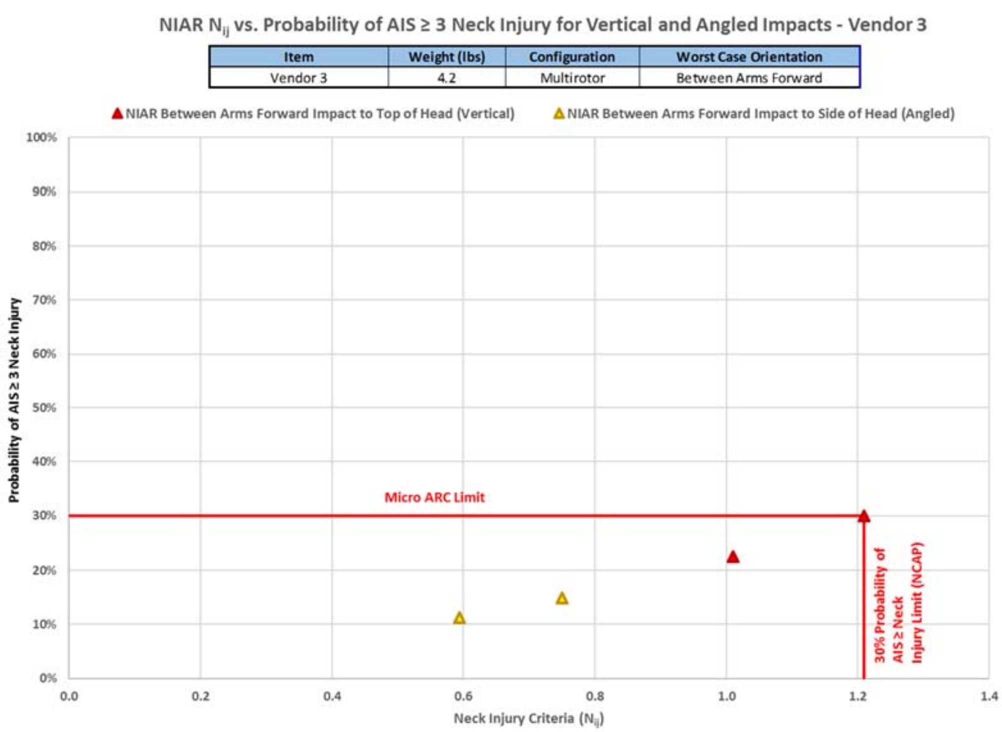

Figure H 10. NIAR N_{ij} vs. Probability of AIS ≥ 3 Neck Injury for Angled Impacts - Vendor 3 Quadrotor

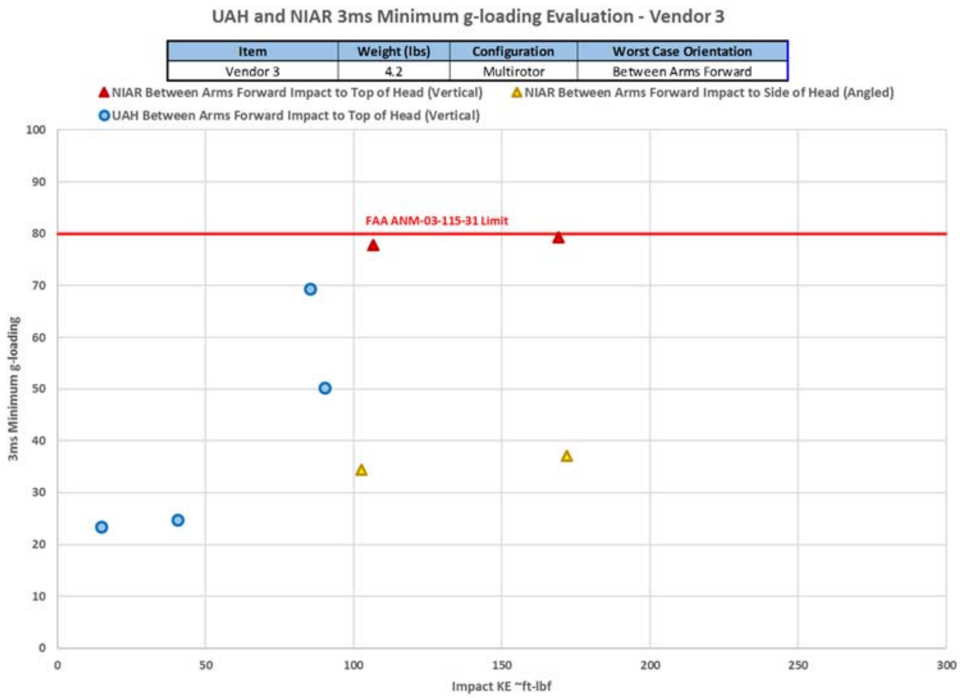

Item	Weight (lbs)	Configuration	Worst Case Orientation
Vendor 3	4.2	Multirotor	Between Arms Forward

Figure H 11. UAH and NIAR 3ms Minimum g-loading Evaluation - Vendor 3 Quadrotor

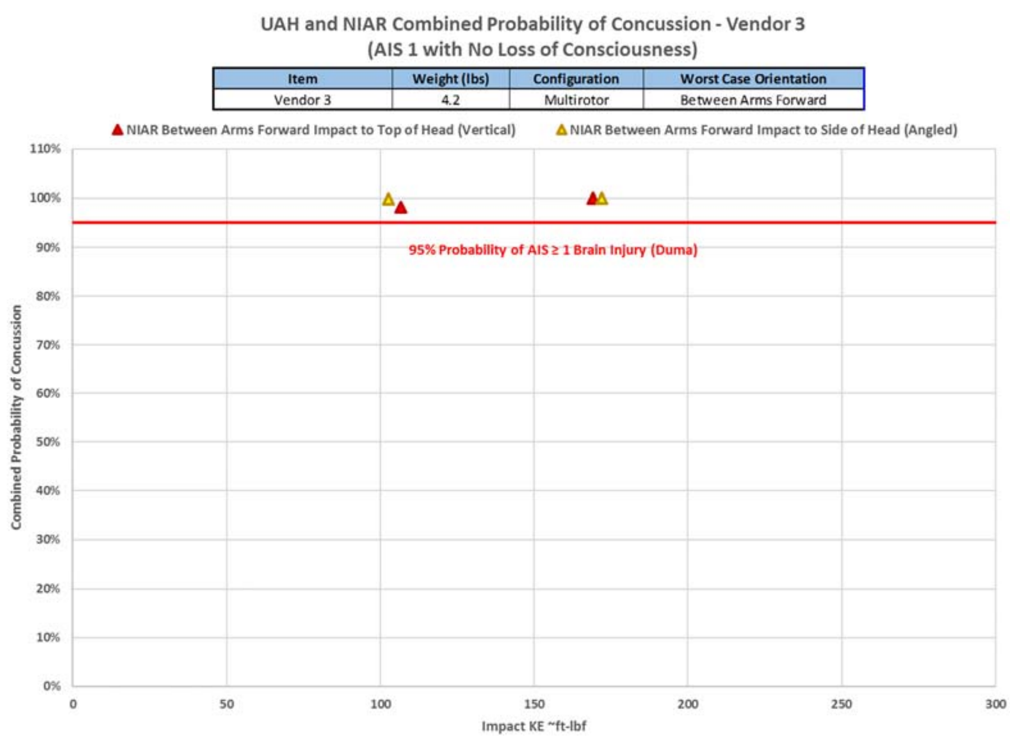

Item	Weight (lbs)	Configuration	Worst Case Orientation
Vendor 3	4.2	Multirotor	Between Arms Forward

Figure H 12. NIAR Combined Probability of Concussion - Vendor 3 Quadrotor

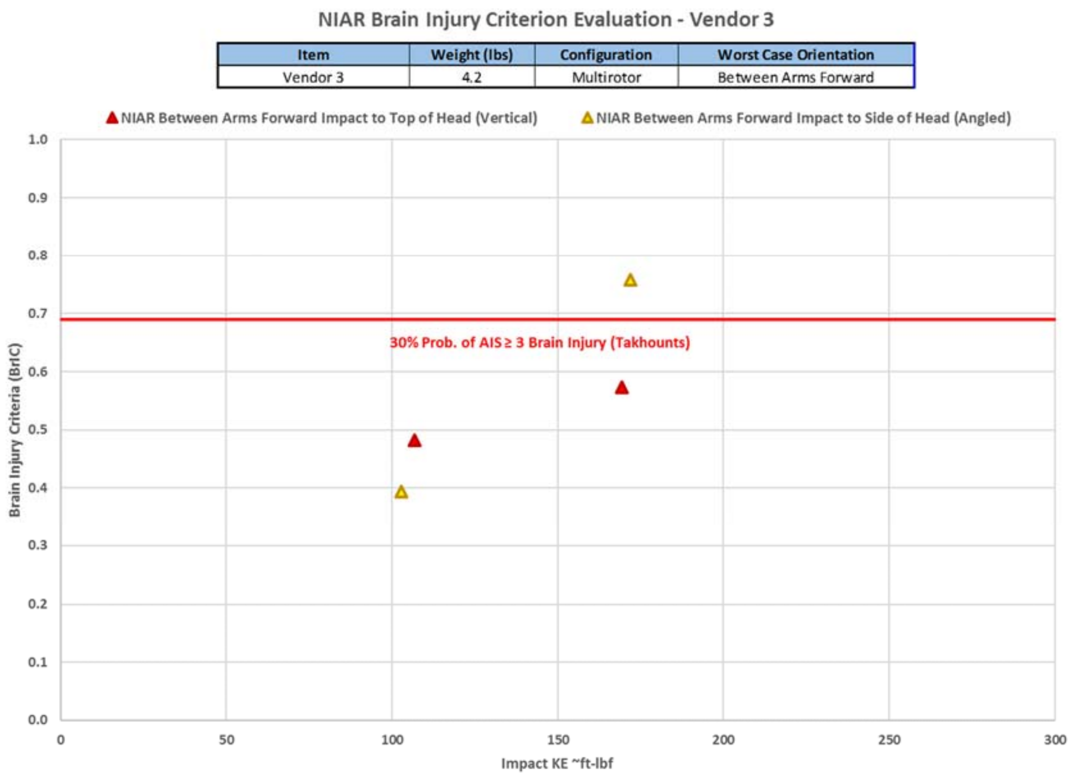

Figure H 13. NIAR Brain Injury Criterion Evaluation - Vendor 3 Quadrotor

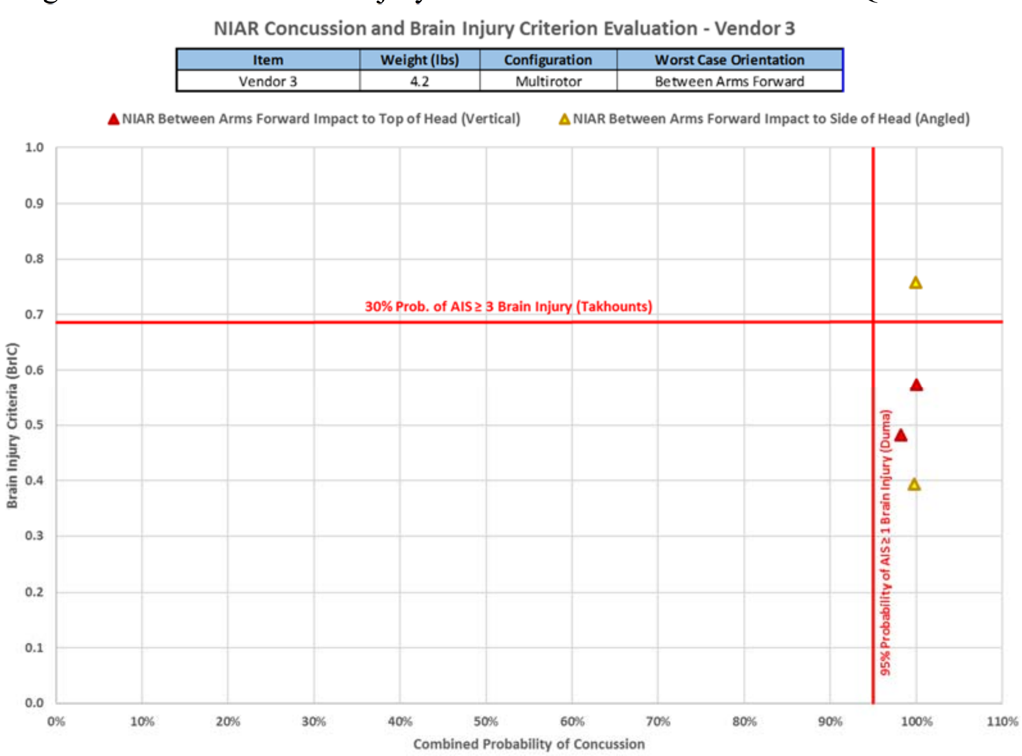

Figure H 14. NIAR Concussion and Brain Injury Criterion Evaluation - Vendor 3 Quadrotor

APPENDIX I – DJI INSPIRE 2 FULL ATD TEST DATA

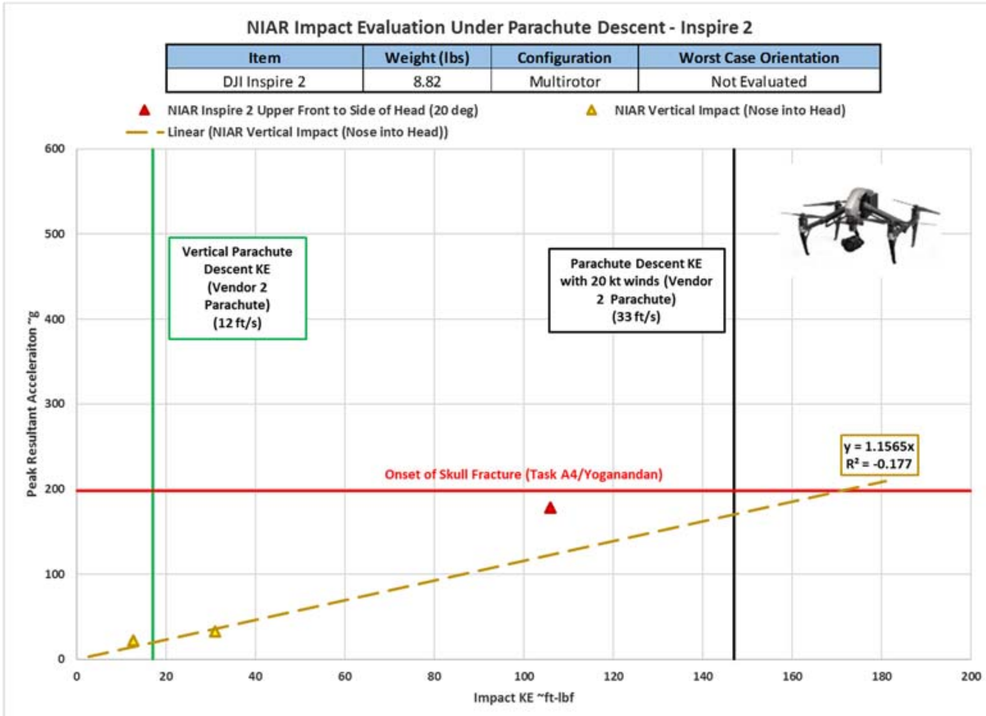

Figure I 1. NIAR Impact Evaluation Under Parachute Descent - Inspire 2

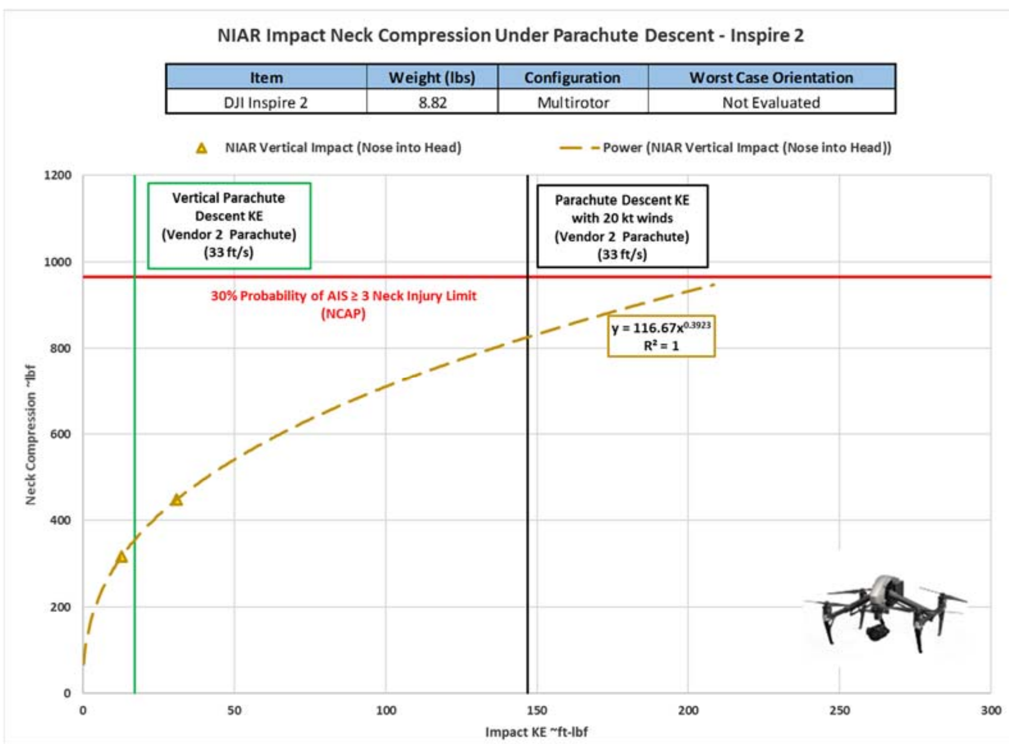

Figure I 2. NIAR Impact Neck Compression Under Parachute Descent - Inspire 2

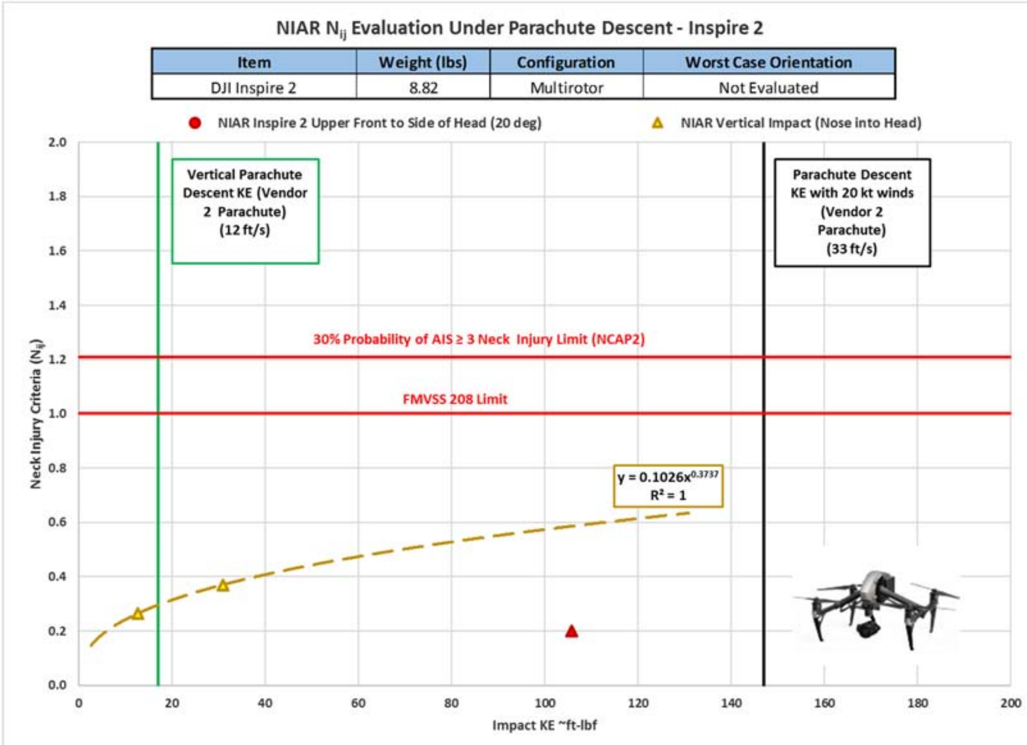

Figure I 3. NIAR N_{ij} Evaluation Under Parachute Descent - Inspire 2

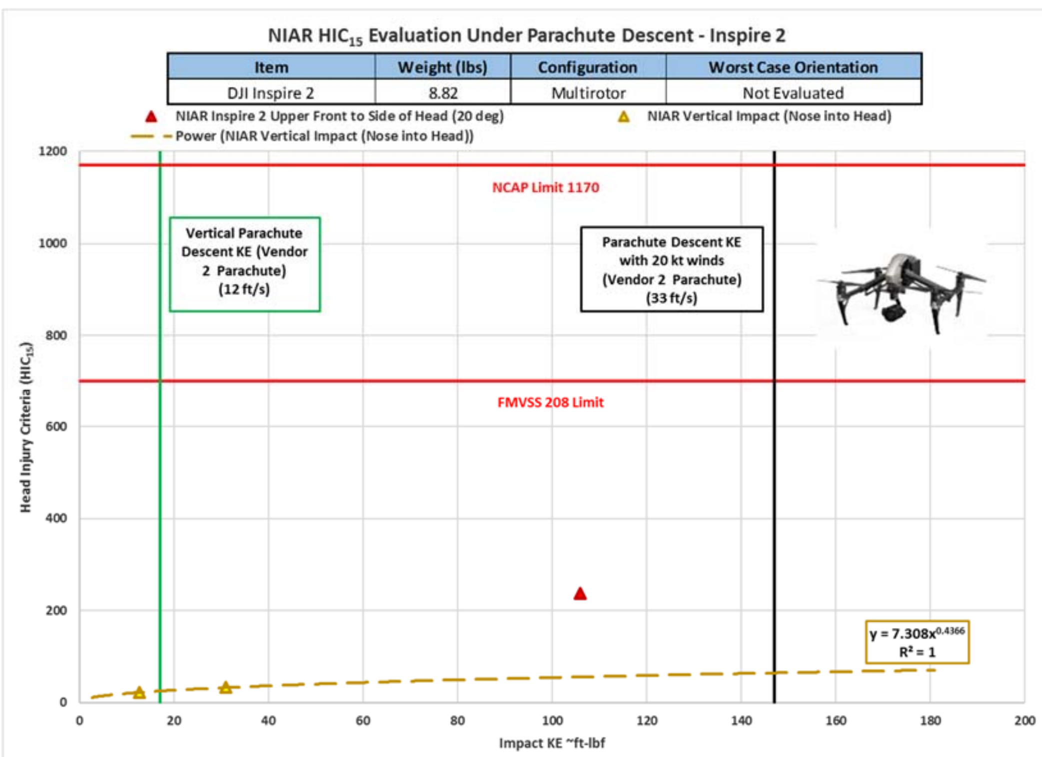

Figure I 4. NIAR HIC_{15} Evaluation Under Parachute Descent - Inspire 2

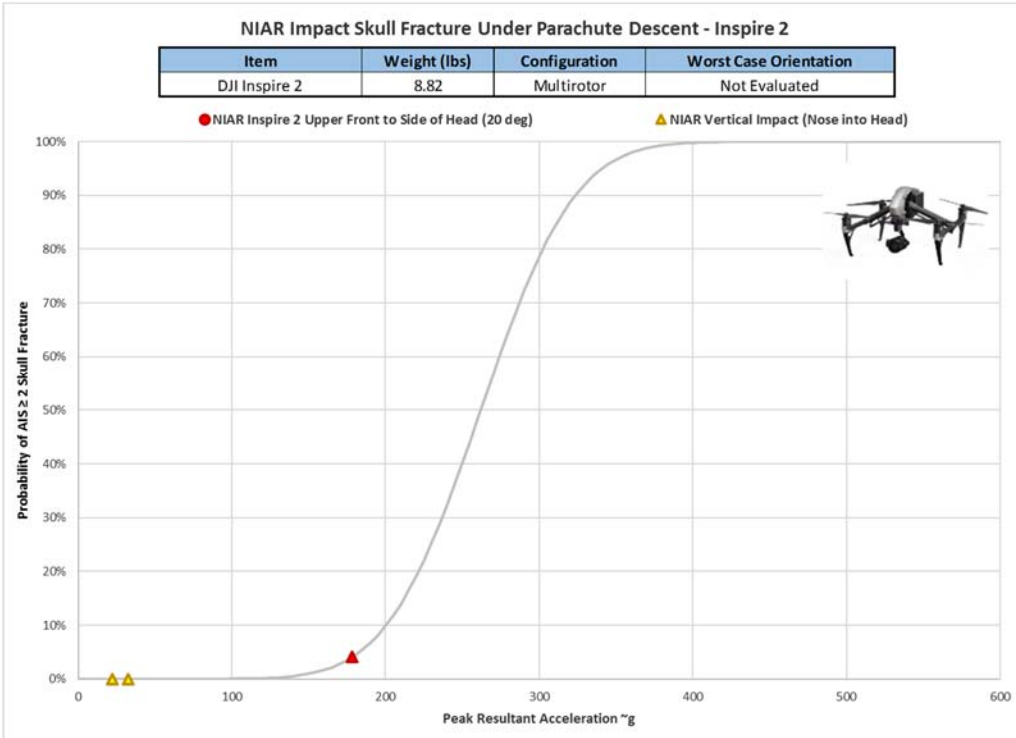

Figure I 5. NIAR Impact Skull Fracture Under Parachute - DJI Inspire 2

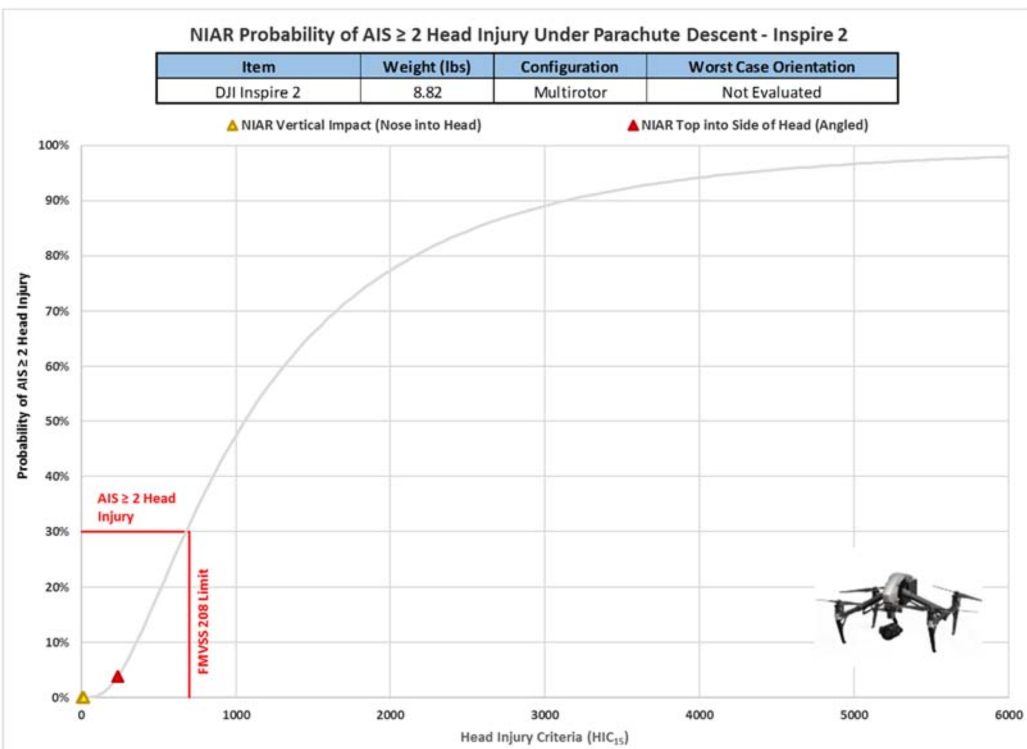

Figure I 6. NIAR Probability of AIS ≥ 2 Head Injury under Parachute Descent - DJI Inspire 2

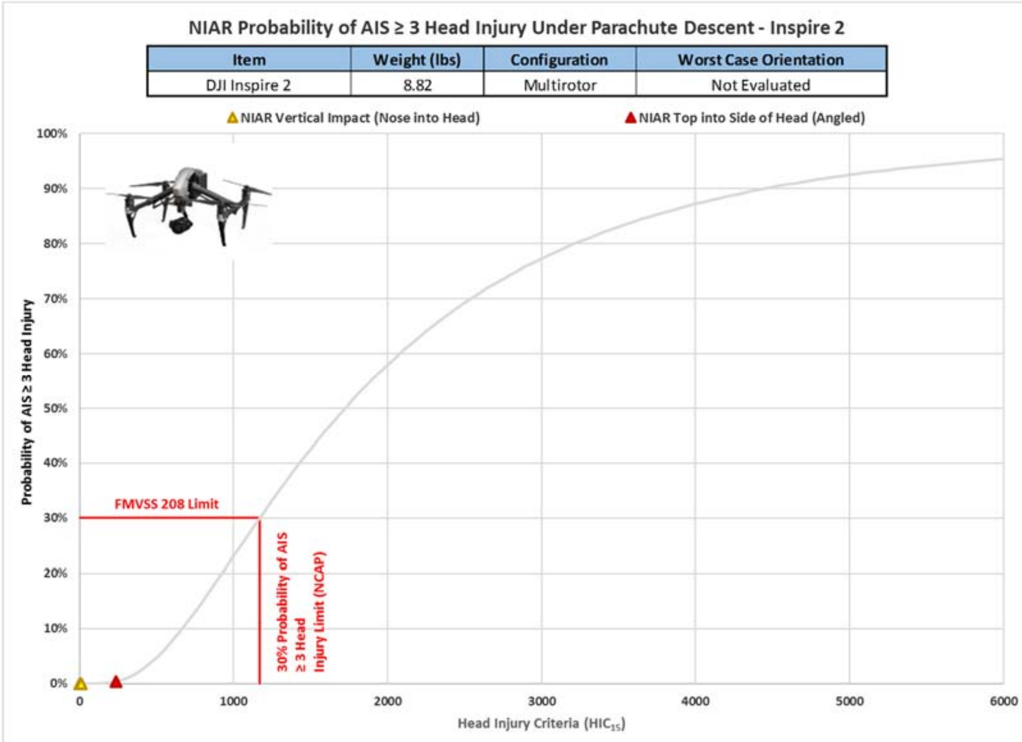

Figure I 7. NIAR Probability of AIS ≥ 3 Head Injury under Parachute Descent - DJI Inspire 2

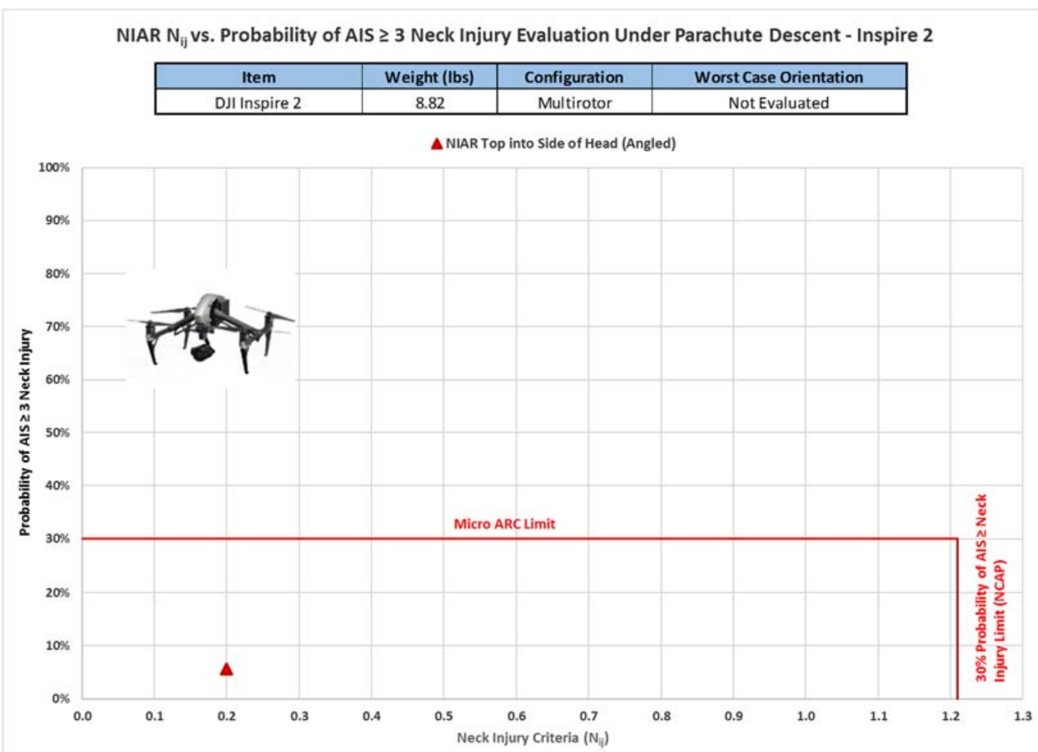

Figure I 8. NIAR N_{ij} vs. Probability of AIS ≥ 3 Neck Injury for Vertical and Angled Impacts under Parachute Descent- DJI Inspire 2

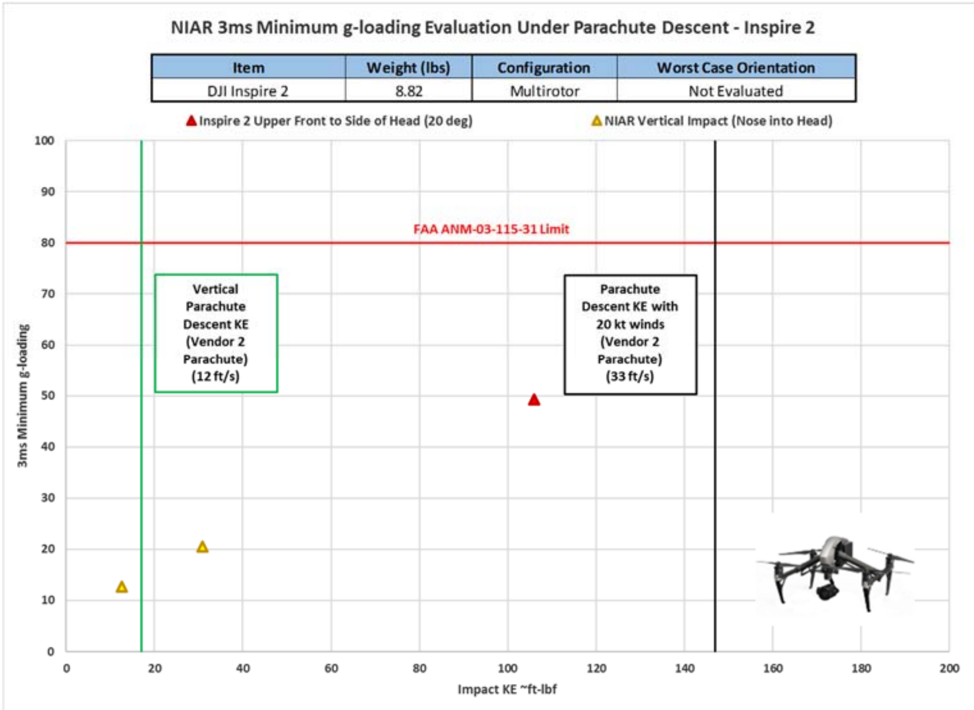

Figure I 9. NIAR 3ms Minimum g-loading Evaluation under Parachute Descent - DJI Inspire 2

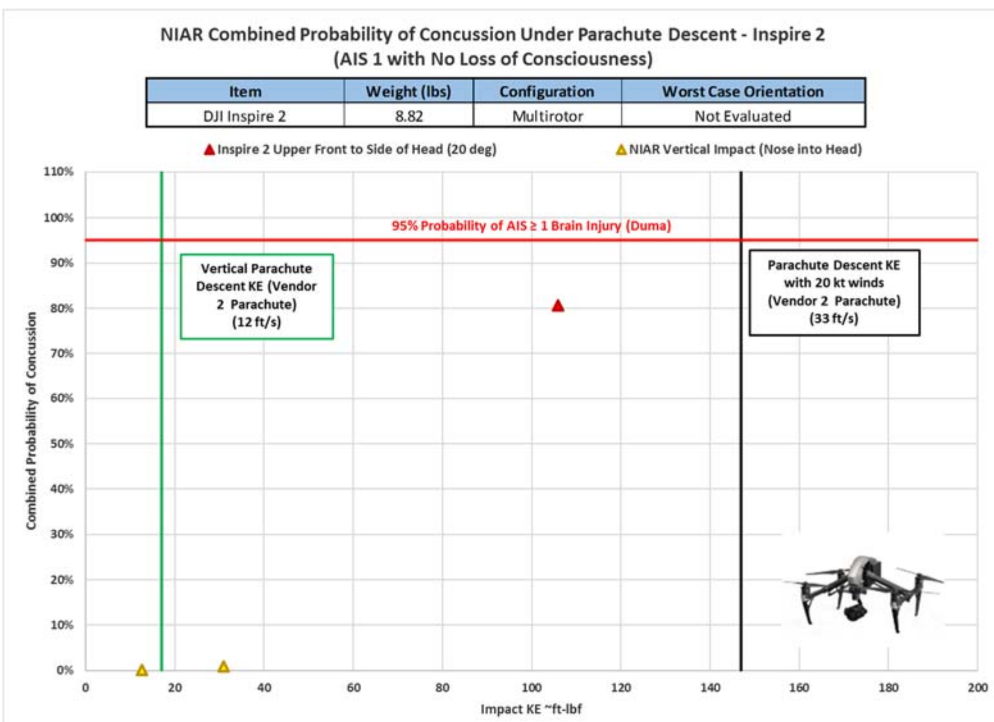

Figure I 10. NIAR Combined Probability of Concussion under Parachute Descent - DJI Inspire 2 (AIS 1 with No Loss of Consciousness)

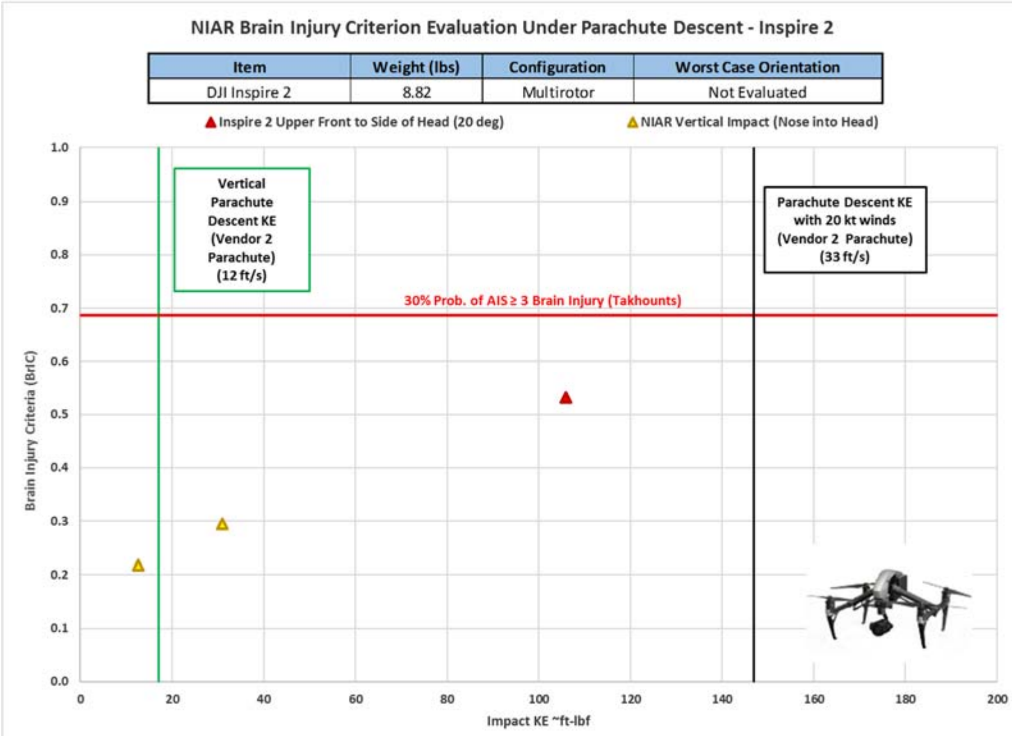

Figure I 11. NIAR Brain Injury Criterion Eval uation under Parachute Descent - DJI Inspire 2

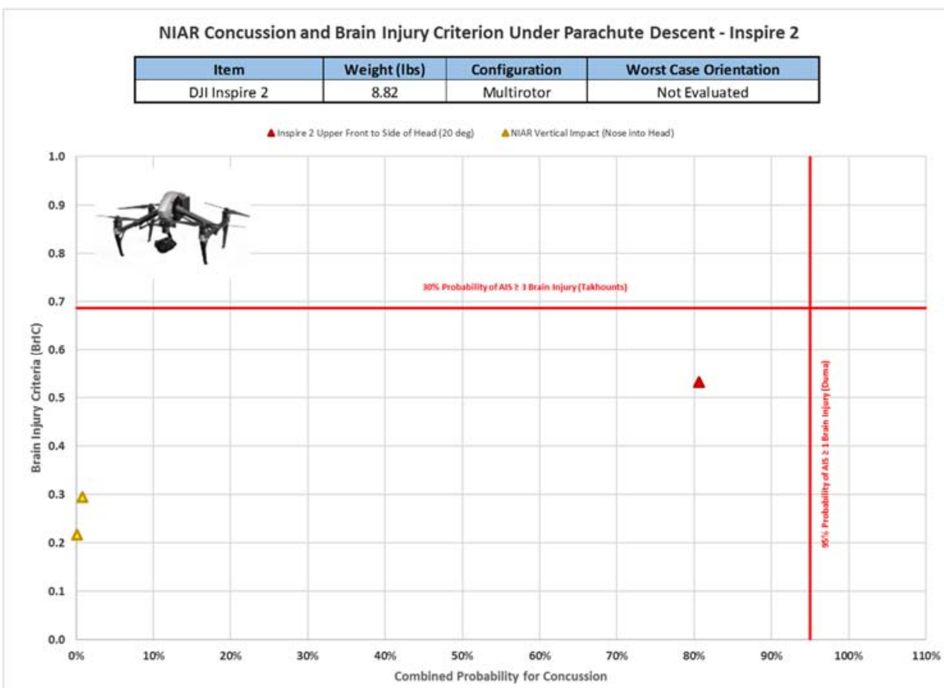

Figure I 12. NIAR Concussion and Brain Injury Criterion Evaluation under Parachute Descent-
DJI Inspire 2

APPENDIX J – DJI S800 SIMPLIFIED TEST DATA

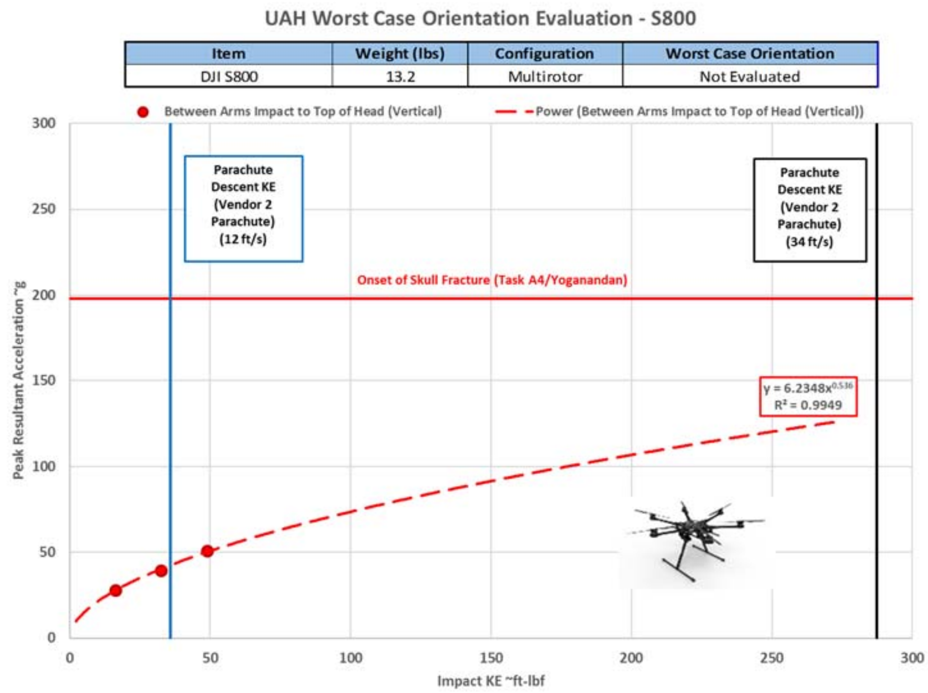

Figure J 1. UAH Worst Case Orientation Evaluation - S800

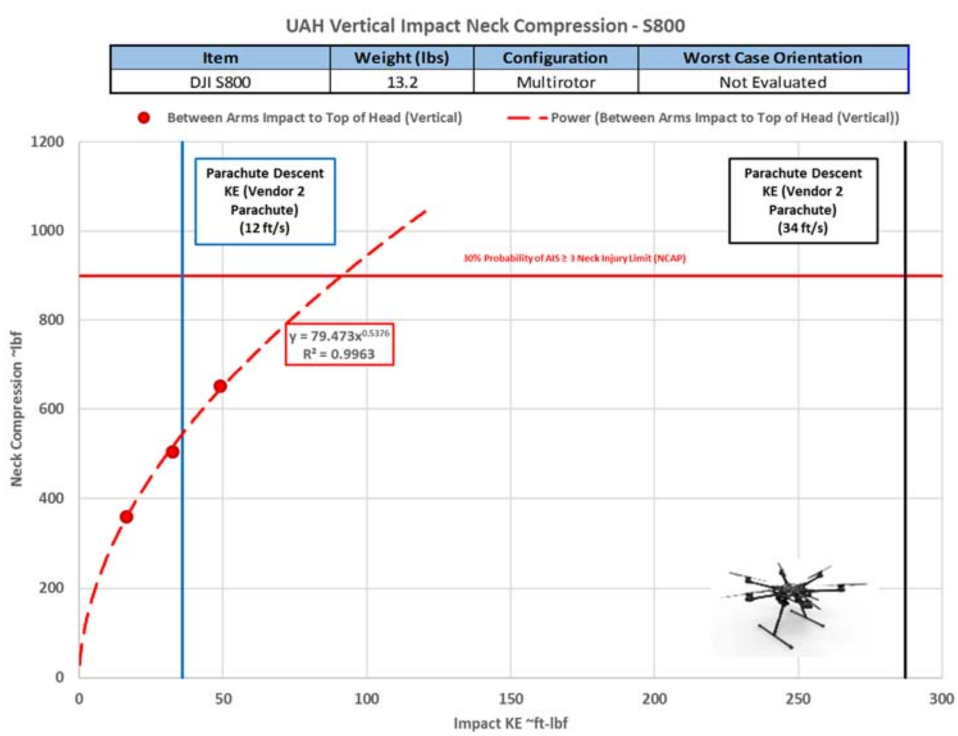

Figure J 2. UAH Vertical Impact Neck Compression - S800

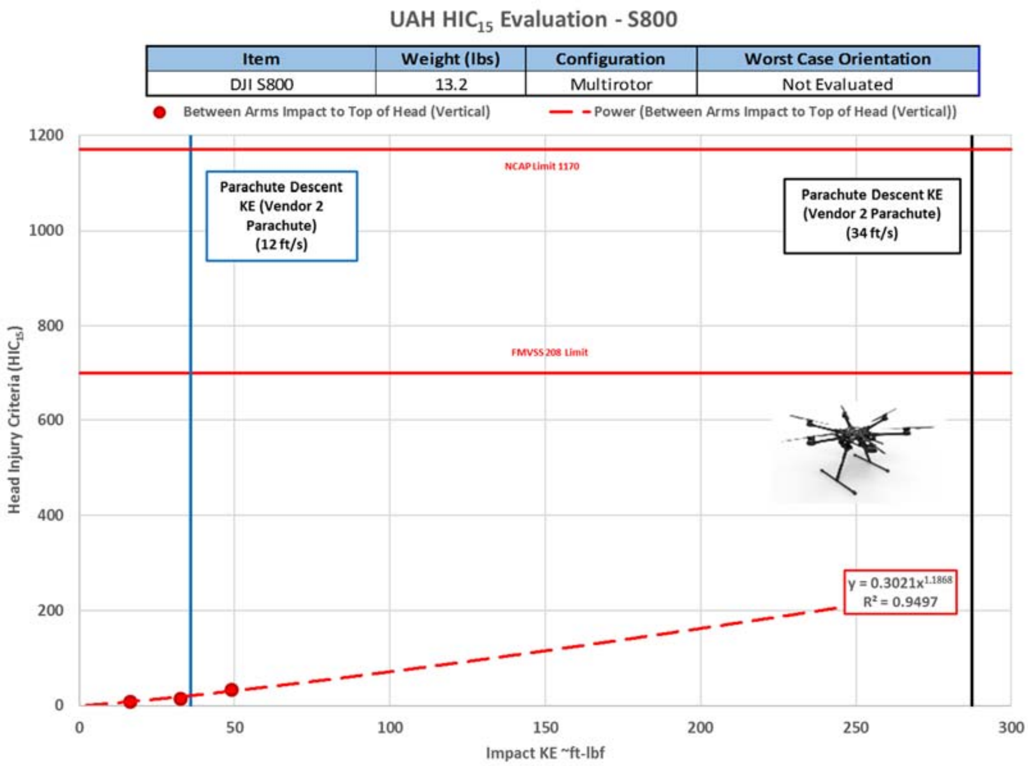

Figure J 3. UAH HIC_{15} Evaluation - S800

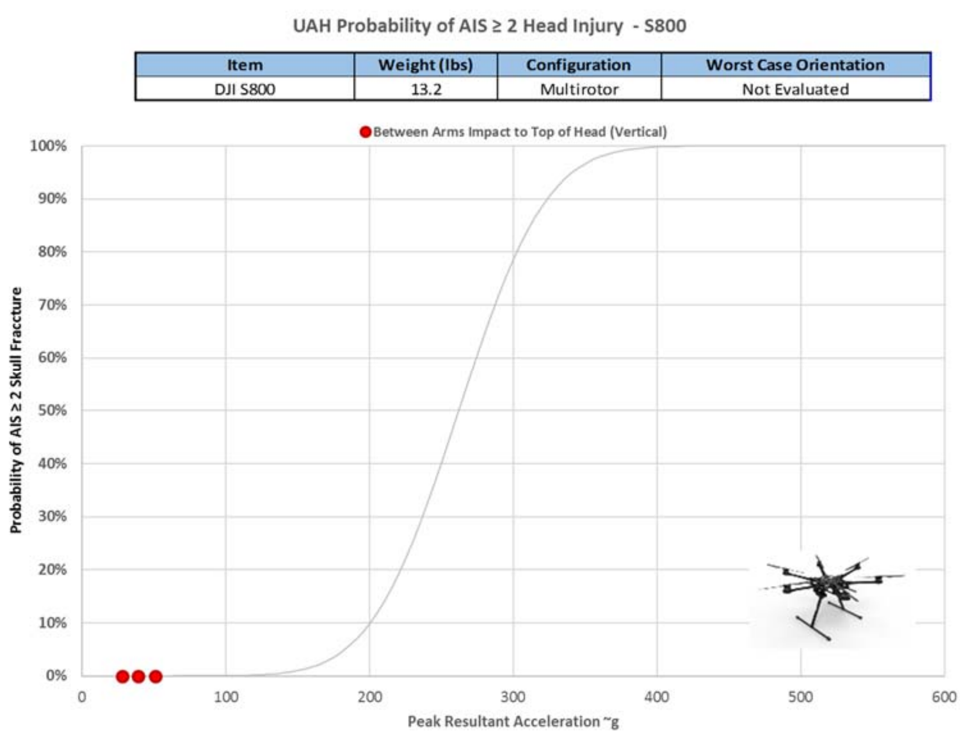

Figure J 4. UAH Probability of AIS ≥ 2 Skull Fracture - S800

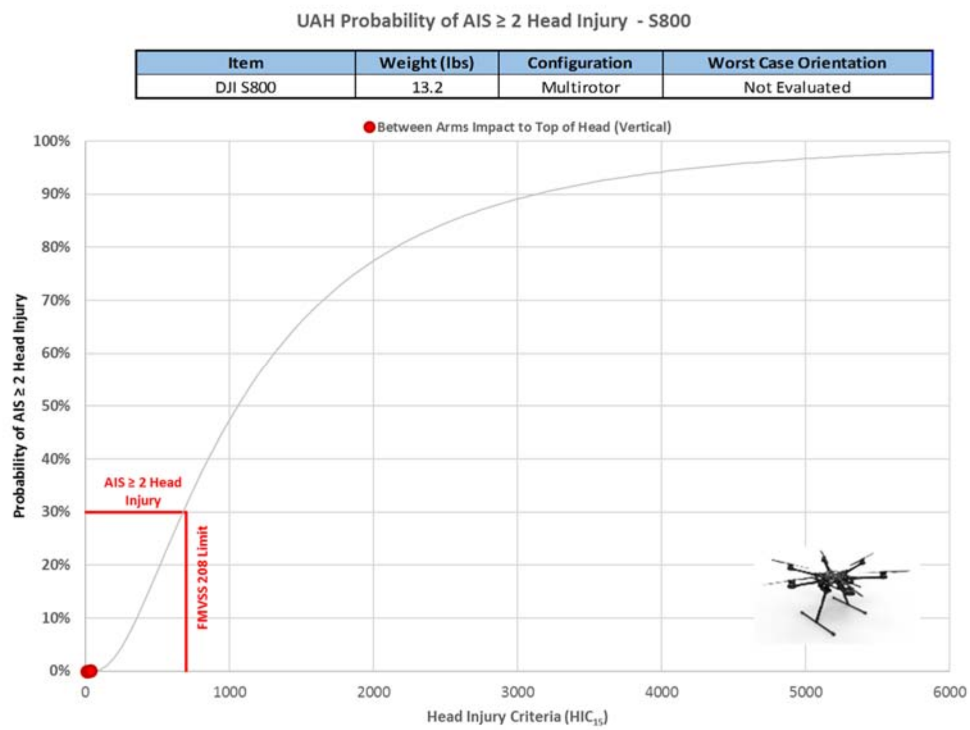

Figure J 5. UAH Probability of AIS ≥ 2 Head Injury - S800

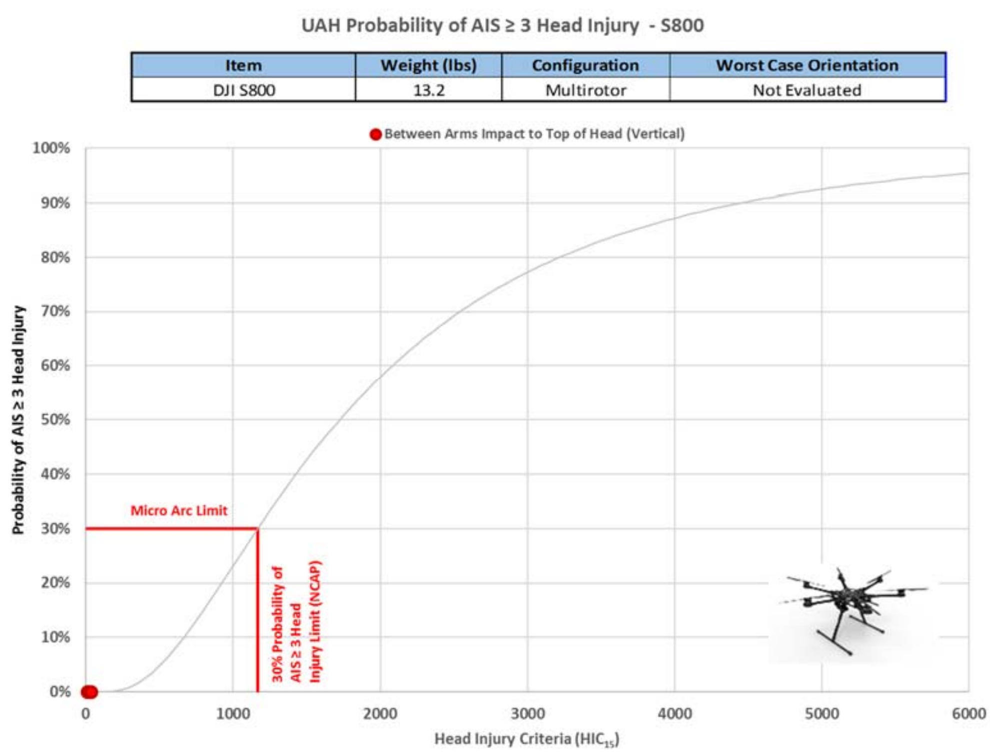

Figure J 6. UAH Probability of AIS ≥ 3 Head Injury - S800

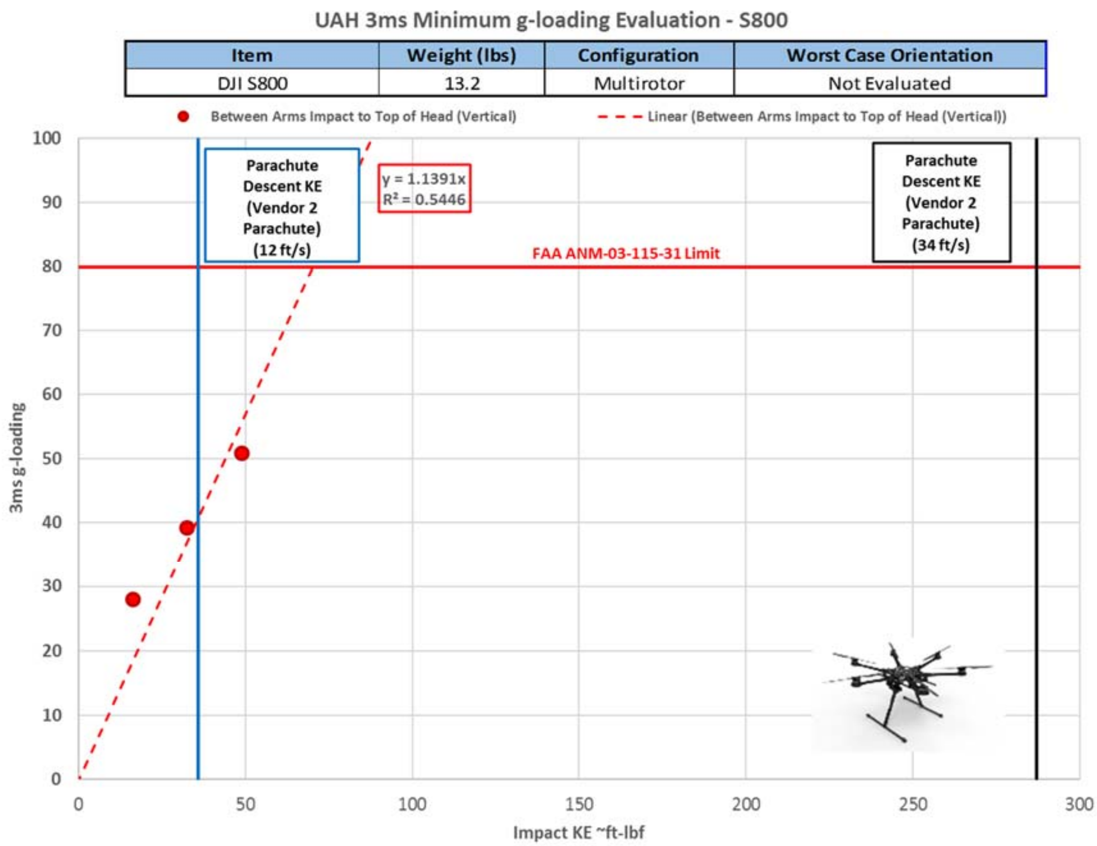

Figure J 7. UAH 3ms Minimum g-loading Evaluation - S800

APPENDIX K – EBEE+ SIMPLIFIED AND FULL ATD TEST DATA

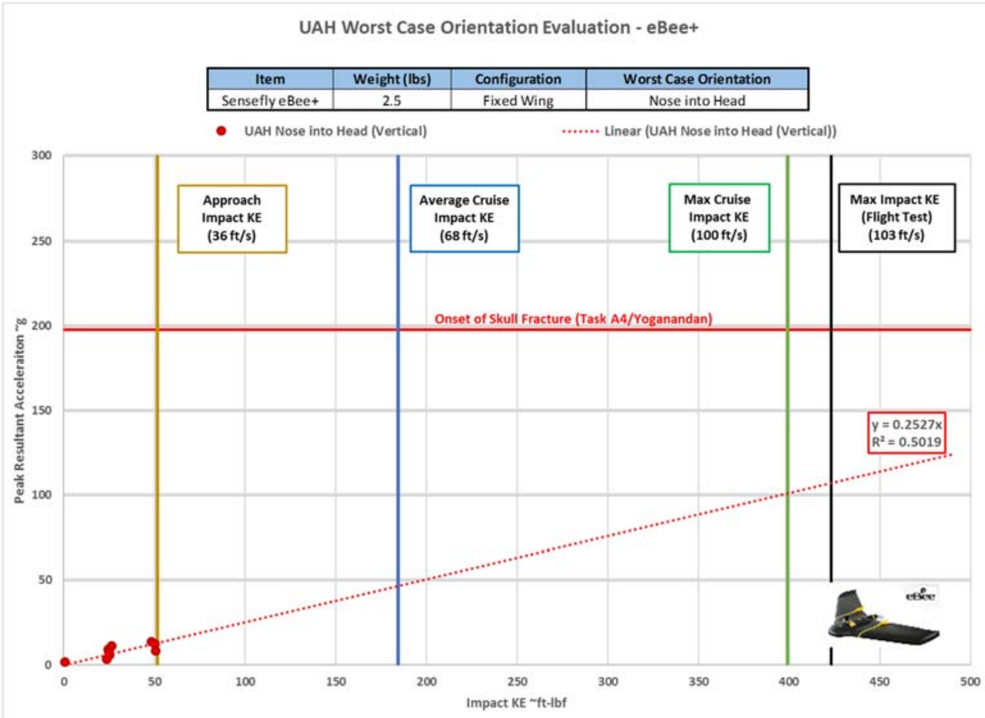

Figure K 1. UAH Worst Case Orientation Evaluation - eBee+

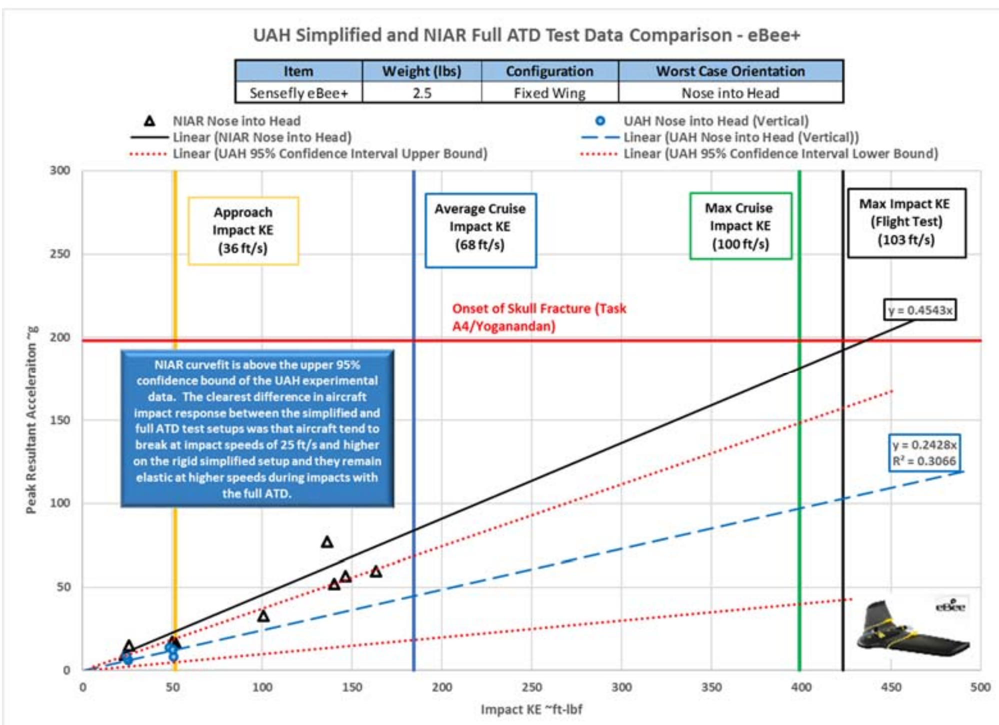

Figure K 2. UAH vs. NIAR Data Comparison – eBee+

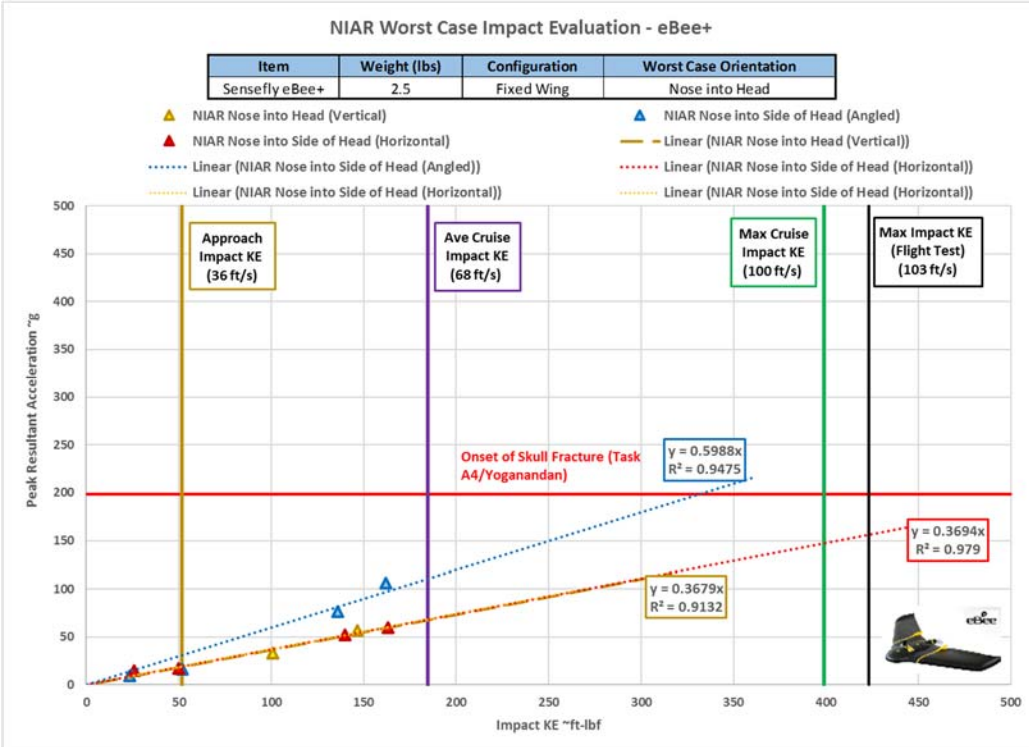

Figure K 3. NIAR Worst Case Impact Evaluation - eBee+

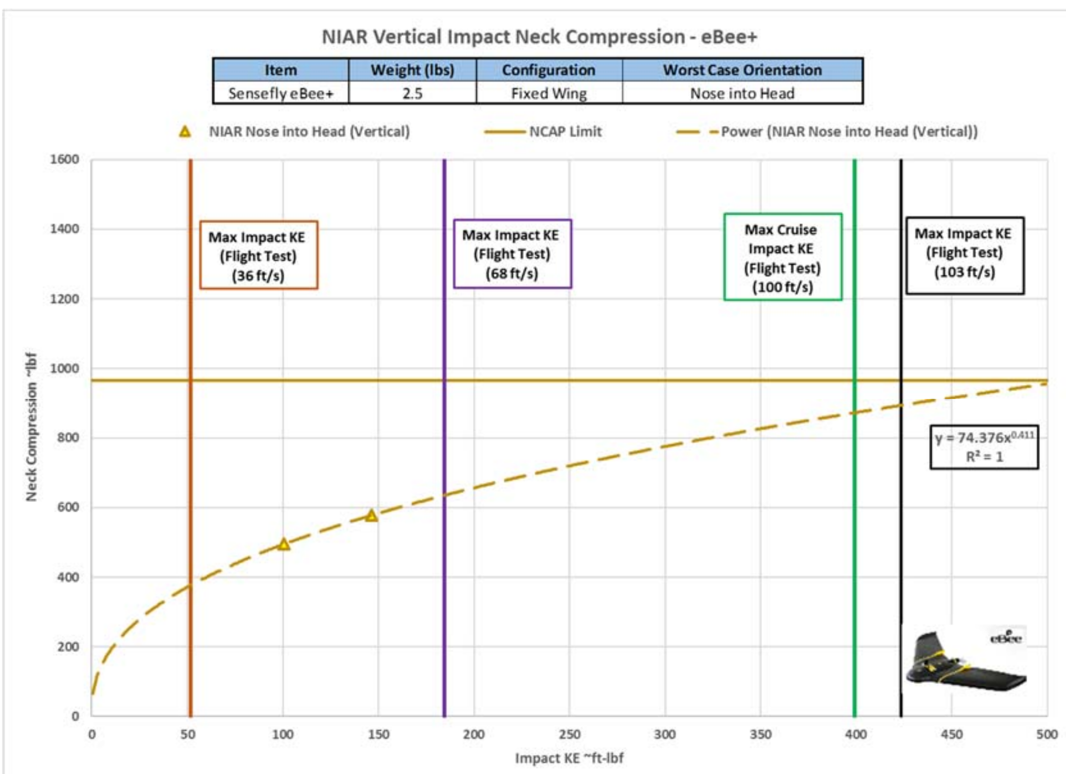

Figure K 4. NIAR Vertical Impact Neck Compression - eBee+

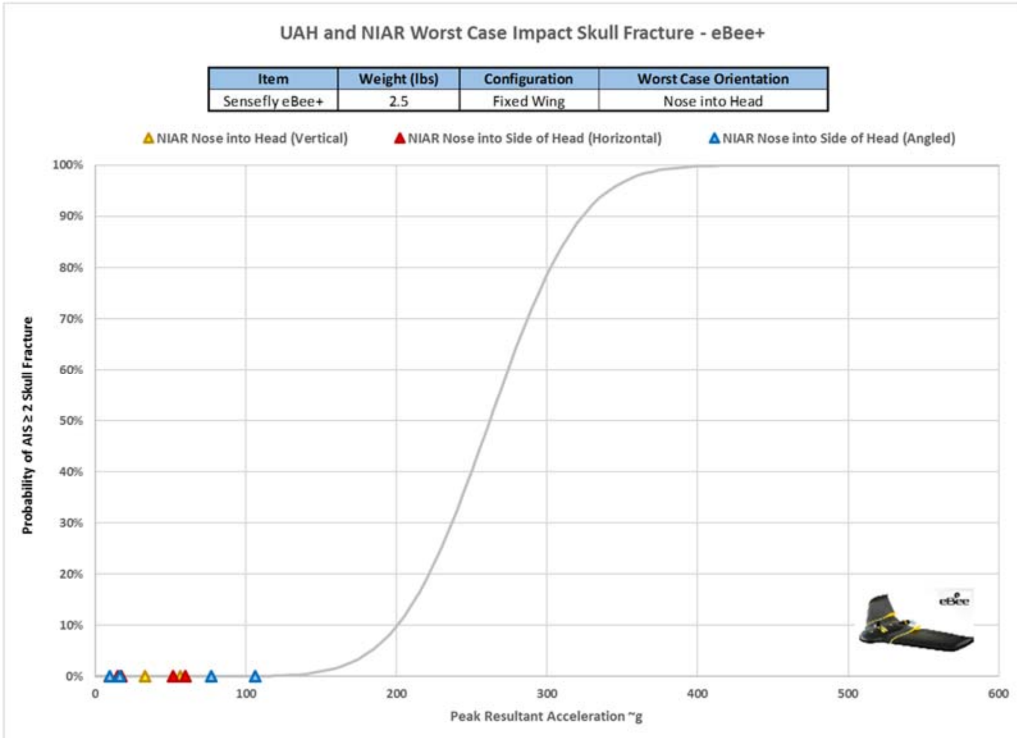

Figure K 5. UAH and NIAR Worst Case Impact Skull Fracture - eBee+

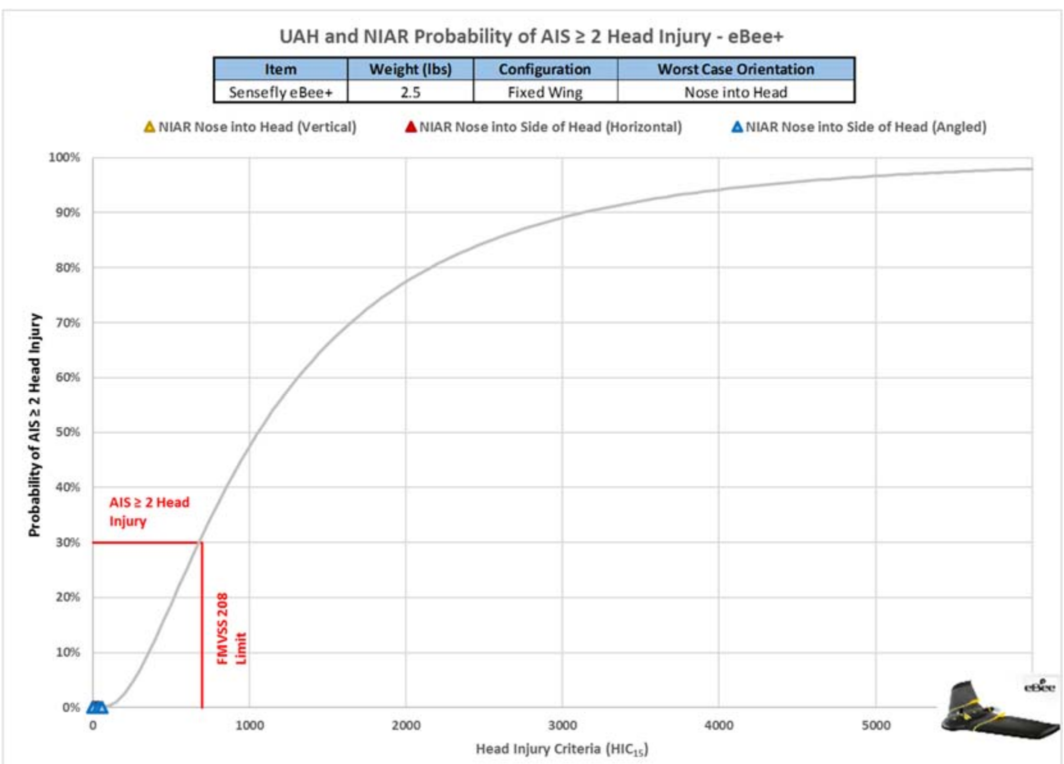

Figure K 6. UAH and NIAR Probability of AIS ≥ 2 Head Injury - eBee+

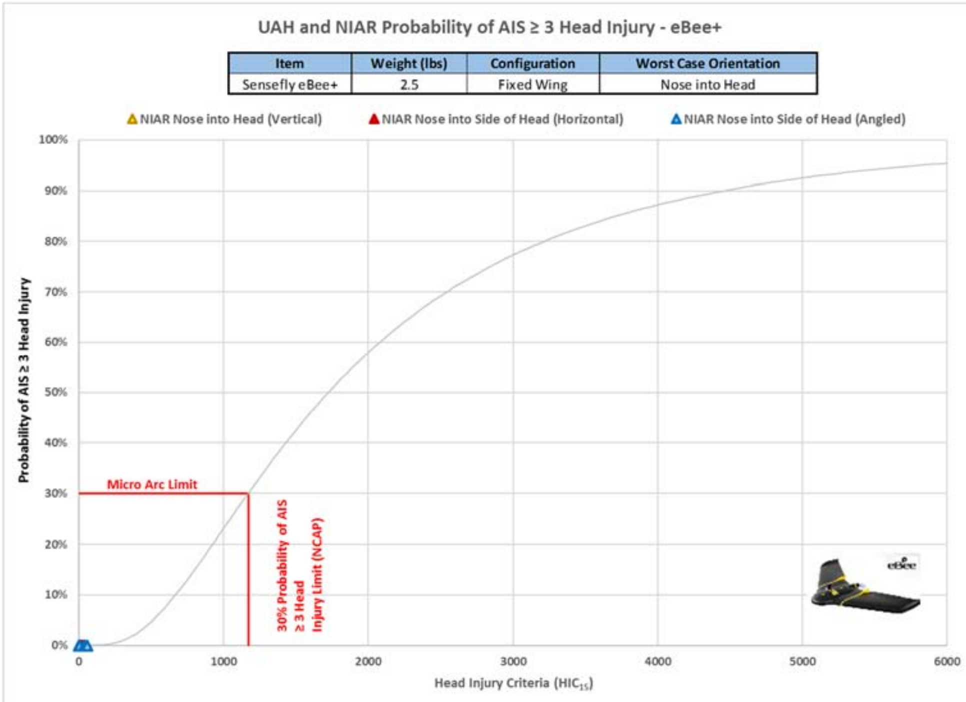

Figure K 7. UAH and NIAR Probability of AIS ≥ 3 Head Injury - eBee+

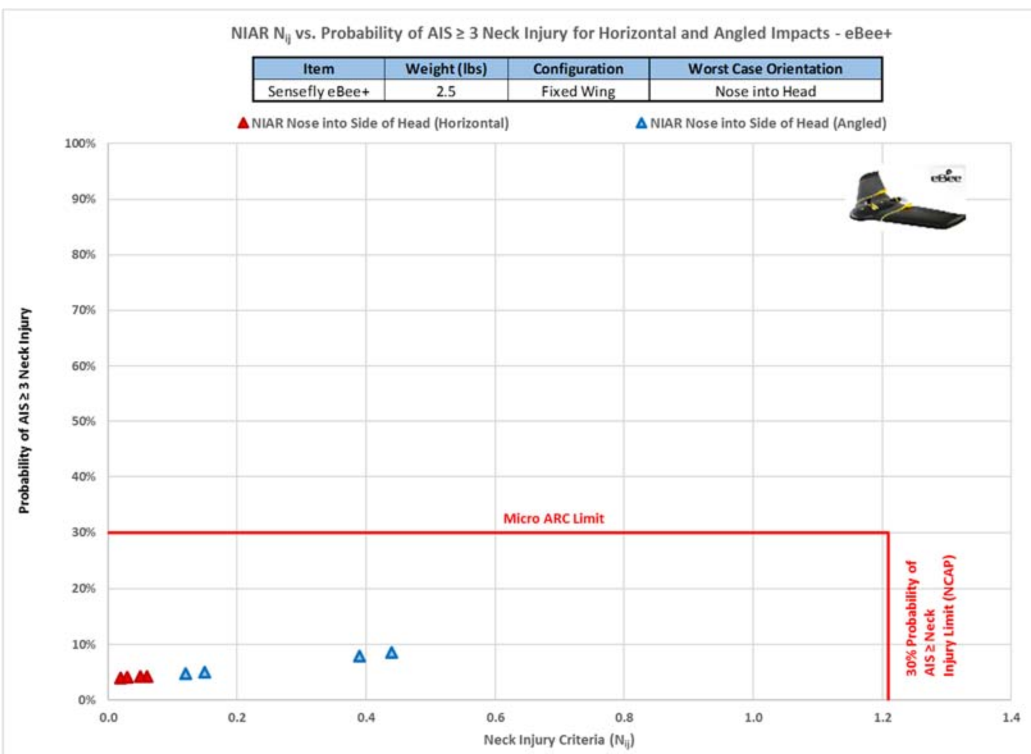

Figure K 8. NIAR N_{ij} vs. Probability of AIS ≥ 3 Neck Injury for Horizontal and Angled Impact – eBee+

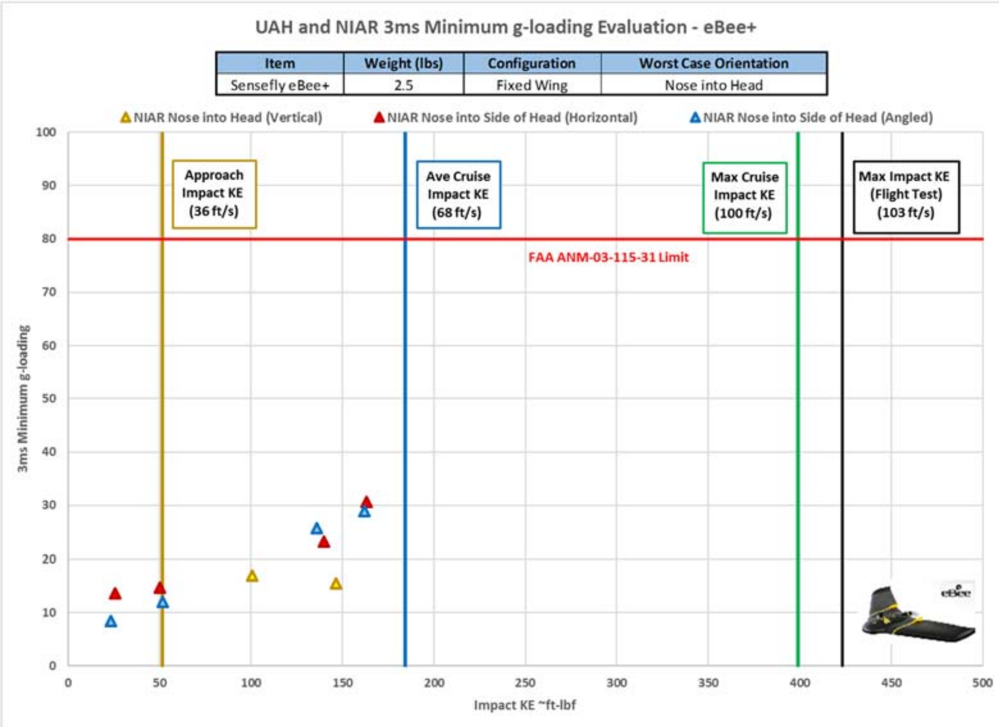

Figure K 9. UAH and NIAR 3ms Minimum g-loading - eBee+

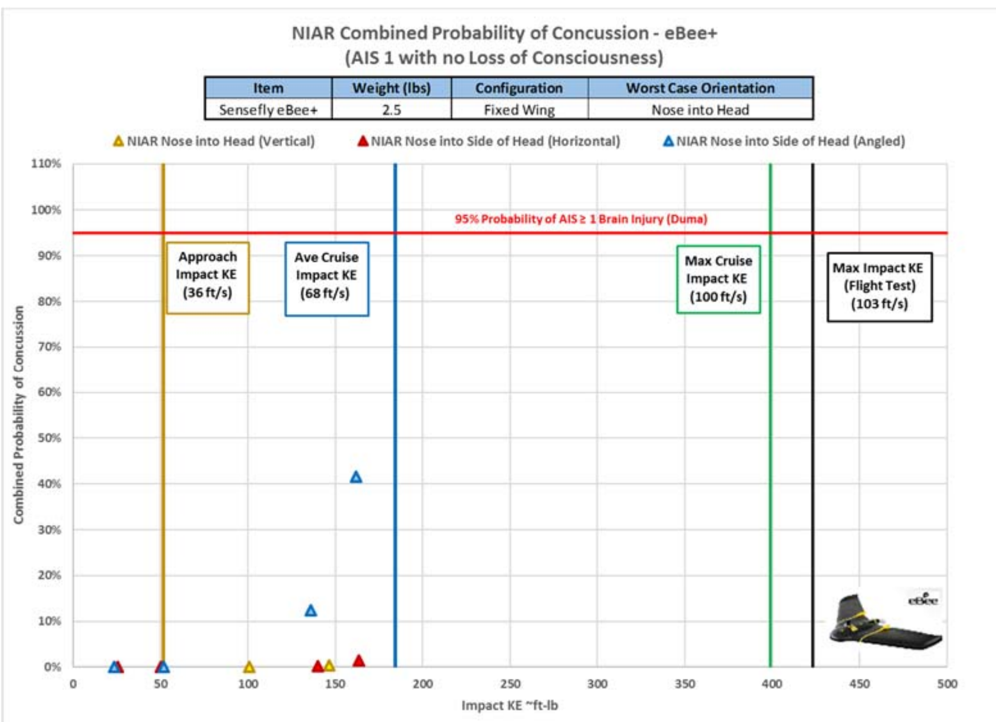

Figure K 10. NIAR Combined Probability of Concussion - eBee+ (AIS 1 with No Loss of Consciousness)

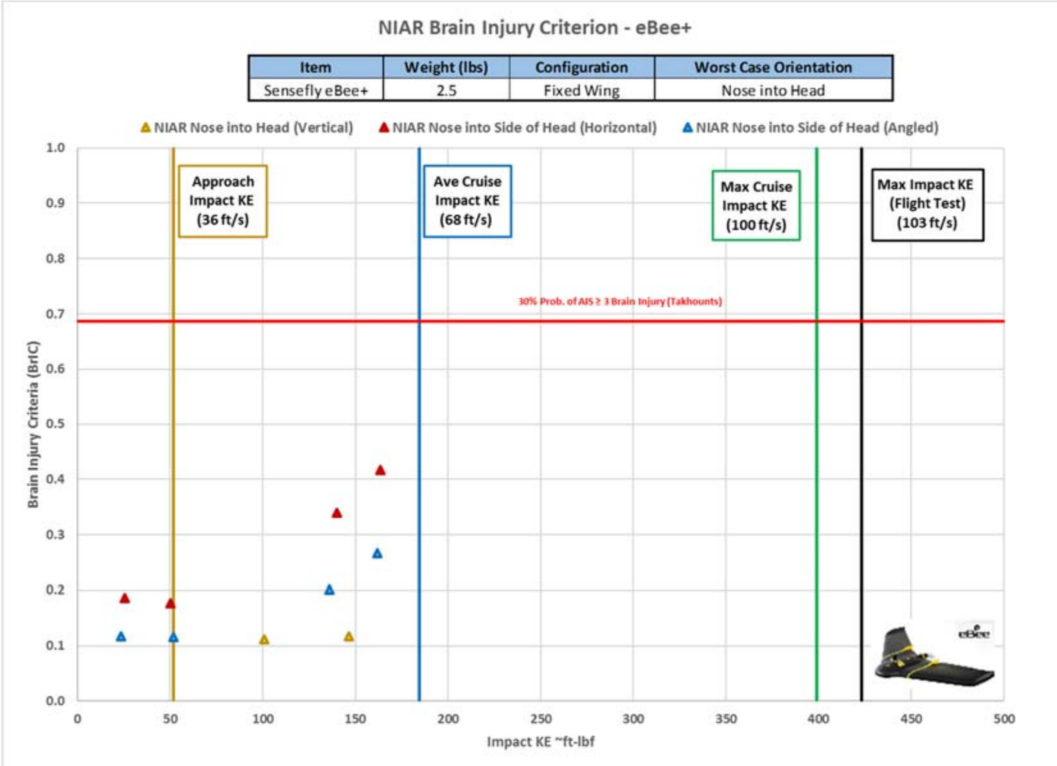

Figure K 11. NIAR Brain Injury Criterion Evaluation - eBee+

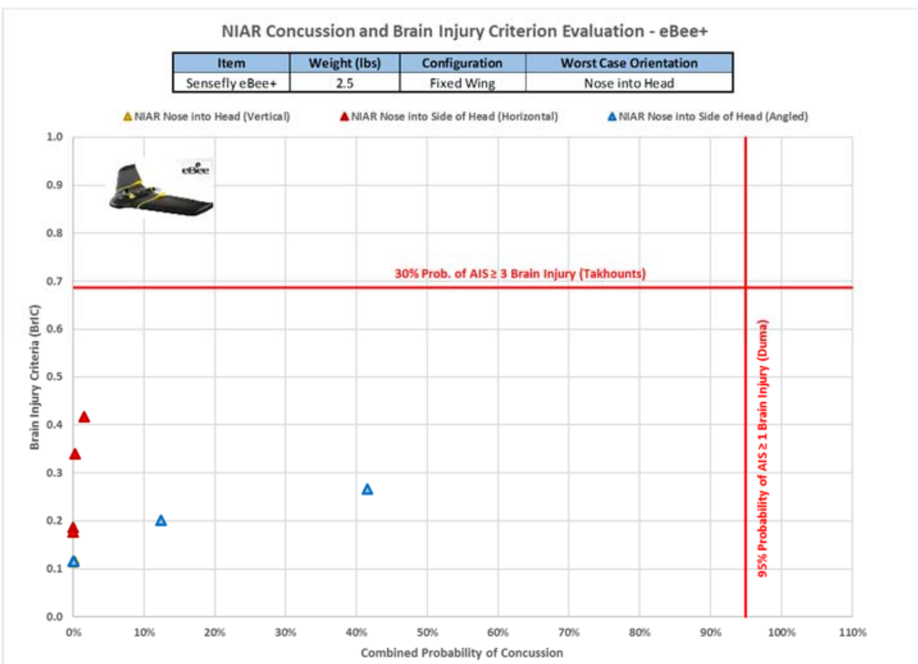

Figure K 12. NIAR Concussion and Brain Injury Criterion Evaluation - eBee+

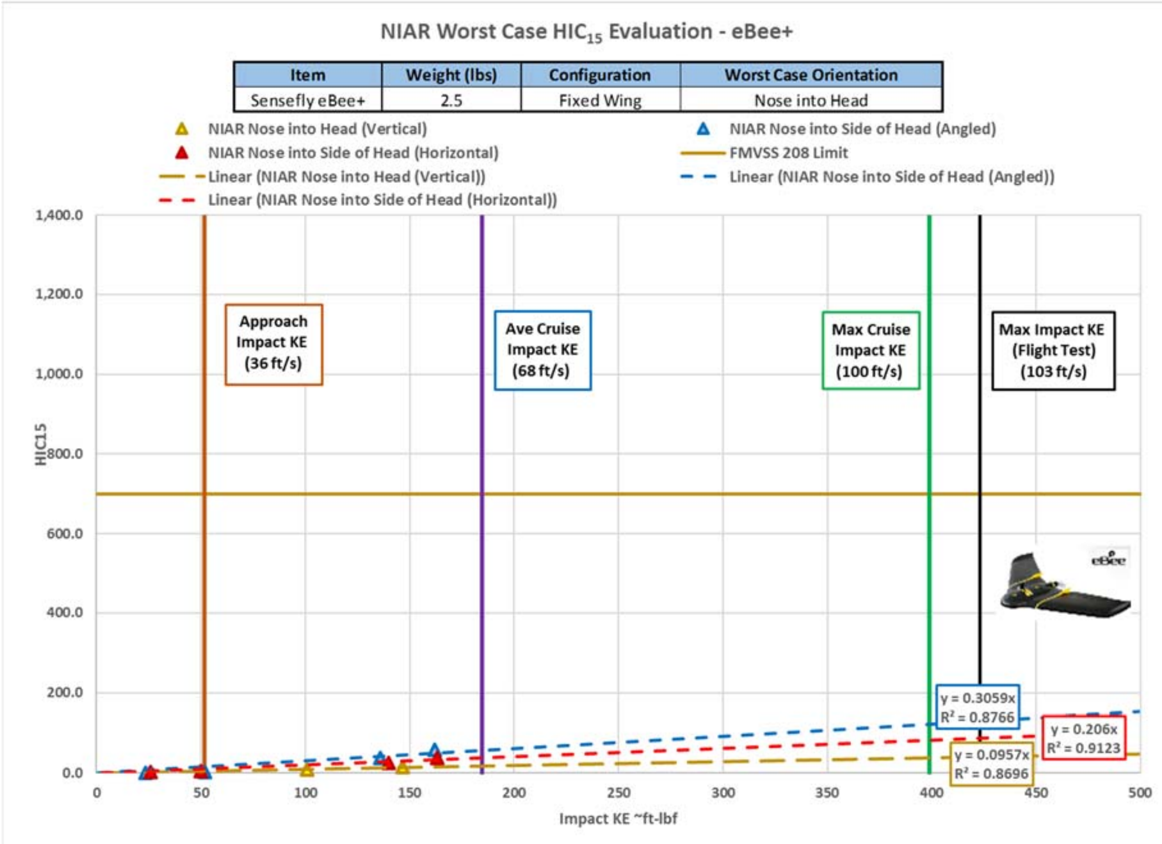

Figure K 13. NIAR Worst Case HIC_{15} Evaluation - eBee+

APPENDIX L – EBEE STANDARD SIMPLIFIED TEST DATA

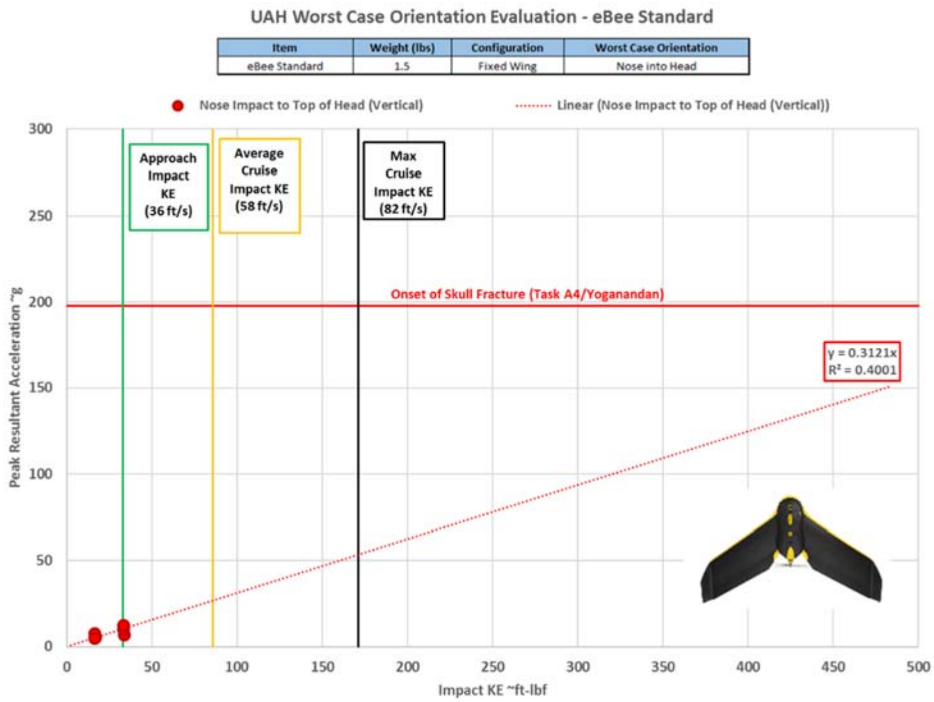

Figure L 1. UAH Worst Case Orientation Evaluation - eBee Standard

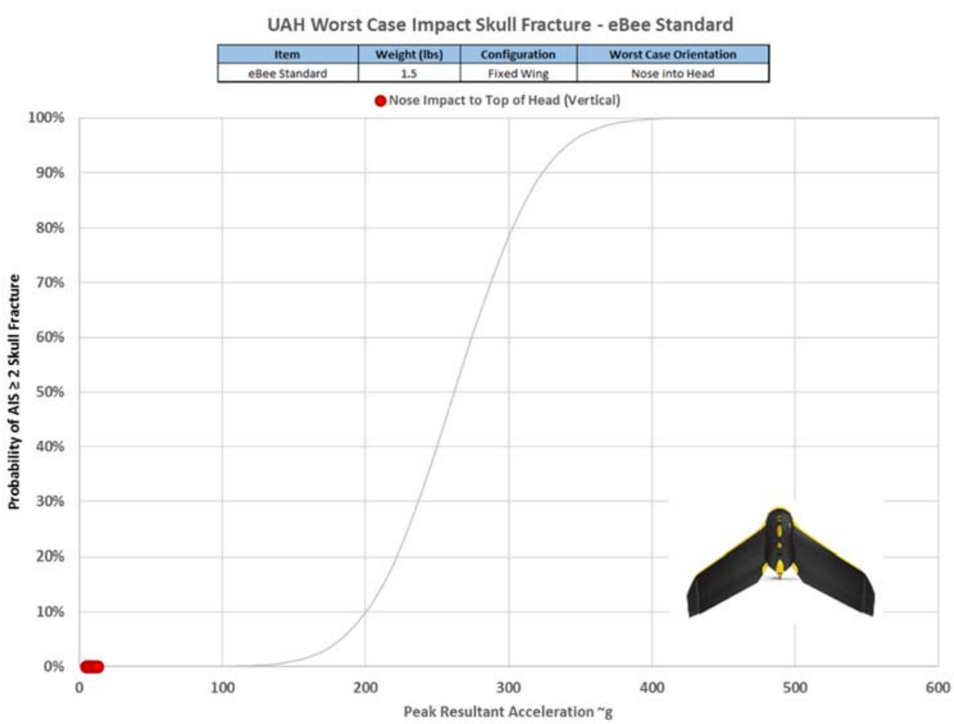

Figure L 2. UAH Worst Case Impact Skull Fracture - eBee Standard

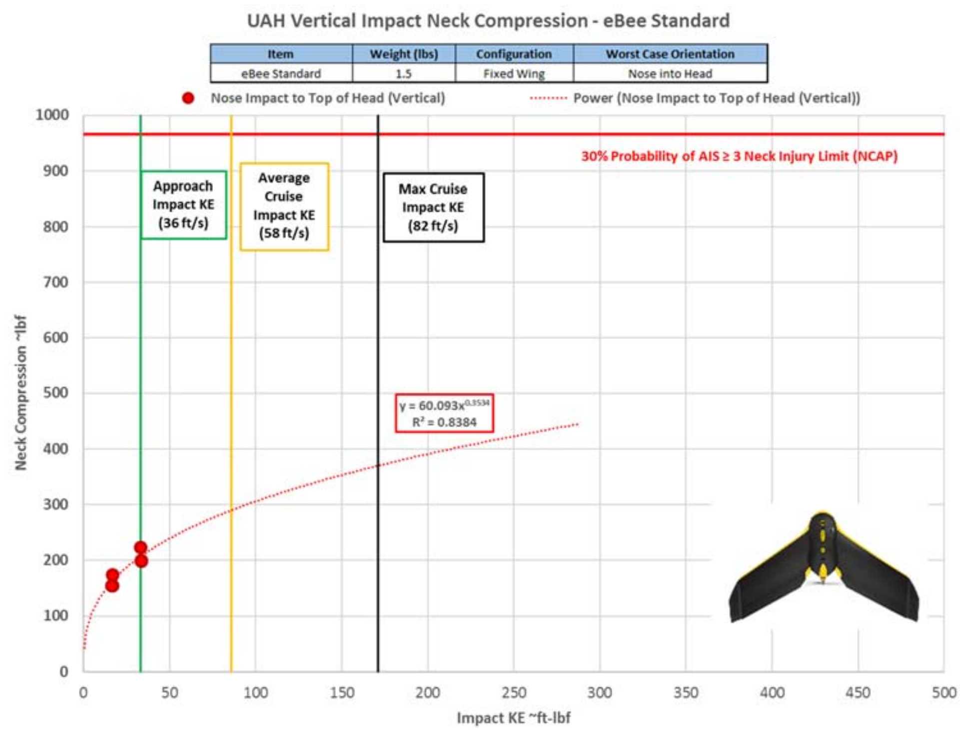

Figure L 3. NIAR Vertical Impact Neck Compression - eBee Standard

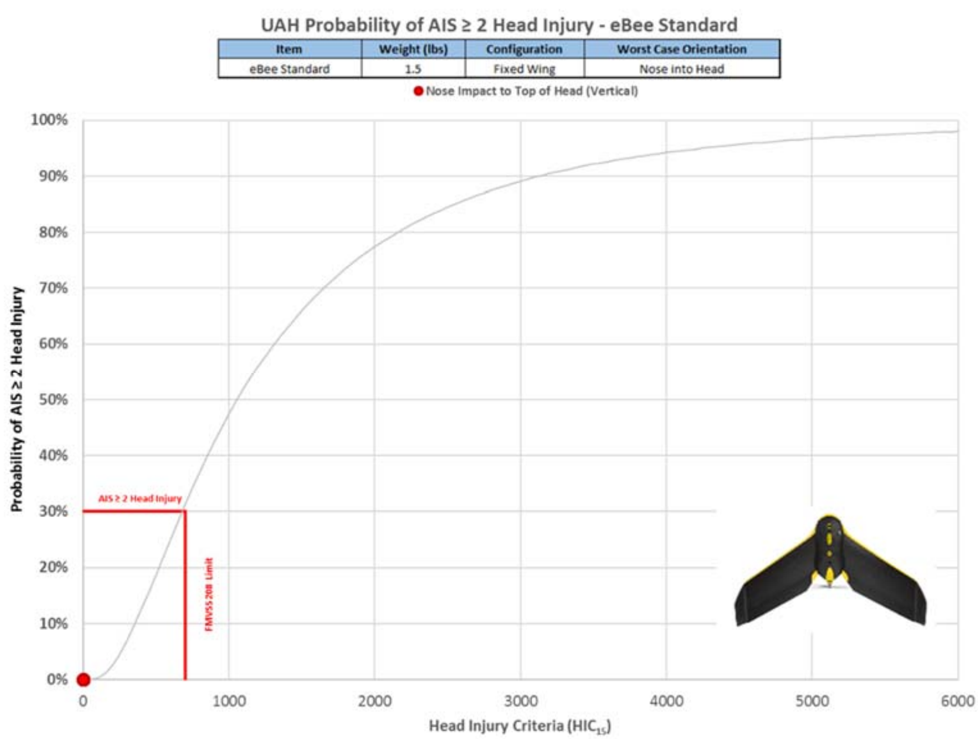

Figure L 4. UAH Probability of AIS $\geq$ 2 Head Injury - eBee Standard

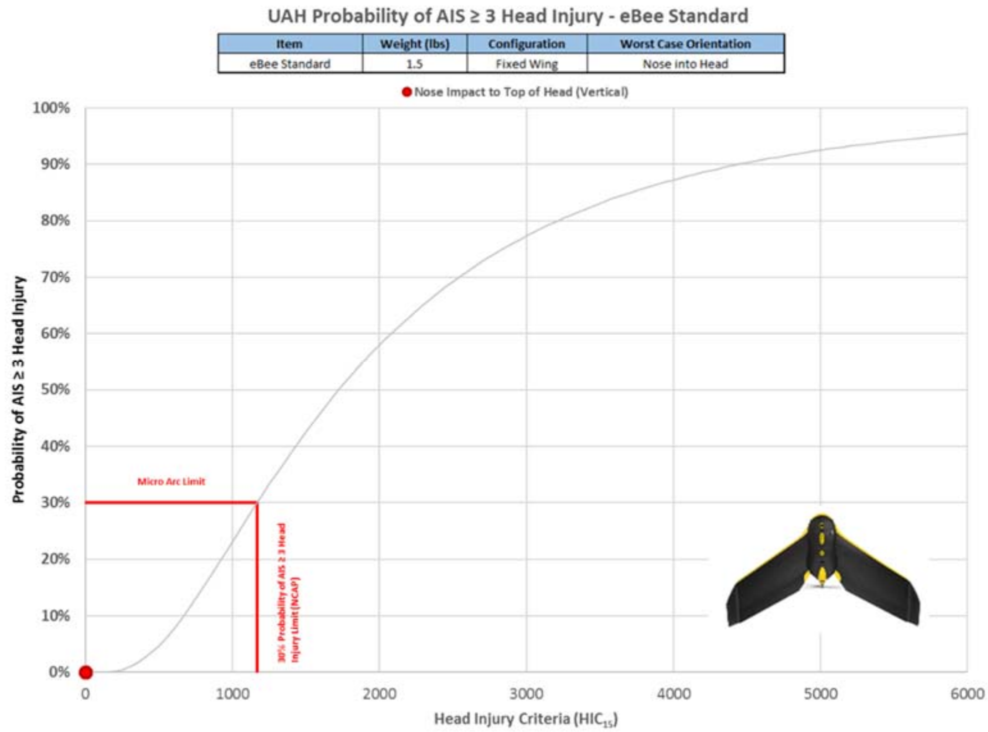

Figure L 5. UAH and NIAR Probability of AIS ≥ 3 Head Injury - eBee Standard

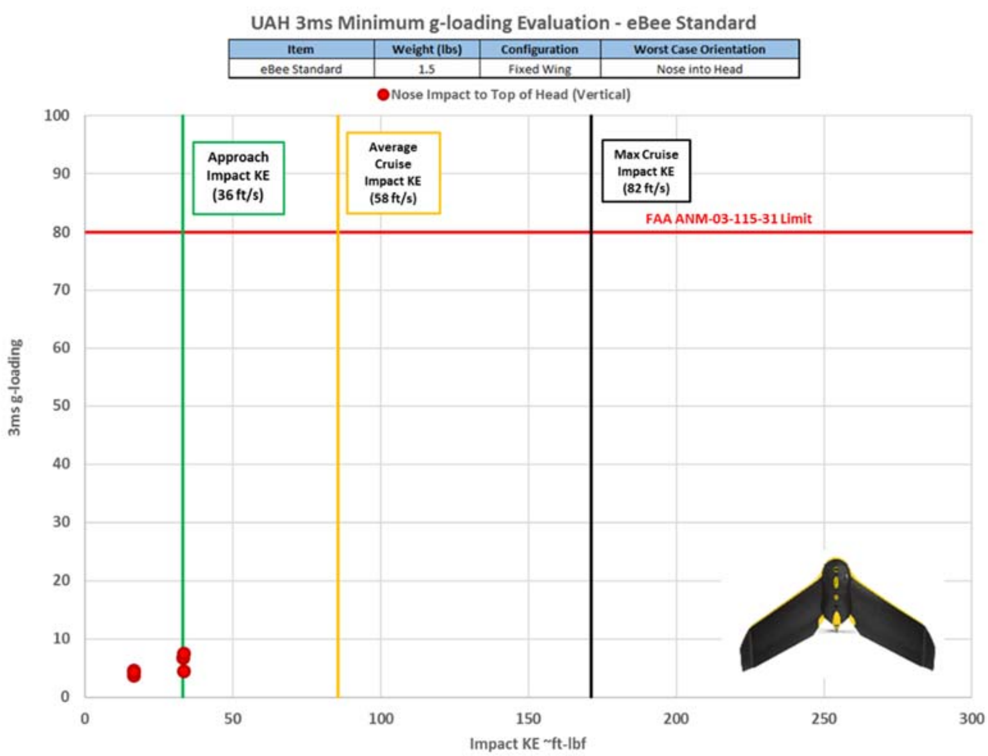

Figure L 6. UAH and NIAR 3ms Minimum g-loading Evaluation - eBee Standard

APPENDIX M – NANO TALON SIMPLIFIED TEST DATA

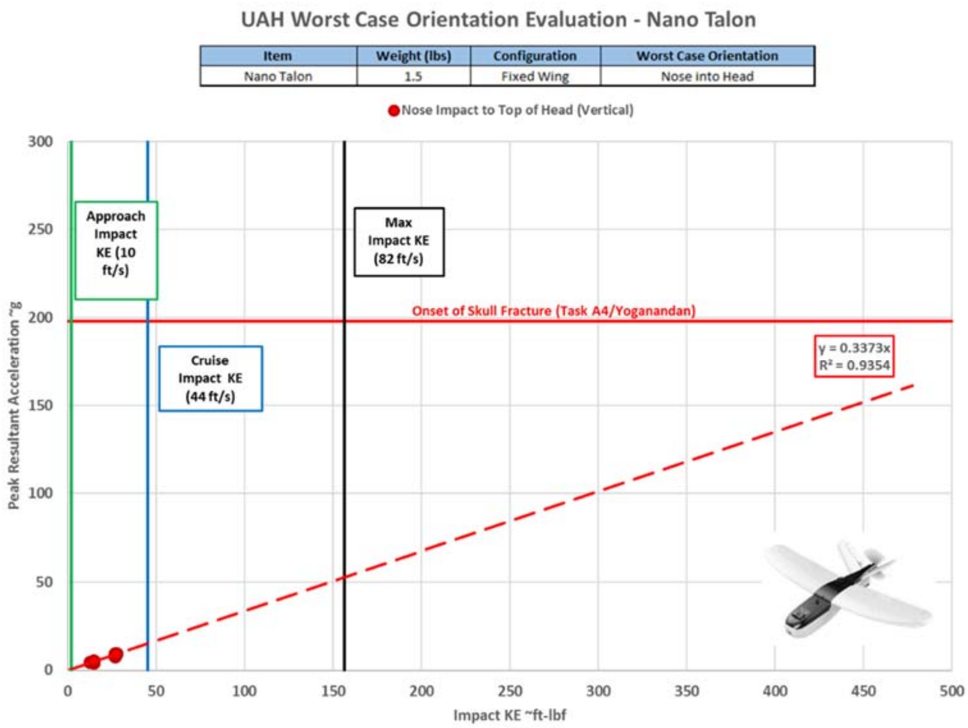

Figure M 1. UAH Worst Case Orientation Evaluation – Nano Talon

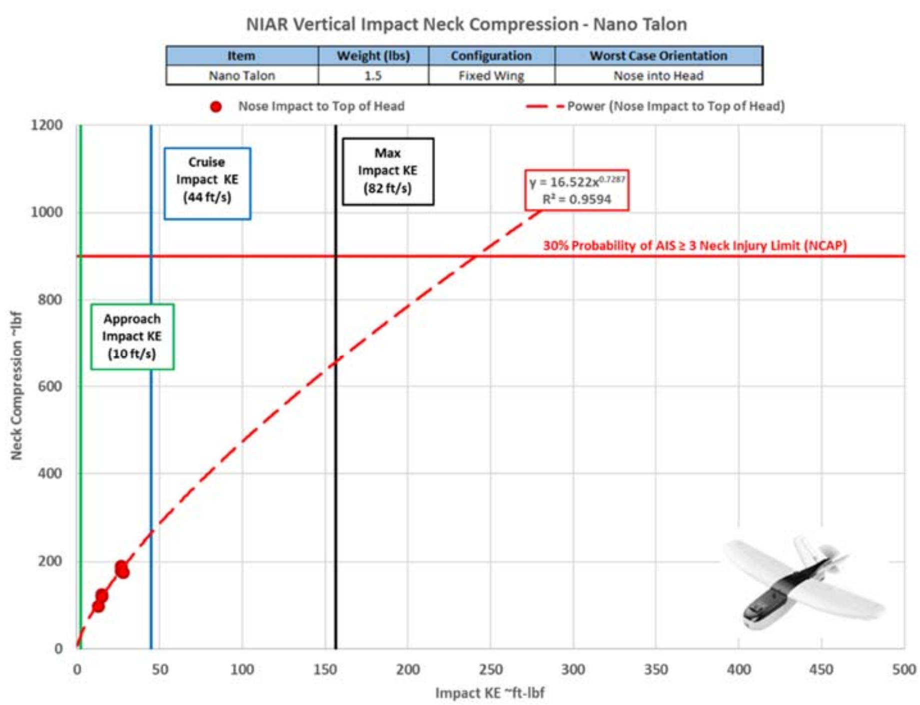

Figure M 2. UAH Vertical Impact Neck Compression - Nano Talon

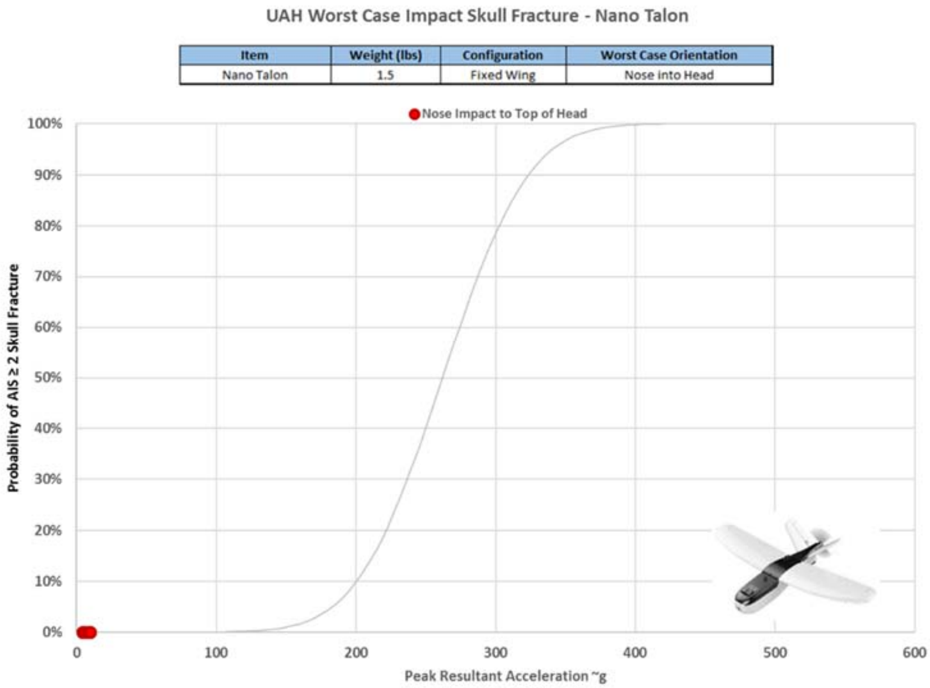

Figure M 3. UAH Worst Case Impact Skull Fracture - Nano Talon

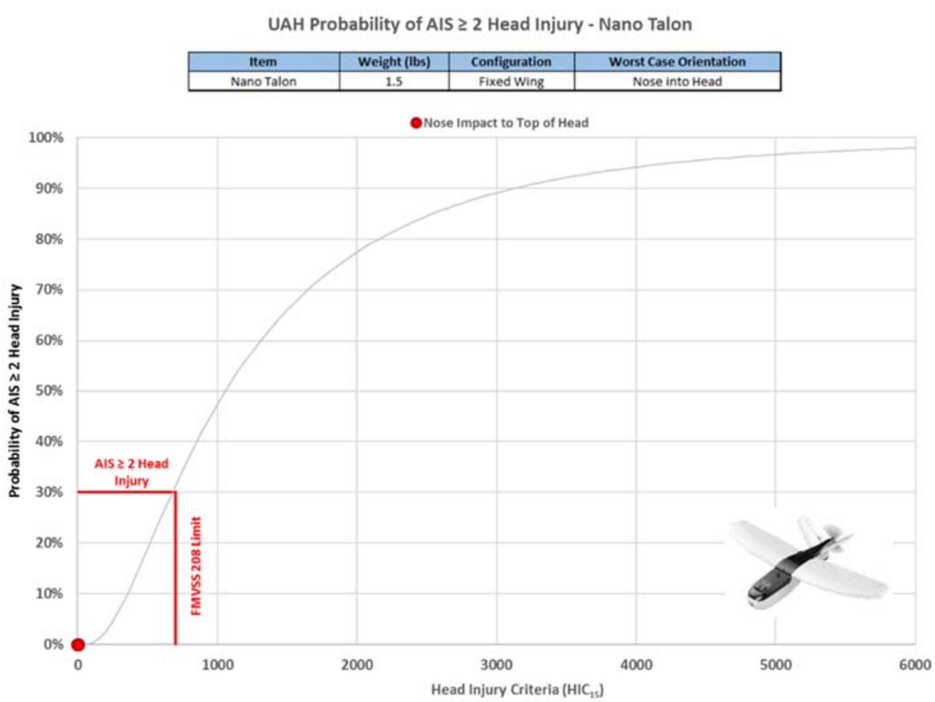

Figure M 4. UAH and NIAR Probability of AIS ≥ 2 Head Injury - Nano Talon

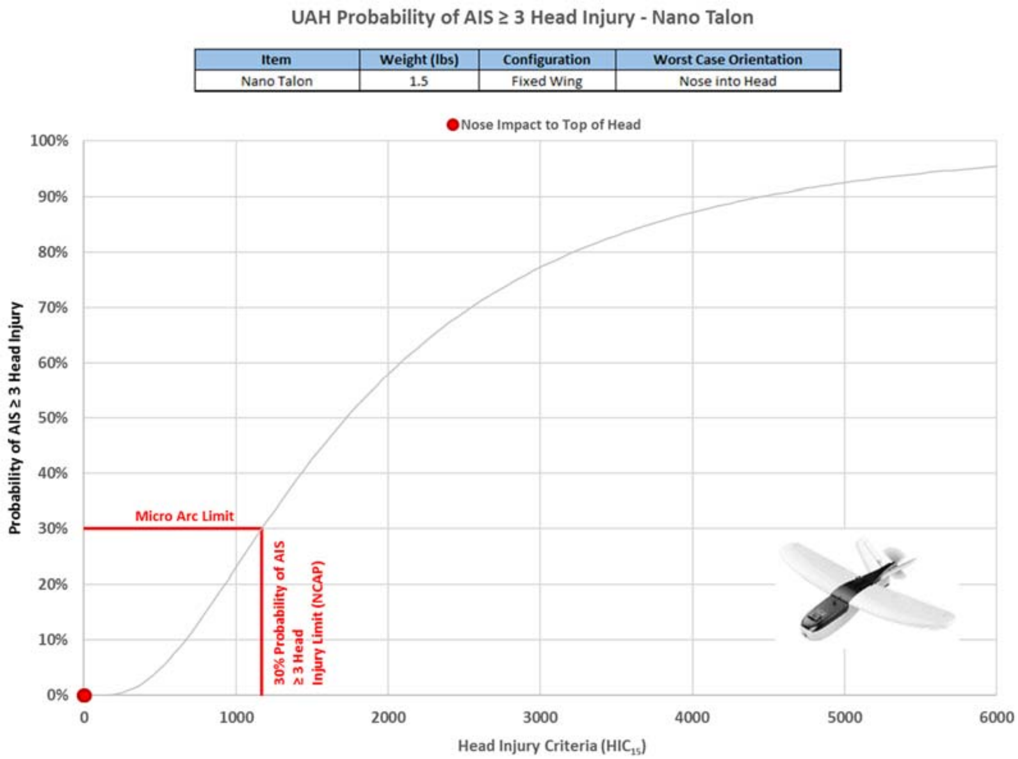

Figure M 5. UAH Probability of AIS ≥ 3 Head Injury - Nano Talon

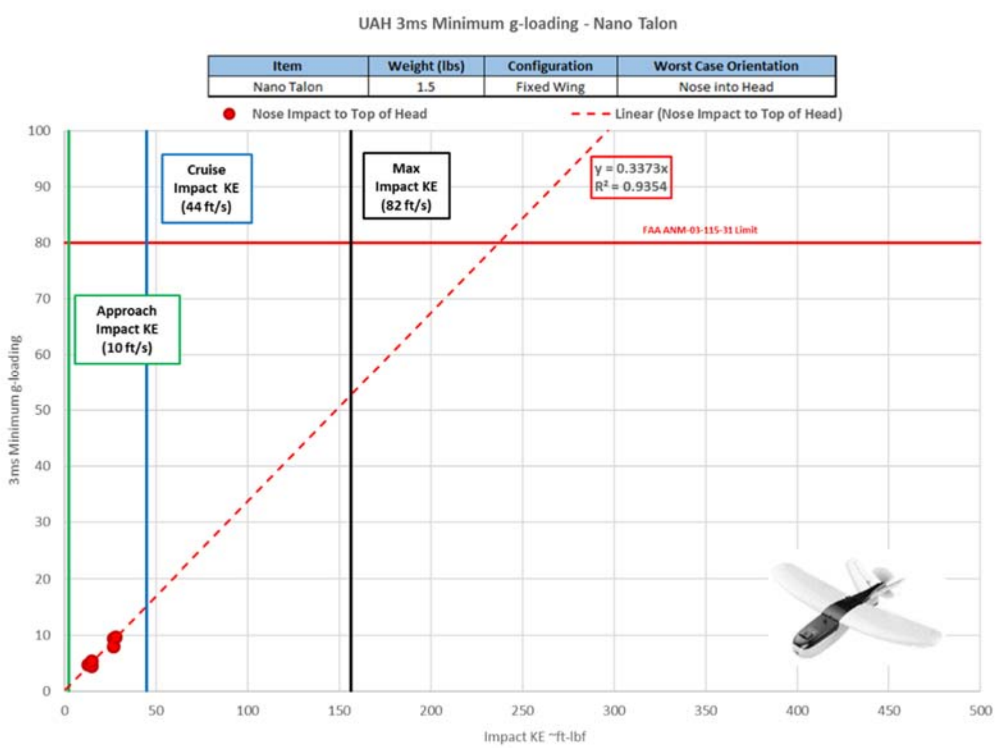

Figure M 6. UAH and NIAR 3ms Minimum g-loading Evaluation - Nano Talon

APPENDIX N – RADIAN SIMPLIFIED TEST DATA

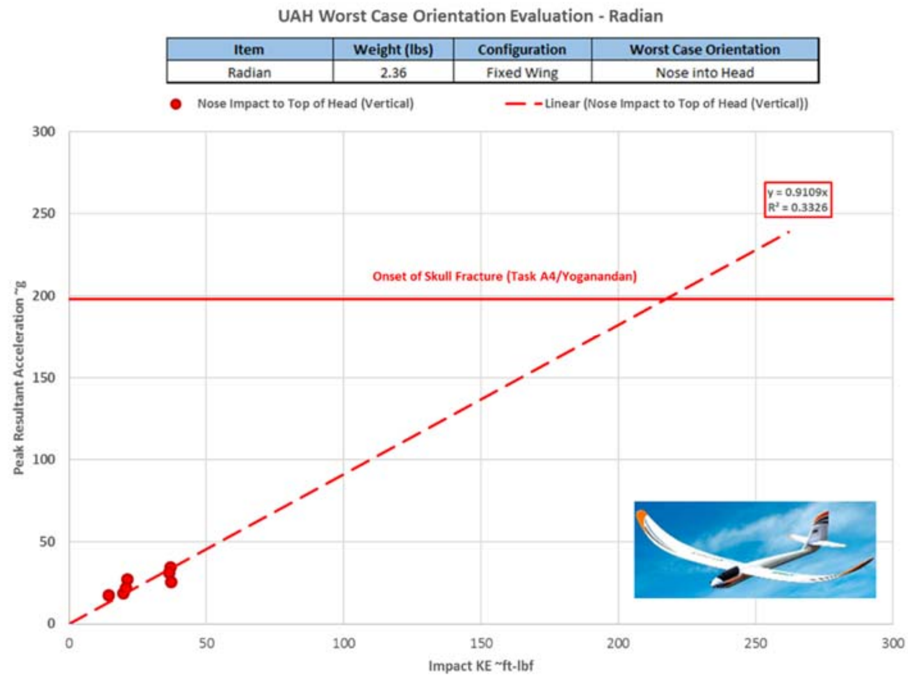

Figure N 1. UAH Worst Case Orientation Evaluation - Radian

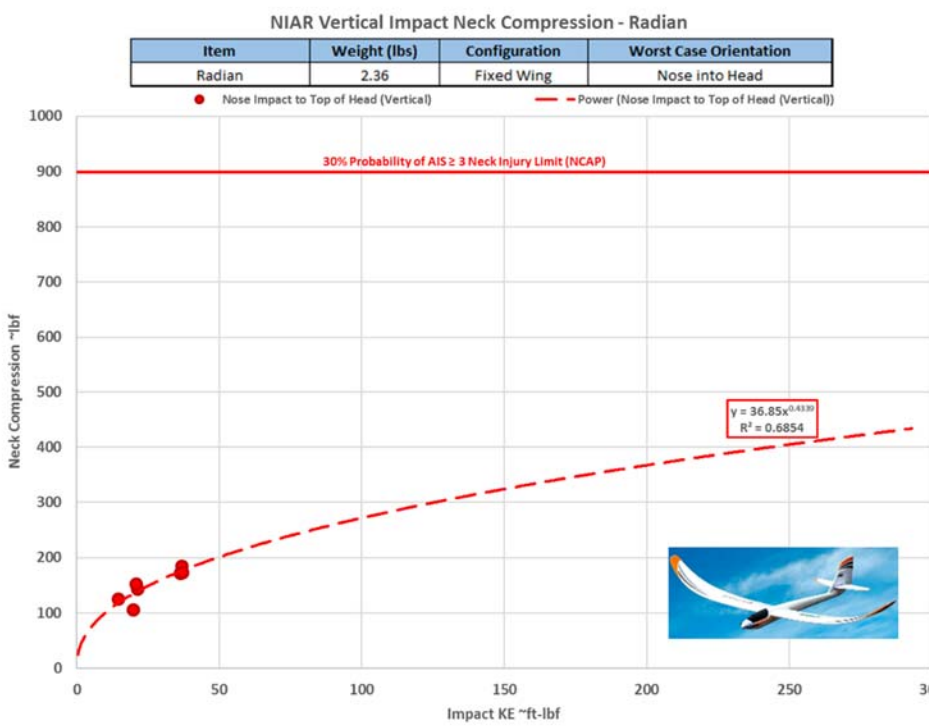

Figure N 2. UAH Vertical Impact Neck Compression - Radian

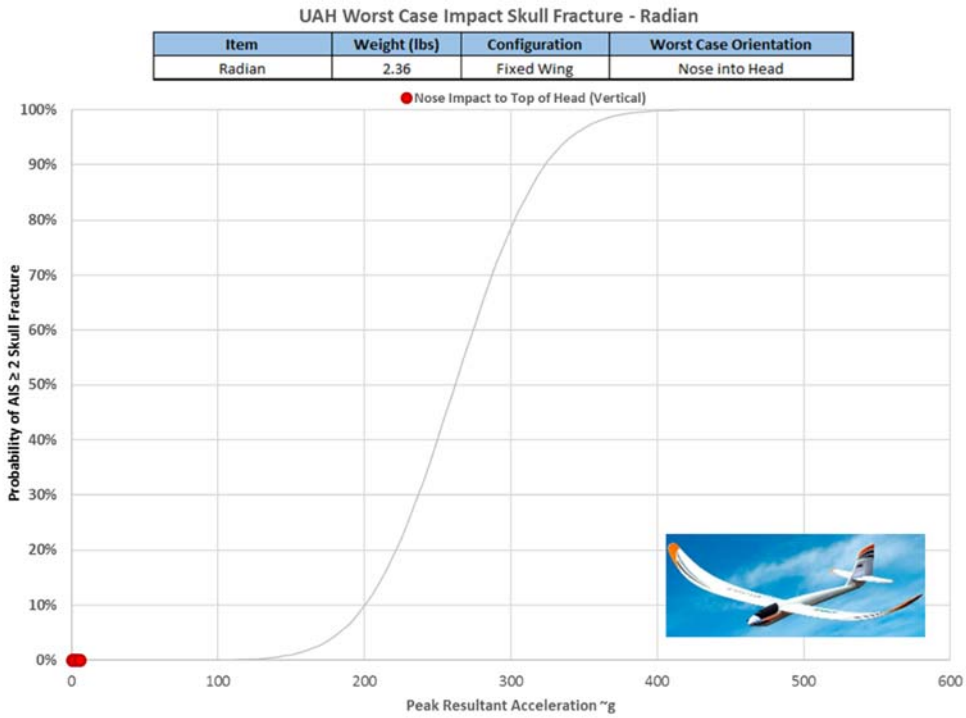

Figure N 3. UAH Worst Case Impact Skull Fracture - Radian

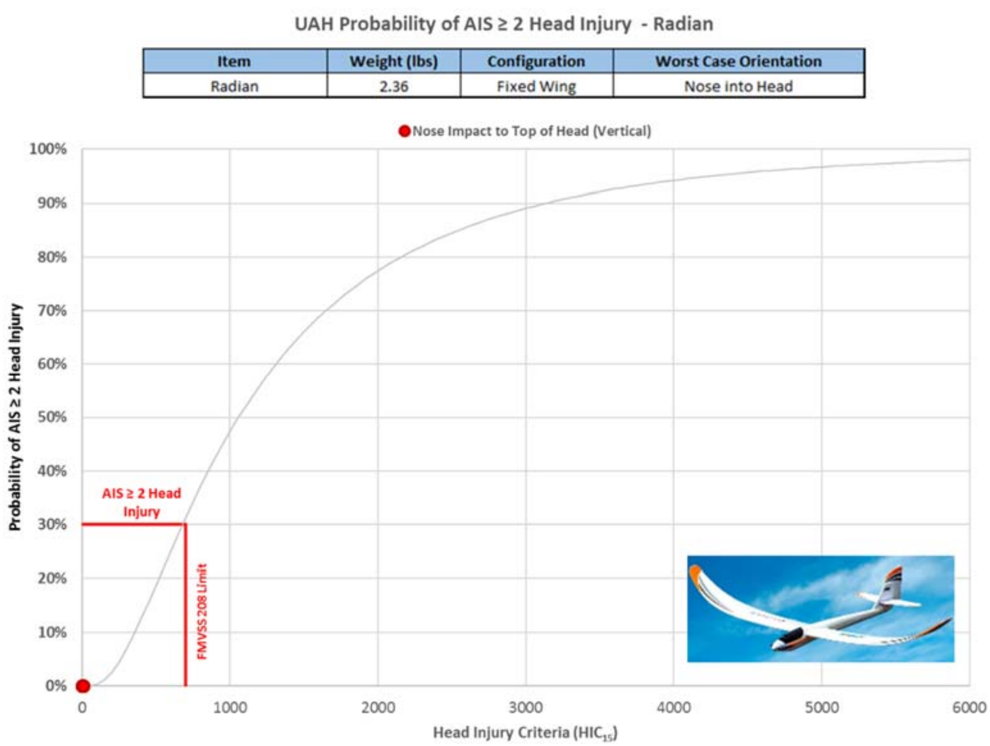

Figure N 4. UAH Probability of AIS ≥ 2 Head Injury - Radian

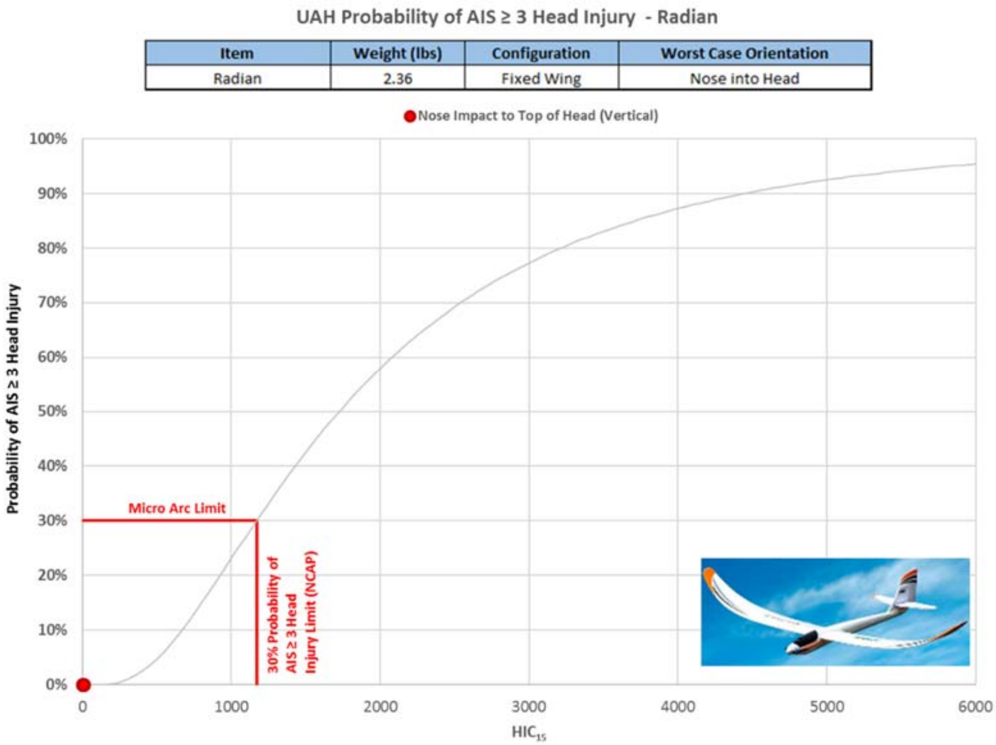

Item	Weight (lbs)	Configuration	Worst Case Orientation
Radian	2.36	Fixed Wing	Nose into Head

Figure N 5. UAH Probability of AIS ≥ 3 Head Injury - Radian

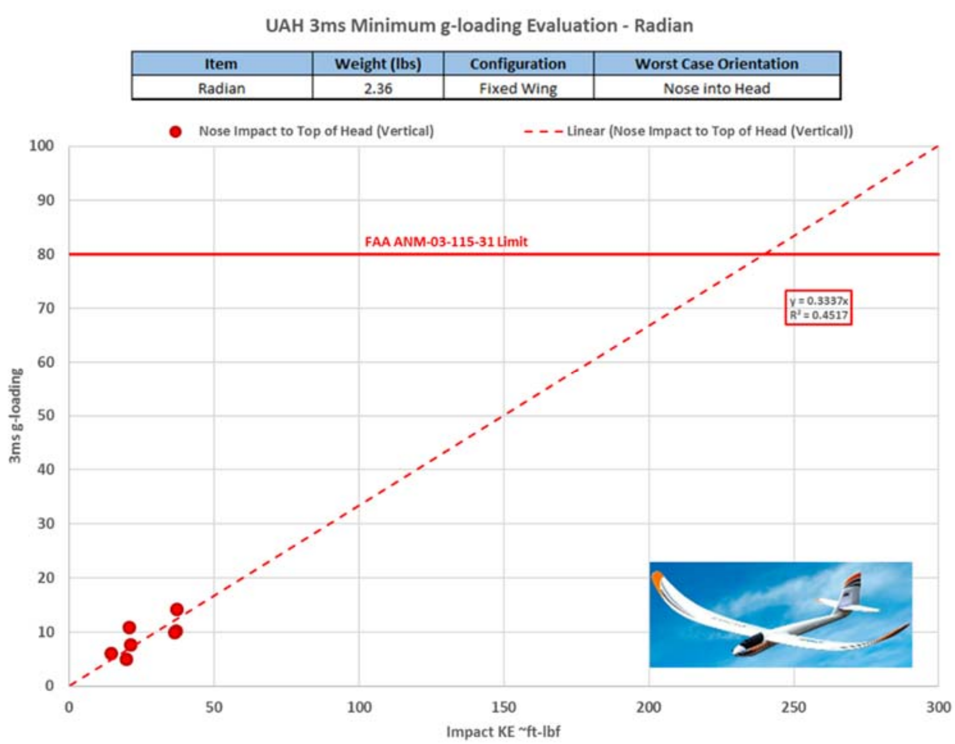

Item	Weight (lbs)	Configuration	Worst Case Orientation
Radian	2.36	Fixed Wing	Nose into Head

Figure N 6. UAH 3ms Minimum g-loading – Radian

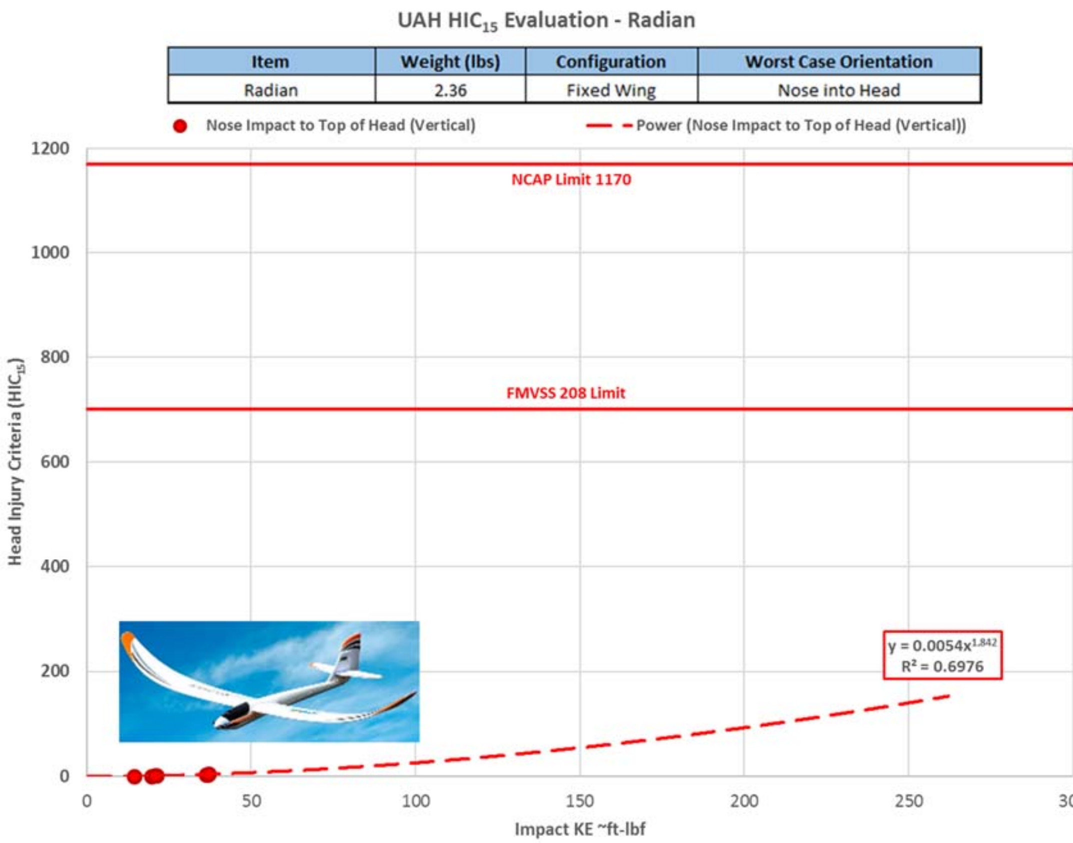

Figure N 7. UAH HIC$_{15}$ Evaluation - Radian

APPENDIX O – SKYHUNTER SIMPLIFIED TEST DATA

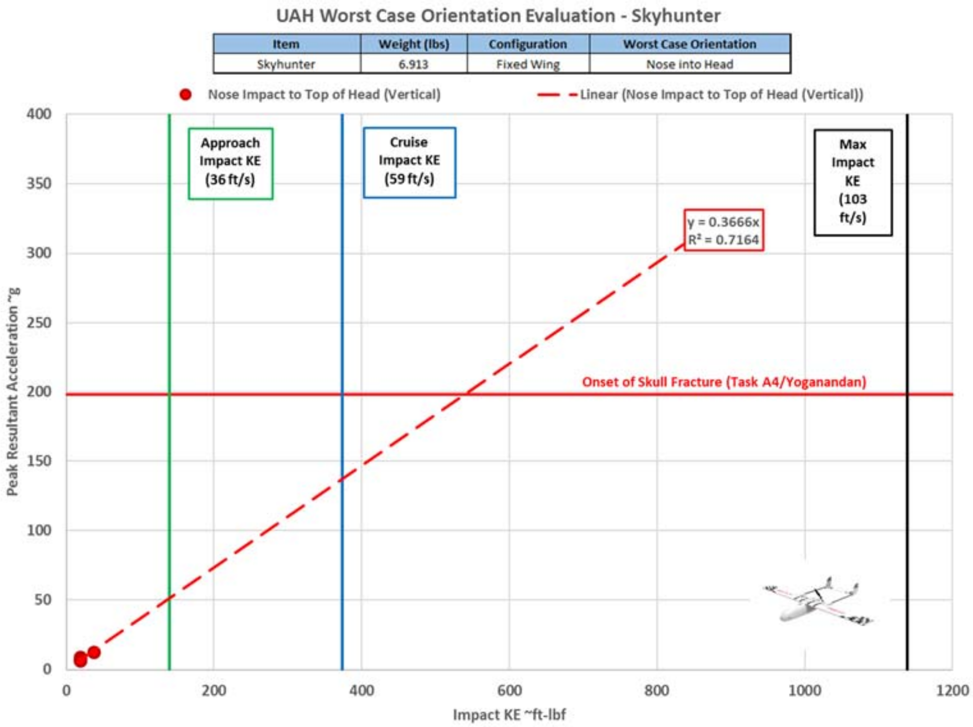

Figure O 1. UAH Worst Case Orientation Evaluation - Skyhunter

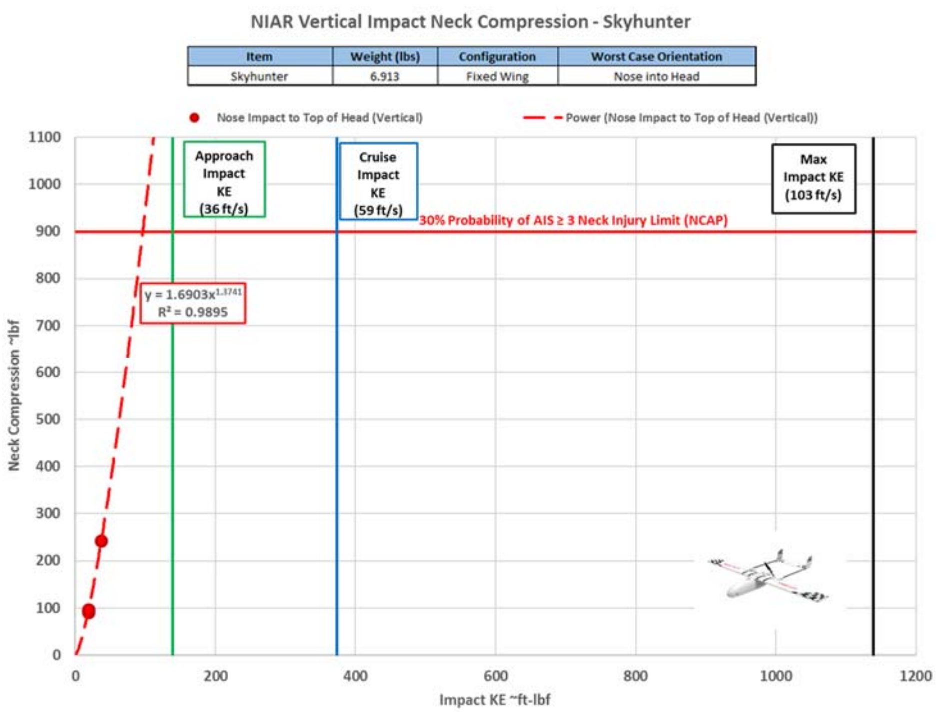

Figure O 2. NIAR Vertical Impact Neck Compression - Skyhunter

UAH Worst Case Impact Skull Fracture - Skyhunter

Item	Weight (lbs)	Configuration	Worst Case Orientation
Skyhunter	6.913	Fixed Wing	Nose into Head

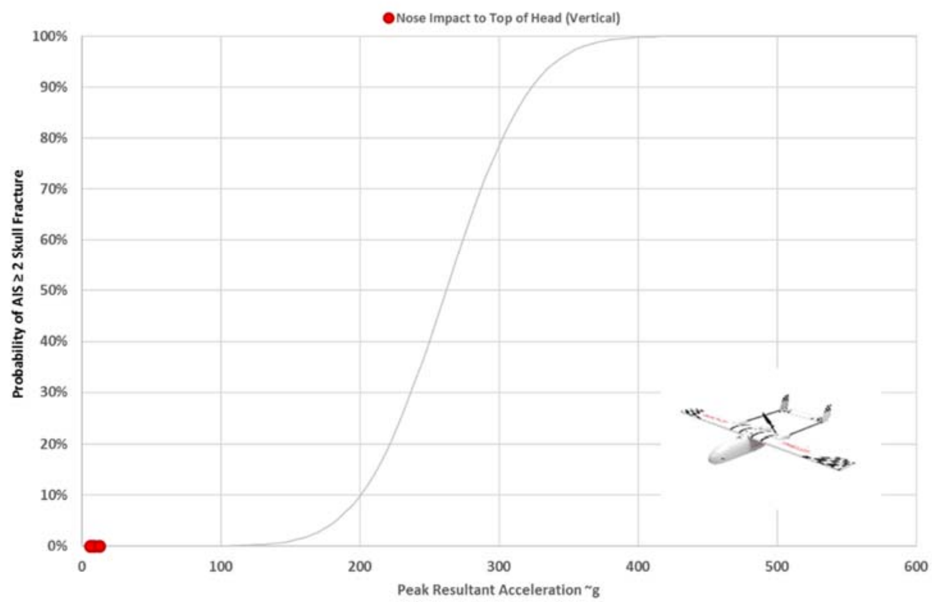

Figure O 3. UAH Worst Case Impact Skull Fracture - Skyhunter

UAH and NIAR Probability of AIS ≥ 2 Head Injury - Skyhunter

Item	Weight (lbs)	Configuration	Worst Case Orientation
Skyhunter	6.913	Fixed Wing	Nose into Head

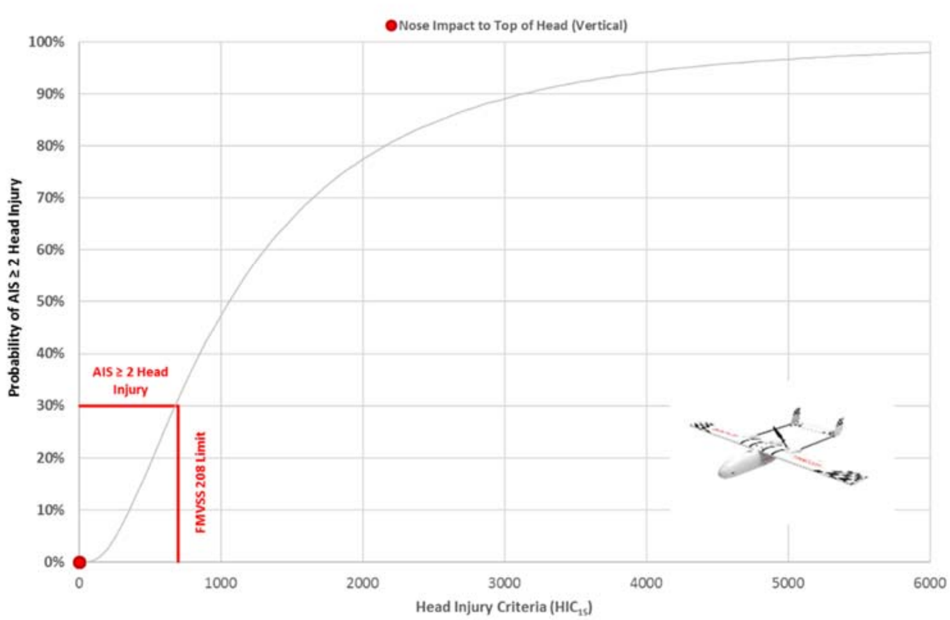

Figure O 4. UAH Probability of AIS ≥ 2 Head Injury - Skyhunter

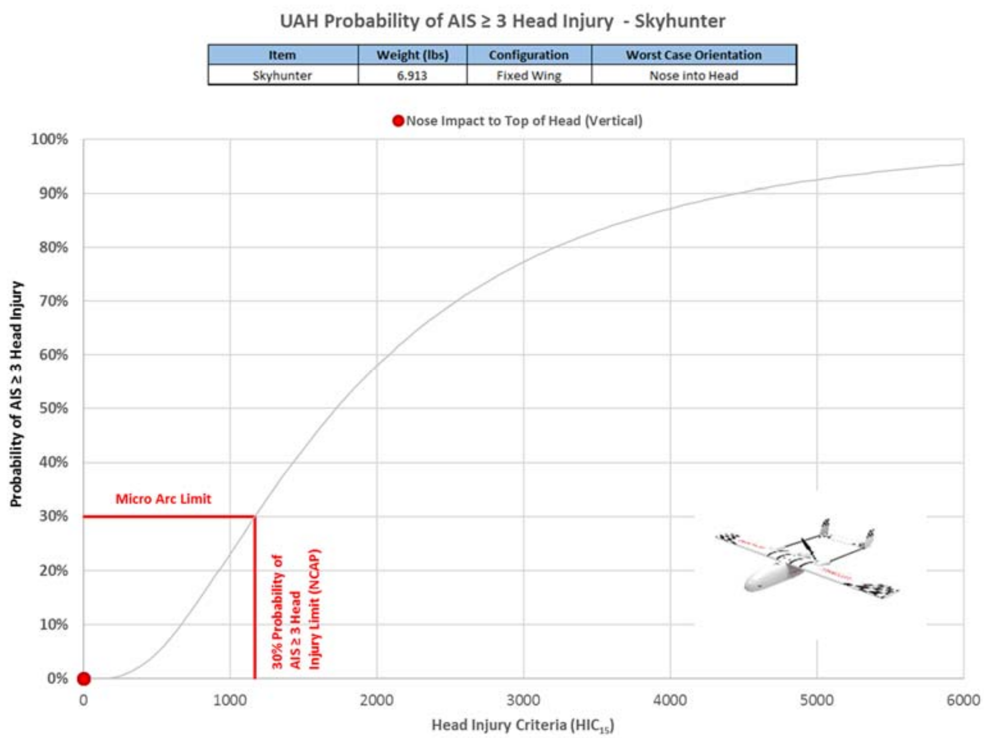

Figure O 5. UAH Probability of AIS ≥ 3 Head Injury - Skyhunter

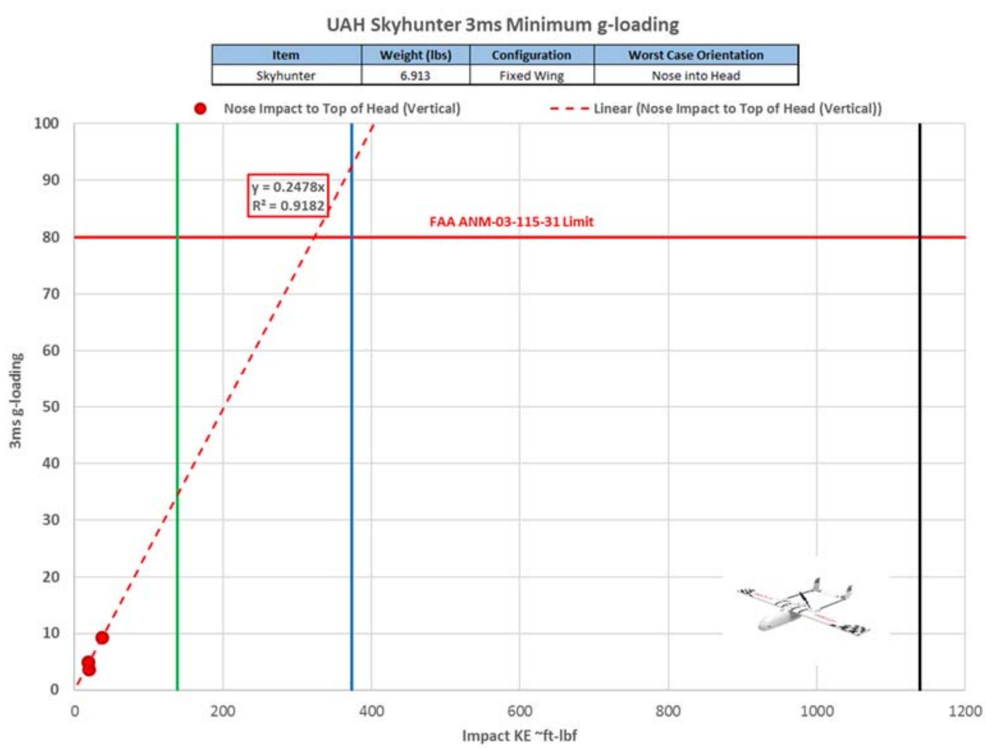

Figure O 6. UAH 3ms Minimum g-loading Evaluation - Skyhunter

APPENDIX P – WOOD BLOCK ATD AND SIMPLIFIED TEST DATA

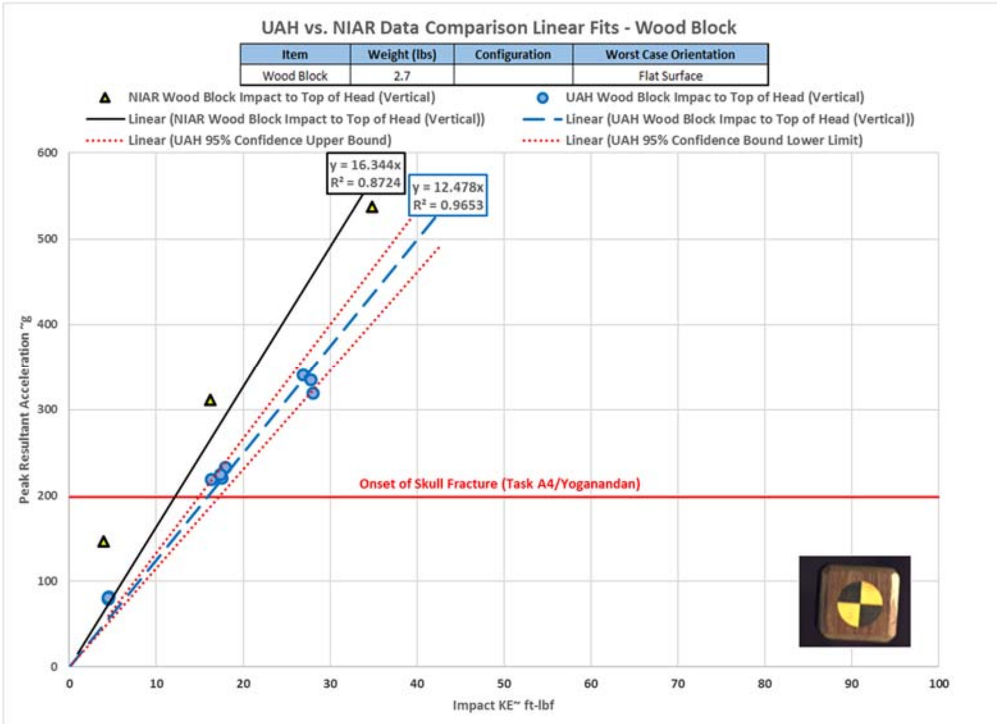

Figure P 1. UAH vs. NIAR Data Comparison Linear Fits - Wood Block

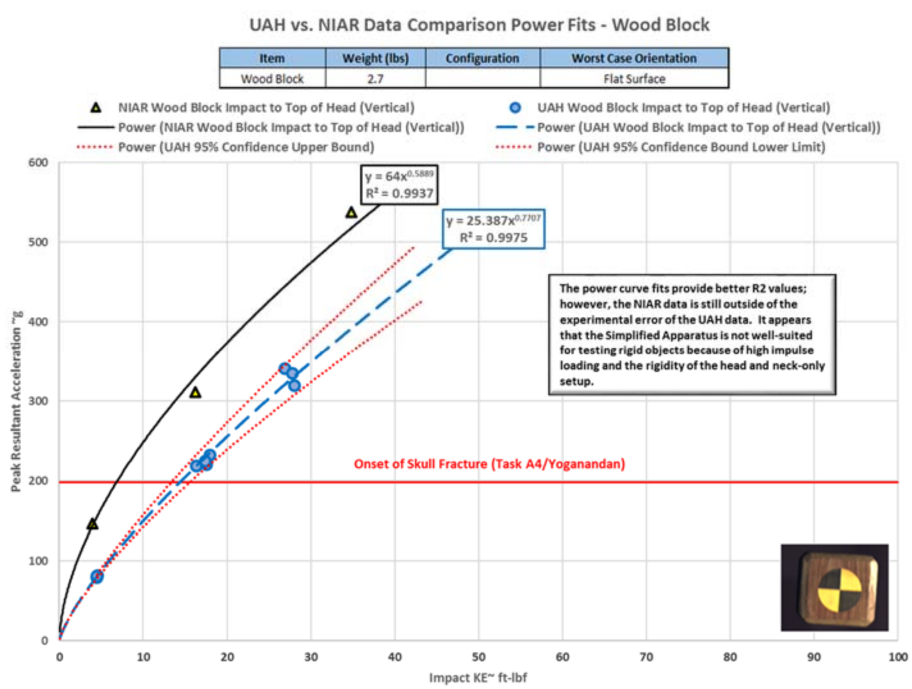

Figure P 2. UAH vs. NIAR Data Comparison Power Fits - Wood Block

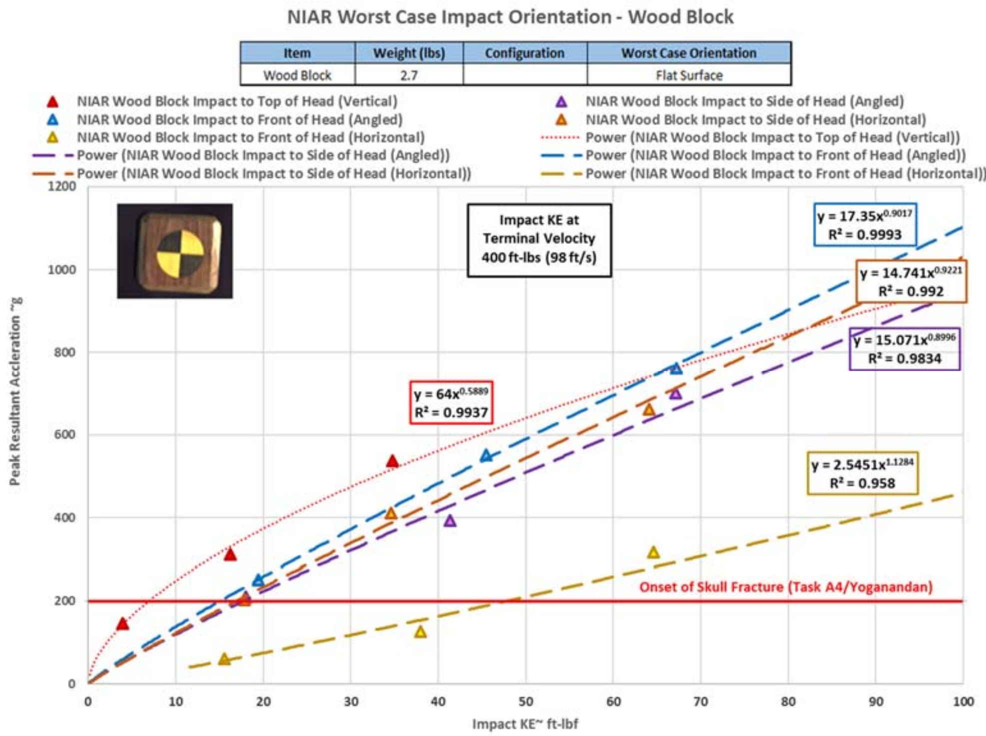

Figure P 3. NIAR Worst Case Impact Evaluation - Wood Block

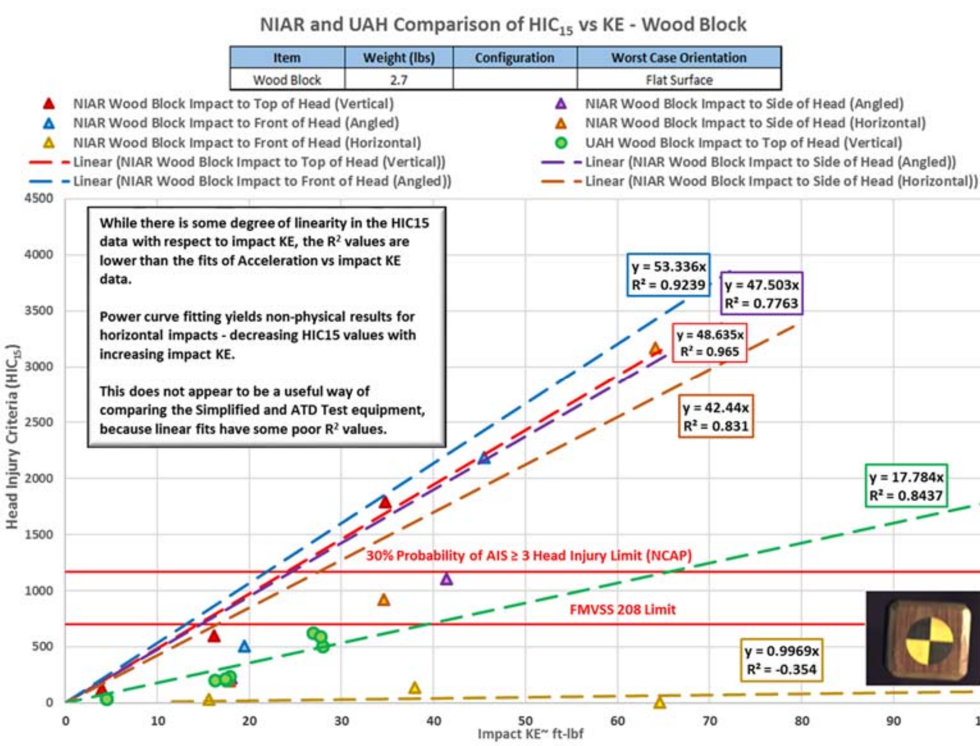

Figure P 4. NIAR and UAH Comparison of HIC_{15} vs KE - Wood Block

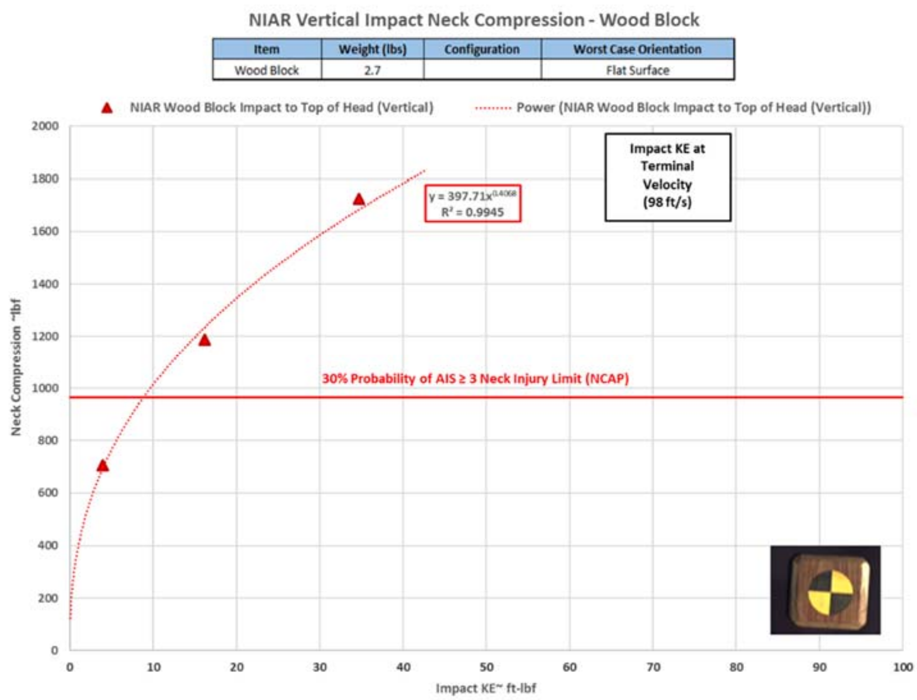

Figure P 5. NIAR Vertical Impact Neck Compression - Wood Block

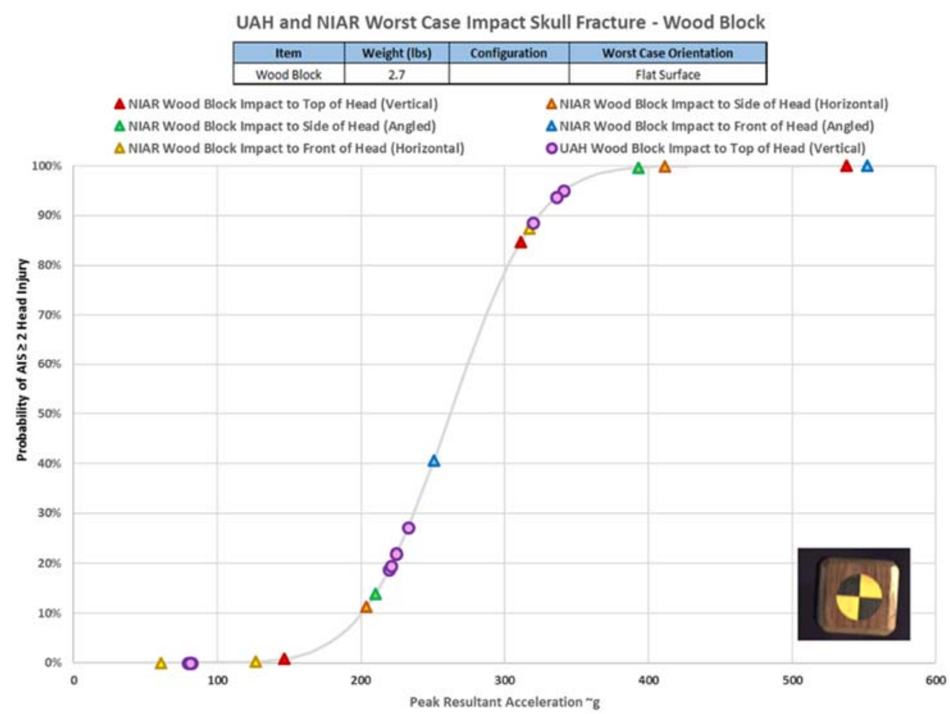

Figure P 6. UAH and NIAR Worst Case Impact Skull Fracture - Wood Block

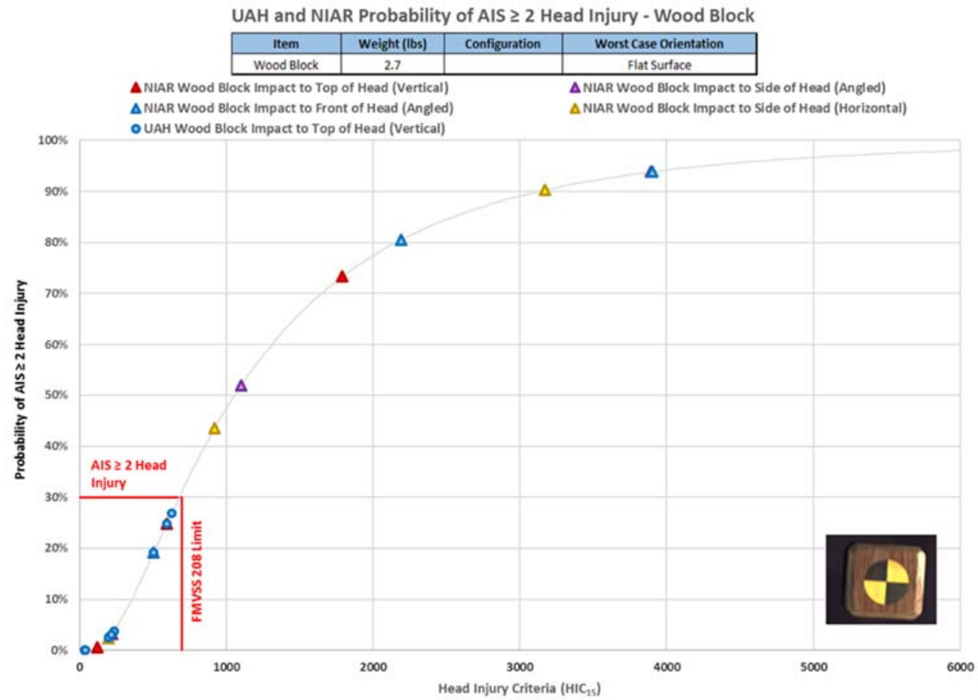

Figure P 7. UAH and NIAR Probability of AIS ≥ 2 Head Injury - Wood Block

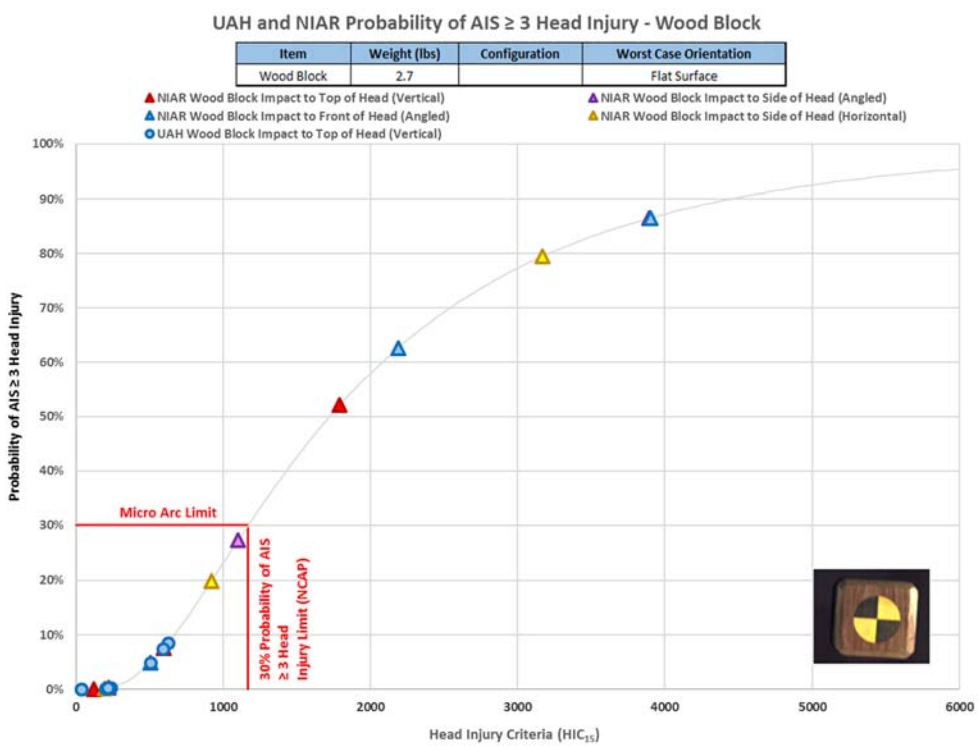

Figure P 8. UAH and NIAR Probability of AIS ≥ 3 Head Injury - Wood Block

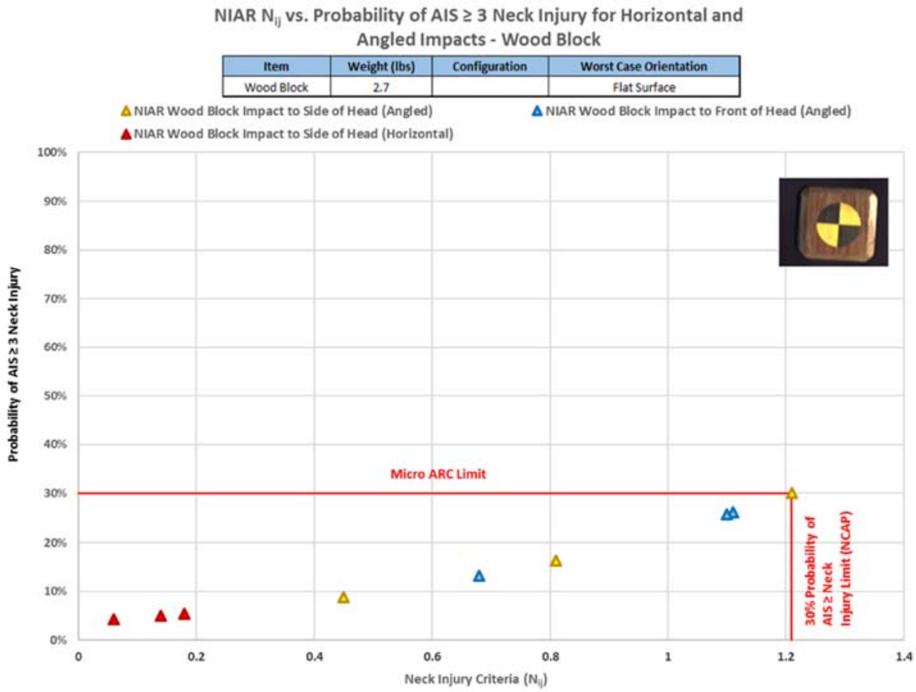

Figure P 9. NIAR N_{ij} vs. Probability of AIS ≥ 3 Neck Injury for Horizontal and Angled Impacts – Wood Block

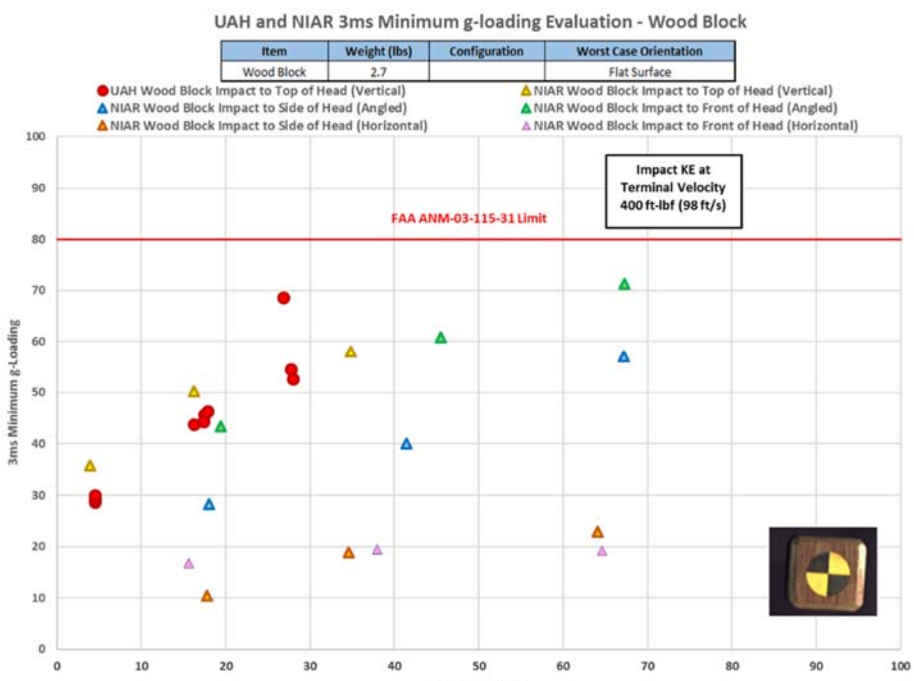

Figure P 10. UAH and NIAR 3ms Minimum g-loading Evaluation - Wood Block

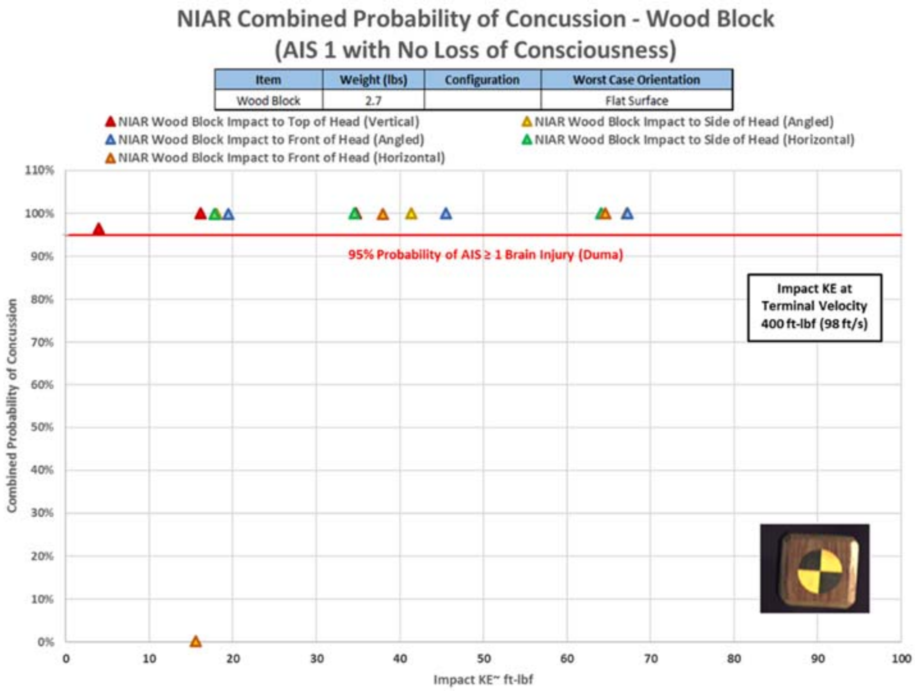

Figure P 11. NIAR Combined Probability of Concussion - Wood Block (AIS 1 with No Loss of Consciousness)

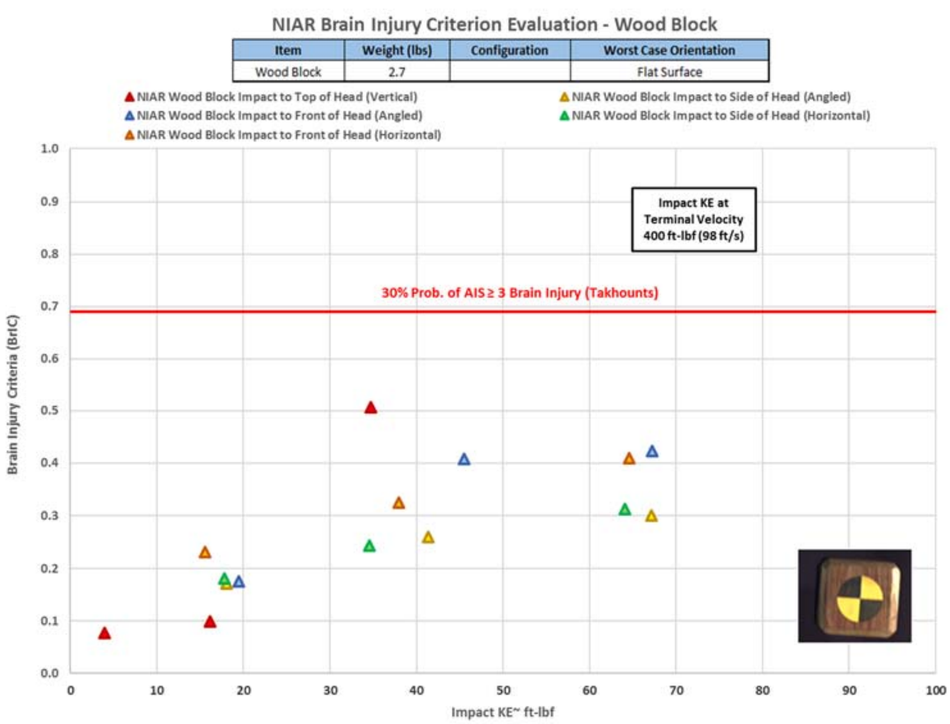

Figure P 12. NIAR Brain Injury Criterion Evaluation - Wood Block

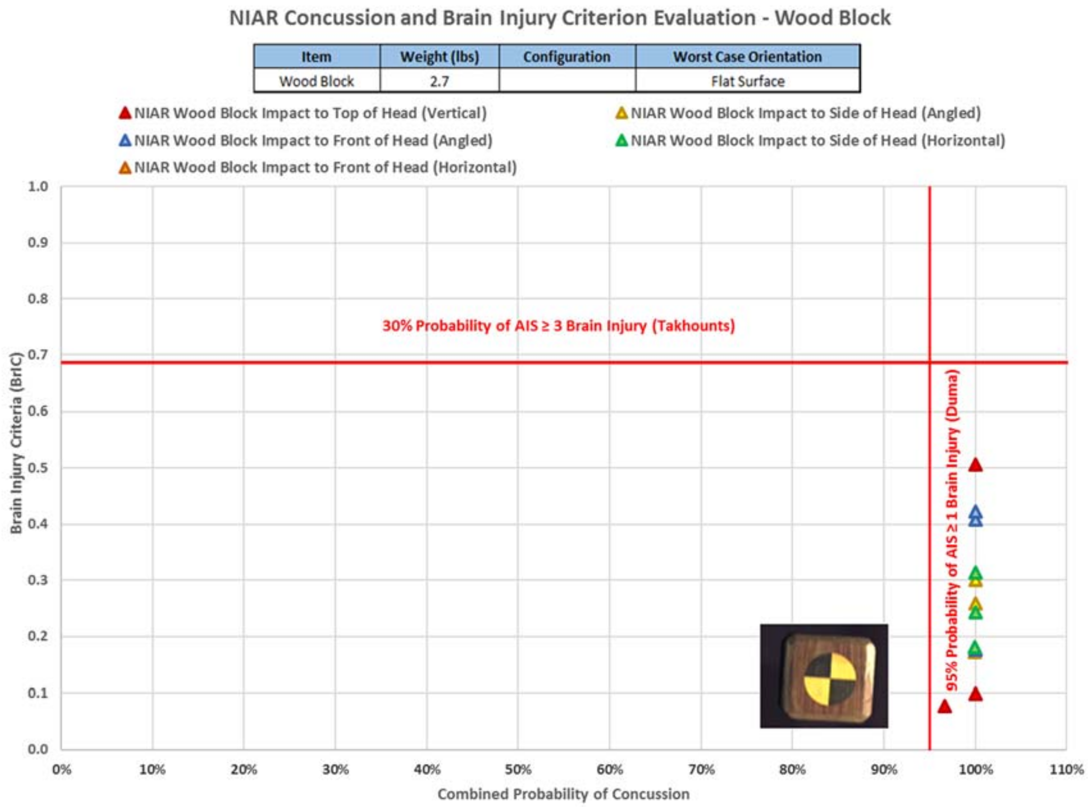

Figure P 13. NIAR Concussion and Brain Injury Criterion Evaluation - Wood Block

APPENDIX Q – STEEL CORE FOAM BLOCK SIMPLIFIED AND ATD TEST DATA

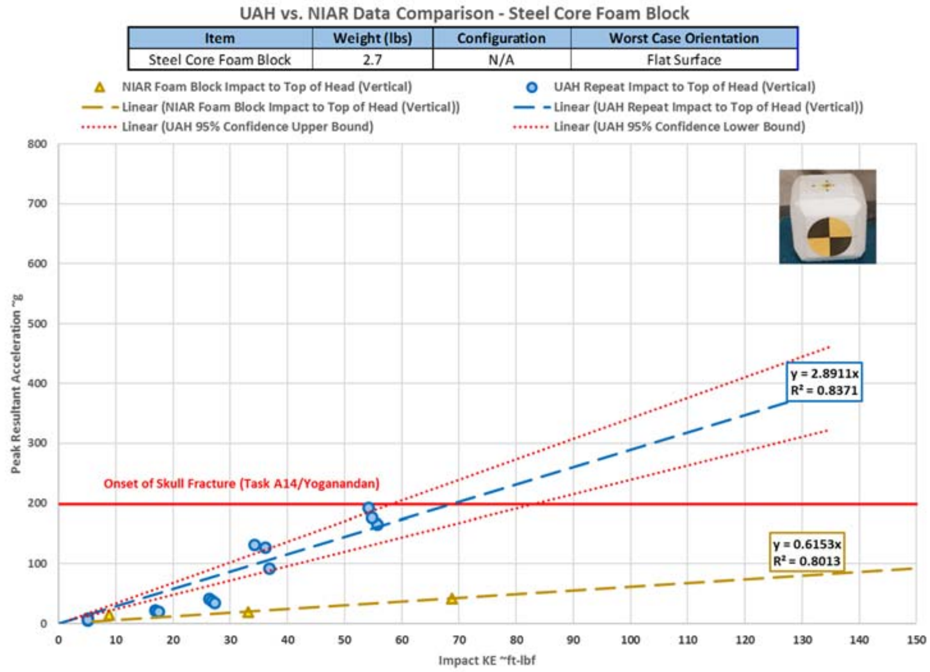

Figure Q 1. UAH vs. NIAR Data Comparison - Steel Core Foam Block

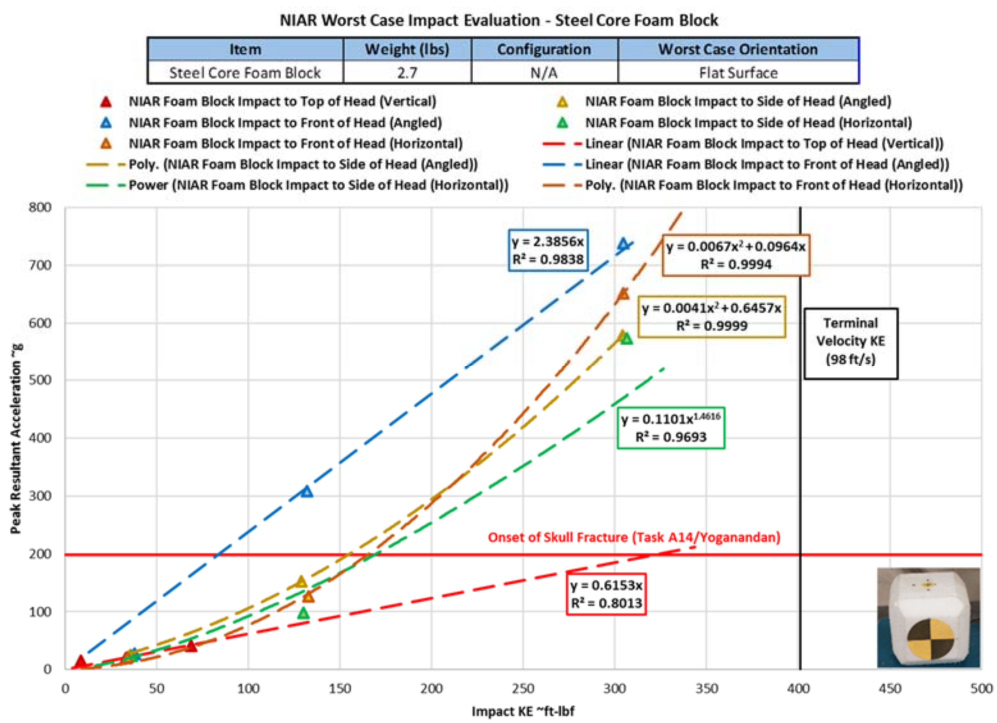

Figure Q 2. NIAR Worst Case Impact Evaluation - Steel Core Foam Block

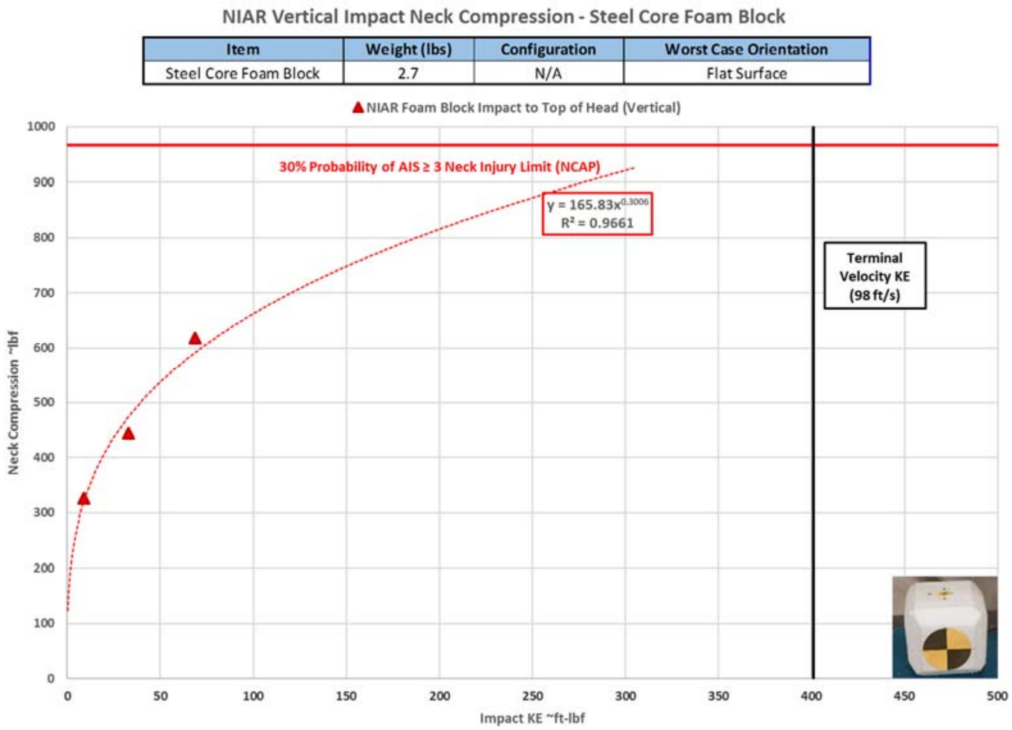

Figure Q 3. NIAR Vertical Impact Neck Compression - Steel Core Foam Block

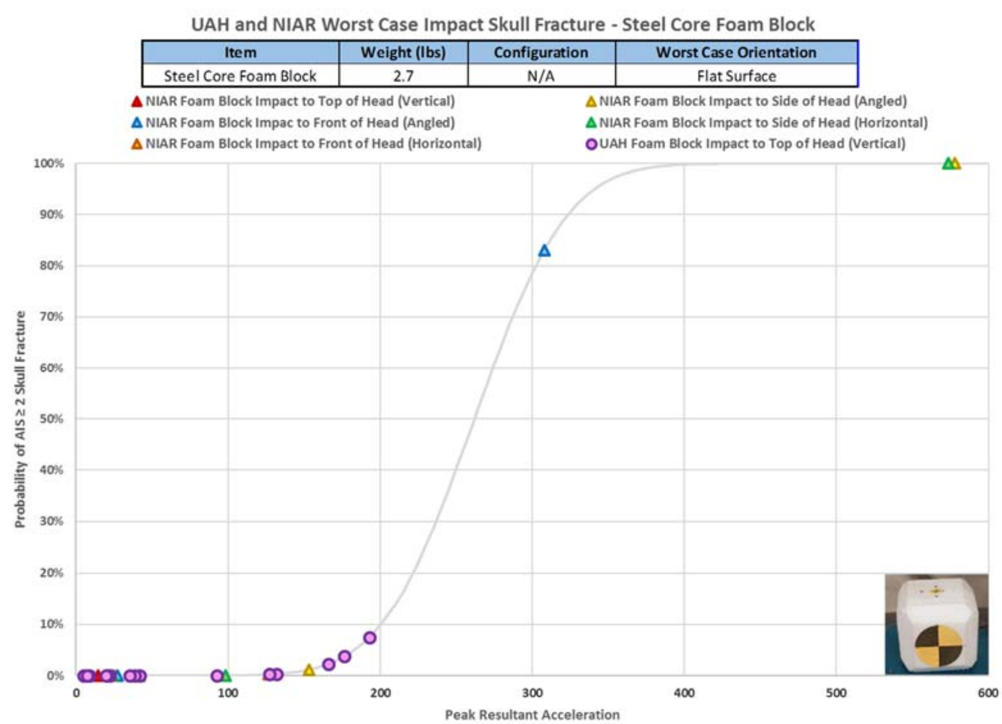

Figure Q 4. UAH and NIAR Worst Case Impact Skull Fracture - Steel Core Foam Block

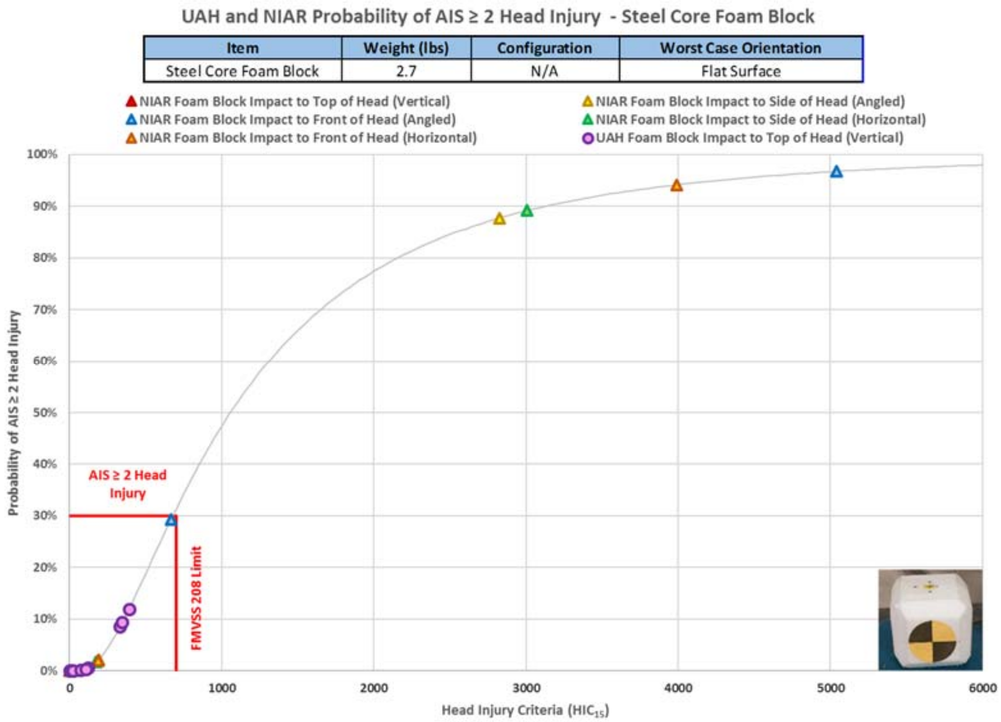

Figure Q 5. UAH and NIAR Probability of AIS ≥ 2 Head Injury - Steel Core Foam Block

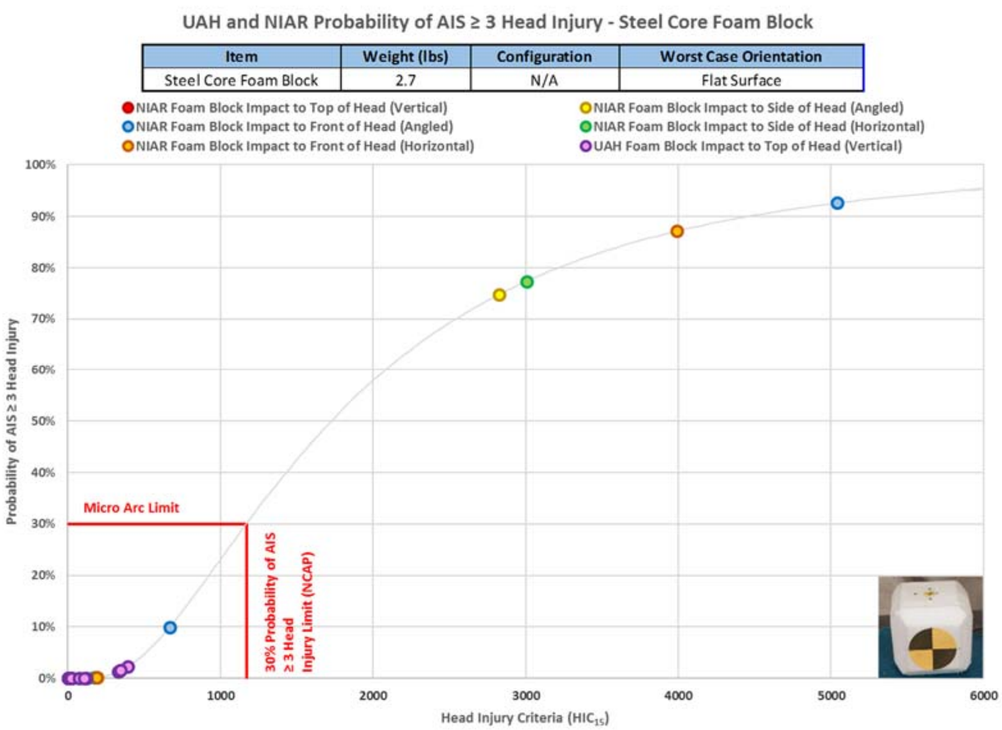

Figure Q 6. UAH and NIAR Probability of AIS ≥ 3 Head Injury - Steel Core Foam Block

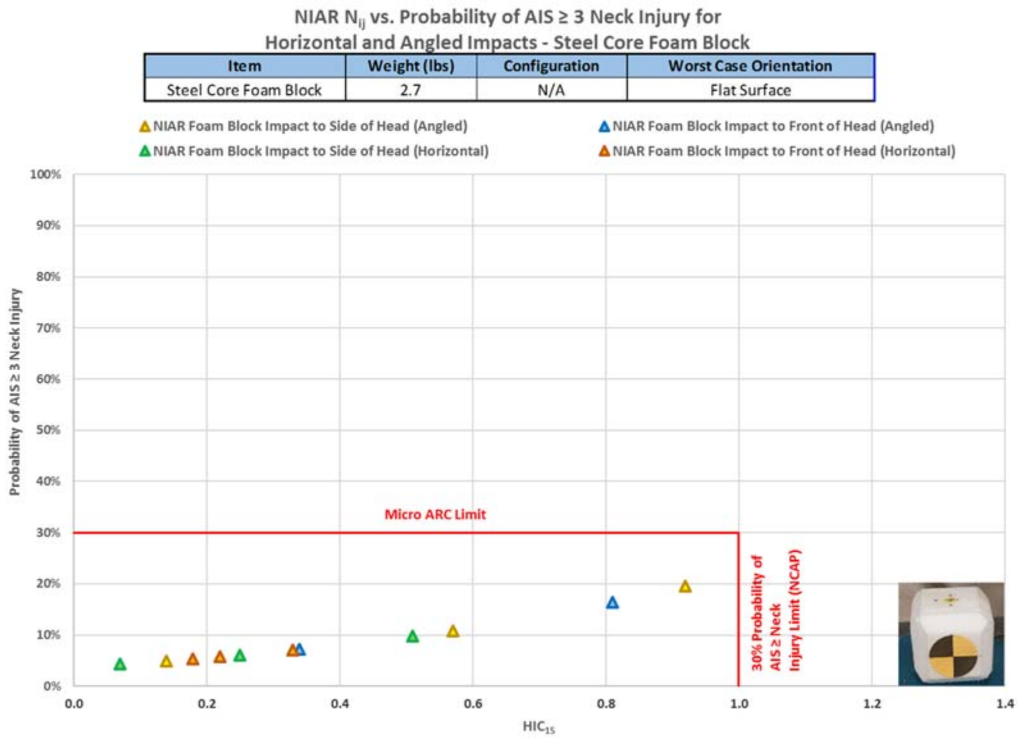

Figure Q 7. NIAR N_{ij} vs. Probability of AIS ≥ 3 Neck Injury for Horizontal and Angled Impact – Steel Core Foam Block

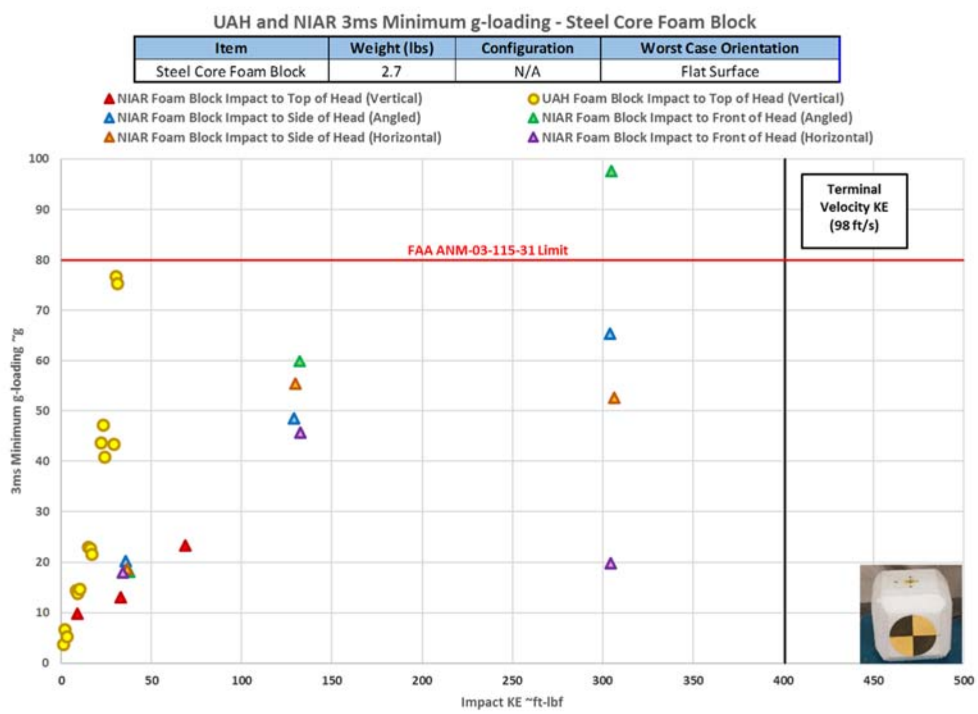

Figure Q 8. UAH and NIAR 3ms Minimum g-loading - Steel Core Foam Block

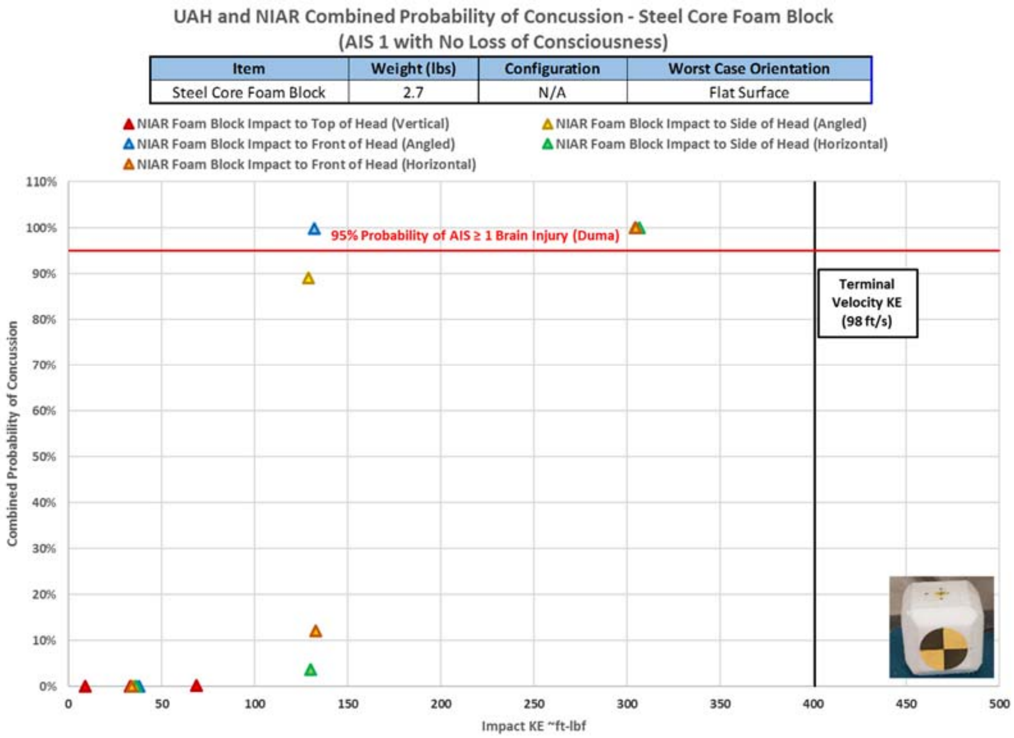

Figure Q 9. NIAR Combined Probability of Concussion - Steel Core Foam Block (AIS 1 with No Loss of Consciousness)

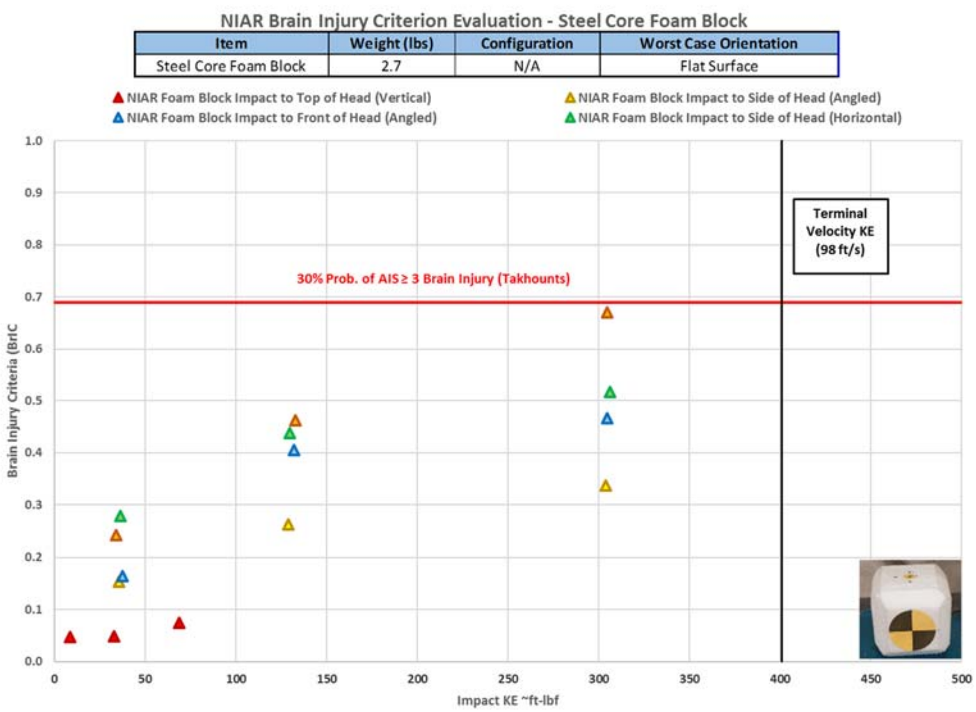

Figure Q 10. NIAR Brain Injury Criterion Evaluation - Steel Core Foam Block

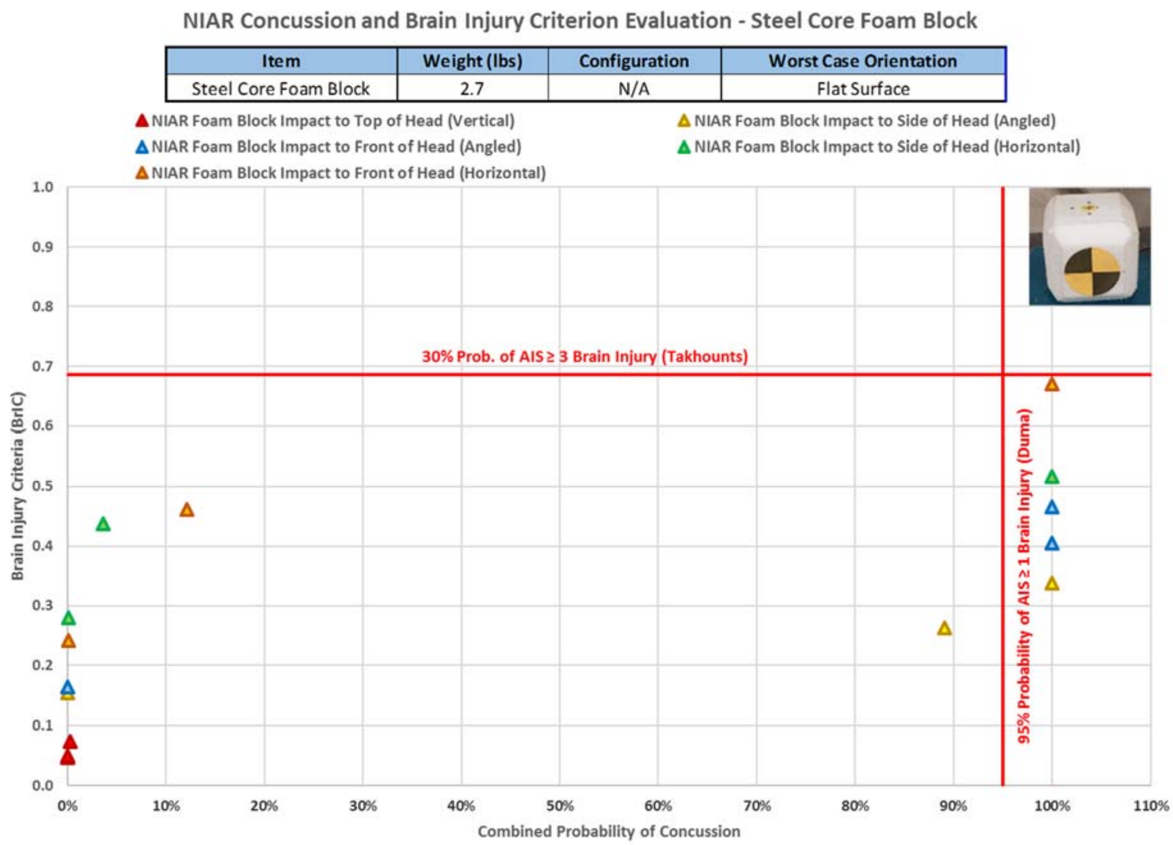

Figure Q 11. NIAR Concussion and Brain Injury Criterion Evaluation - Steel Core Foam Block

APPENDIX R – ALUMINUM CORE FOAM BLOCK SIMPLIFIED TEST DATA

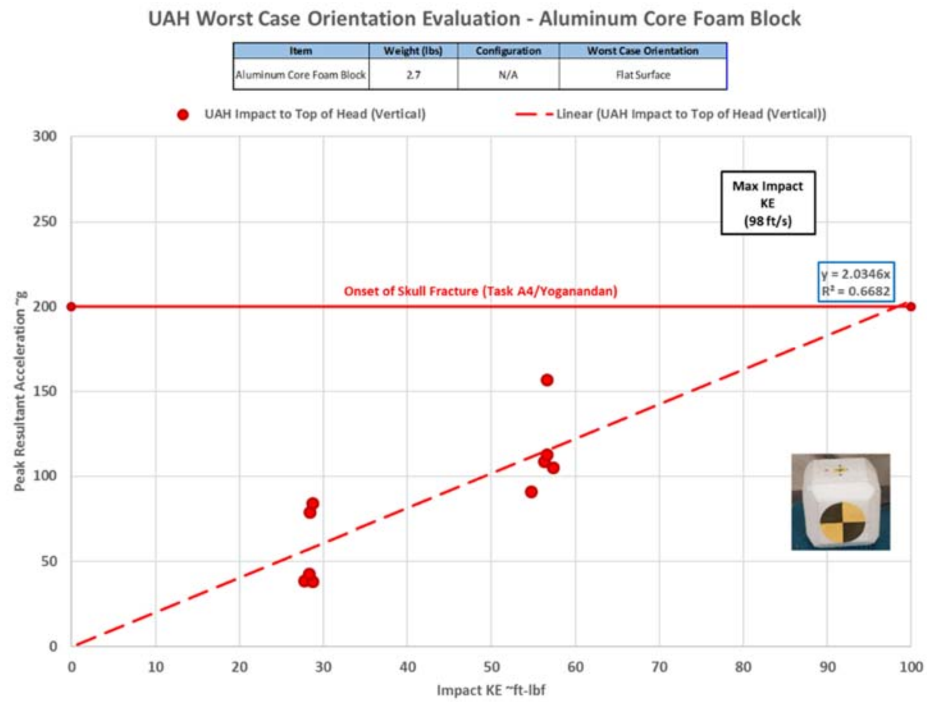

Figure R 1. UAH Worst Case Orientation Evaluation - Aluminum Core Foam Block

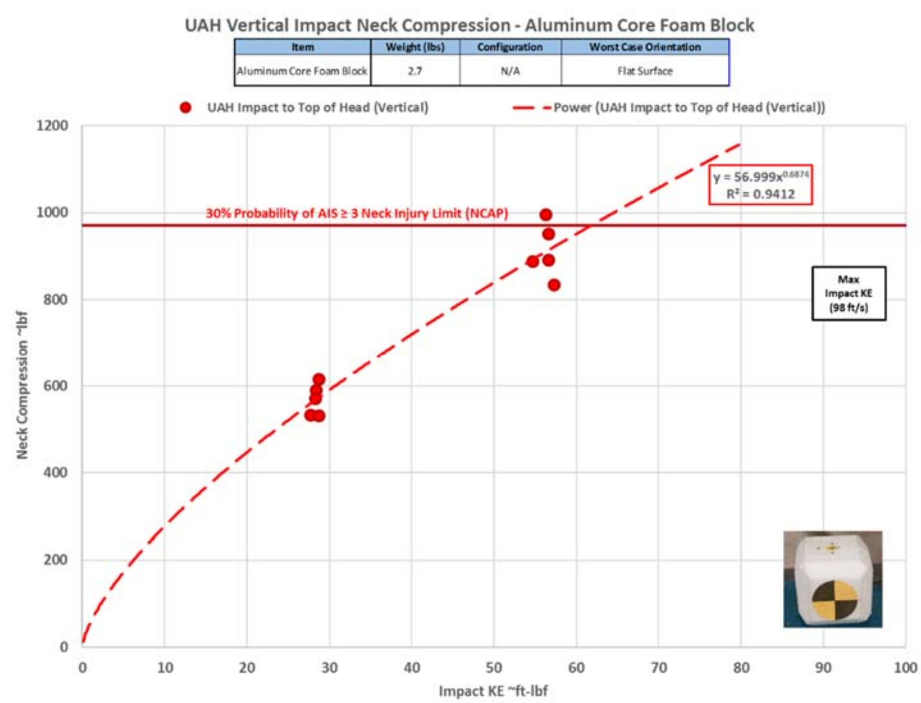

Figure R 2. UAH Vertical Impact Neck Compression - Aluminum Core Foam Block

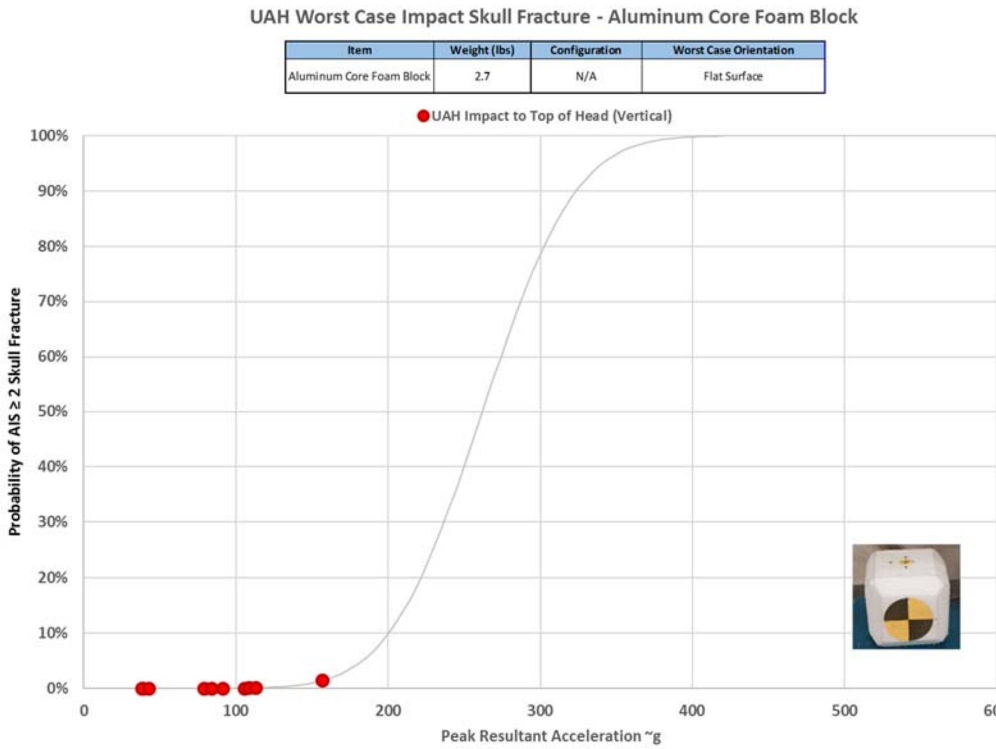

Figure R 3. UAH Worst Case Impact Skull Fracture - Aluminum Core Foam Block

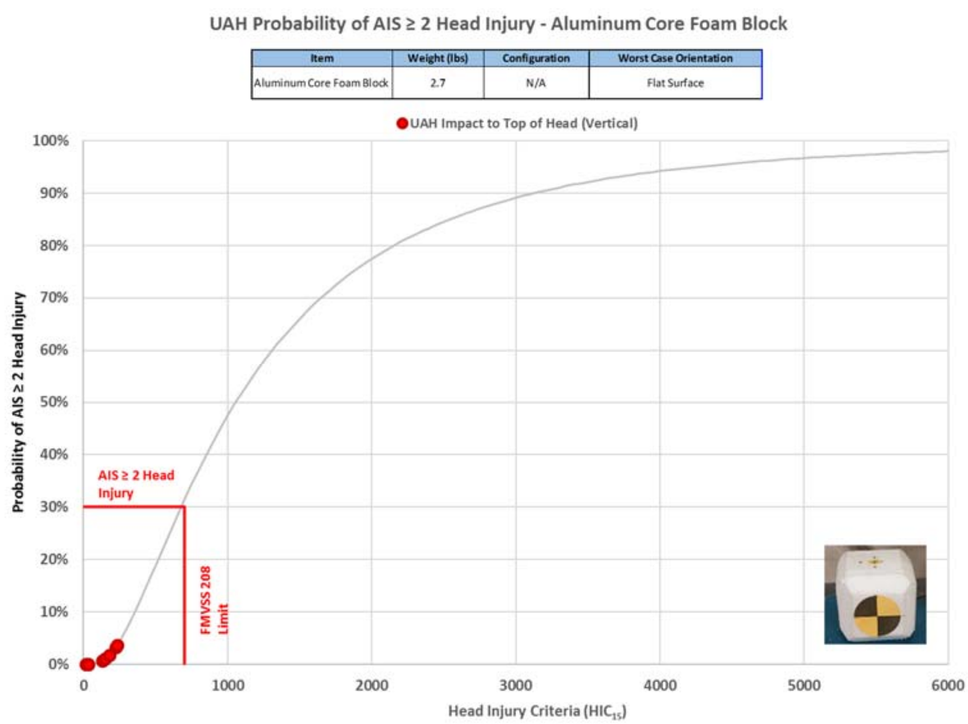

Figure R 4. UAH Probability of AIS ≥ 2 Head Injury - Aluminum Core Foam Block\

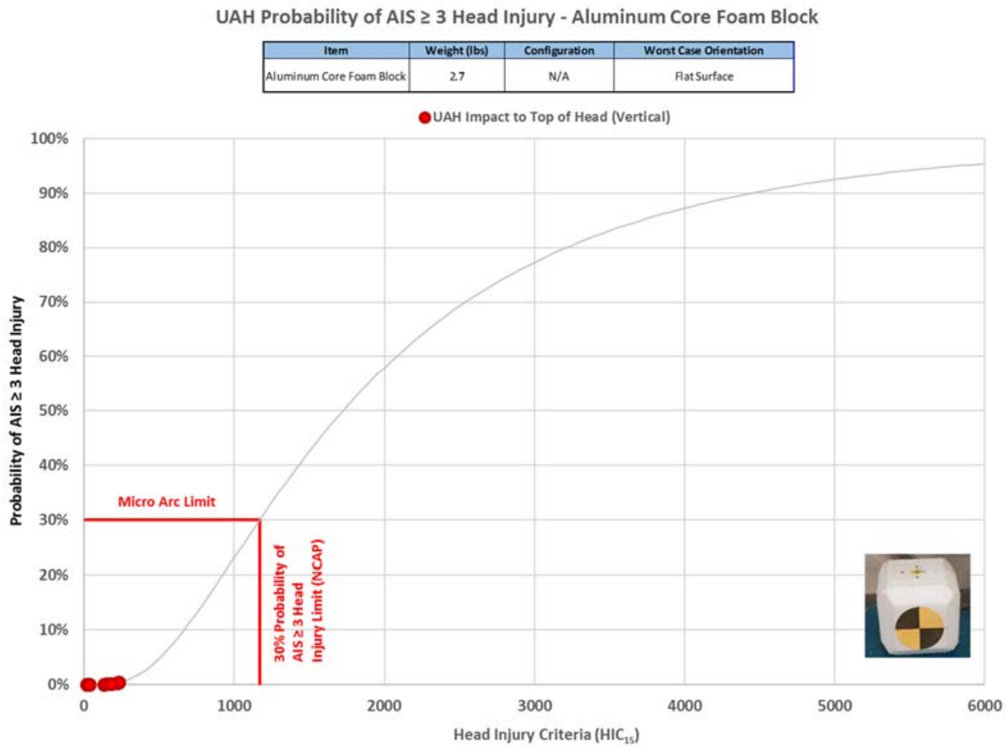

Figure R 5. UAH Probability of AIS ≥ 3 Head Injury - Aluminum Core Foam Block

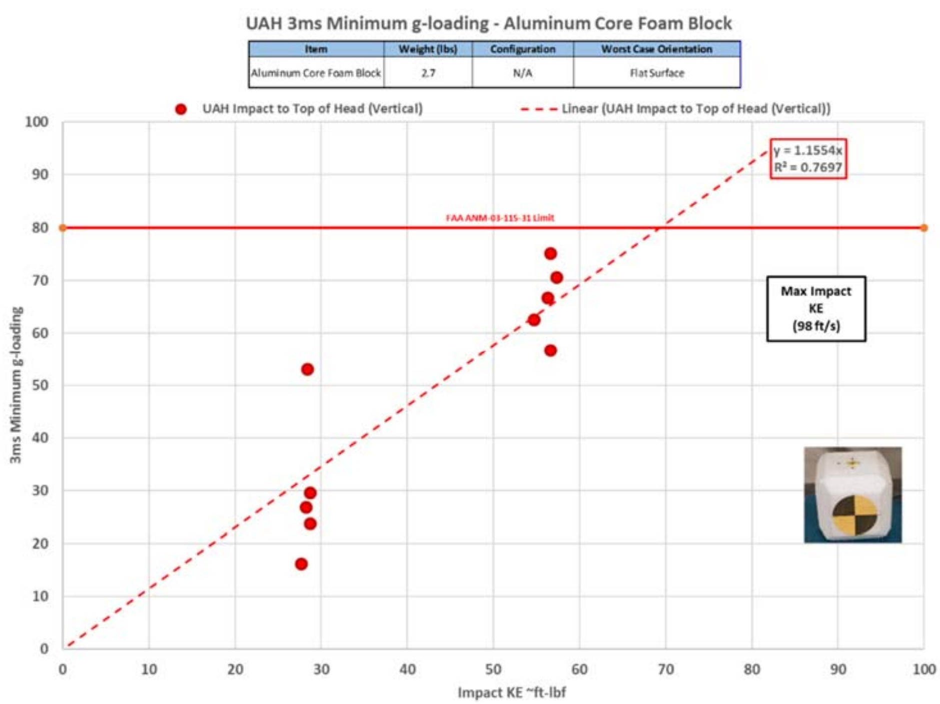

Figure R 6. UAH 3ms Minimum g-loading - Aluminum Core Foam Block

APPENDIX S – DJI PHANTOM 3 BATTERY ATD AND SIMPLIFIED TEST DATA

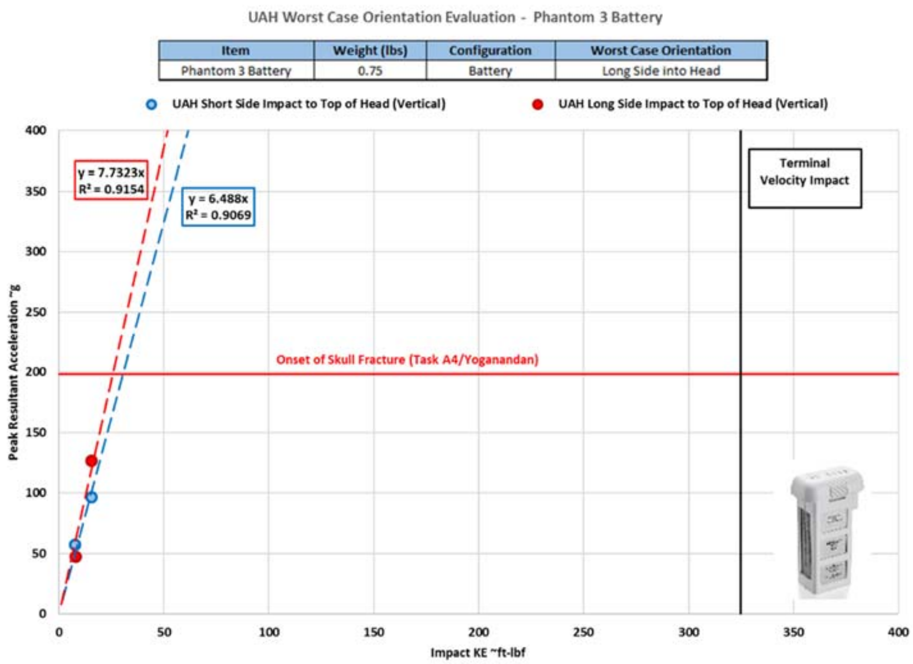

Figure S 1. UAH Worst Case Orientation Evaluation - DJI Phantom 3 Battery

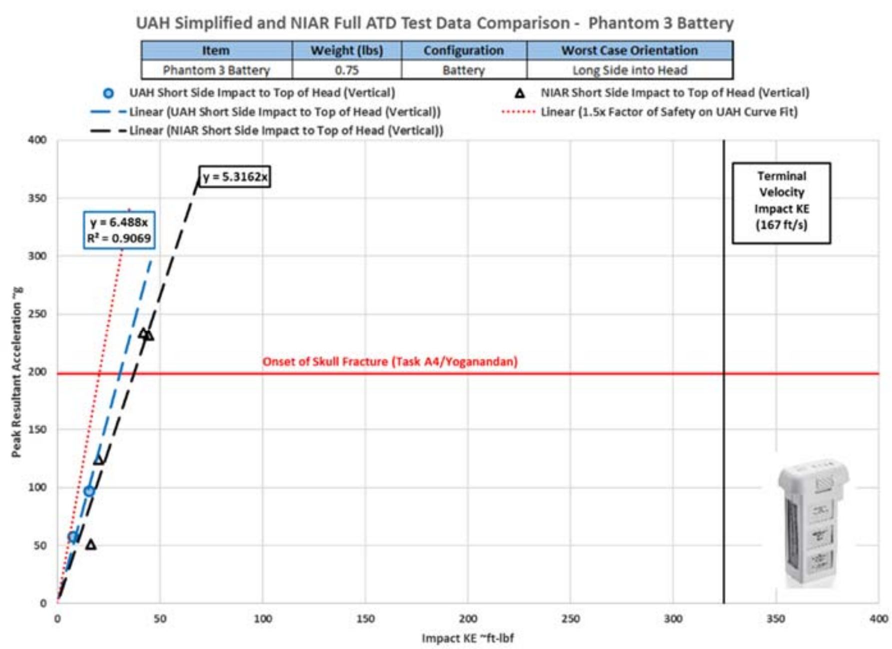

Figure S 2. UAH and NIAR Test Data Comparison - DJI Phantom 3 Battery

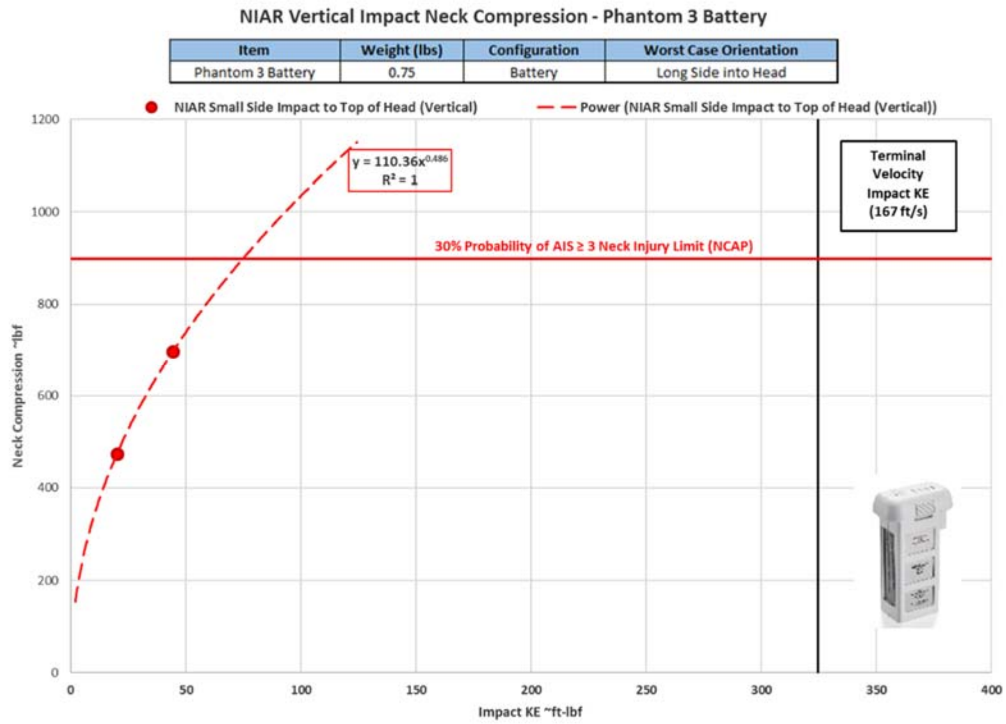

Figure S 3. NIAR Vertical Impact Neck Compression - DJI Phantom 3 Battery

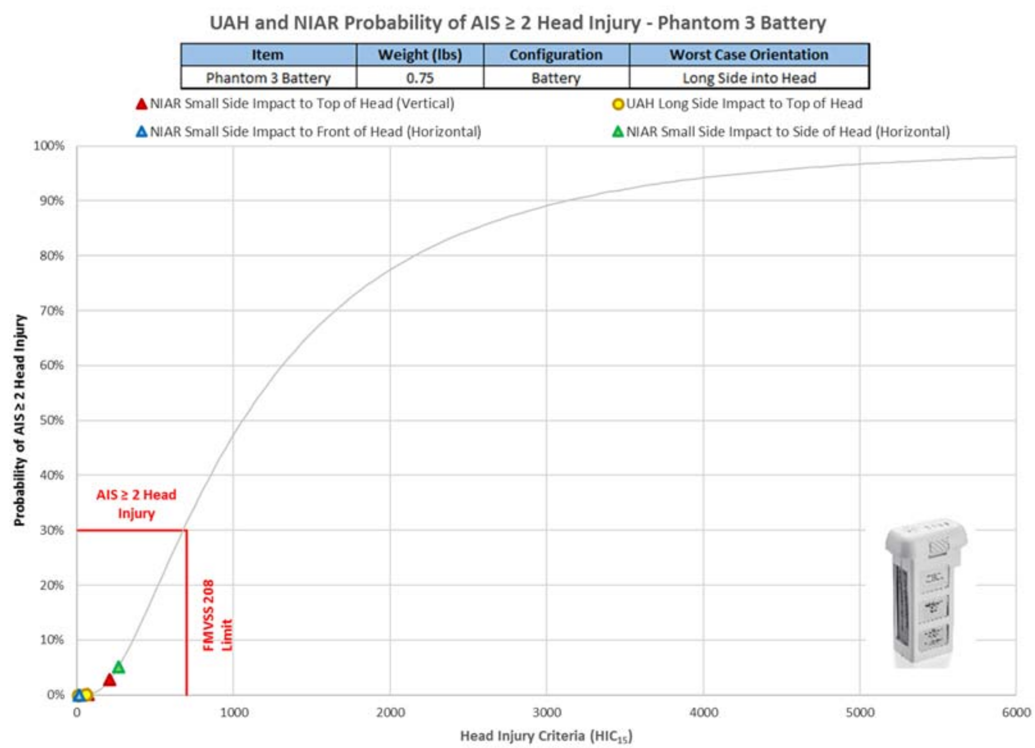

Figure S 4. UAH and NIAR Worst Case Impact Skull Fracture - DJI Phantom 3 Battery

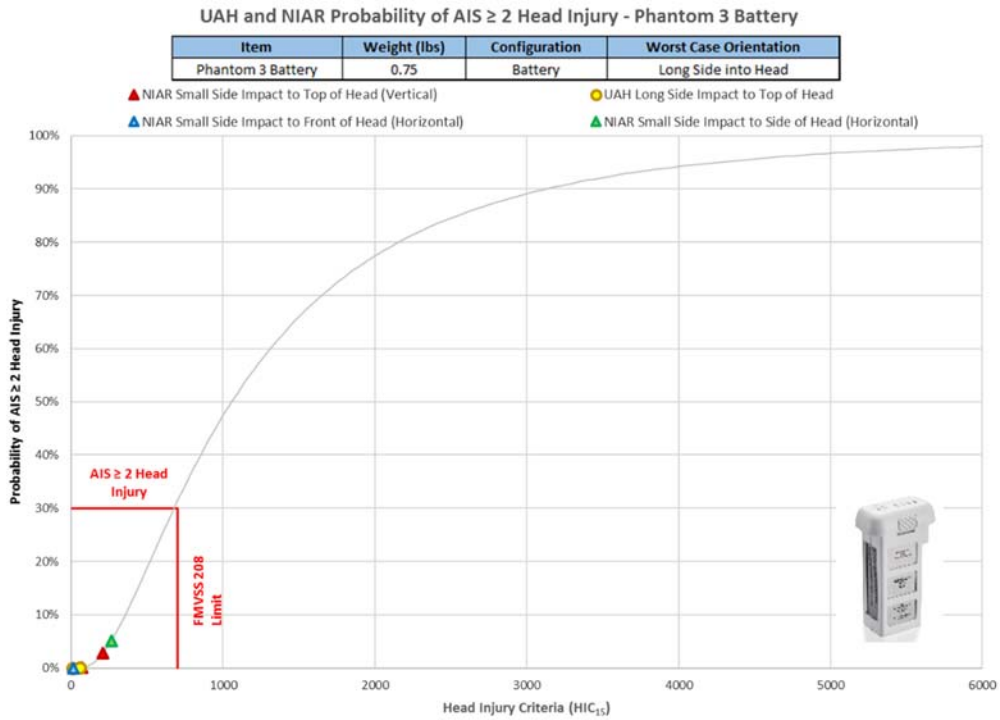

Figure S 5. UAH and NIAR Probability of AIS ≥ 2 Head Injury - DJI Phantom 3 Battery

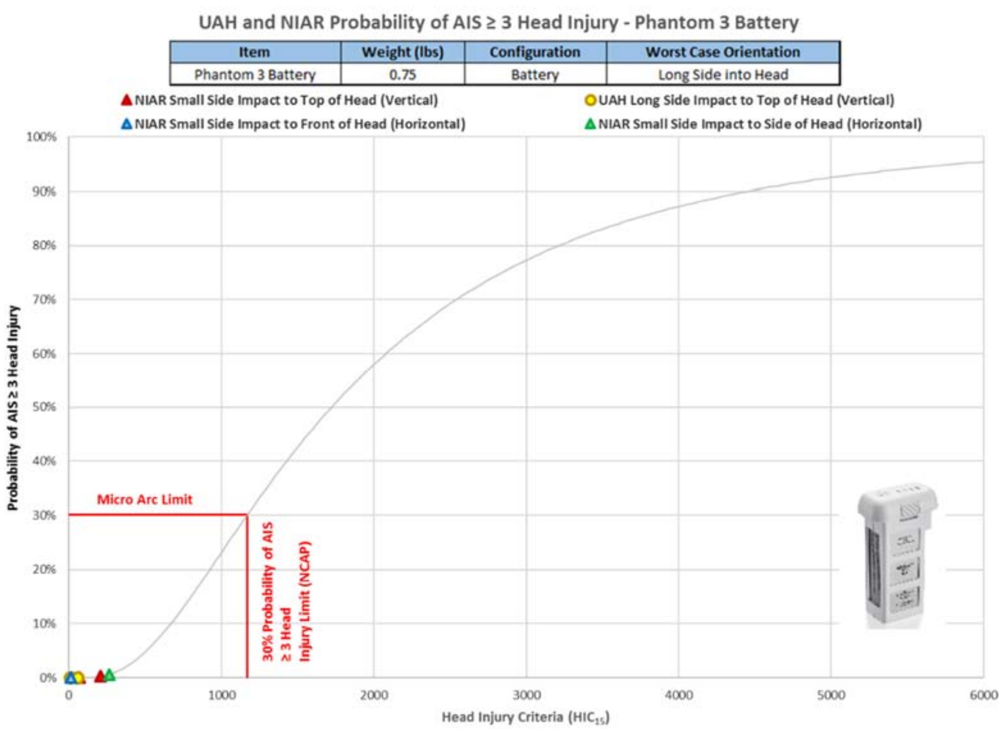

Figure S 6. UAH and NIAR Probability of AIS ≥ 3 Head Injury - DJI Phantom 3 Battery

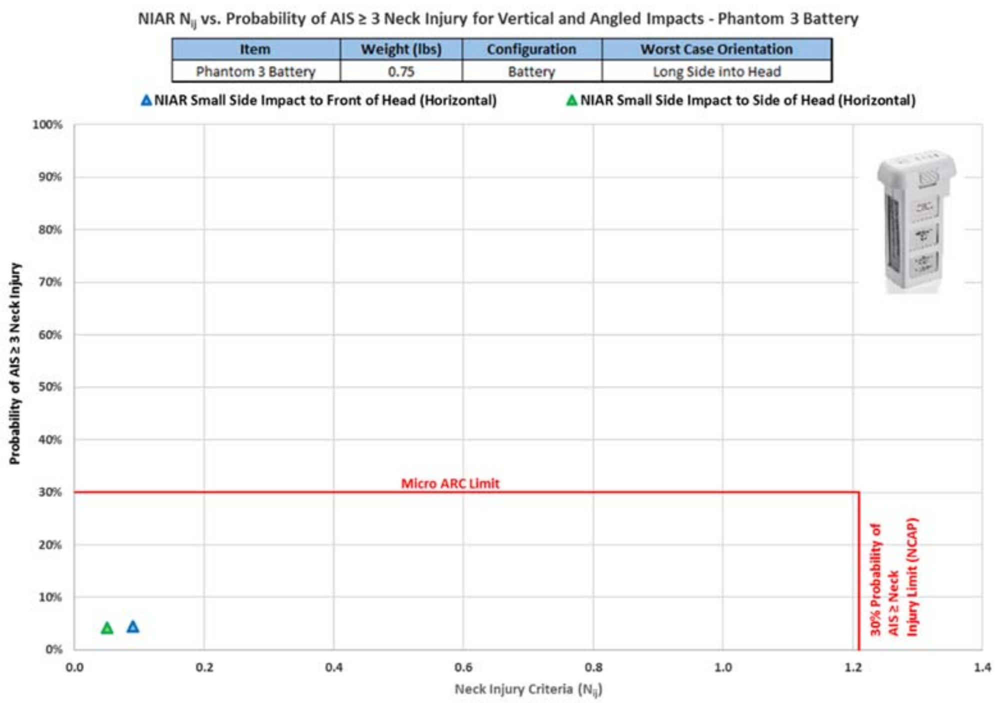

Figure S 7. NIAR N_{ij} vs. Probability of AIS ≥ 3 Neck Injury for Vertical and Angled Impacts - DJI Phantom 3 Battery

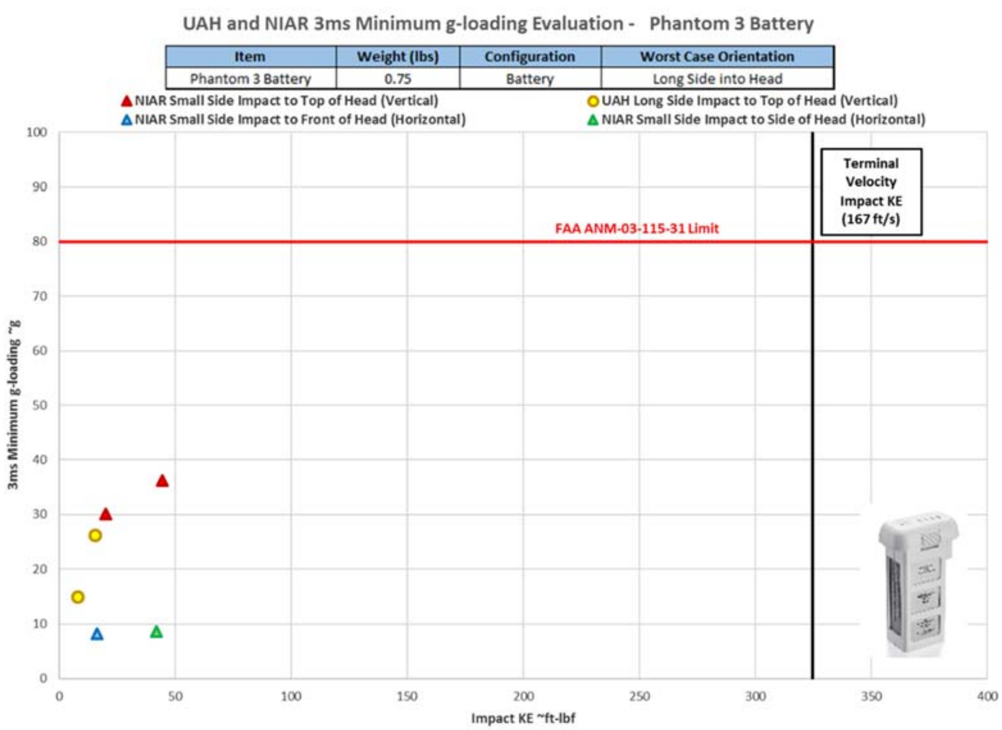

Figure S 8. UAH and NIAR 3ms Minimum g-loading Evaluation - DJI Phantom 3 Battery

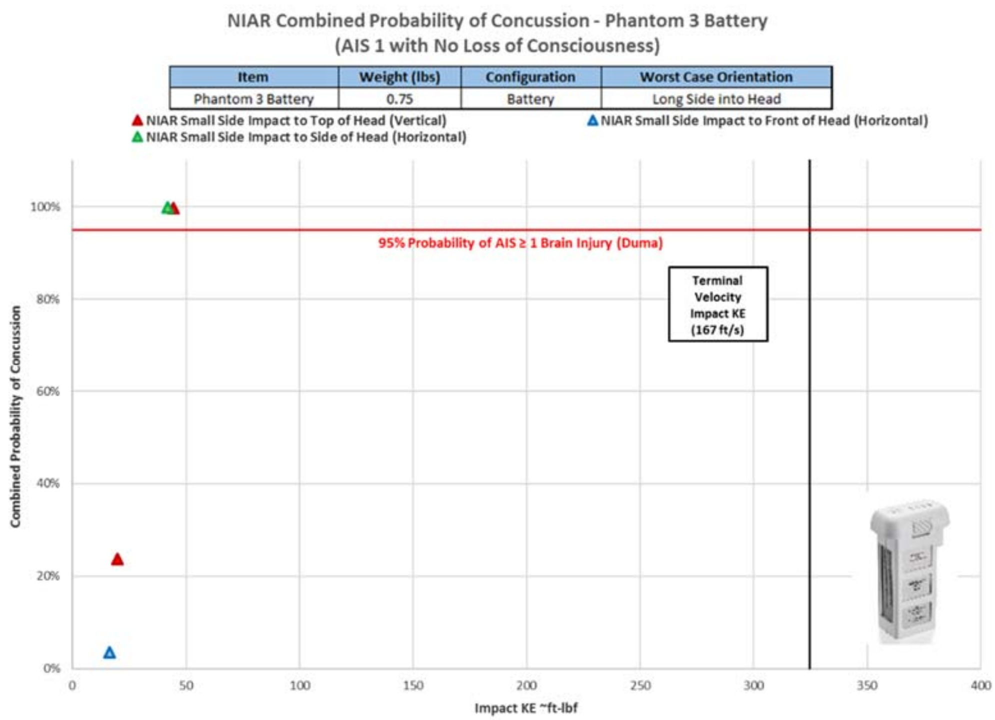

Figure S 9. NIAR Combined Probability of Concussion - DJI Phantom 3 Battery (AIS 1 with No Loss of Consciousness)

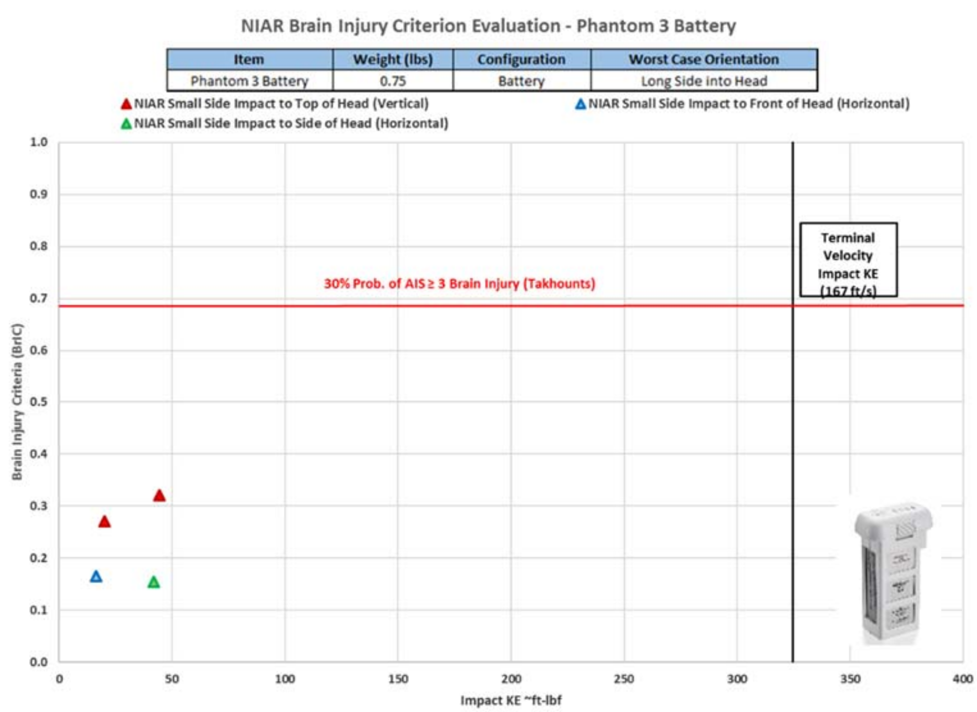

Figure S 10. NIAR Brain Injury Criterion Evaluation - DJI Phantom 3 Battery

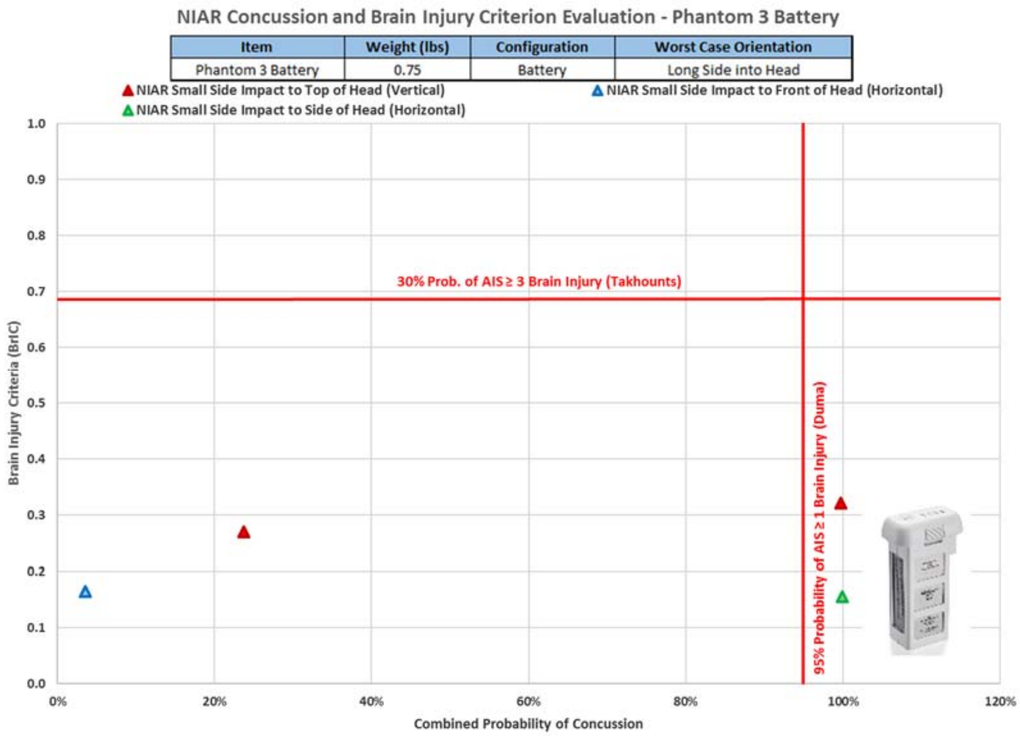

Figure S 11. NIAR Concussion and Brain Injury Criterion Evaluation - DJI Phantom 3 Battery

APPENDIX T – SLR CAMERA SIMPLIFIED TEST DATA

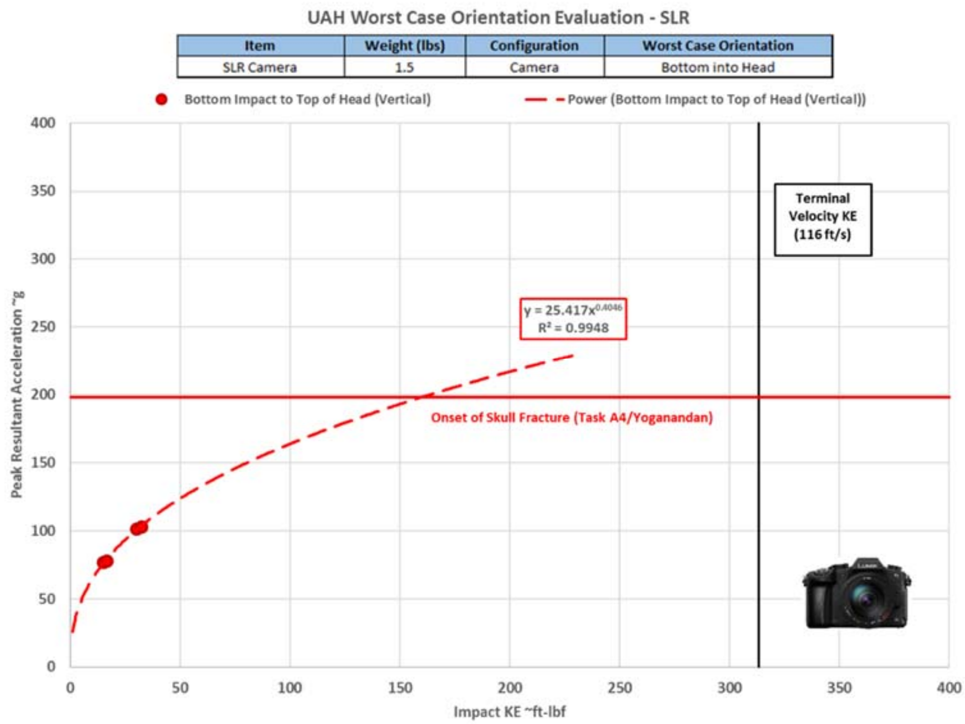

Figure T 1. UAH Worst Case Orientation Evaluation - SLR

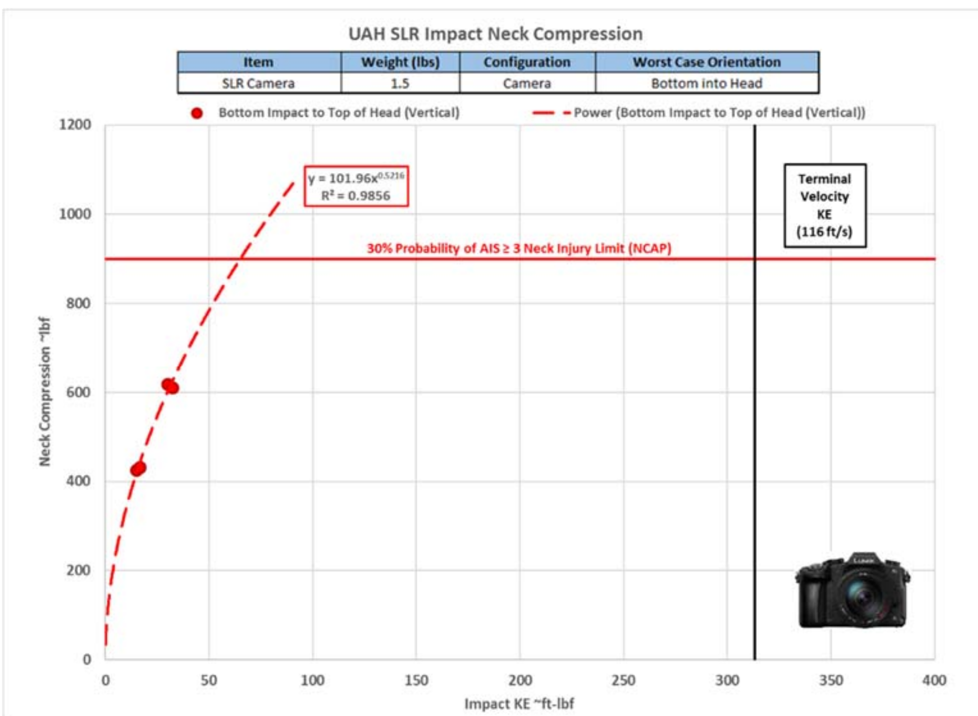

Figure T 2. UAH Vertical Impact Neck Compression – SLR Camera

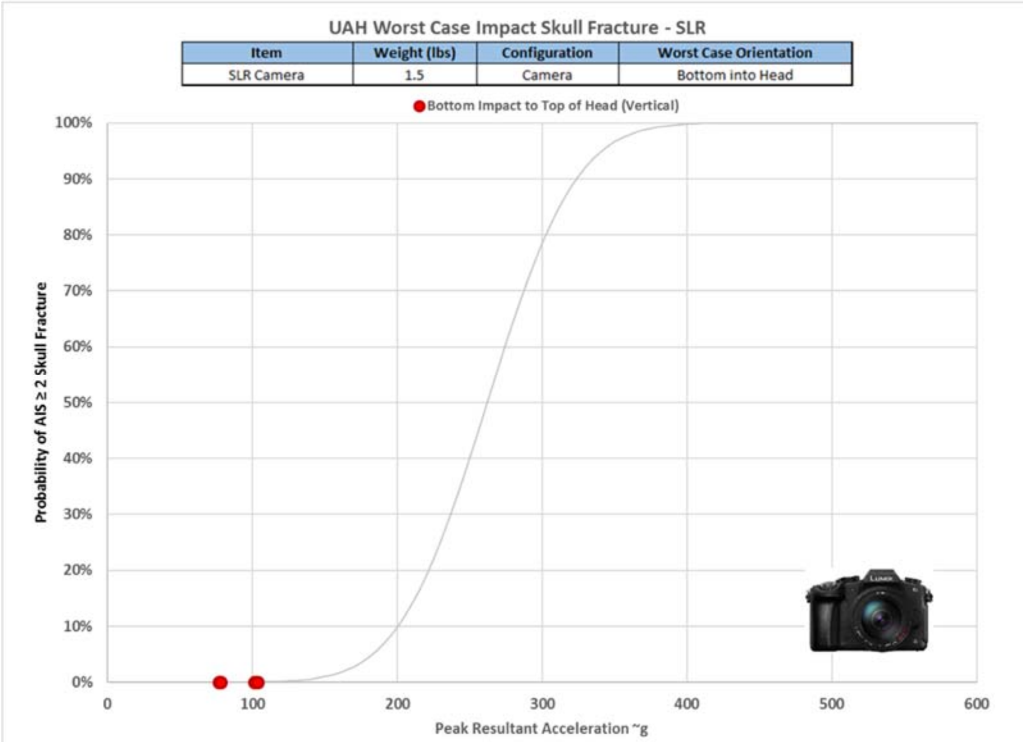

Figure T 3. UAH Worst Case Impact Skull Fracture – SLR Camera

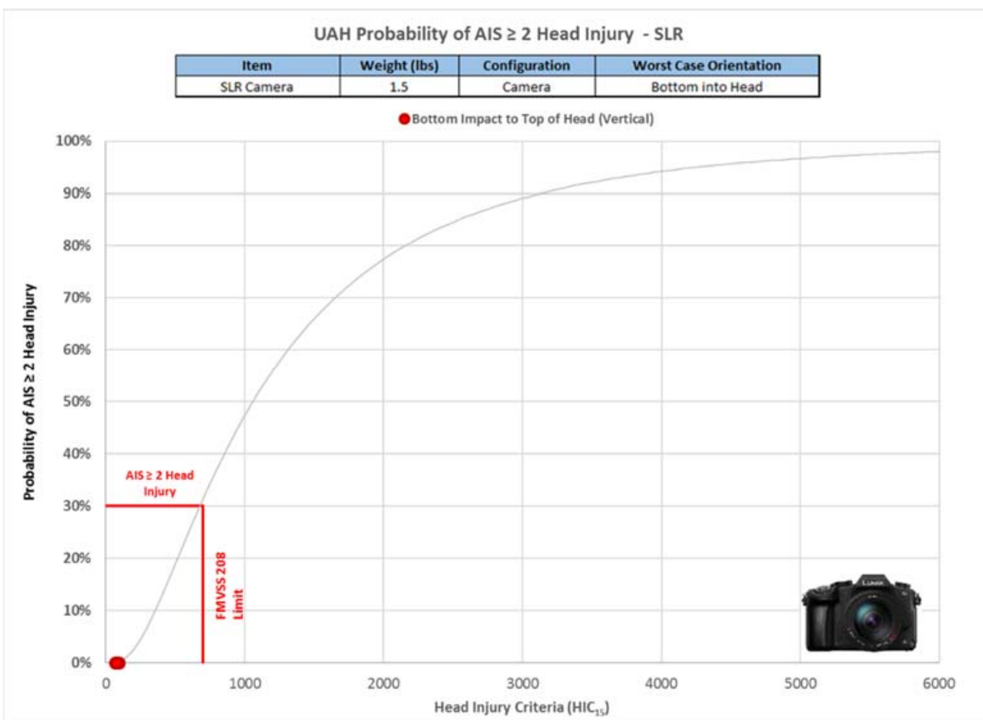

Figure T 4. UAH Probability of AIS ≥ 2 Head Injury - SLR Camera

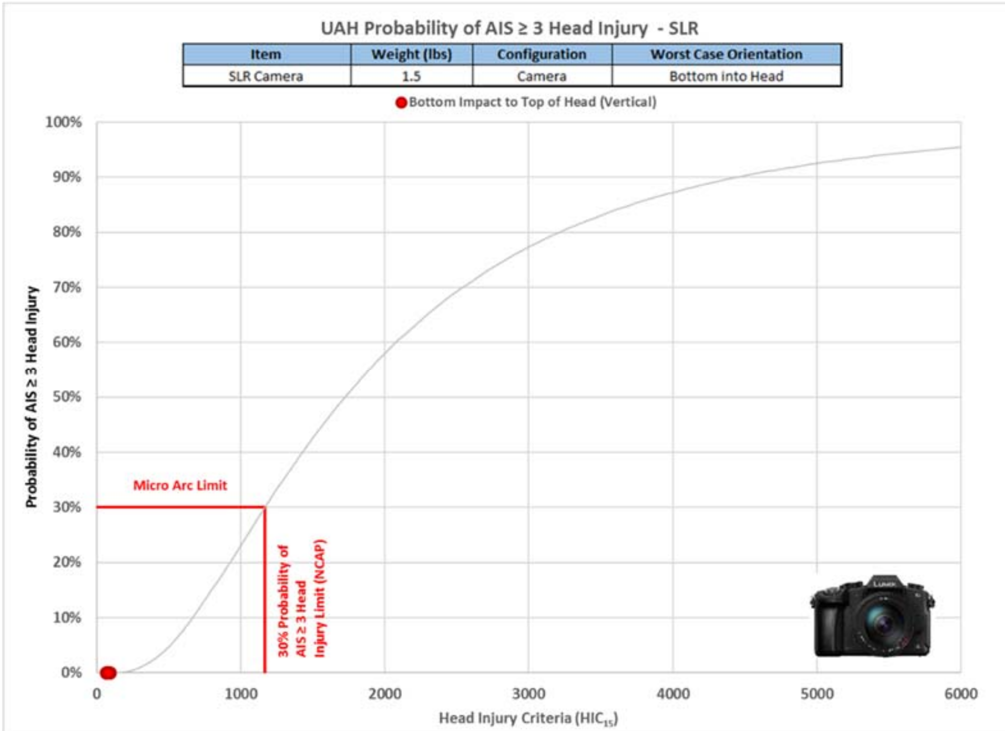

Figure T 5. UAH Probability of AIS ≥ 3 Head Injury - SLR Camera

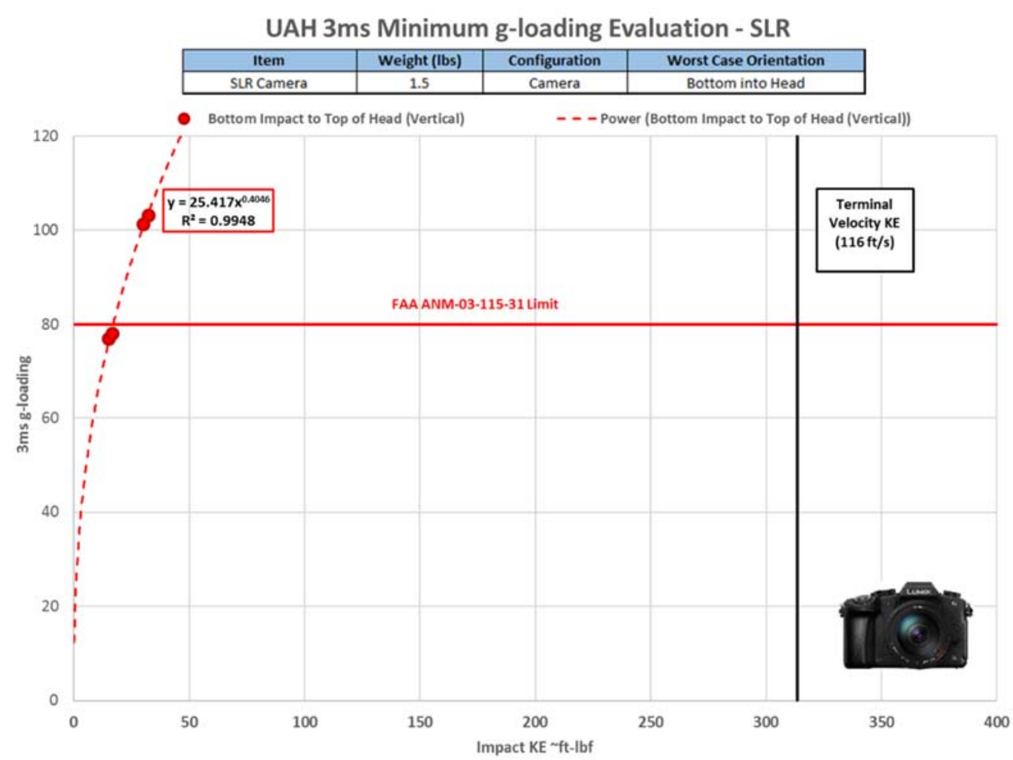

Figure T 6. UAH 3ms Minimum g-loading Evaluation – SLR Camera